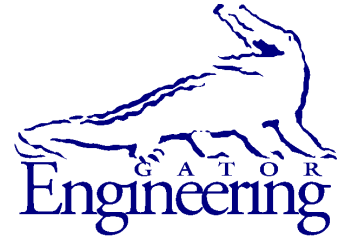




University of Florida
Civil and Coastal Engineering



University of Florida
Civil and Coastal Engineering

Final Report

March 2013

END REGION DETAILING OF PRETENSIONED CONCRETE BRIDGE GIRDERS

Principal investigator:
H. R. Hamilton

Co-Principal investigator:
Gary R. Consolazio

Research assistant:
Brandon E. Ross

Department of Civil and Coastal Engineering
University of Florida
P.O. Box 116580
Gainesville, Florida 32611

Sponsor:
Florida Department of Transportation (FDOT)
Sam Fallaha, P.E. – Project Manager

Contract:
UF Project No. 00072910 & 00074016
FDOT Contract No. BDK75 977-05

DISCLAIMER

The opinions, findings, and conclusions expressed in this publication are those of the authors and not necessarily those of the State of Florida Department of Transportation.

SI* (MODERN METRIC) CONVERSION FACTORS
APPROXIMATE CONVERSIONS TO SI UNITS

SYMBOL	WHEN YOU KNOW	MULTIPLY BY	TO FIND	SYMBOL
LENGTH				
in	inches	25.4	millimeters	mm
ft	feet	0.305	meters	m
yd	yards	0.914	meters	m
mi	miles	1.61	kilometers	km
AREA				
in²	square inches	645.2	square millimeters	mm ²
ft²	square feet	0.093	square meters	m ²
yd²	square yard	0.836	square meters	m ²
ac	acres	0.405	hectares	ha
mi²	square miles	2.59	square kilometers	km ²
VOLUME				
fl oz	fluid ounces	29.57	milliliters	mL
gal	gallons	3.785	liters	L
ft³	cubic feet	0.028	cubic meters	m ³
yd³	cubic yards	0.765	cubic meters	m ³
NOTE: volumes greater than 1000 L shall be shown in m ³				
MASS				
oz	ounces	28.35	grams	g
lb	pounds	0.454	kilograms	kg
T	short tons (2000 lb)	0.907	megagrams	Mg (or "t")
TEMPERATURE (exact degrees)				
°F	Fahrenheit	5(F-32)/9 or (F-32)/1.8	Celsius	°C
ILLUMINATION				
fc	foot-candles	10.76	lux	lx
fl	foot-Lamberts	3.426	candela/m ²	cd/m ²
FORCE and PRESSURE or STRESS				
kip	1000 pound force	4.45	kilonewtons	kN
lbf	pound force	4.45	newtons	N
lbf/in²	pound force per square	6.89	kilopascals	kPa

*SI is the symbol for the International System of Units. Appropriate rounding should be made to comply with Section 4 of ASTM E380.

SI* (MODERN METRIC) CONVERSION FACTORS
APPROXIMATE CONVERSIONS FROM SI UNITS

SYMBOL	WHEN YOU KNOW	MULTIPLY BY	TO FIND	SYMBOL
LENGTH				
mm	millimeters	0.039	inches	in
m	meters	3.28	feet	ft
m	meters	1.09	yards	yd
km	kilometers	0.621	miles	mi
AREA				
mm²	square millimeters	0.0016	square inches	in ²
m²	square meters	10.764	square feet	ft ²
m²	square meters	1.195	square yards	yd ²
ha	hectares	2.47	acres	ac
km²	square kilometers	0.386	square miles	mi ²
VOLUME				
mL	milliliters	0.034	fluid ounces	fl oz
L	liters	0.264	gallons	gal
m³	cubic meters	35.314	cubic feet	ft ³
m³	cubic meters	1.307	cubic yards	yd ³
MASS				
g	grams	0.035	ounces	oz
kg	kilograms	2.202	pounds	lb
Mg (or "t")	megagrams (or "metric ton")	1.103	short tons (2000 lb)	T
TEMPERATURE (exact degrees)				
°C	Celsius	1.8C+32	Fahrenheit	°F
ILLUMINATION				
lx	lux	0.0929	foot-candles	fc
cd/m²	candela/m ²	0.2919	foot-Lamberts	fl
FORCE and PRESSURE or STRESS				
kN	kilonewtons	0.225	1000 pound force	kip
N	newtons	0.225	pound force	lbf
kPa	kilopascals	0.145	pound force per square inch	lbf/in ²

*SI is the symbol for the International System of Units. Appropriate rounding should be made to comply with Section 4 of ASTM E380.

1. Report No.		2. Government Accession No.		3. Recipient's Catalog No.	
4. Title and Subtitle End Region Detailing of Pretensioned Concrete Bridge Girders				5. Report Date March 2013	
				6. Performing Organization Code	
7. Author(s) B. E. Ross, G. R. Consolazio, and H. R. Hamilton				8. Performing Organization Report No.	
9. Performing Organization Name and Address University of Florida Department of Civil & Coastal Engineering P.O. Box 116580 Gainesville, FL 32611-6580				10. Work Unit No. (TRAIS)	
				11. Contract or Grant No. BDK75 977-05	
12. Sponsoring Agency Name and Address Florida Department of Transportation Research Management Center 605 Suwannee Street, MS 30 Tallahassee, FL 32301-8064				13. Type of Report and Period Covered Final Report	
				14. Sponsoring Agency Code	
15. Supplementary Notes					
16. Abstract <p>End region detailing has significant effect on the serviceability, behavior, and capacity of pretensioned concrete girders. In this project, experimental and analytical research programs were conducted to evaluate and quantify the effects of different end region detailing schemes. Two end region design models were developed using results from the experimental and analytical programs. The first model can be used to design confinement reinforcement to prevent lateral-splitting failure at ultimate strength. The second model focuses on serviceability criteria and can be used to calculate bottom flange stresses due to prestressing and thereby assess the likelihood of bottom flange cracking in the end region.</p> <p>The experimental program was conducted using (14) Florida I-Beam (FIB) specimens. Cracking and strain data were collected during prestress transfer and during the months following transfer. These data were used to evaluate serviceability criteria. Following serviceability evaluations, specimens were load tested to determine capacity and behavior due to applied loads. Specimens were loaded in three-point bending at a shear-span-to-depth (a/d) ratio of approximately 2.0. Variables considered in the experimental work included confinement reinforcement, steel bearing plates, horizontal reinforcement, vertical reinforcement, strand quantity, strand shielding, and strand layout.</p> <p>The analytical program was conducted using finite element analysis (FEA). FEA models were validated using data from the experimental program. Variables considered in the analytical program included bearing pad geometry, bearing pad stiffness, steel bearing plates, transfer length, and prestress release sequence.</p> <p>A test program was also conducted to evaluate the shear strength of 1950s era pretension girders used in the Florida highway system. These girders are of interest because they have thin 4 in. webs and very little specified shear reinforcement. Six test girders were removed from an existing bridge and were tested to failure in the laboratory. Results from the testing will be useful in determining the shear strength of similar pretensioned girders.</p> <p>Recommendations are provided with regard to detailing of confinement reinforcement, embedded bearing plates, strand shielding, and crack control. Recommendations are also given regarding evaluation of early pretensioned girders.</p>					
G17. Key Word Prestressed Concrete, End Region, Confinement Reinforcement, Splitting Failure, Shear, Debonding, Strand Shielding, Bridge Girders, Florida I-Beam			18. Distribution Statement No restrictions. This document is available to the public through the National Technical Information Service, Springfield, VA, 22161		
19. Security Classif. (of this report) Unclassified		20. Security Classif. (of this page) Unclassified		21. No. of Pages 581	22. Price

Acknowledgments

The authors would like to thank Florida Department of Transportation (FDOT) for funding the research presented in this report. The project was managed by Sam Fallaha of the FDOT. The authors thank Mr. Fallaha for his technical input and suggestions throughout the project. Special thanks go to staff at the FDOT M.H. Ansley Structures Research Center who assisted in fabrication and load testing of the concrete girders used in this project. In particular the authors acknowledge the contributions from staff members: David Allen, Adam Brennan, Steve Eudy, Tony Hobbs, Will Potter, Paul Tighe, David Wagner, and Chris Weigly. Assistance from FDOT State Materials Office personnel Mark Conley, Alfred Camps, Richard DeLorenzo, and Jordan Nelson is also appreciated.

University of Florida personnel and undergraduates also assisted with this project. UF laboratory managers Chuck Broward and Dr. Christopher Ferraro were helpful in providing equipment, lab space, and technical assistance during the project. Graduate and undergraduate students assisting on this project include Abraham Alende, Rafael Asencio, Natassia Brenkus, David Lavenhagen, Kunal Malpani, Scott Maul, Kinsman Pearson, Abhay Singh, Peter Whitfield, and Michael Willis.

Supplies were donated by CEMEX, Florida Rock, Insteel, and Lenton/Erico. The generous contribution of these companies is appreciated. Test girders were fabricated by Dura-Stress Inc. of Leesburg, FL and Standard Concrete Products of Tampa, FL.

Finally, the authors would like to dedicate this work to the memory of the late Marc Ansley, who managed this project for the FDOT until his untimely death. His suggestions and guidance early in the project provided a positive influence on the direction and completion of the project. Marc will be missed.

Executive Summary

End region detailing has significant effect on the serviceability, behavior, and capacity of pretensioned concrete girders. In this project, experimental and analytical research programs were conducted to evaluate and quantify the effects of different end region detailing schemes. Two end region design models were developed using results from the experimental and analytical programs. The first model can be used to design confinement reinforcement to prevent lateral-splitting failure at ultimate strength. The second model focuses on serviceability criteria and can be used to calculate bottom flange stresses due to prestressing and thereby assess the likelihood of bottom flange cracking in the end region.

The experimental program was conducted using (14) Florida I-Beam (FIB) specimens. Both FIB-54 and FIB-63 specimens were used. Cracking and strain data were collected during prestress transfer and during the months following transfer. These data were used to evaluate serviceability criteria. Following serviceability evaluations, specimens were load tested to determine capacity and behavior due to applied loads. Specimens were loaded in three-point bending at a shear-span-to-depth (a/d) ratio of approximately 2.0. Variables considered in the experimental work included confinement reinforcement, steel bearing plates, horizontal reinforcement, vertical reinforcement, strand quantity, strand shielding, and strand layout.

The analytical program was conducted using finite element analysis (FEA). FEA models were validated using data from the experimental program. Variables considered in the analytical program included bearing pad geometry, bearing pad stiffness, steel bearing plates, transfer length, and prestress release sequence.

A test program was also conducted to evaluate the shear strength of 1950s era pretension girders used in the Florida highway system. These girders are of interest because they have thin 4 in. webs and very little specified shear reinforcement. Six test girders were removed from an existing bridge and were tested to failure in the laboratory. Results from the testing will be useful in determining the shear strength of similar pretensioned girders.

Recommendations are provided with regard to detailing of confinement reinforcement, embedded bearing plates, strand shielding, and crack control. Recommendations are also given regarding evaluation of existing 1950's era pretensioned girders.

Table of Contents

Acknowledgments.....	vi
Executive Summary	vii
List of Figures	ix
List of Tables	xi
1 Introduction	1
1.1 Objectives	2
1.2 Report Outline.....	2
2 Background	4
3 Small Beam Tests.....	7
3.1 Specimen Details and Test Setup.....	7
3.2 Results and Discussion	9
3.3 Conclusions.....	13
4 SR-72 Tests	15
4.1 Specimen Details and Test Setup.....	15
4.2 Results and Discussion	18
4.3 Conclusions.....	20
5 FIB-54 Tests	22
5.1 Specimen Details and Test Setup.....	22
5.2 Results and Discussion	25
5.3 Conclusions.....	34
6 FIB-63 Tests	37
6.1 Specimen Details and Test Setup.....	37
6.2 Results and Conclusions	40
6.3 Conclusions.....	45
7 Finite Element Analyses of End Region	48
7.1 Analyses at Prestress Transfer	48
7.2 Analyses during Loading	53
7.3 Conclusions.....	55
8 End Region Design Models.....	58
8.1 Confinement Reinforcement Design Model	58
8.2 Serviceability Model.....	61
8.3 Ultimate Strength Design of Confinement Reinforcement.....	67
8.4 Conclusions.....	67
9 Recommendations	68
10 References	71
Appendix A–Literature Review	76
Appendix B–Small Beam Tests	77
Appendix C–SR-72 Tests	78
Appendix D–FIB-54 Tests.....	79
Appendix E–FIB-63 Tests	80
Appendix F–Finite Element Analysis of End Region.....	81
Appendix G–End Region Design Models.....	82
Appendix H–Support Data.....	83

List of Figures

Figure 1–Prestressed concrete bridge	4
Figure 2–Florida I-Beam cross-sections	5
Figure 3–Lateral-splitting failure	5
Figure 4–Flange splitting crack (Tadros et al. 2010)	6
Figure 5–Nomenclature and beam details	8
Figure 6–Reinforcement details	8
Figure 7–Test setup	9
Figure 8–Load vs. displacement and strand slip	10
Figure 9–Failure of unconfined (left) and confined (right) specimens	11
Figure 10–Normalized shear capacity	13
Figure 11–SR-72 cross-section and prestressing	16
Figure 12–Specified transverse reinforcement	16
Figure 13–Specified deck and curb reinforcement	16
Figure 14–SR-72 specimens and labels	17
Figure 15–Test setup	18
Figure 16–Crack pattern girder I2B (initial crack shown in red)	19
Figure 17–Experimental and code shear capacities	20
Figure 18–FIB-54 labeling scheme	23
Figure 19–FIB-54 end region reinforcement for HC (left) and VU (right)	24
Figure 20–FIB-54 test setup	24
Figure 21–Test specimen and load frame view of A) top and B) side of girder	25
Figure 22–Flange displaced shapes	26
Figure 23–Web splitting (blue) and flange splitting (brown) cracks	28
Figure 24–Girders W, F, & D web and flange splitting cracks	29
Figure 25–Flange splitting cracks girders W, F, and D	30
Figure 26–Typical flange splitting crack location	31
Figure 27–FIB-54 Peak shear forces	31
Figure 28–Lateral-splitting failure mechanics	32
Figure 29–Bond-shear failure A) bottom view and B) side view	32
Figure 30–Web-crushing failure	33
Figure 31–Transverse forces in confinement reinforcement and bearing plates	34
Figure 32–FIB-63 test specimen labels	38
Figure 33–FIB-63 test specimens during construction	39
Figure 34–FIB-63 test setup	39
Figure 35–Crack growth in specimen CT (flexural cracks in top flange not shown)	41
Figure 36–Photo of FIB-63 end region cracks (cracks enhanced in blue)	42
Figure 37–Web splitting crack length and area	43
Figure 38–Web splitting crack widths	43
Figure 39–Punching failure specimen LB	44
Figure 40–Specimen CT after load tests	45
Figure 41–Hook breakout and load point punching failures	45
Figure 42–FE model details	49
Figure 43–Comparison of experimental and FE model transverse (x-x) strain	50
Figure 44–Element x-x stress and y-z area	50
Figure 45–Transverse (x-x) stress at stages of prestress transfer	51
Figure 46–Transverse force variation as strands are released	52
Figure 47–Transverse force variation with length of prestress transfer	53
Figure 48–FE model configuration	54

Figure 49–Small beam transverse (x-x) strain profile ($V = 15$ kip).....	54
Figure 50–Normalized transverse (x-x) strain vs. bearing pad width, small beam.....	55
Figure 51–Definition of number of strands in outer portion of flange n_f	59
Figure 52–Design model compared to nominal strength of experimental girders	61
Figure 53–Flange splitting in experimental girder.....	63
Figure 54–Strand release conditions.....	63
Figure 55–Analysis sections for FIB bottom flange	64
Figure 56–Bottom flange free body diagram.....	65
Figure 57–Calculated transverse splitting stress vs. experimental crack length.....	66

List of Tables

Table 1–Report organization.....	3
Table 2–Test setup dimensions	18
Table 3–SR-72 girder behaviors at peak load	19
Table 4–FIB-54 test girder and specimen variables.....	23
Table 5–Tensile strain during prestress transfer girders H and V	26

1 Introduction

In January 2009, the Florida Department of Transportation (FDOT) mandated that all new prestressed concrete bridges in Florida be constructed using the new Florida I-Beam (FIB) sections. The standard FIB end region reinforcement is based on historic FDOT details, American Association of State Highway and Transportation Officials (AASHTO) Load and Resistance Factor Design (LRFD) Bridge Design Specifications (LRFD 2010), and constructability considerations. End region detailing has a significant effect on the strength and behavior of pretensioned I-girders. Effective detailing enables the end region to serve two critical functions. First, the end region transfers prestressing forces from the strands to the cross-section. Second, the end region transfers shear force from the girder into the bearing. A limitation in the current AASHTO LRFD is the use of empirical design provisions for portions of the end region reinforcement with no consideration of the flange geometry, prestressing force, or strand pattern.

This report presents the results of experimental and analytical investigations that were conducted to evaluate the effects of end region detailing on strength and serviceability of bridge girders. Also included in the report are proposed models that can be used to design effective end region details.

Experimental work in this project included load tests of 32 pretensioned, precast girder specimens. Specimens were loaded in three-point bending and ranged in size from 28 in. to 63 in. deep. Load tests were conducted as part of four different test programs: Small beam, SR-72, FIB-54, and FIB-63. The SR-72 test program utilized girders salvaged from a bridge demolition, whereas the other three test programs utilized girders constructed specifically for experimental testing.

Analytical work in this project utilized the finite element (FE) analysis method. FE models were linear-elastic and were intended to model the behavior of the end region prior to cracking. FE models were validated using data from the experimental program and were then used to examine parameters that were not investigated experimentally such as bearing pad width, bottom flange geometry, and strand debonding patterns. The effects of applied loads and prestressing forces were considered in the FE analyses.

Building on the experimental and FE results, two analytical models were developed to aid in the design of effective end region details. The first is an ultimate strength model to design confinement reinforcement. The second is for calculating lateral stresses in the bottom flange due to prestressing.

1.1 Objectives

Combined experimental and analytical work was conducted to achieve the following objectives:

- Evaluate strategies for controlling or preventing web splitting cracks including vertical post-tensioning; strand shielding beyond AASHTO LRFD allowances; and strategic use of vertical reinforcement.
- Determine the function(s) of confinement reinforcement during prestress transfer and at ultimate strength.
- Create a model for bottom flange splitting cracks at prestress transfer.
- Create a design model for confinement reinforcement at ultimate strength.
- Evaluate the effects of strand shielding beyond AASHTO LRFD allowances on the ultimate strength and serviceability of FIB girders.
- Evaluate the need (or lack thereof) for confinement reinforcement within the transfer length of partially shielded strands.
- Evaluate the contribution of horizontal vertical reinforcement in end region.
- Develop recommendations regarding end region detailing practices.
- Evaluate the shear strength and behavior of early pretensioned girders used in Florida highway bridges.

1.2 Report Outline

The report is divided into a summary document and several appendixes. This portion of the report is the summary document, which is comprised of nine chapters. Table 1 shows the correspondence between the chapters in this summary document and the appendixes, which present the research in greater detail than the summary document.

Table 1–Report organization

Topic	Summary Chapter	Appendix
Introduction	1	--
Background	2	--
Literature Review	--	A
Small Beam Test Program	3	B
SR-72 Test Program	4	C
FIB-54 Test Program	5	D
FIB-63 Test Program	6	E
Analytical Program (Finite Element Analyses)	7	F
End Region Design Models	8	G
Recommendations	9	--
Support Data	--	H

2 Background

The state of Florida has over 12,000 bridges in its public road system (FHWA 2010). Prestressed concrete is the most utilized material in Florida bridges, with precast-pretensioned concrete I-girders being the most common structural element. Figure 1 shows a typical highway overpass in Florida. It consists of multiple simple spans with each simple span being comprised of multiple individual I-girders.



Figure 1–Prestressed concrete bridge

Because Florida relies heavily on concrete I-girders there is motivation to improve the efficiency and performance of these members. To that end the Florida Department of Transportation (FDOT) introduced the Florida I-Beam (FIB) in 2009 for use in new bridge construction and bridge widening projects. The FIB was designed to be “more efficient to fabricate, safer to construct, and more cost effective” than the formerly used AASHTO and Florida Bulb-T shapes (FDOT 2009). FIB sections range from 36-in. deep to 96-in. deep and have the same top and bottom flange geometry regardless of depth (Figure 2). Because the bottom flange is relatively wide, it can accommodate up to 72 prestressing strands, thus improving the structural efficiency of the sections, particularly for those constructed with concrete strengths greater than 8000 psi.

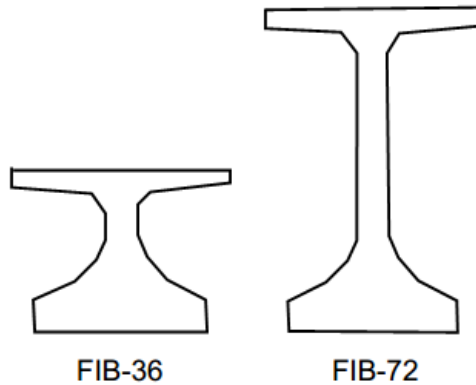


Figure 2–Florida I-Beam cross-sections

Although beneficial with regard to structural efficiency, the relatively wide bottom flange and high prestress forces in FIB girders raise potential concerns for capacity and serviceability. One failure mode accentuated by a wide and narrow flange is lateral-splitting, which occurs when the bottom flange splits laterally above the bearing due to applied loads (Figure 3). This behavior has been observed in experimental testing (Llanos et al. 2009) and in beams with slender bottom flange geometry. If the end region is not appropriately detailed lateral-splitting failure can control the shear capacity of I-girders and can lead to situations where the code calculated shear capacities are unconservative. Investigation of lateral-splitting failure was a primary focus of the experimental and analytical studies presented in this report.

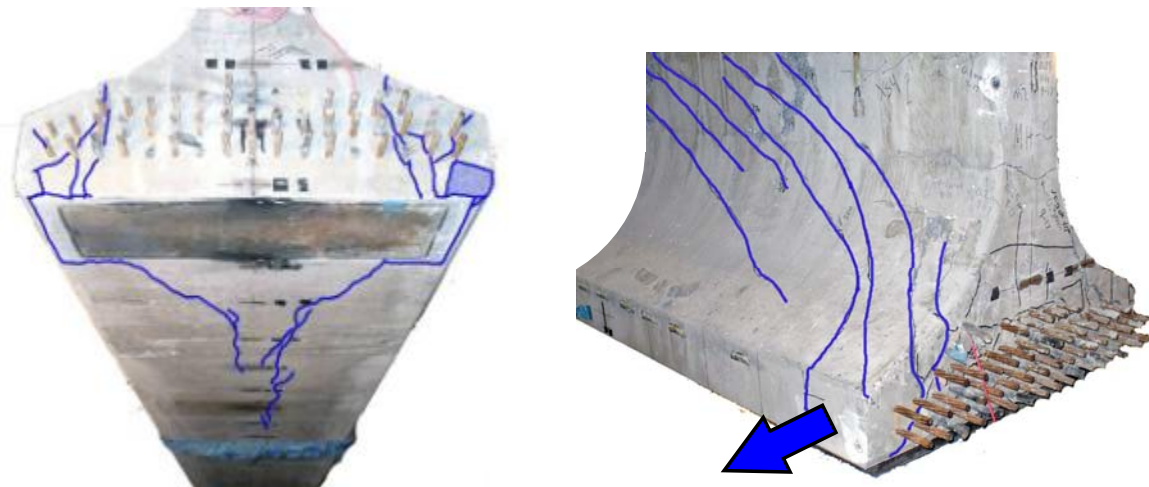


Figure 3–Lateral-splitting failure

Another focus of the research was controlling - and if possible preventing - end region splitting cracks. Web splitting cracks are an ongoing issue in I-girders. These cracks occur due

to vertical tensile stresses that form as prestressing is spread from the bottom flange to the entire cross-section. Splitting cracks in the bottom flange have historically been less common than those in the web. Recently, however, flange splitting cracks have been observed in girders with slender bottom flanges (Figure 4). Because FIB girders have relatively slender bottom flanges there is motivation to investigate flange splitting cracks, as well as, splitting cracks in the web.



Figure 4—Flange splitting crack (Tadros et al. 2010)

This report also presents experimental results of testing on early (circa 1950s) pretensioned girders utilized in Florida. Early girder designs in Florida called for thin 4 in. webs and very little shear reinforcement. Accordingly these girders also have low code-calculated shear capacity, which presents a problem with load rating. To more accurately determine shear capacity, load tests were conducted using specimens salvaged from a demolished bridge. The effect of integral curbs and barriers on shear capacity and behavior was also investigated during load testing. Results of these tests may be useful in load rating the shear capacity of similar girders still in service.

3 Small Beam Tests

The AASHTO LRFD Bridge Design Specifications require that confinement reinforcement be placed around prestressing strands in the bottom bulb of pretensioned concrete beams. Although the AASHTO specifications contain prescriptive requirements for the quantity and placement of confinement reinforcement, the effect of such reinforcement on the end region behavior is not well understood. To evaluate the function and effect of confinement reinforcement, twelve tests were conducted on 28-in. deep precast-pretensioned beams. Beams were loaded in three-point bending at a shear span-to-depth ratio of 1.0. Variables in the test program included strand size, strand quantity, prestressing force, and the presence or lack of confinement reinforcement. See Appendix B for a comprehensive discussion of testing and results.

3.1 Specimen Details and Test Setup

Six precast pretensioned concrete beams from a previous research project (O'Neill and Hamilton 2009) were salvaged for use in testing the end region. That research project conducted tests to measure service stresses at mid-span without loading the beams to their ultimate strength. The ends remained undamaged and were fit for the shear tests reported in this chapter. Strand diameter, strand quantity, prestress force, and confinement reinforcement were included in the variables examined (Figure 5).

The beams were constructed so that each end had identical confinement reinforcement. To create specimens with no confinement reinforcement, one end of each beam was saw-cut to remove the portion containing the confinement steel (Figure 6). Each end of each beam was then tested in three-point bending (Figure 7). Tests on specimens (ends) with confinement reinforcement are referred to as “confined tests” and those on specimens without confinement reinforcement as “unconfined tests”.

Load, strain, displacement and strand slip data were collected during testing.

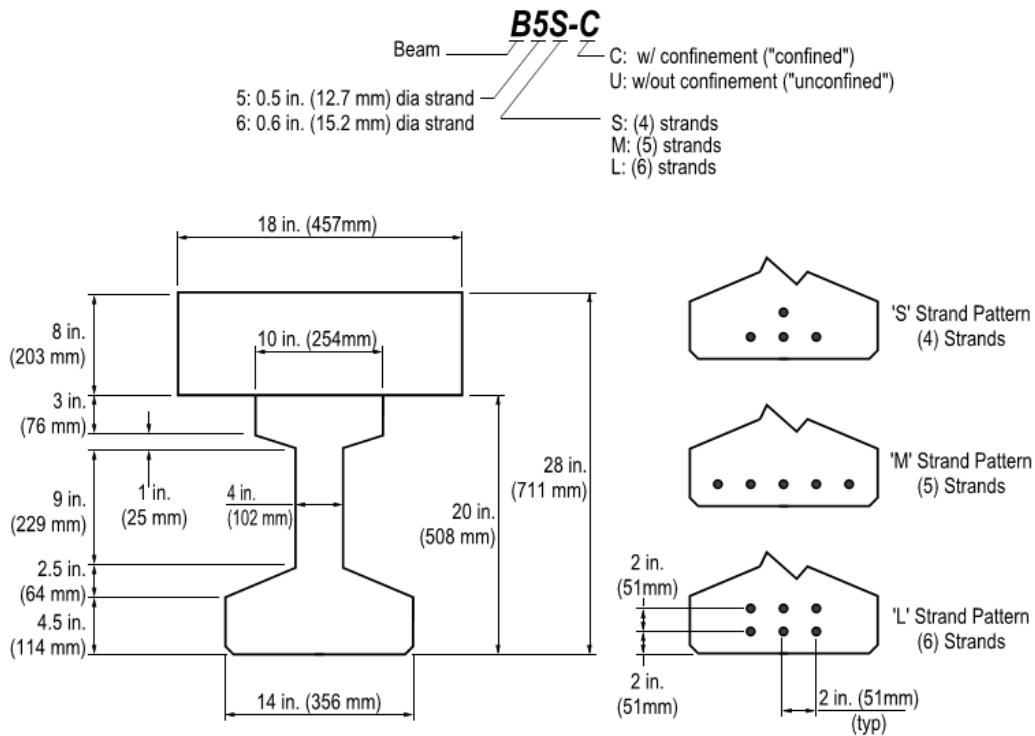


Figure 5—Nomenclature and beam details

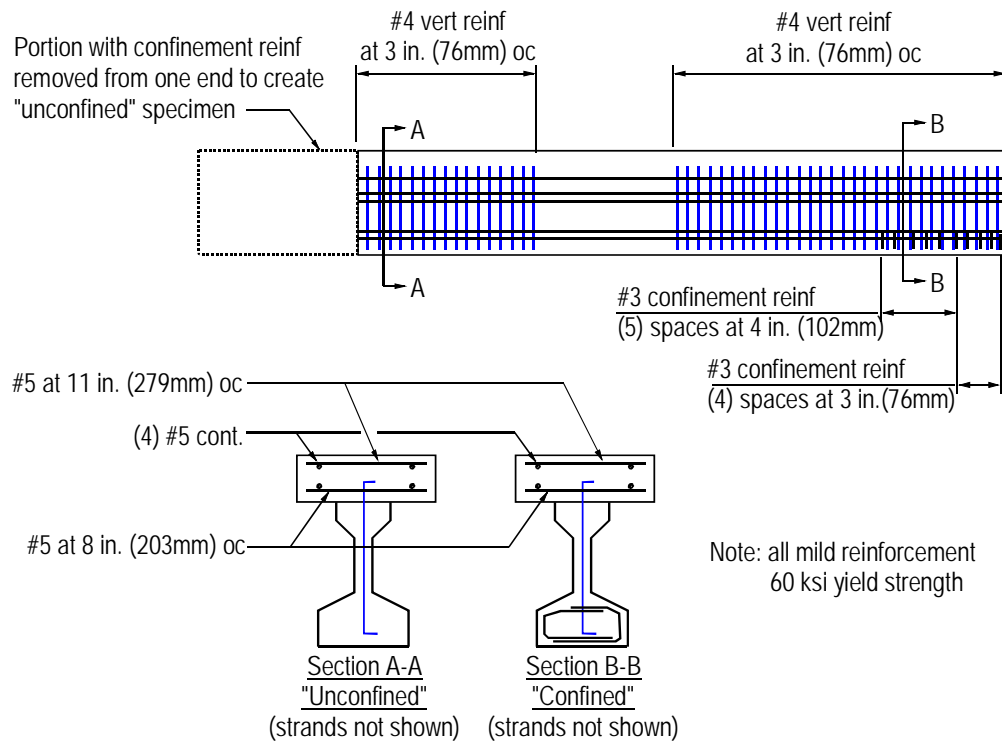


Figure 6—Reinforcement details

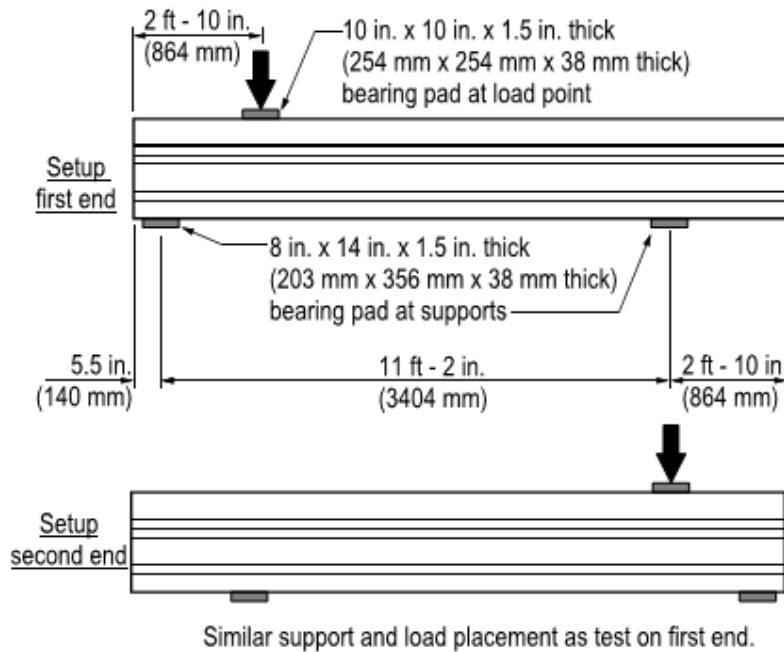


Figure 7–Test setup

3.2 Results and Discussion

To illustrate the general differences in behavior between confined and unconfined specimens, Figure 8 shows the load-displacement and strand-slip results for confined (B5M-C) and unconfined (B5M-U) specimens. The figure shows vertical displacement at the load point and average slip of bonded strands. Since the two tests were conducted on the same beam, the strand pattern, strand size, prestress force, and concrete were identical for both tests, with the confinement reinforcement being the only difference. The qualitative behavior of these specimens is representative of all six pairings of similar confined and unconfined tests.

Both specimens behaved in a linear-elastic manner until reaching a load of approximately 100 kip (445 kN). Initial cracks consistently formed in the web and were inclined between the load point and the support, whether or not the specimen contained confinement reinforcement. Flexural cracks and additional inclined cracks formed as the load was further increased. When the load reached 150kip (668 kN), the inclined cracks in both tests had propagated into the bottom bulb, thereby reducing the available development length of the prestressing strands, and

initiating strand slip. Strand slip was gradual at first, but increased when the load reached approximately 175 kip (779 kN). Slip and displacement characteristics of the confined and unconfined ends remained similar up to a load of 190 kip (846 kN), at which point the unconfined specimen failed in a splitting mode. Splitting failures were characterized by formation of splitting cracks at the end of the beam above the support, accompanied by sudden strand slip and an almost instantaneous loss of capacity.

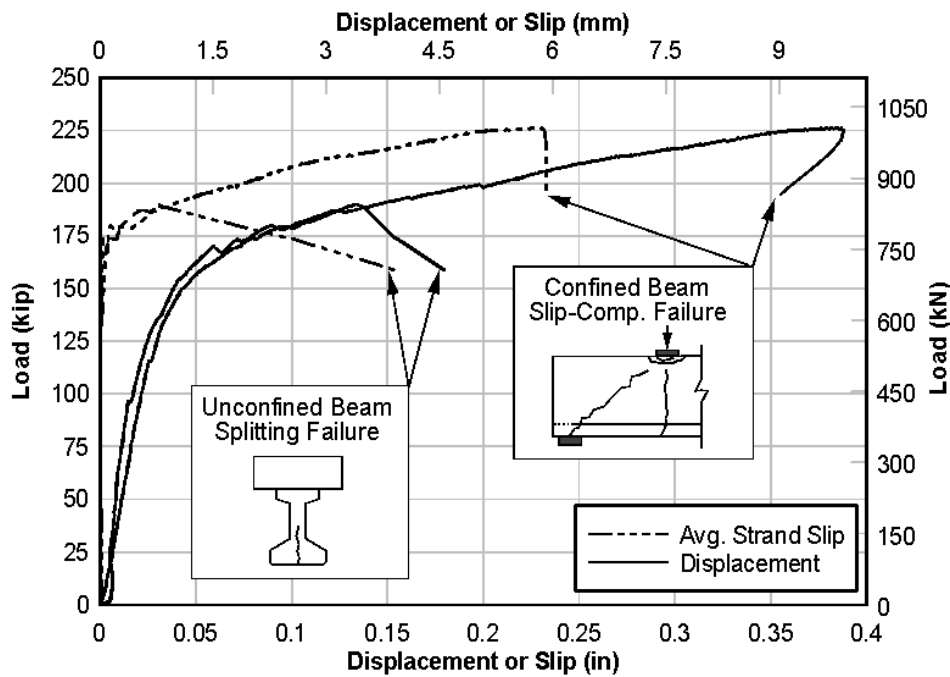


Figure 8–Load vs. displacement and strand slip

For the confined end, load continued to increase until failure occurred at a load of 226 kip (1006 kN). The continued load increase, however, was accompanied by further strand slip indicating that the remaining development length provided sufficient anchorage to maintain stability of the mechanism. As the strands slipped, the diagonal crack opened further, reducing the concrete area available to resist the compression in the top of the section. Capacity was reached when the concrete below the load point was crushed due to the excessive rotation that was allowed, in part, by strand slip. Indeed most of the rotation occurred about the inclined crack, which shortened the available strand development length. Strands in the confined end slipped 0.23 in. (5.8 mm) at failure. Enhanced photographs of the failed test specimens are shown in Figure 9.

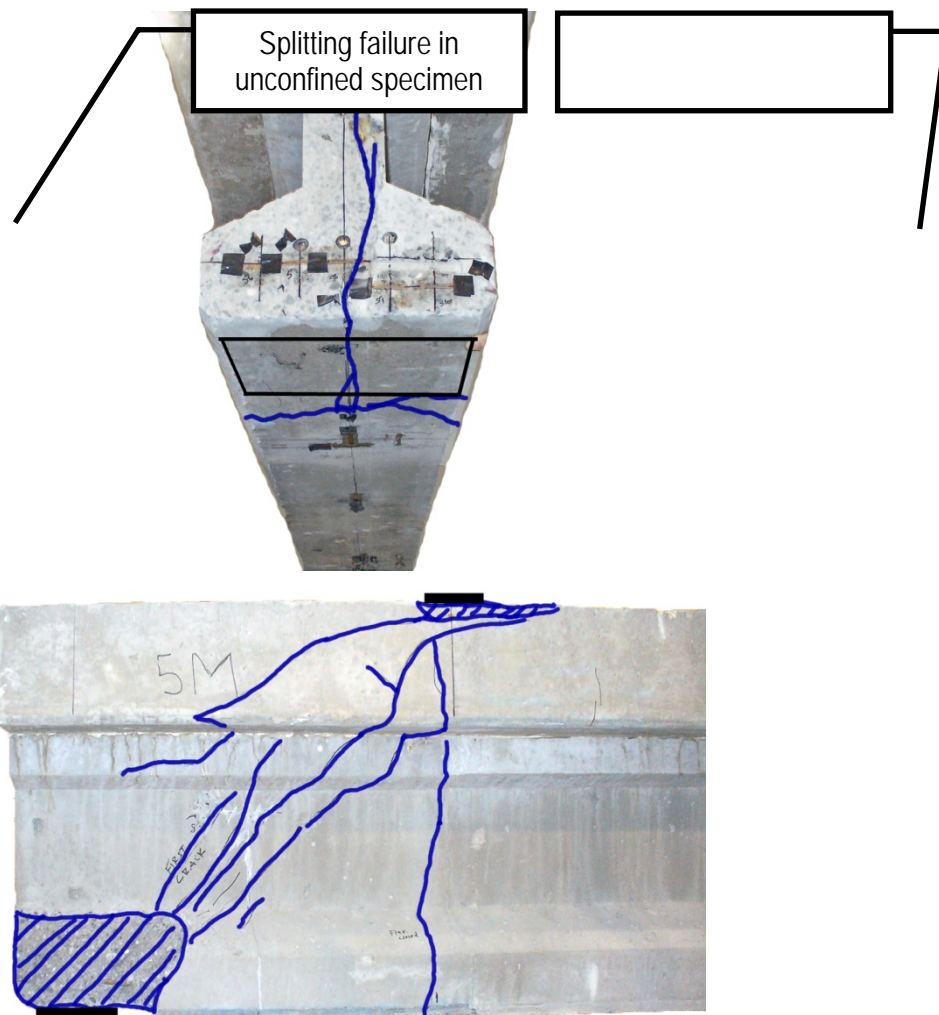


Figure 9–Failure of unconfined (left) and confined (right) specimens

In addition to the typical behavior described above, some common behavioral characteristics were noted in all tests. Strand slip occurred in all specimens after cracks had propagated into the bottom bulb. Furthermore, the load at which this slip occurred was at or near the same load for each pair of confined and unconfined tests conducted on a single beam. Thus confinement reinforcement did not prevent or delay strand slip, but did allow strands in the confined beams to continue carrying tensile forces even as they slipped beyond the point at which the unconfined tests failed in splitting. Slip at maximum load was, on average, over seven times greater in the confined tests than in the unconfined tests. While significant strand slip occurred in the confined beam tests upon reaching peak load, section curvature was not always sufficient at this point to crush the compression zone, thus causing a definitive drop in load and

signal the end of the test. In such cases, an arbitrary amount of additional displacement was imposed to ensure that the ultimate load had indeed been reached.

Figure 10 shows the normalized shear capacity for each test. The experimental shear capacity is defined as the shear force at the near support corresponding to the maximum load. Values have been normalized by the average of the unconfined beam capacities: 138 kip (614 kN). The data clearly indicate that variation in strand diameter had little effect on the shear capacity in unconfined tests. Average capacity of the unconfined tests with 0.5-in. (12.7 mm) diameter strand (B5 in the figure) and 0.6-in. (15.2 mm) diameter strand (B6 in the figure) varied by only 4%, indicating that strand size and area of prestressing steel did not significantly affect the capacity of the unconfined beams.

Confined tests resulted in an average of 25% more shear capacity than that of the unconfined tests and more than twice the displacement ductility. The improved shear capacity was likely due to increased contribution from the mild reinforcement. As the confined beams rotated beyond the point at which the unconfined beams split and failed, forces in the vertical steel increased, leading to improvements in shear capacity. The increased rotation also caused the resultant of the compressive force to move upwards, thereby increasing the moment arm and shear contribution of the prestressing strands. The experimental shear capacities were an average of 34% greater than the shear capacities calculated by the general procedure in section 5.8.3.4.2 of AASHTO LRFD (2007).

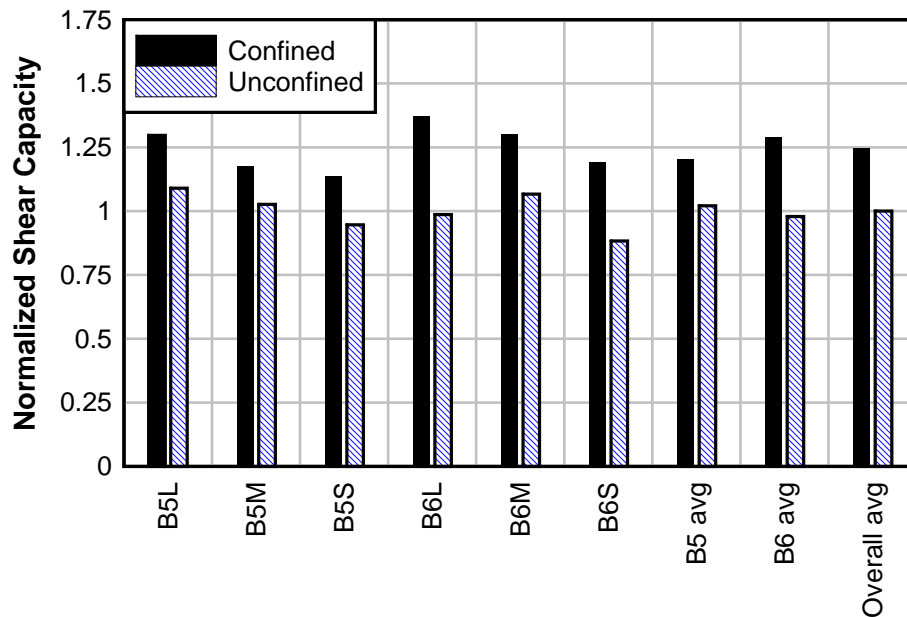


Figure 10–Normalized shear capacity

3.3 Conclusions

Twelve precast-prestressed test specimens were loaded to failure in three-point bending. The load point was placed approximately one member depth away from the support. Half of the specimens had confinement reinforcement and the other half did not. Other variables in the test program included the quantity and size of prestressing strands. Conclusions are listed below. See Appendix B for additional discussion and justification of the conclusions.

- Confinement reinforcement had negligible effect on measured strain distribution in concrete prior to cracking.
- Transverse tensile strains formed in the bottom flange above the bearing pad. The maximum strain occurred at the centerline of the cross-section and the strain diminished to a minimum at the edge of the flange. Transverse tensile strains are believed to have led to splitting failures in the beams without confinement reinforcement.
- Confinement reinforcement did not consistently delay or prevent slipping of prestressing strands. Such reinforcement, however, did provide sufficient slip restraint

to the strands to ensure that they were able to continue supporting tensile forces beyond the point at which the unconfined test specimens failed.

- Confinement reinforcement prevented splitting failure, thereby improving the shear capacity and displacement ductility of the confined tests relative to the unconfined tests. Average shear capacity increase was 25% and the average increase in displacement ductility was 157%.
- Experimental results and strut-and-tie modeling suggest that the strands were 30% developed on average at peak load. Development of the strands in the experimental tests was limited by the formation of cracks within the strand development length.

4 SR-72 Tests

Ultimate load tests were conducted on precast pretensioned girders that were removed from a Florida bridge after nearly 55 years of service. The shear capacity of these girders is of interest because they had relatively thin webs and limited vertical reinforcement. Varying portions of the deck and/or curb were retained with each girder to evaluate the effect of these elements on shear capacity. Girders were loaded in three-point bending at shear-span-to-depth (a/d) ratios ranging from 2.1 to 4.5. Results of this testing will be helpful in evaluating the strength of similar girders that are still in service. A summary of the SR-72 test program is presented in this chapter. See Appendix C for a more comprehensive discussion of testing and results.

4.1 Specimen Details and Test Setup

Test girders were salvaged from a bridge on Highway SR-72, in Sarasota County, Florida. Girders were precast and pretensioned, having the cross-section shown in Figure 11. Varying widths of the composite concrete bridge deck were kept integral with each salvaged girder. Portions of the integral curb were also retained with the two exterior girders used in the test program. Specified reinforcement in the girders and deck is shown in Figure 12 and Figure 13. Destructive and non-destructive investigation indicated transverse reinforcement in the girders was less than specified on the original drawings. Girder labels and cross-sections are shown in Figure 14.

Girders were tested in three-point bending. Dimensions and setup are described in Figure 15 and Table 2. Load, displacement, strain, and strand slip data were collected during testing. As indicated in the table, SR-72 specimens were load tested at one end rather than each end as was done for other specimens in this research project.

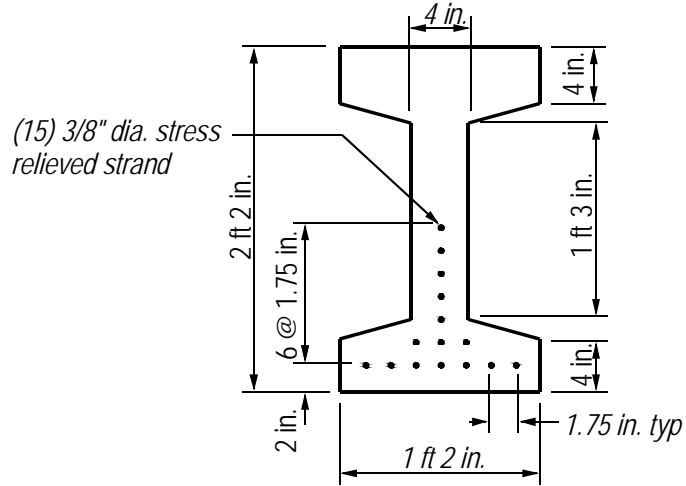


Figure 11–SR-72 cross-section and prestressing

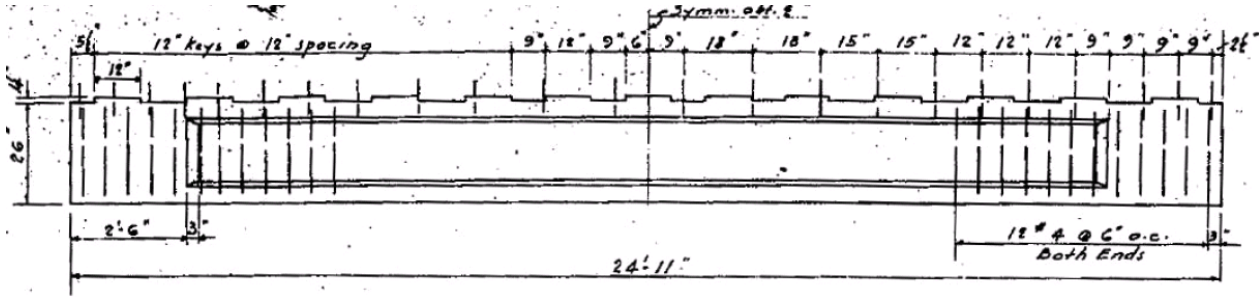


Figure 12–Specified transverse reinforcement

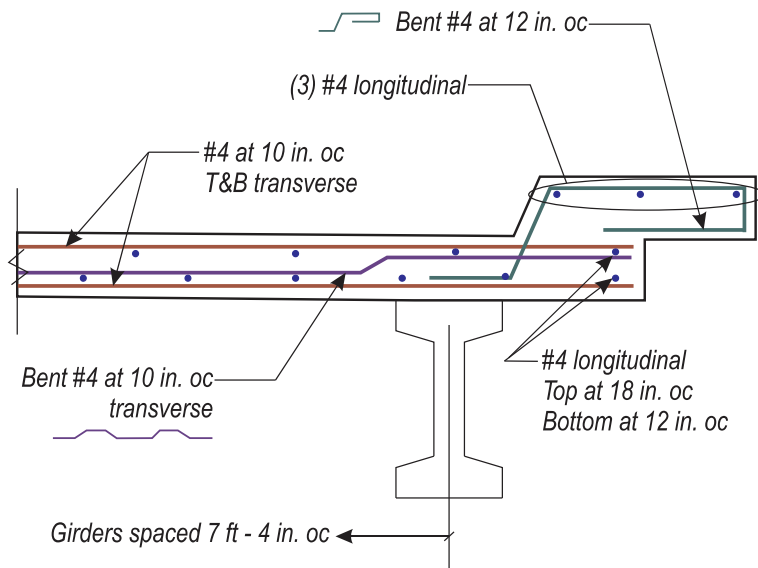


Figure 13–Specified deck and curb reinforcement

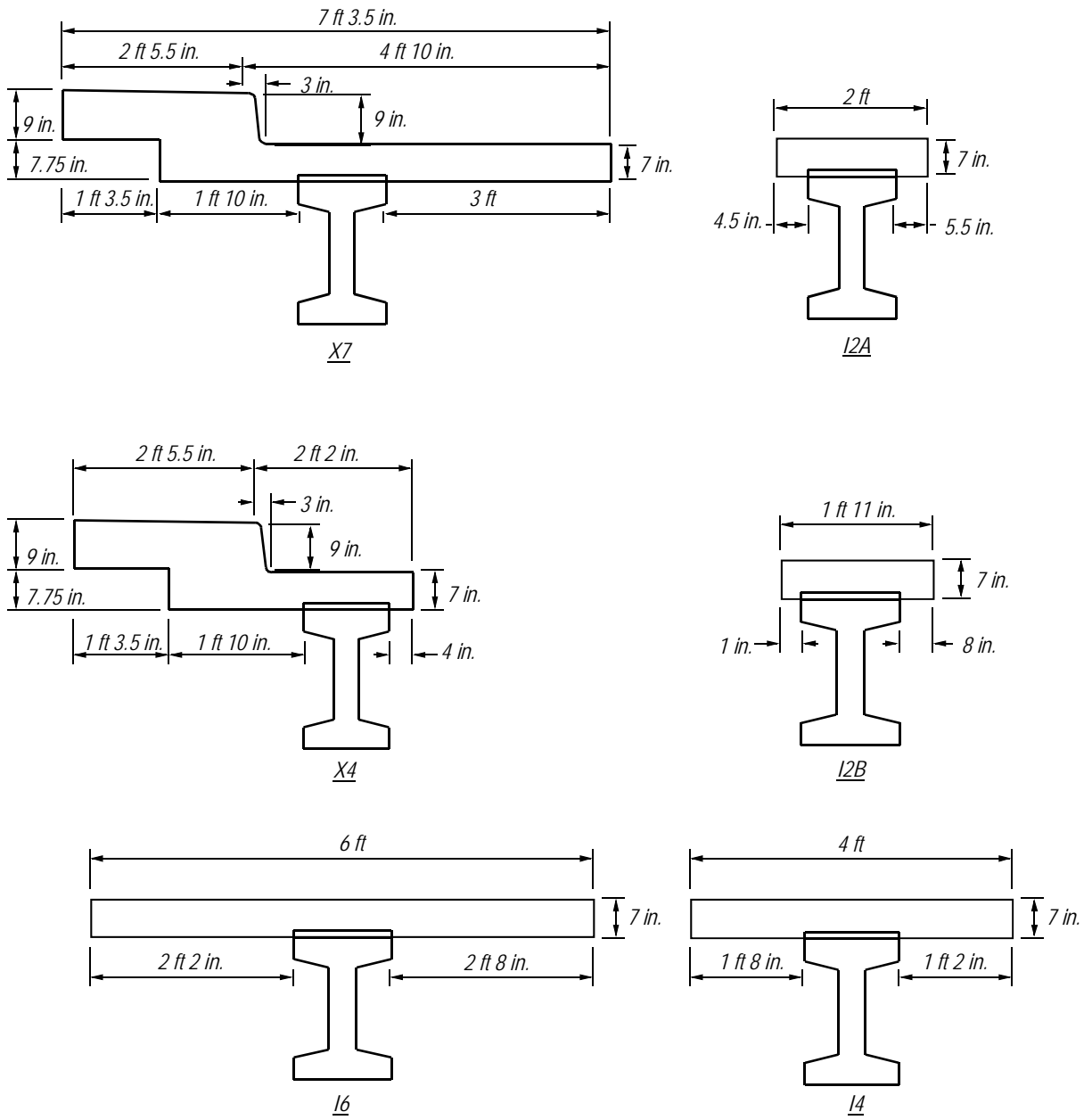


Figure 14–SR-72 specimens and labels

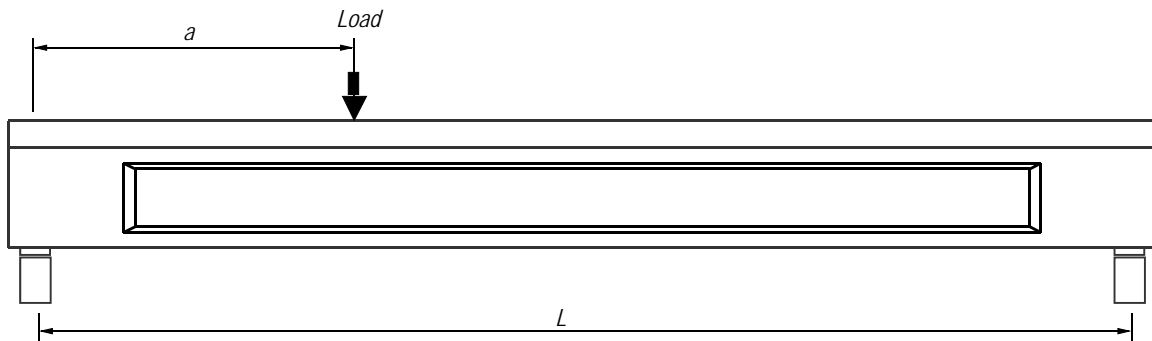


Figure 15–Test setup

Table 2–Test setup dimensions

Girder	A	a/d*	L
X7	8'-2"	3.4	23'-9"
X4	8'-2"	3.4	24'-3"
I2A	10'-11"	4.5	23'-9"
I2B	8'-1"	3.3	24'-11"
I4	5'-2"	2.1	23'-10"
I6	8'-2"	3.4	24'-0"
*d = 29 in.			

4.2 Results and Discussion

As load was applied, behavior was linear- elastic until the formation of a crack, which was typically a flexural crack located below the load point (Figure 16). As the load increased, inclined cracks formed in the web. Additional inclined cracks formed at flatter angles and closer to the supports as testing continued. During the latter stages of loading but before ultimate strength was reached, the inclined cracks were wide enough to allow the passage of light. Peak load was controlled by capacity of the compression zone in girders X7, X4 and I2A, and by formation of inclined cracks in girders I2B, I4 and I6.

Figure 16 shows the crack pattern for specimen I2B. Similar crack patterns were observed in the other girders. Figure 16 also shows the location of vertical reinforcement as determined by non-destructive testing for this specimen. The location and quantity of vertical reinforcement was different from the reinforcement specified in the construction drawings. Inclined cracks in the specimens typically did not intersect vertical reinforcement.

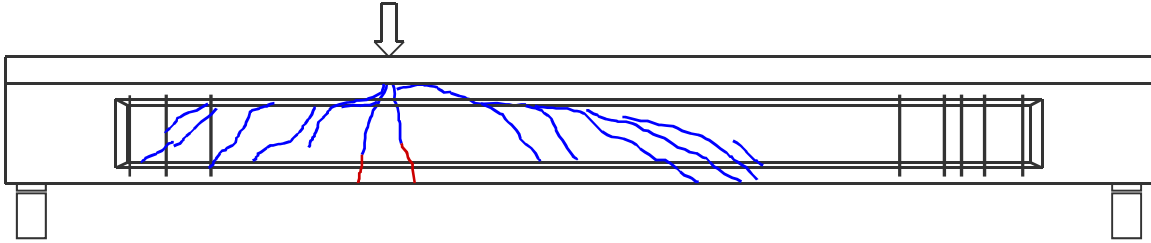


Figure 16–Crack pattern girder I2B (initial crack shown in red)

Because the inclined cracks were relatively wide as the specimen was near ultimate strength, and because the inclined cracks did not typically intersect vertical reinforcement, a plastic truss could not form. Rather, the girders behaved as tied-arches with shear forces being transferred through compression in the concrete arch. Tied-arch behavior was typical for all girders. Truss and tied-arch action are discussed and defined in the literature review contained in Appendix A.

As previously noted, peak load of girders X7, X4 and I2A was controlled by capacity of the compression zone. Peak load for girders I2B, I4 and I6 corresponded to formation of inclined cracks in the web. Table 3 summarizes the behavior at peak load of each girder.

Table 3–SR-72 girder behaviors at peak load

Girder	Behavior at Peak Load
X7	Punching failure of concrete arch below the load point.
X4	Flexure compression failure of concrete near the load point.
I2A	Instability (buckling) of concrete compressive arch.
I2B	Formation of inclined crack in web.
I4	Formation of inclined crack in web.
I6	Formation of inclined crack in web.

Figure 17 compares the experimental capacities with the code-calculated nominal shear capacities. Calculations were based on the specified properties of an interior girder and are plotted in Figure 17 as a function of the shear span a . The abrupt change in capacity at $a = 5.8$ ft corresponds to the specified end of vertical reinforcement. Girders performed well in the load tests in spite of thin webs, minimal shear reinforcement, and 55 years of service. In each case, the experimental shear capacity was greater than the code-calculated capacity.

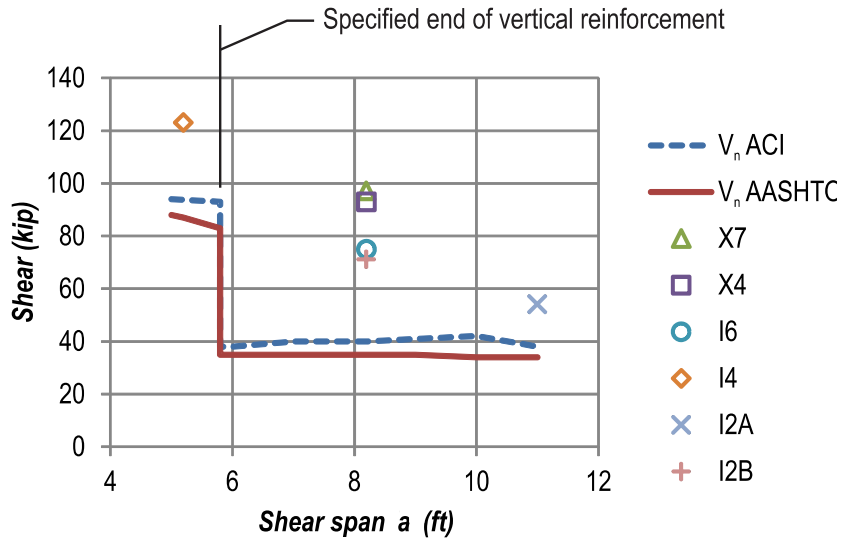


Figure 17–Experimental and code shear capacities

4.3 Conclusions

Six pretensioned concrete girders were salvaged from an existing bridge and tested after nearly 55 years of service. Girders were tested in three-point bending at a/d ratios from 2.1 to 4.5. Varying portions of the existing deck and/or curb were retained with each test girder. The experimental results were compared to theoretical predictions of strength capacity. Key conclusions are listed below. Additional conclusions, as well as discussion and justification of conclusions are presented in Appendix C.

- Test girders behaved as tied arches during the latter stages of loading. This is evident from the relatively wide cracks that did not allow aggregate interlock and from the absence of transverse reinforcement necessary to ensure plastic truss behavior.
- Tied-arch behavior controlled the experimental strength of girders X7, X4 and I2A. Arches in these girders failed due to punching, flexural compression, and arch instability, respectively.
- For girders I2B, I4, and I6 the maximum load occurred just prior to the formation of an inclined crack in the web. These girders behaved as tied-arches during the latter stages of loading, however, their maximum capacities were limited by the capacity of the web to resist inclined cracking.

- For tests at the same a/d ratio, the cast-in-place curb increased the average exterior girder strength by 30% over that of the interior girders with no curb.
- Nominal shear capacities calculated by ACI 318 and AASHTO LRFD methods were conservative relative to the experimental results. On average, the ratio of experimental-to-calculated shear capacity was 2.0 for ACI 318 and 2.1 for AASHTO LRFD calculations.
- The experimentally determined prestress force in specimen I2A was 47% less than the specified prestress. The large difference between the specified and experimental values may indicate quality control issues in addition to higher than expected losses.
- In spite of relatively thin webs, small quantities of vertical reinforcement, and poor quality control during construction, the girders were able to support significant shear force after nearly 55 years of service.

5 FIB-54 Tests

Five 54-in. deep Florida I-Beam (FIB-54) girders were fabricated and load tested to evaluate the effects of different end region details on girder capacity and behavior. Each end of each girder was detailed differently, which resulted in ten unique test specimens. Variables in the end region detailing included: presence or absence of embedded steel bearing plates, quantity and configuration of confinement reinforcement, strand bond pattern, strand quantity, and quantity of horizontal and vertical end region reinforcement.

Strain and crack data were collected during and after prestress transfer to evaluate the effectiveness of each detailing scheme on controlling bottom flange cracking. Load tests were then conducted on each specimen (end) to determine the effects of each detailing scheme had on girder behavior and capacity. Specimens were loaded in three-point bending at a shear span-to-depth ratio of 2.0. Failure modes included web-shear, bond-shear, and lateral-splitting.

5.1 Specimen Details and Test Setup

Five 50-ft. long FIB-54 girders were built according to the schedule of variables shown in Table 4. Each end of each girder was detailed differently, resulting in ten unique specimens. Girder and specimens were labeled using the convention shown in Figure 18. Girders were built in two different phases. Phase 1 girders were built by Dura-Stress of Leesburg, FL. Phase 2 girders were built by Standard Concrete Products of Tampa, FL. Construction plans, materials properties, and construction timelines are presented in detail in Appendix D. Figure 20 shows specimens HC and VU. These specimens had the most (HC) and least (VU) amounts of end region mild reinforcement.

Strain, crack, and material property data were collected during fabrication. Vibrating wire and electrical resistance strain gages were used to collect strain data. Crack data were collected using a tape measure and microscope. Material property data were collected for concrete compressive strength, reinforcement yield strength and elongation, prestressing strand strength, and prestressing strand bond capacity. The Standard Test for Strand Bond (NASP 2009) was used for determining strand bond capacity.

Table 4–FIB-54 test girder and specimen variables

Test Girder	Specimen	Bearing plate	Mild reinforcement		Strand bond pattern	Confinement reinforcement	Phase
			Vertical	Horizontal			
H	HC	Yes	FDOT	Yes	Design	FDOT	1
	HU	Yes	FDOT	Yes	Design	No	1
V	VC	Yes	Mod	No	Design	FDOT	1
	VU	Yes	Mod	No	Design	No	1
W	WN	No	FDOT	No	Web	Mod	2
	WB	Yes	FDOT	No	Web	Mod	2
F	FN	No	FDOT	No	Flange	Mod	2
	FB	Yes	FDOT	No	Flange	Mod	2
D	DC	Yes	FDOT	No	Design	FDOT	2
	DM	Yes	FDOT	No	Design	Mod	2

FDOT: Detailed per FDOT design standards

Mod: Detailed with modifications to FDOT design standards

Web: Fully bonded strands placed below web (24 fully bonded strands)

Flange: Fully bonded strands placed in outer portion of flange (24 fully bonded strands)

Design: Strand pattern based on prototype design (45 fully bonded strands)

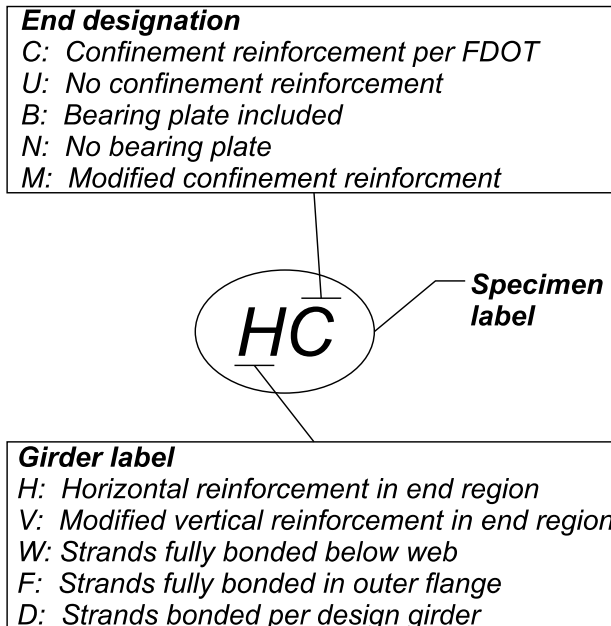


Figure 18–FIB-54 labeling scheme

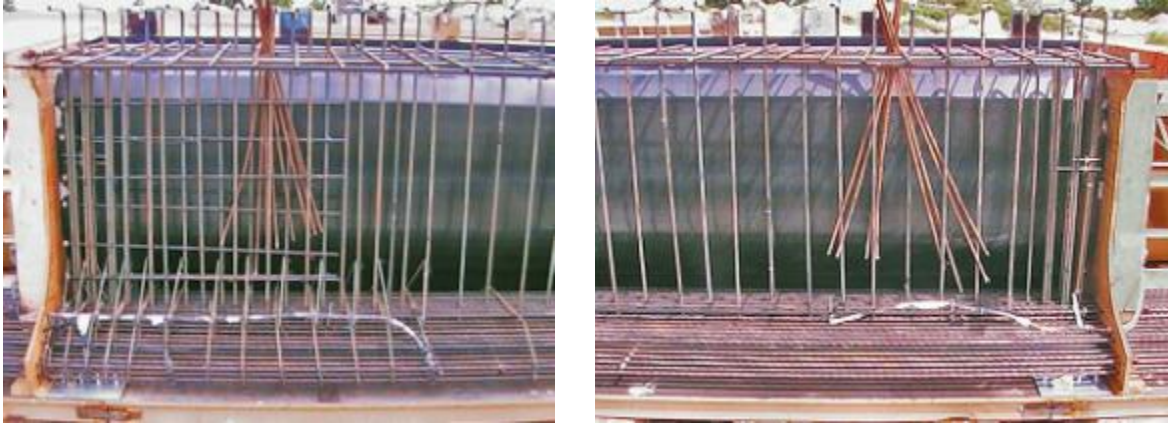


Figure 19–FIB-54 end region reinforcement for HC (left) and VU (right)

After fabrication, girders were trucked to the FDOT M.H. Ansley Structures Research Center in Tallahassee, FL. At the research center cast-in-place composite decks were built on top of each girder. Once the decks were sufficiently cured load tests were conducted. Each end (specimen) was loaded in 3-point bending as shown in Figure 20. After the first end was tested, the load point and supports were moved and the opposite end was tested. Photos of the test setup are shown in Figure 21. Load, displacement, strain, and strand-slip data were collected during load testing.

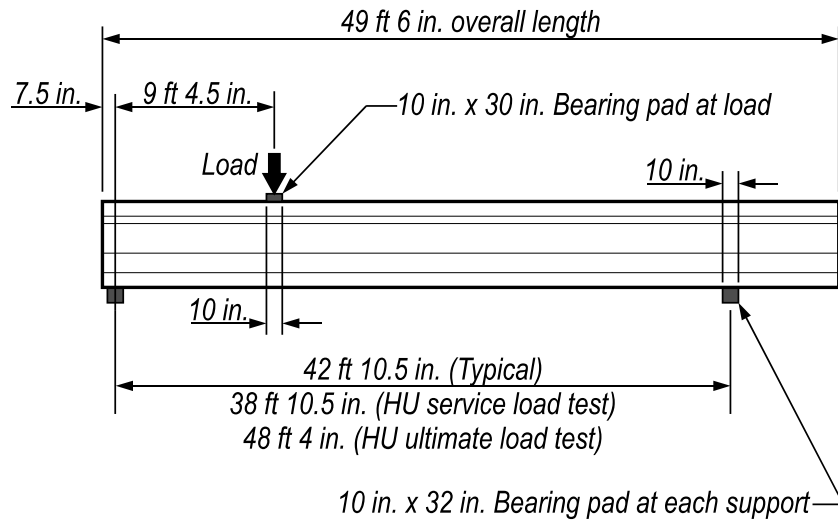


Figure 20–FIB-54 test setup

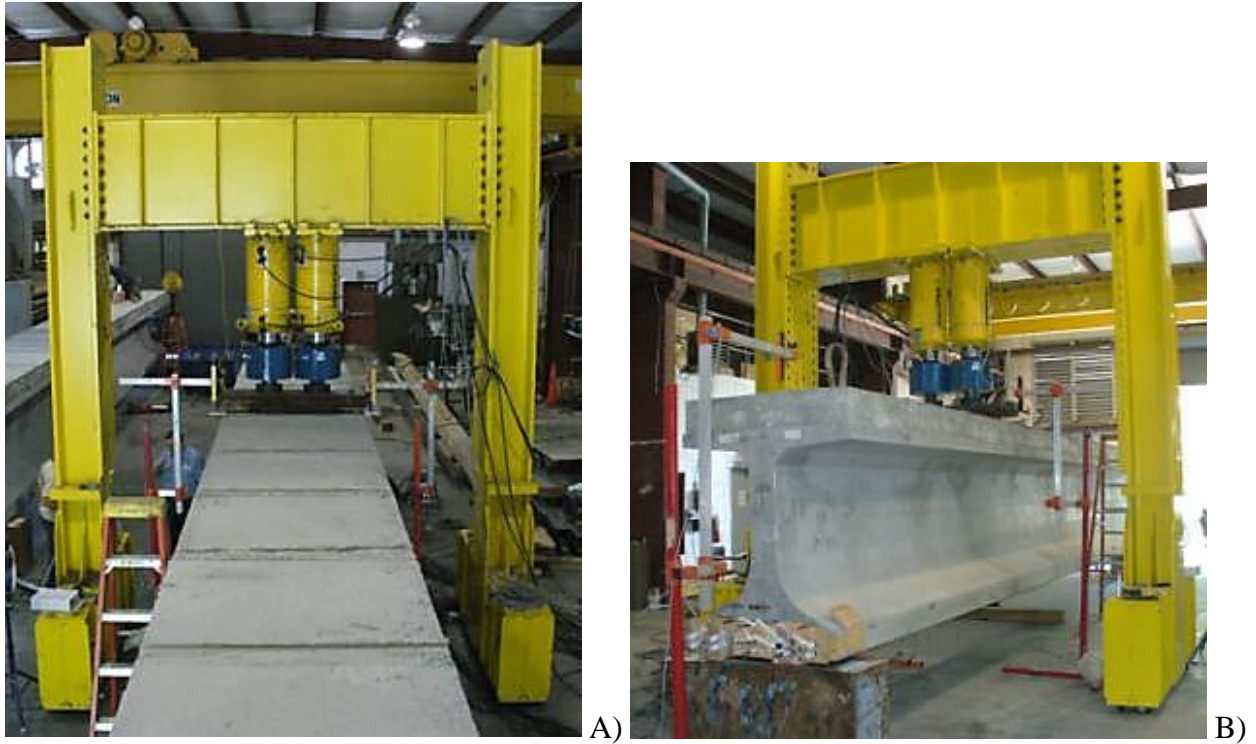


Figure 21–Test specimen and load frame view of A) top and B) side of girder

5.2 Results and Discussion

5.2.1 Strain during Prestress Transfer

Prestressing transfer in Florida is typically accomplished by flame cutting the prestressing strands, beginning with those on the outside of the strand pattern. Strands are cut sequentially starting with the outside strands and working toward the center of the beam. Strain gages labeled ‘XS3’ were placed at the end of specimens HC, HU, VC, and VU to monitor strain in the bottom flange during the prestress transfer (Figure 22).

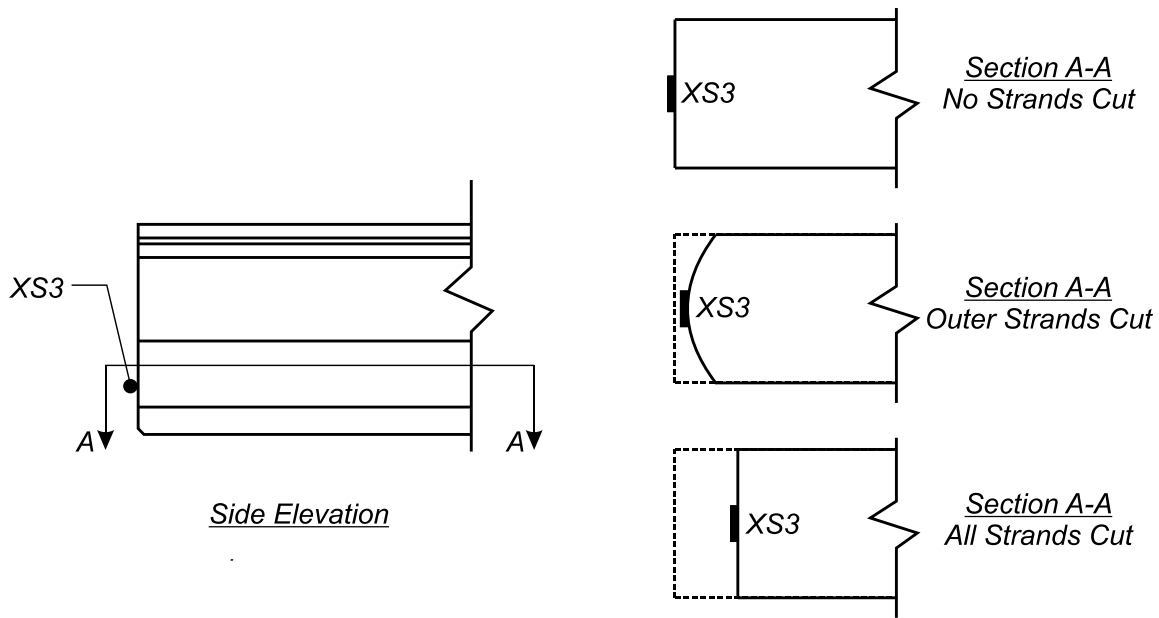


Figure 22–Flange displaced shapes

Data from gages XS3 are summarized in Table 5. The maximum tensile strain reported by XS3 occurred when only those strands in the outer portion of the flange were cut. The tensile strain reported by gages XS3 decreased significantly after the inner strands had been cut. This strain behavior is explained by the deformed shapes shown in Figure 22. Forces from the outer strand deform the edges of the flange resulting in transverse tension. Forces from the inner strands lead to a more uniform displacement across the bottom flange resulting in a reduction of transverse tension.

Table 5–Tensile strain during prestress transfer girders H and V

Gage and condition	Strain in specimens with confinement reinforcement (microstrain)		Strain in specimens without confinement reinforcement (microstrain)	
	HC	VC	HU	VU
X3 maximum tensile strain –outer strands cut	406	177	724	1258
X3 all strands cut (all strands released)	25	15	60	45

Assuming a concrete rupture strength of $7.5\sqrt{f'_c}$ and elastic modulus of $57,000\sqrt{f'_c}$, the expected rupture strain was approximately 135 microstrain. The maximum strain values reported by gages XS3 were larger than 135 microstrain - in some cases much larger - suggesting that cracks may have formed near the gage locations during the strand cutting process. Cracks were not visually observed, however, and it is believed that these cracks closed as the inner strands were cut.

Strain data presented above demonstrate that transverse tension forms in the bottom flange of I-girders due to prestress forces from the outer strands. This transverse tension is partially relieved as inner strands are cut.

5.2.2 Cracks due to Prestress

Crack data were also collected during and in the weeks following prestress transfer.

Three types of cracks were observed:

- Top flange flexural cracks
- Web splitting cracks
- Flange splitting cracks

Top flange cracks formed due to flexural stresses generated by the vertically eccentric prestressing. Top flange cracks are outside the scope of the FIB-54 test program. Web splitting (Figure 23) cracks also formed due to eccentric prestressing. As the prestress force was distributed from the bottom flange to the rest of the cross-section, the attendant vertical tension stresses caused cracks in the web. Flange splitting cracks were of primary interest in the FIB-54 test program. Flange splitting cracks were caused by horizontal eccentricity of prestressing, Hoyer expansion of strands, and self-weight reaction of the girders.



Figure 23–Web splitting (blue) and flange splitting (brown) cracks

Web and flange splitting cracks were first observed nine days after prestress transfer for girders H and V, which were built during the first phase of construction. Girders W, F, and D were built in the second construction phase. Cracks in Girders W, F, and D were first observed during prestress transfer. For all girders, cracks typically grew in length and in quantity after they were first observed. Figure 24 shows the web and flange cracks in girders W, F, and D three months after prestress transfer. Length and area of the bottom flange cracks for these girders are quantified in Figure 25.

Each of the specimens listed in Figure 25 had the same Class of concrete, were fabricated at the same time, and were fabricated using the same procedures. Strand patterns, bearing plates, and confinement reinforcement varied among specimens. The most severe cracking, in terms of total length and area, occurred in specimens FB and FN. Severity of cracking in these specimens is attributed to the strand pattern. All of the fully bonded prestressing strands in these specimens were located in the outer portion of the flange. As discussed in the previous section, prestressing located in the outer portions of the flange caused transverse tension in the bottom flange. This transverse tension is culpable in the cracks observed in specimens FB and FN.

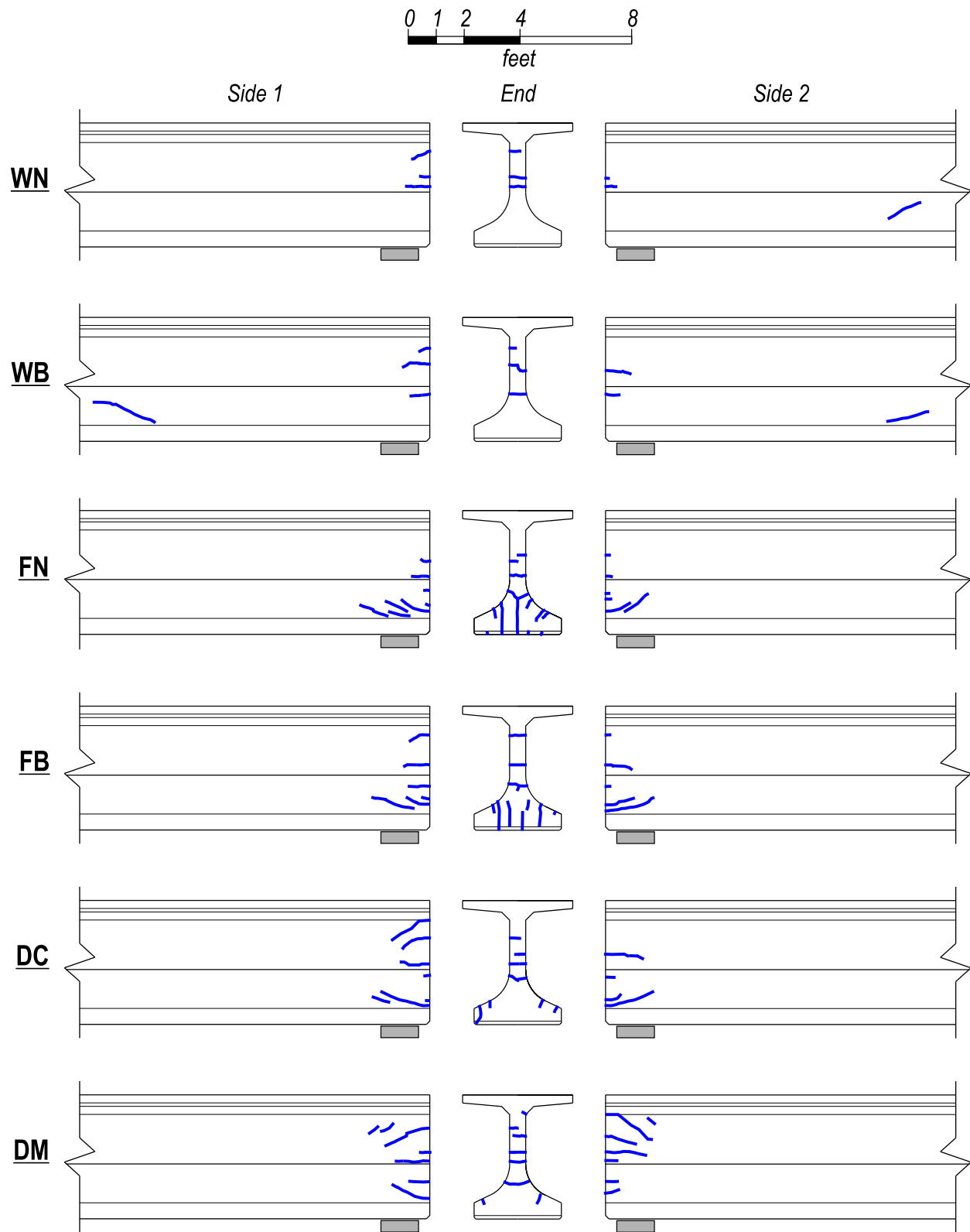


Figure 24–Girders W, F, & D web and flange splitting cracks

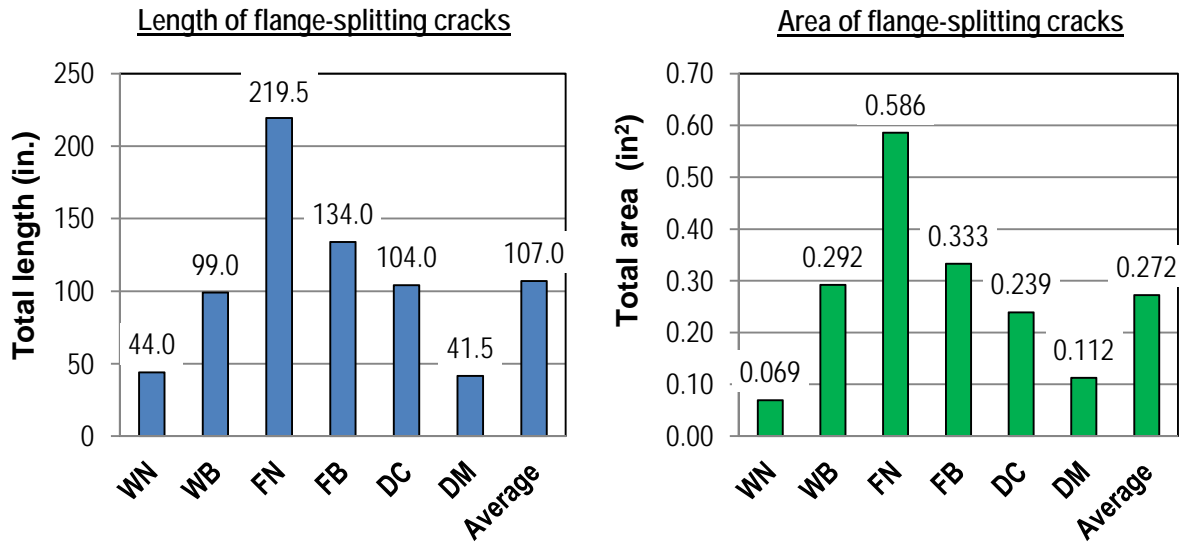


Figure 25–Flange splitting cracks girders W, F, and D

Figure 24 and Figure 25 demonstrate that variation in end region detailing can have a significant effect on the extent of cracking in the bottom flange and web. The effects of specific detailing schemes are discussed in greater detail in Appendix D.

One typical observation among most specimens was the formation of a flange splitting crack that intersected the outermost strand in the third row (Figure 26). This strand had the least amount of clear cover of any strand. Cracks at this location are attributed to the relatively small cover distance. Removing this strand from the pattern may reduce the potential for cracking.

5.2.3 Load Testing

Each specimen was load tested using the test setup shown in Figure 20. Maximum shear forces supported by the specimens and associated failure modes are presented in Figure 27. Forces include applied load and self-weight. End region detailing had significant effect on shear capacity. Specimen HC supported the largest shear force of 793 kip, almost twice as much as specimen FN which had a capacity of 402 kip. Experimental shear strength was increased by confinement reinforcement, bearing plates, and increased quantity of bonded prestressing strands. Strength was decreased when all fully bonded prestressing strands were placed in the outer portions of the bottom flange.

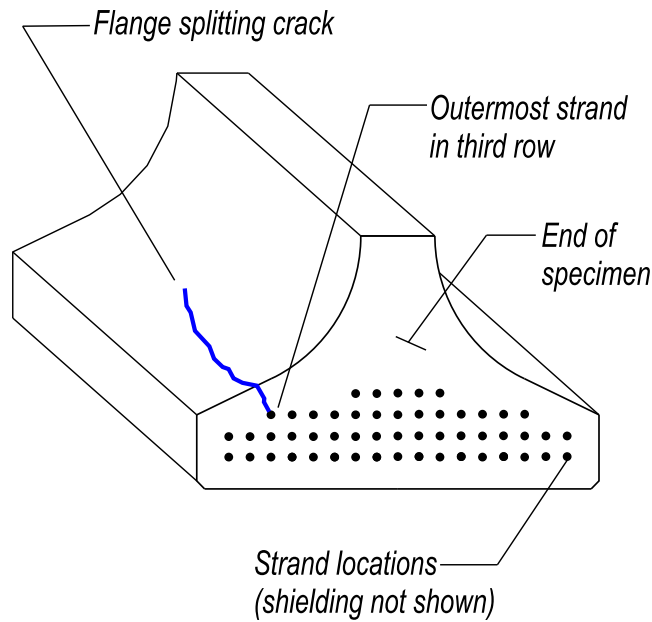


Figure 26–Typical flange splitting crack location

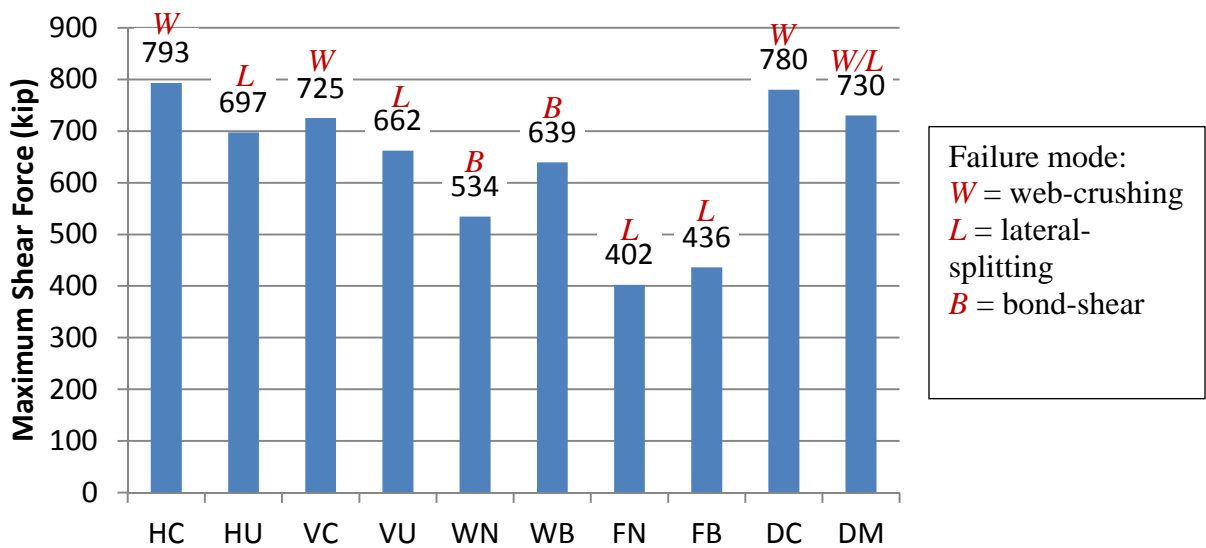


Figure 27–FIB-54 Peak shear forces

Three distinct failure modes were observed: Lateral-splitting failure, bond-shear failure, and web-crushing failure. Lateral-splitting failure occurred due to transverse tensile forces in the bottom flange (Figure 28). Longitudinal cracking through the bottom flange was characteristic of girders failing in lateral-splitting (Figure 3). Bond-shear failure (Figure 29) occurred when cracks formed within the development length of the prestressing strands, thereby interrupting

force transfer between the strands and concrete. Web-crushing failure occurred when diagonal compressive stresses exceeded the strength of the concrete in the web (Figure 30).

Lateral-splitting and bond-shear failures are considered “premature” failure modes because they occur prior to a girder reaching the desired web-crushing capacity. ACI 318 and AASHTO LRFD provisions for shear design both consider web-crushing failure. In the test program, lateral-splitting failures occurred in specimens lacking confinement reinforcement and in specimens with all fully bonded prestressing strands placed in the outer portions of the bottom flange. Bond-shear failure was observed in specimens with the smallest quantity of fully bonded strands.

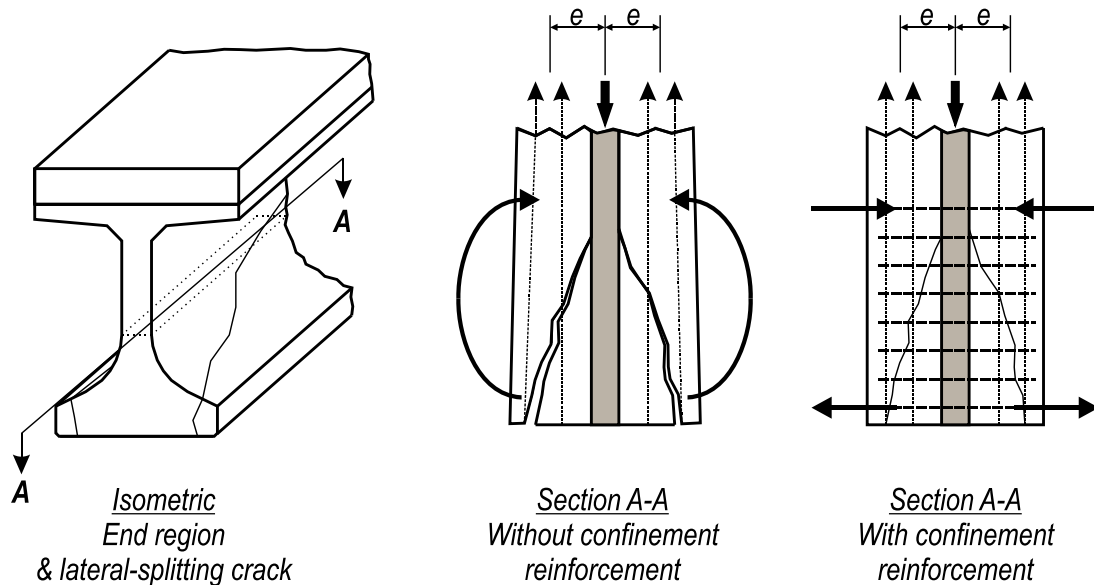


Figure 28–Lateral-splitting failure mechanics

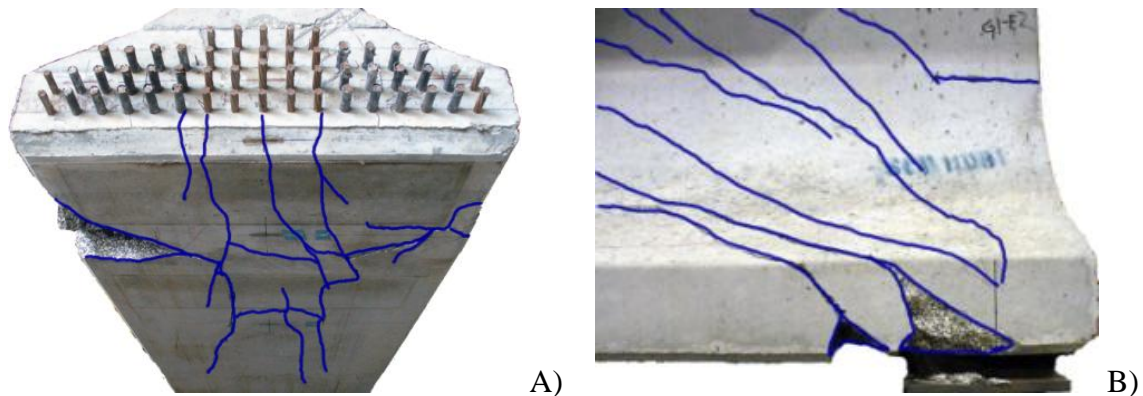
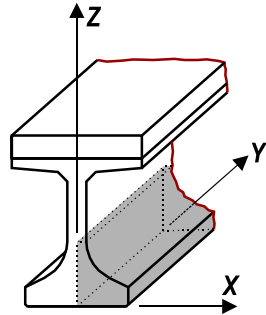


Figure 29–Bond-shear failure A) bottom view and B) side view



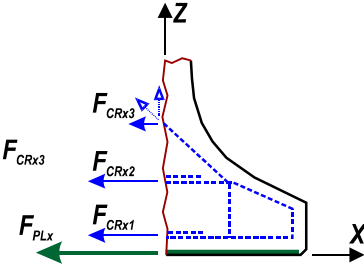
Figure 30–Web-crushing failure

Strain data from the confinement reinforcement and bearing plates were collected during load testing and were used to estimate the transverse forces acting in the bottom flange. Confinement and bearing plate forces are shown in Figure 31 for specimens HC and VC. Forces in the figure were calculated using strain data from ultimate load. Similar calculations were made for all test specimens. Results of these calculations suggest that significant (up to 100 kip) transverse forces were present in the bottom flange. These forces were carried by the confinement reinforcement and where present, embedded steel bearing plates.

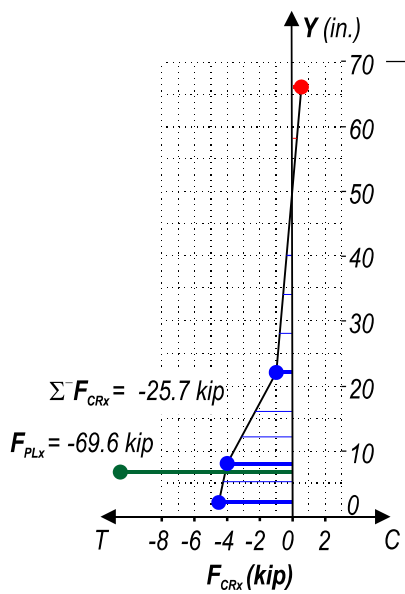


End region
isometric view

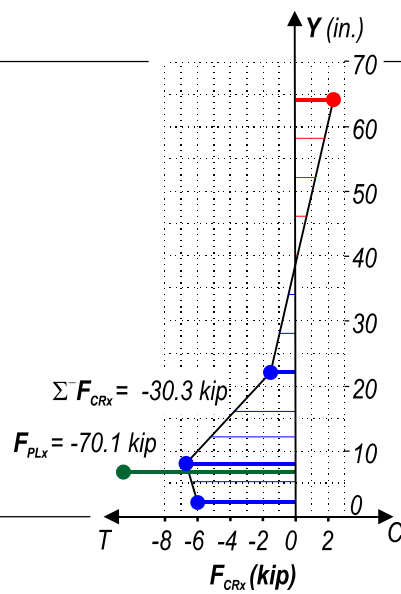
$$F_{CRx} = F_{CRx1} + F_{CRx2} + F_{CRx3}$$



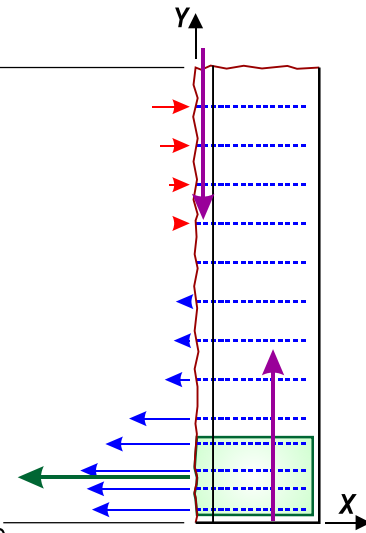
Bottom flange section
end view



Bottom flange forces
specimen HC



Bottom flange forces
specimen VC



Bottom flange section
partial plan view

Figure 31–Transverse forces in confinement reinforcement and bearing plates

5.3 Conclusions

Ten uniquely detailed FIB-54 specimens were fabricated and tested to evaluate the effects of end region detailing on girder serviceability, behavior, and cracking. Variables in the test program included:

- Presence/absence of confinement reinforcement
- Quantity and configuration of confinement reinforcement

- Presence/absence of horizontal reinforcement
- Quantity of vertical reinforcement
- Presence/absence of embedded steel bearing plates
- Strand quantity
- Strand placement

The following is a partial list of conclusions. Additional conclusions and justifications are presented in Appendix D along with a more comprehensive presentation of test program results.

- Transverse tensile strains were measured in the bottom flange, confinement reinforcement and embedded bearing plates during and after prestress transfer. Tensile strains are attributed to a combination of prestressing forces, the Hoyer effect and girder self-weight and are thought to have caused flange splitting cracks.
- Transverse tensile strains are greatest in sections with fully bonded strands placed only in the outer portions of the bottom flange. Bonded strands in the outer flange are eccentric with the resultant internal force, thereby inducing bending in the bottom flange and associated transverse tension at the girder end.
- Differences in detailing have significant effect on end region cracks occurring due to prestress forces. All test specimens used the FIB-54 cross-section, yet the summation of end region crack lengths varied from a maximum of 291 in. to a minimum of 75 in.
- Flange splitting cracks extended up to 30 in. from the test specimens ends. This length is comparable to the AASHTO LRFD transfer length of 36 in. (60 strand diameters) suggesting that this is a reasonable extent for the placement of confinement reinforcement to control flange splitting cracks.
- Splitting cracks in the bottom flange typically intersected the outermost strand in the third row from the bottom. This strand location had the least amount of top cover of any location in the test girders.
- Differences in detailing, such as confinement reinforcement configuration, steel bearing plates, and strand pattern have significant effect on the end region capacity, even for members having the same cross-section. All test specimens used the FIB-54 cross-

section, yet experimental capacities ranged from a maximum of 793 kip to a minimum of 402 kip.

- Test specimens with confinement reinforcement detailed according to current FDOT specifications failed in web-shear mode and at an average load 13% higher than comparable specimens without confinement. Specimens without confinement failed in lateral-splitting.
- Current shear and longitudinal tie provisions resulted in nominal capacities that were unconservative (up to 32% too large) relative to some experimental capacities. Nominal capacities were unconservative in specimens without confinement reinforcement (HU), specimens without steel bearing plates (WN, FN), and specimens with bonded strands concentrated in the outer flange (FB, FN).

6 FIB-63 Tests

Web cracking at the end of the girder during and after prestress transfer is an ongoing problem for pretensioned concrete I-girders. The FIB-63 test program compared four different detailing schemes for controlling and/or preventing web cracking. Schemes include: current Florida Department of Transportation standard detail, 1-in. diameter vertical end zone reinforcement, vertical post-tensioning of the end region prior to prestress transfer, and partial debonding of 45% of prestressing strands. One scheme was implemented on each end of two 63 in. deep Florida I-Beams (FIB-63). Crack locations, lengths, and widths were monitored during prestress transfer, as well as during the weeks and months following transfer. Crack data were used to compare the relative effectiveness of each scheme in controlling web cracking. After crack data were collected and analyzed, each specimen was load tested to determine the effect of the detailing schemes on ultimate load. A more comprehensive presentation of the FIB-63 test program is presented in Appendix E.

6.1 Specimen Details and Test Setup

Two 50 ft. long FIB-63 girders were fabricated and tested for this program. Each end of each girder had unique end region detailing (Figure 32), which results in four different test specimens. Specimen CT served as the control specimen and followed current Florida Department of Transportation (FDOT) details (2010). Vertical end zone reinforcement in CT consisted of (16) #5 bars placed within 16.5 in. of the member end.

Specimen SL had the same end region reinforcement as specimen CT. Strands in SL, however, were 45% partially shielded. This percentage of shielded strands violated AASHTO LRFD requirements.

The end of specimen PT was vertically post-tensioned prior to prestress transfer. The post-tension force was designed to counteract vertical tensile stresses in the web. A post-tension force of 78 kip was applied by tightening nuts on six threaded rods placed in the end region. The area of end region vertical reinforcement was reduced by 33% relative to CT. The post-tension concept used in specimen PT was proposed by the FDOT structures design office.

The fourth and final specimen, LB, had 1-in. diameter threaded rods as vertical end reinforcement. Because it used larger reinforcement, LB had 30% more end reinforcement than CT. Specimen LB was located on the same girder but opposite end as specimen PT.

FIB-63 specimens were built at the same time as the phase 2 specimens from the FIB-54 test program. They were built by Standard Concrete Products of Tampa, FL. Photos of the test specimens during construction are shown in Figure 33

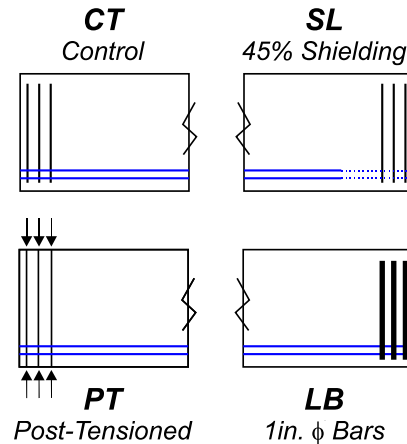


Figure 32–FIB-63 test specimen labels

Strain, crack, and material property data were collected during fabrication. Vibrating wire and electrical resistance strain gages were used to collect strain data. Crack data were collected using a tape measure and microscope. Material property data were collected for concrete compressive strength, reinforcement yield strength and elongation, prestressing strand strength, and prestressing strand bond capacity. The Standard Test for Strand Bond (NASP 2009) was used for determining strand bond capacity.

After fabrication, girders were trucked to the FDOT M.H. Ansley Structures Research Center in Tallahassee, FL for load testing. Each end (specimen) was loaded in 3-point bending as shown in Figure 34. After the first end was tested, the load point and supports were move and the opposite end was tested. Load, displacement, strain, and strand-slip data were collected during load testing.



Specimen CT



Specimen SL



Specimen PT



Specimen LB

Figure 33–FIB-63 test specimens during construction

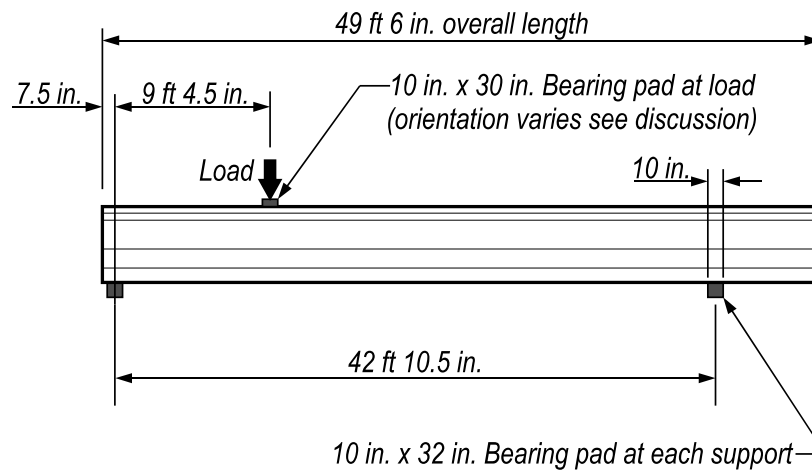


Figure 34–FIB-63 test setup

Orientation of the bearing pad at the load point varied. Specimen LB was tested first and had the pad oriented such that the 30 in. dimension was perpendicular to the span length. This led to failure in top flange, and the pad orientation was rotated 90 degrees for the subsequent tests.

6.2 *Results and Conclusions*

6.2.1 Cracks due to Prestress

Cracking in the end region was monitored during prestress transfer and in the weeks and months following transfer. Figure 35 shows the formation and growth of cracks in the control specimen. Similar figures are shown for the other specimens in Appendix H. Cracks were first observed during prestress transfer and grew in length and quantity in the months following prestress transfer. Load tests were conducted approximately four months after transfer. Photos of the specimens are shown in Figure 36.

Crack data are quantified in Figure 37 and Figure 38. Data presented in these figures were used to compare the relative effectiveness of the different detailing schemes in controlling web cracks. Based on the metrics of total length and total area, the control detail (specimen CT) was the least effective in controlling web splitting cracks. Specimen CT had 28% more length and 53% greater area than the average of all specimens.

Specimen SL was the most effective detail according each metric except total length. SL had 59% less area, and 44% smaller average width than the control specimen. The reduction in crack length, area, and width observed in specimen SL is attributed to the partial strand debonding which reduced tensile stresses in the end region.

In terms of crack length, the post-tensioning detail of specimen PT was the most effective for controlling web splitting cracks. Web splitting crack length in specimen PT was 50% less than the control specimen. Figure 36 shows that the post-tensioning effectively mitigated all web cracks at the end surface of the member. Web cracking did, however, occur away from the end surface.

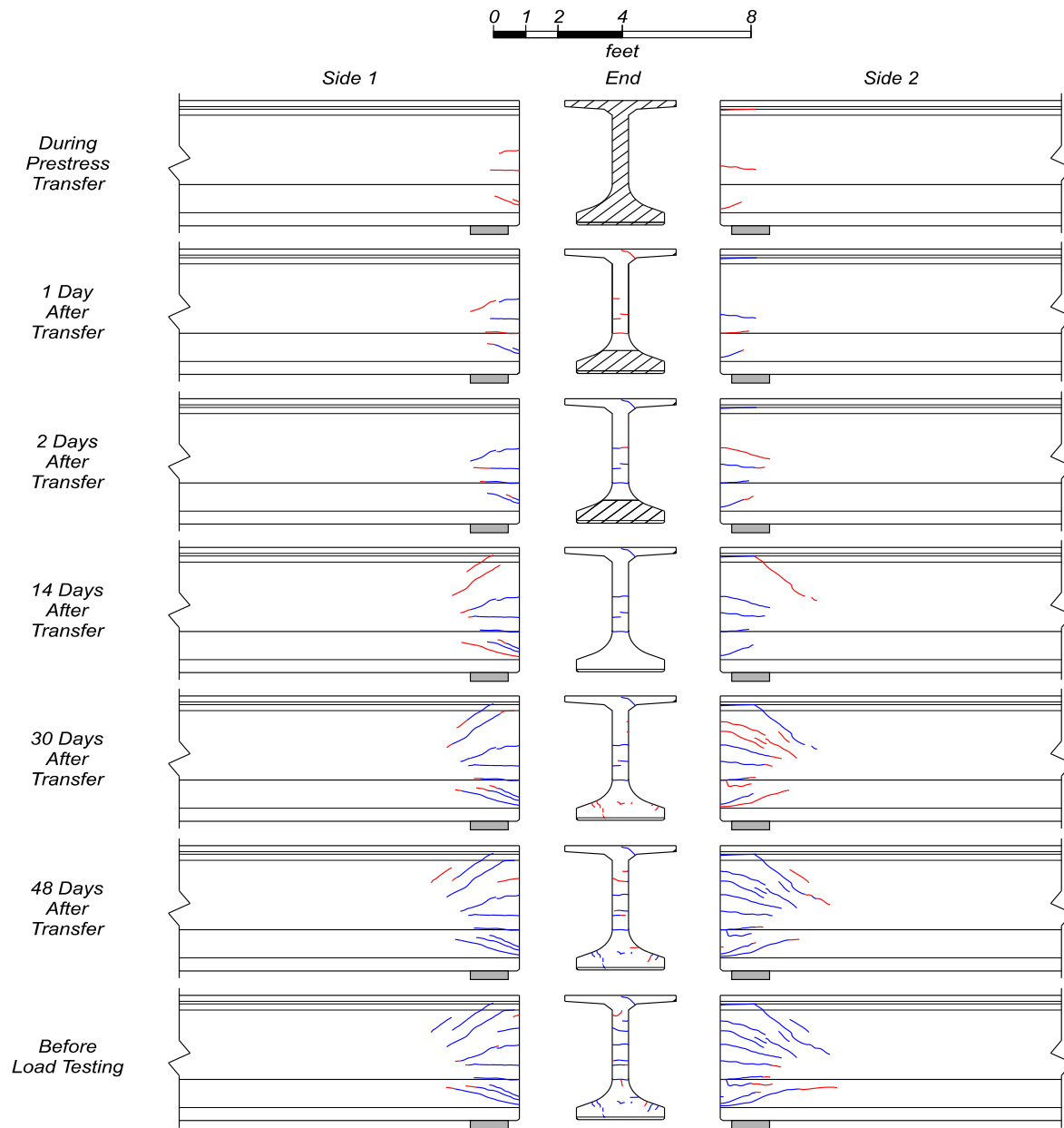


Figure 35–Crack growth in specimen CT (flexural cracks in top flange not shown)

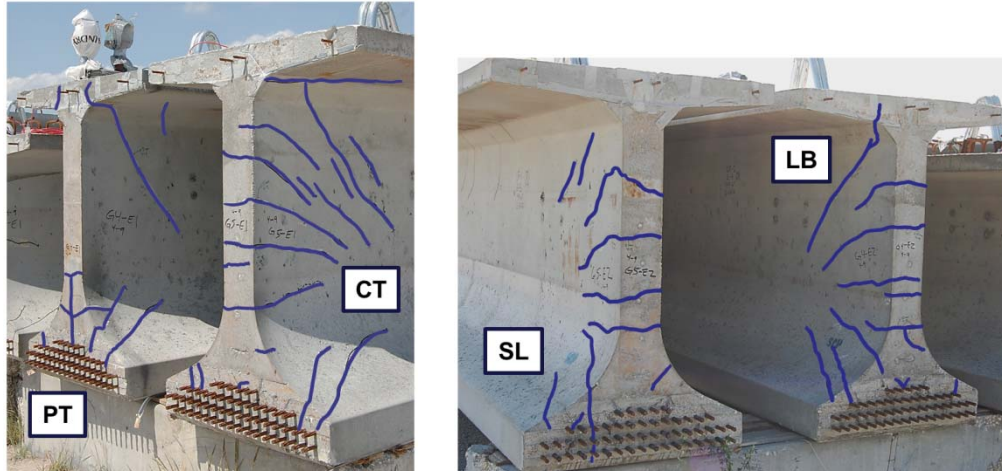


Figure 36–Photo of FIB-63 end region cracks (cracks enhanced in blue)

Web cracks away from the end of specimen PT extended diagonally into the web from the post-tensioning anchor plate. Forces introduced at the plate are believed to have contributed to the formation of the diagonal cracking in specimen PT. The diagonal web crack in PT had the greatest web crack width and the largest average web crack width (~0.006 in.), which was 30% greater than that of the control specimen.

Detailing of specimen PT had a negative effect on the bottom flange spitting cracks. Referring to Figure 36, it can be observed that PT was the only specimen to have a vertical splitting crack on the end surface. This crack is attributed to development of the post-tensioning rods in the bottom flange.

Specimen LB performed better than the control specimen in every metric except maximum crack width. Specimens LB and CT had the same maximum crack width of 0.008in. For LB, the total web crack length was 10% smaller and the average web crack width was 35% smaller than in the control specimen.

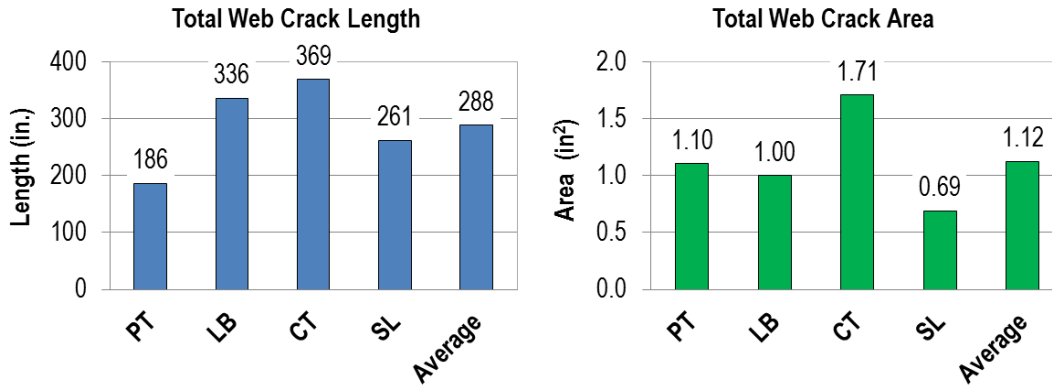


Figure 37–Web splitting crack length and area

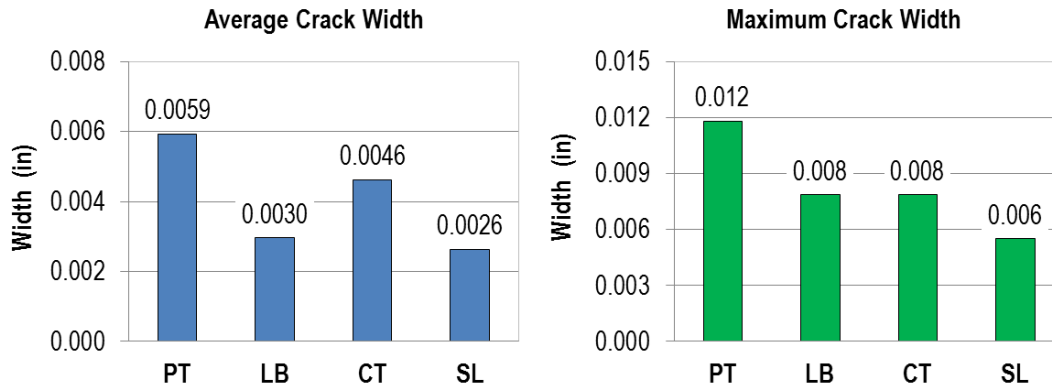


Figure 38–Web splitting crack widths

6.2.2 Load Tests

Specimens were load tested using the setup shown in Figure 34. Specimen LB was first to be tested. The primary variable in LB was the use of eight 1-in. diameter threaded rods as end region vertical reinforcement. LB supported a maximum shear force of 612kip. Peak load was controlled by a punching failure through the flange (Figure 39), which was caused by the orientation of the bearing pad at the load point. Pad orientation was rotated 90 degrees in subsequent tests to prevent this failure mode. Effect of end region detailing in LB on shear capacity could not be determined because of the punching failure in the top flange. In spite of the undesirable failure mode, LB still exhibited capacity that was approximately 20% greater than the code-calculated nominal shear capacity.

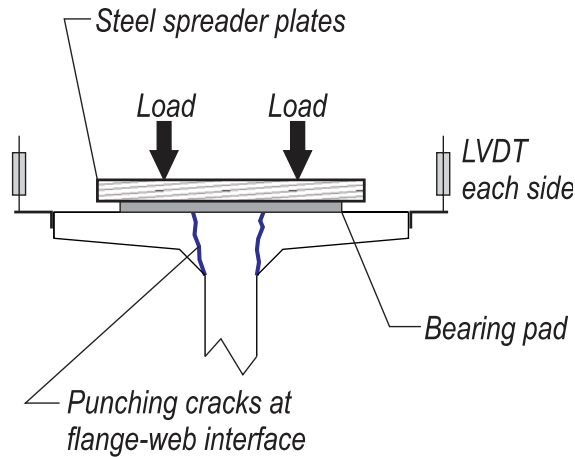


Figure 39–Punching failure specimen LB

The control specimen (CT) supported a maximum shear force of 791 kip. Peak load was controlled by failure of the web (Figure 40). After testing it was observed that the top hooks of the vertical reinforcement experienced breakout failure due to lack of sufficient cover (Figure 41). Top hooks from the vertical reinforcement were embedded in the relatively thin top flange because a topping slab was not cast on the specimen. It is not known if the hook failure precipitated or was a by-product of the web failure. The bearing pad at the load point also punched through the top flange at peak load (Figure 41). Capacity of CT exceeded the code-calculated nominal shear capacity by approximately 50%.

Specimen SL supported a maximum shear force of 609 kip, which is the smallest of any FIB-63 specimen. The primary variable in specimen SL was partial strand shielding of almost half of the prestressing strands. Failure of SL was categorized as a bond-shear failure. The reduced number of fully bonded strands in SL was culpable for the bond-shear failure and lower capacity. Specimens CT, LB, and PT had almost twice as many bonded strands and were less affected by cracks interrupting the strand development length. As such bond-shear failure did not occur in these other specimens.

Specimen PT supported a maximum shear force of 800 kip. The primary variable in PT was the presence of vertical post-tensioning in the end region. The capacity of the testing equipment was reached prior to failure occurring in specimen PT. As such, the controlling failure behavior could not be determined. Based on comparison with the control specimen (CT) it can be concluded that the end region post-tensioning did not adversely affect the shear capacity of specimen PT.

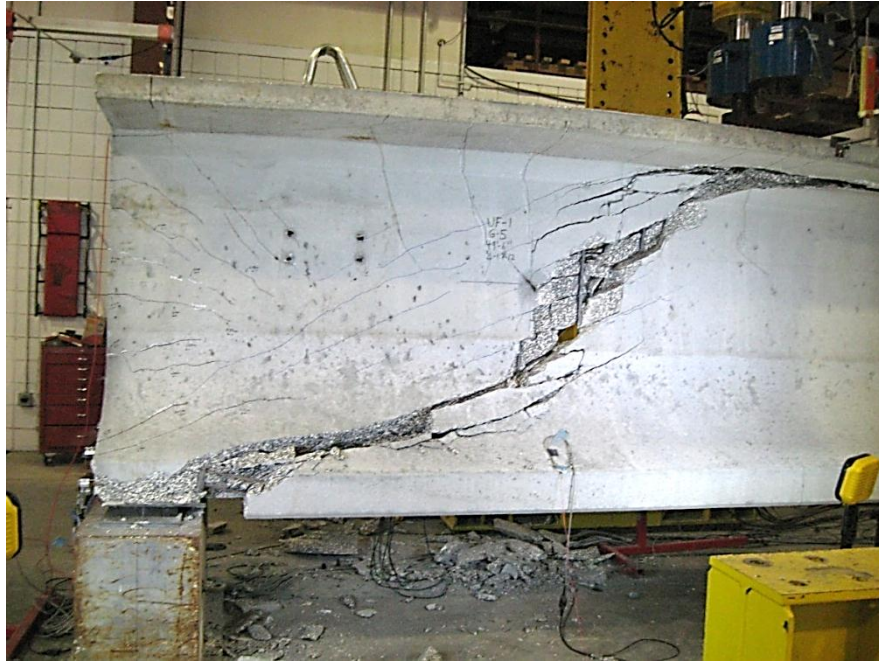


Figure 40–Specimen CT after load tests

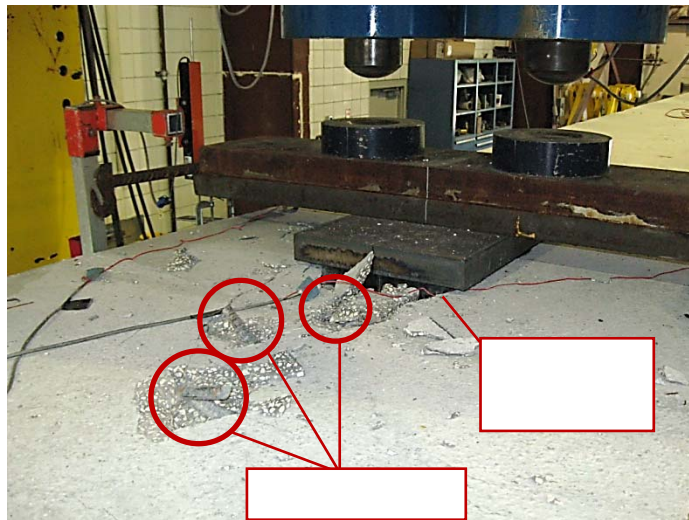


Figure 41–Hook breakout and load point punching failures

6.3 Conclusions

Four FIB-63 test specimens were fabricated and load tested to evaluate the effects of different end region detailing schemes on the control of web splitting cracks. Details in the test program included: 1) #5 vertical end region reinforcement per current FDOT standards (control specimen), 2) vertical reinforcement per FDOT and 45% partial strand shielding, 3) vertical end region post-tensioning, and 4) 1 in. diameter threaded rods as vertical reinforcement. Cracks and

strains were monitored during prestress transfer and in the weeks following transfer. These data were used to compare the relative effectiveness of each detailing scheme in controlling web splitting cracks. Finally, specimens were load-tested in 3-point bending to determine what, if any, effect the end region detailing had on shear capacity and behavior. Key observations and conclusions are as follows:

- Partial strand shielding was an effective means of controlling the length, and width of web splitting cracks. Of the 52 strands in specimen SL 45% were shielded within the end region. Shielding resulted in a 29% reduction in web crack length and a 43% reduction in average web crack width relative to the control specimen.
- Vertical post-tensioning of specimen PT prevented web splitting cracks at the end surface, but affected other web cracks away from the end and in the bottom flange. The largest web cracks in the test program occurred in specimen PT.
- All web cracks in the test program had widths equal to or less than 0.012in. Cracks above this width require corrective action based on FDOT requirements for moderate environments.
- Increasing the end region vertical reinforcement decreased the length and width of web splitting cracks. Specimen LB had 30% more vertical end region reinforcement than the control specimen, and had 10% less web crack length and 35% lower average web crack width.
- Experimental capacity of all specimens was greater than the ACI 318 and AASHTO LRFD calculated nominal shear capacities.
- Increased strand shielding in specimen SL resulted in a reduction in the experimental capacity of specimen SL. Because of strand shielding this specimen had insufficient fully bonded strands to prevent bond-shear failure after cracks formed in the above flange in front of the bearing.
- Vertical post-tensioning in the end region of specimen PT did not affect load capacity. Specimen PT supported the largest load of any specimen. Failure of PT could not be reached due to limitations of the testing equipment.
- Specimen LB experienced a punching shear failure in the top flange due to placement of the applied load. Consequently, the effect on load capacity of

increased vertical reinforcement (relative to the control) in specimen LB could not be evaluated. It is assumed that the additional vertical reinforcement would not have had negative effect.

7 Finite Element Analyses of End Region

FE (finite element) modeling was conducted to evaluate the behavior of the end region during prestress transfer and under applied loads. The FEA (finite element analysis) program Adina (2009) was used to conduct all modeling and analysis. All models were linear elastic and were intended to model the girder behavior prior to cracking. Strain gage and displacement data from the Small Beam and FIB-54 test programs were used to validate the FE models. The validated models were then used in parametric studies to evaluate variables that were not included in the experimental programs. A summary of the analyses are presented in this section. A more comprehensive presentation of the FE modeling is contained in Appendix F.

7.1 Analyses at Prestress Transfer

7.1.1 Model Configuration and Validation

Girder behavior during prestress transfer was evaluated using the FE model configuration shown in Figure 42. The end region was modeled with 27-node 3D solid elements. Beam elements were used away from the end region to reduce computation demand. Transition for solid element to beam elements was achieved using rigid shell elements and links. The FE model was linear-elastic and was intended to model end region behavior prior to cracking.

Prestressing forces were applied as point loads to nodes occurring at strand locations. Prestressing forces were applied over a transfer length of 17.5 in. from the member end. Only the prestressing forces were considered in the model, strands were not explicitly modeled. Loads, boundary conditions, and girder geometry were symmetric about the Z-Y axis as shown in Figure 42. This allowed for use of a half-symmetry model to reduce computation demand.

One critical feature of the model was that prestressing forces were applied sequentially as occurs in physical girders during prestress transfer. To match the transfer process used in the experimental programs, prestressing forces were applied from the outside-in. In this manner the stress and strain state of the end region could be evaluated at different stages of the prestress transfer process. Self-weight was applied using the ‘mass proportional’ load feature of ADINA.

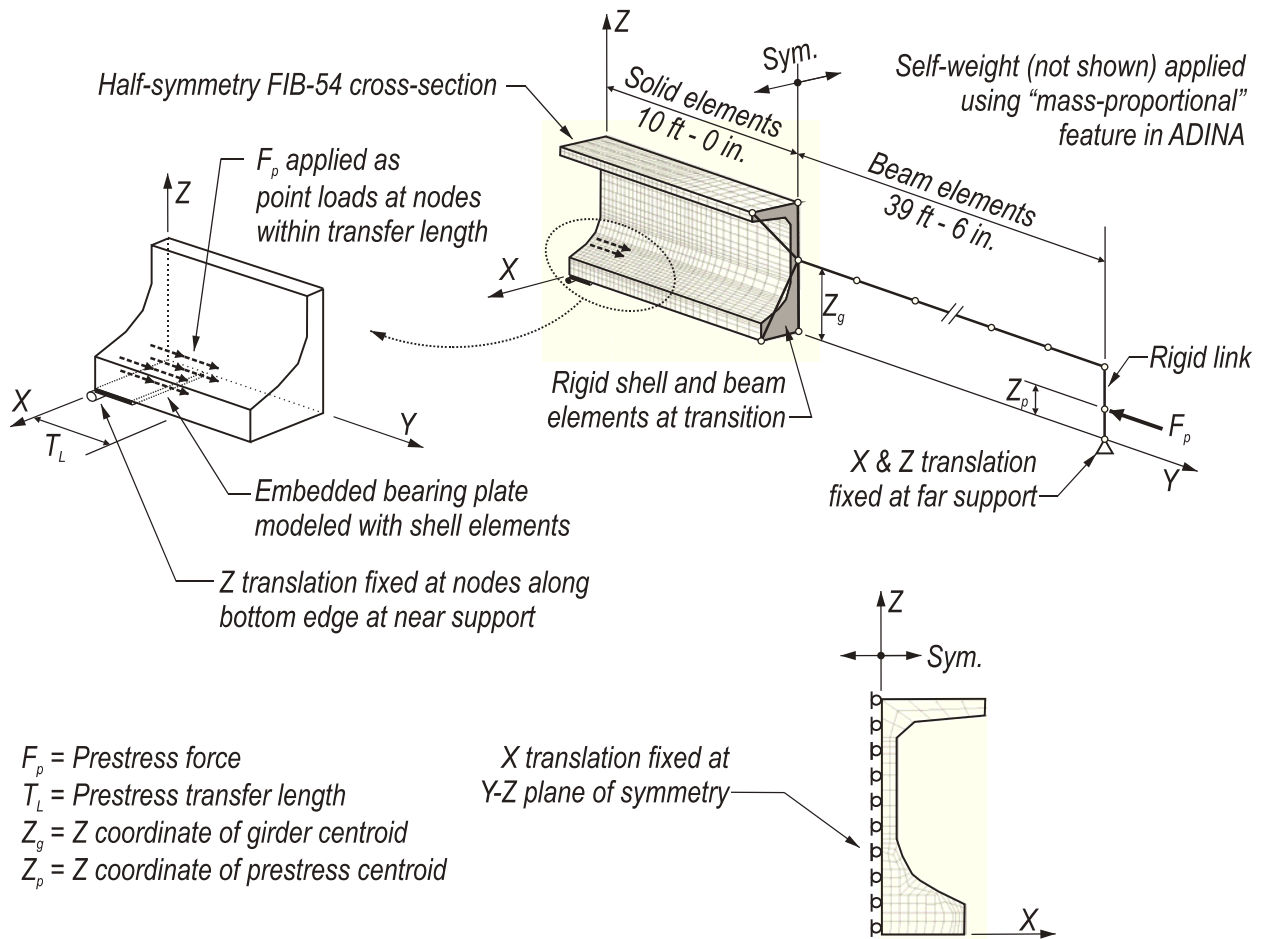


Figure 42–FE model details

The model configuration shown in Figure 42 was validated using experimental data from the FIB-54 test program. Two stages of prestress transfer were considered in the validation. Stage 1 corresponded to the condition when only the strands in the outer portions of the bottom flange had been released. Stage 2 corresponded to all strands being released. Partial results from the validation study are presented in Figure 43. In general the FE model did an excellent job of capturing the strain behavior at both of the stages considered. A mesh convergence study was also conducted to verify the adequacy of the mesh density. Based on the convergence study a mesh density of 2 in. was deemed adequate for the modeling conducted.

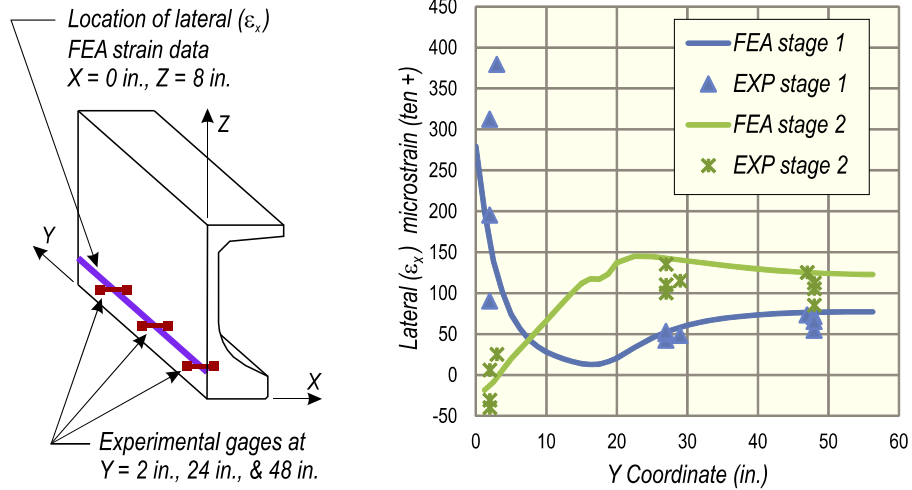


Figure 43–Comparison of experimental and FE model transverse (x-x) strain

7.1.2 Parametric Studies

After validation and verification the model shown in Figure 42 was used to conduct parametric studies of end region behavior during prestress transfer. Parameters included: stages of prestress transfer, steel bearing plates, and transfer length. Studies were also conducted to quantify the transverse stresses and forces at different locations in the bottom. Forces were calculated by integrating stresses over the section of interest as shown in Figure 44. Additional details of the integration procedure are presented in Appendix F.

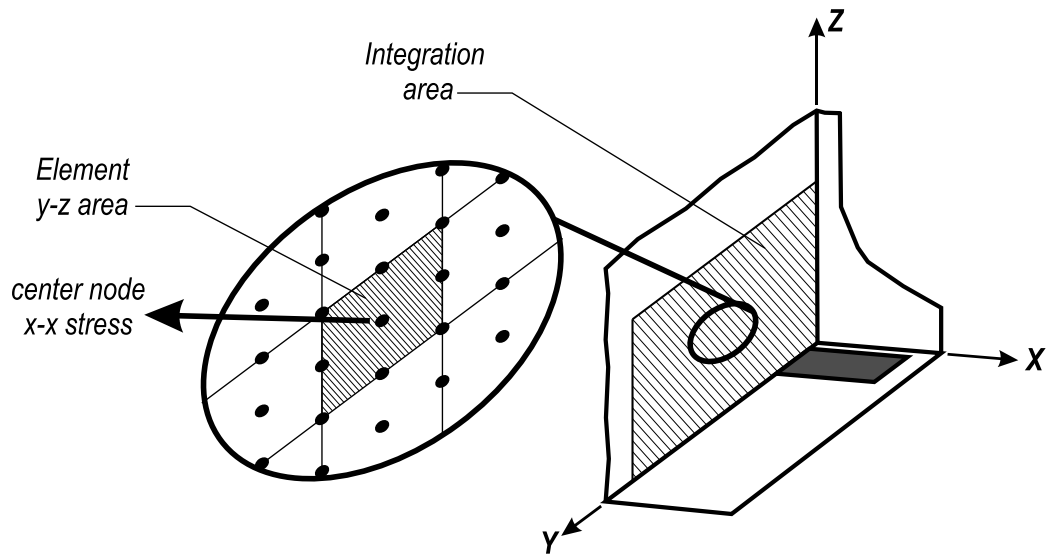


Figure 44–Element x-x stress and y-z area

Results of the strand release parametric study are presented in Figure 45 and Figure 46. In this study prestress forces were sequentially added to the model from outside-in, mimicking the prestress transfer process used in the experimental programs. The horizontal axis of Figure 46 is the percentage of the strands released at a given stage. The vertical axis is the normalized transverse tensile force occurring in the bottom flange above the bearing. Transverse force was obtained by integrating stresses such as those shown in Figure 45. Results indicate that the transverse force is greatest when only the outer strands are cut.

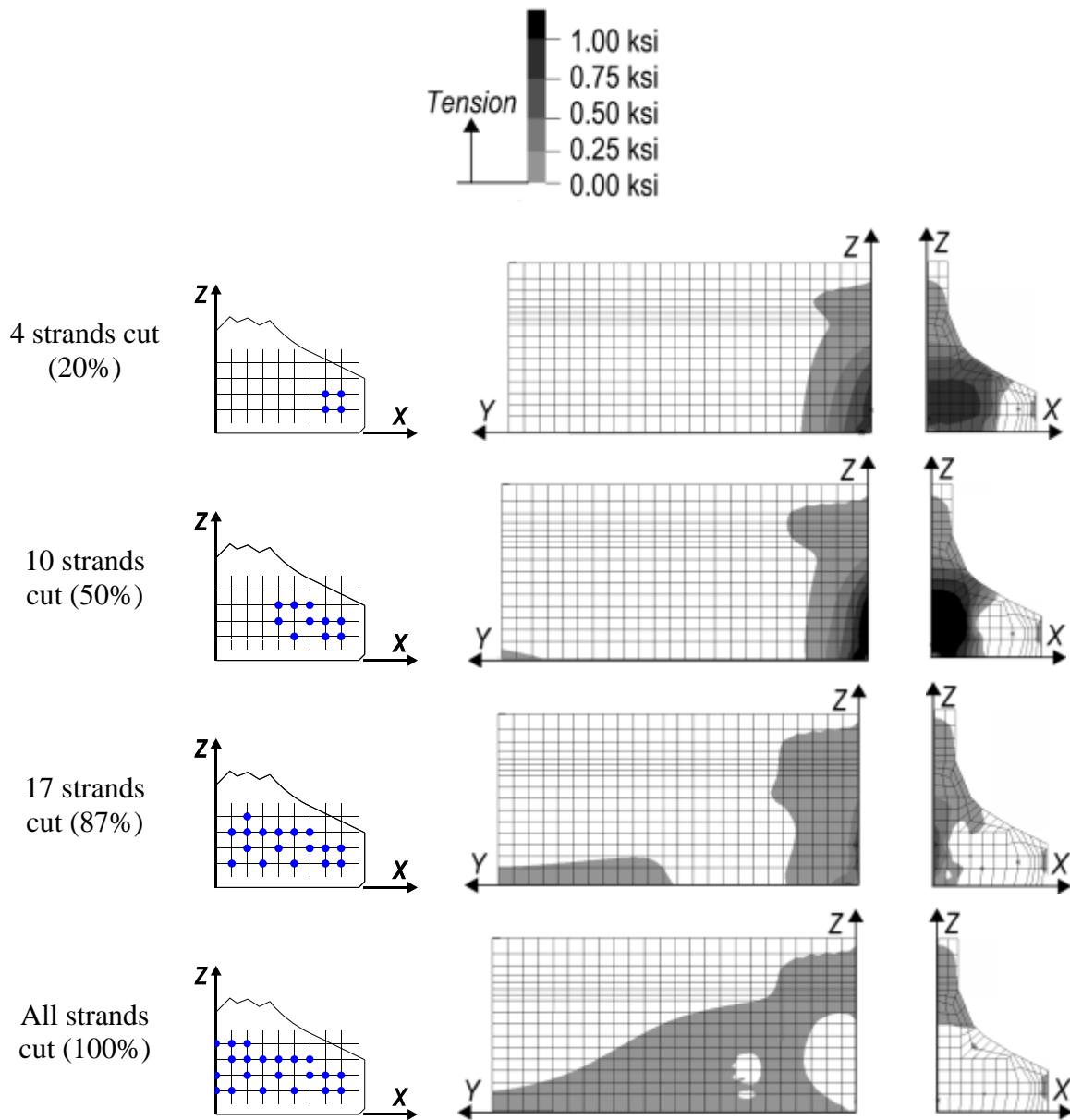


Figure 45–Transverse (x-x) stress at stages of prestress transfer

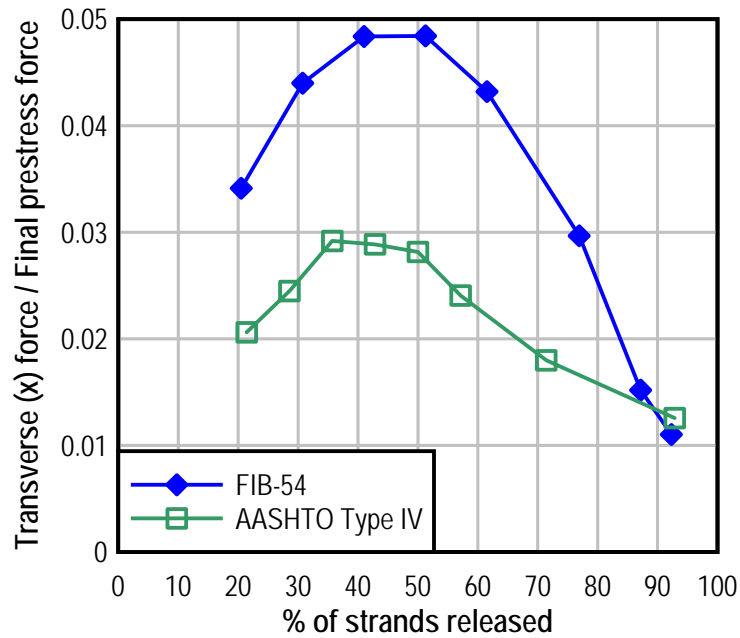


Figure 46–Transverse force variation as strands are released

Effects of transfer length were also studied by varying the length over which prestress forces were applied to the FE model. For each transfer length considered, the transverse force in the bottom flange was quantified using the procedures discussed previously in this section. Figure 47 shows that transverse tensile force in the bottom flange has an inverse linear relationship with transfer length. Shorter transfer lengths create the largest transverse forces.

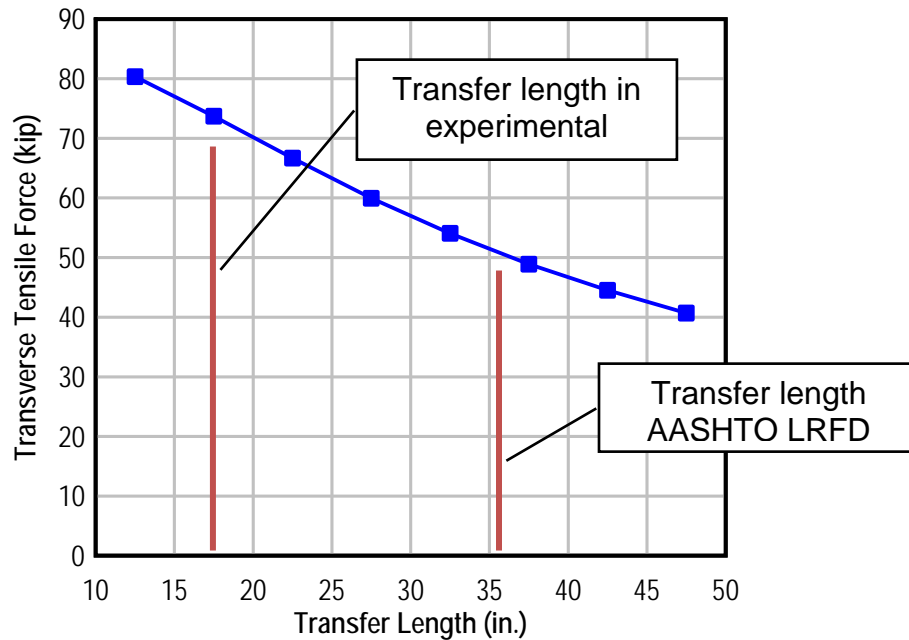


Figure 47–Transverse force variation with length of prestress transfer

7.2 Analyses during Loading

7.2.1 Model Configuration and Validation

End region behavior under applied loads was analyzed using the model shown in Figure 48. This model was similar to the one used to study behavior during prestress transfer (Figure 42), but had specific features to represent girders during load testing. Boundary conditions during the test programs consisted of reinforced neoprene bearing pads. This condition was modeled using a bed of spring elements spread over the bearing pad area. Girders in the test programs were loaded using hydraulic actuators acting on the top flange. This condition was modeled as a pressure load acting over an area similar to the load point in the test specimens.

The FE model was validated using data from the small beam test program. Partial results from the validation study are shown in Figure 49, which compares experimental strain data (black diamonds) with the strain calculated using the FE model. As shown in the figure, the FE model was in good agreement with the experimental data. A mesh convergence study was also conducted to verify the adequacy of the mesh density. Based on the convergence study, a mesh density of 1 in. was deemed adequate for modeling specimens from the small beam test program.

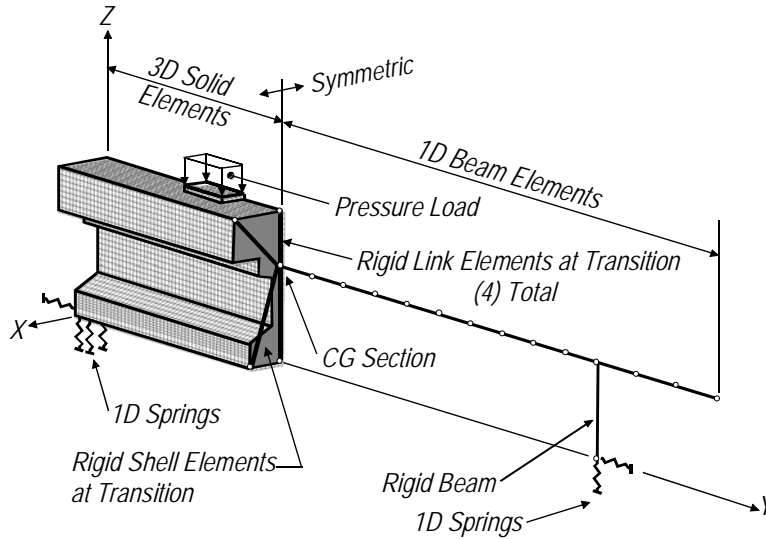


Figure 48–FE model configuration

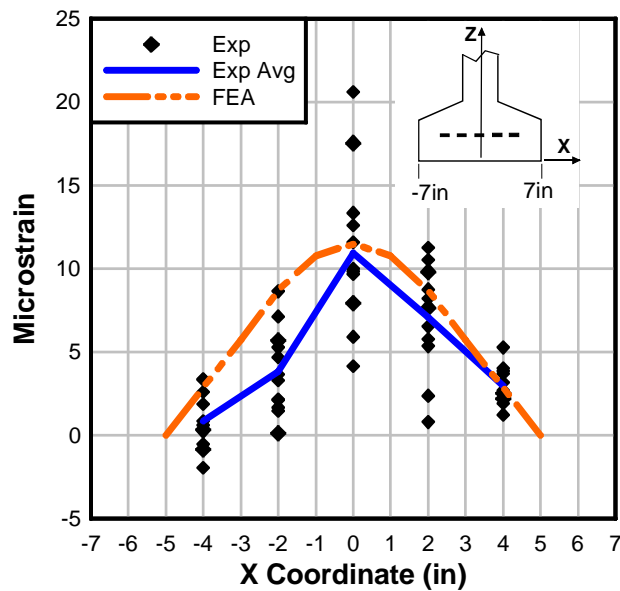


Figure 49–Small beam transverse (x-x) strain profile (V = 15 kip)

7.2.2 Parametric Studies

After validation and verification the model shown in Figure 48 was used to conduct parametric studies of end region behavior during loading. Parameters included: bearing pad width, bearing pad stiffness, and presences of steel bearing plates. Results of the study on bearing pad width are shown in Figure 50. The figure shows how the transverse strain changes as a function of the bearing width. When the bearing width is narrow (relative to the flange) the

maximum strain occurs at the mid height of the bottom flange. When the bearing width was wide the maximum strain occurred at the bottom of the bottom flange. Based on the parametric study it was determined that transverse strain in the bottom flange can be minimized when the bearing pad width is approximately 60% of the flange width. Narrow bearing widths, however, may adversely impact the stability of the girder during construction.

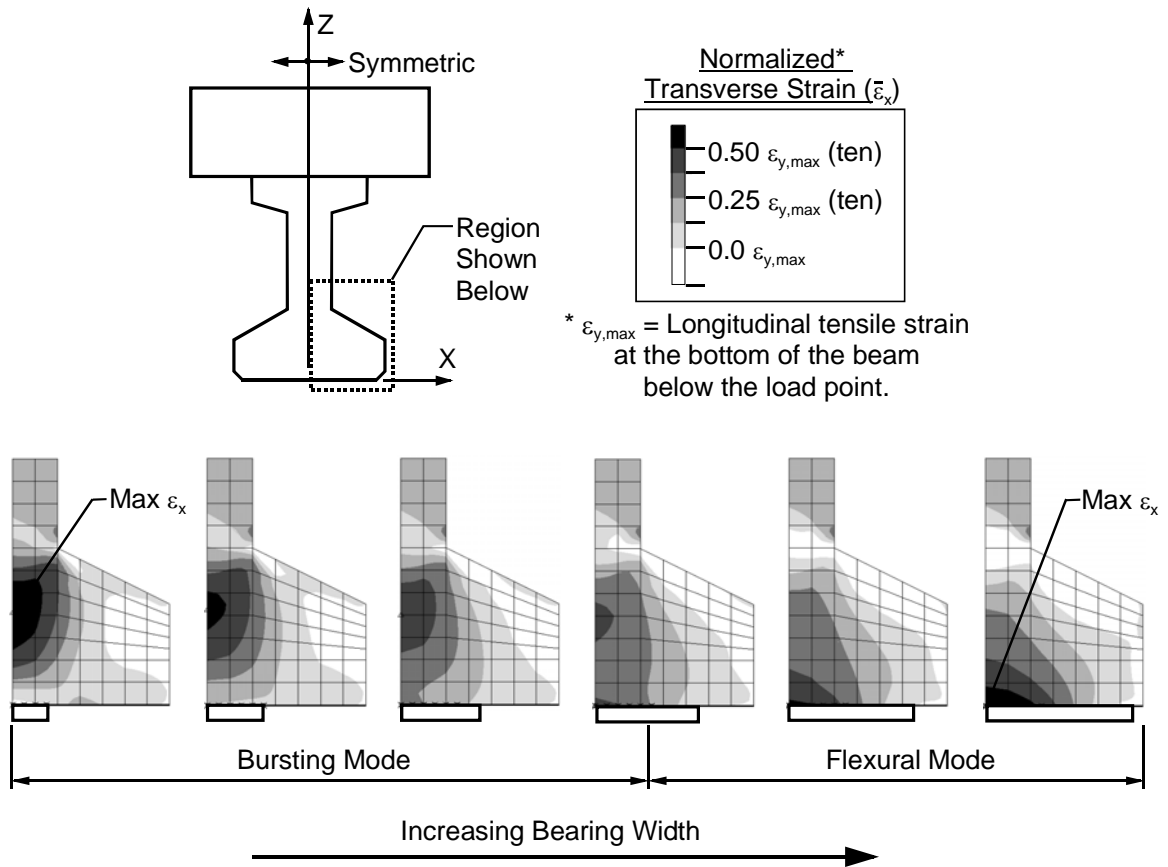


Figure 50–Normalized transverse (x-x) strain vs. bearing pad width, small beam

7.3 Conclusions

Linear-elastic FE models were used to evaluate the effects of prestressing forces and applied loads on the behavior of I-girder end regions. Models were validated using experimental data and were verified through convergence studies. Analyses are discussed in greater detail in Appendix F. The following is a partial list of conclusions regarding behavior during prestress transfer:

- Embedded steel bearing plates carry transverse tension during and after prestress transfer. In the linear-elastic range, plates in FIB girders carry 10% of the tension force due to prestressing. Load testing indicated that the bearing plate carries a significantly greater proportion of the transverse tensile force at ultimate capacity. The portion carried by the plates does not vary during different stages of strand cutting.
- Transverse stress and forces are inversely proportional to strand transfer length. Thus the greatest transverse effects occur in girders with the shortest transfer lengths. A 50% reduction in transfer length causes an increase of approximately 50% in transverse tension.
- During prestress transfer, the maximum transverse tensile stress on an arbitrary vertical line through the bottom flange occurs when only the strands outboard (closer to edge) of the line have been cut. Cutting of strands along or inboard (closer to centerline) of a line relieve tensile stresses on that line.
- Self-weight reaction produces transverse tension forces in the bottom flange above the bearing. For Florida I-beams, the transverse tension force due to self-weight equals 28% of the reaction.

Conclusions were also made with regard to end region behavior due to applied loads:

- For the range of stiffness values reported for neoprene bearing pads, variations in pad shear stiffness have negligible effect ($< 0.1\%$) on the transverse strain in the end region. However, variations in pad axial stiffness can change the transverse strain by $\pm 3\%$.
- Depending on the width of the bearing pad, two types of strain distributions (behaviors) occur in the end region of I-girders. A behavior denoted as ‘bursting’ occurred when the bearing pad width was narrow, and the transverse strain was distributed in a bottle-shaped manner. However, ‘flexural’ behavior occurred when the pad width was large, and transverse strain was dominated by flexural strains in the flange.
- The transition between ‘bursting’ and ‘flexural’ behavior occurred when the bearing pad width was approximately equal to 60% of the bottom flange width. This pad width also corresponded to the minimum transverse tensile strain.

- Steel bearing plates reduced the magnitude of transverse strain in the concrete adjacent to the plate, but the strain dissipates significantly with increasing distance from the plate. This effect was most pronounced when the bottom flange was acting in the ‘flexural’ mode.
- For the applied loads in the analytical study the transverse force in the bottom flange was approximately 25% of the reaction force.

8 End Region Design Models

AASHTO LRFD contains prescriptive requirements for the quantity and placement of confinement reinforcement located in the bottom flange of pretensioned concrete I-girders. A rational model for designing confinement reinforcement was developed as an alternative to the prescriptive requirements of AASHTO LRFD. The model considers a wide range of conditions and variations, yet is intended to be practical enough for use by bridge design engineers. The model is based on the ultimate strength limit state and specifically focuses on preventing lateral-splitting failures.

In addition to ultimate strength, serviceability of I-girder end regions must also be considered. Experimental and analytical research presented in previous sections has demonstrated that transverse tensile stress in the bottom flange of pretensioned I-girders can lead to flange splitting cracks during fabrication. A serviceability design model was developed for quantifying bottom flange splitting stress. Stress from the model can be compared to concrete tensile capacity to determine the likelihood of bottom flange splitting cracks.

Detailed derivations of the confinement reinforcement and serviceability models can be found in Appendix G.

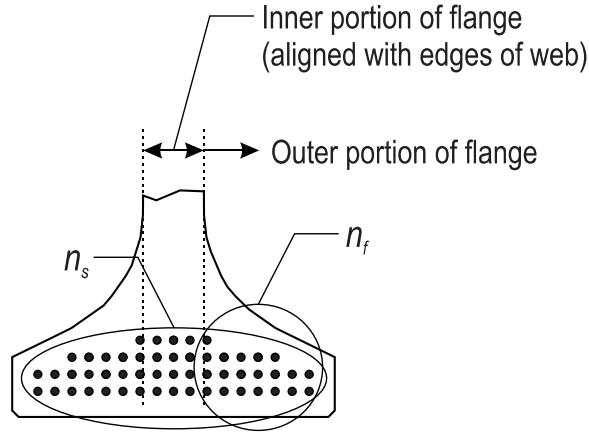
8.1 Confinement Reinforcement Design Model

Experimental and analytical work from the previous sections has shown that confinement reinforcement carries transverse tension forces due to prestressing and applied loads. By carrying these forces the confinement reinforcement functions to prevent lateral-splitting failure and provides a normal force whereby strand tension forces can be transferred to the concrete after strut-and-tie behavior has initiated. The confinement reinforcement design model was created to address each of these functions. Forces generated due to these functions are referred to as the transverse tie force (F_{TTu}), and the strand anchorage force (F_{SAu}). An equation for calculating F_{TTu} was derived using strut-and-tie modeling:

$$F_{TTu} = R_u \left(\frac{n_f}{n_{strands}} \right) \left[\frac{(b_f - b_w)}{3t_f} - 3.1 \left(\frac{W_b}{b_f} \right) + 3 \right] \quad 8-1$$

Where:

- R_u = Factored reaction force
- n_f = Number of strands in the outer portion of the flange (Figure 51)
- $n_{strands}$ = Total number of strands
- b_f = Bottom flange width
- b_w = Web width
- t_f = Minimum thickness of bottom flange
- W_b = Width of bearing pad



- n_s = total number of fully bonded strands in bottom flange
- n_f = number of fully bonded strands in outer portion of flange (one side only)

Figure 51—Definition of number of strands in outer portion of flange n_f

An equation for F_{SAu} was derived using a shear-friction model:

$$F_{SA} = \frac{A_{ps} f_{pe} n_c}{\pi \mu} \quad 8-2$$

Where:

- A_{ps} = Cross-section area of all prestressing strands
- f_{pe} = Effective prestress
- n_c = Number of strands along critical section
- μ = Coefficient of friction between concrete and strand, taken as 0.4

The model requires that the confinement reinforcement be designed for a factored tension force taken as the greater of F_{TTu} and F_{SAu} :

$$F_{CRu} = \text{maximum} (F_{SA}, F_{TTu}) \quad 8-3$$

Where:

F_{CRu} = Factored design force in confinement reinforcement

The quantity of confinement required at ultimate load is equal to the confinement reinforcement design load divided by the specified yield stress of the reinforcement:

$$A_{CR} = \frac{(F_{CRu})}{f_{yCR}} \quad 8-4$$

Where:

A_{CR} = Required area of confinement reinforcement

f_{yCR} = Yield stress of confinement reinforcement

Results from the experimental program demonstrate that confinement reinforcement is most effective when placed near the end of the girder. As such, confinement reinforcement required by Equation 8-4 should be placed as close to the end of the girder as reasonable, but should also be placed over a distance of at least the transfer length.

Where bearing plates are provided the model allows the cross-sectional area of the bearing plate to account for up to 50% of the required confinement reinforcement.

The design model was compared to data from the small beam and FIB-54 experimental programs as well as to experimental results published in the literature. Figure 52 compares confinement reinforcement installed in each test girder with the required confinement reinforcement calculated using the proposed model (Equation 8-4). The factored reaction force used to calculate the transverse tie force (F_{TTu}) was taken as the nominal shear strength. Provided confinement reinforcement, plotted on the vertical axis, was taken as the area of confinement reinforcement placed within the transfer length. If present, the embedded steel bearing plate area was allowed to contribute up to 50% of the confinement requirement. Prestress losses were assumed to be 20 percent.

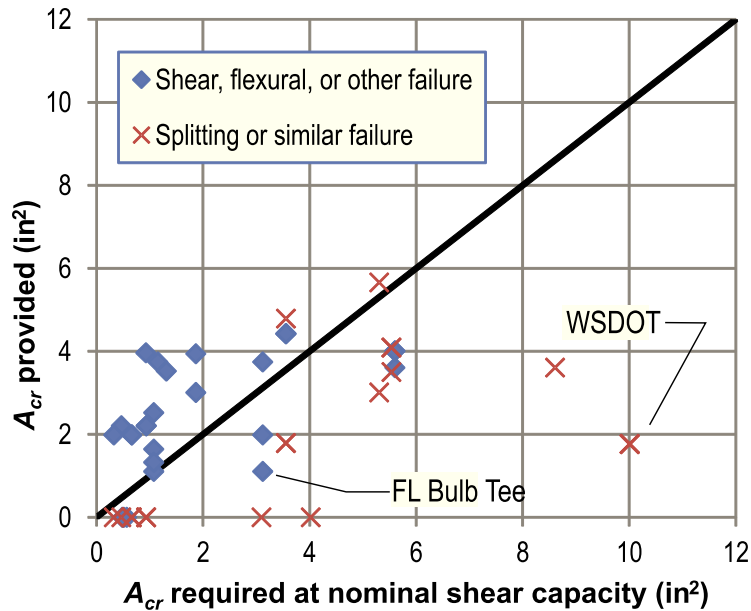


Figure 52–Design model compared to nominal strength of experimental girders

Points below the solid line have less confinement than calculated by the model, and were predicted by the model to fail due to splitting or lateral-bursting. The proposed model correctly identified all but two of the specimens that failed in lateral-splitting, bearing, or similar modes. Splitting and similar failures are denoted by the ‘X’ markers. The model incorrectly predicted failure in eight cases, as denoted by the diamond shaped markers below the solid line. In most cases where the failure mode was not accurately predicted, the provided confinement reinforcement was within 1.5 in² of the calculated requirement, indicating a desirable degree of conservatism in the model.

8.2 Serviceability Model

Experimental results from the FIB-54 and FIB-63 test programs demonstrate that splitting cracks can form in the bottom flange of I-girders due to prestressing forces. A model was developed for calculating tensile stresses that cause the flange splitting cracks. The following phenomena lead to transverse tensile stresses and are thusly considered in the serviceability model:

- Hoyer effect
- Eccentric prestress forces
- Self-weight reaction

Concrete stresses due to eccentric prestress forces are referred to in the design model as “peeling stress”. This term was selected because the eccentric prestress forces act to “peel” the outsides of the bottom flange away from web (Figure 28). Concrete stresses due to the Hoyer effect are referred to as “Hoyer stress.”

FE modeling (Appendix H) has shown that self-weight reaction stresses (due to Poisson’s effect) at the end surface of FIB girders can be neglected at locations in the outer portion of the bottom flange. As such, stress due to self-weight was assumed to be zero for comparison of the serviceability model with experimental results from the FIB-54 and FIB-63 test programs. This assumption may not be reasonable for all cross-sections.

Vertical splitting cracks can occur at multiple locations in the bottom flange (Figure 53). Derivation of the serviceability model focused on splitting cracks through the outer portion of the flange. Bottom flange splitting cracks below the web were not considered because they are associated with extreme strand bond patterns that are not permitted in FDOT production girders.

An outside-in strand release pattern is commonly used in FDOT production girders. As such, this is the pattern considered in the serviceability model. The model does not apply to girders with other strand release patterns.

Two critical conditions (Figure 54) are considered in the design model:

- **Maximum Peeling.** The FIB-54 experimental program (Appendix D) and finite element modeling (Appendix F) have shown that the maximum peeling stress along a given section occurs when only the outboard (closer to the outside edge) strands are cut. This condition is referred to as the “maximum peeling” condition.
- **Combined.** This condition occurs when strands along a given section are cut and Hoyer stresses are superimposed with peeling stress. It is referred to as the “combined” condition.

The model does not consider stress conditions when inboard (closer to the centerline) strands have been cut. FE modeling (Appendix F) has shown that cutting of inboard strands reduces peeling stresses at the end of a girder.



Figure 53–Flange splitting in experimental girder

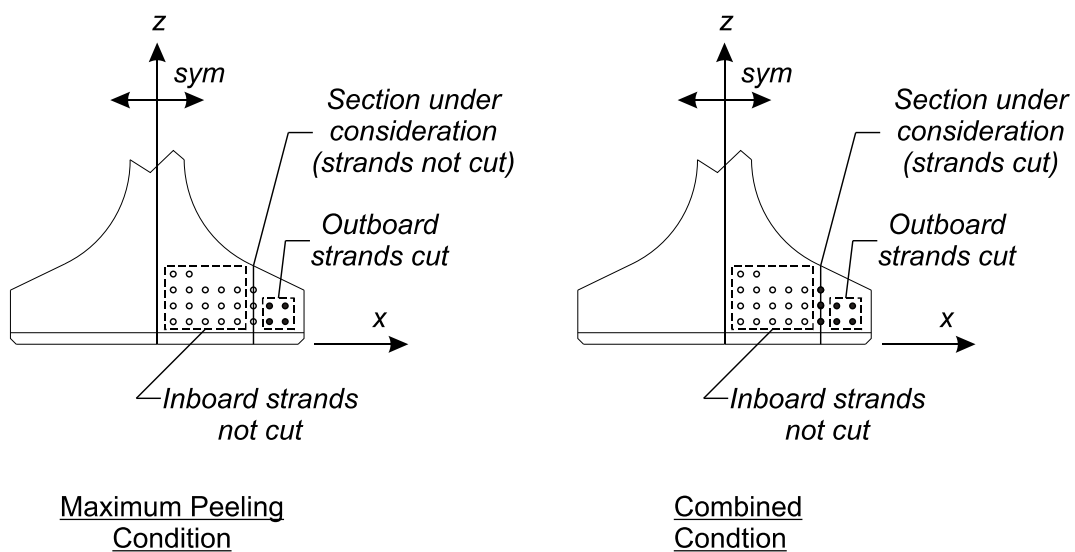


Figure 54–Strand release conditions

The serviceability model can be used to calculate average stress at the end of a girder along a vertical line through the flange. For FIB girders, the model can be used to calculate average stress at the member end along lines A through E as shown in Figure 55. The worst stress along any of these lines, and for either of the critical stress conditions (maximum peeling or combined), is the governing stress that should be used for comparison with the concrete tensile capacity.

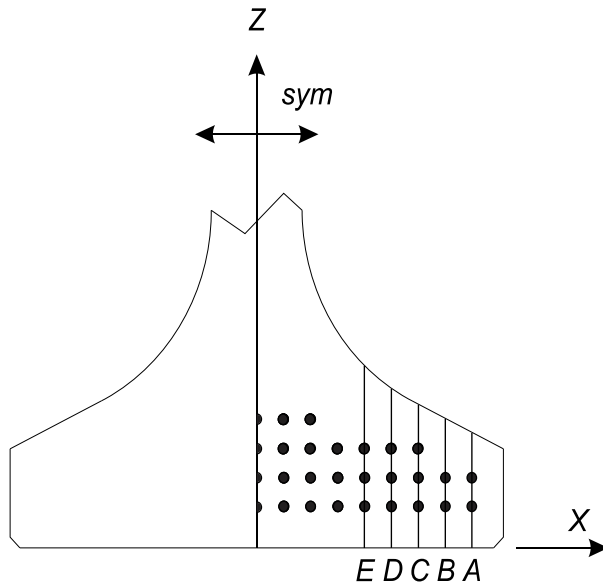


Figure 55–Analysis sections for FIB bottom flange

Peeling stress calculations are based on the free body diagram shown in Figure 56. This figure shows peeling stresses at the end of the member that result from an internal moment in the bottom flange. The internal moment is created by eccentricity between the applied prestressing force and the resultant axial force. Additional details and justification for this approach are given in Appendix G. Equation 8-5 was derived from the free body diagram and can be used for calculating peeling stresses at the end of a member.

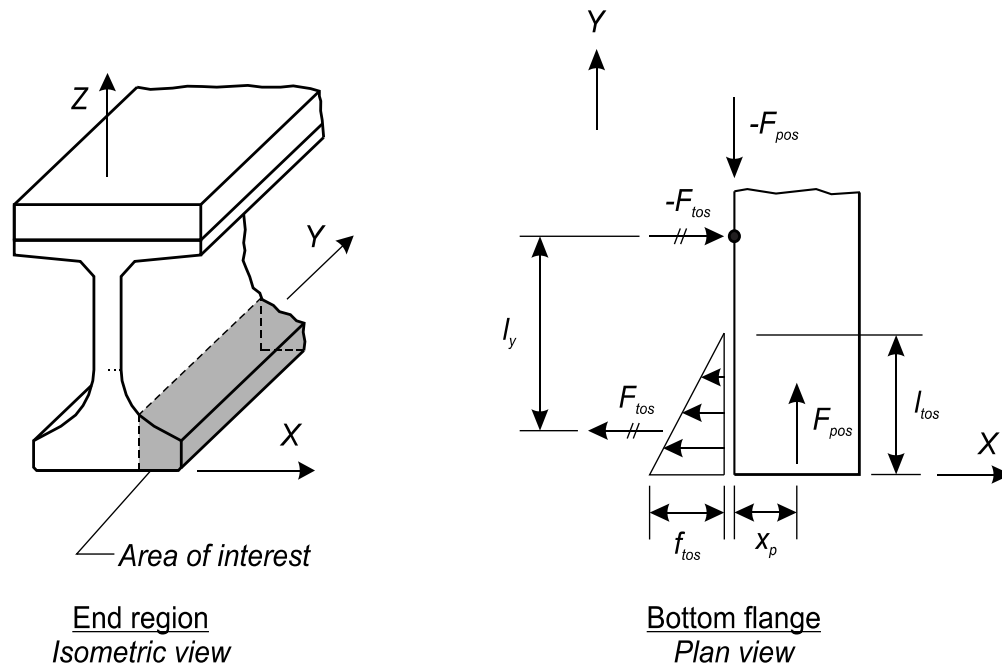


Figure 56–Bottom flange free body diagram

$$f_{tos} = \frac{2F_{pos}x_p}{l_y l_{tos}(h_f - n_{st}d_b)}$$

8-5

Where:

- f_{tos} = Peeling stress at location under consideration
- F_{pos} = Prestressing force from strands outboard of cut plane
- x_p = Distance from cut plane to centroid of prestressing force
- l_y = Internal moment arm in y-direction (see Appendix G for equations)
- l_{tos} = Length of the assumed tensile stress distribution
- n_{st} = Quantity of all strands along location under consideration
- d_b = Diameter of prestressing strands

Hoyer stress calculations are based on a model derived by Oh et al. (2006). The Oh model considers constitutive and geometric properties of steel and concrete as well as the level of prestressing. Building on the Oh model, Equation 8-6 was derived for calculating Hoyer stresses. Stress calculated by this equation is the average stress on a vertical line through the bottom flange at the end of a member. Stressing 0.6-in. diameter strands to 75% f_{pu} causes a 0.21% decrease in strand radius.

$$f_h = \frac{n_s d_b}{(h_f - n_{st} d_b)} \left[\frac{r_o - r_j}{(1 - \nu_p) r_o / E_p + (\nu_c + 1) r_j / E_c} \right]$$

Where:

- f_h = Average stress at location under consideration due to Hoyer Effect
- n_s = Quantity of fully bonded strands along location under consideration
- d_b = Diameter of prestressing strand
- h_f = Thickness of flange at location under consideration
- n_{st} = Quantity of all strands along location under consideration
- r_o = Strand radius before pretensioning
- r_j = Strand radius immediately after pretensioning
- ν_p = Strand Poisson ratio
- E_p = Strand Elastic Modulus
- ν_c = Concrete Poisson ratio
- E_c = Concrete Elastic Modulus

Stresses calculated using the serviceability model correlate well with flange crack data from the FIB-54 and FIB-63 test girders (Figure 57). This can be seen from the linear curve in Figure 57 that is fit to the stress and crack data. The line has an R^2 value of 0.85, indicating a high degree of correlation between calculated stresses and experimental crack lengths. Considering the random nature of cracking in concrete, this level of correlation suggests that the model does an excellent job of capturing the physical phenomenon which cause bottom flange splitting cracks.

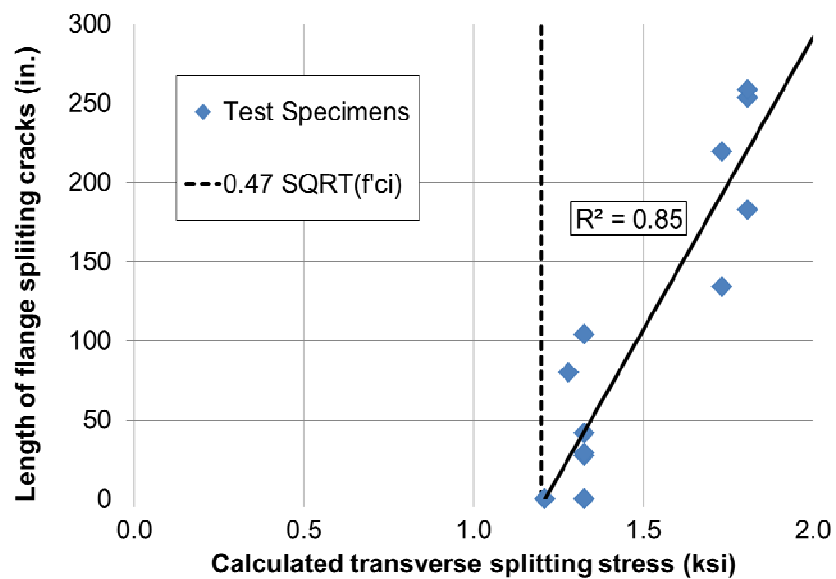


Figure 57–Calculated transverse splitting stress vs. experimental crack length

8.3 Ultimate Strength Design of Confinement Reinforcement

The ultimate strength model derived previously can be used for AASHTO LRFD design using 8-7:

$$\phi A_{CR} f_{yCR} = F_{CRu} \quad 8-7$$

Where:

A_{CR} =	Required area of confinement reinforcement
f_{yCR} =	Yield stress of confinement reinforcement
ϕ =	Resistance factor

The required area of confinement reinforcement is such that the confinement reinforcement must provide a design strength greater than the force generated by the strand anchorage or the transverse tie. The resistance factor should be determined using the AASHTO LRFD reliability analysis of the limit states. In lieu of this it is reasonable to treat this reinforcement the same as tension steel in an anchorage zone ($\phi = 1.0$).

8.4 Conclusions

Models were derived for designing confinement reinforcement and for calculating transverse tensile stresses in the bottom flange of I-girders. The confinement reinforcement model can be used to design confinement reinforcement to resist lateral-splitting failure at ultimate load. The tensile stress model can be used to determine the likelihood of flange splitting cracks at the serviceability limit state. Both models were found to compare favorably with experimental data.

9 Recommendations

Based on the literature review, experimental, and analytical work detailed in this report, the following recommendations are made:

Load rating of lightly reinforced sections similar to SR-72 girders:

- The experimentally determined shear capacities should be considered when evaluating girders similar to the SR-72 test girders. Experimental capacities of interior girders were approximately 70% larger on average than capacities calculated by ACI 318 and AASHTO LRFD methods.
- Concrete shear contribution, as calculated by ACI 318 or AASHTO LRFD methods, are recommended for estimating the cracking load of girders similar to the SR-72 test girders. Concrete contribution as calculated by ACI 318 and AASHTO methods were, respectively, 17% and 32% lower than the experimental cracking loads.
- Strength contribution from integral curbs and barriers can be conservatively neglected when analyzing members similar to the SR-72 test girders. Should evaluations show that contribution of curbs is critical, it is noted that exterior girders with integral curbs had 30% greater shear capacity than similar interior girders without curbs. Test girders with curbs also exhibited increased stiffness over interior girders.
- Evaluations of members similar to the SR-72 test girders should consider the possibility of prestressing forces up to 50% lower than the specified prestress. The large difference between the specified and experimental values may indicate quality control issues in addition to higher than expected losses.

Confinement reinforcement and bearing plates in precast/pretensioned I-girders:

- The end region design procedures developed as part of this research provide a rational approach for designing confinement reinforcement for both service and strength conditions. Full scale testing and the end region design provisions indicate that the current FDOT confinement reinforcement is adequate for girders up to at least FIB-63. The current detail places #3 confinement reinforcement at 3.5-in. spacing over a distance approximately $0.3d$ from the member end and at 6-in. spacing over a distance approximately $1.5d$ from the end. The current detail also includes an embedded steel bearing plate at each member end.
- In special cases where additional bottom flange crack control or lateral-splitting capacity is required, #4 bars should be used for confinement reinforcement in lieu of the currently specified #3 bars. Such cases may include: girders with factored reaction forces larger than the experimental capacities from the test program, girders in aggressive environments wherein flange cracking is a critical durability concern, girders with partially bonded strands clustered below the web, and/or girders without embedded steel bearing plates.

- Embedded steel bearing plates performed well in the research program and are recommended for continued use. Bearing plates utilizing the current FDOT design standards improved the test girders with respect to serviceability and strength criteria.
- Use of longer studs on bearing plates is recommended for future research. It is believed that longer studs will engage a greater portion of concrete, thereby providing additional confinement to the bottom flange. Wider (in the direction of the span length) bearing plates are also recommended for future research. Wider bearing plates may prevent cracking near the member end, and thereby improve bond-shear capacity.

Strand and partial debonding patterns:

- Fully bonded strands should be placed as close to the cross-section centerline and with as much top cover as practical. This practice will reduce the likelihood of bottom flange splitting cracks forming and propagating during and following prestress transfer. In addition, the potential that lateral-splitting failure will control the shear strength will be reduced.
- Current AASHTO LRFD limits on termination of strand shielding at a given section are recommended for controlling flange splitting cracks within the transfer length of partially shielded strands. Confinement reinforcement is believed unnecessary at these locations if shielding termination complies with the AASHTO LRFD limits.
- Although further research is needed, this project has demonstrated that the percentage of shielded strands can reasonably exceed the 25% limit currently specified by AASHTO LRFD if sufficient reinforcement and strands are provided to meet minimum longitudinal steel requirements at the girder end. As currently specified by AASHTO LRFD, any lack of full development must be considered when evaluating the minimum longitudinal steel.
- Partially shielded strands (when used) should be placed towards the outside of the bottom flange. Clustering of shielded strands below the web is strongly discouraged.
- Prestress force in the outermost strands in the bottom two rows should be reduced from the currently specified level for the FIB sections. A prestress force of 10 kip is recommended in order to support reinforcement during fabrication. This practice will reduce the likelihood of bottom flange splitting cracks and lateral-splitting failure.

End region detailing to prevent/control lateral web splitting cracks:

- The current FDOT detail for vertical end region reinforcement is recommended for continued use. In spite of high stresses in the end region of the test specimens, the FDOT detail kept crack widths within the FDOT acceptance criteria for moderate environments.
- Strand shielding is recommended for use in controlling end region stresses and web splitting cracks. Negative effects of shielding on end region capacity and cracking load must be considered when utilizing strand shielding to control web cracks.
- The post-tensioning detail used in the FIB-63 test program is not recommended for use in its current form. Issues with this detail included cracks propagating from the post-tensioning bearing plate and vertical cracking from the end of the bottom flange due to development of the post-tensioning rods.
- Increasing the area of vertical reinforcement in the end region beyond the current FDOT level is recommended when circumstance warrant. The use of 1-in. diameter all-thread

rods is recommended as a means of increasing the area of vertical reinforcement. If used, heavy nuts should be placed top-and-bottom of the rods to aid in development. One option is to anchor bars by threading into tapped holes in bearing plate or nuts welded to top of plate surface.

- Horizontal reinforcement in the end region was omitted from FDOT standard details beginning with the 2010 interim design standard. The decision to omit horizontal reinforcement was validated by the experimental program. Experimental capacity of girders with and without horizontal end region reinforcement differed by a marginal 2%.

10 References

- American Association of State Highway and Transportation Officials (2007), *AASHTO LRFD Bridge Design Specifications* 4th Edition." Washington, D.C.
- American Association of State Highway and Transportation Officials (2010), *AASHTO LRFD Bridge Design Specifications* 5th Edition." Washington, D.C.
- ACI (2008), *Building Code Requirements for Structural Concrete and Commentary ACI 318-08*, American Concrete Institute, Farmington Hills, MI.
- ACI (2011), *Building Code Requirements for Structural Concrete and Commentary ACI 318-11*, American Concrete Institute, Farmington Hills, MI.
- ADINA R&D Inc. (2009), ADINA version 8.6. Watertown, MA.
- Aknoukh, A. (2010), "The Effect of Confinement on Transfer and Development Length of 0.7 Inch Prestressing Strands," Concrete Bridge Conference. Phoenix, AZ.
- ASCE-ACI Task Committee 426. (1973), "The Shear Strength of Reinforced Concrete Members." *Journal of the Structural Division*, 99(6), pp. 1091-1187.
- Barnes, R., Burns, N., and Kreger, M. (1999), *Development Length of 0.6-Inch Prestressing Strand in Standard I-Shaped Pretensioned Concrete Beams* Rep. No. 1388-1, Texas Department of Transportation, Austin, TX.
- Breen, J., Burdet, C., Sanders, D., and Wollmann, G. (1991), *Anchorage Zone Reinforcement for Post-Tensioned Concrete Girders*, National Highway Cooperative Research Program. Transportation Research Board. Washington, D.C.
- Castrodale, R.W., Lui, A., and White, C.D. (2002), "Simplified Analysis of Web Splitting in Pretensioned Concrete Girders." *Proceedings, PCI/FHWA/NCBC Concrete Bridge Conference*, Nashville, TN, October 6-9.
- CEB-FIP (1993), *International Recommendations for the Design and Construction of Concrete Structures*, Comité Euro-International du Béton, Thomas Telford, London.
- Chong, O. and Arthur, P. (1987), "Ultimate Strength of Uniformly Loaded Reinforced Concrete T-Beams." *Structural Engineer, Part B: R&D Quarterly*, 65B(1), pp 10.
- Consolazio, G., Fung, J., and Ansley, M. (2004), "M- ϕ -P Diagrams for Concrete Sections Under Biaxial Flexure and Axial Compression," *ACI Struct.J.*, 101(1), pp 114-123.

Cook, R. and Reponen, M. (2008), *Prevention of Splitting Failure at the Ends of Prestressed Beams during Fabrication*, Rep. No. BD545-30. Florida Department of Transportation, Tallahassee, FL.

Crispino, E.D. (2007), *Anchorage Zone Design for Pretensioned Bulb-Tee Bridge Girders in Virginia*, Thesis, Virginia Polytechnic Institute and State University, Blacksburg, VA, 155 pp.

Csagoly, P. (1991), *A Shear Moment Model for Prestressed Concrete Beams*, Rep. No. 9900-1550, Florida Department of Transportation, Tallahassee, FL.

Davis, R.T., Buckner, C.D., and Ozyildirim, C. (2005), "Serviceability-Based Design Method for Vertical Beam End Reinforcement," *Proceedings of PCI National Bridge Conference*, Palm Springs, CA, 16-19 Oct 2005.

Deatherage, J., Burdette, E., and Chew, C. (1994), "Development Length and Lateral Spacing Requirements of Prestressing Strands for Prestressed Concrete Bridge Girders," *PCI Journal*. Jan-Feb, pp. 70-83.

Dunkman, D. (2009), "Bursting and Spalling in Pretensioned U-Beams," thesis. University of Texas, Austin.

Englekirk, R. E. and Beres, A. (1994), "Need to develop shear ductility in prestressed members," *Concr.Int*, 16(10), 49-56.

Fallaha, S. (2009). Telephone and E-mail correspondence with Brandon Ross.

FHWA (2010), "Federal Highway Administration National Bridge Inventory," <http://www.fhwa.dot.gov/bridge/nbi/mat09.cfm> (accessed December 1, 2010).

Florida Department of Transportation (FDOT) (2008), *Interim Design Standard Index No. 20054*, Florida Department of Transportation, Tallahassee, FL.

FDOT (2009), *Structures Design Guidelines*, Tallahassee, FL.

FDOT (2009a), *Temporary Design Bulletin C09-01*, Tallahassee, FL.

FDOT (2009b), *Temporary Design Bulletin C09-03*, Tallahassee, FL.

FDOT (2009d), *Interim Design Standard Index No. 20510*, Tallahassee, FL.

FDOT (2010), *Interim Design Standard Index No. 20063A*, Tallahassee, FL.

FDOT (2012), *Specification 450 Precast Prestressed Concrete Construction*, Tallahassee, FL.

Gergely, P., Sozen, M.A., and Siess, C.P. (1963), *The Effect of Reinforcement on Anchorage Zone Cracks in Prestressed Concrete Members*, University of Illinois Structural Research Series No. 271, 170 pp.

Giaccio, C., Al-Mahaidi, R., and Taplin, G. (2002), "Experimental study on the effect of flange geometry on the shear strength of point loaded RC T-beams." *Canadian Journal of Civil Engineering*. 29(6) pp. 911-918.

Guyon, Y. (1955), *Prestressed Concrete* 2nd ed. (English translation), F.J. Parsons, London, 543 pp.

Harries, K.A. 2009, "Structural Testing of Prestressed Concrete Girders from the Lake View Drive Bridge," *ASCE Journal of Bridge Engineering*, 14(2), pp 78-92.

Hoyer, E. (1939), *Der Stahlsaitenbeton*, Otto Elsner, Berlin.

Ibell, T., Morley, C., and Middleton, C., (1999), "Strength and behaviour in shear of concrete beam-and-slab bridges," *ACI Struct.J*, 96 (3), pp. 386-391.

Iyengar, K. (1962), "Two-Dimensional Theories of Anchorage Zone Stresses in Post-Tensioned Prestressed Beams," *ACI Journal*, 59(10), pp. 1443-1466.

Kannel, J., French, C., and Stolarski, H., (1997), "Release Methodology of Strands to Reduce End Cracking in Pretensioned Concrete Girders," *PCI Journal*, 42(1), Jan.–Feb., pp. 42–54.

Kotsovos, M., Bobrowski, J., and Eibl, J., (1987), "Behavior of Reinforced Concrete T-Beams in Shear," *Structural Engineer, Part B: R&D Quarterly*, 65B(1), pp1-10, March.

Kaufman, M. K. and Ramirez, J. A. (1988), "Re-Evaluation of the Ultimate Strength Behavior of High-Strength Concrete Prestressed I-Beams," *ACI Struct.J*, 85(3), 295-303.

Kuchma, D., Kim, K. S., Nagle, T. J., Sun, S., and Hawkins, N. M. (2008), "Shear tests on high-strength prestressed bulb-tee girders: Strengths and key observations," *ACI Struct.J*, 105(3), 358-367.

Leonhardt, F., Walter, R. (1962), *The Stuttgart Shear Tests 1961*, Translation III. Cement and Concrete Association Library. London.

Leonhardt, F. and Walther, R. (1961), "The Stuttgart Shear Tests," *Beton - und Stahlbetonbau*, 56(12) and 57(2,3,6,7, and 8), Translation by Amerongen, C.

Llanos, G., Ross, B., and Hamilton, H. (2009). "Shear Performance of Existing Prestressed Concrete Bridge Girders." Rep. No. BD 545-56, Florida Department of Transportation, Tallahassee, FL.

Magus, R. (2010). Brandon Ross notes from pre-construction meeting. Dura-Stress, Leesburg, FL.

Marshall, W. and Mattock, A. (1962), "Control of Horizontal Cracking in the Ends of Pretensioned Prestressed Concrete Girders," *PCI Journal*, 7(10), pp. 56-75.

Maruyama, K. and Rizkalla, S. H. (1988). "Shear Design Consideration for Pretensioned Prestressed Beams," *ACI Struct.J.*, 85(5), 492-498.

Morcous, G., Hanna, K., and Tadros, M., (2010), *Bottom Flange Reinforcement in NU I-Girders*, Nebraska Department of Roads, Lincoln, NE.

Nolan, S. (2009). Telephone and E-mail correspondence with Brandon Ross.

North American Strand Producers Association (NASP) (2009), "Standard Test for Strand Bond"

Patzlaff, Q., Morcous, G., Hanna, K., and Tadros, M., (2010), "Bottom Flange Reinforcement of Precast-Prestressed Bridge I-Girders," 2010 Concrete Bridge Conference.

Oh B., Kim K., and Lew Y., (2002), "Ultimate Load Behavior of Post-Tensioned Prestressed Concrete Girder Bridge through In-Place Failure Test," *ACI Struct J*, V. 99, No. 2, March-April.

Oh, B., Kim E., and Choi Y., (2006), "Theoretical Analysis of Transfer Lengths in Pretensioned Prestressed Concrete Members." *ASCE J of Engineering Mechanics*, October.

O'Neill, C. and Hamilton, H. (2009), *Determination of Service Stresses in Pretensioned Beams*, Rep. No. BD 545-78, Florida Department of Transportation. Tallahassee, FL.

PCI (1999), *PCI Design Handbook*. 5th ed. Chicago, IL

Pessiki, S., Kaczinski, M., and Wescott, H., (1996), "Evaluation of Effective Prestress Force in 28-Year-Old Prestressed Concrete Bridge Beams," *PCI Journal*, v 41, n 6, pp 78-89, Nov-Dec.

Placas, A. and Regan, P., (1971), "Shear Failure of Reinforced Concrete Beams," *ACI J*, October, pp. 763-773.

Ritter, W. (1899), "Die Bauweise Hennebique," *Schweizerische Bauzeitung*, Zurich, February.

Roberts, C. (1990), *Behavior and Design of Local Anchorage Zone of Post-Tensioned Concrete Members*, M.S. Thesis. University of Texas. Austin, TX.

Ross, B., Ansley, M., and Hamilton, H., (2011), "Load Testing of 30-year-old AASHTO Type III Highway Bridge Girders," *PCI Journal*, 56(4), 152-163.

Russell, B. and Burns, N. (1996), "Measured Transfer Lengths of 0.5 and 0.6 in. Strands in Pretensioned Concrete," *PCI Journal*, Sept.-Oct., pp. 44-54.

Ruddle, M., Rankin, G., and Long, A., (2003), "Arching Action – Flexural and Shear Strength Enhancements in Rectangular and Tee Beams," *Proceedings of the ICE – Structures and Buildings*, 156(1), February, pp. 63-74.

Schlaich, J., Schäfer, K., and Jennewein, M. (1987), "Toward a Consistent Design of Structural Concrete," *PCI Journal*, 32(3), pp. 74-150.

Shahawy, M., Robinson, B., and deV Batchelor, B. (1993), "An Investigation of Shear Strength of Prestressed Concrete AASHTO Type II Girders," Florida Department of Transportation, Tallahassee, FL.

Tadros, M., Badie, S., and Tuan, C. (2010), "Evaluation and Repair Procedures for Precast/Prestressed Concrete Girders with Longitudinal Cracking in the Web," National Cooperative Highway Research Program, Report 654, Transportation Research Board, Washington, D.C.

Tuan, C., Yehia, S., Jongpitakseel, N., and Tadros, M., (2004), "End Zone Reinforcement for Pretensioned Concrete Girders," *PCI Journal*, Vol. 49, No. 3, pp. 68-82.

Yura, J., Kumar, A., Yakut A., Topkaya, C., Becker, E. and Collingwood, J., (2001), *Elastomeric Bearing Pads: Recommend Test Methods*," National Cooperative Highway Research Program Report 449, Transportation Research Board, Washington, D.C.

Zararis, I., Karaveziroglou, M., and Zararis, P., (2006), "Shear strength of reinforced concrete T-beams," *ACI Struct.J*, Vol. 103, No. 5, pp. 693-700.

Appendix A–Literature Review

Appendix B—Small Beam Tests

Appendix C—SR-72 Tests

Appendix D—FIB-54 Tests

Appendix E–FIB-63 Tests

Appendix F--Finite Element Analysis of End Region

Appendix G—End Region Design Models

Appendix H–Support Data

Appendix A–Literature Review

Table of Contents

A.1	Introduction	79
A.2	Glossary.....	80
A.3	Confinement Reinforcement	85
A.3.1	End Region Failure Modes	85
A.3.2	Code Requirements	87
A.3.3	Confinement Reinforcement during Prestress Transfer	88
A.3.4	Confinement Reinforcement during Loading.....	89
A.3.5	Hoyer Effect	95
A.3.6	Summary.....	97
A.4	Web Splitting.....	98
A.4.1	Code Requirements	99
A.4.2	Modeling of Web Splitting Cracks	99
A.4.3	Treatment of Web Splitting Cracks	101
A.5	Flange Effect on Shear Strength.....	103
A.6	Curb Contribution to Girder Behavior	109
A.7	Truss and Arch Action	111

List of Figures

Figure 1–Confinement reinforcement	80
Figure 2–End region	80
Figure 3–Strut-and-tie behavior	81
Figure 4–Shear span.....	82
Figure 5–Transfer length.....	82
Figure 6–Development length.....	83
Figure 7–Strand debonding (shielding).....	84
Figure 8–End region strut-and-tie behavior	86
Figure 9–Bond-shear failure.	86
Figure 10–Splitting crack.....	87
Figure 11–Splitting crack at prestress transfer.....	88
Figure 12–Transverse tie above bearing (after Csagoly 1991)	90
Figure 13–End region strut and tie models A) with fully bonded strands below web and B) debonded strands concentrated below web.....	91
Figure 14–Flange cracking in girder with debonded strands concentrated below web A) side view and B) end view.	92
Figure 15–Confinement reinforcement as shear reinforcement.....	93
Figure 16–Shear-friction model (Based on Akhnoukh 2010).....	94
Figure 17–Hoyer effect in A) Strand before stressing, B) strand after prestressing, C) concrete cast around strand, and D) stresses and forces after transfer	96
Figure 18–Web splitting cracks (enhanced in blue).....	98
Figure 19–Free-body diagram based on Gergely-Sozen model (after Gergely et al. 1963)	100
Figure 20–Effect of web width (Leonhardt and Walther 1961).....	103
Figure 21–Effect of flange thickness (Placas and Regan 1971).....	104
Figure 22–T-beam failure after tied-arch behavior	106
Figure 23–Beam-slab test specimen (Ibell et al. 1999).....	107
Figure 24–Shear contribution of flange (Zararis 2006)	108
Figure 25–Cross section of bridge (Harries 2009).....	110
Figure 26–Cross section of test bridge (Oh et al. 2002)	110
Figure 27–Beam behavior (a) truss action and (b) arch action.	111

List of Tables

Table 1–Literature review topics and relevant appendixes	79
Table 2–Crack treatment procedures as recommended by Tadros et al. (2010)	102
Table 3–Crack treatment procedures as recommended by FDOT Specification 450 (2012)	102

1 Introduction

This appendix contains a review of the literature and other background information germane to the experimental and analytical research presented in subsequent appendices. Table 1 lists the sections and topics contained in this appendix and those appendices for which the topics specifically apply. To assist the reader, additional background information is also briefly discussed in the individual appendices.

Table 1–Literature review topics and relevant appendices

Section	Topic	Relevant Appendices
A.2	Glossary	General to entire report
A.3	Confinement Reinforcement	Appendix B – Small Beam Test Program Appendix D – FIB-54 Test Program Appendix F – Finite Element Analyses Appendix G – End Region Design Models
A.4	Web Splitting	Appendix E – FIB-63 Test Program
A.5	Flange Effect on Shear Strength	Appendix C – SR-72 Test Program
A.6	Curb Contribution to Girder Behavior	Appendix C – SR-72 Test Program
A.7	Truss and Arch Action	Appendix C – SR-72 Test Program

2 Glossary

This section discusses some of the terms, phrases, and concepts germane to the study of pretensioned concrete I-girders.

Confinement reinforcement. Confinement reinforcement is mild steel reinforcement placed around prestressing strands in the bottom flange of precast pretensioned concrete girders (Figure 1).

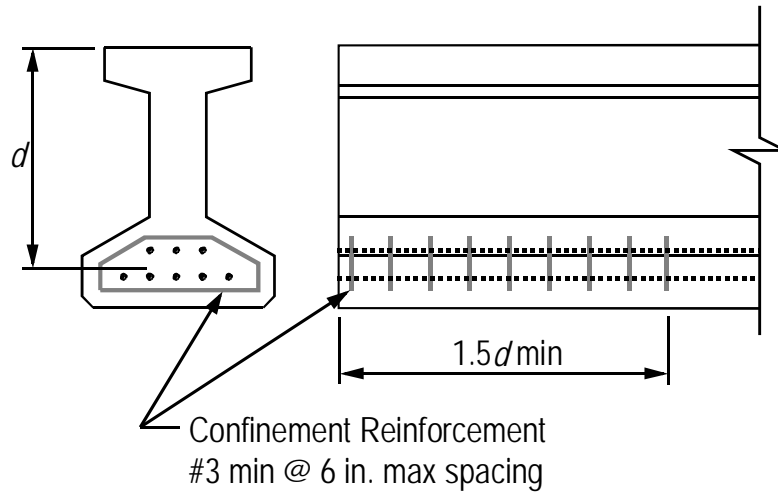


Figure 1–Confinement reinforcement

End region. The end region is loosely defined as the portion of a girder located within one and a half member depths from the girder end (Figure 2). The end region serves two critical functions: 1) Force transfer between the prestressing strands and concrete, and 2) Delivery of shear forces to the support. Mild reinforcement, including confinement reinforcement, is placed in the end region to aid in these functions.

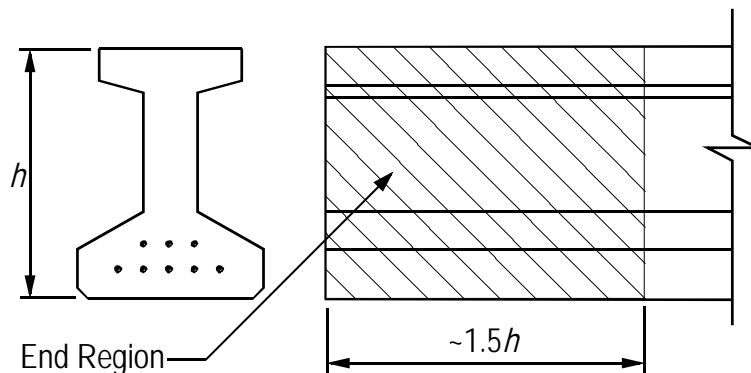


Figure 2–End region

Prestress transfer. In precast pretensioned concrete construction, concrete is cast around steel strands that have been preloaded in tension. After concrete is sufficiently cured, tension force in the strands is released, thereby transferring force into the surrounding concrete. This event is referred to as prestress transfer. Flame cutting of the strands is a common method of releasing the prestress force. The effects of prestress transfer are important considerations in the design of end region reinforcement.

Strut-and-tie behavior. After cracking, the behavior of concrete members can be modeled by a truss analogy. In this analogy, concrete struts carry compressive forces, and steel ties carry tensile forces (Figure 3). Behavior modeled by the truss analogy is referred to as strut-and-tie behavior. Strut-and-tie modeling is one approach for designing of end region reinforcement.

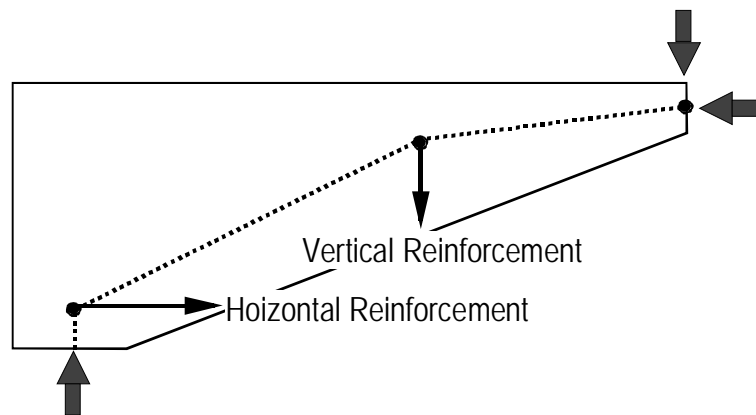


Figure 3–Strut-and-tie behavior

Shear span. Shear span is the horizontal distance from the support to the point of load application (Figure 4). Shear span-to-depth ratio (or a/d ratio) is often used to describe the loading condition of concrete members. Shear behavior is, among other factors, a function of the shear span-to-depth ratio. Strut-and-tie modeling is generally appropriate for members loaded with relatively small shear span-to-depth ratios.

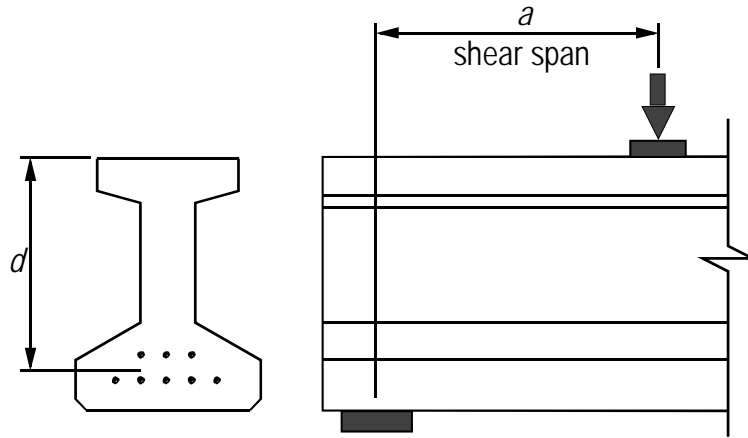


Figure 4–Shear span

Transfer length. Transfer length is the length over which prestressing force is transferred from prestressing strands into the surrounding concrete (Figure 5). Transfer length occurs within the end region. By design the prestress force in a strand is always less than ultimate capacity. Hence transfer length is not equivalent to the length required for full strand development.

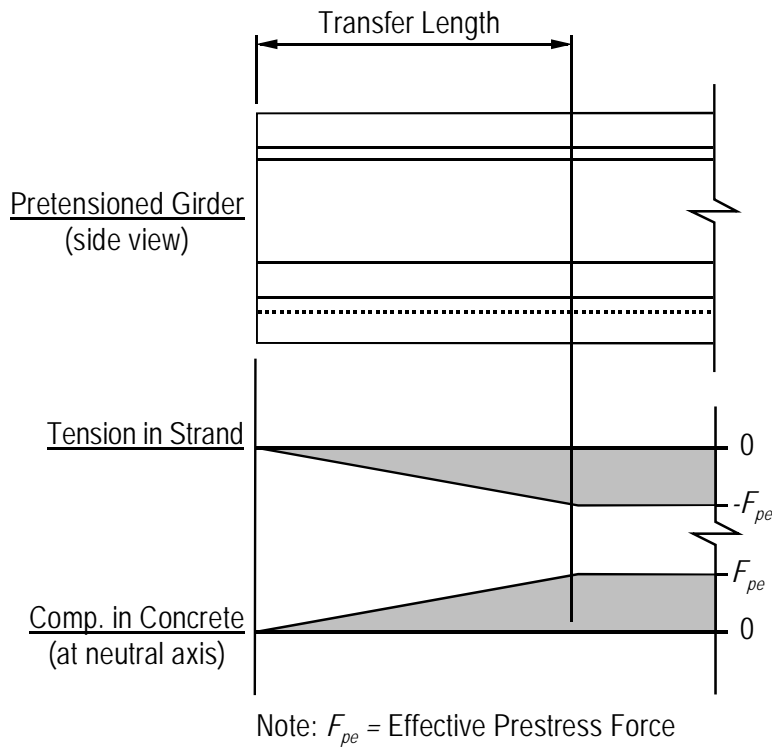


Figure 5–Transfer length

Development length. Development length is the length of concrete embedment required to fully anchor prestressing strands. Strands with full development length can carry their ultimate tensile capacity (Figure 6). Development length is greater than transfer length.

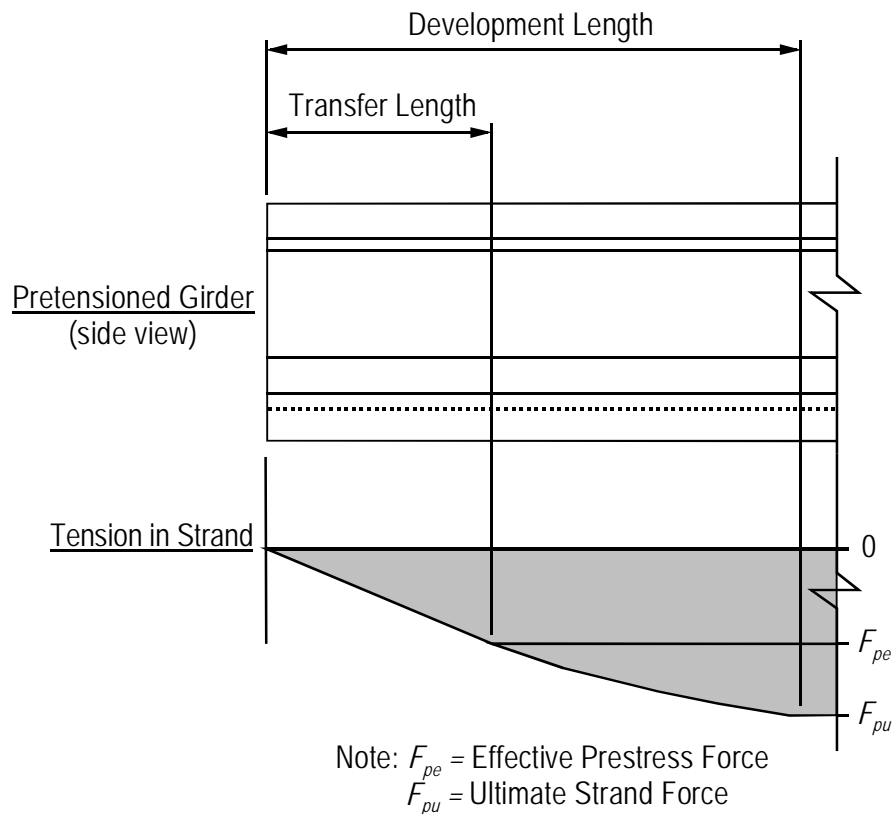


Figure 6–Development length

Strand debonding (shielding). Stress in pretensioned concrete girders can be controlled by selectively preventing force transfer between strands and concrete. To prevent force transfer, strands are debonded (also called shielding), at the ends of the beam. Debonding is accomplished by placing a sleeve over the strand to prevent bond with the concrete. Debonding moves the transfer length of shielded strands away from the girder end (Figure 7).

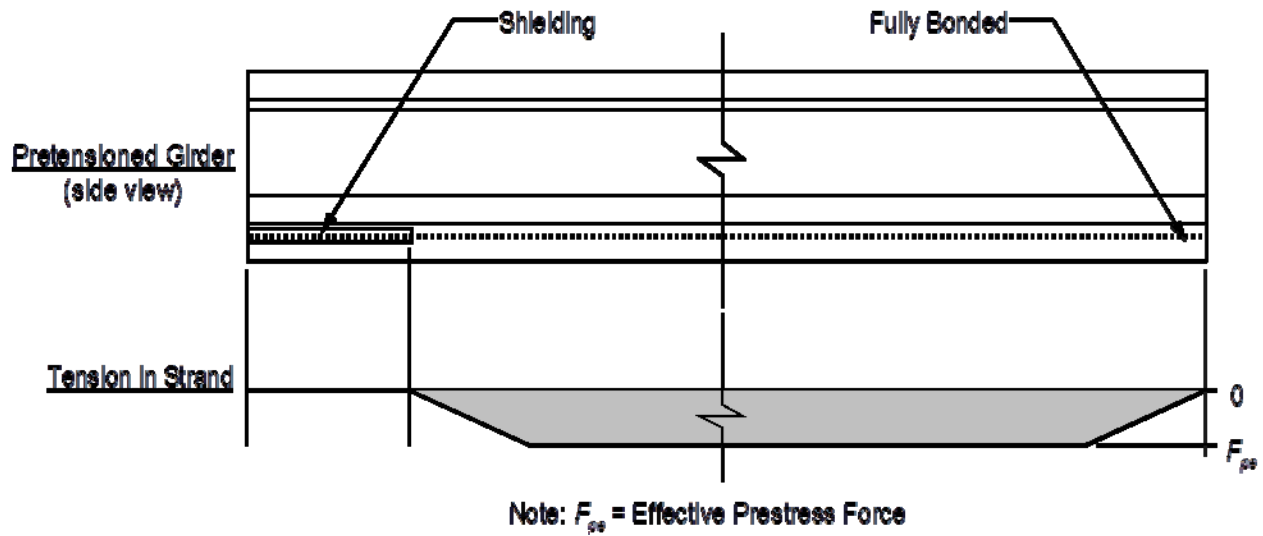


Figure 7–Strand debonding (shielding)

Strand Slip. Strand slip is movement of prestressing strands relative to the surrounding concrete due to applied loads. Strand slip generally occurs after the formation of cracks within the strand development length. These cracks reduce the available bond length for developing the strands, thus leading to strand slip once load on the strands exceeds capacity along the reduced embedment length. Strands can still partially develop even after the onset of slip.

3 Confinement Reinforcement

This chapter summarizes the work of other researchers regarding confinement reinforcement and other relevant topics. It is organized topically, beginning with a discussion of end region failure modes. Code requirements regarding confinement reinforcement and end region detailing are also summarized.

3.1 End Region Failure Modes

The end region of pretensioned girders can fail in modes other than basic “flexural failure” or “shear failure.” Two such failure modes are bond-shear failure and lateral-splitting failure. Both of these modes have been observed experimentally, and have relevance in the study of confinement reinforcement.

3.1.1 Bond-Shear Failure

After cracks form in the end region, load is carried by a strut-and-tie mechanism (Figure 8). If cracks form near the girder end then strand anchorage is interrupted, and the strands may slip (Figure 9). Bond-shear failure occurs when strands can no longer support load, or when the compression zone crushes due to the rotation allowed in-part by strand slip. This type of failure can be very sudden and has also been called “bond-tension failure” or “bond failure.” Bond-shear failure has been observed during load tests of girders without confinement reinforcement (Maruyama and Rizkalla 1988, Kaufman and Ramirez 1988, Englekirk and Beres 1994, Llanos et al. 2009), as well as during tests of girders with confinement reinforcement (Deatherage et al. 1994, Barnes et al. 1999, Kuchma et al. 2008).

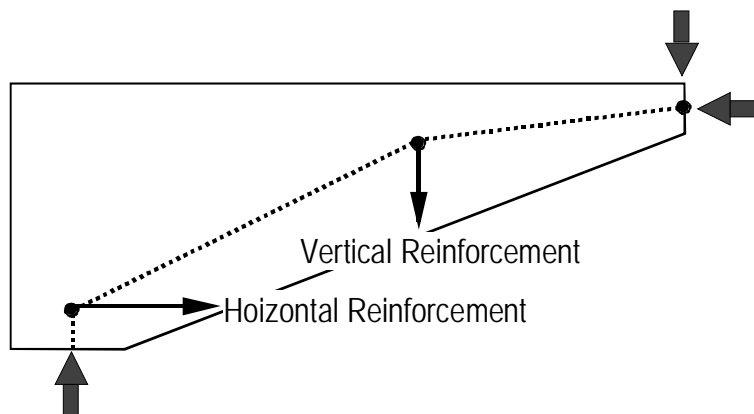


Figure 8–End region strut-and-tie behavior

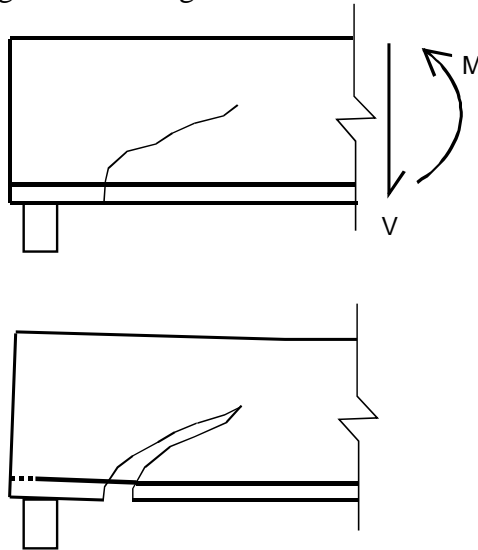


Figure 9–Bond-shear failure.

3.1.2 Lateral-Splitting Failure

As with bond-shear failure, lateral-splitting failure occurs after cracks form in the end region and the girder begins strut-and-tie behavior. In this failure mode, splitting cracks (Figure 10) form due to transverse stresses above the support (Llanos et. al. 2009, Csagoly 1991). Splitting cracks can lead to strand slip relative to the surrounding concrete. In girders without confinement reinforcement the formation of splitting cracks and the associated strand slip can lead to sudden girder failure. Development of transverse forces and their relationship to confinement reinforcement are primary considerations of the research presented in this document.

Figure 10 shows a splitting crack forming at the centerline of the cross-section. Splitting cracks in the outer portion of the bottom flange have also been observed experimentally (Llanos et. al. 2009). Splitting cracks in the flange can also lead to sudden girder failure.

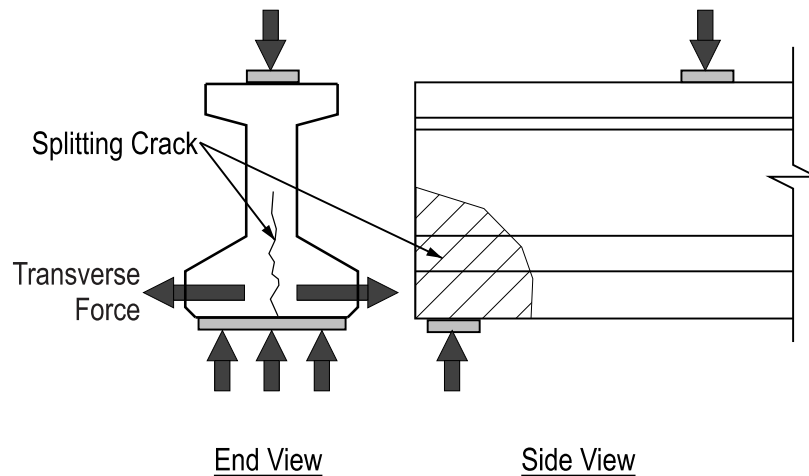


Figure 10–Splitting crack

3.2 Code Requirements

Confinement reinforcement is required by AASHTO LRFD article 5.10.10.2 (AASHTO 2009). Figure 1 graphically presents the confinement reinforcement requirements. The requirements are prescriptive, meaning that confinement reinforcement is not designed, but is rather specified according to the strict “recipe.” The function of confinement reinforcement is not discussed in the code or in the associated commentary.

Strand shielding is addressed by AASHTO LRFD article 5.11.4.3. This article limits shielding to no more than 25% of strands in a girder. Limits are also placed on the percentage of shielded strands in a given row (40%) and the quantity strands that can have shielding terminate at the same section (greater of 40% or four strands). Shielding is required to be symmetric about the cross-section centerline.

Article 5.8.3.5 addresses the amount of longitudinal steel required at any section, including sections near the supports. Requirements at the support are based on a strut-and-tie model similar to that shown in Figure 3. Sufficient steel must be provided to support the horizontal tie force above the bearing. To prevent bond-shear failures the article states that, “Any lack of full development shall be accounted for.”

3.3 Confinement Reinforcement during Prestress Transfer

In addition to design for ultimate loads, pretensioned girders must also be designed and detailed for serviceability criteria arising from fabrication, shipping, deck placement, and service. Loads from prestress transfer in particular can have negative consequences on performance and durability of girders. Llanos et al. (2009) observed splitting cracks at prestress transfer (Figure 11) in the bottom flange of test girders. Splitting cracks formed due to a problematic strand-shielding pattern wherein fully bonded strands were placed in the outer portion of the flange and shielded strands were placed below the web. Splitting cracks were allowed to propagate because confinement reinforcement was not present. Other researchers (Russell and Burns 1996) recommended the use of confinement reinforcement to prevent splitting at prestress transfer.

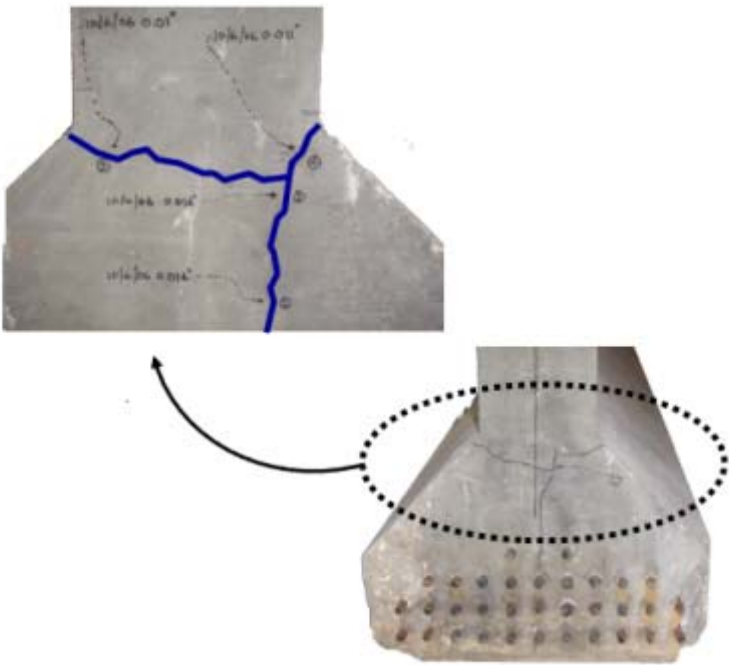


Figure 11–Splitting crack at prestress transfer

Russell and Burns (1996) investigated transfer length for 0.5 and 0.6 in. diameter prestressing strands in girders with and without confinement reinforcement. The authors’ state:

Overall, confining reinforcement had little or no effect in improving the transfer lengths. In fact, the measured transfer lengths for strands confined by mild steel reinforcement were marginally longer than strands where confinement was not provided.

Other authors have reported similar findings for 0.7 in. diameter strands (Patzlaff et al. 2010, Akhnoukh 2010). None of the authors investigating transfer length in confined girders reported splitting cracks during prestress transfer. Each concluded that the negligible impact on transfer length was due to the inactivity of confinement reinforcement in the absence of cracking.

Work regarding confinement reinforcement in the anchorage zone of post-tensioned concrete members has been conducted by Breen et al. (1991) and Roberts (1990). These works, while useful for post-tensioned members, do not apply directly to the design of pretensioned members. In post-tensioned concrete, prestress force is transferred to the concrete in a relatively small local zone. In pretensioned concrete, however, the prestress force is transferred to the concrete over the relatively large strand transfer length. The local zone in post-tensioned members is analogous to an axially loaded column, and confinement reinforcement for the local zone can be designed using an approach similar to columns. As demonstrated in subsequent chapters of this document, confinement in the bottom flange of pretensioned I-girders is used to control cracks and to carry transverse tension forces. These functions are distinct from confinement reinforcement in columns and post-tensioned local zones, which provide confinement to axially loaded concrete.

3.4 Confinement Reinforcement during Loading

Confinement reinforcement has been shown to affect girder performance under applied loads. This section summarizes previous research investigating the effects of confinement reinforcement on girder strength and behavior during loading.

3.4.1 Shear Capacity

Csagoly (1991) tested 16 pretensioned girders, some with confinement reinforcement and some without. Confinement reinforcement improved shear capacity by an average of 13% relative to girders without confinement. Shahawy et al. (1993) also tested girders with and without confinement reinforcement; results indicated that confinement reinforcement improved shear capacity by 10% to 17%.

3.4.2 Transverse Reinforcement

In some cases, equilibrium of strut-and-tie systems requires the formation of tension ties in bottom flange in the transverse direction. If confinement reinforcement is not provided to act as the transverse tie, concrete must carry the tension force. This condition is undesirable, and has been found culpable in splitting cracks by Csagoly (1991) and Llanos et al. (2009).

According to Csagoly, splitting cracks result from “the spreading of the reaction force above the bearing.” This concept is shown graphically in Figure 12. A transverse force T is formed to maintain static equilibrium as the reaction force is spread from the web to the bearing pad. Splitting cracks form when the transverse force exceeds the concrete tensile capacity.

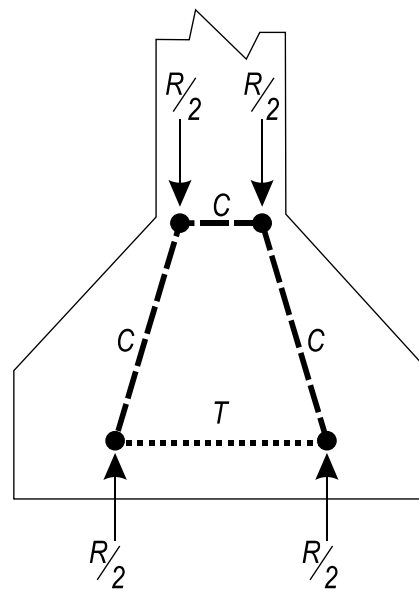


Figure 12–Transverse tie above bearing (after Csagoly 1991)

Llanos et al. (2009) also observed splitting failures in load tests of full-scale girders, and likewise attributed these failures to transverse forces above the support. Mechanics leading to these transverse forces were different from the Csagoly model, and are described by Figure 13. Figure 13a is a model of a girder with bonded strands below the web. Inclined compressive forces travel through the web, arriving at a node above the support. A tie resists the horizontal component of the inclined force. Because strands are fully bonded, they can act as the tie, and equilibrium is maintained. In contrast to Figure 13a, Figure 13b models the condition from the Llanos et al. test girders in which fully bonded strands were located at the edges of the flange. Because only the strands in the outside portion of the flange were bonded near the support, they

were the only strands able to act as ties (Figure 13b). This resulted in a disruption of the node at the support point. Because of the offset between the strut in the web and the two ties (fully bonded strands) in the bottom flange, secondary struts formed to transfer the load laterally to the nodes at the ties. Additional secondary struts were essential between the support and the nodes at the ties to complete the load path to the support. Both pairs of secondary struts induced horizontal components that acted transverse to the beam.

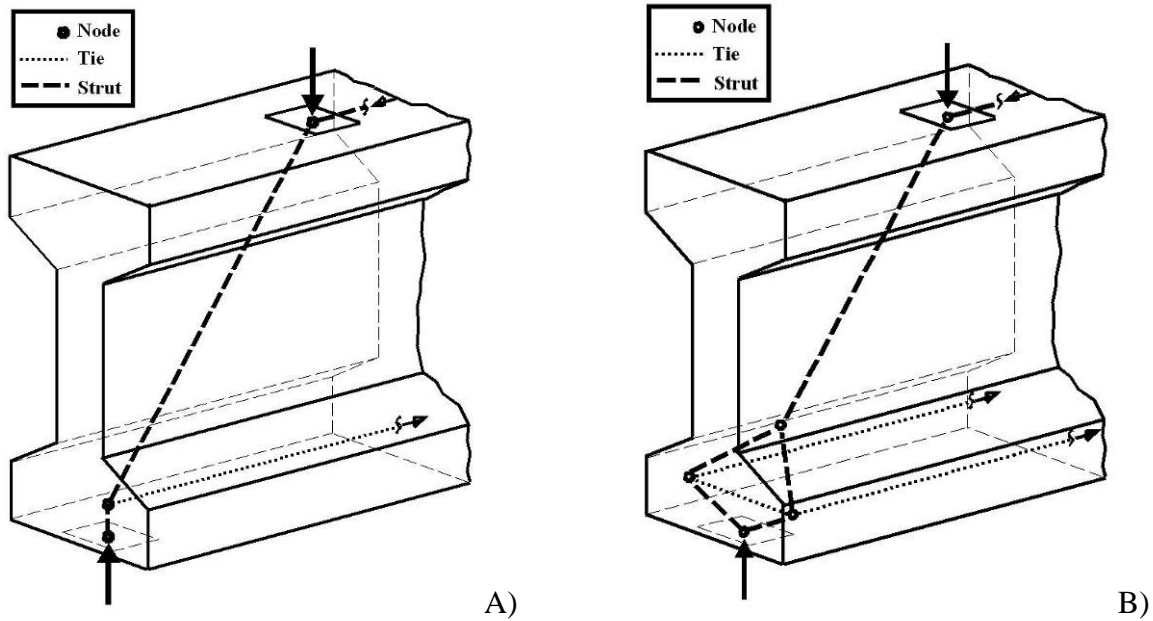


Figure 13–End region strut and tie models A) with fully bonded strands below web and B) debonded strands concentrated below web.

Test beams had no reinforcement (such as confinement reinforcement) to support the transverse force, and edges of the bottom flange peeled or split away at failure (Figure 14). The authors speculate that “[confinement] reinforcement might have held the bulb together after cracking.”

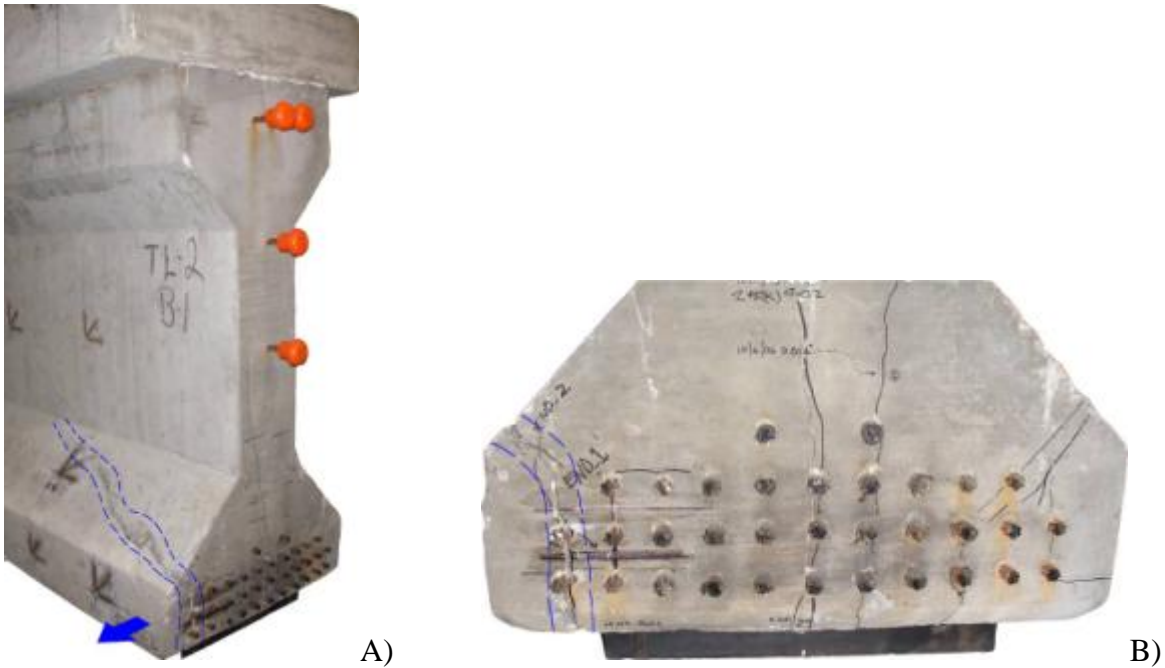


Figure 14–Flange cracking in girder with debonded strands concentrated below web A) side view and B) end view.

3.4.3 Vertical Reinforcement

Another possible function of confinement reinforcement is that of vertical, or “shear” reinforcement. Csagoly (1991) proposed this function and included it in a strut-and-tie model of the end region. In the model, inclined cracks crossing confinement reinforcement mobilize the confinement steel, thereby generating a vertical force that contributes to the end region shear capacity (Figure 15).

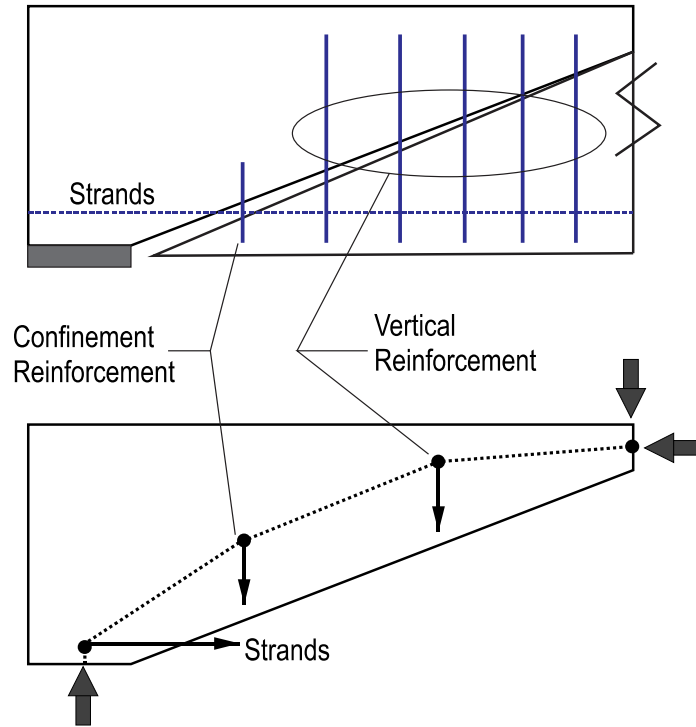


Figure 15—Confinement reinforcement as shear reinforcement

3.4.4 Ductility

Morcous et al. (2010) noted an improvement in ductility in girders with confinement reinforcement. Work presented in Appendix B and Appendix D confirm Morcou's finding and provide information on the mechanisms by which confinement reinforcement leads to improved ductility.

3.4.5 Development Length

By restraining cracks, confinement reinforcement may reduce strand development length. To test this possibility, Patzlaff et al. (2010) load tested (6) pretensioned concrete T-beams with varying configurations of confinement reinforcement. In all cases, the girders failed in flexure, and at loads sufficient to fully develop the strands. Because the strands reached full development in all tests, no conclusions were made regarding the effect of confinement reinforcement on development length.

Akhnoukh (2010) investigated the effects of confinement reinforcement on development length by conducting pullout tests of 0.7 in. diameter strands embedded in 4 ft, 5 ft, and 6 ft long concrete prisms. Specimens also varied in the quantity and spacing of confinement reinforcement. Pullout tests were terminated when the strand ruptured or when the strand

slipped relative to the concrete. The 4 ft specimens with (5) #3 confinement hoops always failed by strand rupture, whereas the majority of the 4 ft specimens with (3) #3 confinement hoops failed by strand slip. The author concluded that confinement reinforcement decreased the development length.

3.4.6 Shear Friction

Akhnoukh (2010) proposed a shear friction method for designing confinement reinforcement. Currently this is the only design method in the literature. The Akhnoukh method is based on an assumed crack running through a row of strands, which engages the confinement reinforcement thereby inducing normal and friction forces on the crack plane (Figure 16). Equilibrium is applied in the longitudinal direction to equate the friction force with the force in the strands, resulting in Equation 1. Akhnoukh applied this model to design confinement reinforcement for the strand pullout tests discussed previously. It was concluded that the shear-friction concept can be used to quantify the effect of confinement reinforcement on strand development.

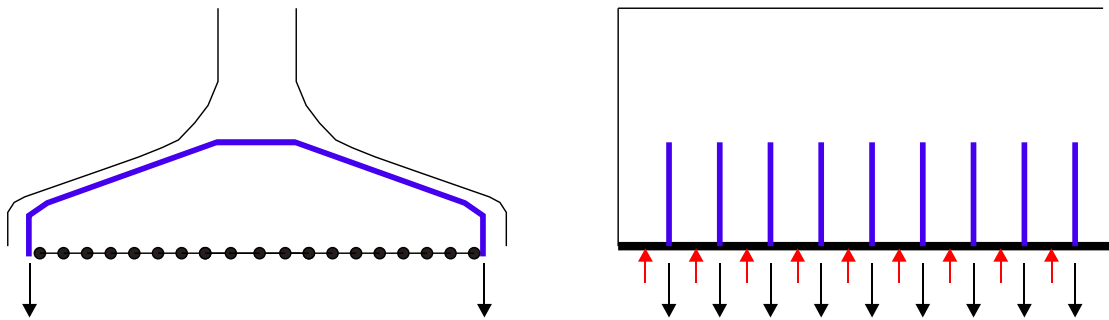


Figure 16–Shear-friction model (Based on Akhnoukh 2010).

$$A_{ts} = \frac{A_{ps} \cdot f_{ps}}{\mu \cdot f_{tsy}} \quad \text{Equation 1}$$

Where:

- A_{ts} = Area of transverse (confinement) reinforcement crossing crack (in²)
- A_{ps} = Total area of prestressing strand (in²)
- f_{tsy} = Yield strength of transverse (confinement) reinforcement (ksi)
- f_{ps} = Stress in prestressing strands at ultimate capacity (ksi)
- μ = Coefficient of friction

3.5 *Hoyer Effect*

The diameter of prestressing strands decreases due to the Poisson effect as strands are pretensioned (Figure 17). Upon release, strand tension at the end of the member is relieved, and the strand diameter increases. The surrounding concrete resists the increase in diameter, which causes tensile stress in the concrete and develops mechanical bond between the strand and concrete. Radial strand expansion and concrete tensile stress are greatest at the member end. Radial strand expansion and the associate concrete tensile stresses are zero at the end of the transfer length. This condition is referred to as the Hoyer Effect and is the primary contributor to strand-concrete bond capacity. This effect is named for Ewald Hoyer, the German Engineer who first discussed radial expansion of prestressing strands (Hoyer 1939).

Oh et al. (2006) derived a model for transfer length that accounts for the Hoyer effect. The Oh model is rigorous, utilizing equilibrium, material constitutive properties, and strain compatibility. The model can be used for calculating stresses at the strand-concrete interface and for calculating tensile concrete tensile stresses. Building on the equilibrium-compatibility portion of the model, Oh then considers the effects of concrete cracking adjacent to the strands within the transfer length. The full model (including crack effects) was compared to experimental tests of transfer length and found to have good correlation.

A) Before Prestressing



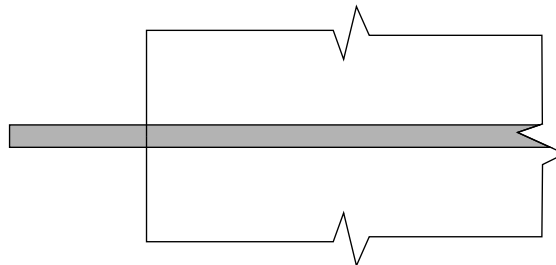
B) Prestressing

Strand elongates longitudinally and contracts transversely



C) Concrete Cast

Concrete around deformed shape



D) Prestress Transfer

Strand expands transversely causing normal and frictional forces

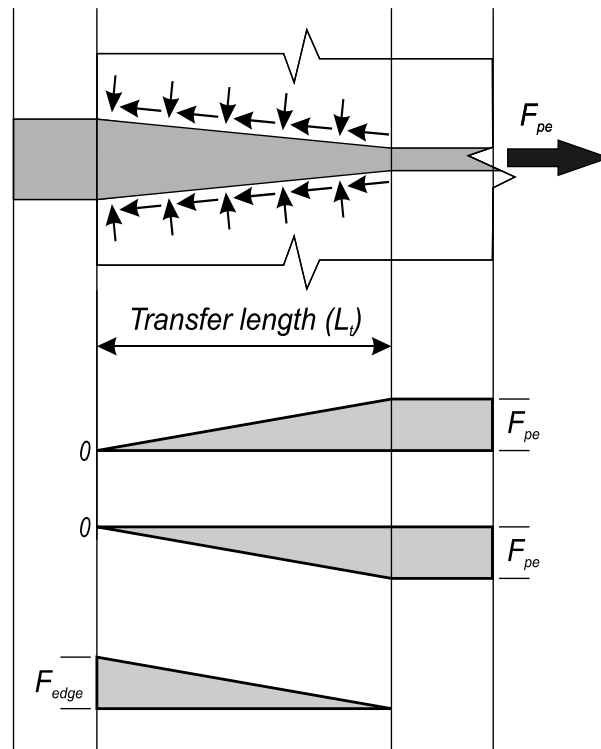


Figure 17—Hoyer effect in A) Strand before stressing, B) strand after prestressing, C) concrete cast around strand, and D) stresses and forces after transfer

3.6 Summary

The following conclusions are made based on the aggregate findings of the relevant literature. Results from two or more authors support each conclusion.

- The presence of confinement reinforcement does not prevent strand slip
- Confinement reinforcement is inactive until engaged by cracks in adjacent concrete
- Confinement reinforcement has negligible effect on transfer length in uncracked concrete
- Confinement reinforcement improves shear capacity and ductility of girders
- Transverse tensile forces forming above the bearing can lead to splitting cracks in concrete girders
- Transverse tensile forces form due to applied loads and the Hoyer effect

Based on limited treatment or complete absence in the literature, the following topics are deserving of additional attention:

- Function of confinement reinforcement at prestress transfer and ultimate strength
- Effect of confinement reinforcement on development length
- Optimal quantity and placement of confinement reinforcement
- Relationship between confinement reinforcement and splitting failure
- Effect of prestress force on bottom flange transverse tensile stress
- Effect of confinement reinforcement on strand-concrete bond capacity
- Interaction of confinement reinforcement with other end region variables
- Rational confinement reinforcement design methods

4 Web Splitting

Web splitting cracks are the horizontal or diagonal cracks that form in the end region of pretensioned concrete I-girders during or following the prestress transfer (Figure 18). Elsewhere these cracks are referred to as “bursting”, “spalling”, or “splitting” cracks. Reinforcement for controlling these cracks is referred to as “bursting” resistance in the 2007 AASHTO LRFD code and “splitting” resistance in the 2010 code. For the purposes of this report these cracks will be referred to as web splitting cracks.



Figure 18–Web splitting cracks (enhanced in blue)

Beginning the 1950s, many researchers have attempted to model stresses in the concrete that lead to web splitting cracks. Other researchers have focused on controlling web splitting cracks through strength evaluation of the vertical reinforcement in the end region. This review of literature will discuss both of the above approaches as well as outlining current code requirements and crack treatment protocols.

4.1 Code Requirements

AASHTO provisions for web splitting reinforcement were first introduced in 1961 and have undergone little revision since that time (Tadros 2010). Provisions were influenced by the work from Marshall and Mattock (1962).

The 2010 AASHTO LRFD Bridge Design Specifications require sufficient vertical reinforcement to resist a force equal to at least 4% of the total prestressing force while limiting the allowable stress in the reinforcement to 20 ksi. The reinforcement must be within $h/4$ (where h is the height of the beam) of the end of the beam and the end bar should be as close to the end of the beam as practicable. The required end region vertical reinforcement can be taken as:

$$A_s = 0.04 \frac{F_{pi}}{f_s} \quad \text{Equation 2}$$

where:

A_s = total area of vertical reinforcement located within the distance $h/4$ from the end of the beam (in²)

F_{pi} = prestress force at transfer

f_s = stress in steel not exceeding 20 ksi

4.2 Modeling of Web Splitting Cracks

As noted by Dunkman (2009) models addressing web splitting cracks have typically been based one of two approaches. The first approach focuses on calculating concrete stresses that lead to web splitting. The other approach focuses on calculating the required strength of the end region, particularly vertical reinforcement, to prohibit excessive crack sizes. Both modeling approaches are discussed in this section.

4.2.1 Stress Modeling

Numerous methods have been used to calculate stresses that cause web splitting cracks. Analytical methods employing elastic, inelastic, and plastic assumptions have all been used with various degrees of success.

Currently finite element analysis (FEA) is the favored analysis approach due to method's ability to model stresses in members with complicated loadings and geometry. FEA has been used by Breen et al. (1994), and Kannel et al. (1997). Other analysis approaches include infinite series (Iyengar 1962) and finite difference approaches (Gergely et al. 1963). Guyon (1955) developed a method of analysis using a symmetric prism method, which is limited to the region

directly adjacent to the prestressed force and subsequently only useful in estimating bursting forces and not splitting forces. This approach has been influential in the development of European codes (Dunkman, 2009).

Inelastic analysis was employed by Gergely et al. (1963) to produce the Gergely-Sozen model. Their approach assumed an initially cracked cross section and was based on equilibrium of the end region. The Gergely-Sozen model gives a conceptual framework for describing the formation of tensile forces in the web (Figure 19).

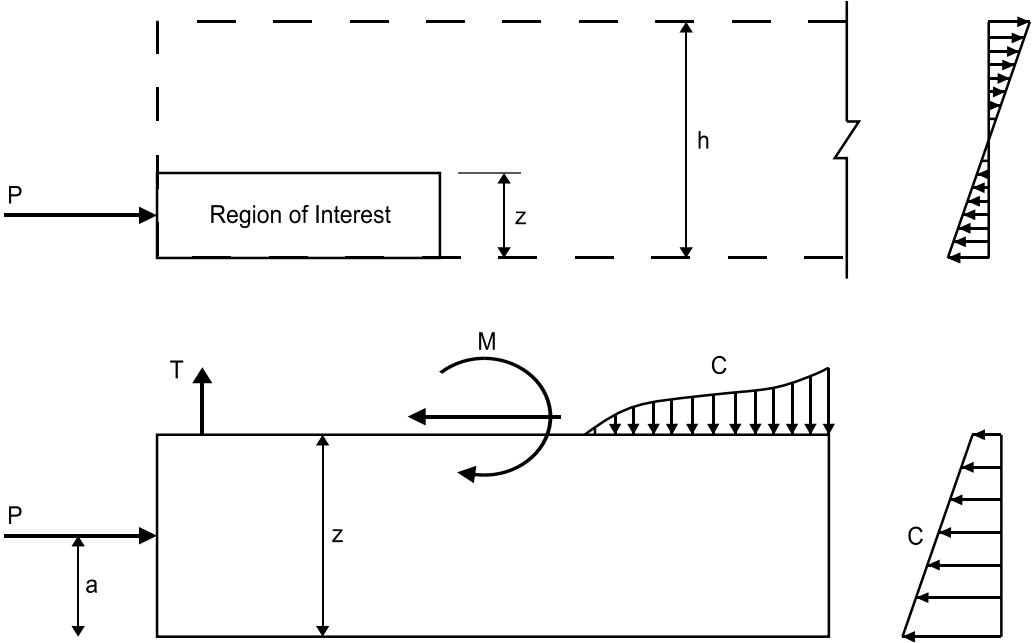


Figure 19–Free-body diagram based on Gergely-Sozen model (after Gergely et al. 1963)

where:

- P = prestress force
- z = height of section analyzed
- h = member depth
- a = height of prestressing force
- T = web splitting tensile force
- M = resulting moment and shear forces
- C = resulting compression fields

4.2.2 Strength Modeling

Marshall and Mattock (1962) and Gergely et al. (1963) are frequently credited as landmark studies that recognized the need to develop a pragmatic approach for designing transverse reinforcing steel in the end region. The Gergely-Sozen model discussed above provides one method for estimating the force to be resisted by the transverse steel. Marshall and Mattock developed Equation 4 for calculating the required area of steel in the end region. This equation was incorporated into AASHTO design standards with slight modifications. To be more conservative the 1962 AASHTO code implicitly changed the ratio of h/l_t to 2. More recently, an experimental investigation by Tuan et al. (2004) has confirmed Marshall and Mattock's equation and suggested that 50% of the area of steel be concentrated to within $h/8$ from the end of the member and the balance between $h/8$ and $h/2$.

$$A_r = 0.021 \frac{P_i h}{f_s l_t} \quad \text{Equation 3}$$

where:

A_r = required transverse reinforcement at the member end

P_i = prestress force at transfer

f_s = maximum allowable stress in reinforcement (20 ksi)

h = member depth

l_t = strand transfer length

Strut-and-tie modeling (STM) has also been used to design reinforcement for controlling web splitting cracks. STM has been influential in the development of European codes and has been investigated by numerous researchers (Schlaich et al. 1987, Castrodale et al. 2002, Davis et al. 2005, and Crispino 2007).

4.3 *Treatment of Web Splitting Cracks*

Treatment protocols for web splitting cracks are typically based on the beam exposure conditions and width and location of cracks. Historical recommendations for the allowable crack widths and treatment procedures are provided in Tadros et al. (2010). Table 2 and Table 3 list treatment procedures from Tadros et al. (2010) and FDOT Specification 450 (2012). Although

not listed in this document, recommendations for treating web splitting cracks have also been made by PCI (1999) and CEB (1993).

Table 2–Crack treatment procedures as recommended by Tadros et al. (2010)

Crack Width	Recommended Action
< 0.012 in.	Left unrepaired
0.012 - 0.025 in.	Repaired by filling the cracks with approved specialty cementitious materials, and the end 4 ft of the girder side faces coated with an approved sealant
0.025 - 0.050 in.	Filled with either epoxy injection or cementitious patching material (depending on crack width) and the surface coated with a sealant
> 0.05 in.	Girder rejected

Table 3–Crack treatment procedures as recommended by FDOT Specification 450 (2012)

Crack Classification	Environment	Action
Cosmetic cracks (< 0.006 in.)	Slight - Moderate	Do not treat
	Extreme	Apply penetrant sealer
Minor cracks (0.006 - 0.012 in.)	Slight	Do not treat
	Moderate	Beam Elevation > 12 ft - Do not treat Beam Elevation < 12 ft - Apply penetrant sealer
	Extreme	Inject epoxy
Major crack (> 0.012 in.)	All	Engineering evaluation required

5 Flange Effect on Shear Strength

Contributions of compressive flanges to shear capacity of concrete beams are typically not considered in design codes. This practice is conservative as multiple researchers have shown that flanges, such as those on T-beams, do indeed contribute to shear capacity. This section summarizes the available research regarding shear contribution of flanges.

Leonhardt and Walther (1961) tested a series of RC beams in which the shear reinforcement, flange width and thickness were held constant while the web thickness varied (Figure 20). Under both uniform and concentrated loads, the shear capacity of the beams increased as the web thickness increased. The increase was less pronounced when the web thickness was greater than about half of the flange width. The increase was also less pronounced for beams tested with concentrated loads.

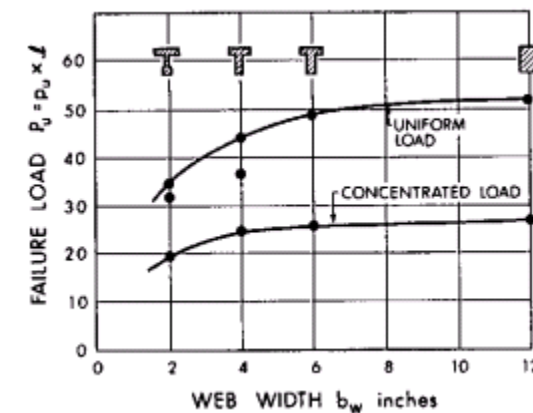


Figure 20—Effect of web width (Leonhardt and Walther 1961)

Placas and Regan (1971) conducted shear tests on beams with constant web width and varying flange sizes. Figure 21 presents the experimental relationship between shear capacity and flange width. For constant web thickness, the presence of a flange increases the shear capacity. The increase in shear capacity, however, is essentially independent of the flange width for the range tested. The shear capacity also increased as flange thickness increased.

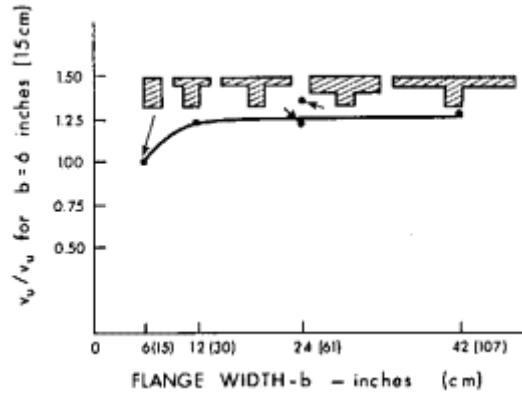


Figure 21–Effect of flange thickness (Placas and Regan 1971)

Placas and Regan (1971) present Equation 4 for calculating the area of the flange that is effective in resisting “shearing failure” of the compression zone. Shearing failure is distinguished from shear-compression failure, which the authors indicate is not a critical mode in T-beams. Because “shearing failure” is only a function of the compression zone, the web is not considered to contribute shear strength for this failure mode.

$$A_f = t(b_w + x) \quad \text{Equation 4}$$

Where:

A_f = Area of the flange effective in resisting shearing failure of the compression zone

t = Thickness of compressive flange

b_w = Web width

$x = 6$ ” (Based on curve fit with available data)

ASCE-ACI committee 426 (1973) presented a document summarizing research on shear capacity of reinforced concrete beams. Research by Leonhardt and Walther (1961) and Placas and Regan (1971) presented in the previous paragraphs was among the work summarized by committee 426. The committee reported that flexural-compression stresses in the flange are distributed over a greater width than are the shear stresses and that only the portion of the flange “immediately adjacent” to the web can contribute to V_{cz} (shear contribution of the compression zone). Accordingly, Equation 5 is presented to address shear contribution from portions of the flange immediately adjacent to the web. This equation assumes that the shear carried by the

concrete in the flange is only a function of the flange thickness. The committee suggests that “For design purposes, however, it seems reasonable to ignore the strengthening effect of the flange [beyond the portion immediately adjacent to the web].”

$$V_c = v_c(b_w d + 2h_f^2) \quad \text{Equation 5}$$

Where:

V_c = Concrete contribution to shear capacity

v_c = Shear stress in the concrete

b_w = Web width

d = Distance from extreme tension fiber to centroid of tensile reinforcement

h_f = Depth of compression flange

Giaccio et al. (2002) conducted a series of tests on 15 RC T-beams to evaluate the flange contribution to shear strength. The test beams were loaded in three-point bending. Variables included the flange width and thickness. The authors report that portions of the flange beyond those adjacent to the web will contribute to the shear capacity if a flange thickness is large enough relative to the beam depth. The flange beyond the web intersection contributed to the shear capacity if the flange thickness was at least $0.25d$ (where d is the distance from the extreme compression fiber to the centroid of the tensile reinforcement). For flanges of sufficient thickness, the width of the flange contributing to the shear capacity was $4b_w$ (where b_w is the web thickness). For beams with wide flanges ($b_f > 4b_w$), the contribution of the flange was governed by its punching strength. The ratio of $b_f > 4b_w$ corresponded to a change in failure mode from a beam shear mechanism to a punching shear mechanism.

Kostovos et al. (1987) conducted a series of four tests on RC beams to evaluate the effect of the flange on the shear capacity. Test beams were loaded uniformly, or with two symmetric point loads. Tied-arch behavior was observed after cracking. Failure of the T-beam shown in Figure 22, was attributed to instability of the concrete arch after the onset of tied-arch behavior. Comparing their test results with data from the literature, the authors found that for a given a/d ratio, the normalized shear carrying capacity of the tested tee beams were as much as 200%

larger than rectangular beams. No attempt was made, however, to quantify the effects of the flange on the shear capacity.



Figure 22–T-beam failure after tied-arch behavior

Chong and Arthur (1987) tested twenty-one RC beams under uniform load. Flange thickness and width were varied. The tee beams behaved as tied-arches, and failed due to instability of the arch. The authors report that increased flange thickness increased the load at the first shear crack, but did not affect the ultimate shear force supported by the beams.

Ibell et al (1999) conducted tests on individual rectangular and T-beams, as well as beam-slab structures (Figure 23). Individual beams were loaded in three-point bending, and failed in shear or flexure. The beam-slab structures were loaded by multiple point loads, and failed in punching-shear, tearing-shear, or flexure. The tearing shear failure was characterized by cracks in the slab running perpendicular to and between the beams. The tears occurred because the slab could not support the load induced by differential movement between adjacent loaded and unloaded beams. Using ACI and BD codes of practice, the authors calculated the predicted capacity of both the beam-slab structures and the individual beams. Comparing the calculated capacities with the experimental results, it is noted that: "...while these codes-of-practice predict relatively accurate two-dimensional beam capacities, they substantially underpredict the enhancement in shear strength that the redundancy of beam-and-slab bridge provides. This underprediction, due to membrane enhancement from the surrounding concrete slab, is in the region of 25 to 35 percent herein, depending on which code-of-practice is used as the basis for

comparison.” Interior beams particularly benefited from membrane effects and load distribution to adjacent girders. By monitoring the reactions in the beam-slab structures during testing, it was observed that the distribution of load was greater than predicted by a grillage analysis, and that the relative load distribution between beams did not change during the course of the test.

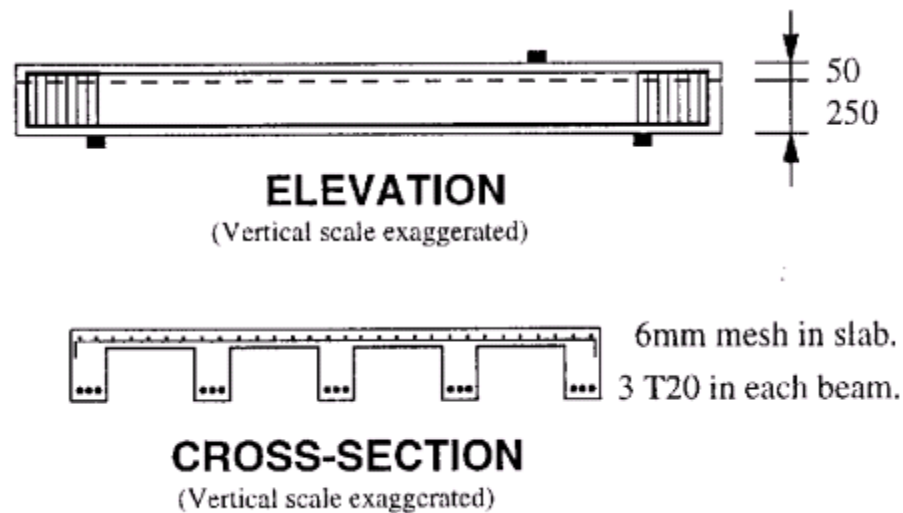


Figure 23–Beam-slab test specimen (Ibell et al. 1999)

Ruddle et al (2003) investigated the effects of arching action on the strength of rectangular and T-beams. The authors report both analytical and experimental work. An analytical model for shear capacity of T-beams was presented, which considers the contribution of the flange away from the web up to $3b_w$ (where b_w is the thickness of the web). The authors report that “the ultimate flexural and shear strength of longitudinally restrained beams are enhanced by the development of arching action.”

Zararis et al. (2006) developed a shear model for concrete T-beams and compared the model with experimental data from the literature. The Zararis model considers shear to be carried by the shaded portion of T-beams shown in Figure 24. Comparisons with the available literature show that the proposed model results in more accurate, but less conservative calculated capacities as compared to the ACI code.

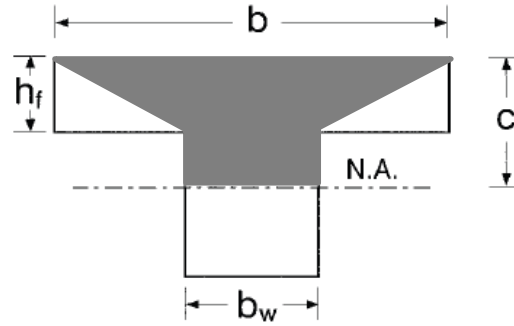


Figure 24—Shear contribution of flange (Zararis 2006)

Although there are differences in approach, the general trend in the literature is that flanges increase the shear capacity of T-beams beyond that of similar rectangular beams. The area of the flange contributing to shear strength is limited to those portions immediately adjacent to the web. Numerous authors suggest that the portion of the flange effective in supporting shear is a function of the geometric properties of the flange and/or web.

The failure modes observed in T-beams can vary from those observed in isolated rectangular beams; punching-shear being one observed failure mode, and arching instability of the compressive zone due to being another. Accordingly, flange contribution to shear capacity can be limited by the flange punching strength and/or compression zone arching capacity.

6 Curb Contribution to Girder Behavior

Concrete curbs, barriers, walls, and other appurtenances are often attached to concrete bridge decks, and are especially common above exterior girders. Although their contribution to the strength and stiffness of the girders are not considered in codes of practice, their effects are still present and can be significant. These effects are greatest when the elements and bridge behave compositely; however detailing of the elements can affect a system's ability to sustain composite action. In addition to affecting the strength and stiffness of individual girders, they can also influence load distribution between girders. Two studies of are presented in this section that demonstrate the effects of curbs, etc. on bridge capacity and behavior.

Harries (2009) tested concrete box girders that were salvaged from the partially-collapsed Lake View Drive Bridge in Pennsylvania. The collapse occurred in one of the exterior girders. Tests were conducted on the other exterior girder as well as the interior girder adjacent to the collapse (Figure 25). The exterior text girder supported a curb and a barrier wall. Test data confirmed a degree of composite action between the curb and the exterior girder; however the composite action deteriorated with increasing load. Because of the composite action, the curb and barrier wall "...clearly increase[d] the capacity of the box girder section, although this increase [was] tempered by an increase in the degree of asymmetry of the section; thus the increased capacity is not as significant as the increase in moment of inertia would suggest." Commenting on the approach designers might take when considering curbs and barrier walls, the author states that "It is not recommended that their contribution to girder capacity be relied upon under ultimate load conditions. Under service load conditions, however, it is likely that they may be considered to be composite with the girder."

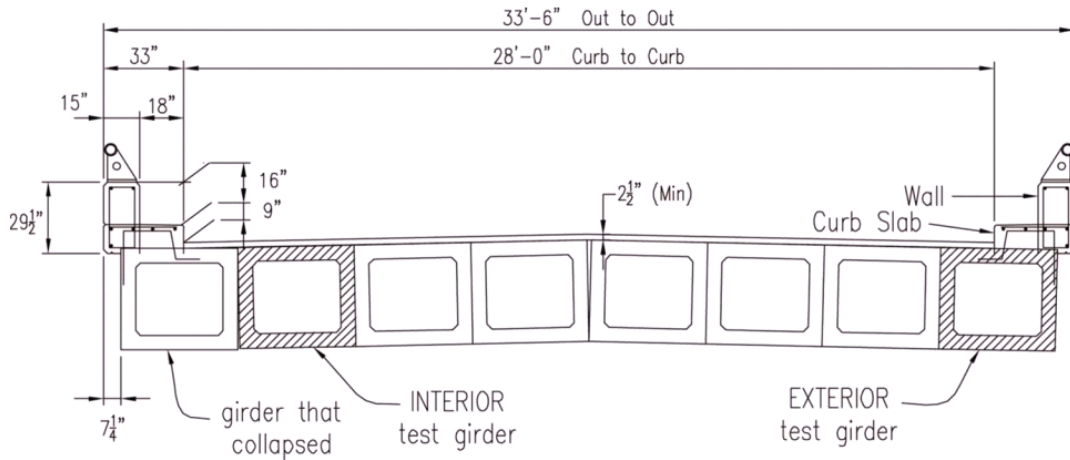


Figure 25–Cross section of bridge (Harries 2009)

Oh et al (2002) conducted an on-site load test of an existing bridge. A cross-section of the bridge is shown in Figure 26. Point loads were applied above the right-most girders near mid-span. The medium curb strip acted compositely with the deck and girders until it separated from the deck when the load reached about 50% of the eventual maximum load. Failure was initiated by compression crushing of the curb near the load points. The test was terminated after crushing occurred in the slab. The authors note that crushing of curbs could be used as a warning indicator preceding failure. Regarding the strengthening of the bridge by the median strip and curb, the authors state that a “...quantitative assessment of [their] contribution greatly depends on the integrity of those elements with the main slab system.”

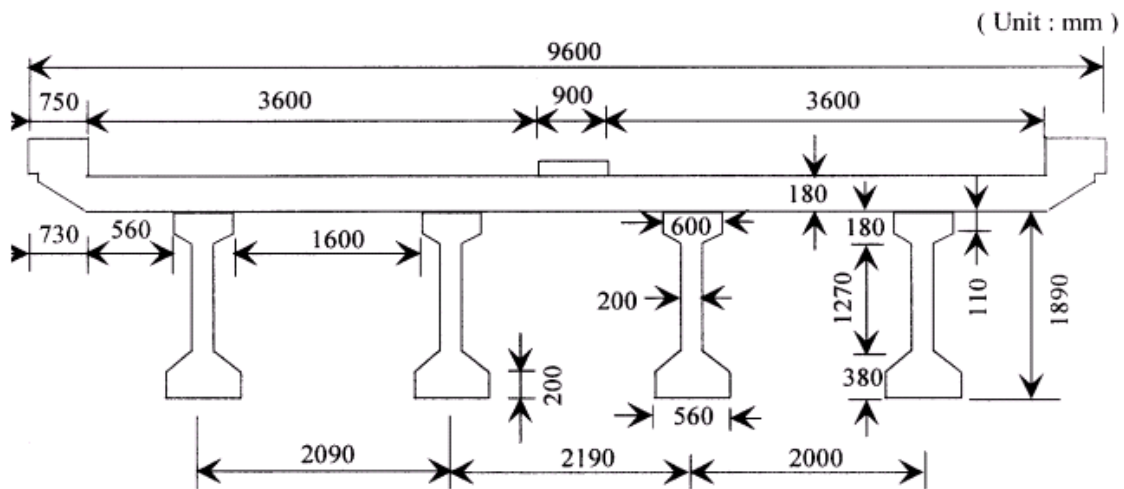


Figure 26–Cross section of test bridge (Oh et al. 2002)

7 Truss and Arch Action

Prior to cracking, RC beams transfer loads according to elastic beam theory. After cracking, loads in RC beams are transferred in “arch action” or “truss action.” Both types of behavior are shown in Figure 27, and are discussed further in the proceeding paragraphs.

Ritter (1899) proposed a truss analogy for modeling the transfer of forces in reinforced concrete beams. In the truss analogy, the concrete at the top of the beam is considered as a compression chord, the steel reinforcement in the bottom of the beam as a tension chord, concrete in the web as diagonal compression struts, and vertical reinforcement as tension members. This type of load transfer will be referred to as “truss action” within this report. In truss action, equilibrium requires that the vertical force component in the compression struts be equal and opposite of the vertical force in the transverse steel ties. Truss action will only occur in beams with transverse reinforcement. Additionally, the formation of cracks at the location of the vertical reinforcement is required to mobilize the reinforcement tie force.

In beams without transverse reinforcement, forces are transferred to the supports by arching of the concrete. To balance the horizontal force component at the supports, a tension tie is formed by the steel reinforcement in the bottom of the beam. This mechanism of load transfer will be referred to as “arch action” within this report.

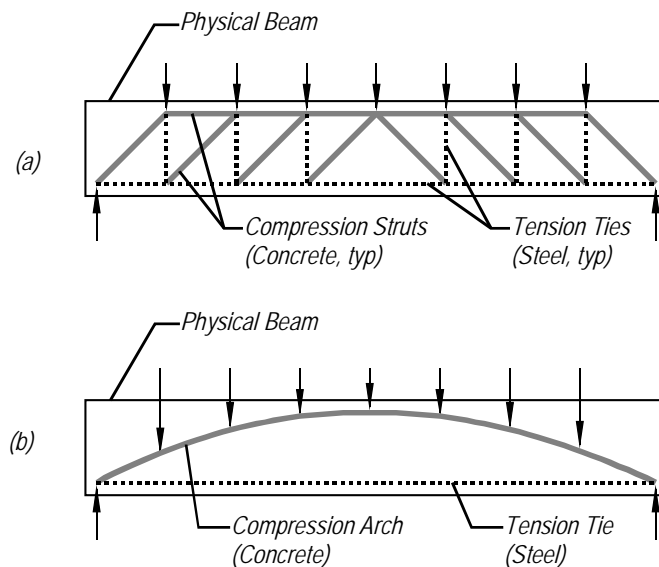


Figure 27–Beam behavior (a) truss action and (b) arch action.

Appendix B–Small Beam Tests

Table of Contents

B.1	Introduction	116
B.2	Beam History.....	117
B.3	Beam Design	118
B.4	Beam Construction and Material Properties.....	121
B.5	Test Setup and Instrumentation.....	123
B.6	Results and Discussion.....	127
B.6.1	B5L-C and B5L-U.....	130
B.6.2	B5M-C and B5M-U.....	131
B.6.3	B5S-C and B5S-U	135
B.6.4	B6L-C and B6L-U.....	138
B.6.5	B6M-C and B6M-U.....	140
B.6.6	B6S-C and B6S-U	143
B.6.7	Transverse Strain	145
B.6.8	Spalling: B5M-C and B6M-C.....	149
B.6.9	Individual Strand Slip.....	150
B.6.10	Shear Capacity	152
B.6.11	Displacement Ductility.....	154
B.7	Strut-and-Tie Model.....	156
B.8	Code Comparison	162
B.9	Summary and Conclusions.....	165

List of Figures

Figure 1–Small beam modification.....	117
Figure 2–Cross-section dimensions of all test beams	118
Figure 3–Vertical and confinement reinforcement	118
Figure 4–Deck dimensions and reinforcement layout	119
Figure 5–Small beam test nomenclature	119
Figure 6–Strand layouts for beams containing 0.5-in. and 0.6-in. strand	120
Figure 7–Finished beam specimens ready for testing	122
Figure 8–Small beam test setup	123
Figure 9–Specimen prior to load test	123
Figure 10–Specimen on bearing pad.....	124
Figure 11–Load point.....	124
Figure 12–Small beam LVDT placement	125
Figure 13–LVDTs at strands.....	125
Figure 14–LVDT frame at end of beam.....	126
Figure 15–Strain gage placement.....	126
Figure 16–Specimen during testing	126
Figure 17–Bottom view of B6M-U with splitting failure mode	128
Figure 18–Bottom view of B6L-C with bond-shear failure mode	128
Figure 19–Bond-flexure failure mode (B6M-C).....	129
Figure 20–Flexural failure mode (B5S-C)	129
Figure 21–Summary of results for B5L-C and B5L-U	132
Figure 22–Summary of results for B5M-C and B5M-U	134
Figure 23–Bottom view of specimen with splitting failure mode (B5M-U).....	135
Figure 24–Bond-flexure failure mode (B5M-C).....	135
Figure 25– Summary of results for B5S-C and B5S-U.....	137
Figure 26– Summary of results for B6L-C and B6L-U	139
Figure 27– Summary of results for B6M-C and B6M-U	142
Figure 28– Summary of results for B6S-C and B6S-U.....	144
Figure 29– Bond-shear failure mode (B6S-C).....	145
Figure 30–Transverse strain above near support (load =15 kip).....	146
Figure 31–Effect of load on transverse strain in confined specimen (B6L-C)	147
Figure 32–Effect of load on transverse strain in unconfined specimen (B5L-U)	148
Figure 33–Strain readings from gage S4 (B5M).....	149
Figure 34–Flange spalling (B5M-C).....	149
Figure 35–Prestressing strand slip in specimen B5S-C	151
Figure 36–Prestressing strand slip in specimen B5S-U	152
Figure 37–Normalized shear capacity.....	153
Figure 38–Effect of area of prestressing on shear capacity	154
Figure 39–Normalized displacement ductility	155
Figure 40–Unconfined specimen strut and tie model	157
Figure 41–Confined specimen strut and tie model	157
Figure 42–Experimental shear capacity vs. area of prestressing steel	161

List of Tables

Table 1–Results for compressive strength and modulus of rupture tests (psi).....	121
Table 2–Failure modes.....	128
Table 3–Comparison of measured and computed shear capacity using STM	158
Table 4–Estimated portion of shear carried by prestressing strand tie (unconfined specimens)	159
Table 5–STM details of confined specimens.....	160
Table 6–Material properties used in calculations.....	162
Table 7–Comparison of calculated shear capacity with maximum experimental shear	163
Table 8–Comparison of calculated moment capacity with maximum experimental moment.....	164

1 Introduction

The AASHTO LRFD Bridge Design Specifications (2007) require that confinement reinforcement be placed around prestressing strands in the bottom bulb of pretensioned concrete beams. Although the AASHTO specifications contain prescriptive requirements for the quantity and placement of confinement reinforcement, the effect of such reinforcement on the end region behavior is not well understood.

To evaluate the function and effect of confinement reinforcement, load tests were conducted using 28-in. deep precast-pretensioned beams. In total, twelve tests were conducted with each specimen loaded in three-point bending at a shear span-to-depth ratio of 1.0. Load, displacement, and strain data were collected during each test. Variables in the test program included strand size, strand quantity, prestressing force, and the presence or lack of confinement reinforcement.

Goals of the test program described in this chapter include:

- Evaluate the effect(s) of confinement reinforcement on specimen capacity and behavior
- Evaluate the interaction(s) between confinement reinforcement and other test variables
- Compile load, strain, and displacement data for use in validating finite element models (See Appendix F)
- Evaluate transverse strain distribution in the bottom flange above the bearing.

Relevant literature is summarized in Appendix A.

2 Beam History

Beams used in the test program were initially fabricated for use in project by O'Neill and Hamilton (2009). The initial test program focused on flexural behavior only, and did not damage the end region of the beams where shear tests were performed the current project. Six beams were fabricated at a precast facility in Leesburg, FL, and then shipped to the FDOT Structures Laboratory in Tallahassee, FL where a cast-in-place deck was added to each beam. After the cast-in-place decks were sufficiently cured, flexural testing by O'Neill and Hamilton was conducted, also at the FDOT Structures Laboratory.

The beams were originally constructed with confinement reinforcement at both ends. After the initial flexural testing by O'Neill and Hamilton, the beams were modified prior to conducting shear tests. This modification consisted of removing the portion containing confinement reinforcement from one end of each beam (Figure 1). Following the modification, shear tests were conducted on each end of each beam resulting in (12) total shear tests. For purposes of this report, each end will be referred to as a separate test specimen.

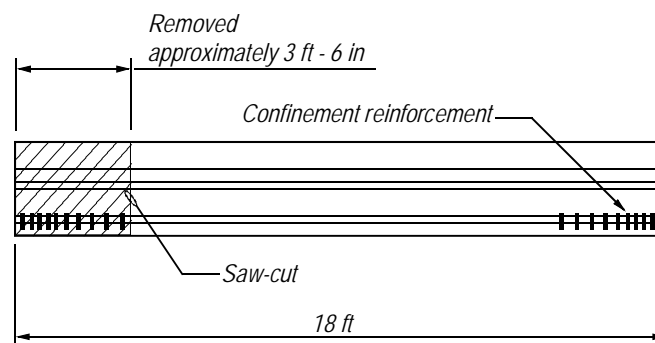


Figure 1–Small beam modification

3 Beam Design

The beam cross section dimensions are shown in Figure 2. Each beam was reinforced with single-leg #4 stirrups at 3 in. o.c. throughout all but the center 3 ft of the beam (Figure 3). Confinement reinforcement consisted of (10) #3 hoops in the end region as shown in Figure 3. An 8 in. thick by 18 in. wide deck was added to the top of each beam. The deck was reinforced with #5 bars longitudinally and transversely as shown in Figure 4.

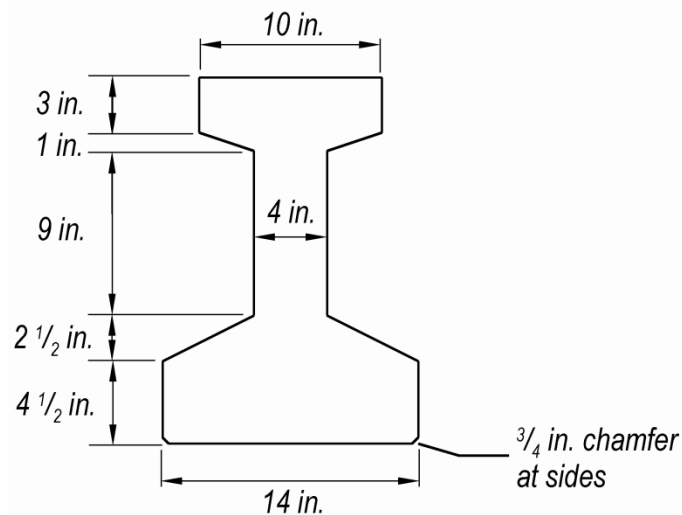


Figure 2–Cross-section dimensions of all test beams

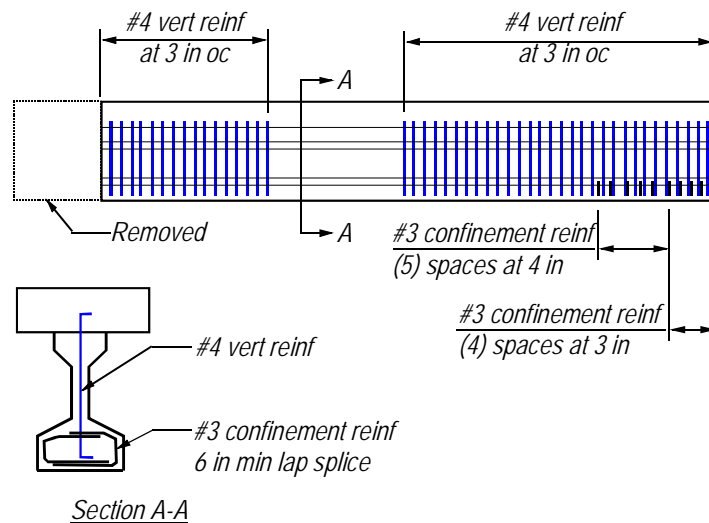


Figure 3–Vertical and confinement reinforcement

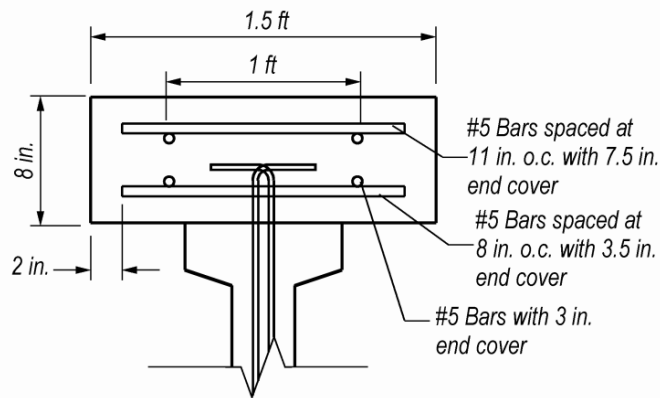


Figure 4–Deck dimensions and reinforcement layout

Three variables were considered in the small beam test program: 1) Strand size, 2) Strand quantity, and 3) Presences or lack of confinement reinforcement. Each variable is denoted in the test nomenclature shown in Figure 5.

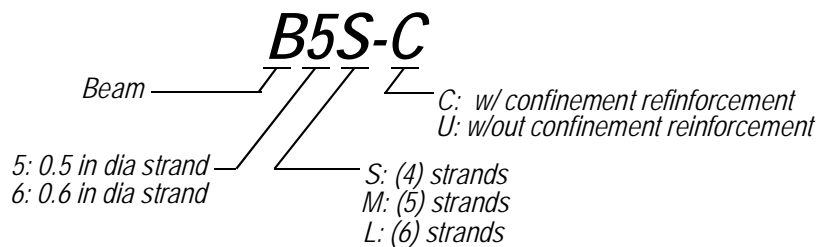


Figure 5–Small beam test nomenclature

Figure 6 shows the three strand patterns used in the specimen design. B5S, B5M, B5L were prestressed with 0.5-in. diameter ASTM A416 seven-wire strand and B6S, B6M, B6L were prestressed with 0.6-in. diameter strand. The 0.5-in. and 0.6-in. prestressing strands were initially stressed to 50% and 74% of the ultimate strength (270-ksi), respectively.

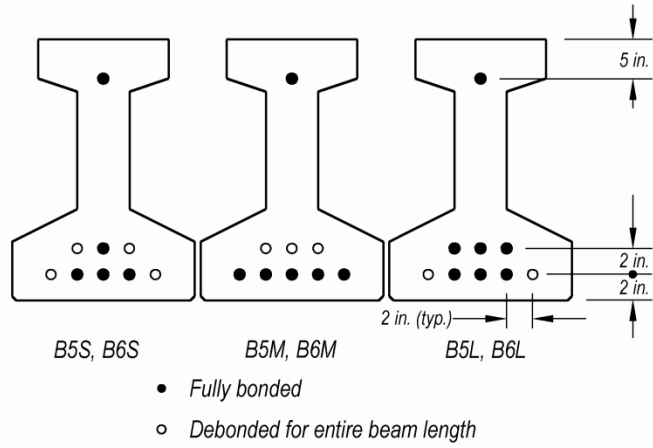


Figure 6—Strand layouts for beams containing 0.5-in. and 0.6-in. strand

4 Beam Construction and Material Properties

Beams B5S, B5M, and B5L were cast from a single batch of concrete. Similarly, beams B6S, B6M, and B6L were also cast from a single mixing batch. The same mix design was used for both batches. The mix contained 90% of granite aggregate equal to or less than 3/8 in. with no aggregates exceeding 0.5 in. For each batch (9) 6 x 12 in. cylinders for compressive strength and modulus of elasticity testing were taken. Additionally, the producer cast 4 x 8 in. cylinders for determining release strength and 28-day compressive strength.

Table 1 shows the cylinder test results at release and at 28-days. Each value is the average of three tests. The design called for a release strength of 3500 psi, which was reached within one day of casting. The B6x beams, however, were not released until four days after casting due to construction scheduling. Note the average 28-day compressive strength from the 6 x 12 in. cylinders is not provided for the B6x. The test machine was thought to have malfunctioned during these cylinder tests, and that the producer tests conducted at 28-day age are a better estimate of the compressive strength.

Table 1—Results for compressive strength and modulus of rupture tests (psi)

Beams	6 x 12 in. cylinders		4 x 8 in. cylinders (Manufacturer)	
	Release*	28 day**	Release*	28 day**
B5x	3900	8400	3980	9750
B6x	5370	N/A	4902	8840

* $f'_{ci} = 3500$ psi ** $f'_c = 6000$ psi

An FDOT Class II concrete deck was cast on each beam ($f'_c = 4500$ psi) after they were delivered to the FDOT Structural Research Center. Figure 7 shows the completed test beams.



Figure 7–Finished beam specimens ready for testing

5 Test Setup and Instrumentation

Load tests were conducted on each end of all six beams, resulting in twelve total tests. For purposes of this report, each end will be referred to as an individual test specimen. Tests were conducted using a three-point loading scheme (Figure 8, Figure 9). The end of the beam not being tested was cantilevered beyond the far support. After the first specimen (end) was tested, the supports and load point were moved and the second specimen was tested. One end of each beam had confinement reinforcement and one end did not. The specimen with confinement reinforcement was tested first in all cases except for B6M-U and B6M-C, for which the unconfined specimen was tested first.

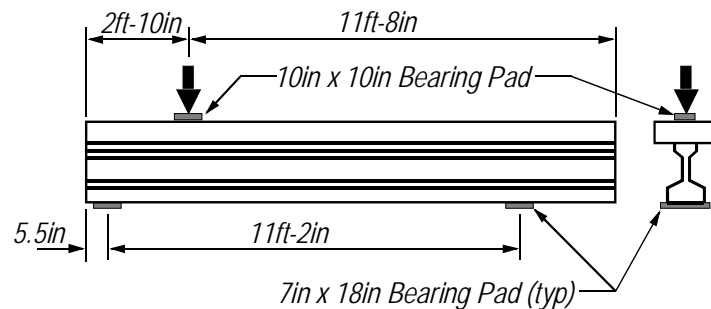


Figure 8—Small beam test setup

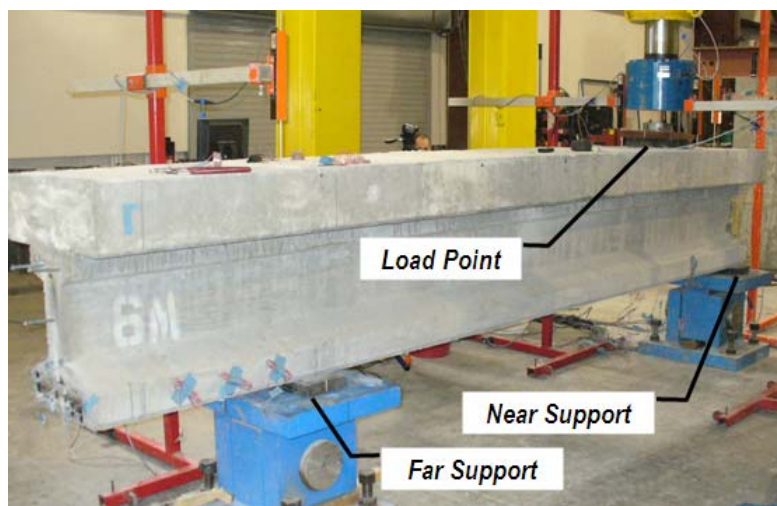


Figure 9—Specimen prior to load test

Beams were supported on 2-in. thick x 7 in. x 18 in. reinforced neoprene bearing pads with the pad oriented such that the 18 in. dimension was perpendicular to the beam axis (Figure 10). Load was applied through a 2-in. thick x 10 in. x 10 in. reinforced bearing pad (Figure 11) at a rate of 0.25 kip/sec. The load was measured by a load cell at the point of application.



Figure 10–Specimen on bearing pad



Figure 11–Load point

Linear variable displacement transducers, LVDTs, were used to measure vertical displacement at the load point, at each support (Figure 12), and to measure strand slip at the end of the beams (Figure 13). A wood frame was used to position the LVDTs at the end of the beam (Figure 14). Electrical resistance foil strain gages recorded strain at discrete locations on the test

beams (Figure 15). Gages were typically 60-mm long, however 30 mm gages were used to measure transverse strain at the end of the beam (S6-S10). Figure 16 shows specimen B6S-C during testing. The load and support points are shown along with strain gage S2 and the LVDTs monitoring strand slip.

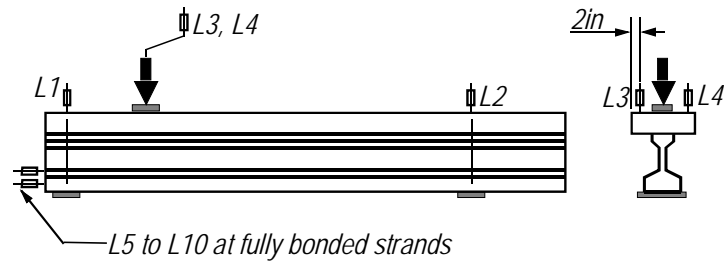


Figure 12–Small beam LVDT placement

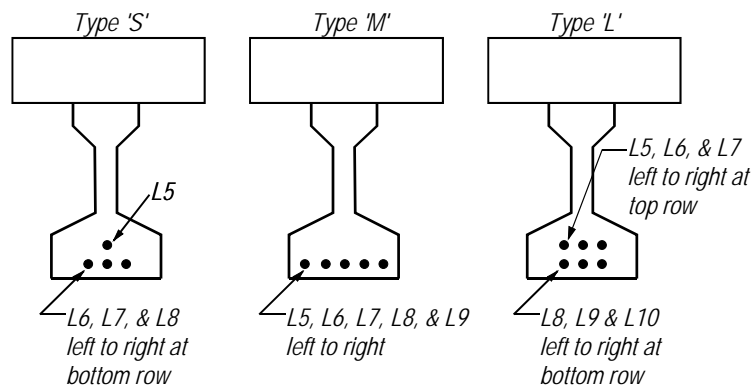


Figure 13–LVDTs at strands



Figure 14–LVDT frame at end of beam

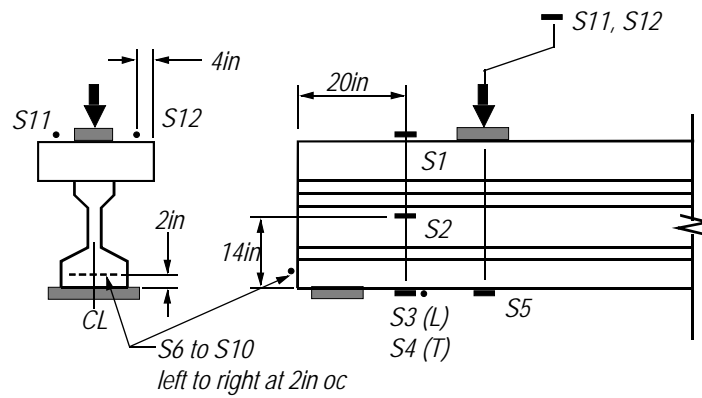


Figure 15–Strain gage placement



Figure 16–Specimen during testing

6 Results and Discussion

Confinement reinforcement was the most significant variable that affected the shear capacity and behavior. As such, test results are presented in pairs of similar confined and unconfined specimens in the following sections. For each pairing, the confined specimen and unconfined specimens were located on opposite ends of the same beam. Because the same beam was used for both tests in each pairing, both specimens had the same prestressing force, strand quantity, and strand pattern. For example, specimens B5L-C and B5L-U each had (6) 0.5-in. diameter strands, and were located at opposite ends of the same beam.

For convenience in reporting test results, the supports are referred to as the “near support” and the “far support.” The near support is the support closest to the load point, and the far support is farthest from the load point.

A summary figure is presented for each pairing of specimens. Each summary figure presents the load-displacement and load-slip results, first and final cracks locations, maximum load, displacement ductility, and failure mode. The displacement shown in the figures is the displacement at the load point, and has been adjusted to remove the effect of the bearing pad displacement. Strand slip presented in the test summaries are the average slip of each fully bonded strand as measured at the near support. Displacement ductility was calculated as the displacement at maximum load divided by the displacement at the on-set of nonlinearity as determined visually from the load-displacement diagram.

Three types of failures were observed in the beam tests: splitting, bond-flexure, and bond-shear. Failure modes and characteristics are presented in Table 2. Photos of specimens with different failure modes are shown in Figure 17 through Figure 20.

Table 2–Failure modes

Failure Mode	No. of Specimens	Characteristics
Splitting	6	Peak capacity is governed by the formation of a splitting crack above the support. Strands cannot support tensile force after formation of splitting crack.
Bond-Flexure	2	Strand slip after the formation of cracks. Peak capacity is governed by crushing of the compression zone. Deformation and rotation leading to crushing is augmented by the strand slip.
Bond-Shear	3	Strand slip after the formation of cracks. Peak capacity is governed by strand-concrete bond capacity.
Flexural	1	Load-displacement plot reaches a plateau indicating yielding of the reinforcement. Applied moment exceeds nominal moment capacity.

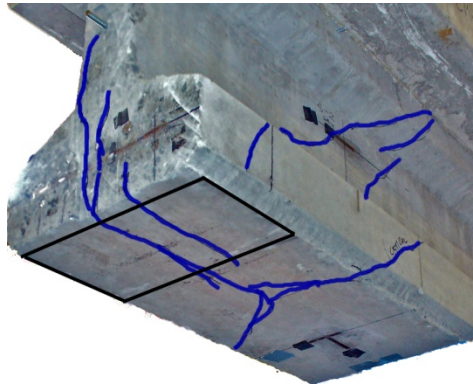


Figure 17–Bottom view of B6M-U with splitting failure mode

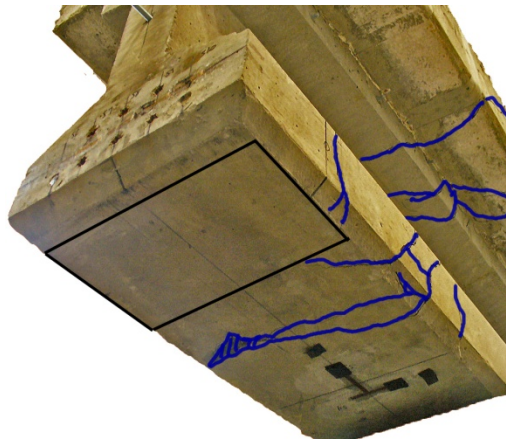


Figure 18–Bottom view of B6L-C with bond-shear failure mode



Figure 19–Bond-flexure failure mode (B6M-C)

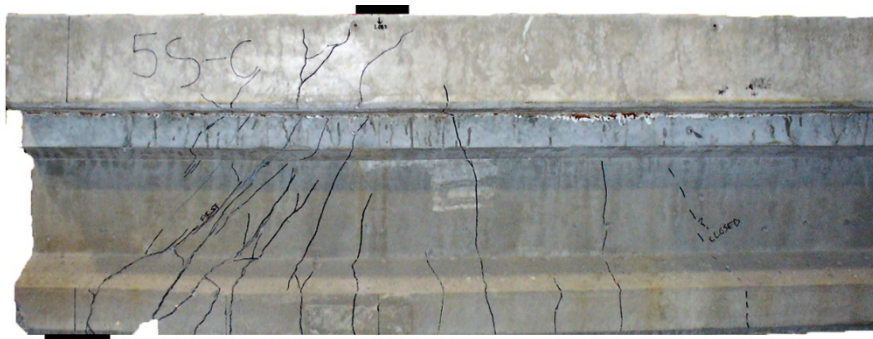


Figure 20–Flexural failure mode (B5S-C)

The specimens used in the testing were constructed and tested under a separate research program (O’Neill and Hamilton 2009), which focused on flexural stresses at mid-span. The beams were loaded in flexure up to and beyond cracking, but not to ultimate flexural capacity. Also, the specimens were modified prior to the current test program by saw-cutting the portion containing confinement reinforcement from one end of each beam (Figure 3). This modification was made to create the unconfined test conditions.

Previous flexural loading of the beams did not result in any visible cracking or damage to the end regions where the shear testing in the current program was focused. Micro-cracking, however, may have formed during the initial load tests and had some influence on the initial cracking loads in the shear tests. Micro-cracks, however, would have had different effects on confined and unconfined specimens. This is because the confined specimen tests used the same

bearing location as the tests by O'Neill and Hamilton, whereas the unconfined tests did not use the same bearing location.

For each pairing of confined and unconfined specimens, cracking always initiated in the confined specimen at a lower load. On average the load at initial cracking was 13% lower in the confined specimens than in the accompanying unconfined specimens. The early cracking in the confined specimens could have been initiated by micro-cracks in the end region that had formed during previous testing. Alternatively, differences in transfer length due to beam modification may also have been a factor influencing the cracking loads. Neither possibility can be evaluated from the available data, however the lower cracking loads in the confined specimens do suggest that the test procedures had some effect on the results. These effects, however, tend to support the results of the test program. For example, the confined specimens cracked at lower loads but still had greater strength and ductility than the unconfined specimens. Consequently, the beam modification and previous testing were concluded to have negligible effect. The FIB-54 girder test program, reported in Appendix D, did not have the same limitations as the small beams and can be used to verify the results and assumptions used in the small beam program.

6.1 B5L-C and B5L-U

Figure 21 summarizes the results for tests B5L-C and B5L-U. Each of these specimens had (6) 0.5 in. diameter strands, and varied only due to the presence or lack of confinement reinforcement. Both specimens behaved linear elastically until the formation of cracks. The first cracks were inclined web cracks occurring between the near support and the load point. Strain data from S2 gages indicated that initial cracks formed at applied loads of 96 kip and 116 kip for B5L-C and B5L-U, respectively. As the load increased, additional cracks formed in each specimen, and the cracks propagated into the flanges and the deck. Stiffness of each specimen was similar throughout loading.

Strands in each specimen began to slip after crack formation. Strands in specimen B5L-C began to slip gradually at an applied load of 96 kip, and more rapidly at load of 170 kip. Strands in B5L-U began to slip gradually at 116 kip and more rapidly at a load of 175 kip. In both cases, rapid strand slip was preceded by the formation of cracks in the bottom bulb that reduced the available development length. Abrupt strand slip in B5L-U occurred at 190 kip in

association with the formation of splitting cracks above the bearing. The strand slip at maximum load was 0.23 in. and 0.03 in. for B5L-C and B5L-U, respectively.

Specimen B5L-U supported a maximum applied load of 190 kip. At this load, a splitting crack formed above the near support and the specimen immediately lost load capacity. Failure of B5L-U was designated as a splitting failure.

Splitting failure did not occur in B5L-C, allowing this specimen to support additional load and displacement beyond the point at which B5L-U failed. Absence of splitting in B5L-C is attributed to the confinement reinforcement that controlled formation of splitting cracks. By preventing splitting, the confinement reinforcement allowed larger loads to be developed in the top strand and vertical reinforcement, which added to the specimen capacity. B5L-C supported a maximum applied load of 226 kip. At this load, testing was terminated because the specimen had almost no stiffness. Slip at peak load was 0.23 in. Continuation of the test would not have resulted in significantly higher load, but would have resulted in additional displacement, rotation, slip, and eventually crushing of the compression zone. Failure of B5L-C is designated as a bond-shear failure.

6.2 *B5M-C and B5M-U*

Figure 22 summarizes the test results of B5M-C and B5M-U. Each of these specimens had (5) 0.5-in. diameter strands and varied only due to the presence or lack of confinement reinforcement. Both specimens behaved linear elastically until the formation of cracks. The first cracks were inclined cracks occurring in the web between the near support and the load point. Strain data from S2 gages indicate that initial cracks formed at applied loads of 93 kip and 103 kip for B5M-C and B5M-U, respectively. As the load increased, additional cracks formed in each specimen, and the cracks propagated into the flanges and the deck. Stiffness of each specimen was similar throughout loading.

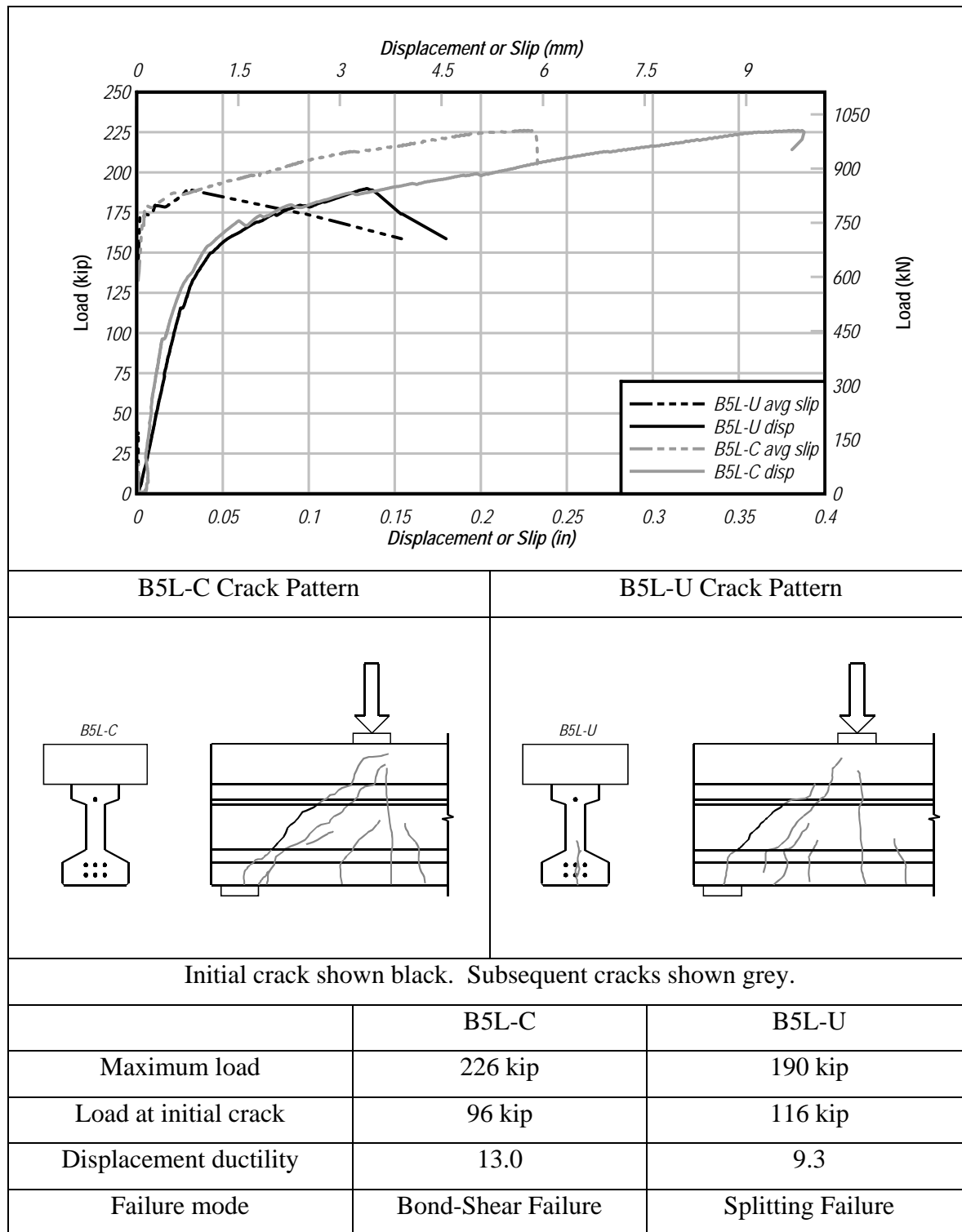


Figure 21–Summary of results for B5L-C and B5L-U

Strands in each specimen began to slip after the formation of cracks. Strands in specimen B5M-C began to slip gradually at an applied load of 113 kip, and more rapidly at load of 162 kip. Rapid slip at 162 kip occurred simultaneously with spalling of concrete from the bottom bulb. Spalling was limited to concrete outside of the confinement reinforcement. Strands in B5M-U did not slip until a load of 155 kip, by which load cracks had formed in the bottom bulb. Abrupt slip in B5M-U occurred at a load of 180 kip in association with the formation of a splitting crack above the bearing point. The strand slip at maximum load was 0.26 in. and 0.03 in. for B5M-C and B5M-U respectively.

Specimen B5M-U supported as maximum applied load of 180 kip. At this load a splitting crack formed above the near support and the specimen almost instantly lost load capacity. Failure of B5M-U is designated as a splitting failure. Figure__ shows the splitting crack at the end and bottom of B5M-U.

Splitting failure did not occur in B5M-C, allowing this specimen to support additional load and displacement beyond the point at which B5M-U failed. Absence of splitting in B5M-C is attributed to the confinement reinforcement which controlled formation of splitting cracks. By preventing splitting, the confinement reinforcement allowed larger loads to be developed in the top strand and vertical reinforcement, which added to the specimen capacity. B5M-C supported a maximum applied load of 205 kip. At this load, the compression zone on either side of the load point crushed. The rotation that led to compression zone crushing was augmented by strand slip. Failure of B5M-C (Figure 24) is designated as a bond-flexure failure.

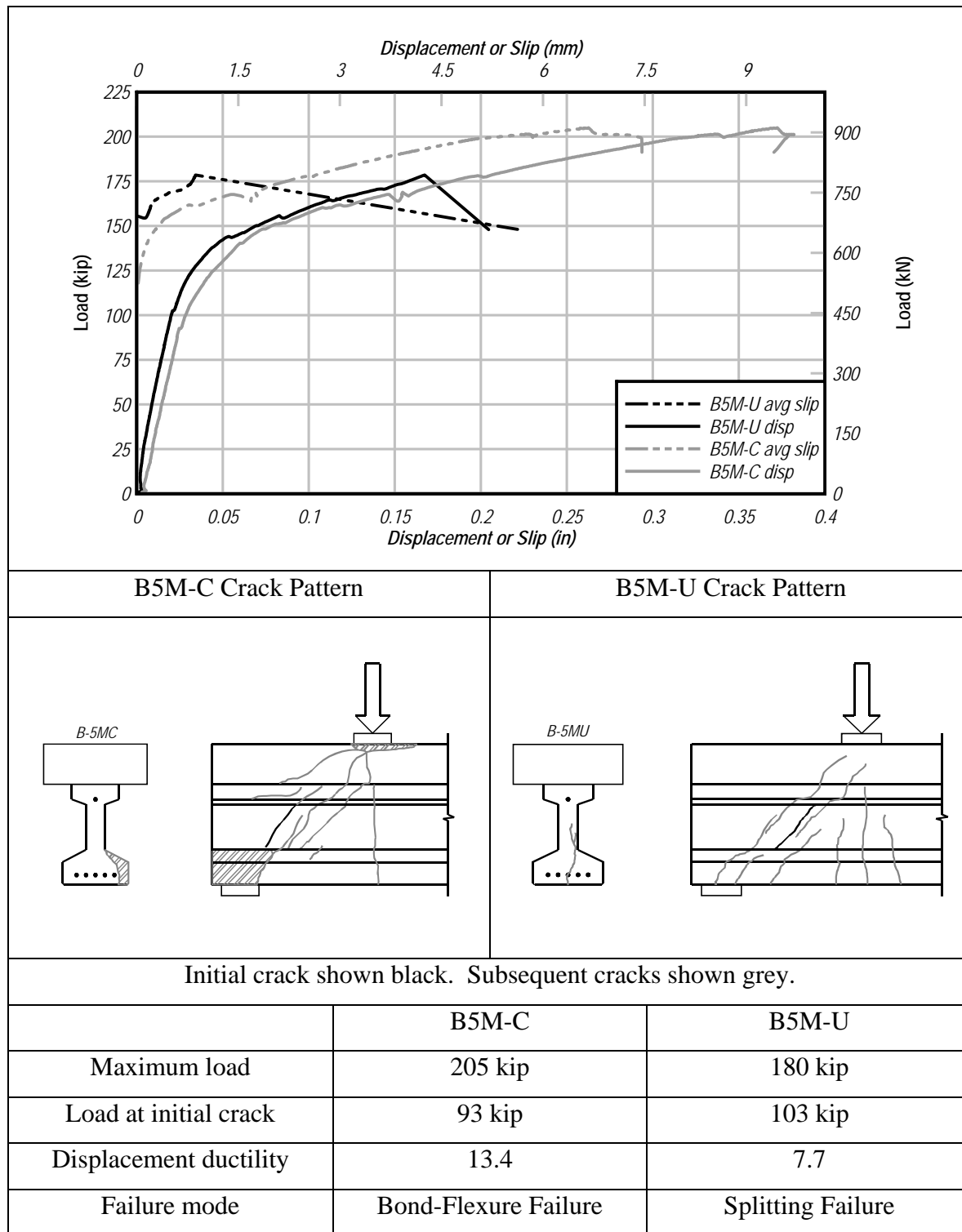


Figure 22–Summary of results for B5M-C and B5M-U

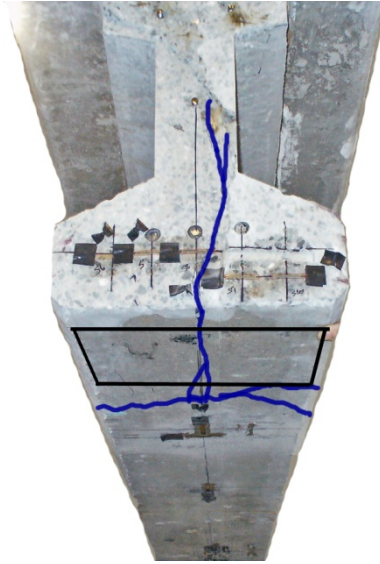


Figure 23–Bottom view of specimen with splitting failure mode (B5M-U)

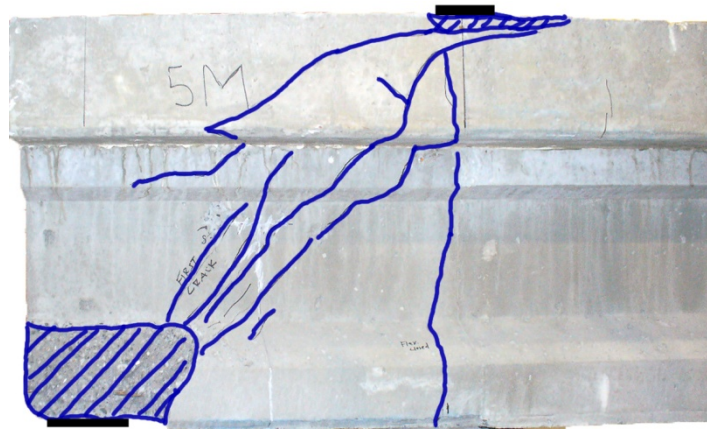


Figure 24–Bond-flexure failure mode (B5M-C)

6.3 B5S-C and B5S-U

Figure 25 summarizes the results from B5S-C and B5S-U. Each of these specimens had (4) 0.5-in. diameter strands, and varied only due to the presence or lack of confinement reinforcement. Both specimens behaved linear elastically until the formation of cracks. The first cracks were inclined web cracks occurring between the near support and the load point. Strain data from S2 gages indicated that initial cracks formed at applied loads of 105 kip and 113 kip for B5S-C and B5S-U, respectively. A flexural crack below the load point also formed in B5S-U at approximately 113 kip. As the load increased, additional cracks formed in each specimen, and

the cracks propagated into the flanges and the deck. Stiffness of each specimen was similar throughout loading.

Strands in each specimen began to slip after the formation of cracks. Strands in specimen B5S-C began to slip gradually at an applied load of 105 kip, and rapidly at load of 149 kip. Rapid slip at 149 kip corresponded to the formation of cracks within the development length. Strand slip in B5S-U was rapid, and began abruptly at load of 150 kip. Abrupt slip in B5S-U also accompanied the formation of a splitting crack above the near support at a load of 166 kip. The strand slip at maximum load was 0.34 in. and 0.07 in. for B5S-C and B5S-U respectively.

Specimen B5S-U supported as maximum applied load of 166 kip. At this load a splitting crack formed above the near support and the specimen almost instantly lost load capacity. Failure of B5S-U is designated as a splitting failure.

Splitting failure did not occur in B5S-C, allowing this specimen to support additional load and displacement beyond the point at which B5S-U failed. Absence of splitting in B5S-C is attributed to the confinement reinforcement which controlled formation of splitting cracks. By preventing splitting, the confinement reinforcement allowed larger loads to be developed in the top strand and vertical reinforcement, which added to the specimen capacity. Specimen B5S-C supported a maximum applied load of 199 kip. At this load, testing was terminated because the specimen had almost no stiffness. Continuation of the test would not have resulted in significantly higher load, but would have resulted in additional displacement, rotation, slip, and eventually crushing of the compression zone. Because B5S-C exceeded its nominal moment capacity, failure was categorized as a flexural failure. Figure 20 shows B5S-C after testing.

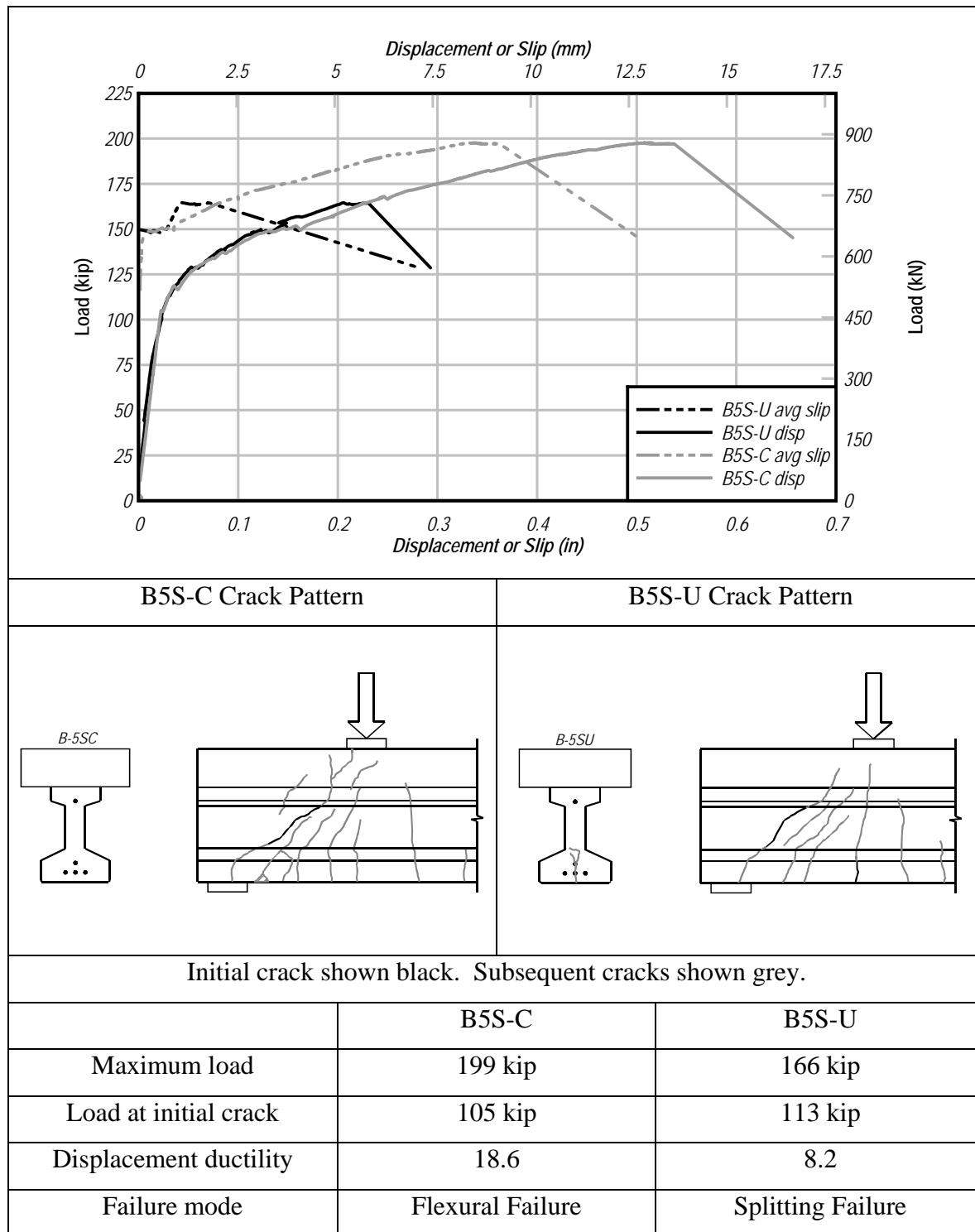


Figure 25– Summary of results for B5S-C and B5S-U

6.4 B6L-C and B6L-U

Figure 26 summarizes test results from B5S-C and B5S-U. Each of these specimens had (6) 0.6 in. diameter strands, and varied only due to the presence or lack of confinement reinforcement. Both specimens behaved linear elastically until the formation of cracks. Inclined web cracks formed between the near support and the load point. Strain data from S2 gages indicate that initial cracks formed at applied loads of 114 kip and 134 kip for B6L-C and B6L-U, respectively. As the load increased, additional cracks formed in each specimen, and the cracks propagated into the flanges and the deck. Stiffness of each specimen was similar throughout loading. The post-cracking stiffness of these and the other B6 specimens was greater than the post-cracking stiffness of the B5 specimens.

Strands in each specimen began to slip after the formation of cracks. Strands in specimen B6L-C began to slip gradually at an applied load of approximately 140 kip, and more rapidly at an applied load of 179kip, after the formation of cracks within the development length. When compared to all other specimens, the strand slip in B6L-C occurred in more discrete events. The magnitude of the slip events increased with increasing load. Strands in B6L-U began to slip at 142 kip. Rapid strand slip in B6L-U accompanied the formation of a splitting crack above the near support at a load of 172 kip. The strand slip at maximum load was 0.12 in. and 0.02 in. for B6L-C and B6L-U respectively.

Specimen B6L-U supported as maximum applied load of 172 kip. At this load a splitting crack formed above the near support and the specimen almost instantly lost load capacity. Failure of B6L-U is designated as a splitting failure.

Splitting failure did not occur in B6L-C, allowing this specimen to support additional load and displacement beyond the point at which B6L-U failed. Absence of splitting in B6L-C is attributed to the confinement reinforcement which controlled formation of splitting cracks. By preventing splitting, the confinement reinforcement allowed larger loads to be developed in the top strand and vertical reinforcement, which added to the specimen capacity. B6L-C supported a peak applied load of 239 kip. Upon reaching 239 kip, the load dropped suddenly to approximately 220 kip. Testing continued after the peak load had been reached, with a series of load increases followed by sudden drops. The sudden drops in load corresponded to strand slip events. The test was terminated once it was apparent that the maximum load had been reached.

Failure of B6L-C (Figure 18) is designated as a bond-shear failure. The 239 kip load support by B6L-C is the largest load supported by any of the test specimens.

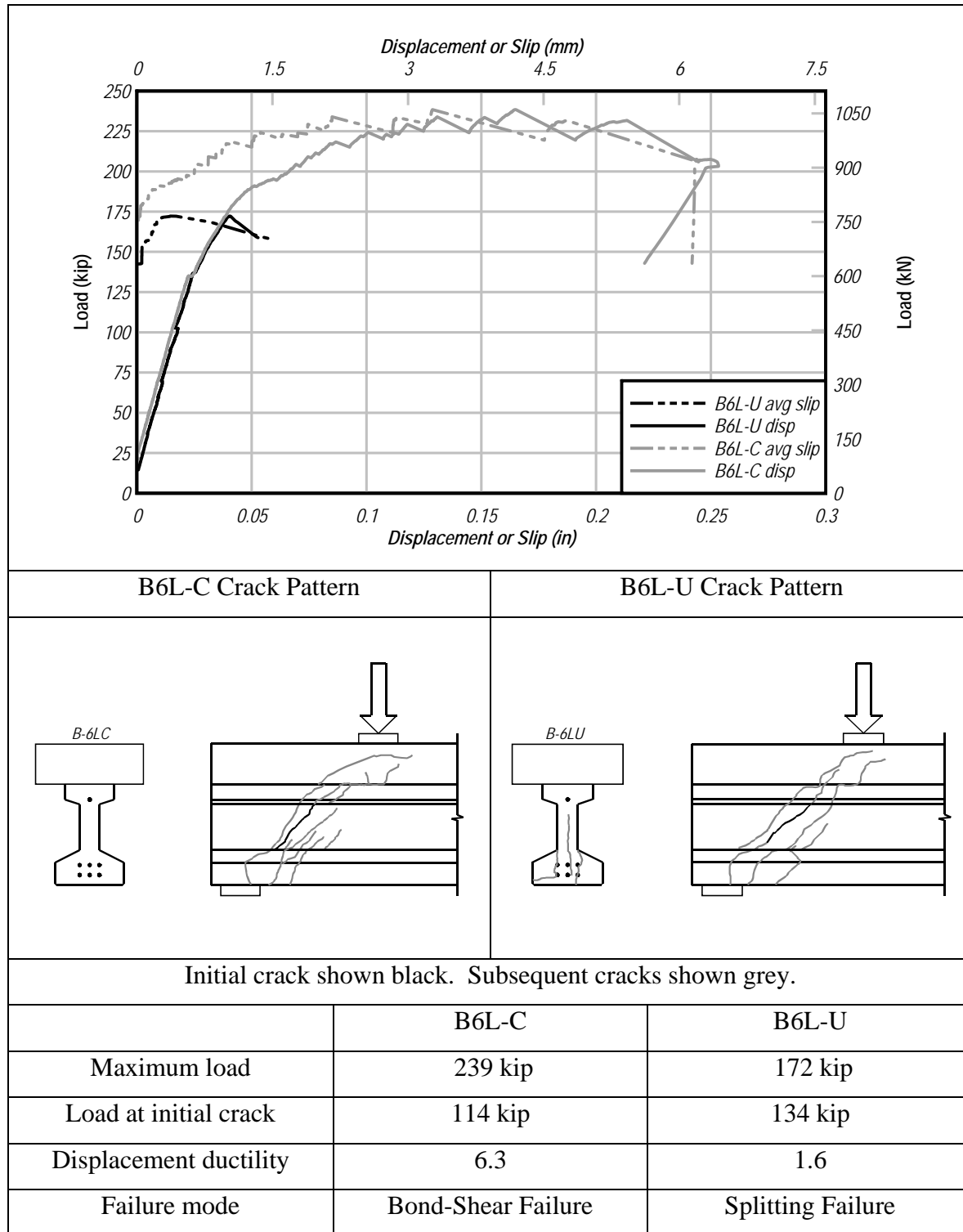


Figure 26– Summary of results for B6L-C and B6L-U

6.5 B6M-C and B6M-U

Figure 27 summarizes test results for B6M-C and B6M-U. Each of these specimens had (5) 0.6 in. diameter strands, and varied only due to the presence or lack of confinement reinforcement. Both specimens behaved linear elastically until the formation of cracks. The first cracks were inclined cracks occurring in the web between the near support and the load point. Strain data from S2 gages indicate that initial cracks formed at applied loads of 131 kip and 143 kip for B6M-C and B6M-U, respectively. As the load increased, additional cracks formed in each specimen, and the cracks propagated into the flanges and the deck.

The pre-cracking stiffness was almost identical for both specimens. However, the post-cracking stiffness of B6M-U could not be directly determined from the available data because the LVDT above the near support malfunctioned in the post-cracking phase of the test. To compensate for the lack of data, the bearing pad displacement at the near support was assumed to be 2.25 times the displacement of the bearing pad at the far support. The 2.25 factor is based on the ratio of the bearing pad displacements prior to the LVDT malfunction. The data presented in Figure 27 includes this assumption.

Strands in specimen B6M-U began to slip gradually at an applied load of about 80 kip, even before the formation of cracks. The 80 kip slip load was the lowest of any of the specimens. Strands in B6M-U began slipping more rapidly at load of 170 kip, after the formation of cracks in the bottom bulb. An abrupt slip event in B6M-U occurred at a load of 185 kip, and was associated with the formation of splitting cracks at the end of the specimen. Strands in specimen B6M-C did not slip until a load of 156 kip, by which load an inclined crack had formed in the bottom bulb. The drops in load at 205 kip and 215 kip correspond to concrete spalling off the bottom bulb above the support. Spalling was limited to portions of the concrete outside of the confinement reinforcement. Strand slip at maximum load was 0.45 in. and 0.03 in. for B6M-C and B6M-U respectively.

Specimen B6M-U supported a maximum applied load of 185 kip. At this load a splitting crack formed above the near support and the specimen almost instantly lost load capacity. Failure of B6M-U (Figure 17) is designated as a splitting failure.

Splitting failure did not occur in B6M-C, allowing this specimen to support additional load and displacement beyond the point at which B6M-U failed. Absence of splitting in B6M-C is attributed to the confinement reinforcement which controlled formation of splitting cracks. By

preventing splitting, the confinement reinforcement allowed larger loads to be developed in the top strand and vertical reinforcement, which added to the specimen capacity. Specimen B6M-C supported a maximum applied load of 227 kip. At this load, the compression zone on either side of the load point crushed. The rotation that led to compression zone crushing was augmented by the strands slipping. Failure of B6M-C (Figure 19) is designated as a bond-flexure failure.

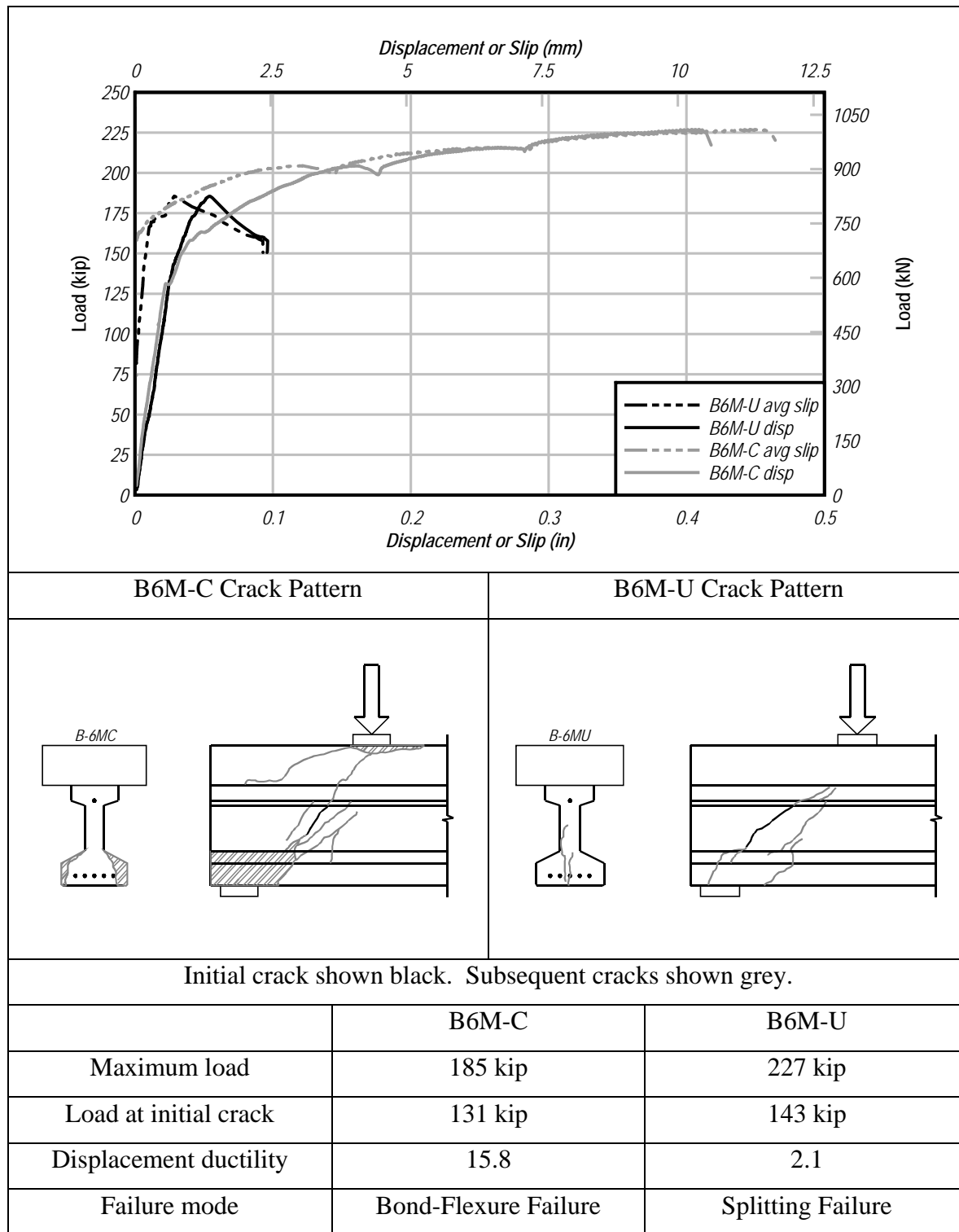


Figure 27– Summary of results for B6M-C and B6M-U

6.6 B6S-C and B6S-U

Figure 28 presents a summary of test results for specimens B6S-C and B6S-U. Each of these specimens had (4) 0.6 in. diameter strands, and varied only due to the presence or lack of confinement reinforcement. Both specimens exhibited linear elastic behavior until the formation of cracks. The first cracks for both specimens were inclined cracks occurring in the web between the near support and the load point. Strain data from S2 gages indicate that the initial cracks formed at applied loads of 110 kip and 132 kip for B5S-C and B5S-U, respectively. As the load increased, additional cracks formed in each specimen, and the cracks propagated into the flanges and the deck. Stiffness of each specimen was similar throughout loading.

Strands in each specimen began to slip after the formation of cracks. Strands in specimen B6S-C began to slip gradually at an applied load of 130 kip and more rapidly at load of 157 kip, corresponding to the formation of a crack within the development length. Strand slip in B6S-U was rapid and began at load of 152 kip. The abrupt slip event in B6S-U at 154 kip accompanied the formation of a splitting crack above the near support. The strand slip at maximum load was 0.34 in. and 0.03 in. for B6S-C and B6S-U respectively.

Specimen B6S-U had the smallest capacity of any test specimen, supporting a maximum applied load of 154 kip. At this load a splitting crack formed above the near support and the specimen almost instantly lost load capacity. Failure of B6S-U is designated as a splitting failure.

Splitting failure did not occur in B6S-C, allowing this specimen to support additional load and displacement beyond the point at which B6S-U failed. Absence of splitting in B6S-C is attributed to the confinement reinforcement which controlled formation of splitting cracks. By preventing splitting, the confinement reinforcement allowed larger loads to be developed in the top strand and vertical reinforcement, which added to the specimen capacity. Specimen B6S-C supported a maximum applied load of 209 kip. At this load, testing was terminated because the specimen had almost no stiffness. Continuation of the test would not have resulted in significantly higher load, but would have resulted in additional displacement, rotation, slip, and eventually crushing of the compression zone. Failure of B5S-C (Figure 29) is designated as a bond-shear failure.

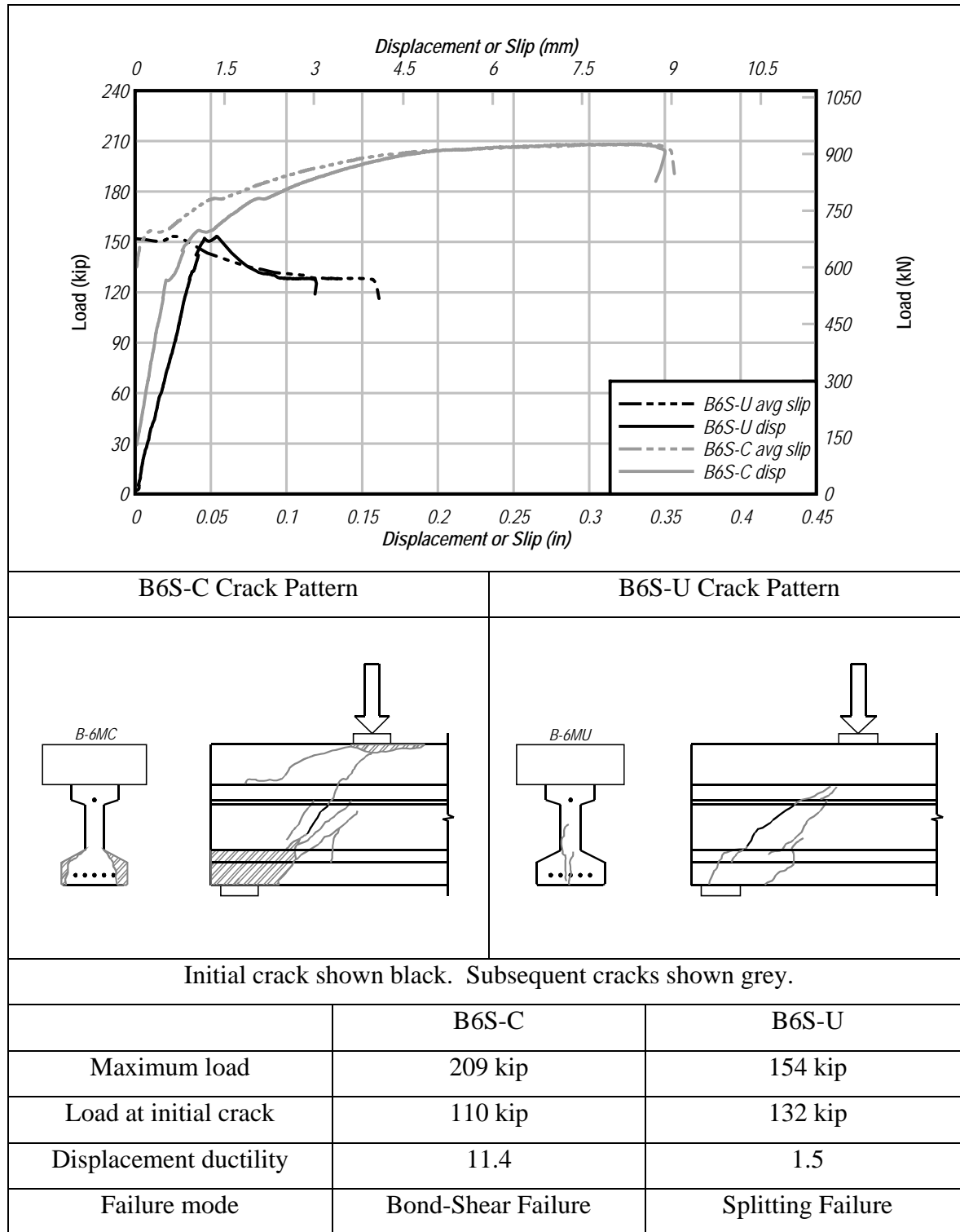


Figure 28– Summary of results for B6S-C and B6S-U

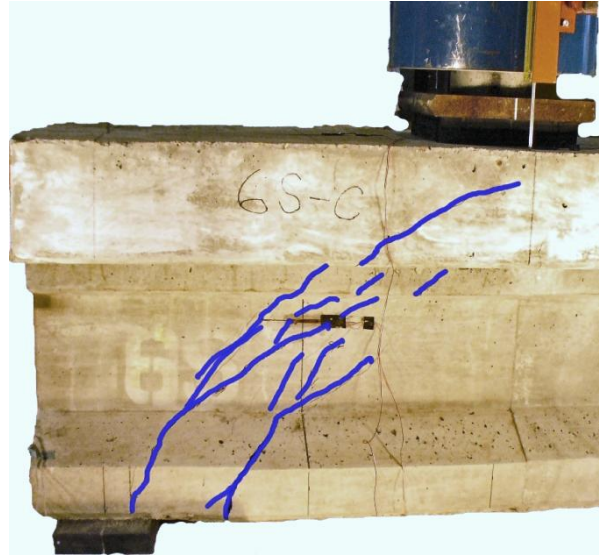


Figure 29– Bond-shear failure mode (B6S-C)

6.7 *Transverse Strain*

Strain gages were placed at the end of the specimens above the near support (Figure 15) to measure the transverse strain in the bottom flange. Figure 30 shows the strains reported by these gages at a load of 15 kip. This load was chosen because it was well within the linear-elastic range of all tests. Strain gages from each specimen reported that transverse strain was greatest below the web and decreased towards the edges of the flange. Figure 30 also shows the results of a finite element analysis which will be discussed in Appendix F.

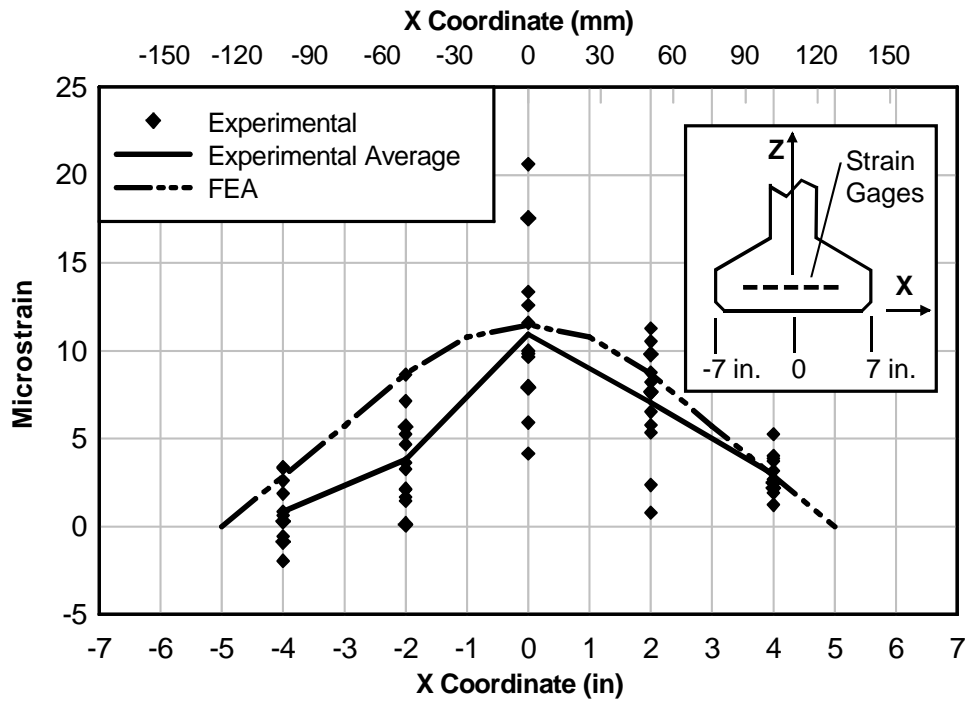


Figure 30–Transverse strain above near support (load =15 kip)

Figure 31 presents the superimposed shear versus transverse strain data from gages on the end of B6L-C. The trends in the figure are representative of all tests with confinement reinforcement. At the beginning of the test the strain was initially proportional to the applied load, indicating linear-elastic behavior. The strain-load relationship became nonlinear after the formation cracking in the web, and changed rapidly after the cracks propagated into the bottom flange and the strands began slipping. Splitting cracks were not visually observed in the confined specimens; however strain data suggest that a vertical splitting crack likely formed at the end of the confined specimens. This can be observed in Figure 31, where gage S8 reported a sudden increase in strain tensile strain at a load of approximately 190 kip. The magnitude of tensile strain reported by S8 is indicative of crack formation. Because of the confinement reinforcement, these cracks were controlled and splitting failure was prevented.

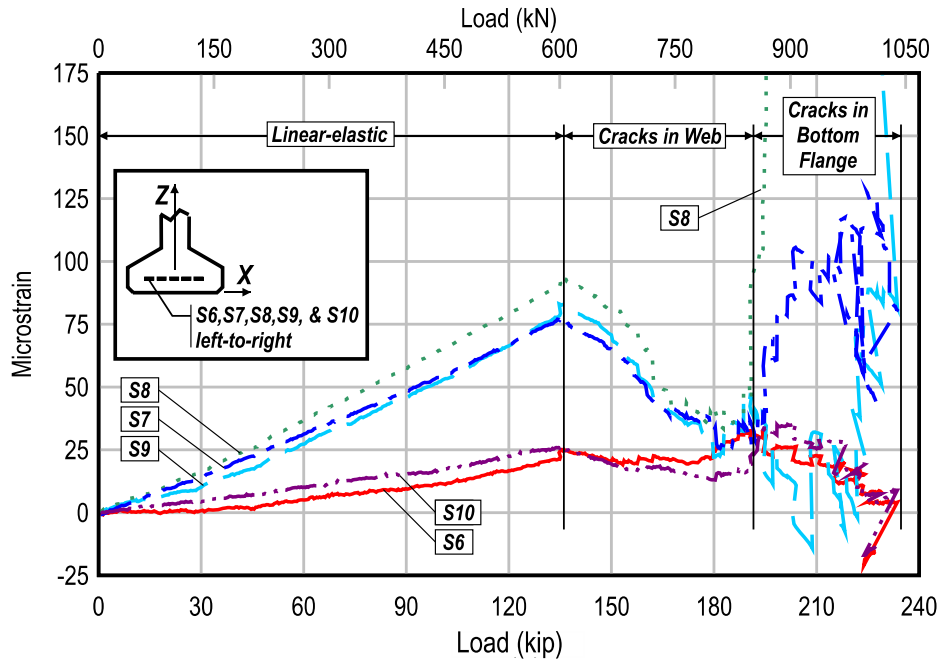


Figure 31–Effect of load on transverse strain in confined specimen (B6L-C).

Figure 32 presents the transverse strain data from gages on the end of B5L-U. Trends in this figure are representative of all unconfined tests. Strain was initially proportional to the applied load, indicating linear-elastic behavior. The strain-load relationship became nonlinear after the formation of cracks in the web. The strain changed rapidly after the cracks propagated into the bottom bulb, then again when splitting cracks formed.

Strain gage S4 was mounted transversely on the bottom on the specimens, approximately 5 in. in from of the bearing pad at the near support. Figure 33 shows load-strain data from gage S4 on B5M-C and B5M-U. The qualitative trends shown in the figure are representative of each pairing of confined and unconfined specimens. The load-strain relationship was initially linear for both the confined and unconfined specimens. The strain was compressive (negative) due to Poisson shortening in the transverse direction as the bottom of the specimen elongated in the longitudinal direction. Nonlinear behavior occurred with the formation of cracks at applied loads of 93 kip and 103 kip for B5M-C and B5M-U, respectively. Strain in B5M-U suddenly became increasingly tensile (positive) starting at a load of about 134 kip; indicating the formation of a crack near the gage location. The tensile strain continued to increase rapidly until splitting failure occurred at a load of 180 kip. For B5M-C, the strain reported by gage S4 continued to become increasingly more compressive (negative) as the load increased, even after the onset of

nonlinearity. Because transverse tensile strains did not occur in the confined specimen, the confinement reinforcement was thought to have prevented the propagation of splitting cracks near gage S4. This conclusion is supported by a visual examination of the specimen, which did not detect any splitting cracks at the end of B5M-C.

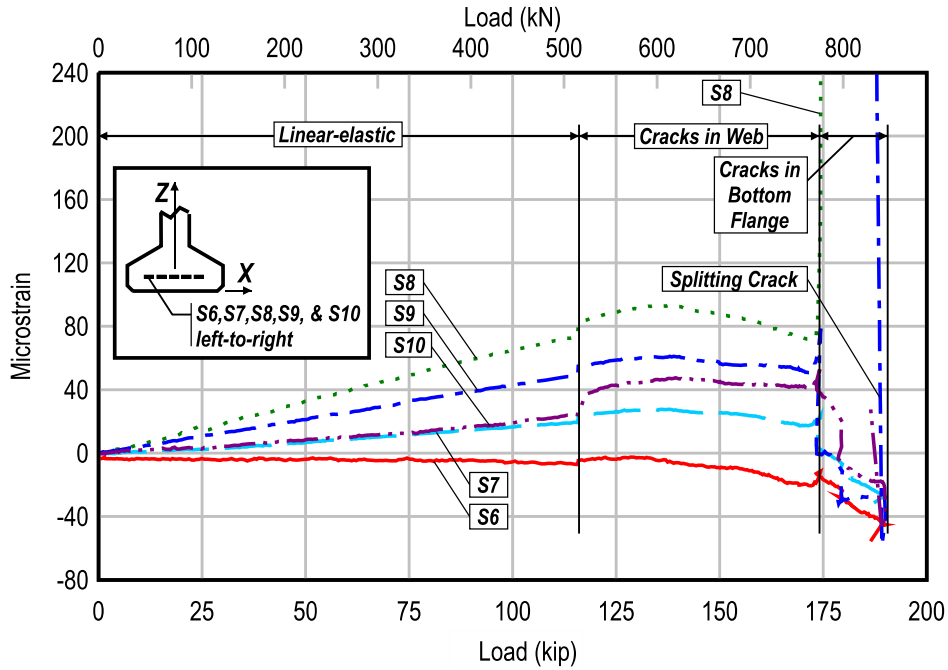


Figure 32–Effect of load on transverse strain in unconfined specimen (B5L-U)

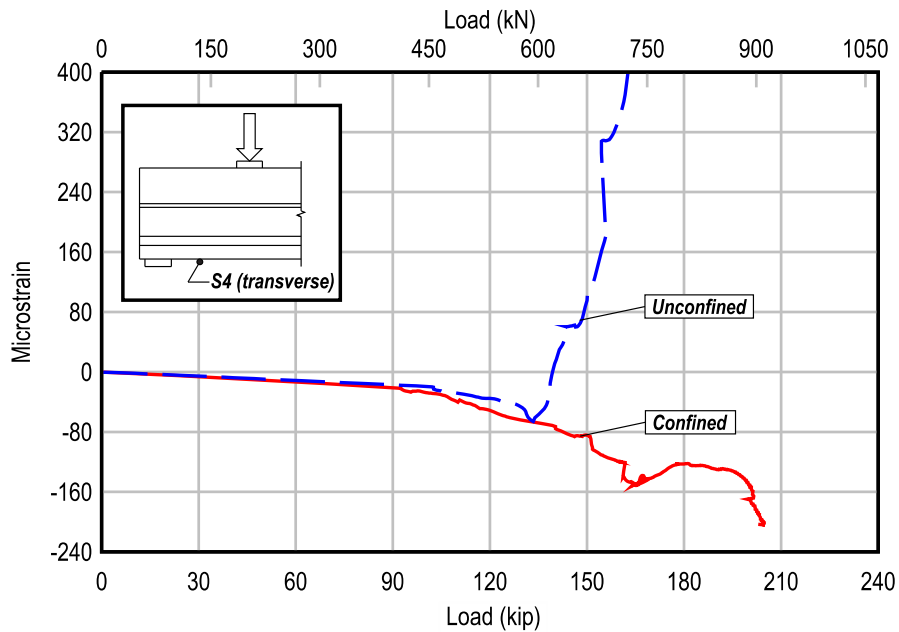


Figure 33–Strain readings from gage S4 (B5M)

6.8 Spalling: B5M-C and B6M-C

Edges of the bottom flanges of specimens B5M-C and B6M-C spalled off during testing. The spalling occurred above the near support, and was limited to the concrete outside of the confinement reinforcement. The confinement reinforcement was visible after the spalling, as shown in Figure 34.

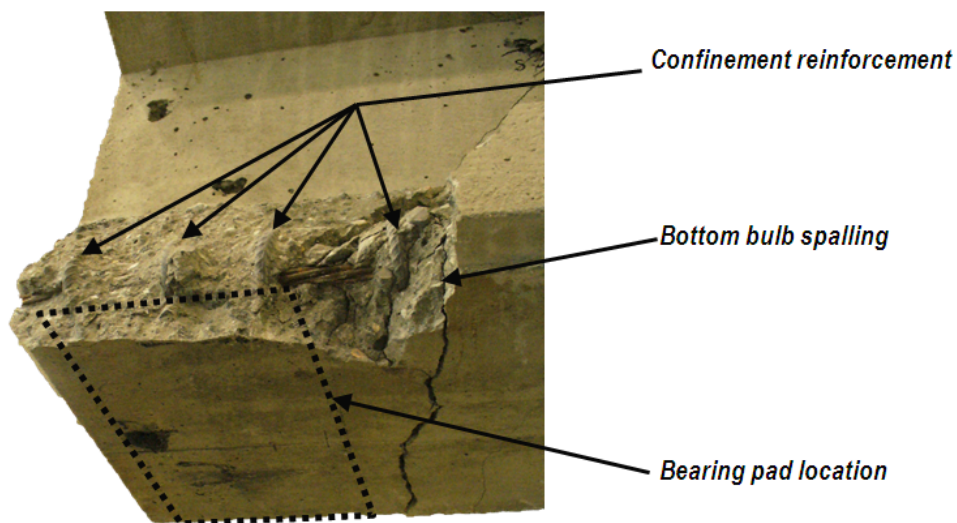


Figure 34–Flange spalling (B5M-C).

For both B5M-C and B6M-C, the load at which spalling occurred was similar to the load at which at which splitting cracks formed in the associated unconfined specimens B5M-U and B6M-U. This observation suggests that the confinement reinforcement had engaged and was supporting transverse forces that would have otherwise caused splitting in B5M-C and B6M-C. This observation is also consistent with the behavior of reinforcement concrete columns, where spalling is indicative that confinement reinforcement is engaged.

It is notable that spalling occurred in specimens B5M-C and B6M-C, both of which have five strands. The five strand layout placed strands near the edges of the bottom flange (Figure 6). Llanos et al (2009), reported that strand patterns with fully bonded strands placed at the edges of the flanges can lead to transverse splitting forces. These splitting forces in specimens B5M-C and B6M-C may have contributed load in the confinement reinforcement thereby leading to spalling. Another possible reason for the spalling in these specimens is that the concrete at the edges of the flanges were under greater compressive load due to the prestress force being applied by the outermost strands.

6.9 Individual Strand Slip

Strand slip data have been presented as the average slip of the bonded strands. Average slip is a convenient way of evaluating overall slip behavior, but load-slip data from individual strands is also instructive. Figure 35 presents the load-slip data for each strand in specimen B5S-C, and demonstrates general trends observed in the slip data from confined tests. Strand slip in B5S-C began gradually after the formation of cracks at load of approximately 120 kip, then increased rapidly as cracks propagated into the bottom bulb at approximately 145 kip. Each strand slipped at approximately the same load and through the same distance.

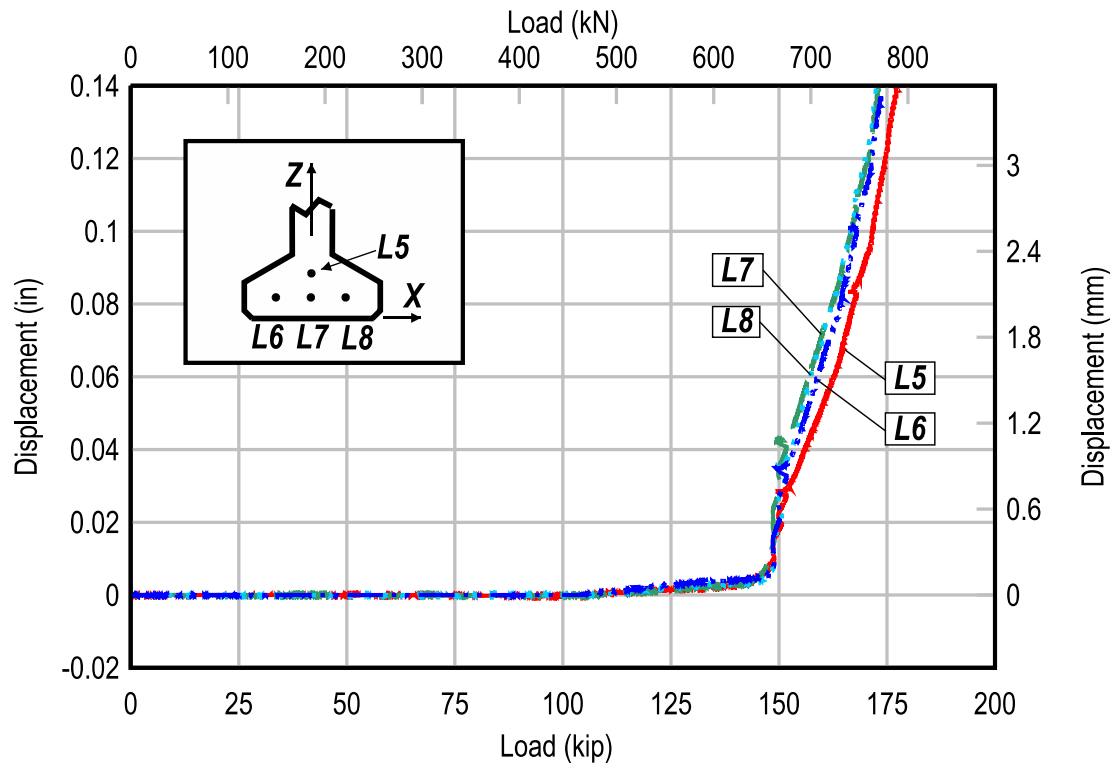


Figure 35–Prestressing strand slip in specimen B5S-C

Figure 36 shows the load-slip behavior for B5L-U, and demonstrates general trends observed in the slip data of the unconfined tests. Strand slip in the B5L-U occurred abruptly, and individual strands did not slip at the same load or through the same distance. The first strands to slip were those located at the centerline of the cross-section below the web. This can be seen in the figure, where strands 5 and 7 (located at the cross-section centerline) slipped first. Strands 6 and 8 were located away from the centerline and slipped later. An “unzipping” mechanism appears to have occurred in the unconfined specimens, where load was transferred to the outer strands after the inner strands began to slip. The outer strands also began to slip after the strand/concrete bond capacity was exceeded. All strands slipped when a splitting crack formed at the peak load of 166 kip.

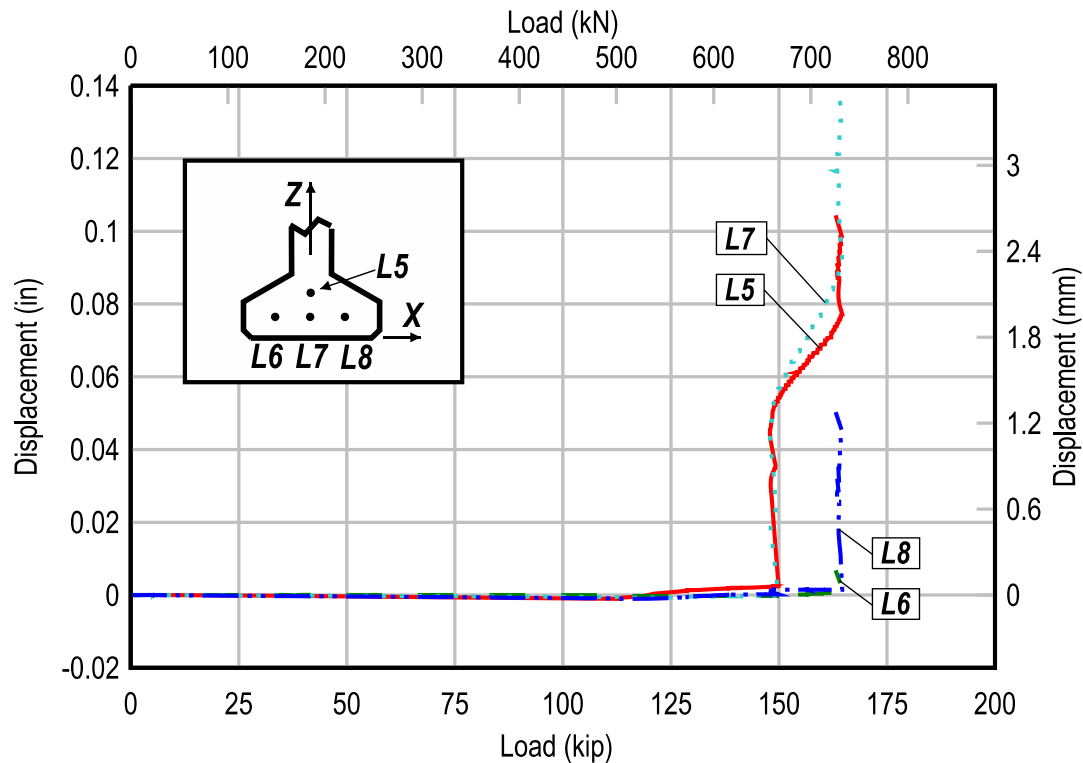


Figure 36–Prestressing strand slip in specimen B5S-U

Differences in load-slip behavior between the confined and unconfined specimens are attributed to the confinement reinforcement. Formation of cracks within the strand development length always preceded rapid strand slip. Cracks in the confined specimens engaged the confinement reinforcement, which then arrested the further propagation of cracking. Because crack propagation was hindered in the confined specimens, crack and slip events were initially less drastic than in the unconfined specimens. In addition to slowing crack propagation, confinement reinforcement is also believed to have created a confining force on the strands and concrete. By arresting the formation of cracks, and/or by providing a confining force, confinement reinforcement lead to more uniform conditions for the strands in confined specimens. This uniform condition is considered culpable for the observation that all strands in the confined specimen tended to slip together.

6.10 Shear Capacity

Figure 37 shows the normalized shear capacity for each test. Note that the shear capacity is taken as the shear force corresponding to the maximum load and occurring at the support

nearest the load point. Values have been normalized by the average of the unconfined specimen capacities, which was equal to 138 kip (614 kN). The data clearly indicate that variation in strand diameter had little effect on the shear capacity in unconfined tests. The average capacity of the unconfined tests with 0.5-in. (12.7 mm) diameter strand (B5 in the figure) and 0.6-in. (15.2 mm) diameter strand (B6 in the figure) varied by only 4%, indicating that strand size and area of prestressing steel did not significantly affect the capacity of the unconfined specimens.

Confined tests resulted in an average of 25% more shear capacity than that of the unconfined tests. Confinement reinforcement prevented splitting failure in the bottom flange, allowing the increased contribution from the vertical reinforcement. As the confined specimens rotated beyond the point at which the unconfined specimens split and failed, the forces in the vertical steel increased, leading to improvements in shear capacity. This presumption is supported by the load-displacement data from the confined specimens. The loss of stiffness as the confined specimens approached maximum capacity indicates that the vertical reinforcement and top strand were at or approaching yielding. The increased rotation also caused the resultant of the compressive force to move upwards in the section, thereby increasing the moment arm and shear contribution of the prestressing strands.

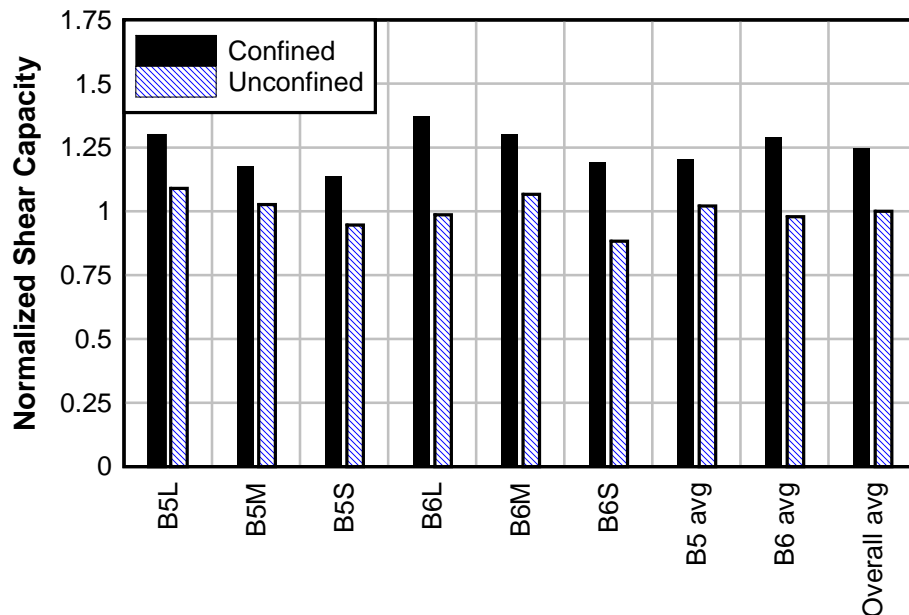


Figure 37–Normalized shear capacity

Figure 38 shows the shear capacity plotted against the area of prestressing steel for confined and unconfined tests. In the unconfined tests there is no clear relationship between shear capacity and area of prestressing steel, indicating that the capacity of the unconfined specimens was not a function the amount of prestressing steel. The confined tests, however, show a proportional relationship between the area of prestressing steel and the shear capacity. This difference is explained by the change in the nature of the failure mode with the addition of confinement reinforcement. In the tests with no confinement reinforcement, specimens reached capacity when end splitting occurred, which effectively eliminated strand bond at the end of the specimen. When confinement reinforcement was present, splitting failure was avoided and the prestressing strands were at least partially mobilized to contribute to shear capacity. This explains the direct proportionality between prestressing steel area and shear capacity in the confined tests.

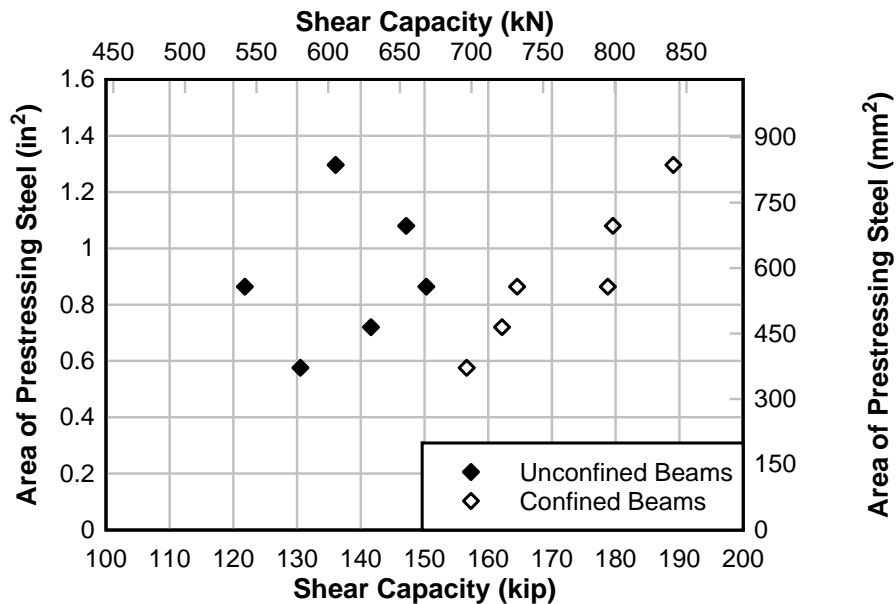


Figure 38–Effect of area of prestressing on shear capacity

6.11 Displacement Ductility

Figure 39 shows the displacement ductility for each specimen, normalized by the average ductility of all specimens. Displacement ductility was calculated by dividing the displacement occurring at maximum load by the displacement occurring at the onset of nonlinearity.

Displacement at maximum load was used in the calculations because the ultimate displacement was arbitrarily determined by the termination of the testing.

The average displacement ductility of the confined tests was 157% greater than that of unconfined tests. The greater ductility of the confined specimens is attributed to the confinement reinforcement, which prevented splitting failure and thereby allowed the confinement specimens to support larger displacements.

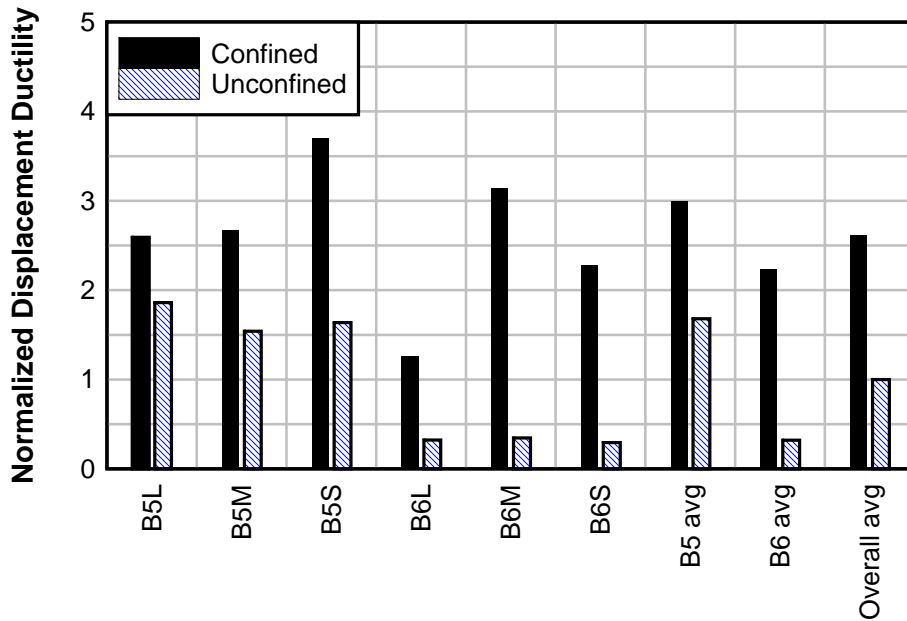


Figure 39–Normalized displacement ductility

7 Strut-and-Tie Model

Using an approach similar to the longitudinal reinforcement provisions in 5.8.3.5 of the 2007 AASHTO LRFD Bridge Design Specifications, strut-and-tie models (STM) were developed to describe the behavior and capacity of the unconfined and confined specimens. Models are presented in Figure 40 and Figure 41 for the unconfined and confined specimens, respectively. The only difference between the models is that the confined model considers the confinement reinforcement to contribute in a manner similar to the vertical reinforcement (Csagoly, 1991). The STM models are based on a series of assumptions:

- A crack is assumed to form between the near support and the load point which crosses the bottom strands (T_1), top strand (T_2), vertical reinforcement (V_s), and confinement reinforcement if present ($V_{s,cr}$).
- The location of the compressive force, point 'C', was assumed to occur at the top of the beam. The STM shear capacity is derived from moment equilibrium about the point 'C'; point. Forces T_1 , T_2 , V_s , and $V_{s,cr}$ (confined specimens only), create moments about point 'C', and thus contribute to the shear capacity.
- Because the available development length of the bottom strands is shortened by the assumed crack, the bottom strands were assumed to be only 30% developed.
- The top strand and vertical reinforcement are fully developed.
- The assumed crack crosses (9) vertical bars. A smeared steel concept was used to place the combined effect of all vertical reinforcement at $a/2$.
- For the confined specimens, the crack was assumed to have engaged a single confinement hoop. Because the hoops are not long enough for full development, 75% development was assumed. The confinement reinforcement is assumed to act at the node directly above the bearing. Consideration of the confinement reinforcement as vertical reinforced was proposed by Csagoly (1991).

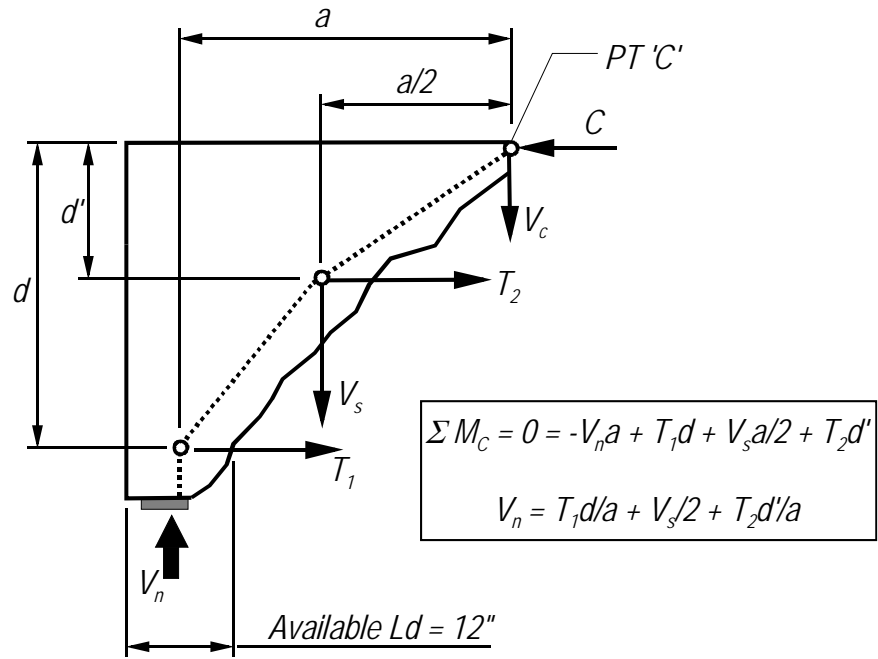


Figure 40–Unconfined specimen strut and tie model

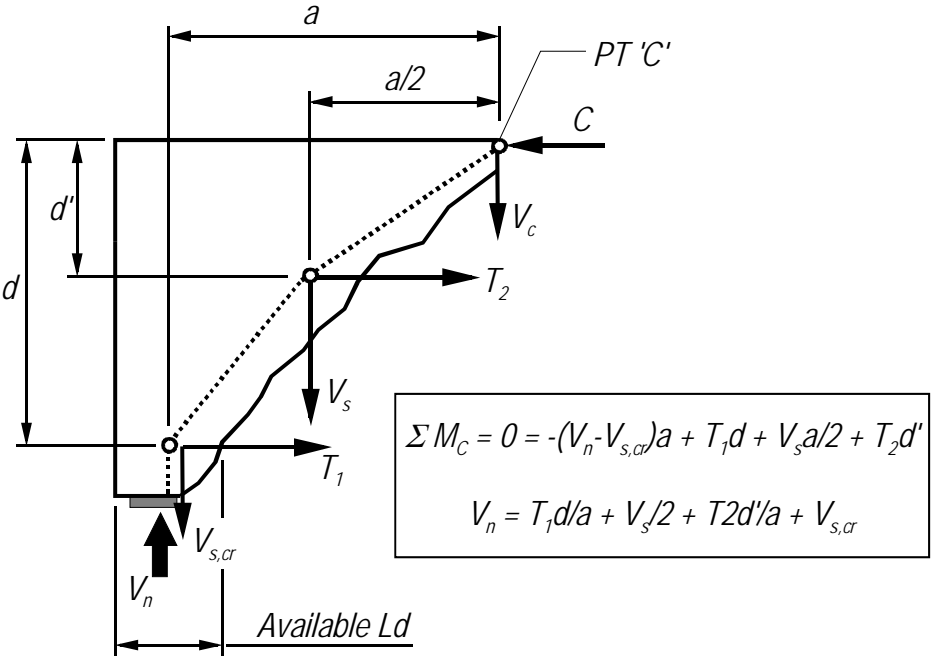


Figure 41–Confined specimen strut and tie model

STM predictions and experimental results are compared in Table 3. On average the STM predictions were within 3% of the experimental results. The STM always under-predicted the capacities of the specimens with 0.5 in. strands (B5), and over-predicted the capacities of

specimens with 0.6 in. strands (B6). Because the same strand development was used regardless of strand size, one possible reason for the difference is that the development was greater than the assumed 30% for B5 specimens and less than 30% for the B6 specimens. This rational is consistent with AASHTO LRFD section 5.11.4., which calculates development length as a function of strand diameter.

Another possible reason for the difference between the 0.5 in. and 0.6 in. strand specimens is that the top strand and mild reinforcement were less developed in the B6 specimens than in the B5 specimens. This is supported by the observation that the B6 specimens had smaller deflections at maximum load, suggesting that the steel in the B6 specimens may have been less developed than steel in the B5 specimens.

Table 3–Comparison of measured and computed shear capacity using STM

Test	V_{EXP} (kip)	V_{STM} (kip)	$\frac{V_{STM}}{V_{EXP}}$
B5L-C	167	181	1.09
B5L-U	149	152	1.02
B5M-C	155	164	1.06
B5M-U	137	144	1.05
B5S-C	142	159	1.12
B5S-U	124	133	1.07
B6L-C	208	191	0.92
B6L-U	190	138	0.73
B6M-C	191	182	0.96
B6M-U	173	149	0.86
B6S-C	173	167	0.97
B6S-U	155	124	0.80
Average			0.97
B5x Avg.			1.07
B6x Avg.			0.87
Bxx-C Avg.			1.02
Bxx-U Avg.			0.92

STM results are compared to the confined and unconfined tests results separately. Looking first at the unconfined tests, Table 4 lists the experimental results along with the STM calculated shear contribution of the top strand and vertical reinforcement. Even when calculated based on potentially unconservative assumptions (i.e. full development), the combined contribution of the top strand and vertical reinforcement do not account for the experimental

capacity. Thus the bottom strands were clearly contributing to the experimental shear capacity at peak load. The shear contribution of the bottom strands can be estimated by subtracting the shear contributions of the top strand and vertical reinforcement from experimental shear capacity. Estimated contributions of the bottom strands are listed in the final column of the table and demonstrate that the strands in the unconfined specimens contributed to the shear capacity up until the point of splitting failure.

Table 4–Estimated portion of shear carried by prestressing strand tie (unconfined specimens)

Test	Experimental shear capacity (kip)	STM shear contribution of vert reinf & top stand (kip)	Estimated shear supported by bottom strand contribution (kip)
	V_{EXP}	V_{VR+TS}	$V_{EXP} - V_{VR+TS}$
B5L-U	152	75	77
B5M-U	144	75	69
B5S-U	133	75	58
B6L-U	138	84	54
B6M-U	149	84	65
B6S-U	124	84	40

Looking now at the confined tests, the experimental results provide a means of evaluating the 30% bottom strand development assumed by the STM. An expression for force in the bottom strands (T_l) can be derived by rearranging the shear capacity equation in Figure 41. Using the derived expression, the bottom strand force can be estimated by substituting the experimental shear capacity (V_{EXP}) for the nominal shear capacity (V_n). An estimate for strand development can then be calculated by dividing the estimated bottom strand force by the ultimate strand capacity. These calculations are carried out in Table 5. The average estimated bottom strand development was calculated to be 32%, similar to the assumed 30%. Results of the calculations also support the previously discussed possibility that the 0.5 in. diameter strands were more developed than the 0.6 in. diameter strands.

Table 5–STM details of confined specimens.

Test	Exp. shear capacity (kip)	Shear contribution of vert. bars, confinement, & top stand (kip)	Estimated force supported by bottom strands (kip)	Ult. bottom strand capacity (kip)	Estimated development (%)
	V_{EXP}	$V_{VR+TS+CR}$	$T_{est} = (V_{EXP} - V_{VR+TS+CR})(a/d)$	T_{ult}	$(T_{est}/T_{ult})*100$
B5L-C	181	93	88	248	35
B5M-C	164	93	71	207	34
B5S-C	159	93	66	165	40
B6L-C	191	102	89	352	25
B6M-C	182	102	80	293	27
B6S-C	167	102	65	234	28
Avg.					32
Avg. B5					36
Avg. B6					27

The relationship between experimental shear capacity and area of prestressing steel provides yet another means of estimating the bottom strand development in the confined specimens. Figure 42 presents the experimental data and a trend line approximating the relationship between shear capacity and area of prestressing. The trend line is expressed mathematically in Equation 1. The area of prestressing strand (A_{ps}) is a variable in the linear term of Equation 1. Accordingly, the linear term is assumed to be the contribution to the shear capacity from the prestressing strands (Equation 2). For the tested a/d ratio of 1.0, the shear contribution of the bottom strands is equal to the force in the strands. Thus, the trend line implies that at maximum capacity, the bottom strands supported 80 ksi. This stress corresponds to 30% strand development, and is in good agreement with the assumed value.

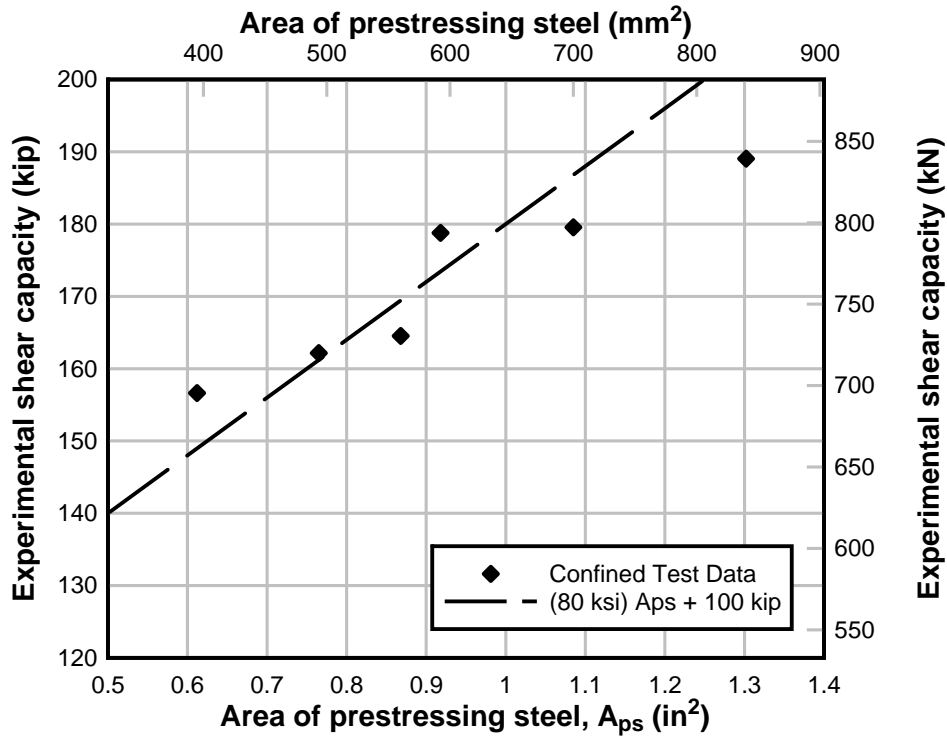


Figure 42—Experimental shear capacity vs. area of prestressing steel

$$V_{EXP} = A_{ps}(80ksi) + 100kip \quad \text{Equation 1}$$

$$\text{Bottom strand shear contribution} = T_1 \left(\frac{d}{a} \right) = A_{ps}(80ksi) \quad \text{Equation 2}$$

The constant term in Equation 1 can also be related to the STM. Equation 3 assumes that the 100 kip constant term is equal to the combined shear contributions of the vertical reinforcement, top strand, and confinement reinforcement. Using the STM, the average combined contribution of these components was calculated to be 93 kip and 102 kip for the B5x and B6x specimens, respectively. The similarity between the experimental trend line and the STM suggests that the assumptions used in the STM are reasonable approximations of the physical system.

$$V_{VR+TS+CR} = 100kip \quad \text{Equation 3}$$

8 Code Comparison

This section compares the experimental results with the nominal capacities calculated using current design codes. All calculations used the material properties shown in Table 6. The geometric properties, reinforcement, and prestressing were based on the specified values presented in section 3.

Table 6–Material properties used in calculations

Material Property	Value
Concrete deck compressive strength (Used in flexural calculations)	6500 psi
Concrete girder compression strength (Used for shear calculations)	8500 psi
Reinforcement yield strength	60 ksi
Prestressing strand ultimate strength	270 ksi

Experimental and code calculated shear capacities are presented in Table 7. Experimental results in the table include shear force due to the self-weight, as well as shear from the applied load. Nominal shear capacities were calculated using three methods:

1. Modified compression field theory (MCFT) from AASHTO LRFD Bridge Design Specification (2007).
2. Detailed method (ACI) from American Concrete Institute ACI 318 (2008).
3. Strut-and-tie modeling as presented in the previous section.

None of the specimens failed in the modes assumed by the MCFT and ACI calculations. Comparisons with these methods are nevertheless useful in evaluating the degree of conservatism in the code provisions. On average, MCFT was more conservative than ACI, predicting shear capacities that were only 75% of the experimental results. The ACI method predicted shear capacity to be 85% of the experimental results, on average.

Table 7–Comparison of calculated shear capacity with maximum experimental shear

Test	V_{EXP} (kip)	MCFT		ACI		STM	
		V_n (kip)	$\frac{V_{EXP}}{V_n}$	V_n (kip)	$\frac{V_{EXP}}{V_n}$	V_n (kip)	$\frac{V_{EXP}}{V_n}$
B5L-C	181	115	1.57	135	1.34	181	1.09
B5L-U	152	115	1.32	135	1.13	152	1.02
B5M-C	164	106	1.55	136	1.21	164	1.06
B5M-U	144	106	1.36	136	1.06	144	1.05
B5S-C	159	89	1.79	137	1.16	159	1.12
B5S-U	133	89	1.49	137	0.97	133	1.07
B6L-C	191	151	1.26	131	1.46	191	0.92
B6L-U	138	151	0.91	131	1.05	138	0.73
B6M-C	182	143	1.27	133	1.37	182	0.96
B6M-U	149	143	1.04	133	1.12	149	0.86
B6S-C	167	115	1.45	135	1.24	167	0.97
B6S-U	124	115	1.08	135	0.92	124	0.80
Average			1.34		1.17		0.97
Bxx-C Avg.			1.48		1.30		1.02
Bxx-U Avg.			1.20		1.04		0.92

The experimental bending moments were also compared with the capacities predicted by theory. Table 8 shows the maximum experimental moments as well as the nominal moment capacity predicted by strain compatibility. In all but one case, the specimens failed prior to reaching the nominal moment capacity. For test B5S-C, the experimental moment was 14% greater than the nominal moment capacity. This was specimens to have failed in flexure.

Table 8–Comparison of calculated moment capacity with maximum experimental moment

Test	M_{EXP} (kip-ft)	M_n (kip-ft)	$\frac{M_{EXP}}{M_n}$
B5L-C	431	488	0.88
B5L-U	362	488	0.74
B5M-C	390	427	0.91
B5M-U	343	427	0.80
B5S-C	379	333	1.14
B5S-U	317	333	0.95
B6L-C	455	673	0.68
B6L-U	329	673	0.49
B6M-C	433	594	0.73
B6M-U	355	594	0.60
B6S-C	398	472	0.84
B6S-U	295	472	0.63
Average			0.78
Bxx-C Avg.			0.86
Bxx-U Avg.			0.70

9 Summary and Conclusions

Twelve precast-prestressed test specimens were loaded to failure in three-point bending. The load point was placed approximately one member depth away from the support. Half of the specimens had confinement reinforcement and the other half did not. Other variables in the test program included the quantity and size of prestressing strands. The following conclusions are made:

- Confinement reinforcement had negligible effect on measured strain distribution prior to cracking.
- Transverse tensile strains formed in the bottom flange above the bearing pad. The maximum strain occurred at the centerline of the cross-section and the strain diminished to a minimum at the edge of the flange. Transverse tensile strains are believed to have led to splitting failures in the beams without confinement reinforcement.
- Confinement reinforcement did not consistently delay or prevent slipping of prestressing strands. Such reinforcement, however, did provide sufficient slip restraint to the strands to ensure that they were able to continue supporting tensile forces beyond the point at which the unconfined test specimens failed.
- Confinement reinforcement prevented splitting failure, thereby improving the shear capacity and displacement ductility of the confined tests relative to the unconfined tests. Average shear capacity increase was 25% and the average increase in displacement ductility was 157%.
- Experimental results and strut-and-tie modeling suggest that the strands were 30% developed on average at peak load. Development of the strands in the experimental tests was limited by the formation of cracks within the strand development length.

Appendix C–SR-72 Tests

Table of Contents

C.1	Introduction	170
C.2	Girder and Deck Design	173
C.3	Test Setup, Procedures, and Instrumentation	176
C.4	Results and Discussion	180
C.4.1	Non-destructive testing to locate transverse reinforcement.....	180
C.4.2	Test X7	181
C.4.3	Test X4	184
C.4.4	I2A-Determination of Effective Prestress	190
C.4.5	Test I2A	192
C.4.6	Test I2B	195
C.4.7	Test I4.....	197
C.4.8	Test I6.....	199
C.5	Comparison with computed strength.....	202
C.6	Summary and Conclusions	206

List of Figures

Figure 1–Existing bridge prior to girder removal	170
Figure 2–Test girder identifications and slab configurations.....	172
Figure 3–Typical girder cross section	173
Figure 4–Transverse reinforcement	174
Figure 5–Deck and curb reinforcement	175
Figure 6–Test setup.....	176
Figure 7–LVDTs at end of girder	177
Figure 8–Strands instrumented with LVDTs	177
Figure 9–X7 far support.....	178
Figure 10–X4 far support.....	178
Figure 11–I6 far support	179
Figure 12–X7 shear vs. vertical displacement	181
Figure 13–X7 lateral displacement at load point	182
Figure 14–X7 cracks (initial crack in red)	183
Figure 15–X7 rosette R7	183
Figure 16–X7 punching failure bottom view	184
Figure 17–X7 Strain contour at shear of 45 kip at section below load point.....	184
Figure 18–X4 shear vs. displacement	185
Figure 19–X4 lateral displacement	185
Figure 20–X4 cracks (initial cracks in red).....	186
Figure 21–X4 shear vs. strain S25	187
Figure 22–X4 strain field at load location at a superimposed shear of 46 kip.....	188
Figure 23–X4 shear vs. compressive strain	189
Figure 24–X4 strand slip vs. shear.....	189
Figure 25–I2A decompression gages.....	191
Figure 26–I2A load vs. decompression strain (crack opening).....	191
Figure 27–I2A shear vs. displacement.....	193
Figure 28–I2A cracks (initial cracks in red)	193
Figure 29–I2A incline cracks in web	194
Figure 30–I2A transverse reinforcement-arch failure.....	194
Figure 31–I2A shear vs. strain S1	195
Figure 32–I2B superimposed shear vs. displacement.....	196
Figure 33–I2B crack pattern (initial cracks in red)	197
Figure 34–I4 shear vs. displacement.....	198
Figure 35–I4 principal strain vs. shear.....	198
Figure 36–I4 cracks (initial crack in red).....	199
Figure 37–I6 shear vs. displacement.....	200
Figure 38–I6 gage S29 vs. shear.	200
Figure 39–I6 cracks (initial crack in red).....	201
Figure 40–Experimental and theoretical shear capacities.....	203
Figure 41–Shear at initial cracking and theoretical concrete contribution.....	204

List of Tables

Table 1–Test setup dimensions	176
Table 2–I2A specified and effective prestress force	191
Table 3–Comparison of experimental and theoretical shear capacities.	203
Table 4–Exterior girder shear strength considering contribution of barrier.....	203
Table 5–Comparison of experimental and theoretical cracking shears.....	205
Table 6–Comparison of experimental moments and nominal moment capacities.....	205

1 Introduction

The Florida highway system includes some of the earliest (circa 1950s) pretensioned concrete bridges in the United States. Shear capacity of Florida's early pretensioned girders is of interest because the early designs had thin webs and only limited vertical reinforcement. This report presents the results of load testing conducted on early girders that were removed from an existing bridge (Figure 1) after nearly 55 years of service. In total, six girders were removed and tested. Girders were loaded in three-point bending at a/d ratios ranging from 2.1 to 4.5. Results of load testing will assist engineers in determining the strength of similar existing girders.

In addition to evaluating shear capacity of early pretensioned girders, this project also had the goal of evaluating the contribution to the shear capacity from the cast-in-place concrete bridge decks. To this end, varying portions of the deck and curb were retained with each salvaged test girder. Width of the retained deck portions ranged from 2 ft to 7 ft. Two of the girders were exterior girders and were removed with the curb portion of the bridge deck intact. The exterior girders allowed the strength and stiffness contributions of the curb to be evaluated.



Figure 1–Existing bridge prior to girder removal

Each girder was given a unique label based width of the retained deck and position as an internal or external girder (Figure 2). Internal girders were labeled with an 'I' and exterior girders with an 'X'. The numeric portion of each label indicates the nominal width of the slab in feet. For example, girder 'I6' was an interior girder with a nominal 6-ft wide deck. Girder 'X4' was an exterior girder with approximately 4 ft of curb and deck remaining. Note that the dimensions for the slab width shown in Figure 2 are nominal dimensions and that the actual dimensions varied slightly along the length of the test girders.

In general the girders performed well in load tests even after 50 plus years of service. In spite of having thin webs and minimal shear reinforcement each of the girders had experimental capacity greater than the code calculated nominal shear capacity. Results indicate that the girders supported load through a tied-arch mechanism wherein the concrete carried compressive loads as an arch, and the prestressing strand acted as ties. The effects of the slab width on shear capacity were not evident from the limited data. The results do demonstrate, however, that the curb increased the strength and stiffness of the exterior girders relative to the interior girders.

A brief discussion of truss and tied-arch mechanisms in concrete beams is presented in the literature review contained in Appendix A. Readers unfamiliar with these concepts may benefit from reviewing this material prior reading the results section of this appendix.

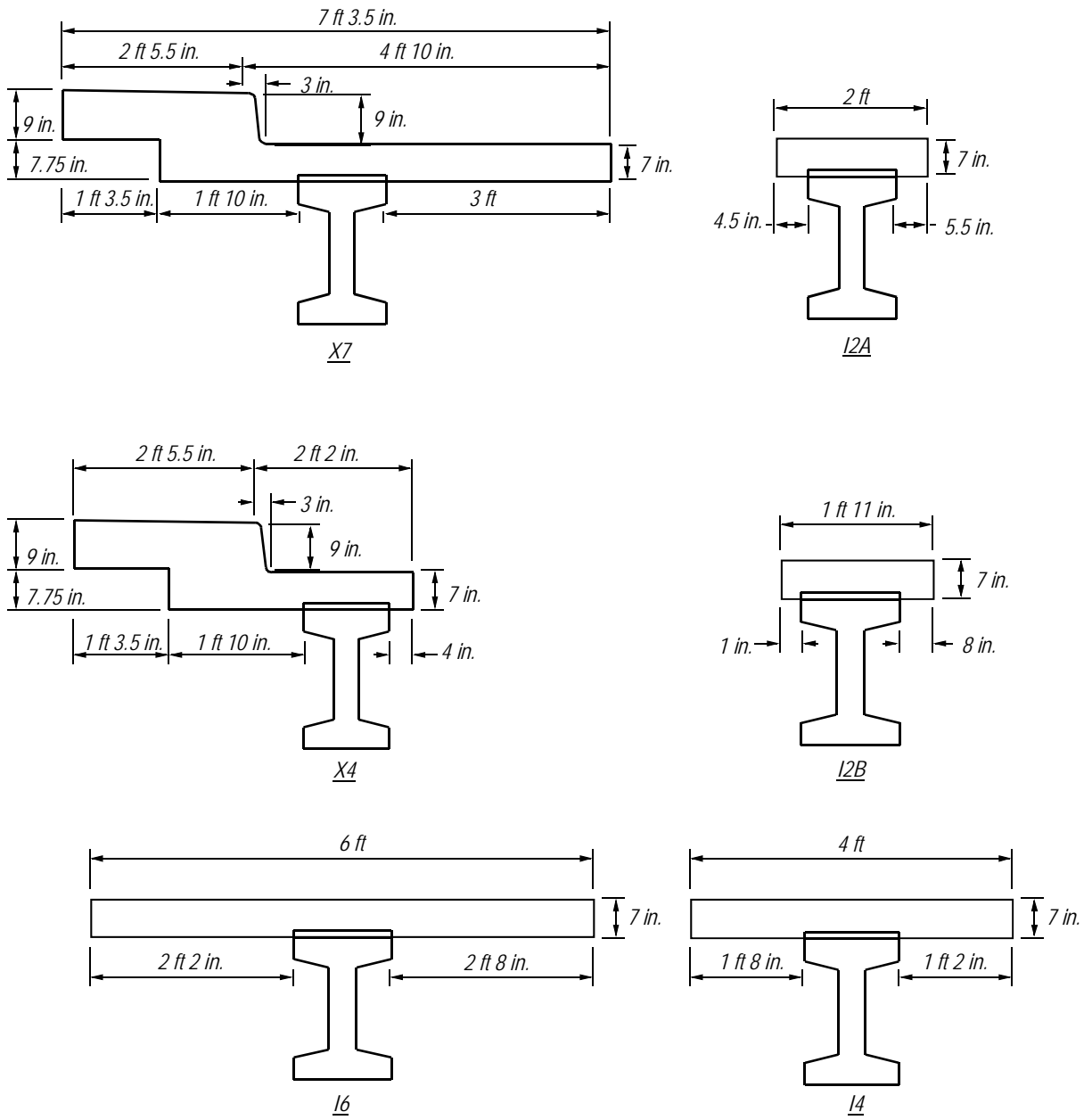


Figure 2–Test girder identifications and slab configurations

2 Girder and Deck Design

Test girders were salvaged from a bridge on Florida Highway SR-72, in Sarasota County, Florida. Girders were precast and prestressed, having the cross section shown in Figure 3.

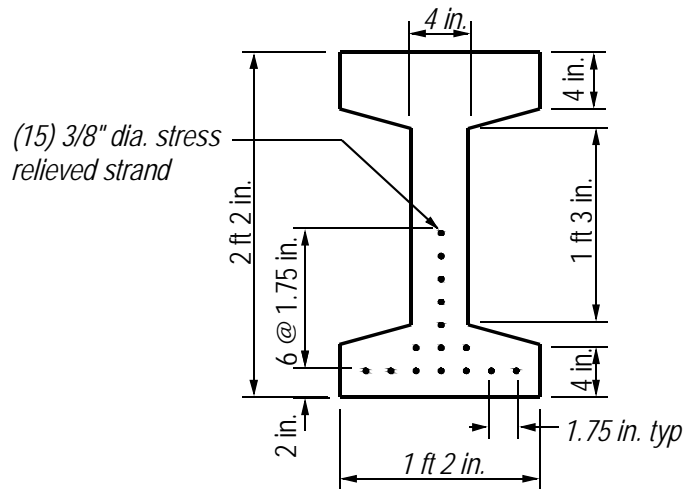


Figure 3—Typical girder cross section

Construction drawings dated February 1954 are shown in Appendix H. These drawings specified that each girder be prestressed with (15) 3/8-in. diameter stress-relieved strands pretensioned to 14 kip each. The strand pattern is shown in Figure 3. No records from pretensioning operations are available, however the effective prestress force of girder I2A was experimentally evaluated using the method presented Pessiki et al. (1996).

The specified 28-day compressive strength was 5500 psi for the girders and 3600 psi for the deck. Core samples from the girders were taken and tested in 2006. Results of the core tests are presented in Appendix H and indicate that the average concrete compressive strength was 3240psi.

Construction drawings specified two #4 longitudinal bars in the top flange and (12) #4 vertical bars spaced at 6 in. o.c. at each end of the girders (Figure 4). The vertical bars did not have hooks specified. End blocks extended 2.5 ft from each end. Non-destructive testing was used to locate the vertical bars in the web. Results of non-destructive testing are presented in section 4.1.

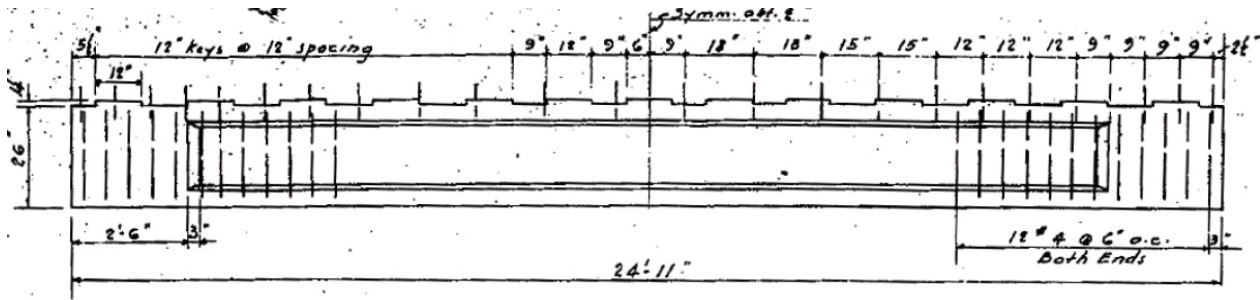


Figure 4–Transverse reinforcement

The girder plans called for shear keys (Figure 4) on top of the girders to create composite action with the cast-in-place deck. Hoops were specified to tie the girders and deck. The hoops were #4 bars and were partially embedded into the top flange, with the remaining portion extending above the girder and embedded into the deck. Plans specified (24) hoops total for each girder, with 9 in. spacing at the ends, and 18 in. spacing near mid-span.

Figure 5 shows the curb and deck reinforcement specified on the original plans. Original plans are included in Appendix H. Plans called for a 7-in. thick cast-in-place deck reinforced with longitudinal and transverse #4 bars top and bottom. Longitudinal bars were specified at an average of 12 in. oc in the bottom of the deck, and 18 in. oc in the top. Specified transverse reinforcement was #4 bars at 10 in. oc in the top and bottom of the deck. Additional transverse #4 bars were spaced at 10 in. oc and were bent such that they support negative moments over the girders and positive moment between girders. Curb reinforcement was (3) #4 bars placed longitudinally near the top of the curb, and bent #4 bars spaced at 12 in. oc transversely to tie the curb to the deck.

End diaphragms were cast between the girders and each end of the bridge and had a specified thickness of 8 in. with 1-in. diameter threaded bar extending through the end diaphragms and girder end blocks to tie the bridge together transversely. Varying portions of the end diaphragms were retained with individual test girders. Relevant details about the end diagrams are given in the next section.

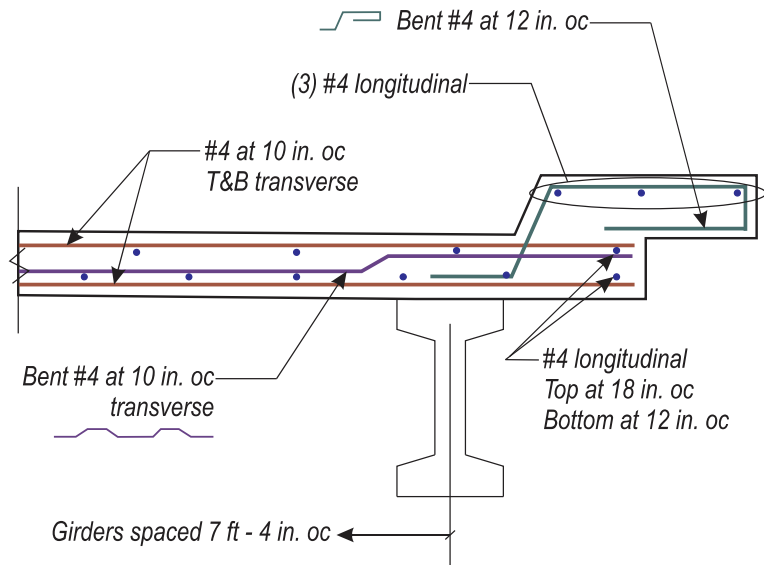


Figure 5–Deck and curb reinforcement

3 Test Setup, Procedures, and Instrumentation

Girders were tested in three-point bending. Dimensions and setup are described in Figure 6 and Table 1. The support nearest the load point is referred to as the near support. The opposite support is referred to as the far support.

The load was transferred from a hydraulic actuator to the girders through a 10-in. x 10-in. x 2-in. thick reinforced neoprene bearing pad at a loading rate of approximately 0.25 kip/second. A load cell was used to measure the applied load. A thin grout pad (1 in. maximum thickness) was placed below the load point on X7, 12B, X4 and I4 to compensate for slight cross-slopes of the deck on those girders.

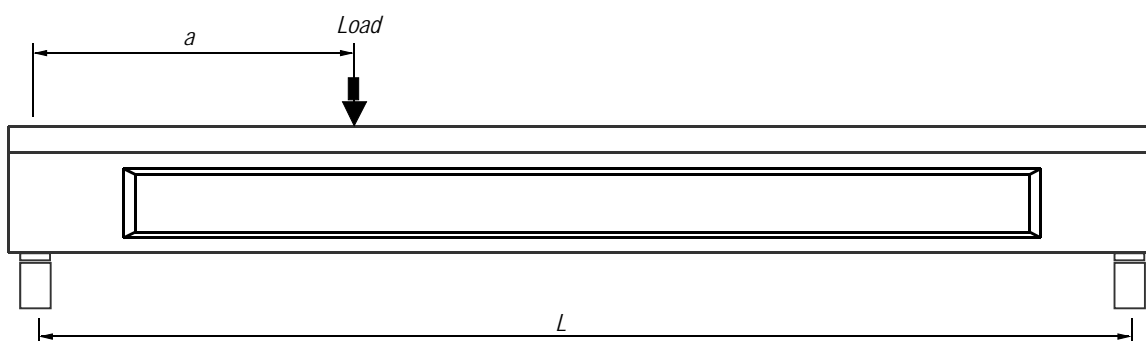


Figure 6–Test setup

Table 1–Test setup dimensions

Girder	A	a/d*	L
X7	8'-2"	3.4	23'-9"
X4	8'-2"	3.4	24'-3"
I2A	10'-11"	4.5	23'-9"
I2B	8'-1"	3.3	24'-11"
I4	5'-2"	2.1	23'-10"
I6	8'-2"	3.4	24'-0"
*d = 29 in.			

Linear Variable Displacement Transducers, LVDTs, were used to measure vertical displacements at the load point and above each support. LVDTs were also used to measure strand slip. A steel frame was bolted to the end of each beam to support the strand slip LVDTs (Figure 7). In total, ten strands were monitored for slip (Figure 8). LVDTs were also used to measure lateral movement at the load point of girders X7 and X4.

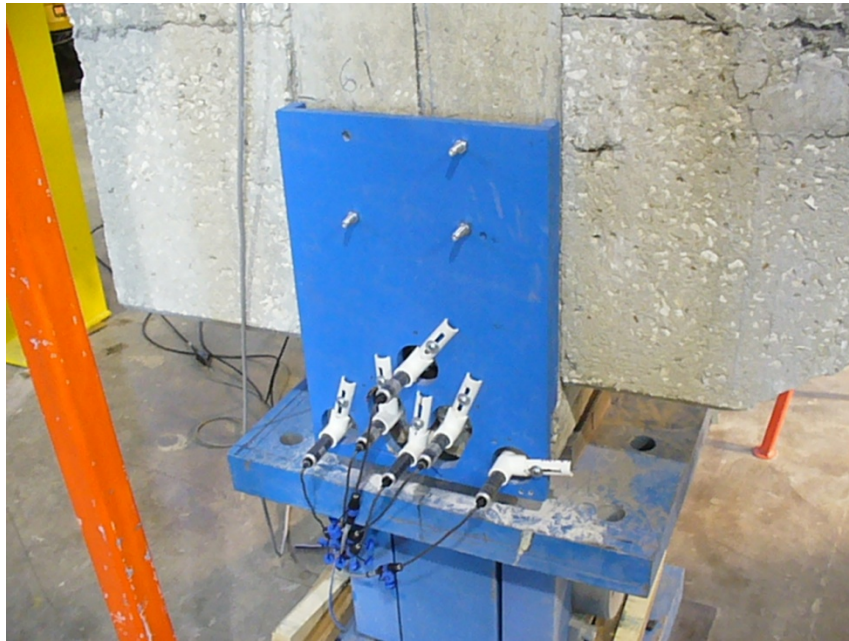


Figure 7–LVDTs at end of girder

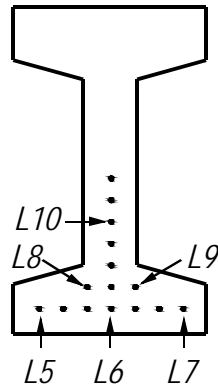


Figure 8–Strands instrumented with LVDTs

Typically, girders were supported at each end on an 8-in. x 14-in. x 2-in. thick (14-in. dimension perpendicular to the length of the girder) reinforced elastomeric bearing pad. Additional bearing points were added at the far support of girders X7, X4 and I6 to provide stability during testing. The additional bearing pads were placed below the end diaphragm or curb as shown in Figure 9, Figure 10, and Figure 11.



Figure 9-X7 far support



Figure 10-X4 far support



Figure 11-I6 far support

Bonded foil strain gages were used to measure concrete surface strain and to detect cracks during testing. Strain gages had a 60-mm gage length. Appendix H contains information on the labels and locations of all strain gages and LVDTs used during load tests.

4 Results and Discussion

Results of the load tests are presented in terms of superimposed shear. Superimposed shear is defined as the shear force at the near support due to the load applied by the hydraulic actuator. The superimposed shear does not include shear force due to girder self-weight.

Displacement results presented in this section are vertical displacement at the load point. Vertical deflection at the load point was taken as the average displacement recorded by the LVDTs on either side of the load point, less the displacement of the girders due to bearing pad compressive reactions. In some cases, the two LVDTs at the load point reported different displacements, indicating that the girder was rotating in addition moving vertically. Rotation of the girders is discussed with the results from in the individual load tests.

Strand slip was monitored using LVDTs mounted on the back of the girders above the near support. Data from the LVDTs indicated that strand slip only occurred during testing of X4. Because strands did not slip in the other tests, slip data is only presented for test X4.

4.1 *Non-destructive testing to locate transverse reinforcement*

Transverse reinforcement in the webs was located using a cover meter. Girder construction drawings specified that (12) #4 single-leg transverse bars be placed vertically at 6 in. o.c. at each end (Figure 4). Of the (12) bars, (6) of the bars were to be placed in the end block and the other (6) placed in the web. The location of the transverse reinforcement in the end blocks could not be determined because the clear cover over the reinforcement was too large for the cover meter to penetrate.

To avoid interference from the prestressing strands, only the top of the web was scanned with the cover meter. Thus, the spacing and quantity of the vertical reinforcement were determined, but the orientation (inclination) of the bars could not be determined. Figures showing the transverse steel locations as determined by the cover meter are presented with the results of the individual girder tests. Note that the presumed vertical orientation of the reinforcement shown in the figures was not confirmed.

Transverse reinforcement in the test girders was generally not consistent with the construction drawings. For example, only two of the twelve ends had the specified number of transverse bars in the web. Four of the twelve ends had only two vertical bars in the web. Inconsistency between the specified and observed vertical reinforce is particularly troubling

because the specified reinforcement was already minimal compared to modern girders. It is recommended that similar girders in Florida be analyzed under the assumption that vertical reinforcement is absent. Alternatively, it is recommended that a cover meter or other means be used to locate vertical reinforcement for the analysis.

4.2 Test X7

Girder X7 was load tested at an a/d ratio of 3.4. Shear-displacement behavior of X7 is shown in Figure 12. As load was applied the girder displaced vertically and laterally, and rotated about its longitudinal axis. Lateral displacement is presented in Figure 13. The maximum rotation was approximately 0.14 degrees, as determined from LVDTs L2 and L3 which were placed on either side of the load point. The rotation and lateral movement are attribute in-part to the asymmetric cross-section and load location which was not through the section's shear-center. Uneven bearing pad deformation may also have contributed to the rotation. As previously discussed, and as presented in Figure 9, multiple bearing points were placed at the far end of X7 to prevent instabilities due to asymmetry of the cross-section and load.

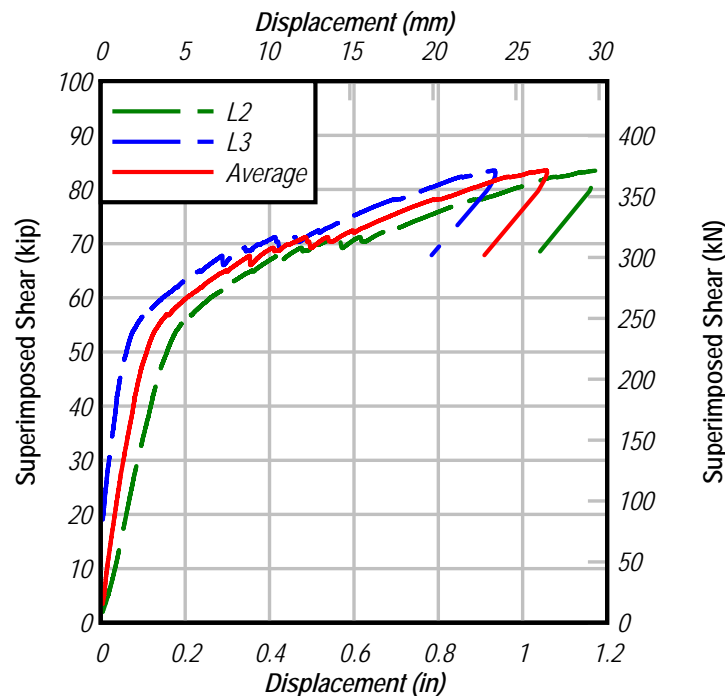


Figure 12–X7 shear vs. vertical displacement

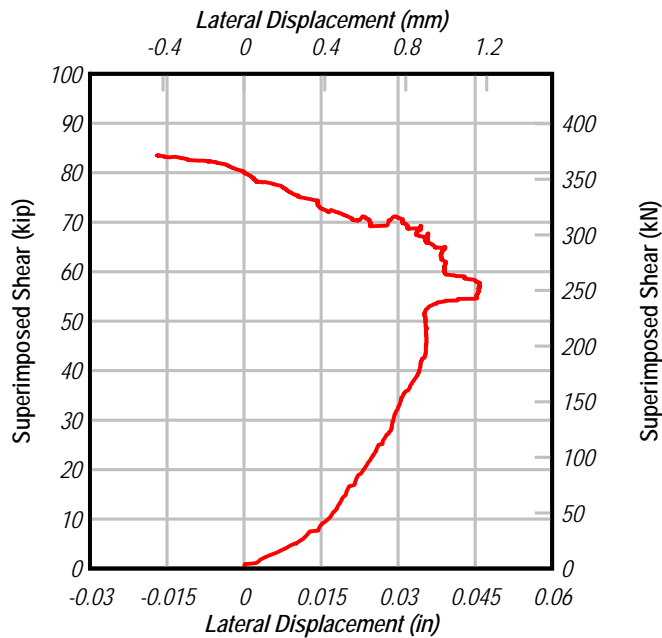


Figure 13–X7 lateral displacement at load point

The girder behaved linear-elastically until the formation of cracks. Visible cracking was first observed in the web at a superimposed shear load of approximately 51kip (Figure 14). Although cracks were not visible prior to 51kip, data from rosette R7 indicates that the crack first formed at a shear of 41kip (Figure 15). At 58kip of shear, the initial crack in the web was observed to have joined with a flexural crack in the bottom flange. This load corresponds to the change in slope on the shear-displacement plot; the change in stiffness being attributed to cracking.

Referring to Figure 12, the abrupt changes in the shear-displacement curve between 65kip and 70kip correspond to the formation of additional cracks. Cracks formed farther from the load point and at shallower angles as the load increased. Comparing the final crack pattern with the location the transverse reinforcement (Figure 14), it is noted that with only one exception, the cracks did not cross transverse reinforcement. Thus, after cracking the load could not have transferred through truss action, but rather was carried through arch action. Girder X7 supported a maximum superimposed shear of 84kip. At this load a punching shear failure occurred in the slab and curb. Figure 16 is a photo of the curb side of X7 showing the location of the punching failure. The red strap in the picture is from the crane which was lifting the girder as the photo was taken.

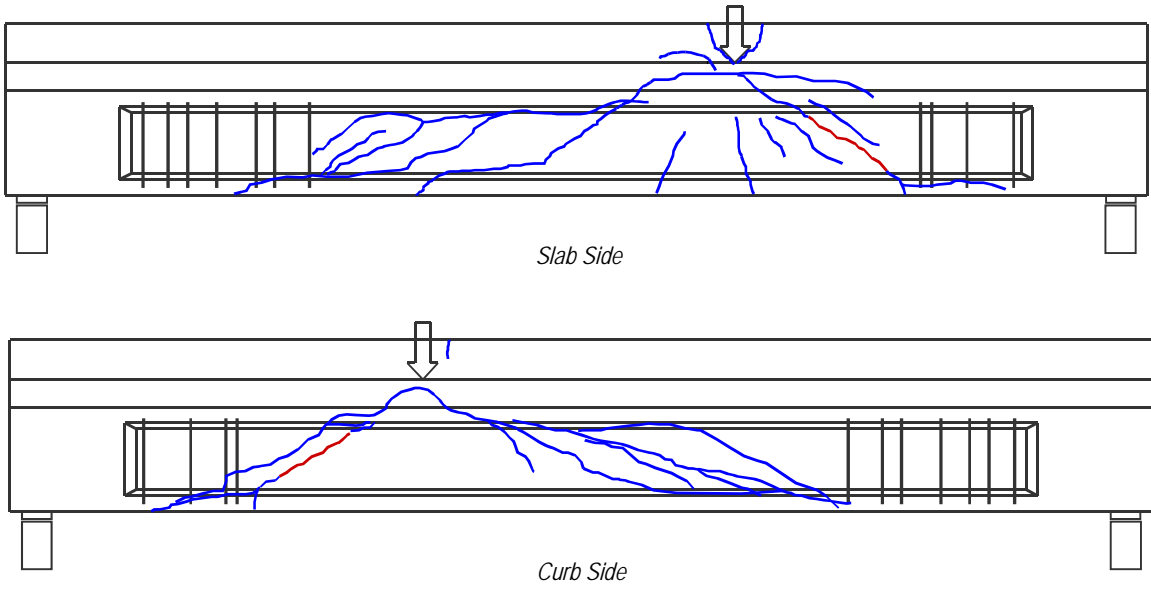


Figure 14–X7 cracks (initial crack in red)

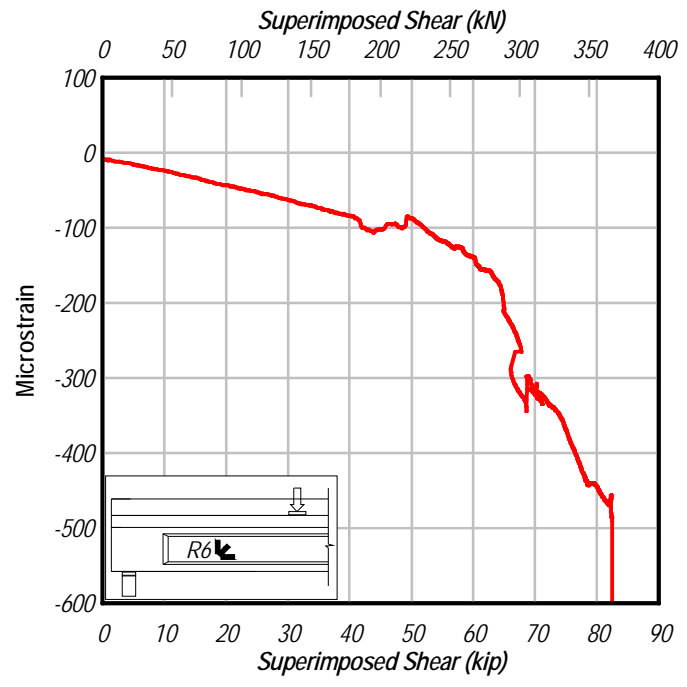


Figure 15–X7 rosette R7



Figure 16–X7 punching failure bottom view

Strain gages were placed around the cross-section at three sections along the length of the girder. Data from these gages were combined via linear interpolation to approximate the strain contour of the section during loading. Figure 17 shows the strain contour at the section below the load point at a shear of 45 kip. The maximum compressive strain occurred at the top corner of the curb. Because the section experienced biaxial bending, the strain contours were inclined.

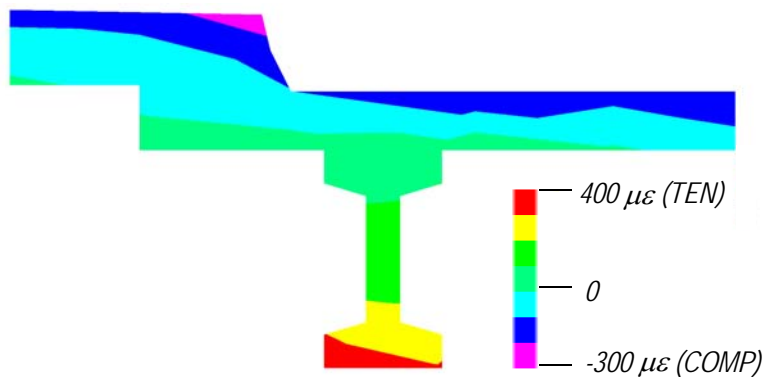


Figure 17–X7 Strain contour at shear of 45 kip at section below load point

4.3 Test X4

Girder X4 was loaded at an a/d ratio of 3.4. During load testing X4 displaced vertically (Figure 18) and laterally (Figure 19), and rotated about its longitudinal axis. The maximum rotation was approximately 0.11 degrees as determined from the differential displacement reported by LVDTs placed on either side of the load point. Rotation and lateral movement are

attributed to the asymmetric cross-section and load location which was not through the shear-center of the section. Uneven bearing pad deformation may also have contributed to the rotation. As previously discussed, and as presented in Figure 10, multiple bearing pads supported X4 at the far end to prevent instabilities due to asymmetry of the cross-section and load.

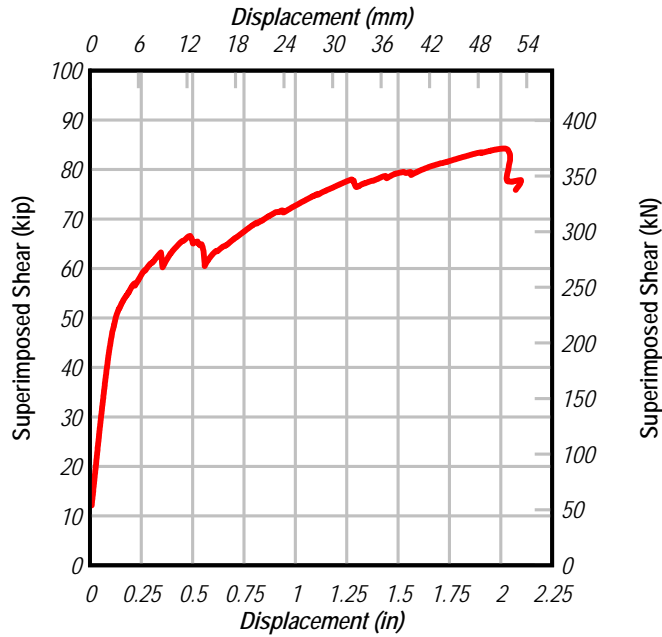


Figure 18–X4 shear vs. displacement

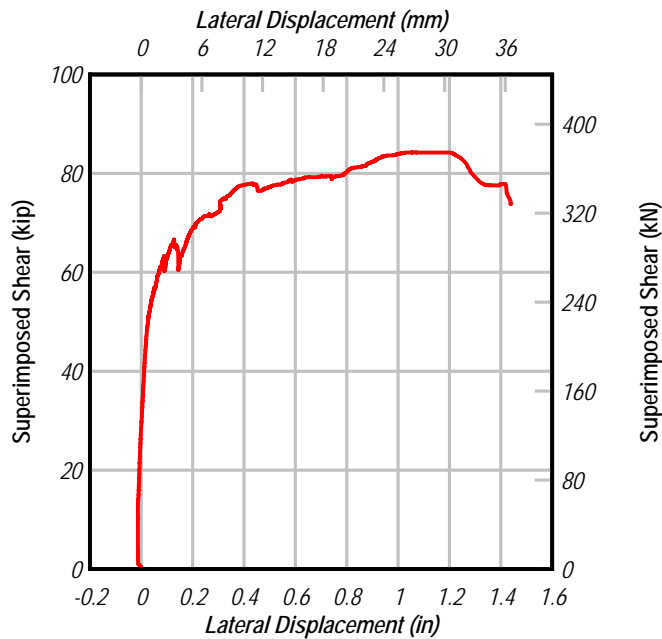


Figure 19–X4 lateral displacement

Referring to Figure 18, girder X4 behaved linear-elastically until a superimposed shear of about 45kip. The transition from linear-elastic behavior corresponded to the formation of flexural cracks at the bottom of the girder below the load point (Figure 20). Data from gage S25 (Figure 21) indicate that cracking initiated at a shear of 44kip. Initial cracks were first visually observed at a shear of 56kip.

The abrupt changes in the shear-displacement plot at 62kip and 66kip correspond to the formation of incline cracks in the web. Cracks continued to form farther from the load point and at shallower angles as the load increased. At the final stages of the load test incline cracks had a maximum width of 1 in. As shown in Figure 20 vertical reinforcement was not engaged by the inclined cracks. The relatively large crack widths and absence of engaged vertical reinforcement suggest that the girder supported load by arch-action.

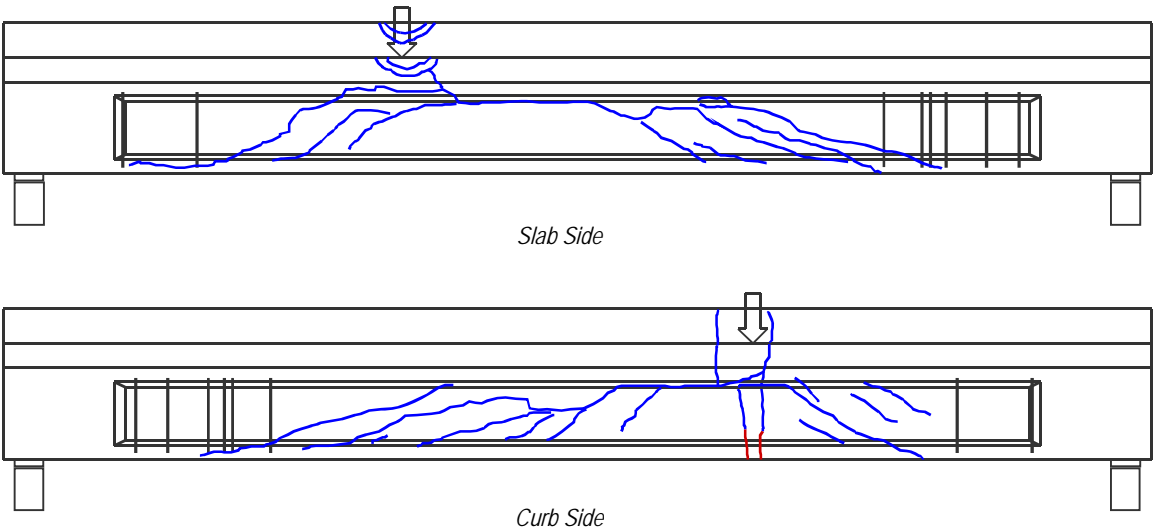


Figure 20-X4 cracks (initial cracks in red)

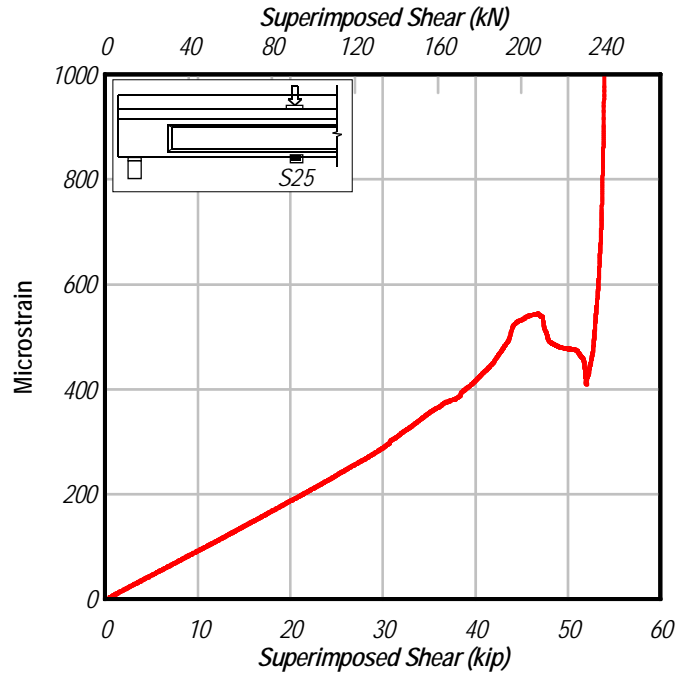


Figure 21–X4 shear vs. strain S25

Strain gages were placed around the cross section to evaluate the flexural strain field during load testing. Figure 22 shows the strain field at the section below the load point at a superimposed shear load of 46k. Contours indicate biaxial bending with the neutral axis inclined at approximately 20 degrees from horizontal. The largest compressive strains occurred in the upper corner of the curb and slab. Formation of the initial flexural cracks on the curb side is consistent with the measured strain field which recorded the largest tensile strains at the location of cracking.

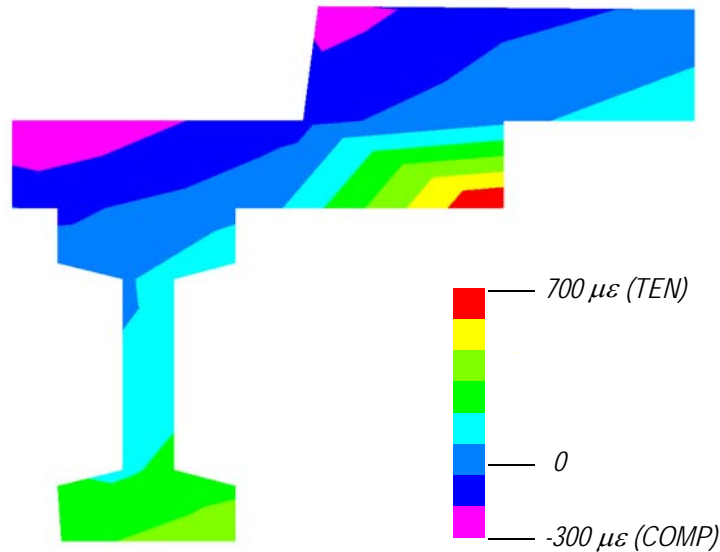


Figure 22–X4 strain field at load location at a superimposed shear of 46 kip

Lateral displacement of girder X4 is presented in Figure 19. As with vertical stiffness, the lateral stiffness of the girder was reduced by the formation of cracks. The relatively flat portion of the shear-displacement curves at the latter stages of the test suggests that reinforcement may have yielded.

Crushing of the compression zone in the slab near gage S15 began at a shear of 71kip. Examining data from S15, the compressive strain reached 2200 microstrain prior to crushing (Figure 23). Crushing is attributed to the superposition of bearing strain from the load point and the flexural strain. The corner of the slab near S15 continued to crush and spall as the shear increased beyond 71kip. The corner of the curb near gage S17 began to crush at a shear of 76 kip. According to gage S17, the strain at the corner of the curb reached 2550 microstrain immediately prior to crushing (Figure 23). Girder X4 supported additional load after the initial crushing at the corners of the slab and curb, reaching a maximum superimposed shear of 84kip. As previously noted, the girder behaved as a tied-arch in the final stages of loading. The failure mode of Girder X4 was flexural compression failure of the concrete. The moment at failure was 95% of the calculated nominal moment capacity. Details of nominal capacity calculations are presented in a later section.

Girder X4 was the only test in which the strands exhibited significant slip (Figure 24). The strand monitored by LVDT L7 was located the curb side in the bottom row. This strand was in the region of highest tension in the bottom flange (Figure 22). Slipping of the strands in X4

contributed to the rotation about the load point and crushing of the compression zone. Because X4 failed in flexural the strands in this girder likely supported higher loads than in other girders, making slip more likely. Slip was also augmented by the asymmetric bending as demonstrated by the slip L7.

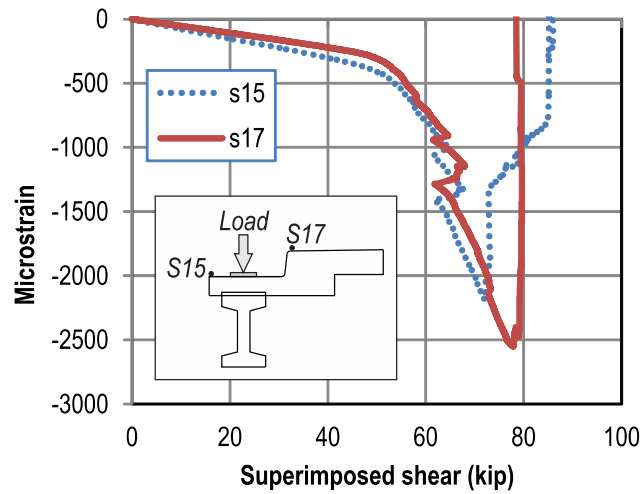


Figure 23–X4 shear vs. compressive strain

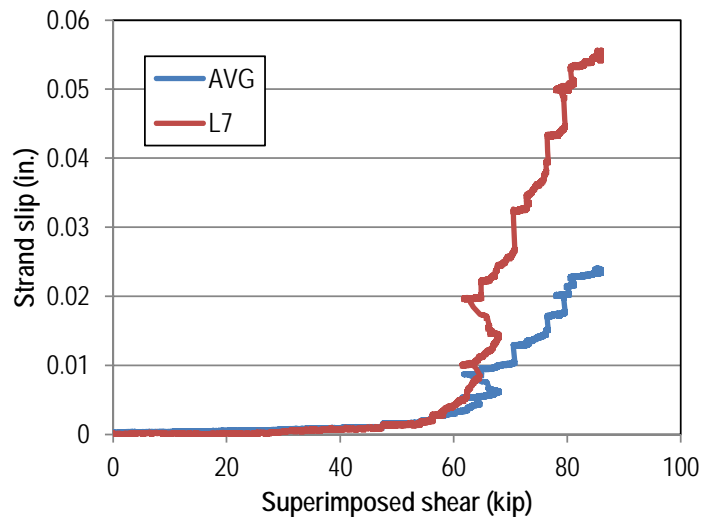


Figure 24–X4 strand slip vs. shear

4.4 I2A-Determination of Effective Prestress

The effective prestress force of Girder I2A was determined using the procedure presented by Pessiki et al. (1996). Based on this procedure, girder I2A was loaded until flexural cracks formed. Two flexural cracks were visually observed at a superimposed shear reached 36k (Figure 28). The load was held constant at this force so that the cracks could be marked. After cracks were marked the girder was unloaded and strain gages (oriented longitudinally) were placed as close as possible to, and on each side of both cracks (Figure 25).

Girder I2A was loaded to failure after the initial cracks were marked and strain gages were installed. Figure 26 shows applied load vs. strain data from each strain gage placed adjacent to the flexural cracks. Theoretically, as load is increased, the cracks should open when the tension due to bending equals the precompression from the effective prestress force. This behavior is indicated by a bilinear shape in the load-strain plots shown in Figure 26. At a load of 40kip (22kip shear) the load-strain relationship became nonlinear due to reopening of the flexural cracks. Knowing this load at which the cracks reopened (i.e. precompression force was overcome), the effective prestress force in the girder was calculated using flexural theory. Specified initial prestress force, effective prestress force and total losses are shown in Table 2. Note that calculation of the experimental prestress force utilized flexural stiffness properties derived from the experimental load-displacement data.

An effective prestress force of 112kips was calculated from the experimental data. Assuming an initial prestress force of 210kip as per the construction drawings, the experimental data indicate a 47% loss in prestress force. This value of prestress loss is unusually high suggesting that the initial prestress force may have been less than specified. This would not be unreasonable considering other inconsistencies between the girders and plans, such as placement of vertical reinforcement. It is not known if the experimentally evaluated prestress force from I2A was representative of all test girders.

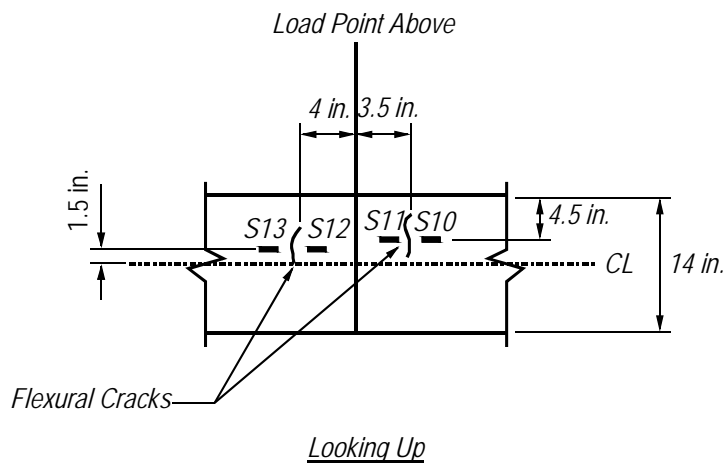


Figure 25–I2A decompression gages

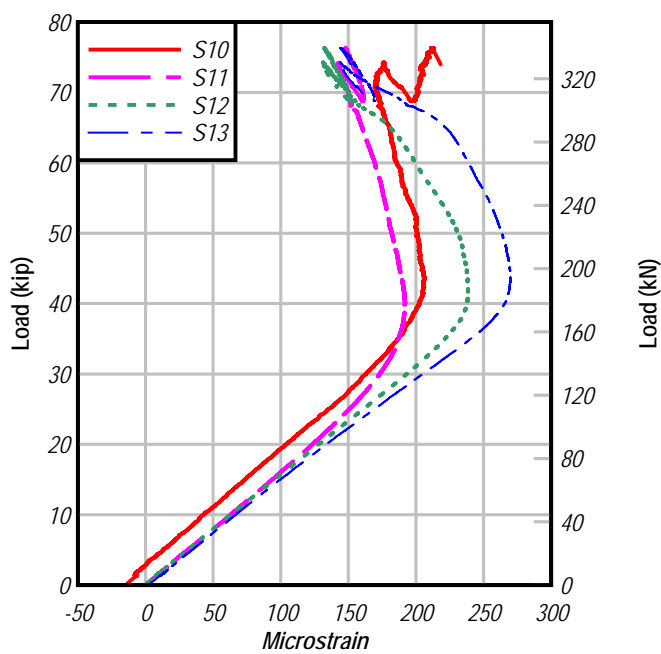


Figure 26–I2A load vs. decompression strain (crack opening)

Table 2–I2A specified and effective prestress force

Specified Initial Prestress Force	Experimental Effective Prestress Force	Total Losses
210 kips	112 kips	47%

4.5 Test I2A

After evaluating I2A for effective prestress, the specimen was loaded to ultimate load. Load was applied at an a/d ratio of 4.5. Shear-displacement data from the ultimate load test is presented in Figure 27. Contrary to X4 and X7, girder I2A did not rotate about its long axis during loading. Flexural cracks reopened at a load 40 kip, corresponding to 22 kip superimposed shear. According to the shear-displacement plot, significant deviation from linear-elastic behavior did not occur until the shear reached 36k. Softening of the girder corresponded to the propagation of flexural cracks. The abrupt changes in the shear-displaced data at shear forces near 40 kip were due to the formation of inclined cracks in the web. As the load increased, additional cracks formed farther from the load point and at shallower angles. Cracking in the web between the load point and the near support was particularly severe, as noted by the shaded area in Figure 28 and shown in Figure 29.

Cracks along the web-flange interface in the shear span prevented the transverse reinforcement from developing and carrying forces. On the far support side of the load, the cracks did not engage the transverse reinforcement. Incline cracks on both ends of the beam were too wide to allow force transfer by aggregate interlock. Without aggregate interlock and effective transverse reinforcement, the girder behaved as a tied-arch during the final stages of loading.

Failure was precipitated by the formation of tensile cracks in the top of the arch between the near support and load point. After the cracks formed, the arch became unstable, buckled upward (Figure 29) and lost load carrying capacity. Failure occurred at a superimposed shear of 51 kip. This behavior was captured by gage S1 (Figure 31) located on top of the girder. After inclined cracks formed in the web, the compressive strains on top of the slab at gage S1 decreased suddenly. As testing continued strain reported by S1 became tensile. This tensile action at the top of I2A resulted in cracking and instability of the compression load path. This type of failure has also been reported by Kostovos (1987).

Girder I2A was one of two tests (I4 being the other) in which cracks formed in the end block. LVDT data indicate that the end block cracks did not affect strand slip.

Extensive cracking and spalling in the web exposed the transverse reinforcement (Figure 29). Orientation and spacing of the transverse bars were not consistent with the girder plans.

Rather than being oriented vertically, bars were inclined towards the load point. Also, the bars were spaced much closer than the specified 6" o.c. spacing.

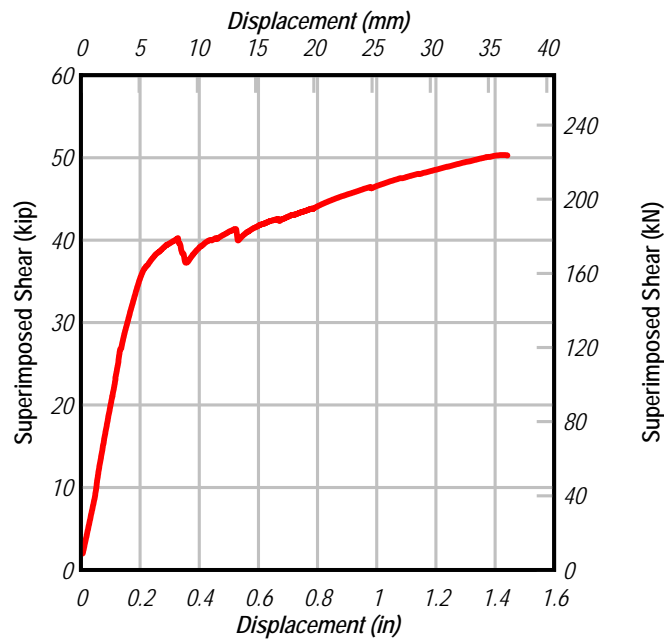


Figure 27-I2A shear vs. displacement

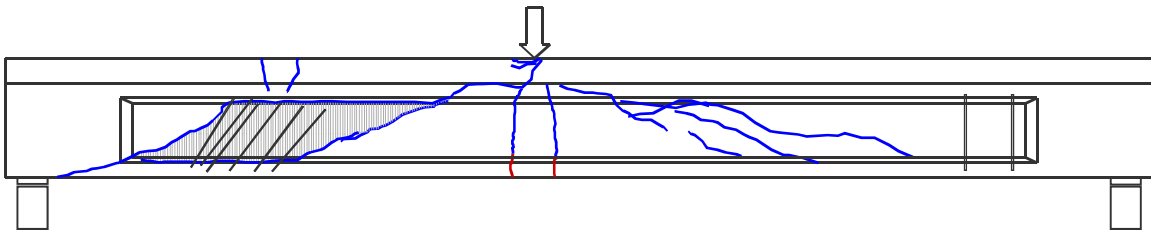


Figure 28-I2A cracks (initial cracks in red)



Figure 29-I2A incline cracks in web



Figure 30-I2A transverse reinforcement-arch failure

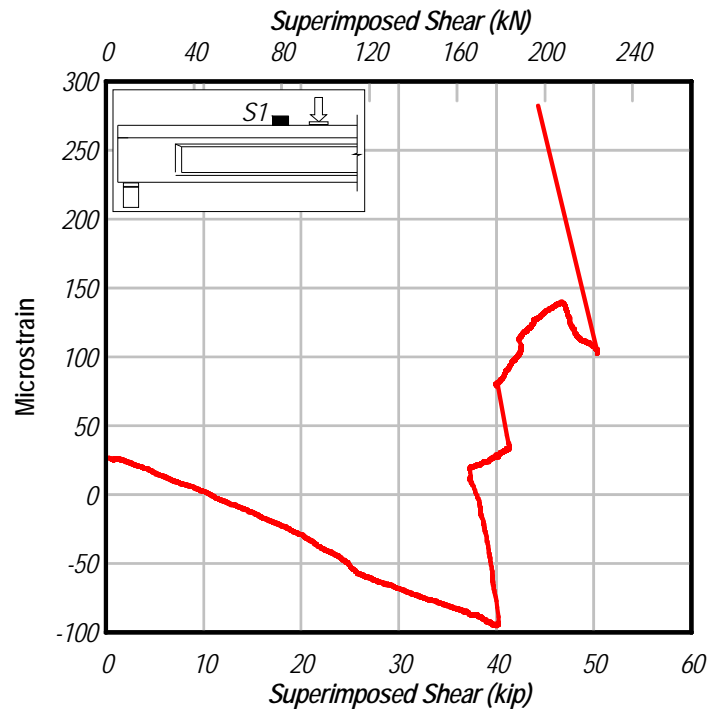


Figure 31-I2A shear vs. strain S1

4.6 Test I2B

Girder I2B was loaded at an a/d ratio of 3.3. Figure 32 shows the superimposed shear vs. load point displacement. I2B rotated 0.22 degrees about its long axis as the shear increased from 0kip to 5kip. The girder maintained this rotated orientation for the remainder of the test. Girder I2B behaved linear-elastically until the shear reached about 43kip, at which point flexural cracks formed below the load point (Figure 33). After formation of the initial cracks, load was held constant and the cracks were marked. After loading was resumed, inclined cracks formed in the web and additional flexural cracks formed in the bottom flange. Loading was stopped again to mark the cracks at 50kip of shear. The abrupt change in the shear-deflection plot at 50kip was due to relaxation of the load while cracks were being marked. Loading was again resumed, and additional shallower cracks formed farther from the load point towards the far support. One of these cracks formed at the peak load of 67kip. The load supported by the girder dropped after the formation of the crack at 67kip, and the load was held to mark cracks for the final time. After loading resumed, the inclined cracks near the far support continued to open and propagate,

however the girder was unable to support the previous peak load. The test was terminated when the load dropped to 64kip.

Comparing the locations of cracks and transverse reinforcement (Figure 33), it can be seen that cracks between the load and near support intersected transverse bars whereas cracks towards the far support did not. As the cracks towards the far support were large, it is unlikely that shear was carried by aggregate interlock at that end of the beam. Thus it is believed that the near side of the girder supported load by some combination of arch and truss action, and the far side supported load by arch action.

The limiting factor on ultimate strength of I2B was capacity of the web near the far support to withstand the formation and propagation of inclined cracks. Additional displacement beyond peak displacement would have resulted in failure of the truss and/or arch mechanisms; however it is unlikely that additional displacement would have accompanied load in excess of the previous peak. It is concluded that the girder strength was controlled by the web capacity, and it is presumed that the displacement capacity would have been controlled by failure of the arching action.

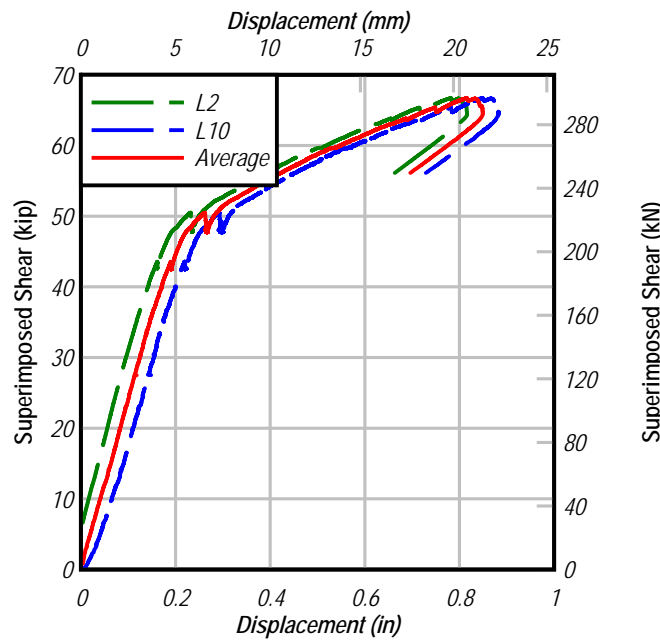


Figure 32–I2B superimposed shear vs. displacement

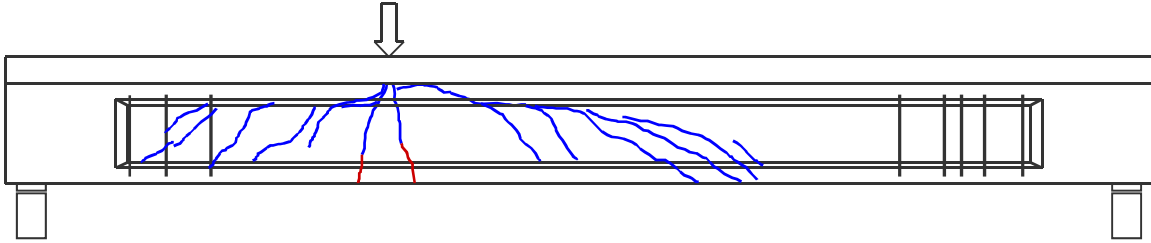


Figure 33–I2B crack pattern (initial cracks in red)

4.7 Test I4

Girder I4 was loaded at an a/d ratio of 2.1. Figure 34 shows the superimposed shear vs. load point displacement. I4 began rotating about its long axis as soon as load was applied. The angle of rotation increased with increasing load, reaching a maximum of 0.57 degrees just before failure.

The first crack formed at a shear of 38 kip as reported by rosette R2 on the web (Figure 35). The initial crack was an incline crack in the web (Figure 36), and appears to have had little effect on the girder stiffness as measured by the shear-displacement relationship. Stiffness of the girder changed at a shear of 75 kip. This is the same load at which the inclined crack near gage R2 was first visually observed.

As the load was increased additional cracks formed in the web on the far support side. The cracks formed farther from the load point and at shallower angles at higher loads. The abrupt changes in the shear-displacement plot near 112 kip and 118 kip correspond with formation of inclined cracks towards the far support. During the final stages of loading cracks in the web were wide approximately 0.5in wide. As shear could not transfer across the cracks, and as the cracks did not engage transverse reinforcement, it is believed that the end of the girder towards the far support behaved as a tied arch during the final stages of loading. The peak superimposed shear supported by girder I4 was 118k.

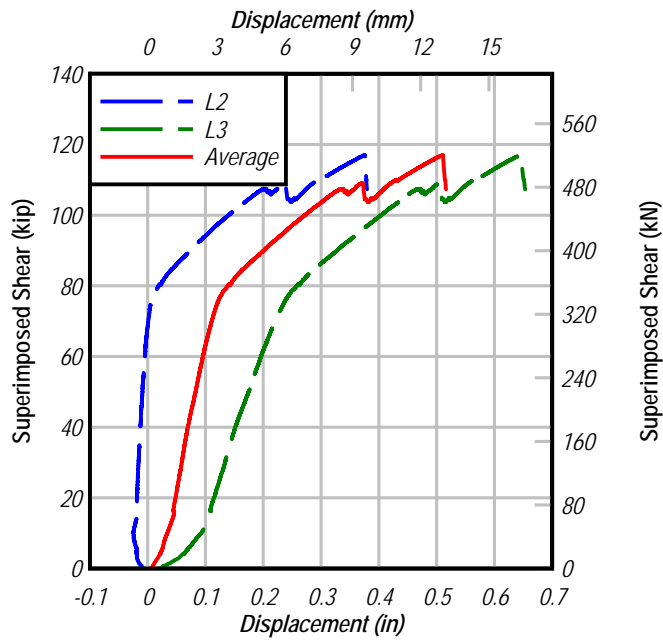


Figure 34-I4 shear vs. displacement

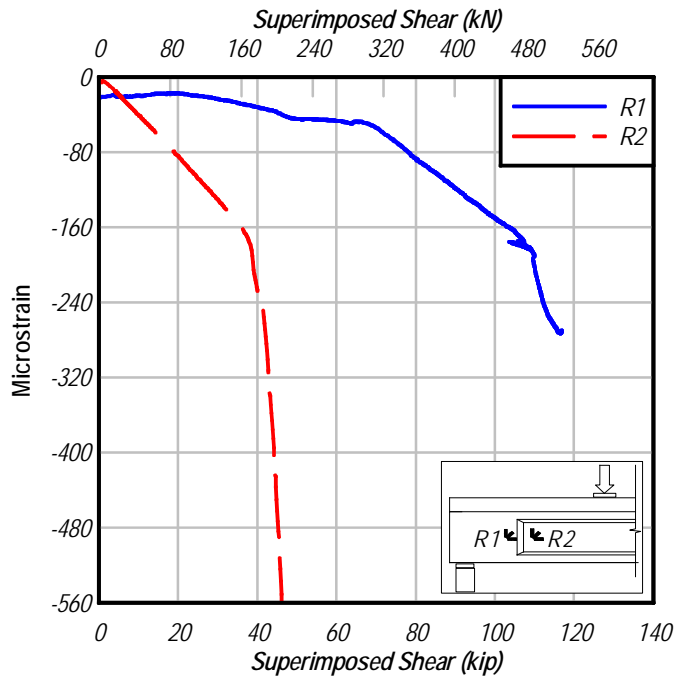


Figure 35-I4 principal strain vs. shear

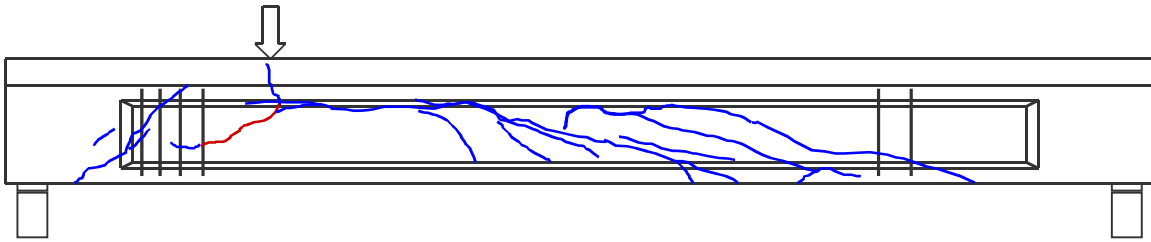


Figure 36–I4 cracks (initial crack in red)

Cracks towards the near support engaged transverse reinforcement (Figure 36). The transverse reinforcement slowed the propagation and opening of these cracks as compared to cracks at the far end of the girder. The shear load transferred to the near support is believed to have been carried by truss action. The shear transfer towards the far support was likely carried by arch action.

The limiting factor on girder strength was capacity of the web on the far support side to withstand the formation and propagation of inclined cracks. Additional movement beyond peak displacement would have resulted in failure of the truss and/or arch mechanisms, however it is unlikely the additional displacement would have resulted in that the loads in greater than the observed peak. It is concluded that the girder strength was controlled by the web capacity and that the displacement capacity was controlled by the arching and/or truss action.

Although cracks formed in the end block, no strand slip was reported by the LVDTs.

4.8 Test I6

Girder I6 was loaded at an a/d ratio of 3.5. Figure 37 shows the superimposed-shear versus load-point displacement. The girder behaved linear elastically until the first crack formed at a shear of 43kip. Load at cracking was determined by data from gage S29 (Figure 38). The initial crack was a flexural crack below the load point (Figure 39). Inclined cracks formed in the web toward the near support at a shear of 48kip. Shallower cracks formed farther from the load point as the load was increased. The load test was terminated after a sudden drop in load caused by the formation of an incline crack at the far end of the girder. The maximum superimposed shear was 68kip. Girder I6 did not rotate as load was applied.

Comparing the cracks with the locations of transverse steel (Figure 36), cracks intersected transverse reinforced on the near side of the beam, but not on the far end. Shear was carried by truss action to the near support, and arch action to the far support.

The limiting factor on girder strength was capacity of the web on the far support side to withstand the formation and propagation of inclined cracks. Additional displacement beyond the tested peak would likely have resulted in failure of the truss and/or arch mechanisms, however it is unlikely the additional displacement would have resulted in that the loads in excess of the observed peak. Girder strength was controlled by the web capacity and it is presumed that displacement capacity would have been controlled by failure of the arch and/or truss mechanisms.

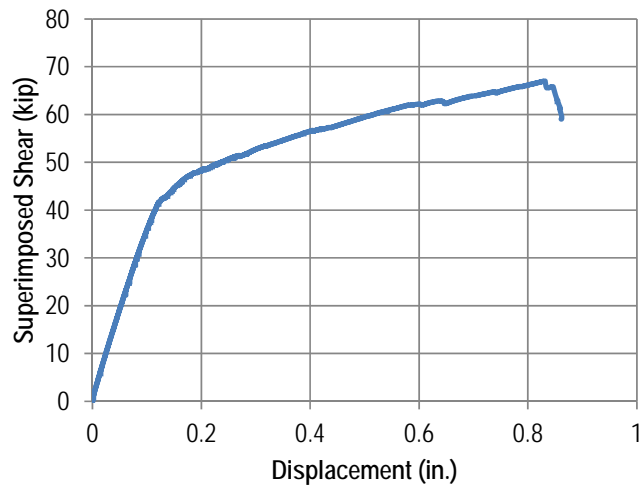


Figure 37-I6 shear vs. displacement.

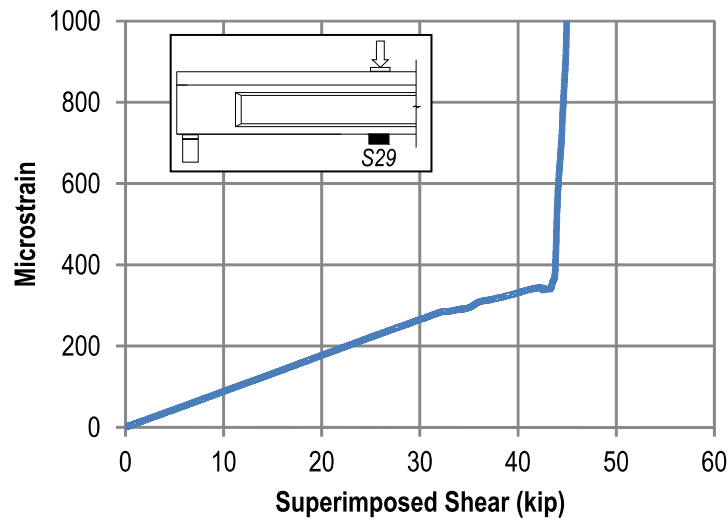


Figure 38-I6 gage S29 vs. shear.

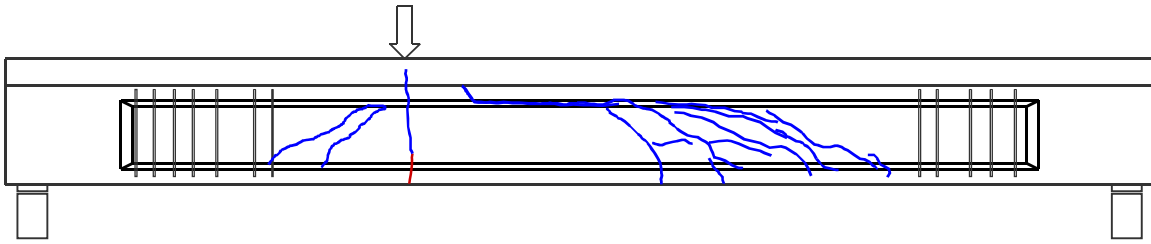


Figure 39-I6 cracks (initial crack in red).

5 Comparison with computed strength

Experimental ultimate capacity was compared with the nominal shear and moment strength calculated using the detailed procedure from ACI 318 (ACI 2008) and the general (MCFT based) procedure from AASHTO LRFD (AASHTO 2007). Nominal shear capacities were calculated for an interior girder using the specified reinforcement, prestressing, geometric properties, and material properties. This approach was used because physical properties were not tested for each girder and because this is the likely approach of an engineer performing a load rating on the bridge.

Based on the girders for which concrete compressive strength and effective prestress were tested, it is assumed that the specified properties are unconservative relative to the physical properties. Thus the approach used for shear calculations resulted in nominal capacities larger than the capacities calculated using the available tested properties. This effect of the approach is inconsequential considering that the experimental capacities were significantly higher than the nominal capacities as shown in Figure 40 and Table 3.

Figure 40 shows the code calculated nominal capacities plotted against the shear span length (a). The discontinuity at $a = 5.7$ occurs due to the specified termination of transverse reinforcement at that location. Point data on the figure represent the experiment shear capacity of the test girders. The experimental capacity of the girders was taken as the maximum superimposed shear plus the dead load shear. In each case, the experimental capacities of the girders were greater than the theoretical capacities predicted by ACI and AASHTO codes. Also note that the exterior girders exhibited 30% greater shear capacity than the interior girders tested at the same shear span.

Data from Figure 40 are tabulated in Table 3. The average experimental shear capacities were 1.96 and 2.10 times larger than the capacity of the standard girder predicted by ACI and AASHTO, respectively. The average experimental-to-nominal capacity ratio for the exterior girders was 2.56 (ACI) and 2.71 (AASHTO), compared to 1.66 (ACI) and 1.79 (AASHTO) for the interior girders. This increased capacity of the exterior girders is attributed to the shear capacity of the curb. As the test girders tended to behave as tied-arches prior to failure, the presence of the curb contributed to the strength of the arch and thus to the shear capacity of the girder.

The increase in nominal shear strength of the test specimens due to the curb can be conservatively approximated by multiplying the shear nominal capacity of an interior girder by the ratio of the exterior girder depth to interior girder depth. This is demonstrated by the calculations shown in Table 5.

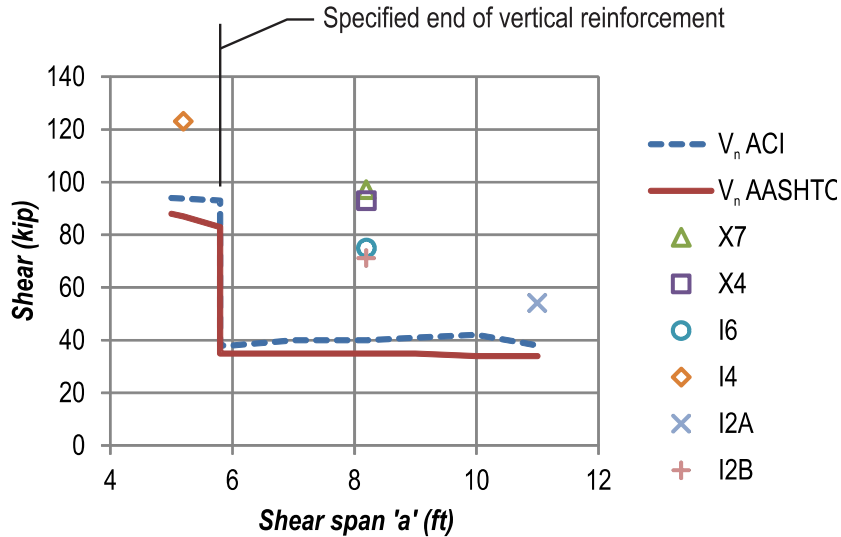


Figure 40–Experimental and theoretical shear capacities.

Table 3–Comparison of experimental and theoretical shear capacities.

	V_{e-max} (kip)	V_n ACI (kip)	V_n AASHTO (kip)	V_{e-max}/V_n ACI	V_{e-max}/V_n AASHTO
X7	96	37	35	2.59	2.74
X4	94	37	35	2.54	2.69
I6	75	37	35	2.03	2.14
I4	123	94	87	1.31	1.41
I2A	54	38	34	1.42	1.59
I2B	71	38	35	1.87	2.03
Avg.				1.96	2.10
X only Avg.				2.56	2.71
I only Avg.				1.66	1.79

Table 4–Exterior girder shear strength considering contribution of barrier

	V_{e-max} (kip)	Depth ratio (d^*) exterior/interior	$d^* \times V_n$ ACI (kip)	$d^* \times V_n$ AASHTO (kip)	$V_{e-max}/$ $(d^* \times V_n)$ ACI	$V_{e-max}/$ $(d^* \times V_n)$ AASHTO
X7	96	1.4	52	49	1.85	1.96
X4	94	1.4	52	49	1.81	1.92
Avg.					1.83	1.94

The least conservative results came from girder I4, which was tested at a shear span of 2.1. This placed the critical section at the load point within the limits of the specified transverse reinforcement. As such, I4 was the only girder for which the nominal capacity included the contribution of shear reinforcement. Figure 36 shows that each of the inclined cracks in the shear span of girder I4 engaged transverse reinforcement, thus consideration of the reinforcement contribution is reasonable.

Experimental loads at the initiation of cracking provide another means of comparison with the theoretically calculated capacities. This comparison is useful for evaluating service behavior and cracking for similar in service girders. Figure 41 shows the theoretical concrete contribution as calculated by the ACI and AASHTO provisions. The theoretical concrete contribution represents the nominal strength of the standard section without shear reinforcement. The point data on this figure mark the total (dead plus superimposed) shear load of the first inclined cracking in the web. Load at first web cracking was determined from the strain gage data. Cracking load indicated by the strain gages was lower than the load at which cracking was visually observed. Data from Figure 41 are tabulated in Table 5. The average ratio of the experimental shear at cracking to the concrete contribution was 1.17 and 1.32 for the ACI and AASHTO procedures, respectively.

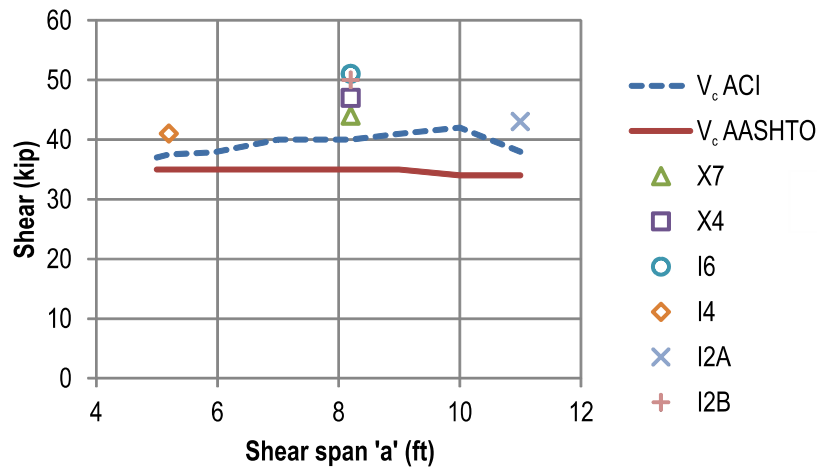


Figure 41–Shear at initial cracking and theoretical concrete contribution.

Table 5–Comparison of experimental and theoretical cracking shears.

	V_{cr-exp} (kip)	V_c ACI (kip)	V_c AASHTO (kip)	V_{cr-exp}/V_c ACI	V_{cr-exp}/V_c AASHTO
X7	44	40	35	1.10	1.26
X4	47	40	35	1.18	1.34
I2A	43	38	34	1.13	1.26
I2B	50	40	35	1.25	1.43
I4	41	37	35	1.11	1.17
I6	51	40	35	1.28	1.46
Avg.				1.17	1.32

Experimental moments and nominal moment capacities are summarized in Table 6. The theoretical moment capacities were calculated using the individual section properties from each test girder rather than from the properties of the standard section. A moment-curvature MathCAD worksheet developed by Consolazio et al. (2004) was used to calculate the theoretical moment capacity of the section. Calculations were rigorous, employing strain compatibility, equilibrium, nonlinear concrete stress-strain model (tension and compression), nonlinear steel stress-strain model for strands and mild steel, and biaxial bending.

Girder X4 was the only specimen to fail in flexure, with the experimental moment capacity being within 5% of the predicted capacity. During testing, crushing occurred in the extreme compression fibers of girder X4 at 2550 microstrain, confirming that girder was at or nearing flexural capacity. As none of the other girders failed in flexure, the experimental moments are less than the calculated moment capacities.

Table 6–Comparison of experimental moments and nominal moment capacities.

	M_{exp} (kip-ft)	M_n (kip-ft)	M_{exp}/M_n
X7	752	934	0.80
X4	745	782	0.95
I2A	572	693	0.83
I2B	560	675	0.83
I4	626	721	0.87
I6	585	743	0.79

6 Summary and Conclusions

Six pretensioned concrete girders were salvaged from an existing bridge and tested after nearly 55 years of service. Girders were tested in three point bending at a/d ratios from 2.1 to 4.5. A varying portion of the existing deck and/or curb was retained with each test girder. The experimental results were compared to theoretical predictions of strength capacity. Based on the experimental and analytical results, the following conclusions are made:

- Test girders behaved as tied arches at the latter stages of loading. This is evident from the relatively wide cracks which did not allow aggregate interlock and from the absence of transverse reinforcement necessary to allow truss action.
- Tied-arch behavior controlled the experimental strength of girders X7, X4 and I2A. Arches in these girders failed due to punching, flexural compression, and arch instability, respectively.
- For girders I2B, I4, and I6 the maximum load occurred just prior to the formation of an inclined crack in the web. These girders behaved as tied-arches during the latter stages of loading, however, their maximum capacities were limited by the capacity of the web to resist inclined cracking.
- The serviceability limit for girders tested at a/d ratios of 3.4 and less was formation of inclined cracks in the web. The thin 4 in. webs were culpable in the relatively small loads required to initiate web cracks.
- For tests at the same a/d ratio, the cast-in-place curb increased the average exterior girder strength by 30% over that of the interior girders with no curb.
- Nominal shear capacities calculated by ACI and AASHTO methods were conservative relative to the experimental results. On average ratio of calculated-to-experimental shear capacity was 2.0 for ACI calculations and 2.1 for AASHTO calculations.
- The concrete shear contribution, as calculated by ACI or AASHTO methods are recommended for estimating the cracking load of similar in-service girders. Concrete contribution as calculated by ACI and AASHTO methods were, respectively, 17% and 32% lower than the experimental cracking loads.

- End blocks effectively supported end region loads, preventing cracking in the end region in all but two tests, and strand slip in all but one test.
- Location and quantity of the transverse reinforcement in the test girders and the construction drawings. It is recommended that presence of vertical reinforcement be confirmed using non-destruction methods when analyzing the shear capacity of similar in-service girders. If the presence of transverse reinforcement is not verified, then it is recommended that shear contribution for the vertical steel be neglected.
- The experimentally determined prestress force in specimen I2A was 47% less than the specified initial prestress. The large difference between the specified and experimental values may indicate quality control issues in addition to higher than expected losses.
- In spite of relatively thin webs, small quantities of vertical reinforcement, and poor quality control during construction, the girders were able to support significant shear force after nearly 55 years of service.

Appendix D–FIB-54 Tests

Table of Contents

D.1 Summary	214
D.1.1 Introduction	214
D.2 Girder Design and Construction.....	218
D.2.1 Test Girder Classification.....	218
D.2.2 Test Girder Design	221
D.2.3 Girder Construction.....	231
D.2.4 Material Properties	241
D.3 Test Setup and Procedures	245
D.3.1 Data Collection during Fabrication	245
D.3.2 Load Test Setup and Procedures	246
D.3.3 Coordinate System.....	248
D.4 Instrumentation.....	250
D.4.1 Types and Descriptions	250
D.4.2 Strain Gage Coordinates.....	257
D.5 Results and Discussion: Fabrication.....	265
D.5.1 Strain Data	265
D.5.2 Crack Data.....	287
D.5.3 Prestress Loss	301
D.5.4 Variable Comparison and Discussion.....	302
D.5.5 Summary and Conclusions	304
D.6 Results and Discussion: Load Tests	308
D.6.1 Failure Modes.....	308
D.6.2 Load Test Results	311
D.6.3 Confinement Reinforcement and Bearing Plates.....	335
D.6.4 Variable Comparisons	345
D.6.5 Code Comparisons.....	352
D.7 Summary and Conclusions.....	356

List of Figures

Figure 1–I-Girder highway bridge	215
Figure 2–Cross-section 54-in. deep Florida I-Beam	215
Figure 3–End region reinforcement.	216
Figure 4–FIB-54 end region reinforcing detail (FDOT 2009b)	217
Figure 5–Labeling scheme	218
Figure 6–Specimen labels and graphical descriptions	220
Figure 7–Cross-section of FIB-54.....	221
Figure 8–Strand layout and prestressing details	222
Figure 9–Strand bond and shielding patterns.....	223
Figure 10–Reinforcement for girder H	225
Figure 11–Reinforcement for girder V	226
Figure 12–Reinforcement for girders W and F.....	227
Figure 13–Reinforcement for girder D	228
Figure 14–Reinforcement and bearing plate details.....	229
Figure 15–Confinement reinforcement schemes	230
Figure 16–Cast-in-place deck reinforcement.....	230
Figure 17–Girder orientation during fabrication.....	232
Figure 18–Tension pattern and wire break locations	233
Figure 19–Girder H reinforcement A) Specimen HC and B) Specimen HU.....	233
Figure 20–Girder V reinforcement A) Specimen VC and B) Specimen VU.....	234
Figure 21–Girder W reinforcement A) Specimen WN and B) Specimen WB	234
Figure 22–Girder F reinforcement A) Specimen FN and B) Specimen FB	234
Figure 23–Girder D reinforcement A) Specimen DC and B) Specimen DM	235
Figure 24–Concrete placement and internal consolidation phase 1	235
Figure 25–Concrete placement phase 2	236
Figure 26–Girder finished surface	236
Figure 27–Girders covered with tarps.....	237
Figure 28–Strand release patterns	238
Figure 29–Test girder lifted by crane.....	239
Figure 30–Girder resting on dunnage above stressing bed	239
Figure 31–Girder H on truck prior to transit.....	240
Figure 32–Deck construction A) reinforcement and B) formwork.....	240
Figure 33–Concrete placement A) unloading and B) placement with bucket	241
Figure 34–Test setup.....	247
Figure 35–Test setup at A) bearing and B) load point.....	248
Figure 36–Test specimen and load frame A) top of girder and B) end of girder.....	248
Figure 37–Coordinate system relative to load and supports	249
Figure 38–MS gage A) before protective covering and B) with protective cover and label	251
Figure 39–XS gage installation.....	251
Figure 40–ES gage A) vertical and B) horizontal orientation.....	252
Figure 41–V gage (view from above).....	253
Figure 42–Wire harness and plywood bulkhead.....	253
Figure 43–S gage A) on top of bottom flange and B) close-up	254
Figure 44–LVDT placement and labels	254
Figure 45–LVDT and support frame	255
Figure 46–Girder H and V strands monitored by LVDT	255
Figure 47–Wood frame and LVDTs	256
Figure 48–Girder W, F, and D strands monitored by potentiometer	256
Figure 49–Aluminum brackets and linear potentiometers on strands.....	257

Figure 50–Load cells below hydraulic actuators	257
Figure 51–Girders H and V strand cutting stages	266
Figure 52–Transverse strain HC	266
Figure 53–Flange displaced shapes for specimen HC	267
Figure 54–Shear and moment during release, lifting, storage (prestressing not shown)	269
Figure 55–Girders W and F strand cutting stages	270
Figure 56–Girders W and F strand bond patterns	271
Figure 57–Bearing plate strain	271
Figure 58–Flange displaced shapes specimens FN and FB	273
Figure 59–Displaced shapes specimen WB and WN	274
Figure 60–WB Confinement reinforcement strain at 2 in. and 9 in. from end of girder	275
Figure 61–WN Confinement reinforcement strain at 2 in. and 9 in. from end of girder	276
Figure 62–FB confinement reinforcement strain at 2 in. and 9 in. from end of girder	278
Figure 63–FN Confinement reinforcement strain at 2 in. and 9 in. for end of girder	279
Figure 64–Confinement reinforcement average strain at prestress release	279
Figure 65–Forces in reinforcement and plates after prestress transfer	282
Figure 66–Strain gages for measuring transfer length	285
Figure 67–Transfer length in girders H and V	285
Figure 68–Transfer length in girder F	286
Figure 69–Web splitting and flange splitting cracks	288
Figure 70–Girder H and V cracks prior to load tests	291
Figure 71–Flange splitting crack intersecting outer strand	292
Figure 72–Web splitting cracks in specimens H and V	293
Figure 73–Maximum crack widths in girders H and V	294
Figure 74–Flange splitting crack data in girders H and V	295
Figure 75–Girders W, F, and D web and flange splitting cracks	297
Figure 76–End of bottom flange covered by portion of steel bulkhead	298
Figure 77–Girder F flange splitting cracks in A) specimen FN and B) specimen FB	299
Figure 78–Flange splitting cracks in girders W, F, and D	299
Figure 79–Maximum crack widths in girders W, F, and D	300
Figure 80–Web splitting cracks in girders W, F, and D	300
Figure 81–Girder D flange splitting cracks in A) specimen DC and B) specimen DM	301
Figure 82–Web-shear failure	309
Figure 83–Lateral-splitting failure A) bottom view and B) side-end view	309
Figure 84–Lateral-splitting failure mechanics	310
Figure 85–Bond-shear failure A) bottom view and B) side view	311
Figure 86–Specimen HC load test summary A) shear-displacement and B) crack pattern	312
Figure 87–HC after load testing (cracks shown blue; spalling in brown)	314
Figure 88–Close-up of web crushing and spalling	314
Figure 89–Cracks at end of HC after testing	315
Figure 90–Specimen HU load test summary A) shear-displacement and B) crack pattern	316
Figure 91–Bottom and end of HU after testing	317
Figure 92–Bottom view of splitting cracks in HU	317
Figure 93–Specimen VC load test summary A) shear-displacement and B) crack pattern	318
Figure 94–VC after load test	320
Figure 95–Specimen VU load test summary A) shear-displacement and B) crack pattern	321
Figure 96–Bottom view of splitting cracks in VU	322
Figure 97–Specimen WN load test summary A) shear-displacement/slip and B) crack pattern	323
Figure 99–Specimen WB load test summary A) shear-displacement/slip and B) Crack pattern	325
Figure 100–Specimen FN load test summary A) shear-displacement/slip and B) crack pattern	327
Figure 101–Strut and tie behavior specimen FN	329

Figure 102–Longitudinal splitting cracks on bottom of specimen FN (release cracks shown black; final cracks shown blue)	329
Figure 103–Confinement reinforcement strain specimen FN	330
Figure 104–Specimen FB load test summary A) shear-displacement/slip and B) crack pattern	331
Figure 105–Specimen DC load test summary A) shear-displacement/slip and B) crack pattern	333
Figure 106–Specimen DM load test summary A) shear-displacement/slip and B) crack pattern	335
Figure 107–Strain gage placement girders W, F, and D	336
Figure 108–Confinement stress at shear = 375 kip	337
Figure 109–Confinement stress at ultimate capacity	337
Figure 110–Transverse (x-x) stress profiles at bearing plate centerline	340
Figure 111–Strain gage placement girders H and V	341
Figure 112–Specimens HC and VC confinement reinforcement and bearing plate transverse (x-x) forces due to maximum applied load	342
Figure 113–Bearing plate stress due to applied load	343
Figure 114–Bearing plate force due to applied load	344
Figure 115–Percent of transverse force due to applied loads carried by bearing plate.....	344
Figure 116–Percent of transverse force carried by bearing plate in WB and FB.....	345
Figure 117–Maximum superimposed shear	345
Figure 118–Girder D bottom flange cracking A) specimen DC with limited bottom flange cracking in front of bearing and B) specimen DM with severe bottom flange cracking in front of bearing	349
Figure 119–Relationship between strand quantity and end region capacity	350
Figure 120–Comparison of FB (left) and WB (right) (release cracks shown black; final cracks shown blue).....	351

List of Tables

Table 1–Test girder and specimen variables.....	219
Table 2–Specified material properties	231
Table 3–Construction and testing chronology	231
Table 4–Tested concrete compressive strengths	242
Table 5–Prestressing steel properties	243
Table 6–Grout strength for NASP tests	243
Table 7–NASP Test Results.....	243
Table 8–Steel reinforcement properties	244
Table 9–Load test chronology.....	246
Table 10–Instrumentation types and labels.....	250
Table 11–Specimen HC strain gage coordinates	258
Table 12–Specimen HU strain gage coordinates	259
Table 13–Specimen VC strain gage coordinates	260
Table 14–Specimen VU strain gage coordinates	261
Table 15–Specimen WN strain gage coordinates	261
Table 16–Specimen WB strain gage coordinates.....	262
Table 17–Specimen FN strain gage coordinates	262
Table 18–Specimen FB strain gage coordinates	263
Table 19–Specimen DC strain gage coordinates	263
Table 20–Specimen DM strain gage coordinates.....	264
Table 21–Girders H and V fabrication chronology.....	265
Table 22–Tensile strain girders H and V	269
Table 23–Girders W and F fabrication stages.....	270
Table 24–Confinement reinforcement strain after prestress transfer	280
Table 25–Confinement and plate forces	283
Table 26–Girders H and V construction events and inspection dates.....	290
Table 27–Recommended action for web splitting cracks (Tadros et al. 2010).....	294
Table 28–Girders W, F, and D construction events and inspection dates.....	296
Table 29–Prestress losses girders F and W	301
Table 30–Prestress losses girder H, V, and D	301
Table 31–Transverse forces in W and F specimens.....	339
Table 32–Maximum superimposed shear	346
Table 33–Variable comparisons.....	347
Table 34–Material properties for capacity calculations	352
Table 35–Experimental moments and nominal moment capacities.....	353
Table 36–Experimental shear and nominal shear capacities.....	354

D.1 Summary

Confinement reinforcement is placed near the end of pretensioned concrete I-girders to enclose prestressing strands in the bottom flange. Experimental and analytical test programs were conducted to investigate the function of confinement reinforcement and to provide the basis for a confinement reinforcement design model. Five 54-in. deep Florida I-Beam (FIB-54) girders were fabricated and load tested in the experimental program. Each end of each girder had a different combination of variables, which resulted in ten unique test specimens. Variables included: presence or absence of embedded steel bearing plates, quantity and configuration of confinement reinforcement, strand bond pattern, strand quantity, and quantity of horizontal and vertical end region reinforcement. Data were collected during and after prestress transfer to evaluate the effects of test variables on bottom flange cracking. Load tests were then conducted on each specimen (end) to determine the effects of test variables on girder behavior and capacity. Specimens were loaded in three-point bending at a shear span-to-depth ratio of 2.0. Failure modes in the test program included web-shear, bond-shear, and lateral-splitting. Primary outcomes of the research include an improved understanding of the function of confinement reinforcement during prestress transfer and at ultimate load, and an improved understanding the interaction between confinement reinforcement and the other end region variables.

D.1.1 Introduction

Of the almost 12,000 bridges in Florida's public road system, approximately half utilize prestressed concrete as the structural system (FHWA, 2010). Simple-span pretensioned concrete I-girders are the most common type of prestressed concrete structures, and are ubiquitous in Florida's highway system (Figure 1). In 2009, the Florida Department of Transportation (FDOT) introduced the Florida I-Beam (FIB) (Figure 2) for use in highway bridges. The FIB girders "were developed to be more efficient to fabricate, safer to construct, and more cost effect when compared to the [previously] used prestressed beams" (FDOT 2009a).



Figure 1–I-Girder highway bridge

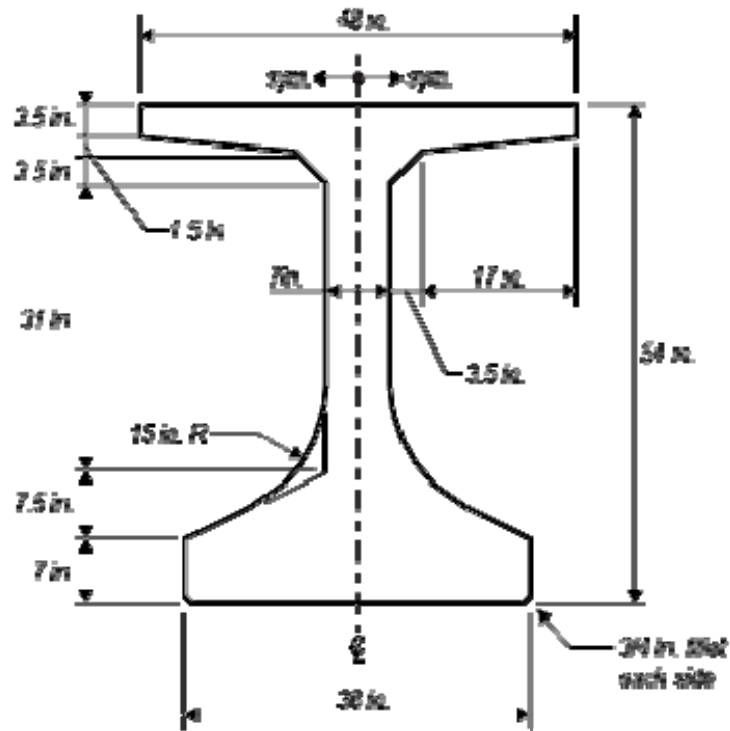


Figure 2–Cross-section 54-in. deep Florida I-Beam

To further improve the efficiency of FIB girders, it is desirable to investigate the feasibility of reducing reinforcement placed in the end region (Figure 3). End region reinforcement is specified by FDOT standard details (Figure 4), which are based on historic FDOT details, code requirements, and constructability considerations (Nolan 2009; Fallaha 2009). There is particular incentive to investigate confinement reinforcement, which is placed in the bottom flange around prestressing strands (Figure 3). The current use of confinement reinforcement is limited by the following:

- Confinement reinforcement approximately doubles the amount of time required to place reinforcement in I-girders (Magus 2010).
- Code provisions governing confinement reinforcement are based on limited experimental data. The interaction of confinement reinforcement and other end region design variables has not been studied.
- Code provisions governing confinement reinforcement are prescriptive and do not provide a rational model for design.

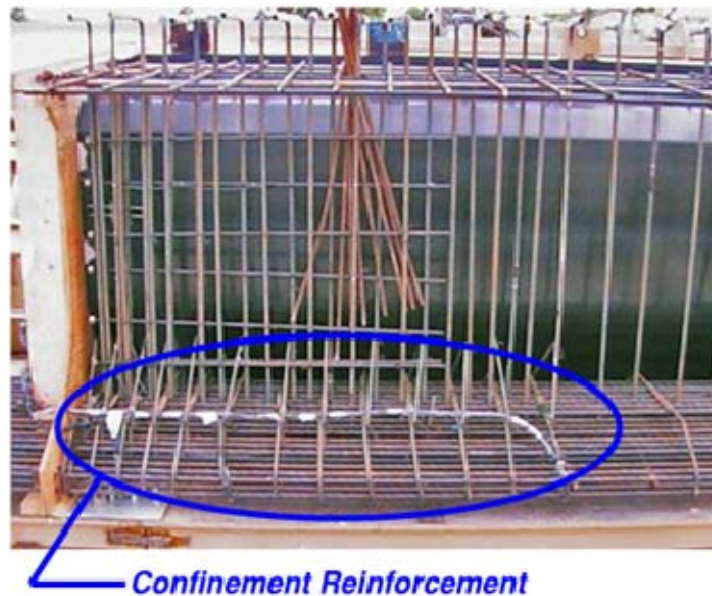


Figure 3–End region reinforcement.

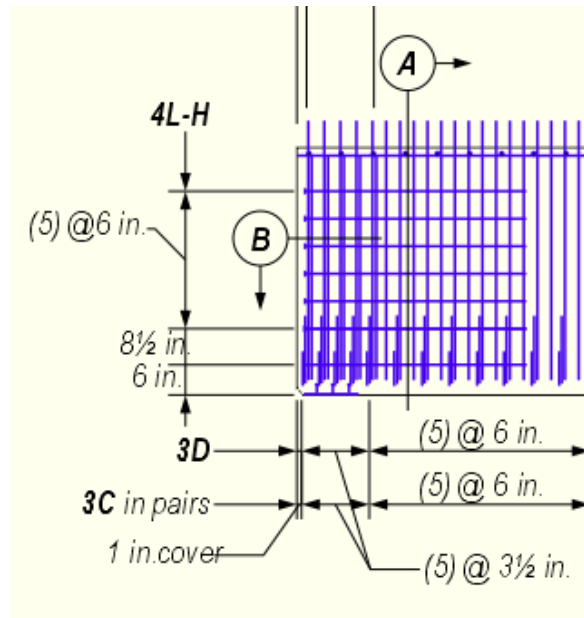


Figure 4–FIB-54 end region reinforcing detail (FDOT 2009b)

Previous research (see Appendix A) has focused on the effects of confinement reinforcement but does little to address its function. For purposes of this document, the “function” of confinement reinforcement is defined as how, why, where, and when confinement reinforcement acts in the end region structure.

Research presented in this document made use of analytical and experimental methods to investigate the function of confinement reinforcement. Interaction between confinement reinforcement and other end region variables was also considered. One goal of the research was to provide a rational model for the design of confinement reinforcement. Experimental results coupled with a rational model may justify a reduction in the quantity of reinforcement in the end region, thereby improving the efficiency of pretensioned I-girders.

In addition to having sufficient strength pretensioned I-girders must also satisfy serviceability requirements. Bottom flange splitting cracks are a particular serviceability concern in girders with relatively slender bottom flanges such as the FIB. Accordingly, development of a serviceability design model for the bottom flange of FIB girders was part of the research program. Such a model can improve the efficiency of FIB girders by giving engineers a tool for designing bottom flanges that are less prone to splitting cracks.

D.2 Girder Design and Construction

Five 54 in. deep Florida I-Beam (FIB-54) girders were fabricated and tested to evaluate the effects of end region detailing on girder behavior and capacity. Variables in the test program included: quantity of horizontal and vertical mild reinforcement in the end region, quantity or lack of confinement reinforcement, strand debonding pattern, and presence or lack of embedded steel bearing plates. This chapter presents details of the girders, construction procedures, and material properties. The labeling convention used to identify the different girders and specimens is also presented.

D.2.1 Test Girder Classification

Each end of each girder had a unique combination of variables. Because of the unique detailing, each end will be referred to as a separate “specimen” in this document. Figure 5 presents the nomenclature used to label specimens and girders. The first letter in the label identifies the girder and the second letter is used to designate the end. Both letters combine to form a specimen label. Letters used in the labels describe the key variables associated with each girder and specimen. A complete description of variables is contained in Table 1. Schematic representations of each specimen and the associated variables are shown in Figure 6.

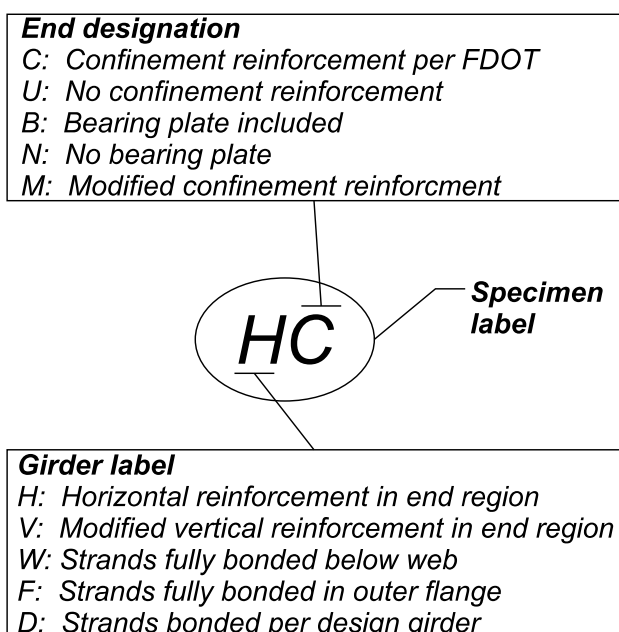


Figure 5–Labeling scheme

Table 1–Test girder and specimen variables

Test Girder	Specimen	Bearing plate	Mild reinforcement		Strand bond pattern	Confinement reinforcement	Phase
			Vertical	Horizontal			
H	HC	Yes	FDOT	Yes	Design	FDOT	1
	HU	Yes	FDOT	Yes	Design	No	1
V	VC	Yes	Mod	No	Design	FDOT	1
	VU	Yes	Mod	No	Design	No	1
W	WN	No	FDOT	No	Web	Mod	2
	WB	Yes	FDOT	No	Web	Mod	2
F	FN	No	FDOT	No	Flange	Mod	2
	FB	Yes	FDOT	No	Flange	Mod	2
D	DC	Yes	FDOT	No	Design	FDOT	2
	DM	Yes	FDOT	No	Design	Mod	2

FDOT: Detailed per FDOT design standards
 Mod: Detailed with modifications to FDOT design standards
 Web: Fully bonded strands placed below web
 Flange: Fully bonded strands placed in outer portion of flange
 Design: Strand pattern based on prototype design

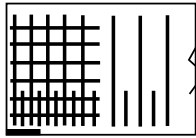
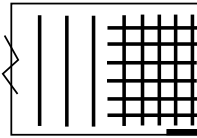

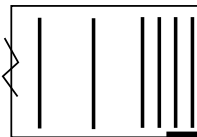
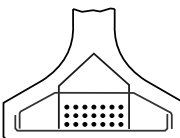
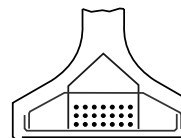
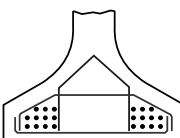
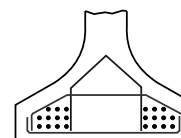

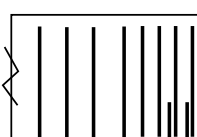
	<i>End 1</i>	<i>End 2</i>
<i>Girder H</i>	<p><i>HC</i></p> 	<p><i>HU</i></p> 
<i>Girder V</i>	<p><i>VC</i></p> 	<p><i>VU</i></p> 
<i>Girder W</i>	<p><i>WN</i></p> 	<p><i>WB</i></p> 
<i>Girder F</i>	<p><i>FN</i></p> 	<p><i>FB</i></p> 
<i>Girder D</i>	<p><i>DC</i></p> 	<p><i>DM</i></p> 

Figure 6–Specimen labels and graphical descriptions

Girders were constructed in two phases. The final column in Table 1 notes the construction phase for each test girder. Phase 1 girders were constructed at Dura-Stress Inc. in Leesburg, FL in August of 2010. Phase 2 girders were constructed at Standard Concrete Products in Tampa, FL in February of 2012.

Meetings were held with the FDOT, the project sponsor, prior to each construction phase to solicit input on test variables. Variables in phase I include the presence or lack of confinement

reinforcement and quantity of mild steel reinforcement in the end region. Variables tested in phase II include confinement reinforcement configuration, the presence or lack of steel bearing plates, and the strand bond pattern.

D.2.2 Test Girder Design

Test girder prototype design was based on girders used in an existing bridge in Clay County, FL, which had the FIB-54 cross-section (Figure 7) and spanned approximately 120 ft. The strand pattern and reinforcement for the prototype girder were designed based on these conditions. Due to laboratory space restrictions, the test girder length was reduced to 49.5 ft. The shorter length, however, still allowed for evaluation of the end region detailing, which was the primary focus of the research program.

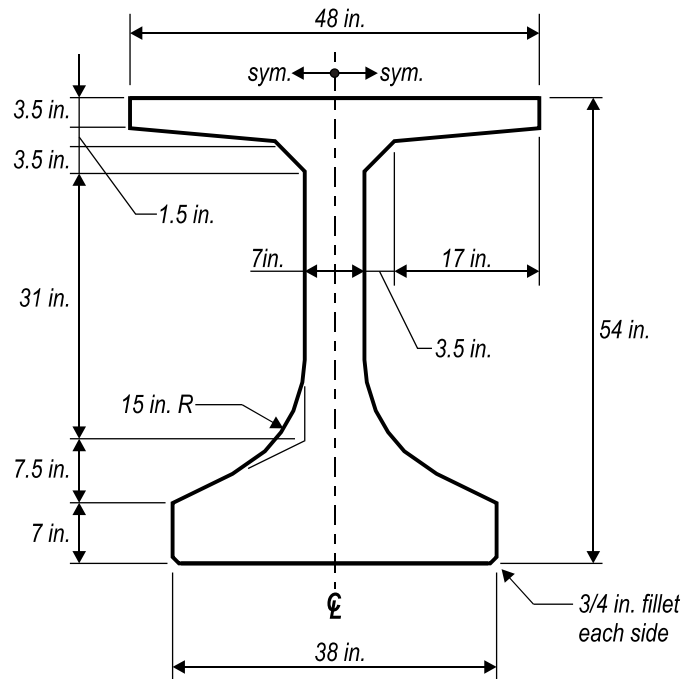


Figure 7–Cross-section of FIB-54

The prototype design called for (52) 0.6-in. diameter prestressing strands in the bottom flange and (4) 3/8-in. diameter strands in the top flange (Figure 8) using the strand bond pattern designated as “design pattern” in Figure 9. While strand bond patterns were varied among the specimens as indicated in Figure 9, the strand diameter, positions, and total prestress force were constant. The design pattern had six partially shielded strands and seven fully shielded strands.

Fully shielded strands in the test girders correspond to locations in the prototype with shielding lengths of 20 ft or 35 ft. Because test girders were shorter than the prototype, these shielding lengths resulted in fully shielded strands in the test girders.

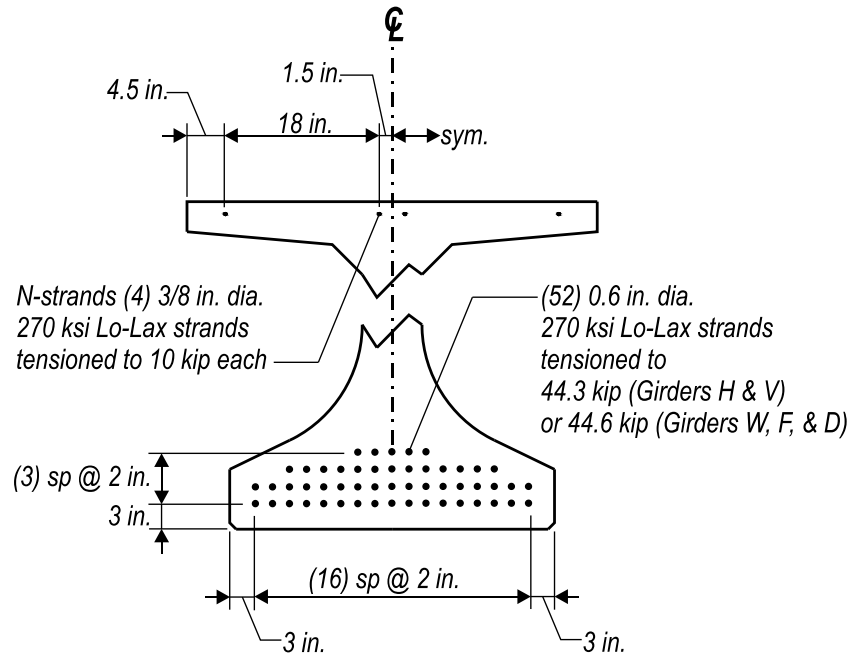


Figure 8—Strand layout and prestressing details

Some strands in Figure 9 are denoted at “Shielded entire length”. This designation is not strictly accurate for girders W, F, and D. All strands in these girders were bonded to the concrete for at least 18 in. at the girder center span. This was done for safety reasons so that the strands would be restrained from dangerous whipping movements during release of prestress forces. Bonding at the center 18 in. did not affect the end regions where load tests were conducted.

The “web pattern” and “flange pattern” (Figure 9) were designed to test the effect of strand placement on end region behavior and capacity. These patterns were created by partially shielding strands in select locations. Both patterns violate current AASHTO LRFD requirements for quantity and placement of shielding, but were useful for research purposes. The two outermost strands in each pattern were fully bonded so that confinement reinforcement could be secured to these strands during fabrication.

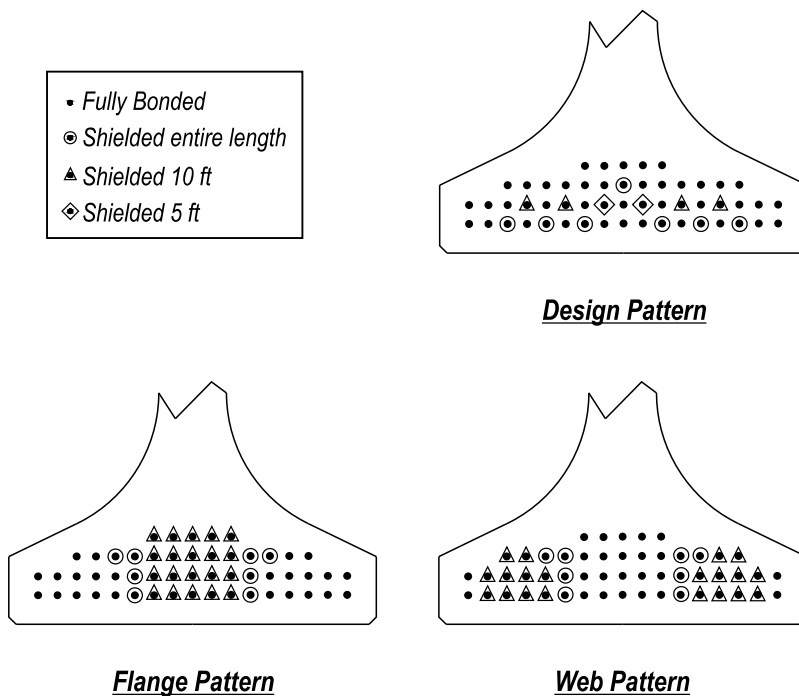


Figure 9–Strand bond and shielding patterns

Mild reinforcement details (Figure 10 through Figure 13) were based on the prototype girder and on FDOT Florida-I 54-Beam Interim Standard Details (FDOT, 2008, 2010). Bar labels are similar to those used in FDOT standards. The numeric portion of each label indicates the size of bar (i.e. 5A is a #5 bar). Reinforcement bending and bearing plates details are shown in Figure 14. The different types of bars will be described in the following paragraphs.

5A. Bars placed longitudinally in the top flange and were continuous for the entire length of the girder. Splices of 5A bars were at least 36 in. long.

BP. Galvanized steel bearing plates with headed studs embedded in the concrete at the girder bearing. Plates in girders H and V had eight studs, whereas plates in girders W, F, and D had six studs. Changes in stud quantity and width were made to follow the FDOT bearing plate detail which changed after girders H and V were constructed. Changes to the FDOT bearing plate detail were unrelated to the current research program.

3C, 4C, 3D, 4E and 4F. Bars placed in the bottom flange as confinement reinforcement around the prestressing strands. Both FDOT and modified confinement schemes were used in the test program and are shown in Figure 15. The FDOT confinement scheme used #3 bars and the modified scheme used #4 bars. Fewer bars were used in modified scheme and all bars were

placed directly above the bearing. The D and E bars in the modified scheme did not splice at the cross-section centerline as did the C bars in the FDOT scheme.

7G and 8G. Bars placed longitudinally in the top flange. These bars were included to control cracking in the top flange after prestress transfer, and are not specified in FDOT standards. The G bars did not extend into the end regions where load testing took place. Girders H and V had #7 G bars. Girders W, F, and D had #8 G bars.

5K and 5Ks. Bars were placed vertically in the web with hooks top and bottom. These bars protruded through the top flange to help develop composite action with the cast-in-place deck. They also acted as shear reinforcement. The bottom hook on 5K bars was 16 in. long to assist in constructability. The bottom hook on 5Ks bars was only 6 in. long. To eliminate any incidental confinement effects from the bottom hooks, 5Ks bars were used in lieu of 5K bars within the end region.

4L and 4L-H. Bars were placed horizontally in the end region of girder H. The 2008 FIB details specify that 4L bars extend beyond the girder end and hook into a cast-in-place end diaphragm. Test girders did not have end diaphragms. In the absence of a diaphragm to anchor the 4L bars, 4L-H bars with headed anchors were used in the web and bottom flange where development was critical. The 4L bars did not have headed anchors and were placed in the top flange. For reasons unrelated to the experimental program the 2010 FDOT standard detail eliminated the use of end diaphragms and horizontal bars in the end region. Girders W, F, and D were designed using the 2010 detail and did not have 4L or 4L-H bars.

4M. Bars placed transversely in the top flange.

N-Strands. Strands placed in the top flange. These strands are sometimes called “dormant” strands. Their primary purpose is to support mild reinforcement during fabrication. They also provide a nominal amount of crack control to the top flange at prestress transfer.

5Y. Vertical bars bundled with 5Ks and 5Z bars at girder ends. These bars are used to control web splitting cracks that form due to prestressing.

5Z. Bars placed vertically within the end region to control web splitting cracks.

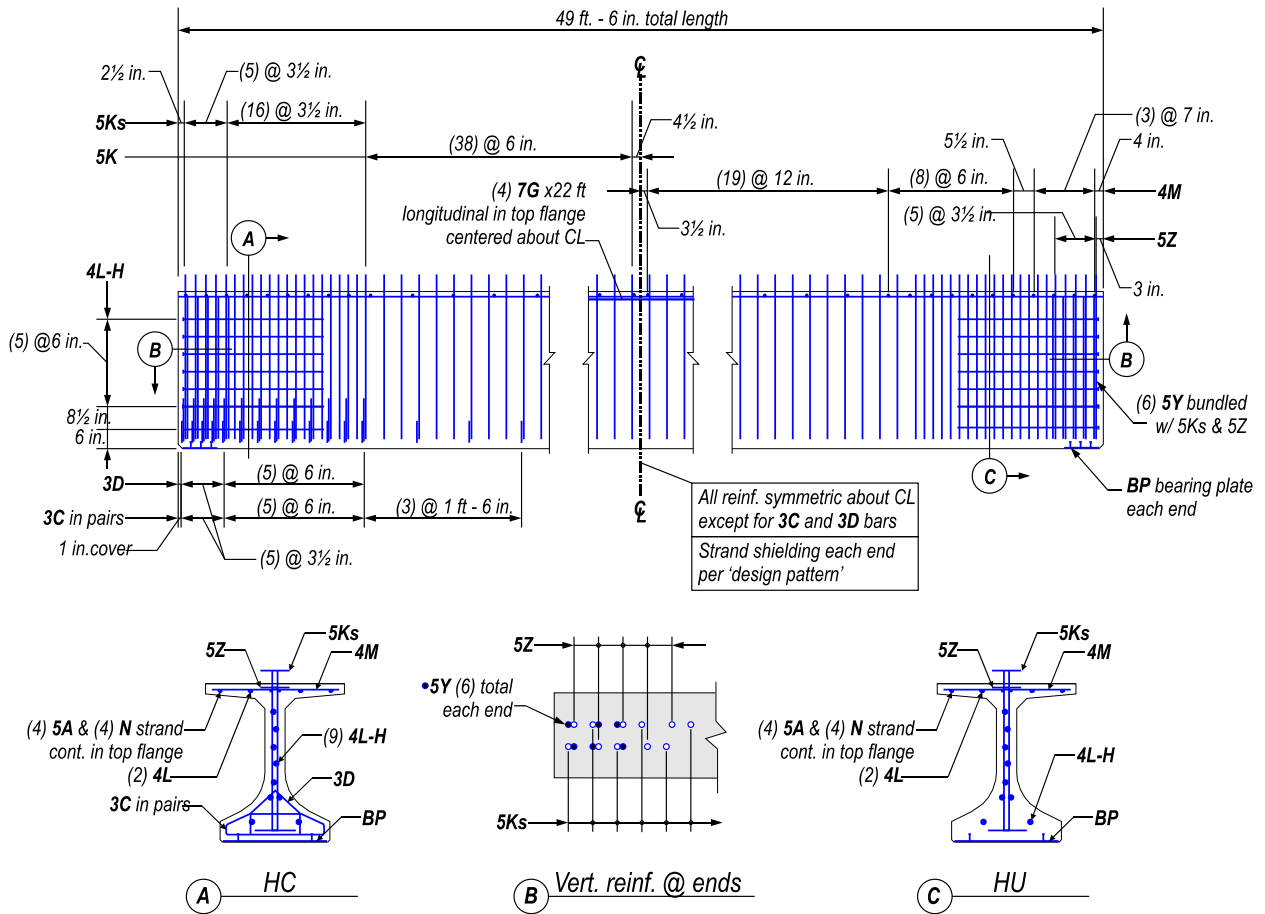


Figure 10—Reinforcement for girder H

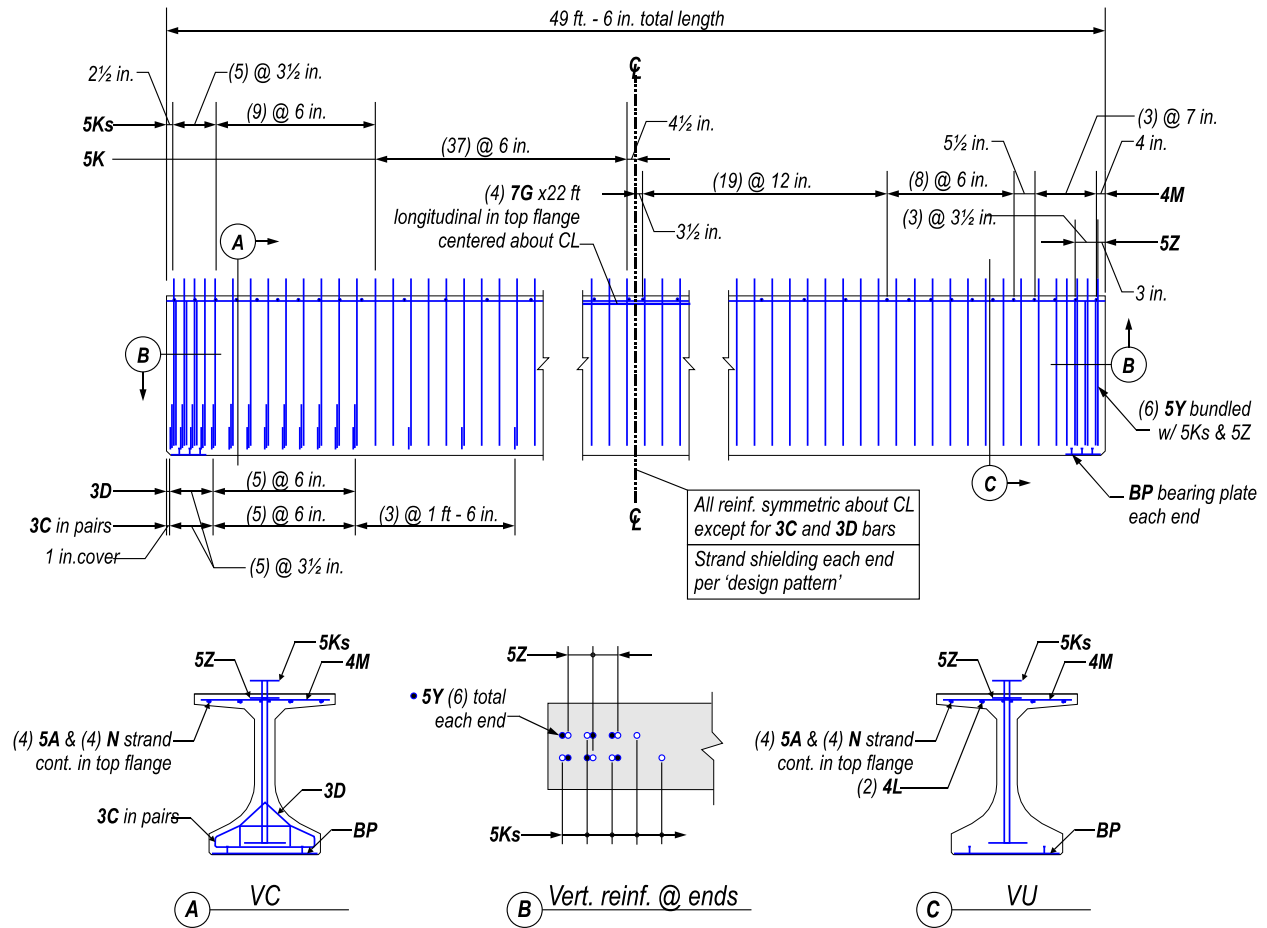


Figure 11–Reinforcement for girder V

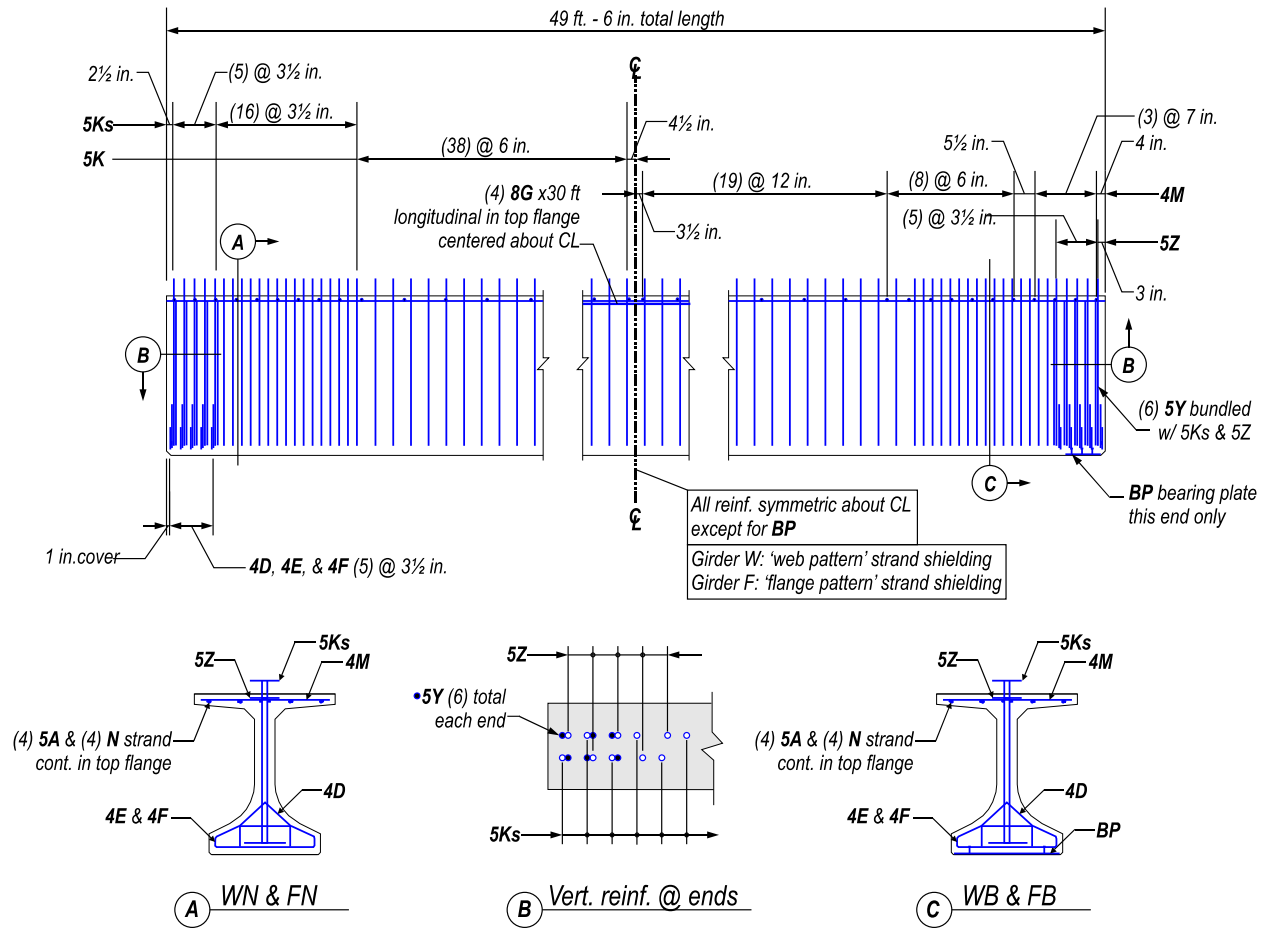


Figure 12—Reinforcement for girders W and F

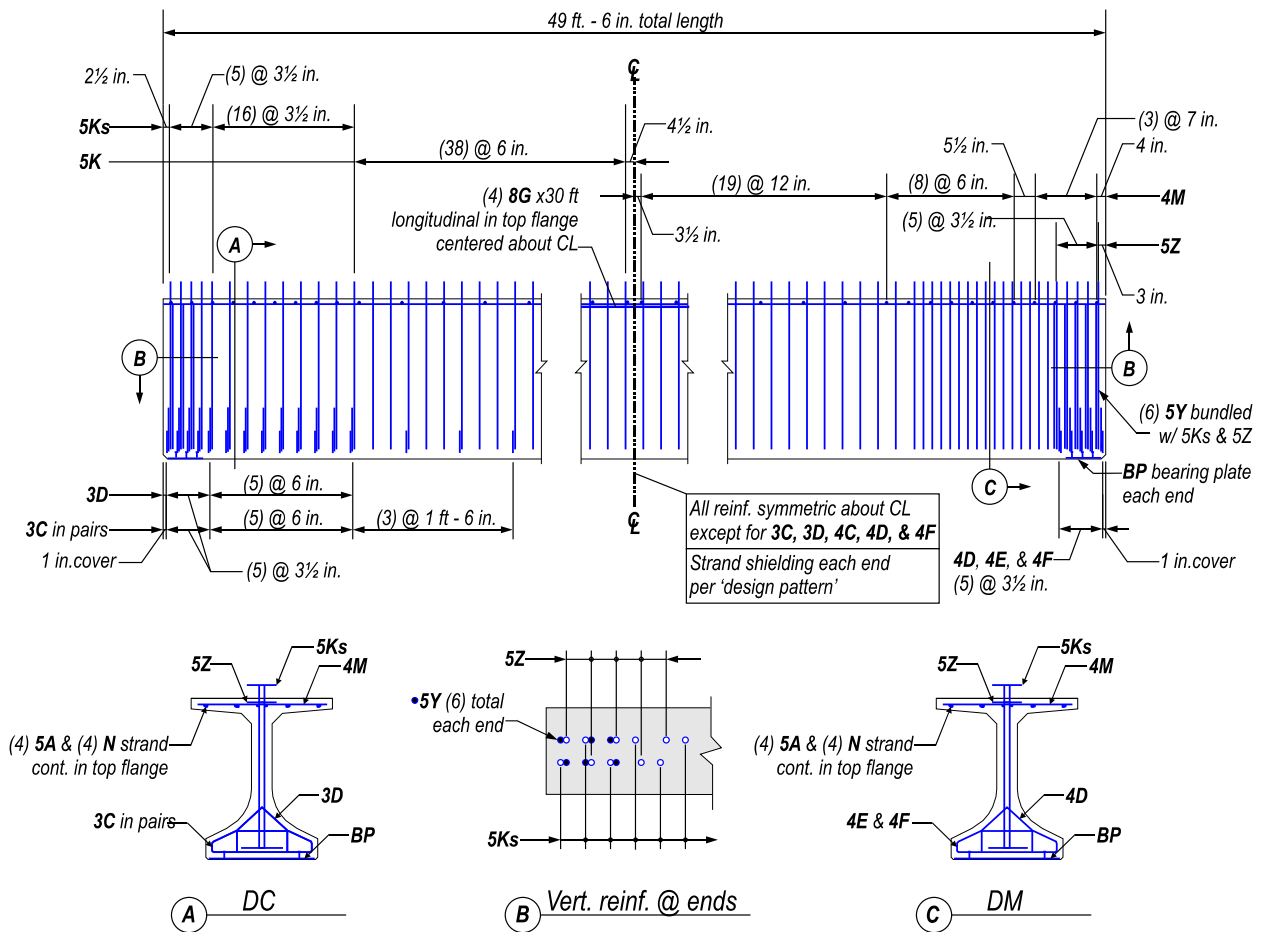


Figure 13—Reinforcement for girder D

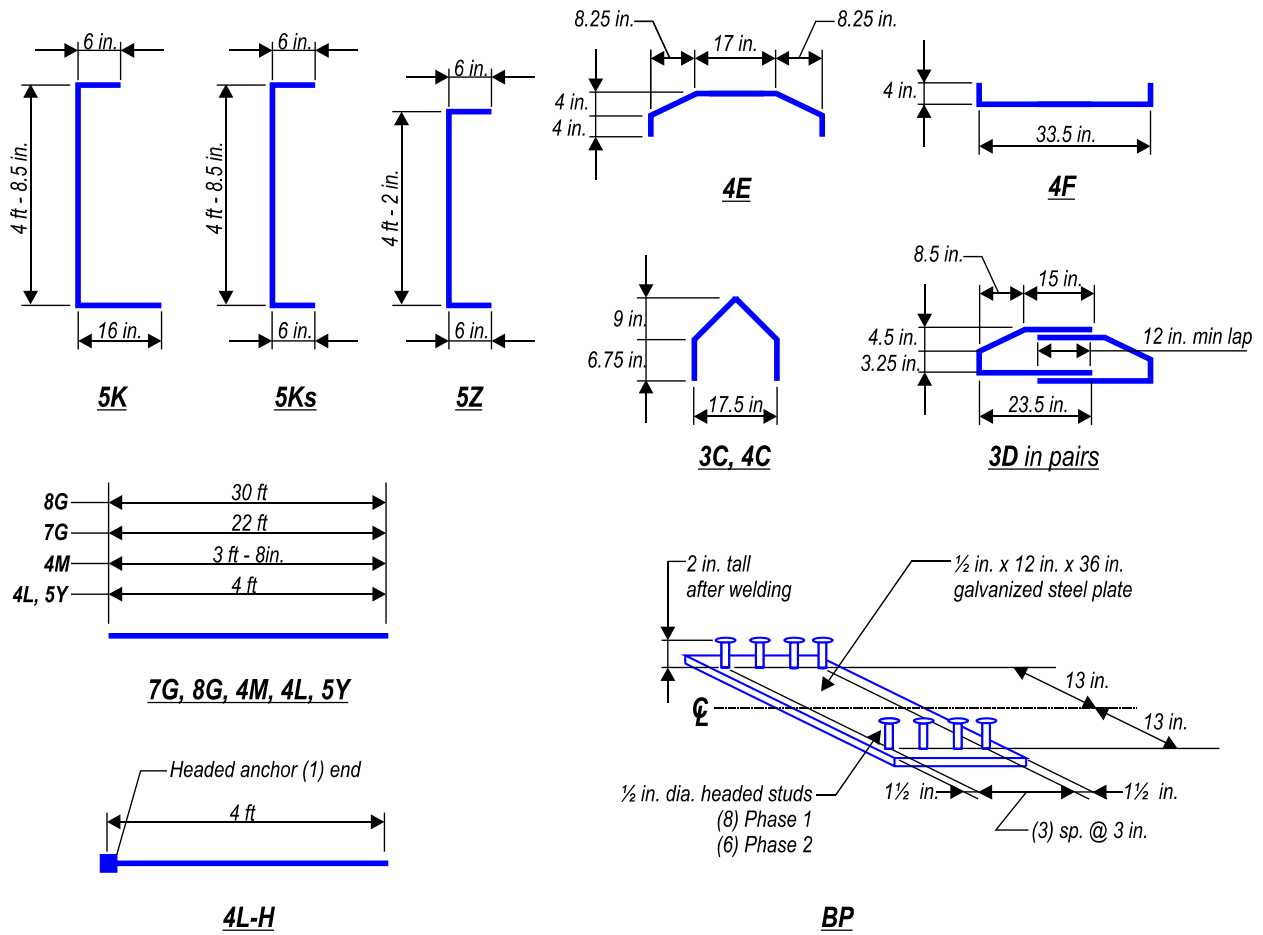


Figure 14–Reinforcement and bearing plate details

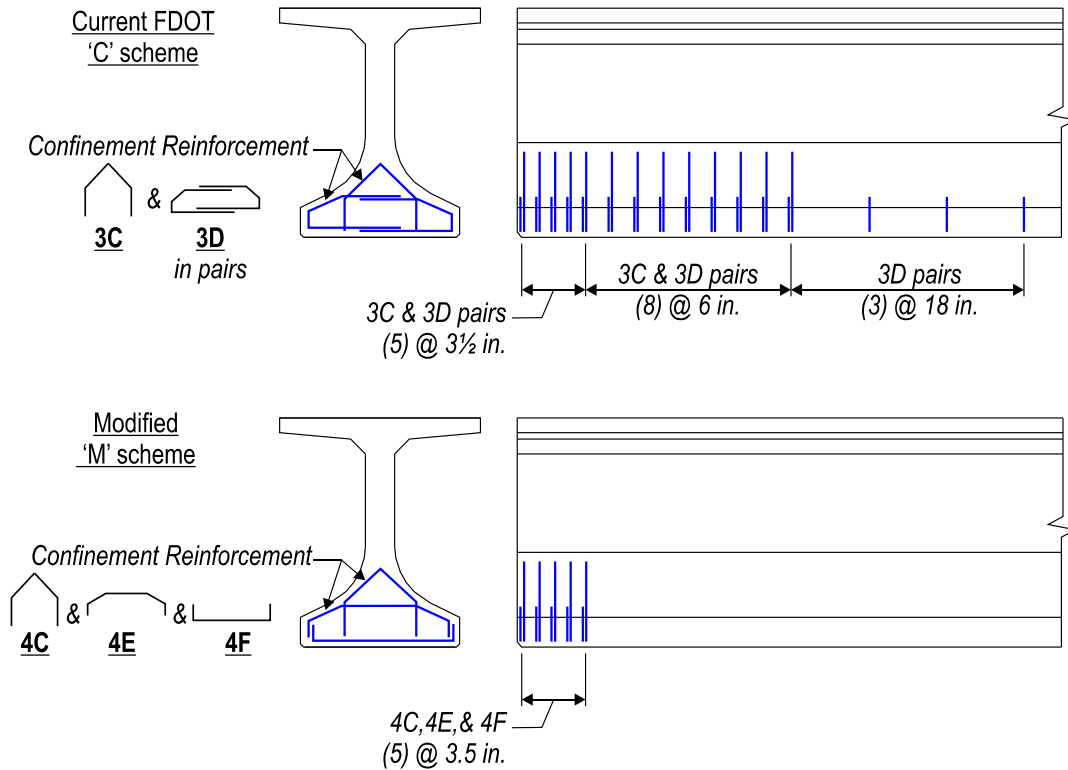


Figure 15–Confinement reinforcement schemes

Cast-in-place concrete slabs were built on top of the test girders to mimic a bridge deck. The slab was 8-in. thick, 48-in. wide and was reinforced longitudinally and transversely (Figure 16).

Specified material properties matched FDOT standards. Specifications are listed in Table 2. Tested material properties will be discussed in a later section.

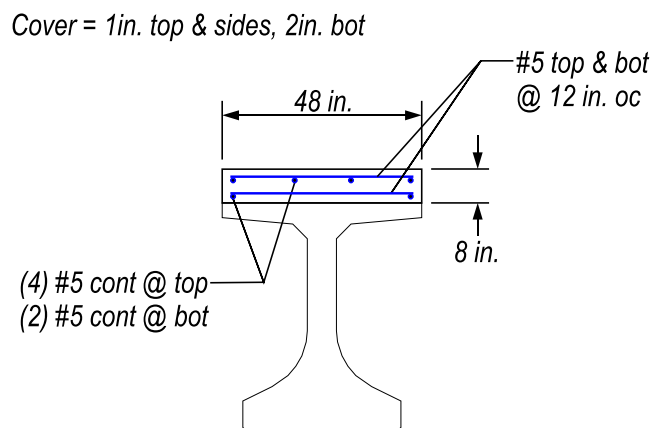


Figure 16–Cast-in-place deck reinforcement

Table 2–Specified material properties

Material	Specification
Girder Concrete	FDOT class VI 8500 psi 28-day compressive strength 6000 psi compressive strength at prestress transfer
Deck Concrete	FDOT class II 4500 psi 28-day compressive strength
Prestressing Strand	ASTM A416 270 ksi ultimate strength Low relaxation
Mild Reinforcement	ASTM A615 60 ksi yield strength

D.2.3 Girder Construction

Girders H and V were fabricated at Dura-Stress, Inc. in Leesburg, FL during the first phase of construction. Girders W, F, and D were fabricated in the second phase at Standard Concrete Products in Tampa, FL. The fabrication process was similar for both phases. Differences are specifically noted in the text in this section. Table 3 presents a summary of the construction events and dates for both phases.

Table 3–Construction and testing chronology

Event	Phase 1 Date	Phase 2 Date
Strands tensioned	August 30, 2010	February 13, 2012
Concrete poured	September 1, 2010	February 17, 2012
Concrete exceeds release strength	September 3, 2010	February 20, 2012
Forms removed	September 7, 2010	February 20, 2012
Prestress released	September 8, 2010	February 21, 2012
Moved to storage	September 8, 2010	February 22, 2012
Trucked to FDOT laboratory	February 23, 2011	April 30, 2012
Deck cast	April 6, 2011	May 7, 2012
Load testing	May 9, 2011 to May 17, 2011	May 23, 2012 to June 1, 2012

Fabrication began with the placement prestressing strands and form bulkheads. Plywood bulkheads were used during phase one. Holes were cut in the plywood for strands to pass through. Steel bulkheads were used in phase two. The steel bulkheads were installed in segments after the strands were tensioned.

A hydraulic jack was used to tension the strands. Jacking force was determined from pressure in the hydraulic line and was verified by measuring strand elongation. Girders were oriented on stressing beds as shown in Figure 17. Dormant strands in the top flange were tensioned first followed by strands in the bottom flange. The same tensioning pattern (Figure 18) was used for both phases.

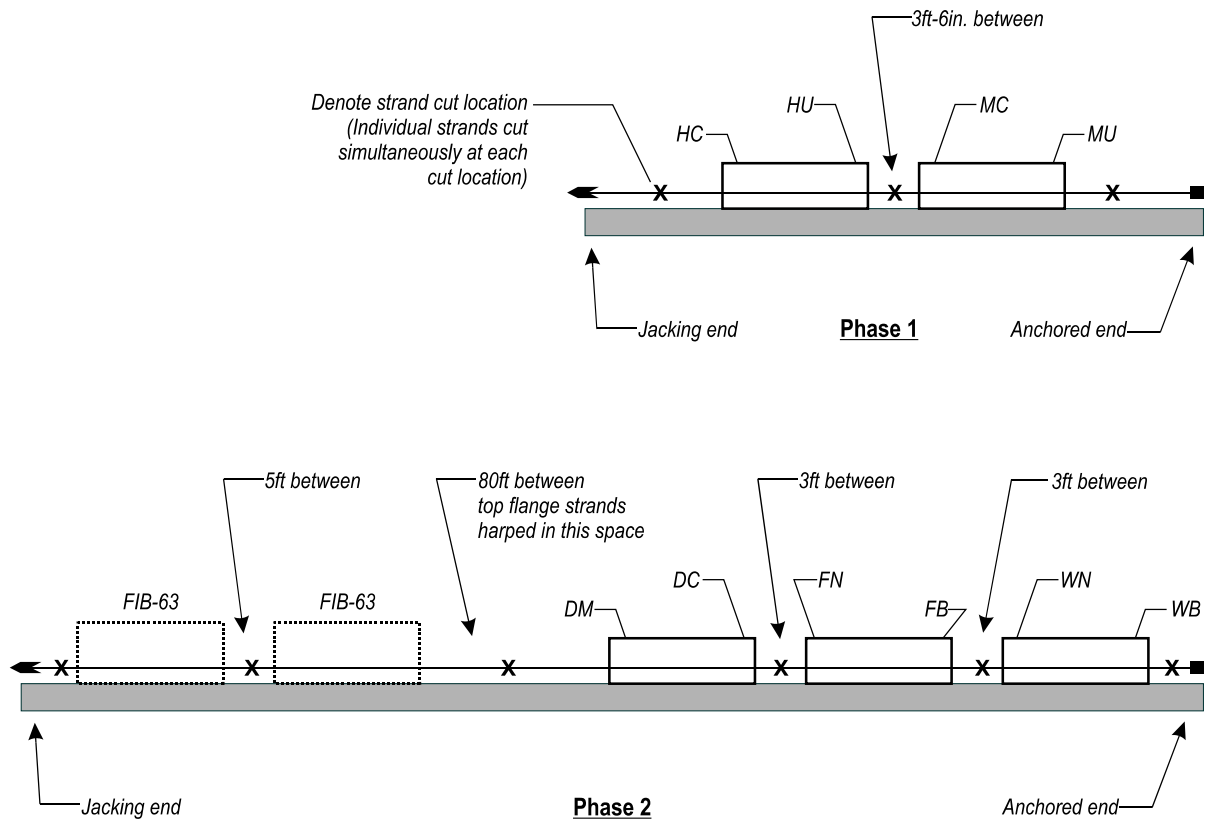


Figure 17–Girder orientation during fabrication

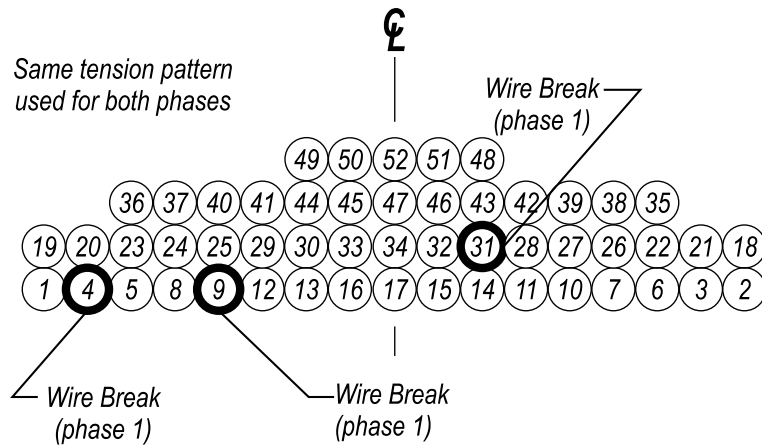


Figure 18–Tension pattern and wire break locations

Wire breaks occurred in three different strands during phase one (Figure 18). The wire breaks did not occur inside the test girders so the strand cross-section within the girders was not compromised. The jacking force of the strands with broken wires could not be checked by the elongation method, however the jacking force as determined by pressure in the hydraulic line was still within the specified range. No wires broke during the second construction phase.

After tensioning, mild steel reinforcement was placed. Select bars were instrumented with strain gages prior to placement in the girders. Figure 19 through Figure 23 show the reinforcement in each specimen.

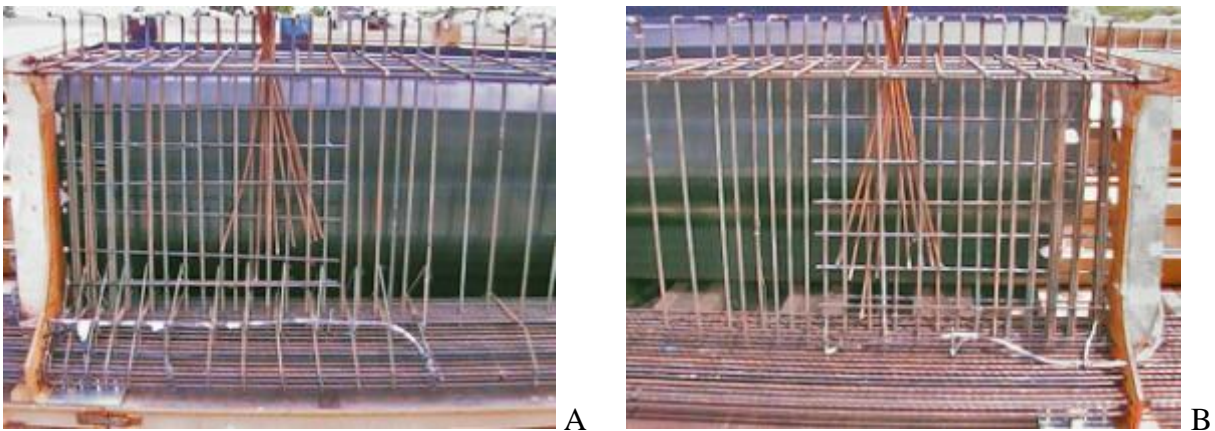
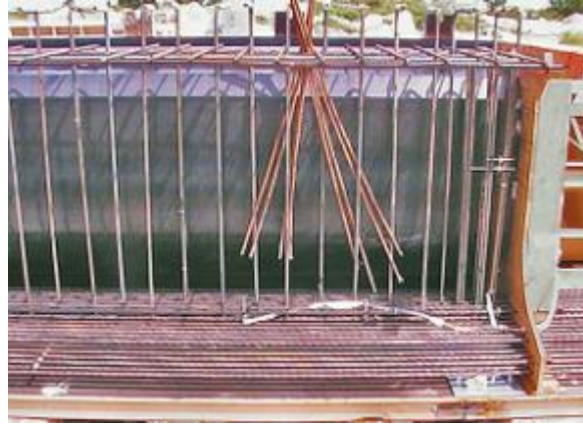


Figure 19–Girder H reinforcement A) Specimen HC and B) Specimen HU



A



B

Figure 20–Girder V reinforcement A) Specimen VC and B) Specimen VU



A



B

Figure 21–Girder W reinforcement A) Specimen WN and B) Specimen WB



A



B

Figure 22–Girder F reinforcement A) Specimen FN and B) Specimen FB

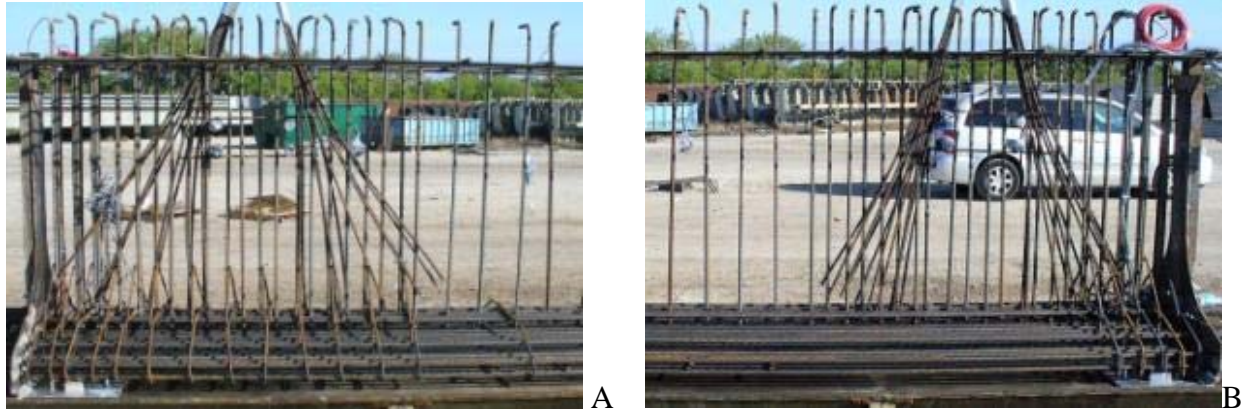


Figure 23–Girder D reinforcement A) Specimen DC and B) Specimen DM

Concrete was mixed at on-site batch plants. For phase one girders, concrete was placed in two lifts and was consolidated with internal and external vibrators after each lift (Figure 24). The internal vibrator was only used on the north side of the web to keep the vibrator away from internal strain gages which were primarily placed on the south side. A self-consolidating concrete mix was used for phase two (Figure 25) and vibration was not necessary. Test cylinders were taken by the fabricators and by the research team from each batch of concrete. The top surface of each girder was raked to intentionally roughen the surface (Figure 26). Girders were covered with heavy tarps during curing (Figure 27).



Figure 24–Concrete placement and internal consolidation phase 1



Figure 25–Concrete placement phase 2



Figure 26–Girder finished surface



Figure 27–Girders covered with tarps

Forms were removed six days after casting during phase one and three days after casting during phase two. Prestress was transferred to the girders the day after form removal. The time between form removal and prestress transfer was used to install bonded foil strain gages and to connect the data acquisition system.

Two 4x8 field cured cylinders were tested on the day of prestress transfer. The average compressive strength was 6880 psi for phase one and 7320 psi for phase two. Both values are above the specified release strength of 6500 psi.

Flame cutting was used in both phases to release the prestressing strands. Individual strands were cut simultaneously at points shown in Figure 17. Dormant strands in the top flange were cut first, followed by the bottom strands, which were cut from the outside-in and from bottom-to-top (Figure 28). This release pattern was selected because it is relatively easy to execute and because it is typical of precast girders in Florida. Strand cutting was stopped intermittently at multiple stages to obtain strain readings from the vibrating wire strain gages and to check the girders for cracking.

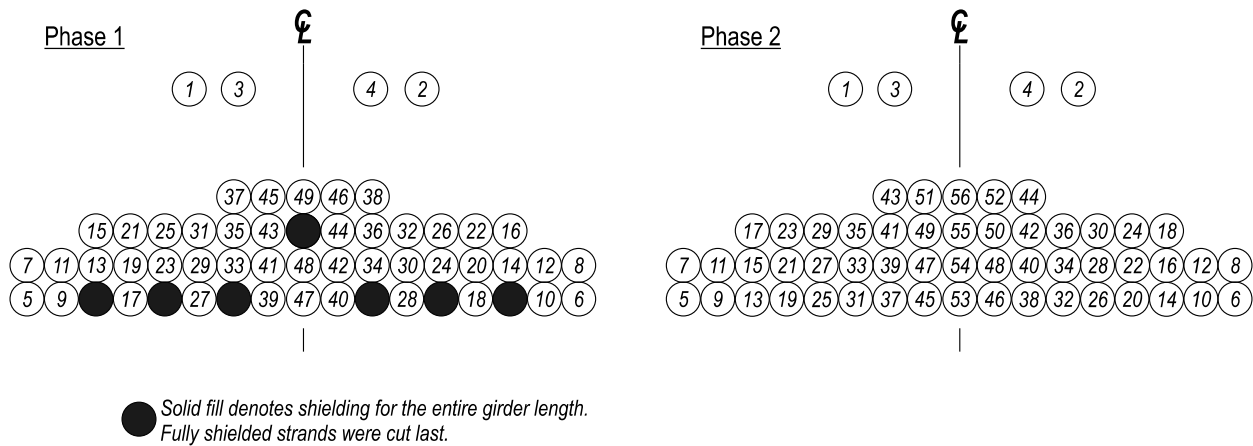


Figure 28—Strand release patterns

For safety reasons, the fully shielded strands in phase one were cut last and were released by a single cut between girders H and V. In some cases the fully shielded strands completely slipped out of the girders upon release. This was not an issue in phase two because each strand was at least partially bonded to each girder.

The girders in both phases shifted slightly (less than 1 in.) along the length of the stressing bed multiple times during prestress transfer. Movement events always corresponded to strand cuts. A more pronounced shift occurred during phase one as the final bonded strand was cut. Just after the final bonded strand was cut, girders H and V each slid approximately 2 ft. along the stressing bed. After sliding, the gap between girders was approximately 7 ft-6in.

To investigate changes in strain due to lifting (Figure 29), girders H and V were lifted by crane immediately after prestress transfer was completed. Girders were supported by the crane momentarily and then placed on dunnage on the stressing beds (Figure 30). Strain data were collected during lifting and as girders were placed on dunnage. After the data were collected, the girders were taken to a storage yard to await shipping. Girders were examined for cracking periodically while in they were held in storage at the prestress fabrication facilities.



Figure 29–Test girder lifted by crane



Figure 30–Girder resting on dunnage above stressing bed

Girders were trucked to the Marcus H. Ansley FDOT structures laboratory in Tallahassee, FL for deck construction and load testing. Strain gages were used to monitor strain

in girder H (phase one) during transport. Figure 31 shows girder H being transported. The black box on top of the girder in the picture housed the data acquisition system.



Figure 31–Girder H on truck prior to transit

After unloading of the test girders in Tallahassee, forms were constructed and reinforcement was placed for the concrete deck. Wood forms were affixed to the top flange of the girders using pipe clamps (Figure 32). Concrete was prepared by a local ready mix plant.

Cast-in-place decks were poured inside the lab. Concrete was transported from the mix truck to the girders via a bucket and crane (Figure 33). Concrete was consolidated using hand-held and form-mounted vibrators. After consolidation and screeding, the decks were troweled to a smooth finish. Cylinders of the concrete were taken for material testing.



A



B

Figure 32–Deck construction A) reinforcement and B) formwork

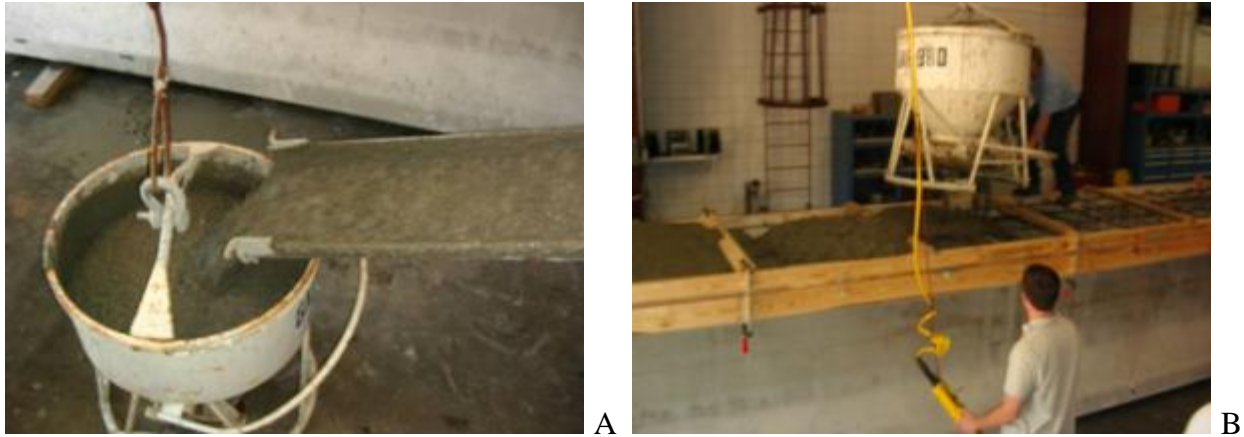


Figure 33–Concrete placement A) unloading and B) placement with bucket

D.2.4 Material Properties

Concrete, mild steel, and prestressing strand were detailed to match FDOT specifications. FDOT class VI concrete ($f'_c = 8500$ psi) was specified for the girders, and FDOT class II concrete ($f'_c = 4500$ psi) for the deck. Concrete compressive strength was tested using both 4x8 and 6x12 cylinders. Table 4 presents the tested concrete strengths.

Prestressing strands were Grade 270 low-relaxation, conforming to ASTM A416. Tested strand properties are shown in Table 5.

Bond capacity of phase one prestressing strands was tested in accordance with the proposed standard recommended by the North American Strand Producers (NASP 2009). This test method consists of pull-out tests of strand samples embedded in mortar. The method places tight requirements on flow and strength of the mortar. Flow must be between 100 and 124, and the strength at the time of the pull-out tests must be between 4500psi and 5000psi. The pull-out tests must be conducted between 22 and 26 hours after mixing and placing the grout. In spite of efforts to create a grout that would meet specifications, the grout used in the NASP tests failed to achieve the required strength. Table 6 lists the grout strengths. Low grout strength was the only deviation from the test method. Flow of the grout was 107.5. Table 7 lists results of the NASP tests. Because the grout strength was less than the value specified by the method, results from NASP tests are conservative when compared to tests that strictly meet the grout strength requirements.

Table 4–Tested concrete compressive strengths

Material	Cast date	Test date	Average strength (psi)	Sample size	Testing agent*	Cure Method
Phase 1 Girder Concrete	8-31-10	9-3-10	6400	(2) 4x8 cylinders	1	Wet
		9-8-10	6940	(2) 4x8 cylinders	1	Field
		9-8-10	6880	(3) 6x12 cylinders	2	Field
		9-29-10	9185	(3) 4x8 cylinders	1	Wet
		9-29-10	8235	(3) 6x12 cylinders	2	Field
		9-28-10	8790	(3) 4x8 cylinders	3	Wet
		5-10-11	10,950	(4) 6x12 cylinders	4	Wet
		5-17-11	11,610	(3) 4x7 cores girder FH	4	Core
		5-18-11	10,510	(3) 4x7 cores girder MH	4	Core
Phase 1 Deck Concrete	4-6-11	5-4-11	6615	(3) 6x12 cylinders	4	Field
		5-18-11	6950	(3) 6x12 cylinders	4	Field
Phase 2 Girder Concrete	2-17-12	2-20-12	7050	(2) 4x8 cylinders	1	Wet
		2-21-12	7330	(2) 4x8 cylinders	1	Field
		3-02-12	8790	(2) 4x8 cylinders	1	Wet
		3-16-12	8250	(3) 6x12 cylinders	2	Wet
		3-16-12	9210	(3) 4x8 cylinders	1	Wet
		5-30-12	10,520	(3) 6x12 cylinders	4	Field
Phase 2 Deck Concrete	5-7-12	5-30-12	6400	(9) 6x12 cylinders	4	Field
* 1. Tested by girder fabricator 2. Tested by FDOT State Materials Office 3. Tested by FDOT District Office 4. Tested by FDOT Structures Research Center						

Table 8 presents the tested material properties for mild steel reinforcement. All reinforcement was ASTM A615 grade 60, with the exception of the 4L-H headed bars placed in girder H. The supplier of the headed bars provided reinforcing bars that met ASTM A706. During phase one the #3 bars came from two separate suppliers; Table 8 presents values from both suppliers.

Table 5–Prestressing steel properties

Material	Stress at 1% elongation	Ultimate stress	Elongation at ultimate stress	Testing agent*
Phase 1 Prestressing Strand	259 ksi	285 ksi	5.47%	1
	271 ksi	284 ksi	4.59%	2
Phase 2 Prestressing Strand	261 ksi	287 ksi	5.38%	1
	259 ksi	285 ksi	NA	2
* 1. Strand supplier 2. FDOT State Materials Office (average of 4 samples)				

Table 6–Grout strength for NASP tests

Time of test (Time zero at mixing of grout)	Grout Strength* (average of (3) cubes)
22 hr	4210 psi
23 hr	4380 psi
24 hr	4030 psi
25 hr	4280 psi
26 hr	4340 psi
* Test method requires a strength between 4500 and 5000 psi	

Table 7–NASP Test Results.

Test Number	Load at 0.1 in. strand slip
1	22.08 kip
2	22.80 kip
3	24.09 kip
4	22.93 kip
5	22.98 kip
6	22.57 kip
Average	22.91 kip

Table 8–Steel reinforcement properties

Material	Yield Stress	Ultimate Stress	Elongation at Ultimate Stress	Testing agent*
Phase 1 #4 Headed rebar	68.8 ksi	90.8 ksi	19%	1
	64.6 ksi	89.6 ksi	18%	2
Phase 1 #3 confinement rebar	72.9 ksi	114.8 ksi	11%	1
	78.6 ksi	121.3 ksi	9%	1
	69.5 ksi	106.2 ksi	9%	2
Phase 1 #5 vertical rebar	66.1 ksi	100.7 ksi	17%	1
	68.6 ksi	105.7 ksi	9 %	2
Phase 2 #3 confinement rebar	73.6 ksi	113.3 ksi	12%	1
	85.2 ksi	115.4 ksi	12%	2
Phase 2 #4 confinement rebar	70.0 ksi	109.1 ksi	11%	1
	76.4 ksi	106.8 ksi	11%	2
Phase 2 #5 vertical rebar	64.5 ksi	103.2 ksi	11%	1
	63.2 ksi	103.5 ksi	13%	2
* 1. Rebar supplier 2. FDOT State Materials Office (average of 2 samples minimum)				

D.3 Test Setup and Procedures

D.3.1 Data Collection during Fabrication

Strain and crack data were collected during various stages of fabrication including: prestress transfer, lifting, storage, trucking, and deck construction. This section describes the procedures used to collect data during each stage of construction.

Data from strain gages were monitored and logged using a computerized data acquisition system powered by portable generators. Data from vibrating wire strain gages were monitored using an electronic readout box and logged manually. Crack data were collected through visual observation and using a microscope. Instrumentation details are presented in Chapter D.5.

Prestress transfer. Data were collected from each girder during prestress transfer. Prior to transfer girders were examined for cracks and null readings were taken from all gages. For girders H and V, the acquisition system and generator were secured to the top of the girders. For girders F, W, and D the acquisition system was placed in a van adjacent to the stressing bed. Strand cutting was paused at various times during prestress transfer to allow for visual evaluations and to take readings from the vibrating wire gages. Visual evaluations and vibrating wire readings were also conducted after prestress transfer was complete. Crack widths were measured by microscope at few locations on each specimen. Crack locations were marked with a crayon or marker and documented by photograph.

Lifting. Data were collected during lifting of girders H and V only. Immediately following the conclusion of prestress transfer, girder H and V were lifted by crane, held in place for approximately four minutes, and then placed onto dunnage. Strain data were collected throughout this process. The data acquisition systems and generators were strapped to the top of the girders to secure them during lifting. Vibrating wire gage readings were taken and visual crack evaluations were conducted during each step.

Storage. All girders received periodic visual evaluations while they were in storage at the precast facilities. Cracks were marked then documented by photograph. Crack widths were measured by microscope at few locations on each specimen. Dates of visual evaluations are listed in Table 3. Vibrating wire gage data were also collected while the girders were in storage.

Trucking. Internal and external strain gages were used to monitor concrete strains in girder H during trucking from the precast facility to the laboratory. The data acquisition system

and generator were strapped to the top of the girder to secure them during transport. Vibrating wire readings were taken before and after trucking. A visual evaluation was given to all girders upon arrival at the laboratory.

Deck construction. All girders were visually evaluated for cracks before and after construction of the cast-in-place decks. Vibrating wire gage readings were also taken before and after deck construction.

Material properties. Samples of reinforcement, strand, and concrete were taken during each construction phase and were tested to determine the associated material properties. Documentation regarding material properties was also obtained from the supplier of each material.

D.3.2 Load Test Setup and Procedures

Load tests were conducted at the FDOT M. H. Ansley Structures Research Center in Tallahassee, FL. Test dates are listed in Table 9. Load tests were conducted on both ends of each girder. After the first end was tested, the supports and load point were moved and the opposite end was tested.

Table 9–Load test chronology

Specimen	Service load test	Ultimate strength test
HC	May 11, 2011	May 11, 2011
HU	May 9, 2011	May 10, 2011
VC	May 13, 2011	May 13, 2011
VU	May 17, 2011	May 17, 2011
WN	May 23, 2012	May 23, 2012
WB	May 25, 2012	May 25, 2012
FN	May 29, 2012	May 29, 2012
FB	May 30, 2012	May 30, 2012
DC	May 31, 2012	May 31, 2012
DM	June 1, 2012	June 1, 2012

For purposes of this document each end will be referred to as a separate specimen. Each specimen was loaded at least twice. The first loading simulated the service load. The simulated service load was approximately 300kip and was determined from the prototype girder that was used as a basis for the test girder designs. Once the service load was reached, the load was held constant and cracks were identified and marked. After the cracks were marked the load was removed. The second loading determined the specimen’s ultimate strength. A load-displacement

plot was monitored real-time during the ultimate load test. Load was applied until it was apparent from the load-displacement plot that a peak load had been reached. Cracking was documented after the ultimate load test was complete.

Load and support geometry are shown in Figure 34. Each support consisted of a 10 in. x 32 in. reinforced bearing pad. Pads were “Type E” pads constructed according to FDOT design interim design standards (FDOT 2009d). The bearing pad at the near support was centered below the embedded steel bearing plate (Figure 35). Load was applied to the specimen using side-by-side hydraulic actuators. The load rate was controlled by adjusting a pump that pressurized the hydraulic system. The combined load rate varied from 0.1 kip/sec to 0.6 kip/sec, with the typical rate being approximately 0.4 kip/sec. Load was spread from the actuators to the girders through steel plates and a 10 in. x 30 in. reinforced neoprene bearing pad. A reaction frame was used to transmit load from the actuators to the strong floor (Figure 36).

Load, displacement, strand slip, and strain data were continuously collected during the service and ultimate load tests. Strain from the vibrating wires strain gages was collect at discrete points during load testing. Concrete samples were tested in conjunction with the load tests to determine compressive strength at the time of load testing.

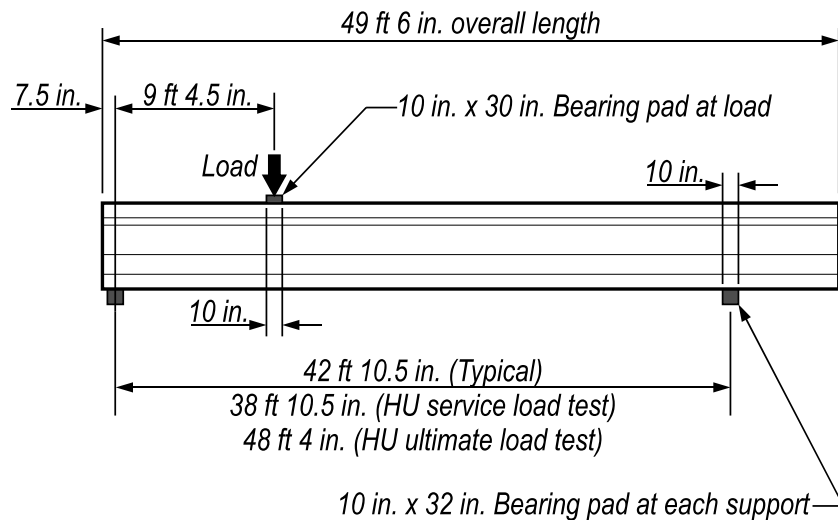


Figure 34—Test setup

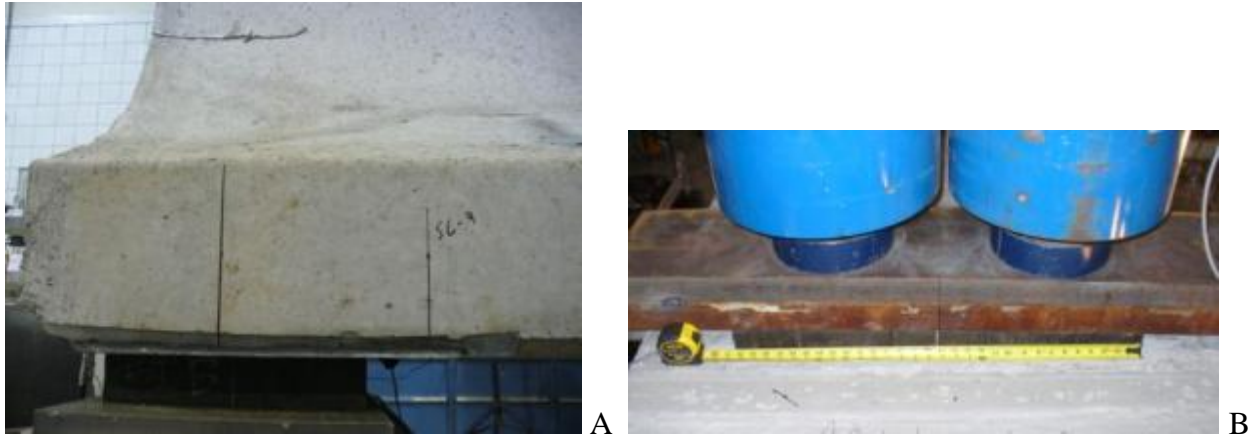


Figure 35–Test setup at A) bearing and B) load point



Figure 36–Test specimen and load frame A) top of girder and B) end of girder.

D.3.3 Coordinate System

A consistent coordinate system is used throughout this document. The system is used to define instrumentation locations and to identify the direction of strains, stress, and forces. The origin for the coordinate system is placed at the centerline of the cross-section, at the bottom of the girder, and at the girder end (Figure 37). The z-direction is vertical, the x-direction is

horizontal across the width of the girder, and the y-direction is horizontal along the span length. The support nearest the origin is denoted as the near support, and the opposite end is denoted as the far support.

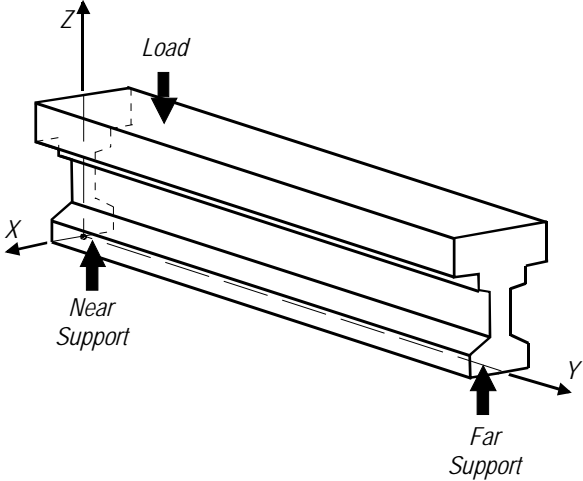


Figure 37–Coordinate system relative to load and supports

D.4 Instrumentation

Strain, displacement, force, and crack data were collected during fabrication and load testing. This chapter describes the instrumentation used to collect data and the labeling scheme that was used to identify the various instruments.

D.4.1 Types and Descriptions

Data were collected using load cells, LVDTs, linear potentiometers, variable resistance strain gages and vibrating wire strain gages. Table 10 lists the different types of instrumentation and the associated labels. With the exception of the vibrating wire strain gages, all data were logged electronically. Vibrating wire gage data were logged manually from an electronic readout box.

Table 10–Instrumentation types and labels

Label	Type	Placement
MS	Foil strain gage	Reinforcement and bearing plates
XS	Foil strain gage	Concrete surface
ES	Embedded strain gage	Concrete interior
V	Vibrating wire strain gage	Concrete interior
S	Foil strain gage	Concrete surface
R	Foil strain rosette	Concrete surface
L	Linear variable displacement transducer (LVDT)	Load point, supports, and strands
P	Linear potentiometer	Strands
--	Load Cell	Load point

MS strain gages were attached to select mild reinforcement and to bearing plates prior to placement in the test girders (Figure 38). MS gages had a gage length of 5mm and were used to monitor strain during prestress transfer and load testing.

XS strain gages (Figure 39) were attached to the surface of test girders immediately after formwork was removed. These gages were used to measure concrete strains during prestress transfer, lifting, and trucking. XS gages had a 60mm gage length.

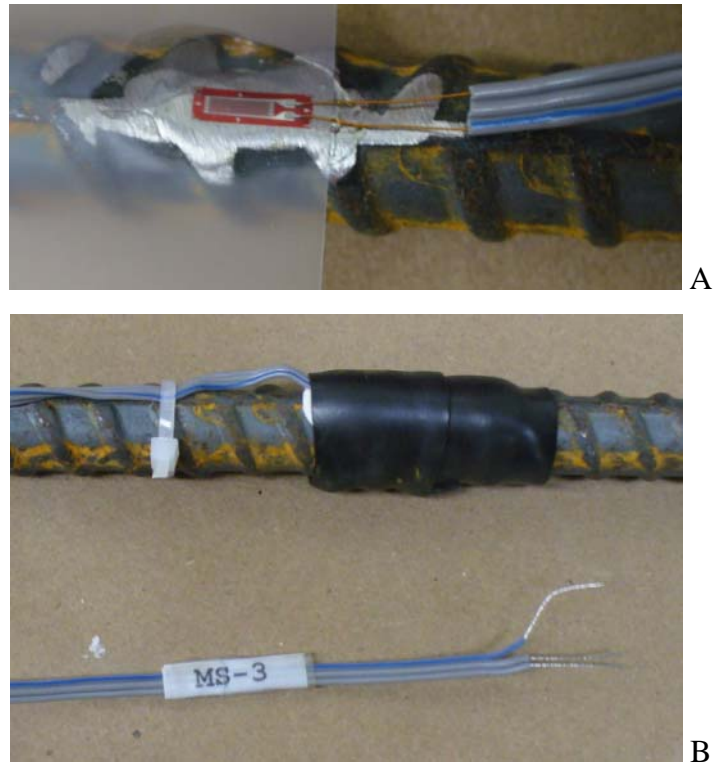


Figure 38–MS gage A) before protective covering and B) with protective cover and label



Figure 39–XS gage installation

ES gages were embedded in the test girders and were used to monitor concrete strain during all phases of fabrication and load testing. ES gages had a gage length of 60mm. Figure 40 shows ES gage installations prior to concrete placement.

V series gages were vibrating wire strain gages which were embedded in the test girders. These gages had a gage length of 152mm and were used to measure concrete strain during all phases of fabrication and load testing. Figure 40 shows a V series gage installation prior to

concrete placement. Because vibrating wire gages do not experience electronic drift over time, they were particularly useful in monitoring long term prestress losses.

Wire leads were collected into harnesses after all internal instrumentation (MS, ES, and V series gages) had been placed in the girders. Harnesses in girders F and V were routed to the ends of the girders and exited through holes in the wood bulkheads (Figure 42). Harnesses in girders F, W, and D were routed to the top of the girders. Wire harnesses were covered with a rubber sleeve and duct tape to protect the wires during concrete casting. A label was placed at the end of each wire lead for identification purposes.

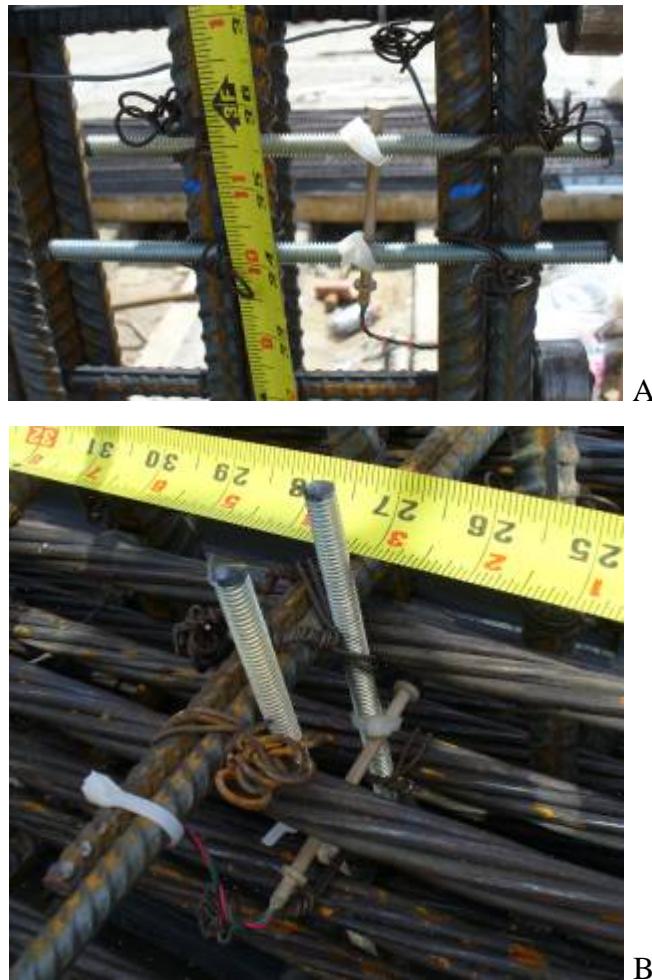


Figure 40–ES gage A) vertical and B) horizontal orientation



Figure 41–V gage (view from above)



Figure 42–Wire harness and plywood bulkhead

Prior to load testing S and R series strain gages were installed at discrete locations on girder surfaces (Figure 43). These gages had 60mm gages lengths. R series gages were strain rosettes built-up from three individual strain gages.

L series instruments were LVDTs used to monitor vertical displacement during load tests. Labels and locations of the LVDTs measuring vertical displacement are shown in Figure 44. LVDTs were mounted to fixed support structures as shown in Figure 45.

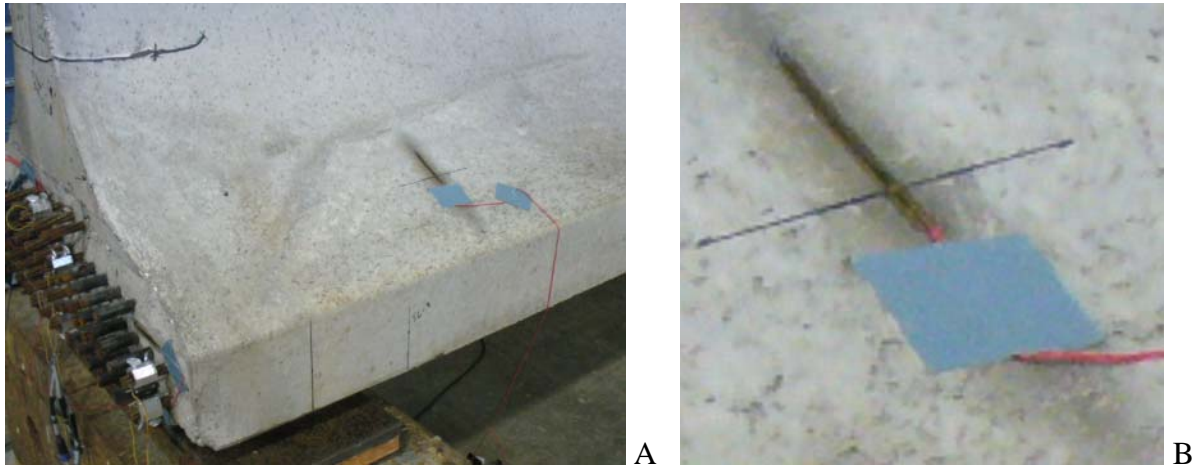


Figure 43—S gage A) on top of bottom flange and B) close-up

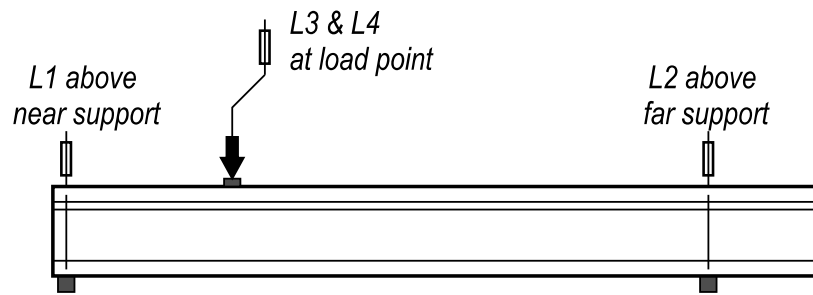


Figure 44—LVDT placement and labels



Figure 45–LVDT and support frame

LVDTs were also used to monitor strand slip for girders H and V. Monitored strands are shown in Figure 46. LVDTs for monitoring strand slip were mounted to a wooden bracket affixed to the girder end (Figure 47). This setup was unreliable because cracking in the concrete caused the LVDT frame to shift during load testing.

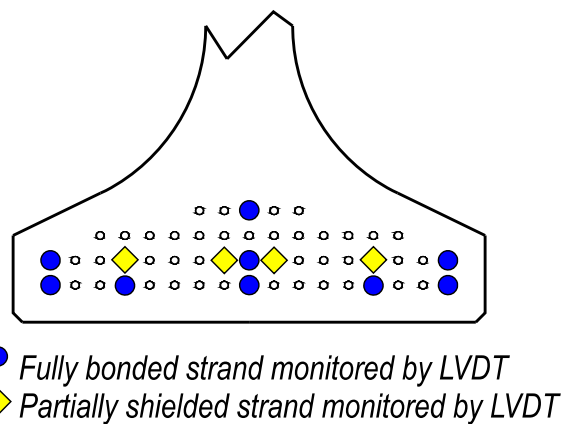


Figure 46–Girder H and V strands monitored by LVDT



Figure 47–Wood frame and LVDTs

Rather than LVDTs, P series variable resistant potentiometers were used to measure strand slip for girders F, W, and D. Instrumented strands are shown in Figure 48. P series instruments were mounted directly to the strands using custom-machined aluminum brackets and set-screws (Figure 49). This setup did not have the problems associated with the wooden frame used for girders H and V.

Load cells (Figure 50) were used to measure the force applied during the load tests. A hydraulic system was used to apply the loads, and a pressure transducer was used to measure pressure in the hydraulic line during testing. Both force and pressure data were logged electronically, along with displacement and strain data from the other instruments.

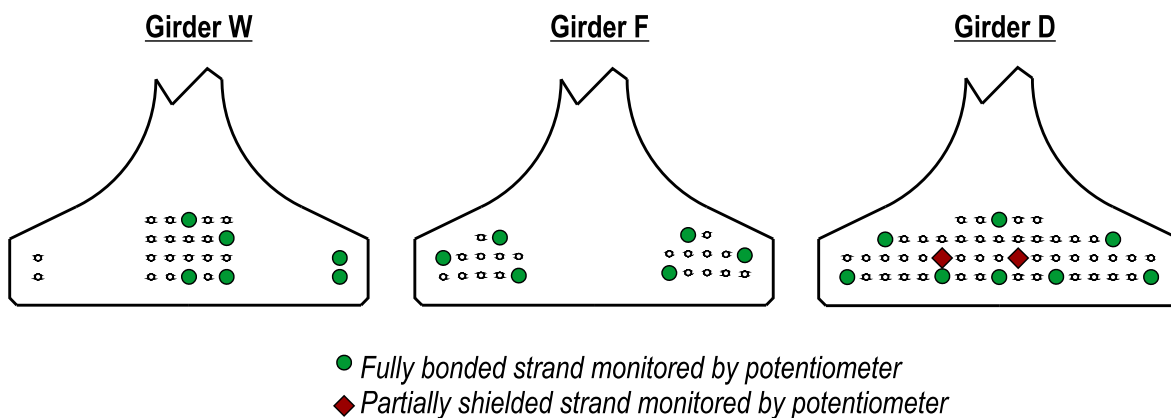


Figure 48–Girder W, F, and D strands monitored by potentiometer

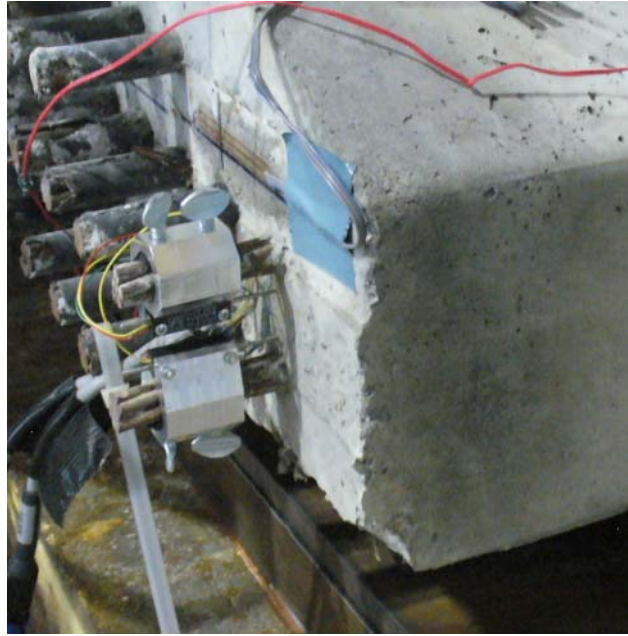


Figure 49–Aluminum brackets and linear potentiometers on strands



Figure 50–Load cells below hydraulic actuators

D.4.2 Strain Gage Coordinates

Figures in this document that present strain data typically also contain information regarding the location of gage(s) from which the data were collected. Information in the figures gives a general idea of the gage orientation and position but doesn't always give specific coordinates. Table 11 through Table 20 give specific coordinates of gages referenced in this document. Coordinates are based on the system defined in Figure 37.

Table 11–Specimen HC strain gage coordinates

Instrument	X (in.)	Y (in.)	Z (in.)	Orientation	Reference(s)
XS3	0	0	12	X	Figure 52, Figure 53, and Table 22
XS5	-19	18	6	Y	Figure 66 and Figure 67
XS6	-19	30	6	Y	Figure 66 and Figure 67
XS7	-19	36	6	Y	Figure 66 and Figure 67
XS8	-19	42	6	Y	Figure 66 and Figure 67
XS9	-19	48	6	Y	Figure 66 and Figure 67
XS10	-19	54	6	Y	Figure 66 and Figure 67
XS11	19	18	6	Y	Figure 66 and Figure 67
XS12	19	54	6	Y	Figure 66 and Figure 67
ES2	-3	27	8	X	Figure 52, and Table 22
ES3	-3	47	8	X	Figure 52, and Table 22
MS1	-0.5	2	0.5	X	Figure 110
MS2	0	13	0.5	X	Figure 110
MS10	0	2	10	X	Figure 110
MS14	0	2	2	X	Figure 110
MS15	-1	2	16	X-Z	Figure 110
MS20	0	8	10	X	Figure 110
MS24	-13	8	2	X	Figure 110
MS25	-1	9	16	X-Z	Figure 110
MS30	0	22	10	X	Figure 110
MS34	0	22	2	X	Figure 110
MS35	-1	22	16	X-Z	Figure 110
MS40	0	66	10	X	Figure 110
MS44	0	66	2	X	Figure 110
MS45	-1	67	16	X-Z	Figure 110
MS51	0	2	0	X	Figure 110
MS52	0	13	0	X	Figure 110
V1	-1	292	7.5	X	Table 30

Table 12–Specimen HU strain gage coordinates

Instrument	X (in.)	Y (in.)	Z (in.)	Orientation	Reference(s)
XS3	0	0	12	X	Figure 53, and Table 22
XS5	-19	18	6	Y	Figure 66 and Figure 67
XS6	-19	30	6	Y	Figure 66 and Figure 67
XS7	-19	36	6	Y	Figure 66 and Figure 67
XS8	-19	42	6	Y	Figure 66 and Figure 67
XS9	-19	48	6	Y	Figure 66 and Figure 67
XS10	-19	54	6	Y	Figure 66 and Figure 67
XS11	19	18	6	Y	Figure 66 and Figure 67
XS12	19	54	6	Y	Figure 66 and Figure 67
ES2	3	27	8	X	Figure 52, and Table 22
ES3	3	48	8	X	Figure 52, and Table 22
MS1	0	2	0.5	X	Figure 110
MS2	0	13	0.5	X	Figure 110
MS51	0	2	0	X	Figure 110
MS52	0	13	0	X	Figure 110

Table 13–Specimen VC strain gage coordinates

Instrument	X (in.)	Y (in.)	Z (in.)	Orientation	Reference(s)
XS3	0	0	12	X	Figure 53, and Table 22
XS5	-19	18	6	Y	Figure 66 and Figure 67
XS6	-19	30	6	Y	Figure 66 and Figure 67
XS7	-19	36	6	Y	Figure 66 and Figure 67
XS8	-19	42	6	Y	Figure 66 and Figure 67
XS9	-19	48	6	Y	Figure 66 and Figure 67
XS10	-19	54	6	Y	Figure 66 and Figure 67
XS11	19	18	6	Y	Figure 66 and Figure 67
XS12	19	54	6	Y	Figure 66 and Figure 67
ES2	-3	29	8	X	Figure 52, and Table 22
ES3	-3	48	8	X	Figure 52, and Table 22
MS1	-0.5	2	0.5	X	Figure 110
MS2	0	13	0.5	X	Figure 110
MS10	0	2	10	X	Figure 110
MS14	0	2	2	X	Figure 110
MS15	-1	3	16	X-Z	Figure 110
MS20	0	8	10	X	Figure 110
MS24	-13	8	2	X	Figure 110
MS25	-1	8	16	X-Z	Figure 110
MS30	0	22	10	X	Figure 110
MS34	0	22	2	X	Figure 110
MS35	-1	22	16	X-Z	Figure 110
MS40	0	64	10	X	Figure 110
MS44	0	64	2	X	Figure 110
MS45	-1	64	16	X-Z	Figure 110
MS51	0	2	0	X	Figure 110
MS52	0	13	0	X	Figure 110
V1	-1	297	7.5	X	Table 30

Table 14–Specimen VU strain gage coordinates

Instrument	X (in.)	Y (in.)	Z (in.)	Orientation	Reference(s)
XS3	0	0	12	X	Figure 53, and Table 22
XS5	-19	18	6	Y	Figure 66 and Figure 67
XS6	-19	30	6	Y	Figure 66 and Figure 67
XS7	-19	36	6	Y	Figure 66 and Figure 67
XS8	-19	42	6	Y	Figure 66 and Figure 67
XS9	-19	48	6	Y	Figure 66 and Figure 67
XS10	-19	54	6	Y	Figure 66 and Figure 67
XS11	19	30	6	Y	Figure 66 and Figure 67
XS12	19	54	6	Y	Figure 66 and Figure 67
ES2	3	27	8	X	Figure 52, and Table 22
ES3	3	48	8	X	Figure 52, and Table 22
MS1	0	2	0.5	X	Figure 110
MS2	0	13	0.5	X	Figure 110
MS51	0	2	0	X	Figure 110
MS52	0	13	0	X	Figure 110

Table 15–Specimen WN strain gage coordinates

Instrument	X (in.)	Y (in.)	Z (in.)	Orientation	Reference(s)
MS10	-1	2.5	17.5	XZ	Figure 61 and Figure 106
MS11	0	2.5	10	X	Figure 61 and Figure 106
MS12	0	2	2	X	Figure 61 and Figure 106
MS20	-1	9	18	XZ	Figure 61 and Figure 106
MS21	0	9	10	X	Figure 61 and Figure 106
MS22	0	10	2	X	Figure 61 and Figure 106
MS30	-1	16.5	17.5	XZ	Figure 61 and Figure 106
MS31	0	16.5	10	X	Figure 61 and Figure 106
MS33	0	16	2	X	Figure 61 and Figure 106Figure 106
V1	0	276	10	X	Table 30

Table 16–Specimen WB strain gage coordinates

Instrument	X (in.)	Y (in.)	Z (in.)	Orientation	Reference(s)
MS3	0	0.5	0.5	X	Figure 59 and Figure 106
MS4	0	7.5	0.5	X	Figure 59 and Figure 106
MS5	0	13.5	0.5	X	Figure 59 and Figure 106
MS10	1.5	2.5	18	XZ	Figure 60 and Figure 106
MS11	0	2	10.5	X	Figure 60 and Figure 106
MS12	0	2	2	X	Figure 60 and Figure 106
MS20	1.5	9	18	XZ	Figure 60 and Figure 106
MS21	0	9	10.5	X	Figure 60 and Figure 106
MS22	0	8	2	X	Figure 60 and Figure 106
MS30	1.5	16	18	XZ	Figure 60 and Figure 106
MS31	0	15.5	10.5	X	Figure 60 and Figure 106
MS33	0	15	2	X	Figure 60 and Figure 106

Table 17–Specimen FN strain gage coordinates

Instrument	X (in.)	Y (in.)	Z (in.)	Orientation	Reference(s)
XS1	19	14.5	6.25	Y	Figure 68
XS2	19	23	5.25	Y	Figure 68
XS3	19	30	6.25	Y	Figure 68
XS4	19	121	6.5	Y	Figure 68
XS5	19	128	6	Y	Figure 68
XS6	19	135.5	6.5	Y	Figure 68
XS7	19	142.5	6.5	Y	Figure 68
MS10	-1	2	18	XZ	Figure 63 and Figure 106
MS11	0	2	10.5	X	Figure 63 and Figure 106
MS12	0	3	2	X	Figure 63 and Figure 106
MS20	-1	9	18.5	XZ	Figure 63 and Figure 106
MS21	0	9	10.5	X	Figure 63 and Figure 106
MS22	0	7	2	X	Figure 63 and Figure 106
MS30	-1	16	18.5	XZ	Figure 63 and Figure 106
MS31	0	15.5	10.5	X	Figure 63 and Figure 106
MS33	0	14.5	2	X	Figure 63 and Figure 106
V1	0	276	10.25	X	Table 29

Table 18–Specimen FB strain gage coordinates

Instrument	X (in.)	Y (in.)	Z (in.)	Orientation	Reference(s)
XS1	19	14	5.5	Y	Figure 68
XS2	19	22	6	Y	Figure 68
XS3	19	29.5	5.25	Y	Figure 68
XS4	19	119	6	Y	Figure 68
XS5	19	127	6.25	Y	Figure 68
XS6	19	135	6	Y	Figure 68
XS7	19	142	6.25	Y	Figure 68
MS3	0	0.5	0.5	X	Figure 58
MS4	0	7	0.5	X	Figure 58
MS5	0	13.5	0.5	X	Figure 58
MS10	0.5	2	17	XZ	Figure 62 and Figure 106
MS11	0	2	10	X	Figure 62 and Figure 106
MS12	0	1.5	2	X	Figure 62 and Figure 106
MS20	1	9	18	XZ	Figure 62 and Figure 106
MS21	0	8.5	10	X	Figure 62 and Figure 106
MS22	0	7.5	2	X	Figure 62 and Figure 106
MS30	0.5	16.5	17.5	XZ	Figure 62 and Figure 106
MS31	0	16	10	X	Figure 62 and Figure 106
MS33	0	14	2	X	Figure 62 and Figure 106

Table 19–Specimen DC strain gage coordinates

Instrument	X (in.)	Y (in.)	Z (in.)	Orientation	Reference(s)
MS3	0	3	0.5	X	Figure 106
MS4	0	9	0.5	X	Figure 106
MS5	0	15	0.5	X	Figure 106
MS10	1	2	18	XZ	Figure 106
MS11	0	1.5	10.5	X	Figure 106
MS12	0	2	3	X	Figure 106
MS20	1	9	18	XZ	Figure 106
MS21	0	9	10	X	Figure 106
MS22	0	8.5	3	X	Figure 106
MS30	2	16	18	XZ	Figure 106
MS31	0	16.5	10.5	X	Figure 106
MS33	0	16	3	X	Figure 106
V1	0	276	10	X	Table 30

Table 20–Specimen DM strain gage coordinates

Instrument	X (in.)	Y (in.)	Z (in.)	Orientation	Reference(s)
MS3	0	2.5	0.5	X	Figure 106
MS4	0	8	0.5	X	Figure 106
MS5	0	15	0.5	X	Figure 106
MS10	3	2.5	18	XZ	Figure 106
MS11	0	2.5	10	X	Figure 106
MS12	0	3	2.5	X	Figure 106
MS20	3	9.5	18	XZ	Figure 106
MS21	0	9	10.5	X	Figure 106
MS22	0	8	2.5	X	Figure 106
MS30	3	16	18.5	XZ	Figure 106
MS31	0	16	10	X	Figure 106
MS33	0	15	2.5	X	Figure 106

D.5 Results and Discussion: Fabrication

Strain and crack data were collected during multiple stages of fabrication including prestress transfer, lifting, storage, trucking, and deck placement. Data were collected to analyze the effects of fabrication events on end region behavior. The effects of end region detailing, particularly confinement reinforcement, were also of interest. Strain data are presented and discussed first followed by crack data.

D.5.1 Strain Data

D.5.1.1 Concrete Strain

Concrete strain data were primarily collected from girders H and V. These girders had the same strand shielding pattern, instrumentation scheme, material properties, and timing of construction events. To facilitate review of the strain-time history, the strand flame-cutting sequence is divided into the stages shown in Table 21. Stages A through D listed in Table 21 are graphically depicted in Figure 51.

General trends in the strain-time history for specimen HC (Figure 52) are representative of the other specimens in girders H and V. Any differences between the specimens were in the strain magnitudes, which are discussed later.

Table 21–Girders H and V fabrication chronology

Stage	Event
A	strands 1-4 cut
B	strands 5-12 cut
C	strands 13-32 cut
D	strands 33-49 cut
E	All bonded strands cut, girder resting on bed
F	Girder held aloft by lifting loops
G	Girder resting on dunnage

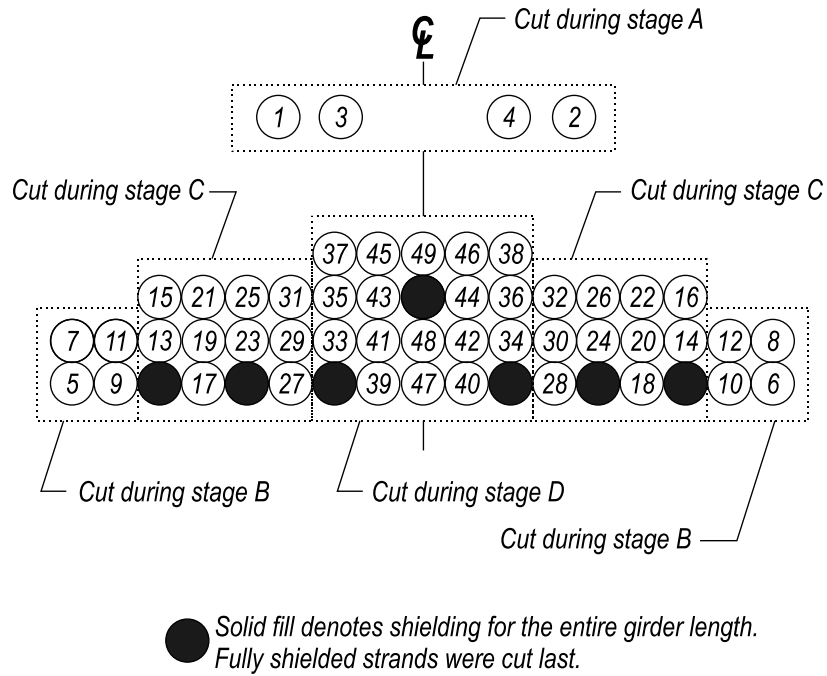


Figure 51–Girders H and V strand cutting stages

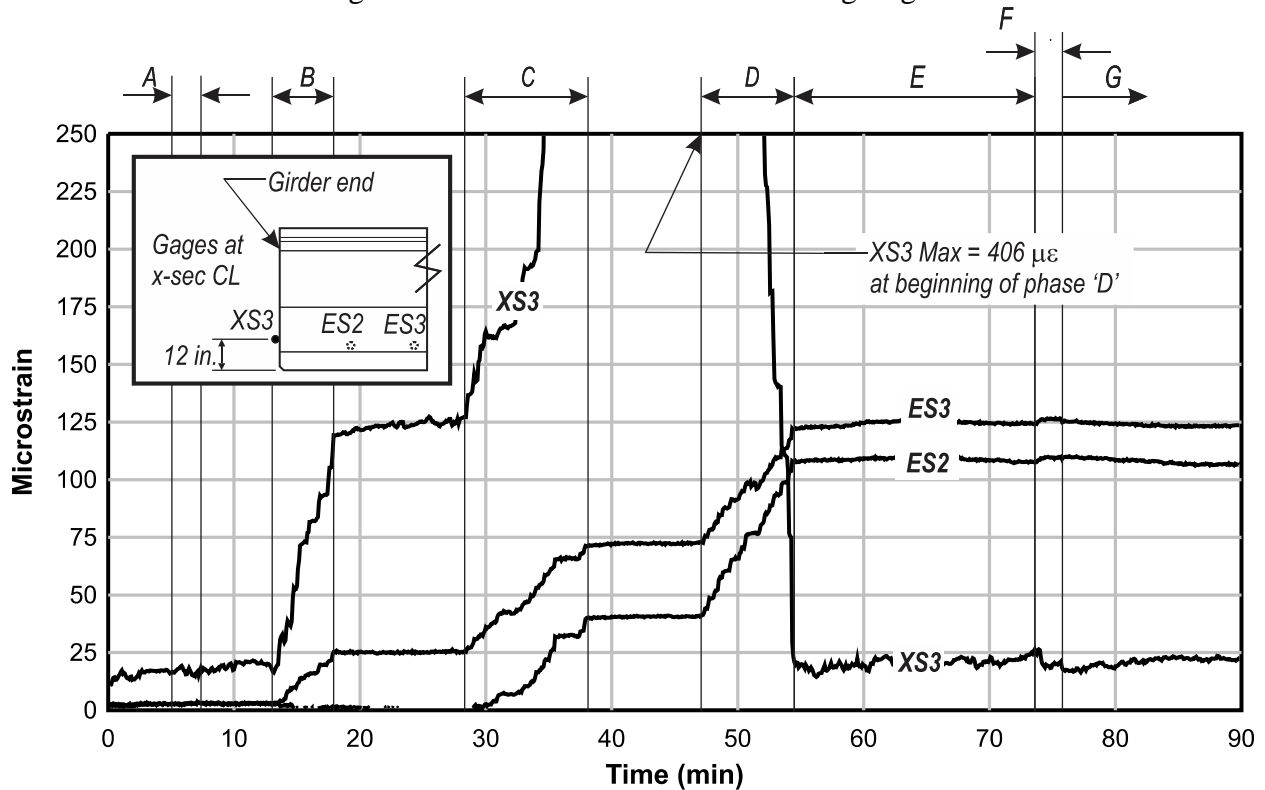


Figure 52–Transverse strain HC

Strands in the top flange were the first to be cut; this stage is denoted A in Figure 52. Data indicate that the transverse strain change was negligible when the top strands were cut. Cutting the bottom strands (stages B, C, and D) had significant impact on transverse tensile strain. The largest measured transverse tensile strain in specimen HC was 406 microstrain reported by gage XS3. This gage was located on the end of the girder, at the cross-section centerline, 3in. above the strands. The maximum strain occurred at the beginning of stage D after all strands in the outer flange had been cut and before any of the strands below the web had been cut. For this chapter, strands in the outer portion of the flange are referred to as “outer strands” and strands below the web are referred to as “inner strands”.

Transverse strain at gage XS3 decreased as inner strands were cut during stage D. The strain-time history from gage XS3 can be understood by considering the strand release pattern (Figure 51) and the resulting deformed shapes (Figure 53). As the outer strands were cut during stage B, the outside edges of the bottom flange deformed as shown in Figure 53. This deformed shape corresponded with the formation of tensile strains at the location of XS3. After the inner strands were cut, deformation of the bottom flange was more uniform and the tensile strain at XS3 was partially relieved. Once all of the strands were cut (stage E), the reported tensile strains at XS3 settled to approximately 25 microstrain.

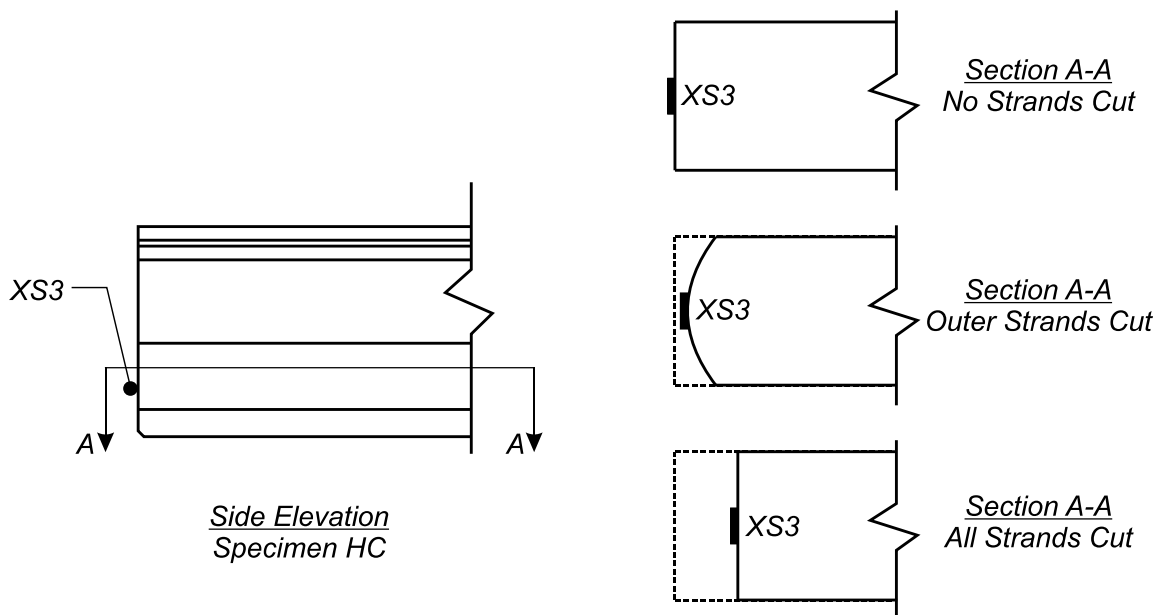


Figure 53–Flange displaced shapes for specimen HC

Concrete strain was monitored for all specimens in girders H and V using gages placed at the same location as XS3 on specimen HC. Results from these gages are summarized in Table 22. While the overall behavior of the other specimens in girder H and V were similar to that shown in Figure 52, the magnitudes of the reported strains differed.

Several observations can be made from the strain data in Table 22. First, although cracks were not visually observed during prestress transfer, the strain magnitudes suggest that cracks had likely formed in each specimen, with the possible exception of specimen VC. Expected rupture strain for the concrete used in the specimens is approximately 132 microstrain. This value of expected rupture strain was derived from empirical equations for concrete elastic and rupture moduli from ACI 318 (2011). Second, the average maximum tensile strain in the unconfined specimens (HU and VU) was 3.4 times greater than the average maximum tensile strain in the confined specimens (HC and VC). Cracks forming in the unconfined ends would not have been impeded by confinement reinforcement, resulting in greater maximum transverse strains than in the confined ends. Finally, the average concrete tensile strain during stage E (all strands cut) was 2.6 times greater in the specimens without confinement reinforcement. The presence of confinement reinforcement significantly reduced the concrete tensile strain at the end of specimens HC and VC relative to specimens HU and VU.

Internal concrete strain gages (ES2 and ES3 in Figure 52) reported increases in tensile strain as prestress force was transferred. In contrast to gage XS3, the tensile strain reported by these gages increased as the inner strands were cut during stage D. Based on this observation and the location of the internal gages, it is concluded that the bending behavior captured by gage XS3 only occurred at or near the end of specimen HC. ES gages in HU, VC, and VU confirmed similar behavior in those specimens. In each specimen strain magnitudes reported by ES gages (Table 22) suggest that concrete near the internal gages remained linear-elastic (i.e. no cracking) during prestress transfer.

Confinement reinforcement did not affect the magnitude of concrete strain at the ES gages. Similar strain magnitudes were reported by specimens with and without confinement reinforcement (Table 22). Gages ES2 and ES3 were placed approximately 2ft and 4ft from the specimen ends, respectively. It is concluded that confinement reinforcement only affected concrete strain at the end of the test specimens.

Stage F on Figure 52 denotes lifting of girder H. Figure 54 shows the supports conditions, loading, shear, and moment diagrams for the girders before, during, and after lifting. The change in support conditions had negligible effect on strain in the end region. None of the gages in the end region of girders H or V reported more than a 25 microstrain change during lifting and placement on dunnage.

Table 22–Tensile strain girders H and V

Gage	Strain in specimens with confinement reinforcement (microstrain)		Strain in specimens without confinement reinforcement (microstrain)	
	HC	VC	HU	VU
X3 maximum tensile strain	406	177	724	1258
X3 Stage E (all strands released)	25	15	60	45
ES2 Stage E	109	113	100	135
ES3 Stage E	125	88	111	105

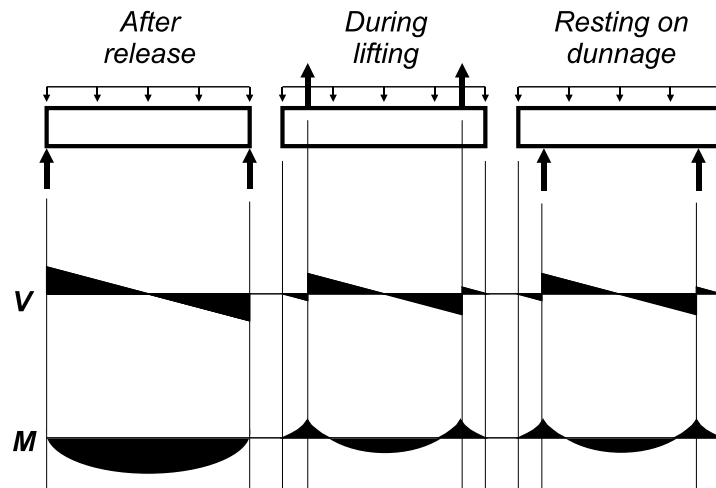


Figure 54–Shear and moment during release, lifting, storage (prestressing not shown)

D.5.1.2 Confinement Reinforcement and Bearing Plate Strain

Girders W and F were fabricated during phase 2 and had the same material properties, instrumentation scheme, and timing of construction events. Instrumentation was designed to

capture confinement reinforcement and bearing plate behavior. To facilitate discussion of data, strand cutting events were broken into the stages listed in Table 23. Strand cutting events listed in Table 23 are keyed to the strand cutting pattern shown in Figure 55.

The strand bond patterns in girders W and F (Figure 56) had significant influence on the observed strain behavior. Girder W had fully bonded strands placed primarily below the web and partially shielded strands placed in the outer portion of the flange. Girder F had fully bonded strands in the outer portion of the flange and partially shielded strands below the web.

Three strain gages were placed on the bearing plates in specimens FB and WB. Gages were oriented to monitor the transverse (x-x) strain during prestress transfer. Gage locations and strain data are shown in Figure 57. Gage MS3 in specimen FB malfunctioned during prestress transfer and data from this gage is not shown in figure.

Table 23–Girders W and F fabrication stages

Stage	Event
J	strands 1-4 cut
K	strands 5-30 cut
L	Pause
M	strands 30-56 cut
N	all strands cut

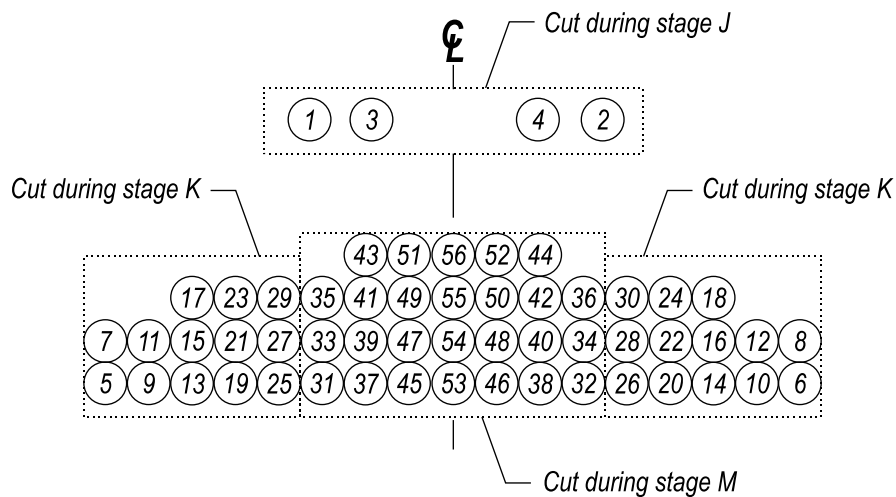


Figure 55–Girders W and F strand cutting stages

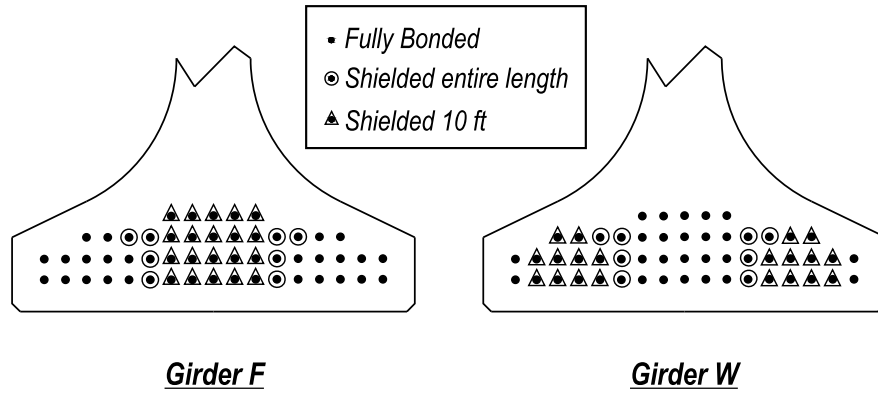


Figure 56–Girders W and F strand bond patterns

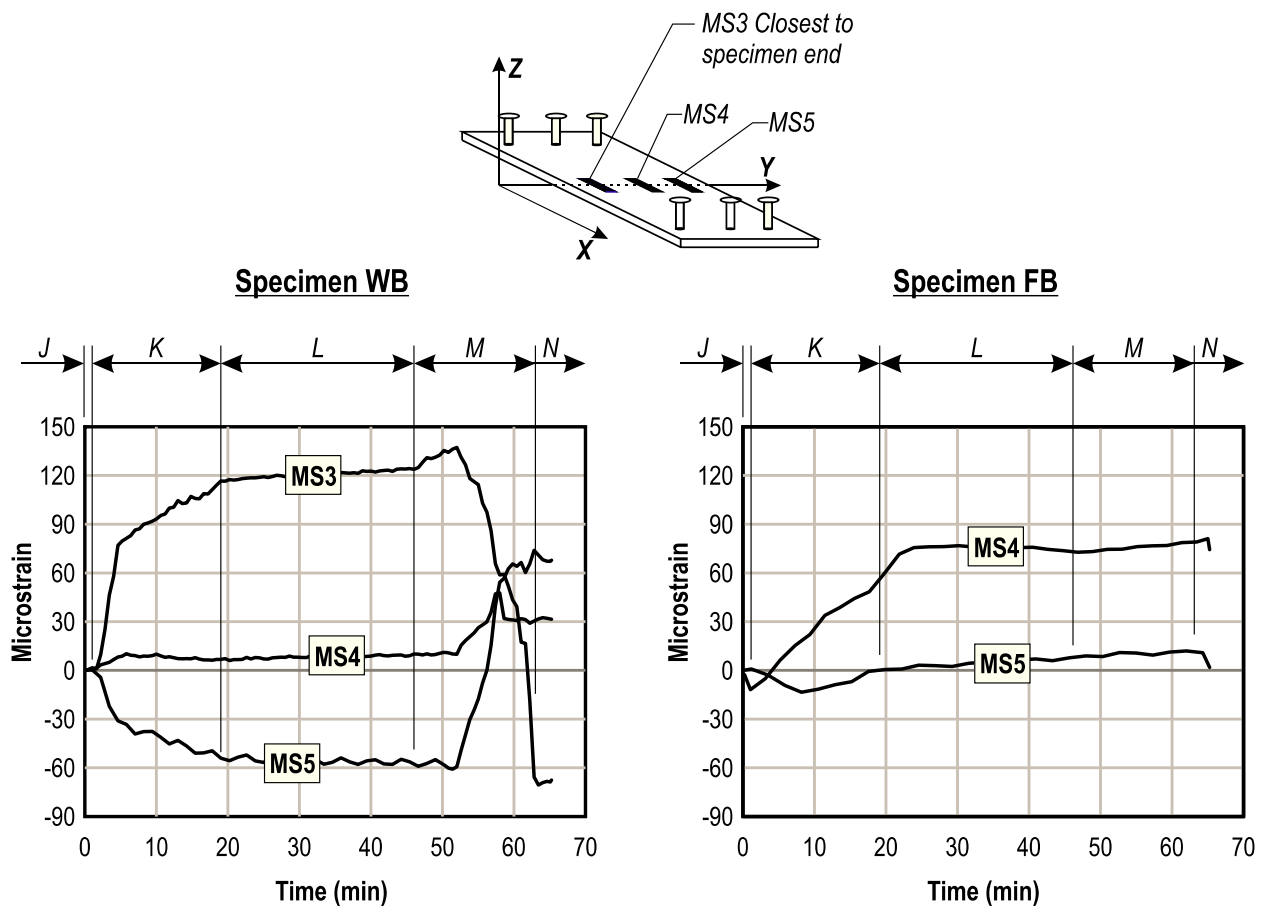


Figure 57–Bearing plate strain

Strain at MS4 in specimen FB grew in tension as the outer strands were cut during stage K. Outer strands were fully bonded in specimen FB and caused the flange and plate to bend as shown in Figure 58. Strain in the plate was fairly constant after stage K. This is because no

strands were cut during stage L and because the strands released during stage M were shielded in specimen FB. The difference in strain between gages MS4 and MS5 indicates in-plane bending of the plate due to the eccentric prestress force.

Data from gages on the plate in specimen WB also indicate in-plane bending during and after strand cutting. The direction of plate bending in specimen WB changed when the strands below the web were cut during stage M. This behavior is attributed to the strand bond pattern in specimen WB, which placed a few fully bonded strands in the outer portion of the flange and many fully bonded strands below the web. This pattern is thought to have caused the deformations and internal forces shown schematically in Figure 59. Release of the outermost strands at the beginning of stage K led to tension in the bearing plate at MS3 and compression in the bearing plate at MS5. The strain sense in the bearing plate reversed after the inner strands were released during stage M. After all strands were released (stage N) the bearing plate was in compression at MS3 and tension at MS5. The net strain in the plate after all strands were cut was approximately 32 microstrain tension, as calculated from the average of gages MS3, MS4, and MS5. The average strain from these gages is also equal to the strain reported at MS4, indicating that the strain reported by MS4 is also a reasonable measure of net strain.

Transverse forces in the bearing plates were calculated by multiplying the net bearing plate strains by the plate cross-sectional area and elastic modulus. Assuming that the net bearing plate strain is equal to the strain at MS4 (center of plate) the net plate strain at stage N was 32 microstrain tension for specimen WB and 79 microstrain tension for specimen FB. Accordingly, net tensile stresses in the plates were 0.9ksi, and 2.3ksi, and the net tensile forces in the plates were 5.2kip and 13.6kip for specimens WB and FB, respectively.

Select confinement reinforcement assemblies were instrumented with strain gages to monitor confinement reinforcement strain during prestress transfer. A confinement assembly is defined as the reinforcing bars placed together at the same y-ordinate (Figure 60). One strain gage was placed on each of the three reinforcement layers in each assembly.

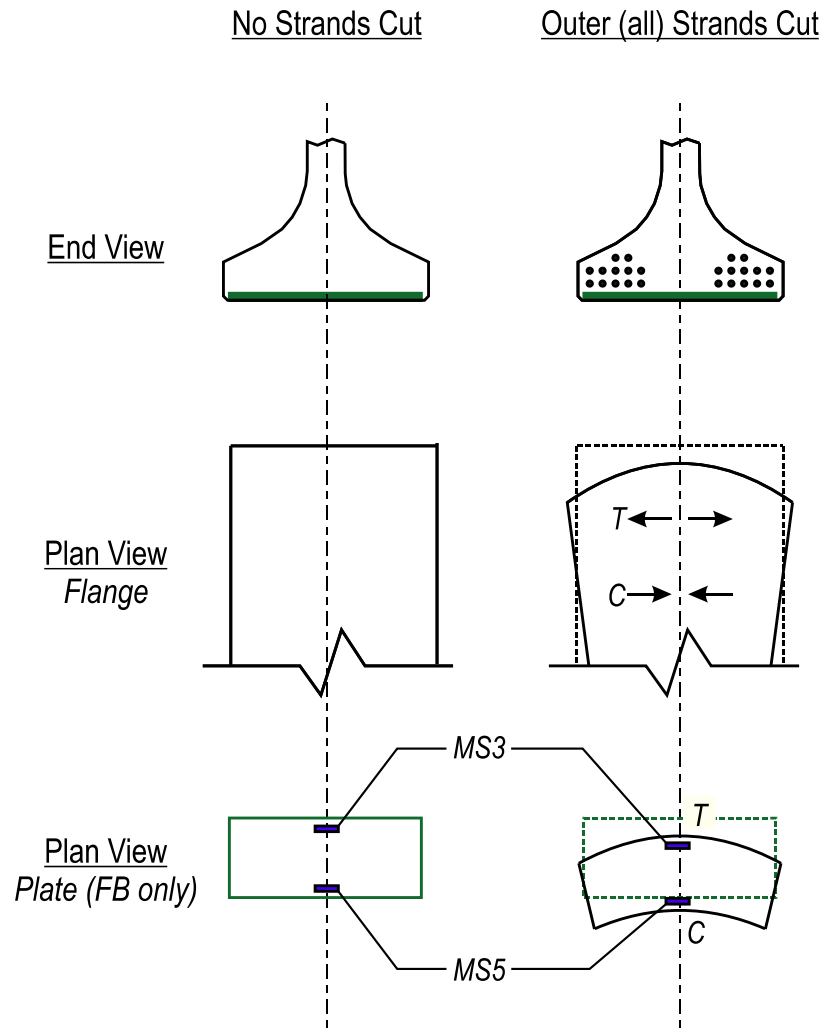


Figure 58–Flange displaced shapes specimens FN and FB

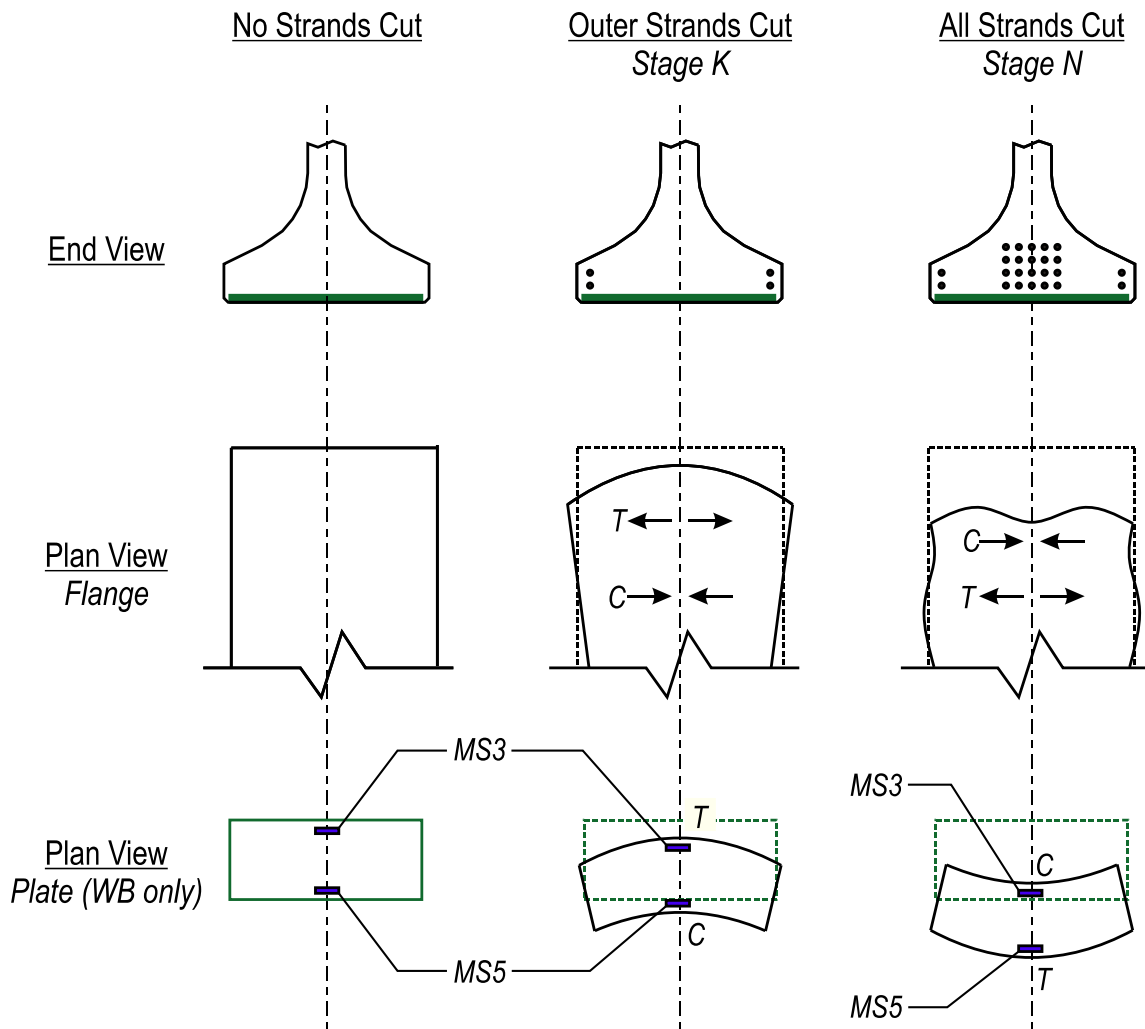


Figure 59–Displaced shapes specimen WB and WN

Figure 60 shows confinement reinforcement strain from specimen WB. Reinforcement nearest to the end of the girder ($y=2\text{in.}$) was initially in tension due to release of the outermost strands during stage K. The strain later became compressive as the inner strands were released during stage M. This strain behavior is similar to the bearing plate strain in WB and is also attributed to flange bending behavior described in Figure 59. Confinement reinforcement placed 9in. from the end had very little strain until the innermost strands were released at the end of stage M. General strain behavior from the confinement assembly at 9 in. is representative of the strain behavior reported by gages on the confinement assembly placed 15 in. from the end (not shown).

Specimen WN had the same strand bond pattern as WB. The only significant difference in strain data between WN (Figure 61) and WB was that the confinement reinforcement located 2in. from the end of specimen WN did not move all the way into compression during stage M. This difference may have been due to the absence of a bearing plate in specimen WN. Without a bearing plate there was less confinement in specimen WN and tensile strains were not relieved during stage M.

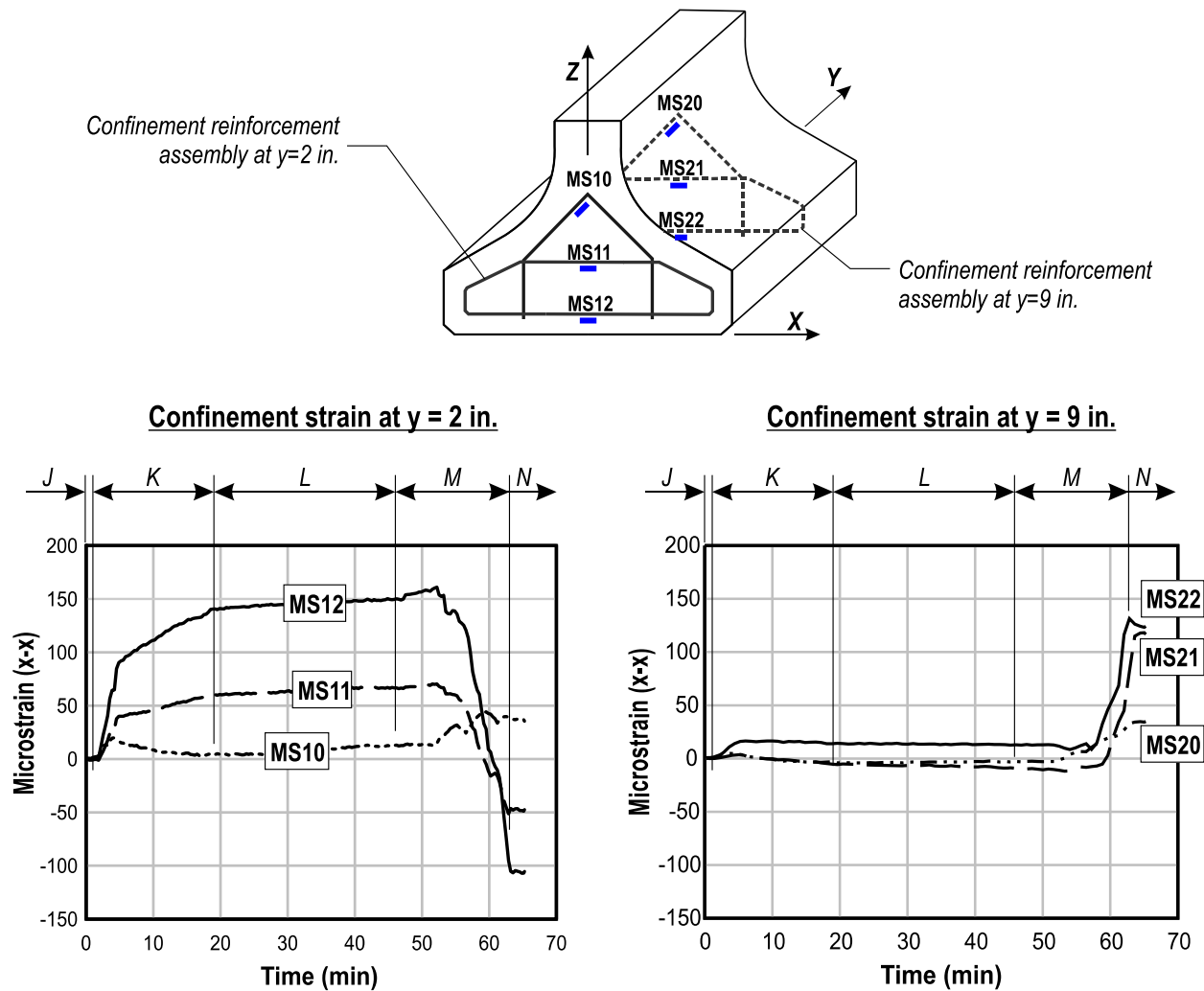


Figure 60–WB Confinement reinforcement strain at 2 in. and 9 in. from end of girder

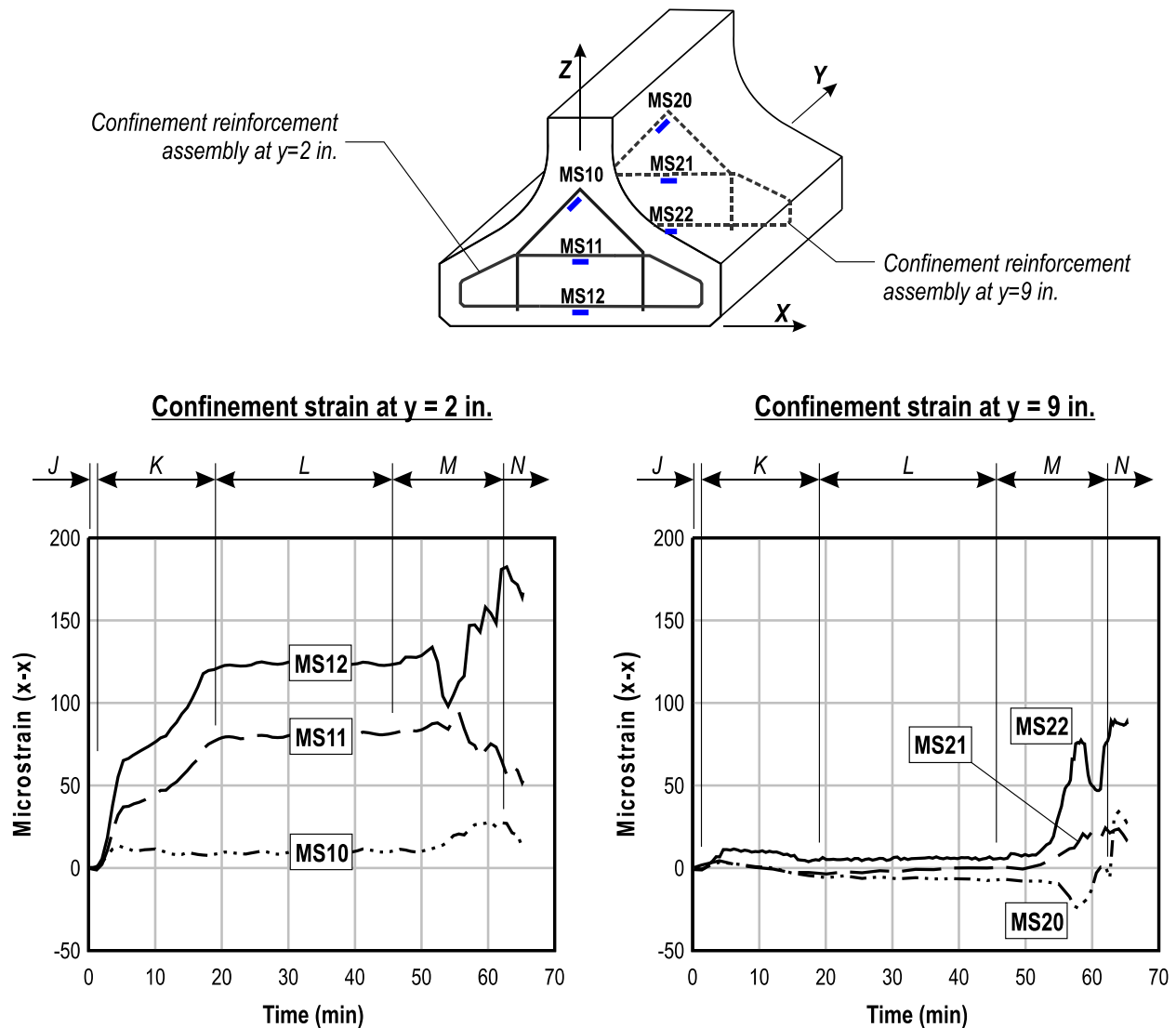


Figure 61–WN Confinement reinforcement strain at 2 in. and 9 in. from end of girder

Specimen FB had fully bonded strands in the outer flange, all of which were cut during stage K. As such, confinement strain in FB (Figure 62) increased during stage K. No fully bonded strands were cut after stage K and the strain did not change in the subsequent stages. Confinement reinforcement was in tension throughout and after the strand cutting process.

Specimen FN had the same strand bond pattern as FB with fully bonded strands located in the outer portion of the flange. Strain behavior in specimen FN (Figure 63) was similar to FB up until the inner strands were released during stage M. During stage M the strain increased rapidly in the bottom (MS12) and middle (MS11) layers of confinement reinforcement. The strain magnitude during stage M suggests that cracking occurred in the nearby concrete. This

result is puzzling because inner strands in specimen FB were shielded for 10ft from the specimen end. It appears that the shielded strands may have induced stresses in the concrete as they expanded after being cut. The thin plastic used to shield the strands may have been insufficient to absorb the strand expansion and prevent normal stresses at the strand-concrete interface. These stresses could have caused the strain changes at gages MS12 and MS11 that occurred during stage M.

Strain data at the end of stage N (all strands cut) is listed in Table 24 for each specimen. Several observations can be made by averaging the stage N strain data (Figure 64). First, strain was greatest in the bottom layer of reinforcement for each test specimen. On average strain in the bottom layer was 1.4 times greater than the middle layer strain and almost 3 times greater than the top layer strain. Second, the largest confinement reinforcement strain occurred in specimens FN and FB in the confinement assemblies 2 in. from the member ends.

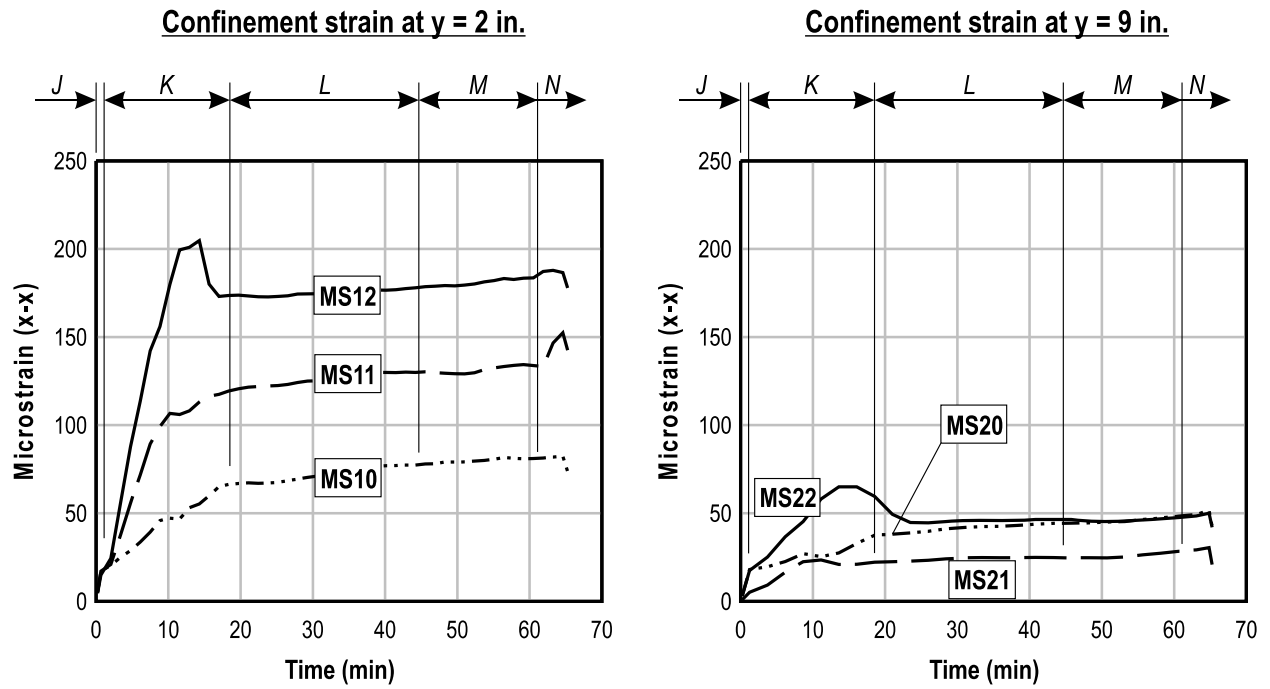
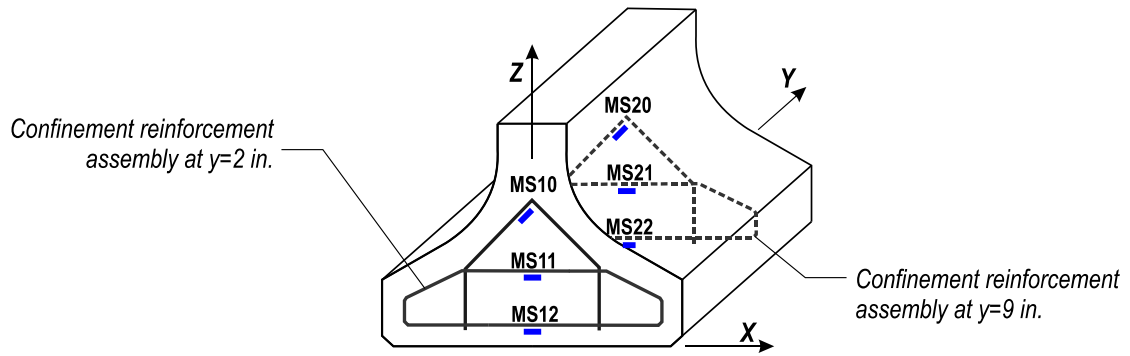


Figure 62–FB confinement reinforcement strain at 2 in. and 9 in. from end of girder

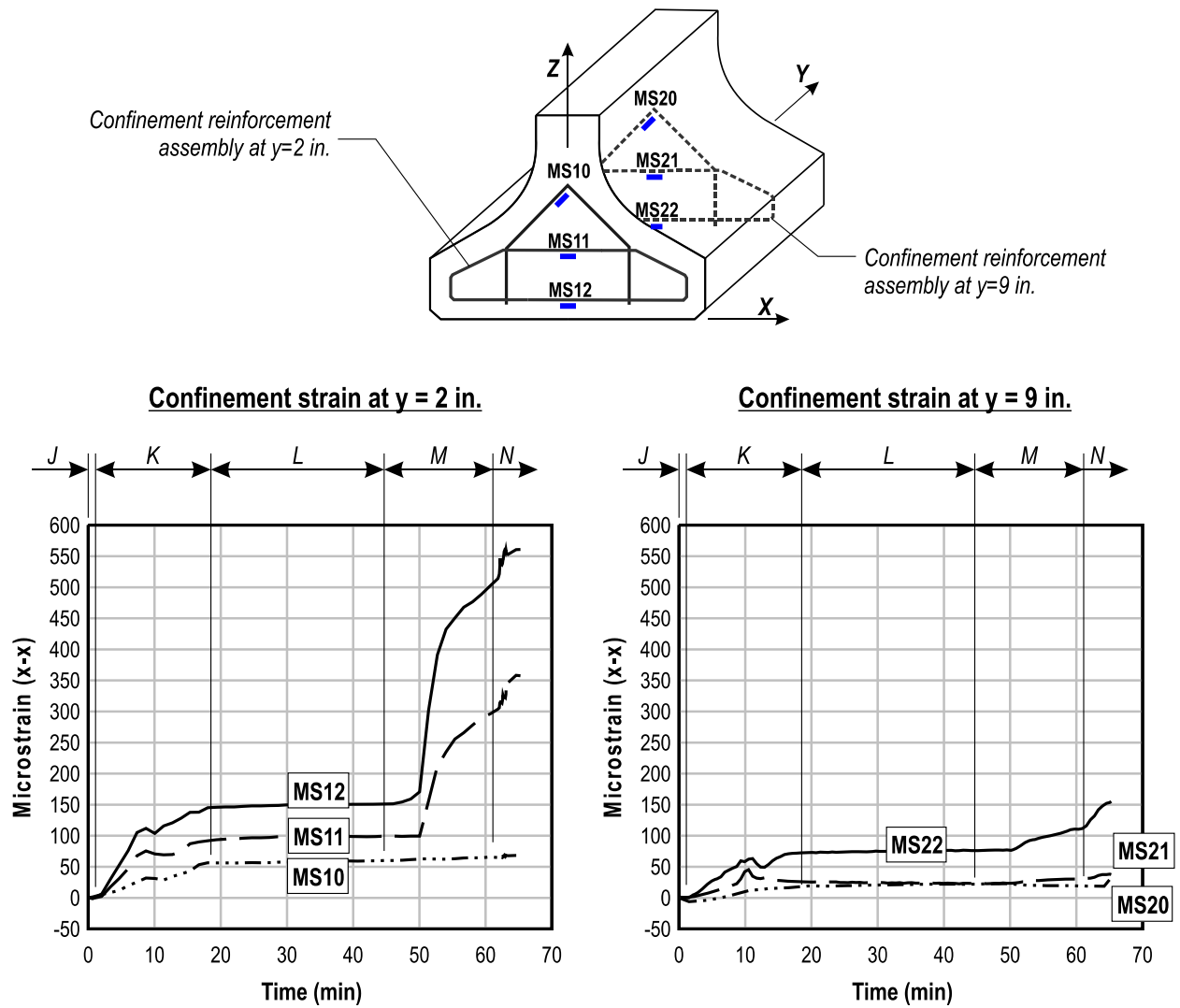


Figure 63–FN Confinement reinforcement strain at 2 in. and 9 in. for end of girder

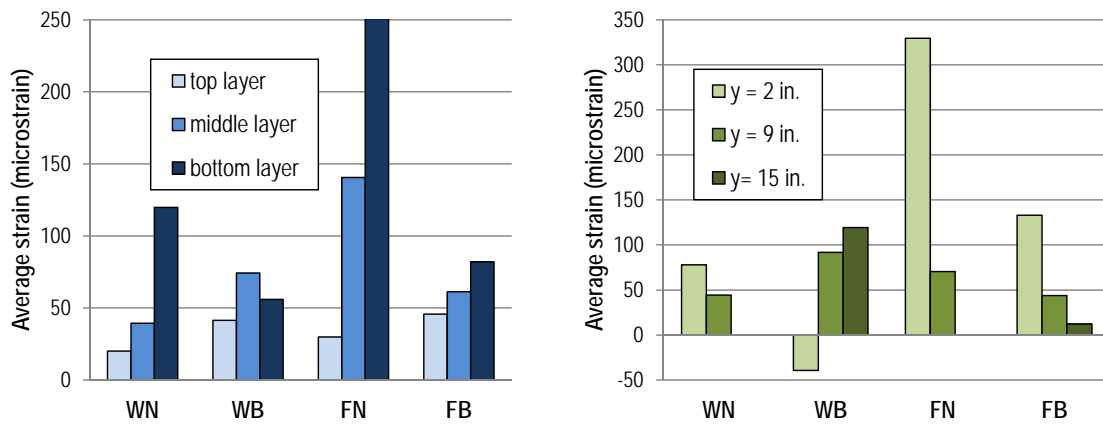


Figure 64–Confinement reinforcement average strain at prestress release

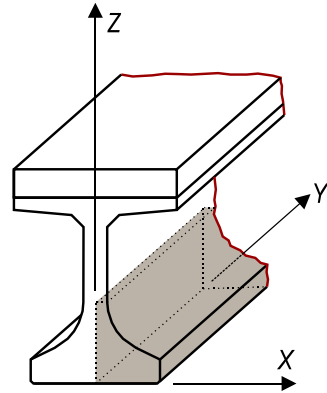
Table 24–Confinement reinforcement strain after prestress transfer

Specimen	Confinement reinforcement layer	Confinement strain (microstrain)		
		y = 2in.	y = 9in.	y = 15in.
WN	Top	7	19	not recorded
	Middle	47	28	not recorded
	Bottom	160	87	not recorded
WB	Top	37	34	53
	Middle	-49	117	155
	Bottom	-106	124	150
FN	Top	70	18	not recorded
	Middle	358	38	not recorded
	Bottom	560	155	not recorded
FB	Top	81	51	5
	Middle	134	30	20
	Bottom	184	50	12

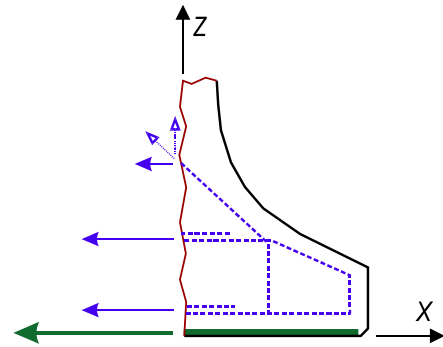
Confinement reinforcement strain at 2 in. from the end of FN and FB was almost 4 times greater on average than confinement strain at 9 in. This is due to the bending behavior of the FN and FB described in Figure 58. Third, confinement strain in specimen FN was typically larger than in FB. The average confinement strain was over 2 times larger in specimen FN than FB. The difference in strain magnitude is attributed to the bearing plate in FB which carried transverse forces thereby reducing the strain in the confinement reinforcement. Finally, the maximum confinement strains in FN and FB were larger than the maximum confinement strains in WN and WB. On average the maximum strain in the FX specimens was 2.6 times greater than the WX specimens

Strain data were used to estimate the total force in each confinement reinforcement assembly after all strands had been cut (stage N). Forces were calculated by multiplying strains from Table 24 by the reinforcement area and steel elastic modulus. Two of five assemblies in specimens WB and FB were not monitored with strain gages. Strains in these assemblies were determined using linear interpolation. In specimens WN and FN three of five confinement assemblies were not monitored. Strains in the unmonitored assemblies were interpolated using the available strain data, or were extrapolated using the available data as well as the relationships between assemblies in specimens WB and FB. Results for each specimen are shown in Figure

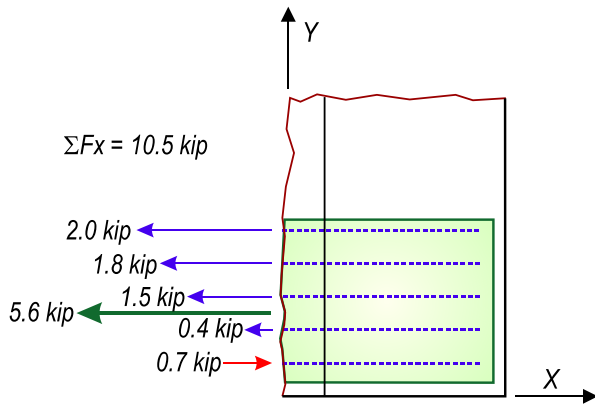
65 along with the estimated forces in the bearing plates. Only the x-direction force component in the inclined top layer of reinforcement was included in the results shown in the figure.



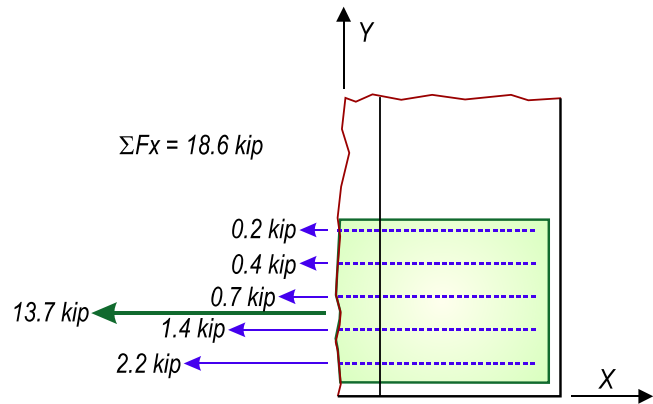
End region
isometric view



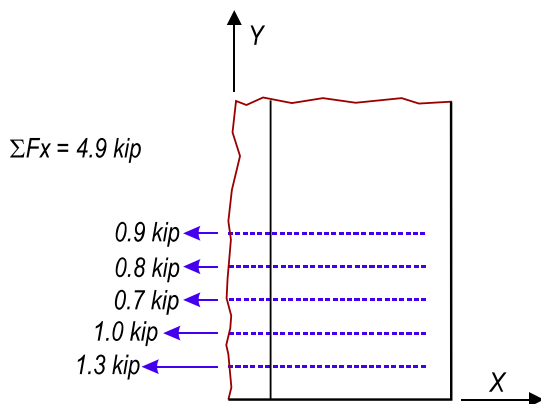
Bottom flange section
end view



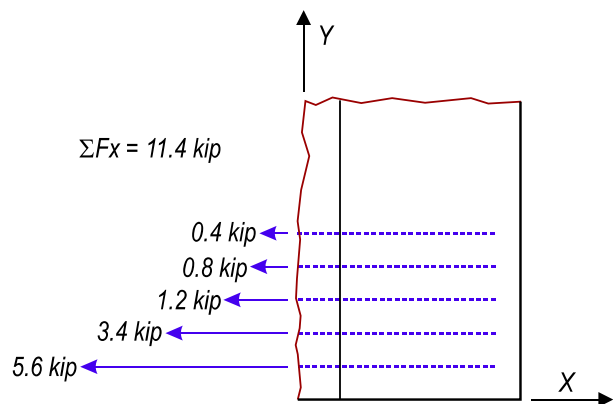
WB bottom flange
partial plan view



FB bottom flange
partial plan view



WN bottom flange
partial plan view



FN bottom flange
partial plan view

Figure 65—Forces in reinforcement and plates after prestress transfer

Total transverse force in the confinement reinforcement and bearing plate (where present) was 63% larger on average in specimens FB and FN than in specimens WB and WN. The additional force is attributed to the strand bond pattern in specimens FB and FN, which placed fully bonded strands in the outer portion of the flange. These fully bonded strands led to additional tension at ends of FN and FB. Most outer strands in specimens WB and WN were partially shielded and did not affect tension at the specimen ends. Transverse forces are compared to the jacking forces in Table 25. Combined transverse forces were equal to 0.6% to 1.7% of the jacking force in the fully bonded strands. Once again, due to the strand bond pattern, the relationship of transverse force to jacking force was larger for FN and FB than for WN and WB.

Data were not collected to estimate confinement reinforcement and bearing plate forces in specimens DC and DM. Strands in these specimens were placed in the ‘design’ strand bond pattern. Fully bonded strands were evenly distributed throughout the bottom flange in this pattern, placing it somewhere between the W_x and F_x specimens in terms of transverse tensile behavior. The transverse force in specimens with the design pattern would likely be smaller than F_x specimens because inner strands in the design pattern relieved tension due to the outer strand. Also, specimens with the design pattern likely had greater transverse force than the W_x specimens because the design pattern included outside strands.

Table 25–Confinement and plate forces

Specimen	Confinement reinforcement transverse force	Bearing plate transverse force	Combined force in reinforcement and plate	Jacking force in fully bonded strands	Transverse force / jacking force
WN	6.2 kip	--	6.2 kip	1070 kip	0.6%
WB	4.3 kip	5.6 kip	9.9 kip	1070 kip	0.9%
FN	11.1 kip	--	11.1 kip	1070 kip	1.0%
FB	4.9 kip	13.7 kip	18.6 kip	1070 kip	1.7%

D.5.1.3 Transfer Length

Longitudinal strains in the bottom flange of I-girders increase through the transfer length as prestress force is transferred from strands to concrete. At locations beyond the transfer length

longitudinal strain is approximately constant. Transfer length in the test girders was experimentally determined by identifying the location at which longitudinal strain in the bottom flange transitioned to constant strain. This was accomplished using strain gages placed at intervals along the bottom flange (Figure 66).

When sufficient data are available, the 95% Average Maximum Strain (AMS) Method is a well-established method for determining transfer length from experimental strain data (Russell and Burns 1993). The available strain data in the current study were insufficient to apply the AMS method, but were still sufficient to estimate the transfer length by other means.

Figure 67 presents strain gage data from the bottom flange of girders H and V immediately after prestress transfer. Blue markers on the figure indicate the strain values reported by individual gages. Values reported by the gages were effectively constant (with some experimental scatter) for the monitored positions along the specimen lengths. This indicates that the gages were placed too far from the end of the girder to capture strain in the transfer length. A bilinear curve representing the apparent strain profile is also shown in Figure 67. The apparent profile shows that the strain must be zero at the end of the girder and must increase to the experimental values recorded at 18in. Beyond 18in. the experimental strains and apparent strain were approximately constant. Thus the transition to constant strain occurred prior to 18in. and it is concluded that the transfer length is not greater than 18in. for girders H and V.

Figure 68 shows experimental strain data from girder F. As before, the blue markers on the figure are data points from individual gages. A piecewise linear curve representing the apparent strain profile is also shown in the figure. Girder F had fully bonded strands in the outer portion of the flange. Strands below the web were shielded for 10ft from the end. Gages were placed near the end of the girder and 10ft from the end in order to evaluate the transfer length of both fully bonded and partially shielded strands.



Figure 66–Strain gages for measuring transfer length

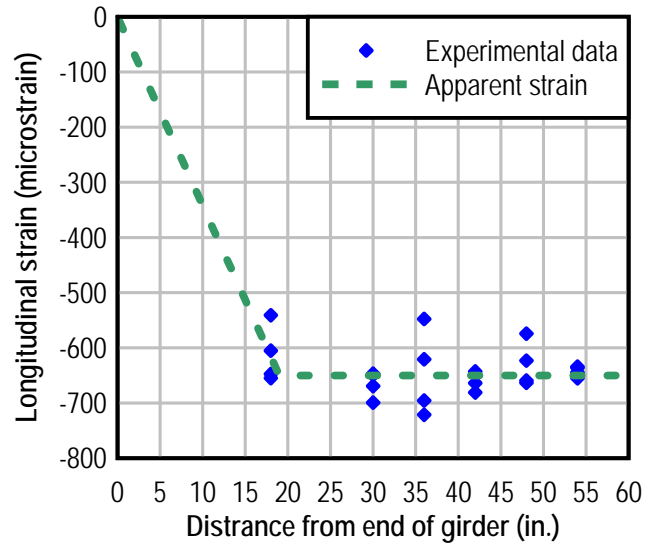


Figure 67–Transfer length in girders H and V

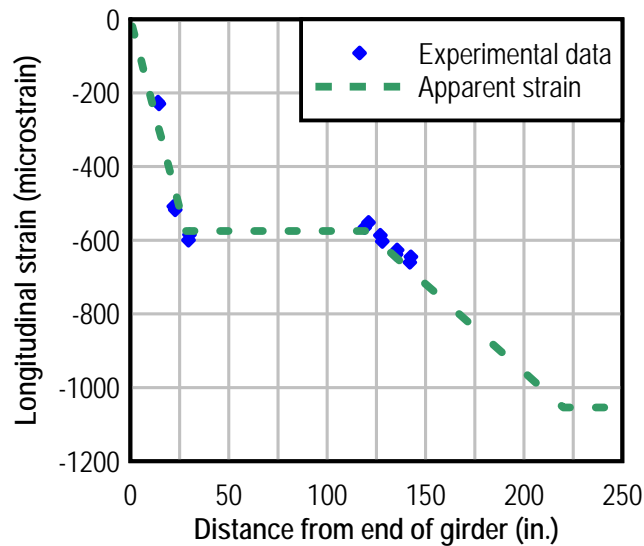


Figure 68–Transfer length in girder F

Gages placed near the ends of girder H reported increasing strain indicative of the transfer length. Beyond 30in. the strain was approximately constant until 120in. at which point the partially shielded strands began to transfer prestress force. Thus the change to constant strain occurred approximately 30in. from the girder end indicating that transfer length for the fully bonded strands was also approximately 30in.

Gages placed between 120in. and 144in. from the end reported increasing strain along the girder length. This indicates that they were within the transfer length of the partially shielded strands. Data were not available beyond 144in. and the transition to constant strain was not observed. As such transfer length of the partially shielded strands cannot be obtained directly from the available data. Transfer length can be estimated by assuming linear-elastic behavior of the concrete and strands. The 24 fully bonded strands affected a microstrain of 575 at the end of their transfer length. The 20 partially shielded strands should have added a proportional amount of strain, resulting in 1054 microstrain at the end of their transfer length. Slope of the apparent strain profile is based on the available data points. Extending the strain profile along this slope shows that the apparent strain intersects 1054 microstrain at a distance 220in. from the member end. Prestress transfer of the partially shielded strands is thus estimated to have occurred between 120in. and 220in. from the member end. The estimated strand transfer length is 100in. This is significantly longer than the transfer length of the fully bonded strands. Additional data

are necessary, though unavailable, for making a more accurate determination of transfer length in the partially shielded strands.

Transfer length was not measured in the other phase two girders (W and D) due to constraints with the data acquisition system. The transfer lengths in girders W and D were likely similar to girder F because the same strand and concrete materials were used for all phase two girders.

Measured transfer length for girders H and V was different from girder F. This difference is attributed to the different strand and concrete materials used in phase one (girder H and V) and phase two (girder F). Measured transfer lengths for fully bonded strands in both phases were less than the AASHTO LRFD calculated transfer length of 36in. Differences between experimental and code values may partially be due to the fact that strain data collected immediately after prestress transfer were used to determine the experimental transfer lengths. Barnes et al. (1999) observed that the transfer length grows by 10% to 20% in the weeks following prestress transfer.

Gages used to measure transfer length were placed at the outside edge of the bottom flange. Longitudinal strain at this location occurred due to axial shortening of the girder and due to shear lag from prestressing forces in the outer stands. Because of the shear lag component, the apparent transfer lengths measured by the gages were likely somewhat longer than the effective transfer length. This effect would be greatest near the end of the girder. Barnes et al. (1999) used finite element modeling to quantify the effect of shear lag on transfer length measurements in AASHTO Type I girders. For fully bonded stands and an apparent transfer length of 18in. Barnes et al. calculated that the effective transfer length would be 16.5 in. For the test girders, the shear lag component of the strain will be affected by the relatively slender and wide bottom flange of the FIB. Thus the correction due to shear lag in the test girders would likely be slightly larger than calculated by Barnes et al.

D.5.2 Crack Data

Girders were inspected periodically during the time between form removal and load testing. When observed crack lengths and widths were measured and documented. Crack widths were determined using a microscope that was precise to +/- 0.001in. Crack lengths were

determined by visual inspection with the naked eye. Three types of cracks were observed in the test girders:

- Top flange flexural cracks
- Web splitting cracks
- Flange splitting cracks

Top flange cracking was due to flexural stresses generated by the vertically eccentric prestressing and is outside the scope of this end region research. Web splitting (Figure 69) cracks were also due to eccentricity of prestressing. Vertical tension stress formed in the web at the end of the specimens as the prestress force was distributed to the cross-section. Flange splitting cracks are of primary interest in the current investigation of confinement reinforcement and were caused by horizontal eccentricity of prestressing, Hoyer expansion of strands, and self-weight reaction of the test girders. Transverse tensile stress formed in the bottom flange as prestressing forces were distributed through the cross-section from eccentric strands in the outer portion of the flange. Additional tensile stresses formed due to the Hoyer effect, in which strand expansion after cutting was restrained by the concrete. Self-weight caused tensile stresses above the support due to Poisson and flange bending effects. Cracks in the top flange, web, and bottom flange occurred when the tensile stresses described above exceeded the concrete strength.



Figure 69–Web splitting and flange splitting cracks

Presentation of crack data is divided according to the two phases of construction. This was done because the materials properties, construction procedures, and curing conditions varied between the construction phases. Within each phase, crack data were further divided between flange splitting cracks and web splitting cracks.

Cracking was quantified and compared in terms of total crack length, total crack area, and maximum crack width. Total crack length was calculated by summing the length of individual cracks for a specimen. Total crack area was calculated by summing the length of each crack multiplied by its representative width. Representative widths were determined from microscope measurements taken at selected points along cracks. Maximum crack width was determined from the microscope readings.

As part of an NCHRP research project, Tadros et al. (2010) recommended criteria for acceptance, repair, and rejection of girders with web splitting cracks. Criteria are based on laboratory data and from field data from Nebraska and Virginia. More stringent criteria may be warranted in aggressive environments such as along Florida coasts. Nevertheless, the recommendations shown in Table 27 and were used as a benchmark for evaluating crack widths in the test specimens.

In general, cracking behavior differed between the two phases of construction. Cracks were first observed in phase one girders (H and V) in the days following prestress transfer, whereas cracks were first observed in phase two girders (W, F, and D) during prestress transfer. Another difference was that cracks in the phase one girders typically did not grow after they were first observed. Cracks in the phase two girders continued to grow in length during the weeks after they were first observed. It is not clear why this occurred. Cracks appearing after some time may be due to tensile creep. If so, then differing environments, plant practices, and mixture properties would have an effect on this behavior.

D.5.2.1 Girders H and V

Girders H and V were fabricated together during the first phase of construction. Girders were inspected for cracking ten times between form removal and load testing (Table 26). Figure 70 shows web and flange splitting cracks observed during inspections. Flexural cracking in the top flange cracking is not shown in the figure.

Cracks were first observed in girders H and V nine days after prestress transfer. The day that cracks formed is unknown because girders H and V were not inspected during the days

immediately following prestress transfer. Web splitting cracks were observed in each specimen. Flange splitting cracks were only observed in specimens without confinement reinforcement (HU and VU). At the end of these specimens the flange cracks intersected with the outermost strand in the third row (Figure 71). Strands at this location had 2.5 in. of clear cover to the top surface of the flange, which was the least amount of top cover for any strand in the test girders.

Table 26–Girders H and V construction events and inspection dates

Event	Date	Days after prestress transfer	Notes
Form Removal	September 7, 2010	--	No cracks observed
Prestress Transfer	September 8, 2010	0	No cracks observed
Lifting and setting on dunnage	September 8, 2010	0	No cracks observed
Girders in storage	September 17, 2010	9	Splitting cracks observed (all specimens)
Girders in storage	September 23, 2010	15	Additional web splitting crack observed (HC)
Girders in storage	October 10, 2010	49	No additional cracks
Girders in storage	January 7, 2011	121	No additional cracks
Trucking	February 23, 2011	167	No additional cracks
Casting deck	April 6, 2011	204	No additional cracks
Begin load tests	May 5, 2011	237	No additional cracks

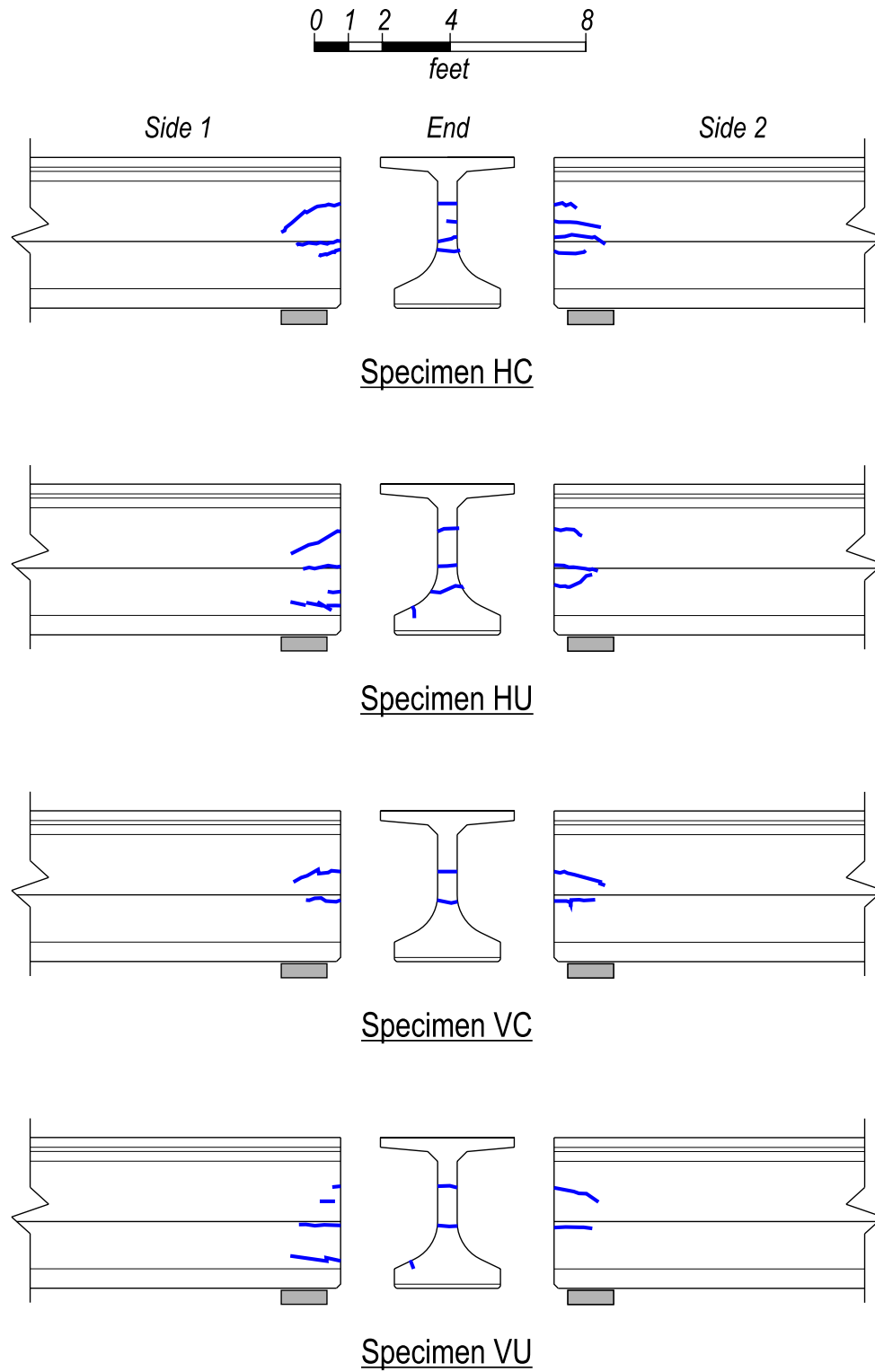


Figure 70–Girder H and V cracks prior to load tests

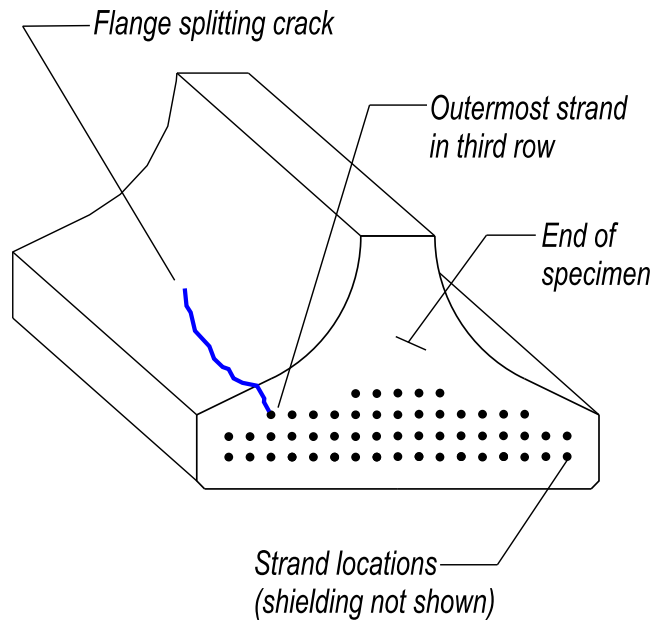


Figure 71–Flange splitting crack intersecting outer strand

Cracks in specimens H and V changed little after they were first observed. An additional web splitting crack was observed in specimen HC during an inspection fifteen days after prestress transfer. No other significant changes in crack quantity, width or length were observed during subsequent inspections of girders H and V.

Web splitting cracks in specimens with the greater amount of end region reinforcement (HC and HU) were an average of 72% longer than the cracks in specimens with less reinforcement (VC and VU)(Figure 72). One possible reason that web cracks were longer in HC and HU was that horizontal bars at the ends of these specimens created a path where horizontal cracks could form and propagate. Web cracks in HC and HU always occurred at the location of horizontal bars.

Although the additional reinforcement increased the total web crack length, it was also more effective in controlling web crack widths. The maximum web splitting crack width was 0.008in. in specimens HC and HU, whereas maximum crack widths were 0.012in. and 0.02 in. in VC and VU, respectively (Figure 73). The additional vertical bars in specimens HC and HU appear to have increased the post-cracking stiffness thereby reducing maximum crack width relative to VC and VU.

For girders H and V the maximum crack widths were typically less than 0.012 in., which according to the criteria in Table 27 do not require repair. Only specimen VU had a crack with a

width greater than 0.012 in. One of the web splitting cracks in this specimen had a maximum width of 0.02 in. According to the criteria in Table 27 this crack would require repair by filling with cementitious material and application of a sealant to the girder end.

Total crack area (Figure 72) was derived from both length and width data, and provides a quantitative comparison of end cracking. Web cracks in specimens HC and HU were longer but narrower than web cracks in VC and VU. Because of this, there is less variation in total web crack area than was observed in total web crack length and maximum web crack width. Variation in total web crack area varied by 24% between HX and VX specimens.

Flange splitting cracks only occurred in specimens HU and VU, which did not have confinement reinforcement. The total length and area of flange cracks were similar between HU and VU (Figure 74). The maximum width of flange splitting cracks was 0.004 in (Figure 73). Presumably, confinement reinforcement in HC and VC controlled the formation and propagation of flange cracks in those specimens.

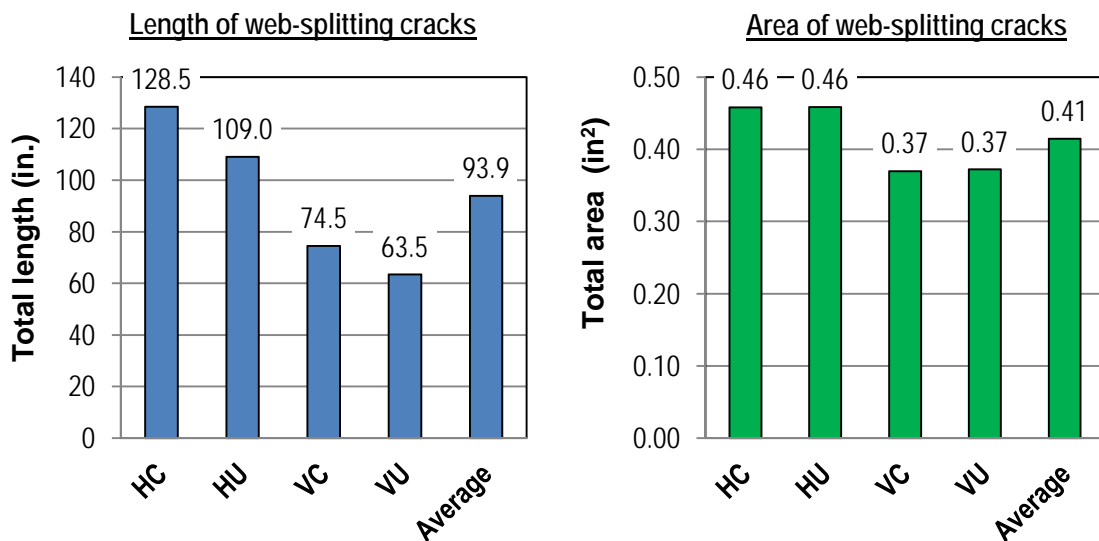


Figure 72–Web splitting cracks in specimens H and V

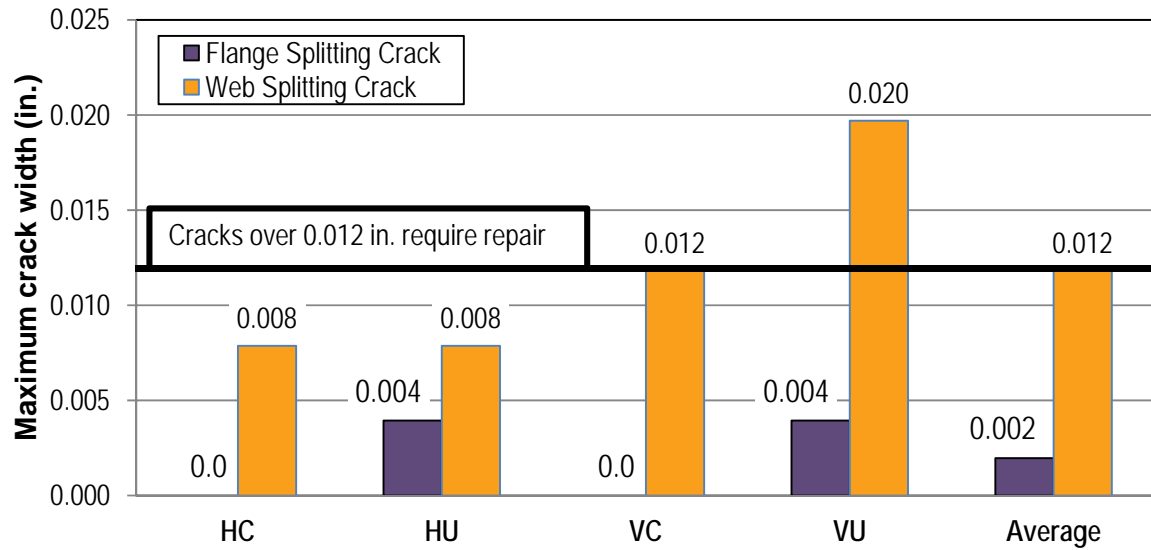


Figure 73–Maximum crack widths in girders H and V

Table 27–Recommended action for web splitting cracks (Tadros et al. 2010)

Crack Width (in.)	Required Action
Less than 0.012	None
0.012 to 0.025	Fill cracks with cementitious material and apply surface sealant to end 4 ft of girder
0.025 to 0.05	Fill cracks with epoxy and apply surface sealant to end 4 ft of girder
Greater than 0.05	Reject girder unless shown by detailed analysis that structural capacity and long-term durability are sufficient

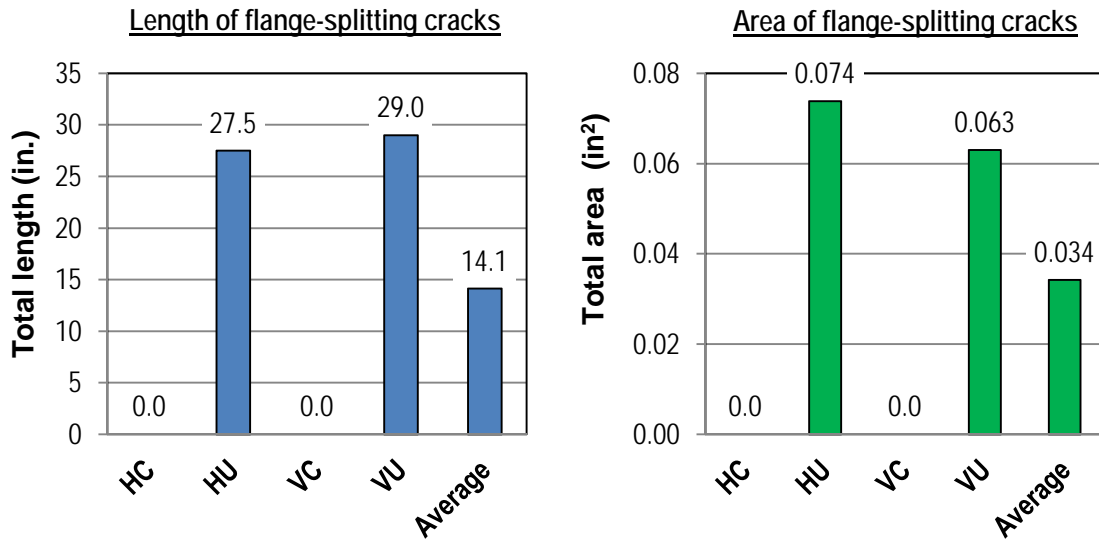


Figure 74—Flange splitting crack data in girders H and V

D.5.2.2 Girders W, F, and D

Girders W, F, and D were fabricated together during the second phase of construction. Construction events, inspection dates, and notes from girders W, F, and D are listed Table 28. Flange and web splitting cracks were first observed in these girders after the outer strands had been cut during prestress transfer. Cracks grew in quantity and length in the days and weeks following prestress transfer. Figure 75 shows the web and flange splitting cracks observed prior to load testing. Flexural cracks in the top flange are not shown.

Steel bulkheads were used during construction of girders W, F, and D. A portion of the bulkhead covering the end of the bottom flange (Figure 76) remained with each test girder for approximately two weeks after prestress transfer. Bottom flange ends covered by the bulkheads were inspected for the first time 30 days after transfer. Cracks were observed at the girder ends during this inspection. Because the ends were previously covered, it is not known when splitting cracks at the end of the bottom flanges first formed.

The location of cracks shown in Figure 75 can be understood by considering the strand bond patterns in the test specimens. For example, specimens WN and WB had flange splitting cracks located 10ft from their ends. These cracks formed within the transfer length of partially shielded strands. Strands in WN and WB were 45% partially shielded, with all shielding located

in the outer portion of the flange. It is believed that the flange cracks in WN and WB occurred due to Hoyer stresses and lateral-splitting stresses associated with the partially shielded strands.

Table 28–Girders W, F, and D construction events and inspection dates

Event	Date	Days after prestress transfer	Notes
Form Removal	February 20, 2012	--	No cracks observed
Prestress Transfer	February 21, 2012	0	First cracks observed after outer strands released.
In storage immediately after lifting	February 22, 2012	1	Additional splitting cracks and extension of previous cracks observed.
In storage	February 23, 2012	2	Additional splitting cracks and extension of previous cracks observed.
In storage	February 24, 2012	3	Additional splitting cracks and extension of previous cracks observed.
In storage	March 6, 2012	14	Additional splitting cracks and extension of previous cracks observed.
In storage	March 22, 2012	30	Additional splitting cracks and extension of previous cracks observed. Bottom flange at ends examined for first time. Previously the bulkhead plates were covering the flange end.
In storage	April 9, 2012	48	Additional splitting cracks and extension of previous cracks observed.
Trucking	April 30, 2012	69	Additional splitting cracks and extension of previous cracks observed.
Casting deck	May 7, 2012	76	No additional cracking observed.
Begin load testing	May 23, 2012	92	Bottom of girder inspected for first time. Flange splitting cracks observed prior to load tests.

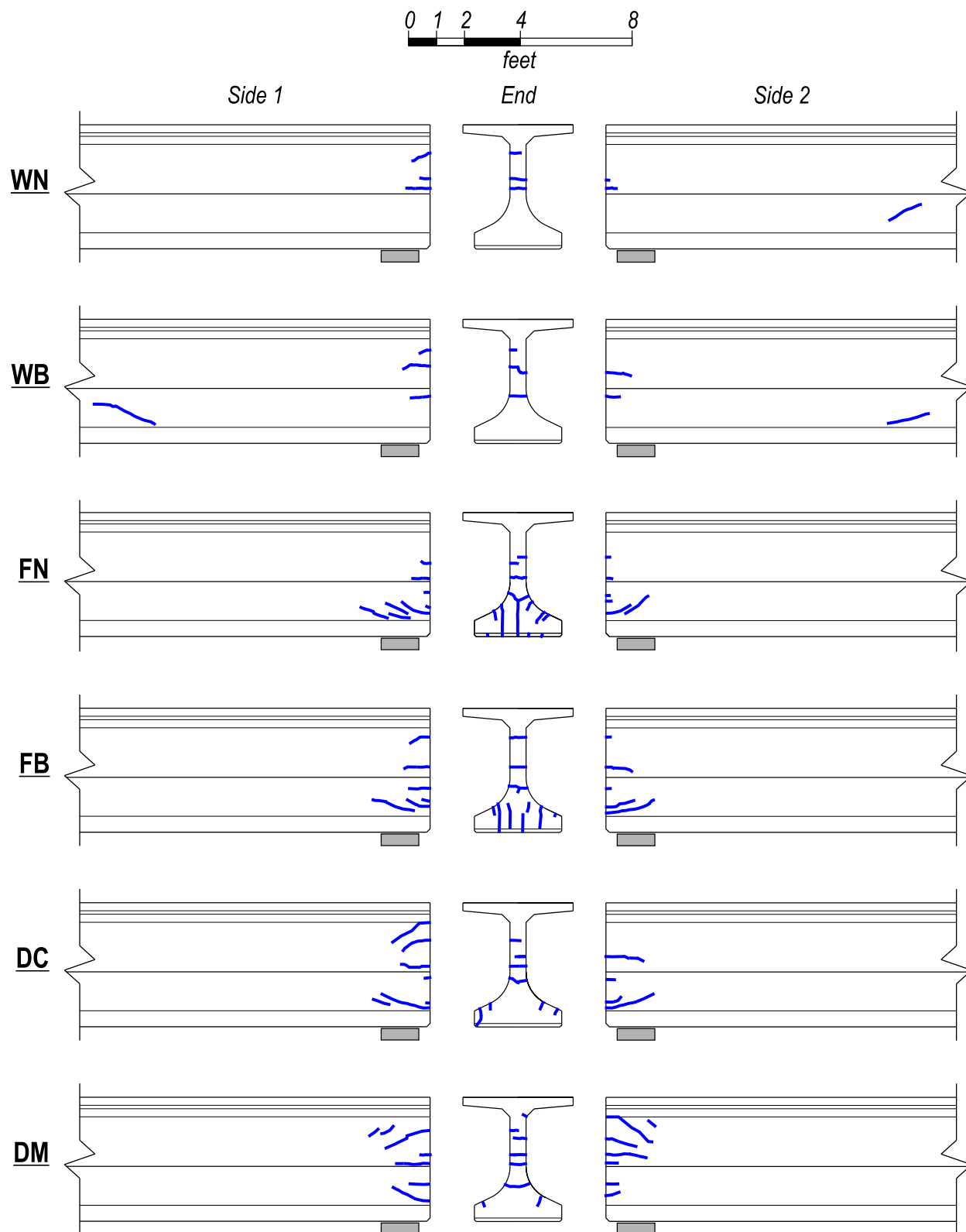


Figure 75—Girders W, F, and D web and flange splitting cracks



Figure 76–End of bottom flange covered by portion of steel bulkhead

Strands in specimens FN and FB were also 45% shielded, with all shielding located below the web and all shielding terminating 10ft from the specimen ends. This pattern placed fully bonded strands in the outer portion of the flange and led to tensile stresses in the bottom flange as illustrated by Figure 58. Flange splitting cracks formed when tension stresses at the end of the flange exceeded the concrete tensile strength. Flange cracks at the ends of FN and FB intersected strands (Figure 77) suggesting that the Hoyer effect also contributed to the tensile stresses and crack formation. Flange splitting cracks in FN and FB were greater in total length and in total area than all other specimens (Figure 78). The maximum width of flange splitting cracks was also greater for FN and FB (Figure 79) than other specimens.

Specimens DC and DM had the largest number of fully bonded strands (39) in the phase 2 test girders. As such the web stresses and web splitting cracks were greatest in DC and DM. All other specimens had only 24 fully bonded strands. The total length of web splitting cracks in specimens DC and DM were 132 in. and 179 in., respectively (Figure 80). The maximum width of web splitting cracks was 0.008 in. specimens DC and DM (Figure 79).

Specimens DC and DM had flange splitting cracks (Figure 81) in addition to web cracks. At the end of these specimens the flange splitting cracks intersected strands, suggesting that the Hoyer effect contributed to crack formation. In specimen DC the cracks intersected the outermost strands in the second and third rows.

The maximum crack width in girders W, F, and D was 0.008 in. This width does not warrant repair using the criteria from Table 27.

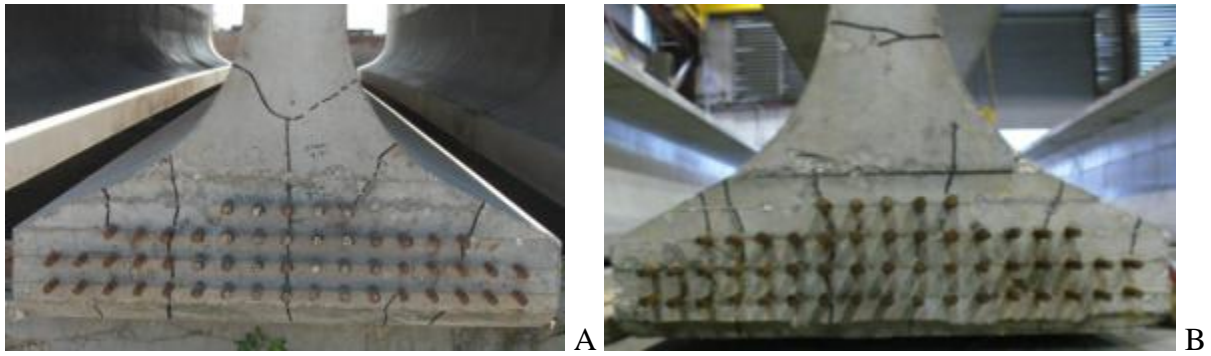


Figure 77–Girder F flange splitting cracks in A) specimen FN and B) specimen FB

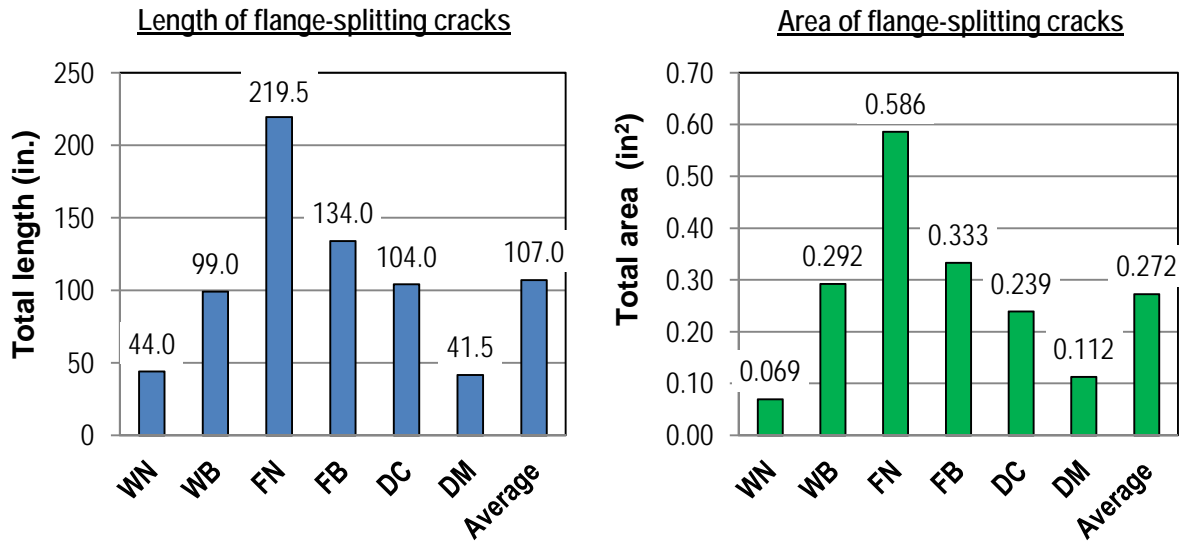


Figure 78–Flange splitting cracks in girders W, F, and D

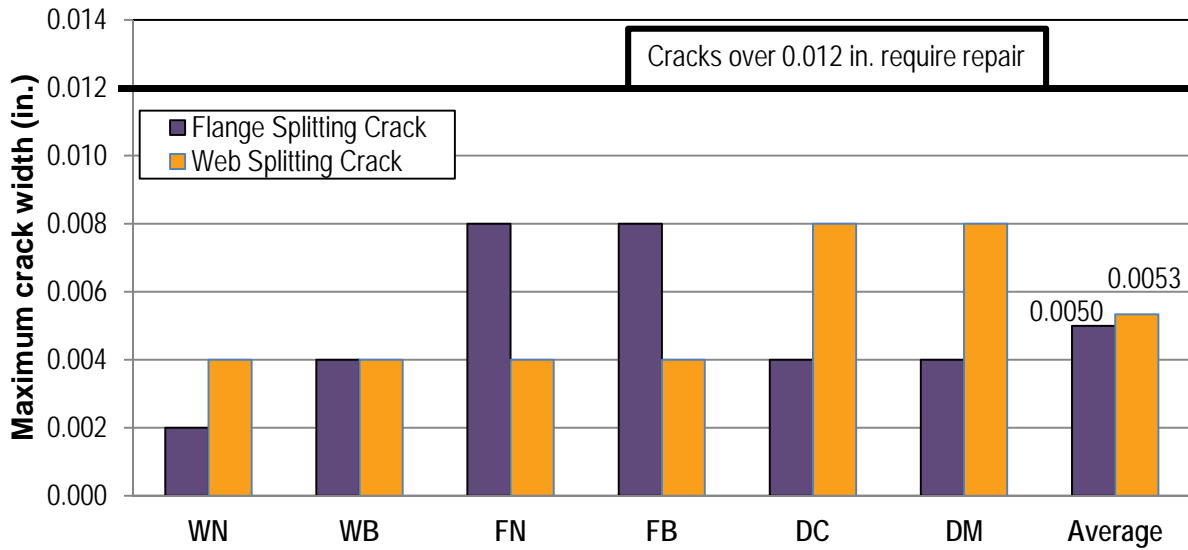


Figure 79–Maximum crack widths in girders W, F, and D

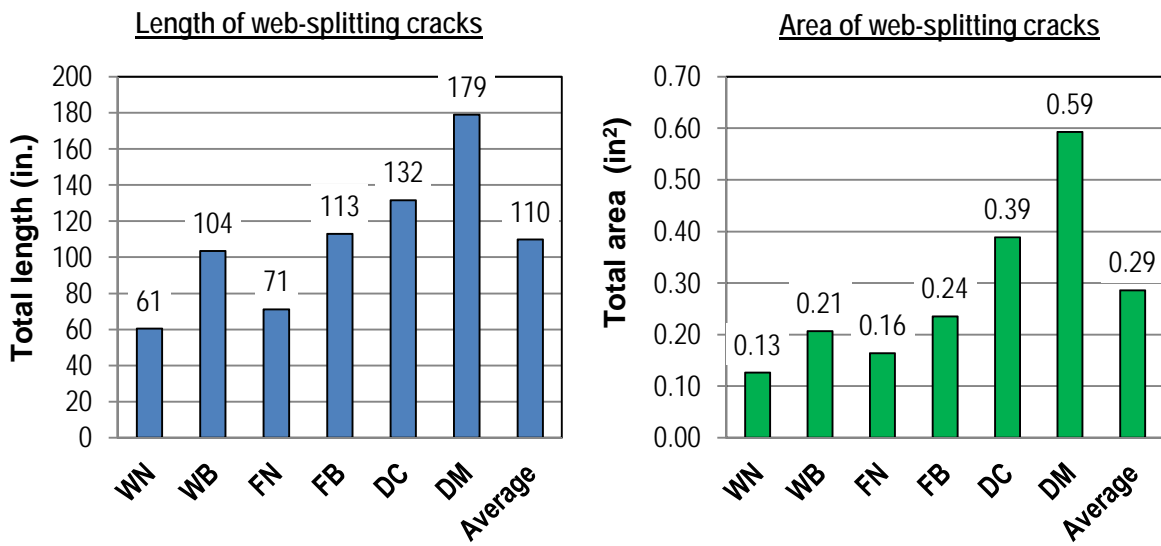


Figure 80–Web splitting cracks in girders W, F, and D

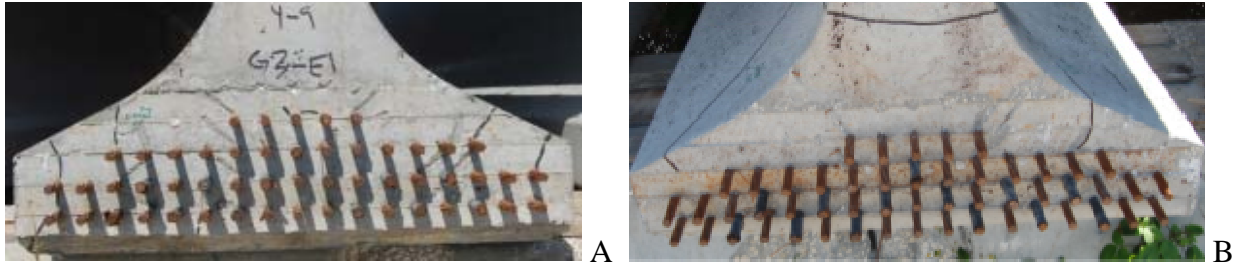


Figure 81–Girder D flange splitting cracks in A) specimen DC and B) specimen DM

D.5.3 Prestress Loss

Vibrating wire gages were placed near mid-span of each girder to monitor prestress losses. Null values were taken just prior to prestress transfer. Additional data were taken from these gages at discrete intervals throughout fabrication, storage, and deck construction. Elastic and long term loss losses were calculated using the strain data. Experimentally calculated loss values are listed in Table 29 and Table 30 along with code estimated losses from the AASHTO and PCI methods using the specified material properties. Experimental and code estimated losses vary between girders with different magnitudes of prestress force.

Table 29–Prestress losses girders F and W.

Prestress Losses	Experimental		Code	
	F	W	AASHTO	PCI
Elastic Losses (%)	14.0%	16.9%	13.4%	10.4%
Long Term Losses (%)	10.1%	13.2%	14.1%	24.3%
Total Losses (%)	24.1%	30.1%	27.5%	34.6%
Measurement Period (days)	76	76	-	-
Initial Prestress (kip)	2002			

Table 30–Prestress losses girder H, V, and D.

Prestress Losses	Experimental			Code	
	H	V	D	AASHTO	PCI
Elastic Losses (%)	14.6%	13.9%	12.4%	13.5%	10.5%
Long Term Losses (%)	11.9%	11.0%	9.2%	14.3%	24.4%
Total Losses (%)	26.5%	24.9%	21.6%	27.8%	34.9%
Measurement Period (Days)	242	242	76	-	-
Initial Prestress (kip)	2046				

The estimated prestress losses from the AASHTO and PCI methods were generally higher than the experimentally determined losses. One possible reason for the difference is that

the experimental losses occurred over a few months, whereas long the AASHTO and PCI methods assume longer time periods. The PCI method predicted higher losses than the AASHTO method.

D.5.4 Variable Comparison and Discussion

This section compares crack behavior across specimens and variables. Trends identified in the test specimens will be useful in detailing end regions to prevent and control cracking during and after prestress transfer.

Flange splitting cracks (Figure 74) formed in phase one specimens without confinement reinforcement (HU and VU) but not in specimens with confinement (HC and VC). This result suggests that confinement reinforcement controls flange splitting cracks that form due to prestressing. It is presumed that confinement reinforcement in HC and VC prevented flange splitting cracks from opening and propagating.

The quantity of bonded strands affected the total length and area of web splitting cracks. This is evident from Figure 80 which compares specimens DC and DM (39 strands each) with specimens WN, WB, FN, and FB (24 strands each). On average the total crack length and total crack area were 78% and 168% larger, respectively, in specimens with 39 fully bonded strands than in the specimens with only 24 strands. The maximum web crack width was twice as large in specimens with 39 fully bonded strands as in those with 24. These results indicate that reducing the quantity of fully bonded strands through partial shielding can successfully control the length, area, and maximum width of web splitting cracks.

The location of shielded strands within the bottom flange (inner flange or outer flange) was not a factor in length, area, or maximum width of web splitting cracks. Web splitting cracks in specimens with shielded stands placed in the outer portion of the flange (WN and WB) had similar total length, total area (Figure 80), and maximum width (Figure 79) as comparable specimens with shielded strands placed below the web (FN and FB).

The effect of confinement reinforcement and bearing plates on web splitting cracks is not obvious from the test data. Comparing total crack areas for girder H and V (Figure 72), it can be seen that specimens with confinement reinforcement had similar crack area but longer lengths than specimens without confinement. Specimens WN and FN without bearing plates had more crack length and area (Figure 79 and Figure 80) as specimens WB and FB with bearing plates.

One possible explanation for the greater amount of cracking in FB and WB is that bottom flange confinement provided by the bearing plates resulted in shorter transfer lengths and higher end stresses than in specimens without bearing plates.

Specimens FN and FB had the worst flange cracking and had all bonded strands placed in the outer portion of the flange. Severity of flange cracking specimens FN and FB is attributed to this strand bond pattern. The total length and total area (Figure 78) of flange cracks in FX specimens were both 2.5 times greater on average than the same metrics in the other phase 2 specimens. Similarly, the maximum flange crack width (Figure 79) was twice as large in FX specimens as in the other phase 2 specimens. Based on these results it is recommended that strands be placed as near to the centerline of the bottom flange as practical in order to maximize cover and minimize flange splitting cracks.

Six of the ten specimens had flange splitting cracks at the member end. In five of the six with flange cracks at the end, flange cracking intersected the outermost strand in the third row (Figure 71). Strands at this location had only 2.5 in. of clear cover to the top of the bottom flange. This was the least amount of cover of any strand in the test specimens. It is recommended that this location be avoided when designing strand patterns. Furthermore it is recommended that strand patterns be designed with the maximum amount of top cover.

Flange cracks were observed within the transfer length of the partially shielded strands in specimens WB and WN. Approximately 45% of strands in these specimens were partially shielded, and all shielding terminated at the same section 10 ft from the specimen ends. Both the overall shielding percentage and the termination of shielding violated AASHTO LRFD requirements. Flange cracks were not observed within the transfer length of partially shielded strands in specimens that complied with the AASHTO requirements.

Similar to specimens WB and WN, specimens FB and FN also violated the AASHTO requirements for total percentage of shielded strands and quantity of strand shielding that terminated at a section. Unlike specimens WB and WN, however, specimens FB and FN had partially shielded strands placed below the web and did not have flange cracks within the transfer length of the partially shielded strands. This demonstrates that the overall percentage of shielded strands was not a factor in flange cracking. The location of shielding was more critical to flange cracking than was the percentage of strand shielding that terminated at a given section.

Flange cracking in specimen end regions extended up to 30 in. from the member end. This length is 6 in. shorter than the code calculated transfer length of 36in. The similarity between these values suggests that code specified transfer length may be a good estimate of flange splitting crack lengths and that the code transfer length is a reasonable guideline for placement of confinement. The correlation between flange splitting crack length and transfer length is attributed in-part to the Hoyer effect which causes tensile splitting stresses within the transfer length.

Embedded steel bearing plates were excluded from specimens WN and FN. Absence of a bearing plate in specimen FN led to 64% greater total crack flange crack length and 76% greater total crack area when compared to specimen FB which had a bearing plate. Both specimens had fully bonded strands placed only in the outer portion of the flange.

Absence of a steel bearing plate did not adversely affect cracking in specimen WN relative to WB which had a bearing plate. Neither specimen had flange cracks at the member end. Thus presence of a bearing plate had the beneficial effects of reducing crack length and area, but only in specimens with fully bonded strands placed in the outer portion of the flange.

Configuration of confinement reinforcement can be compared using results from specimens DC and DM. Specimen DC had #3 confinement reinforcement as currently specified by FDOT. DM had #4 confinement reinforcement, but had fewer total confinement bars than DC. Specimen DC had 151% greater total flange crack length, and 113% greater total flange crack area than did specimen DM. Average flange crack width was not significantly different between the specimens. These results suggest that the modified confinement reinforcement performed better at controlling flange splitting cracks than the FDOT configuration. This is attributed to the fact that specimen DM had more reinforcement placed closer to the end than did specimen DC.

D.5.5 Summary and Conclusions

Cracking and strain data were collected in pretensioned FIB girders during multiple stages of construction including: prestress transfer, lifting, storage, transport, and deck construction. Each end of each girder had a different set of variables. Variables included: the quantity or lack of confinement reinforcement, the presence or lack of a steel bearing plate, and the strand bond pattern. Two of the tested strand bond patterns were intentionally designed to

violate current AASHTO LRFD requirements. Strain data from the reinforcement and bearing plates were used to estimate the transverse forces developed during prestress transfer. The following conclusions are made based on results from the strain data:

- Transverse tensile strains were observed in the bottom flange, confinement reinforcement and embedded bearing plates during and after prestress transfer. Tensile strains are attributed to prestressing forces, the Hoyer effect and girder self-weight and are thought to have caused flange splitting cracks.
- Transverse tensile strains are greatest in sections with fully bonded strands placed only in the outer portions of the bottom flange. Bonded strands in the outer flange are eccentric with the resultant internal force, thereby inducing bending in the bottom flange and associated transverse tension at the girder end.
- Transverse tensile strains are smaller in sections with fully bonded strands placed below the web than in sections without fully bonded strands below the web. This is because prestress forces from the inner (below the web) strands counteract the transverse tension caused by prestress forces from strands in the outer portions of the flange.
- Confinement reinforcement can be effective in controlling transverse tensile strain and associated splitting cracks in the bottom flange during and after prestress transfer. Specimens without confinement reinforcement had average transverse tensile strains in the bottom flange concrete that were 3.4 times greater than specimens with confinement reinforcement.
- The greatest strain in confinement reinforcement typically occurs in the lowest layer of reinforcement. In the test specimens, the bottom layer of confinement had strains 1.4 times greater on average than the middle layer.
- Confinement strains are largest near the end in members with fully bonded strands placed in the outer portion of the flange. In test specimens with fully bonded outer strands the strain was 4 times larger in bars 2in. from the end than in bars 9in. from the end.
- Transverse tensile forces in confinement reinforcement and bearing plates were approximately 50% larger on average in members with bonded strands in the

outer flange only, as compared to members with bonded strands in the inner flange only.

- The combined transverse tensile force in confinement reinforcement and bearing plate was estimated (based on strain data) to be between 0.6% and 1.7% of the total jacking force in fully bonded stands. These values represent lower and upper bounds for extreme strand bond patterns.
- Lifting of test girders and placement on dunnage had little effect on the transverse and vertical strain in the end region. The maximum change in strain during this process of 25 microstrain.

Cracking was monitored in test specimens from the time forms were removed until the time of load testing. The following conclusions are made based on results from the crack data:

- In some cases web and flange splitting cracks occur during and immediately following prestress transfer. In other cases cracking occurs during the days or weeks following transfer.
- Length and width of web and flange cracks were affected by detailing of the end region, even in specimens having the same cross-section.
- Flange splitting cracks in test specimens had maximum widths between 0.002 in. and 0.008 in. These cracks widths would not warrant repair according to the criteria set forth by Tadros et al. (2010).
- Flange splitting cracks extended up to 30 in. from the test specimens ends. This length is comparable to the code calculated transfer length of 36 in. (30 strand diameters) suggesting that the code transfer length is a reasonable extent for the placement of confinement reinforcement to control flange splitting cracks.
- Confinement reinforcement appeared to have effectively controlled flange splitting cracks in specimens HC and VC based on the splitting cracks that were observed in comparable specimens (HU and VU) without confinement reinforcement.
- Absence of a steel bearing plate affected the lengths and widths of flange splitting cracks in specimens with fully bonded strands placed only in the outer portion of the flange. For example, the total flange crack length was 64% greater and total

flange crack area 76% greater in specimen FN (no plate) than in specimen FB (with plate).

- The total length and area of flange splitting cracks were dependent on the strand bond pattern. Specimens with bonded strands placed only in the outer flange had 2.5 times greater total flange crack length and area than specimens with bonded strands distributed throughout the bottom flange. Splitting cracks did not occur in the end region in specimens where bonded strands were placed only in the inner portion of the flange.
- Flange splitting cracks formed within the transfer length of partially shielded strands in two specimens. These cracks were affected by the placement of shielded strands in the outer portion of the flange, and the quantity of shielding that terminated at a same section. The total percentage of shielded strands did not affect cracking.
- Flange splitting cracks were not observed in the transfer length of shielded strands in specimens complying with AASHTO LRFD requirements for quantity of shielding that can terminate at a given section.
- Splitting cracks in the bottom flange typically intersected the outermost strand in the third row from the bottom. This strand location had the least amount of top cover of any location in the test girders.
- Length and area of web splitting cracks was a function of the quantity of fully bonded strands. Web splitting cracks in specimens with 39 fully bonded strands were 78% longer and had 168% more area than web cracks in specimens with 24 fully bonded strands.
- Position of fully bonded strands in the bottom flange did not affect the length, area, or width splitting cracks in the web.

D.6 Results and Discussion: Load Tests

Five 54 in. deep Florida This chapter presents the results of load testing conducted on ten FIB-54 specimens. Test results are presented in terms of superimposed shear, which is referred to as shear in this chapter. Superimposed shear is defined as the shear force due to the applied load acting at the support nearest the load point. Self-weight is not included in the superimposed shear.

Displacement results are presented as the vertical displacement occurring at the load point. Displacement at the load point was calculated as the average of the displacements reported by LVDTs that were placed on either side of the load. The effect of bearing pad displacement has been removed.

Strand slip data are presented as the average slip from all monitored fully bonded strands. Displacement data from partially shielded strands are not included. Locations of monitored strands are presented in Chapter D.5.

D.6.1 Failure Modes

Three different modes of failure were observed in the test program: Web-shear, lateral-splitting and bond-shear. This section defines each type of failure and discusses the characteristics associated with each failure mode.

Web-shear failure is distinguished by crushing of the concrete web at peak load. This type of failure is controlled by the capacity of the web to carry diagonal compression between the top and bottom flanges. A post-peak characteristic of web-shear failure includes sliding of the top portion of the girder relative to the bottom along a shear plane through the web (Figure 82). This type of failure mode is considered in the shear design provisions of AASHTO LRFD and ACI 318.

Lateral-splitting failure is characterized by longitudinal cracks in the bottom flange and by peeling (outward) movement at the edges of the bottom flange (Figure 83.) Peeling movement of the bottom flange is caused by eccentricity between prestressing forces in the outer flange and the resultant equal and opposite force centered in the web (Figure 84.) This condition creates a moment which opens bottom flange cracks, and peels the edges of the bottom flange outward. In specimens with sufficient bottom flange confinement, peeling movement and longitudinal cracks are restrained, and peeling failure is mitigated.

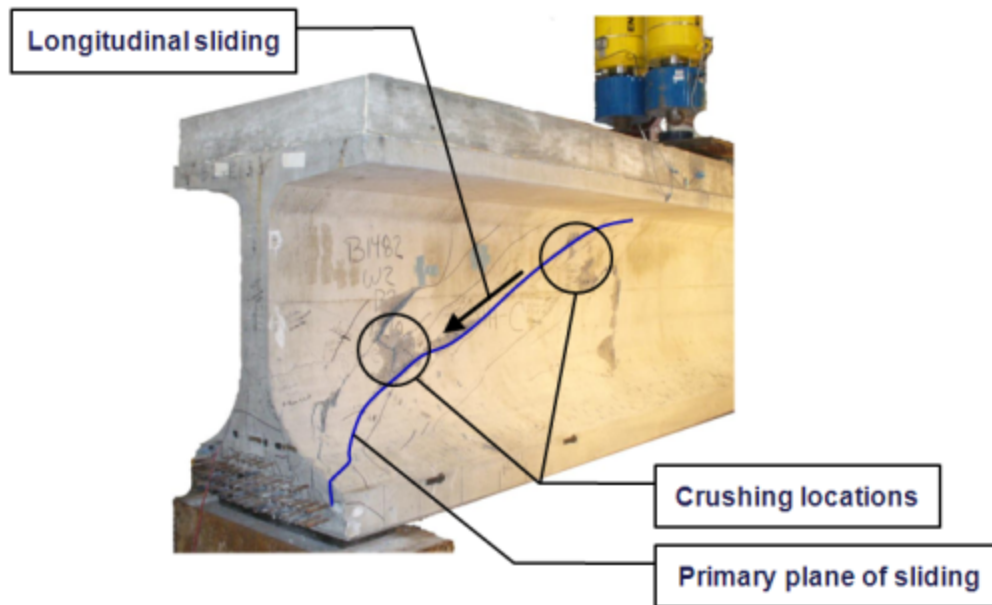


Figure 82–Web-shear failure

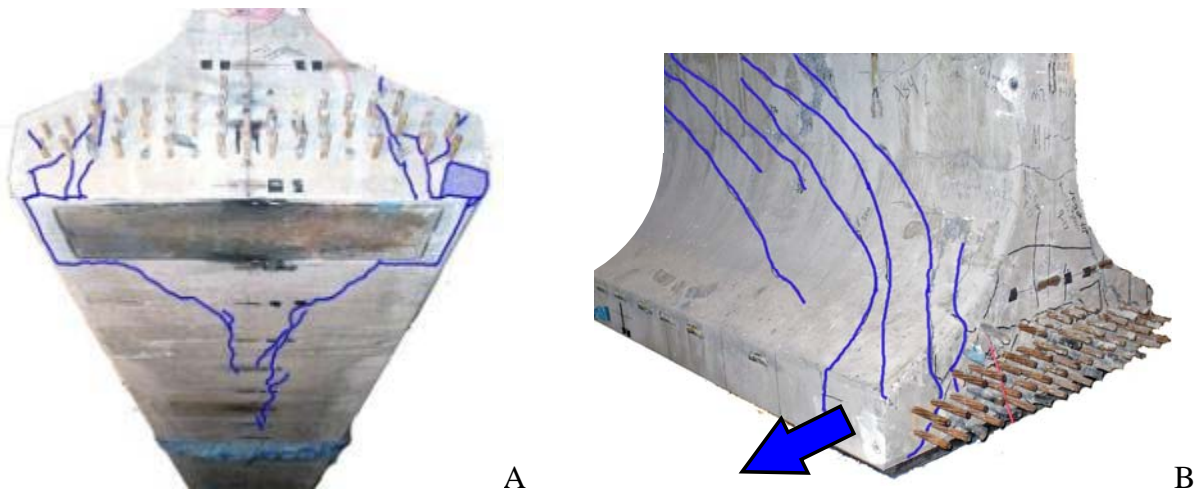


Figure 83–Lateral-splitting failure A) bottom view and B) side-end view

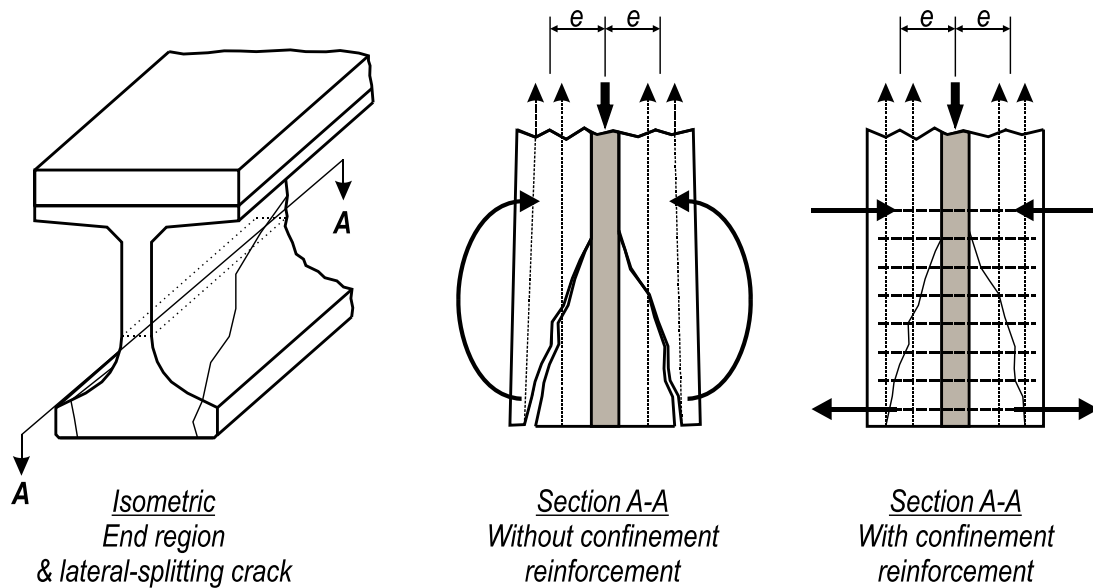


Figure 84–Lateral-splitting failure mechanics

Strand slip is observed in some specimens failing in lateral-splitting mode. Flange splitting cracks are a precursor to strand-slip in lateral-splitting failures. Once strands start to slip cracks open wider and capacity is lost in a sudden manner.

Longitudinal cracking along the specimen bottom (Figure 83) is also a characteristic of lateral-splitting failure. Cracks on the bottom are another manifestation of lateral-splitting cracks on the top surface of the bottom flange.

Bond-shear failure is characterized by strand-slip at peak load. This type of failure is governed by concrete-strand bond capacity and by specimen propensity for cracking within the strand development length. Cracking in the development length is always a precursor to strand slip (Figure 85). Cracks interrupting strand development reduce the embedment length to the distance between the crack and the girder end. After strands start slipping the cracks opened wider and new cracks form. An abrupt slip event occurs at peak load followed by a subsequent loss of capacity. Longitudinal splitting cracks can also be observed on the bottom of specimens that failure in bond-shear (Figure 85).

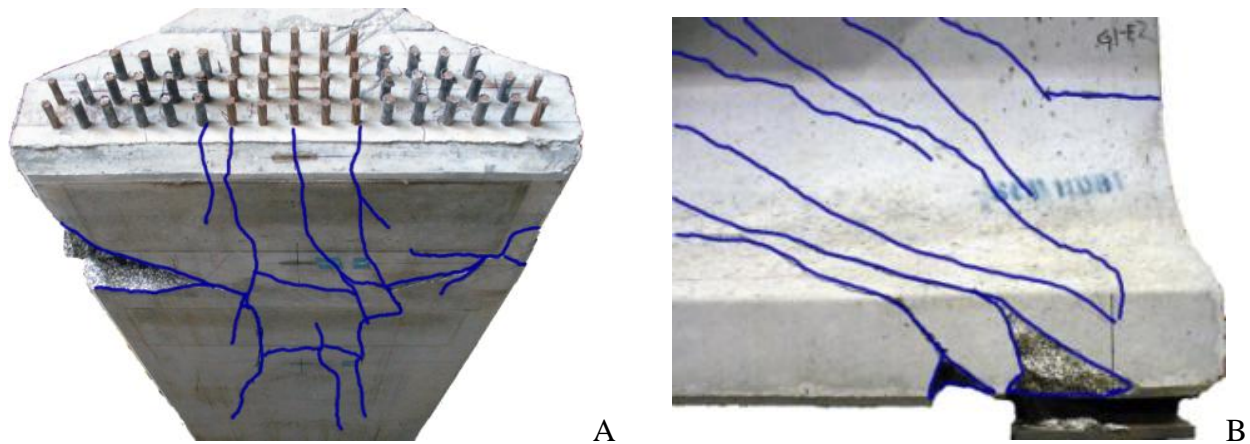


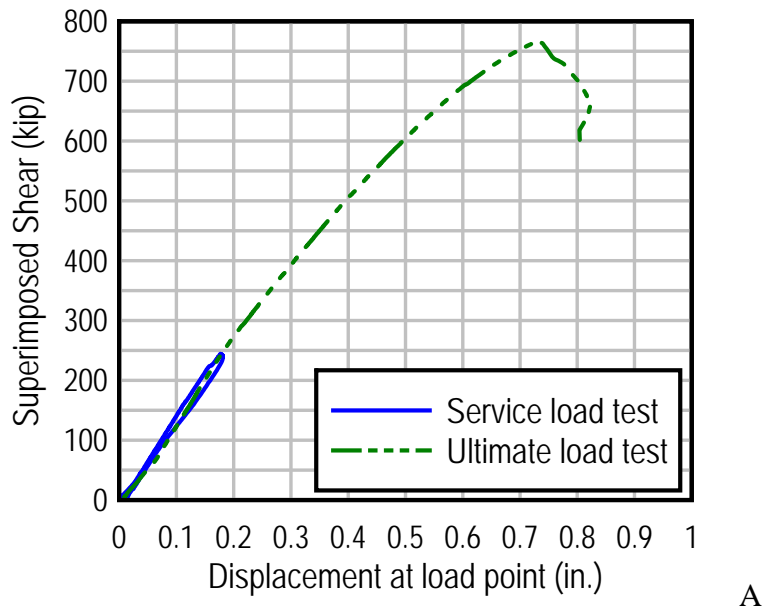
Figure 85–Bond-shear failure A) bottom view and B) side view

As described above, similar characteristics are associated with lateral-splitting and bond-shear failures. One subtle difference between these failure modes is the cause of cracking in the bottom flange. In lateral-splitting failures bottom flange cracking is caused by shear forces and transverse tensile forces due to eccentric prestressing. Bottom flange cracking in bond-shear failures are caused primarily by shear forces. Magnitude of strand slip is a more obvious distinction between bond-shear and lateral-splitting failures. In the test program, specimens failing in bond-shear reported maximum average strand slip over 0.25in. When slip was observed in specimens failing in later-splitting maximum the average slip was less than 0.1in.

D.6.2 Load Test Results

D.6.2.1 HC

Detailing of specimen HC (Figure 10) was effectively identical to the 2008 FDOT Interim Design Standards (FDOT, 2008). Variables in specimen HC included FDOT specified confinement reinforcement and bearing plate in the bottom flange, horizontal reinforcement in the end region, and the ‘design’ strand bond pattern (Figure 9) which had (39) fully bonded strands. Specimen HC failed in web-shear mode. Shear-displacement and crack pattern are shown in Figure 86.



Release cracks not shown.
 Initial cracks shown bold in red
 Final cracks shown blue.

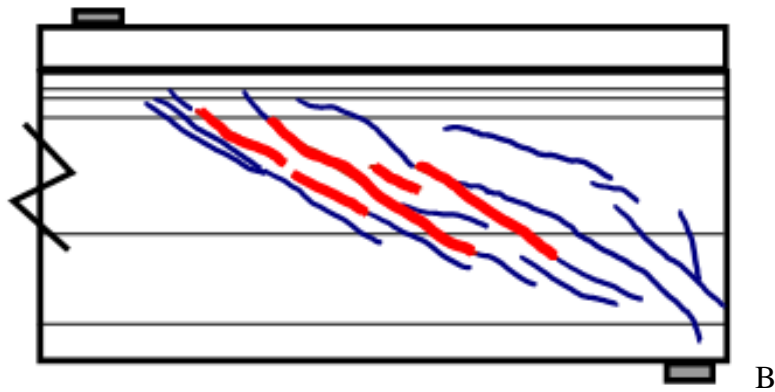


Figure 86–Specimen HC load test summary A) shear-displacement and B) crack pattern

Cracks in HC were first observed during the service load test at a shear of 225 kip. Inclined web cracks between the load point and support were the first to be observed. The service load test reached a peak shear of 244kip. Cracks partially closed during the unloading stage of the service load test. Web cracks in specimen HC had a maximum width of 0.004 in. at a shear of 244kip, and 0.002 in. after load was removed.

Following service load testing specimen HC was loaded to ultimate capacity. Stiffness decreased gradually as load increased beyond the level of the service load tests. Because flexural cracks were not observed, loss in stiffness is attributed to formation and growth of diagonal cracks. Ultimate capacity was signaled by web crushing followed immediately by sliding movement of the specimen's top portion relative to the bottom. Sliding movement occurred along the inclined cracks in the web. Areas of the web surface spalled off at the peak load (Figure 87). Spalling near the load point was a secondary effect, occurring immediately after the load had dropped. No splitting cracks were observed on the bottom of the girder.

Failure of HC is classified as a web-shear failure. Loss of capacity after the web-shear failure was abrupt. Specimen HC supported a maximum shear of 766 kip, the most of any specimen in the test program.

Strand slip data are not presented in Figure 86. LVDT data indicate that strand slip was negligible at lower loads. At higher loads cracks caused shifting of the frame holding the LVDTs thereby compromising the strand slip data. Specimens DC and DM used the same strand bond pattern as HC, but used different strand slip instrumentation that did not shift during testing. Slip data from the DC and DM suggest that strand slip was not a factor in the failure mode of specimens (such as HC) with the design strand pattern. The lack of slip observed in the specimens with this pattern is attributed to the relatively large quantity of fully bonded strands.

After the test the wood frame holding the LVDTs was removed, revealing cracks at the end of HC that intersected most of the strands (Figure 89). These cracks are believed to have occurred at or subsequent to the peak load.

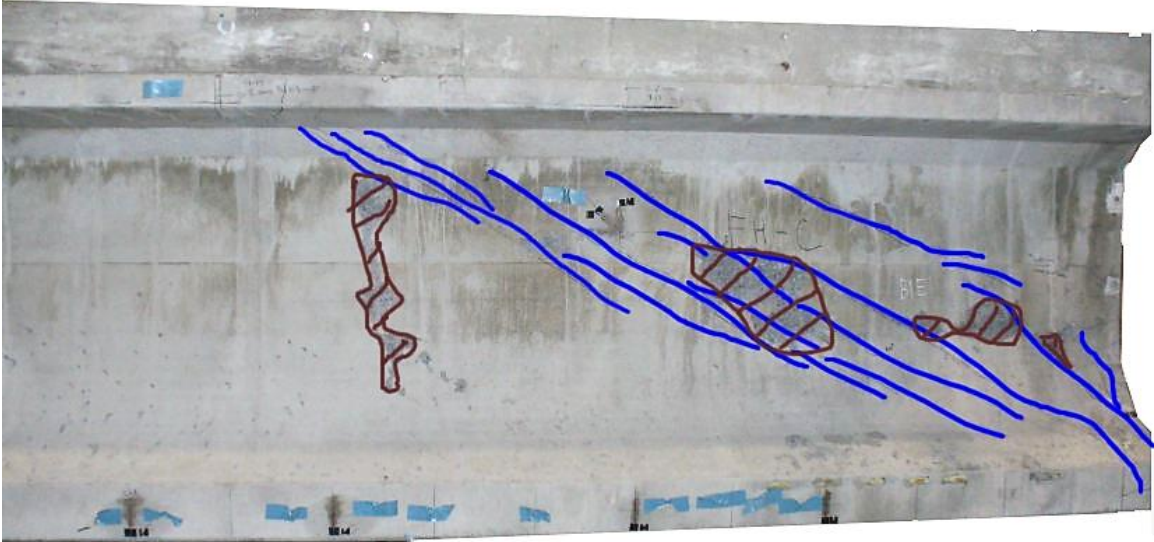


Figure 87–HC after load testing (cracks shown blue; spalling in brown)

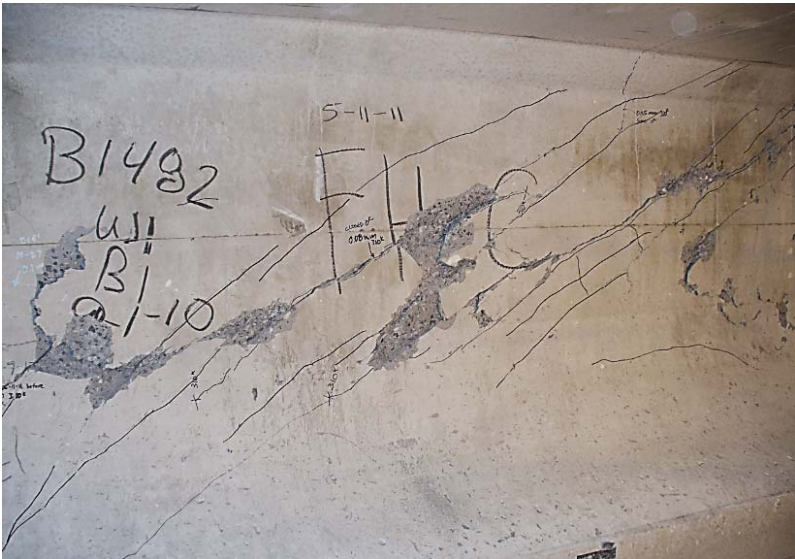


Figure 88–Close-up of web crushing and spalling

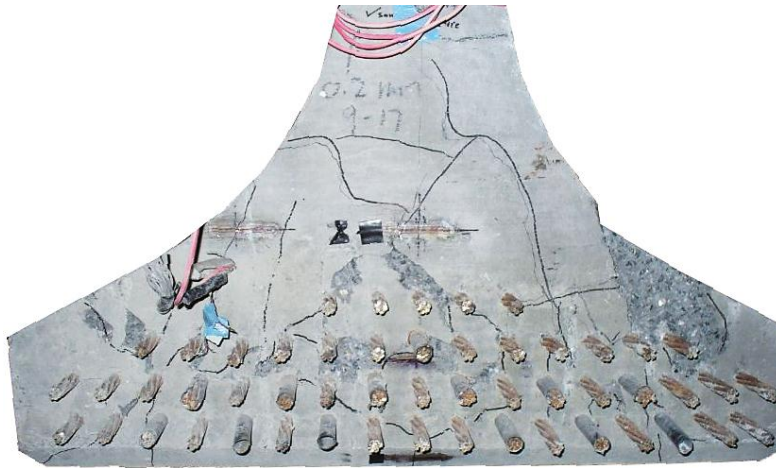


Figure 89–Cracks at end of HC after testing

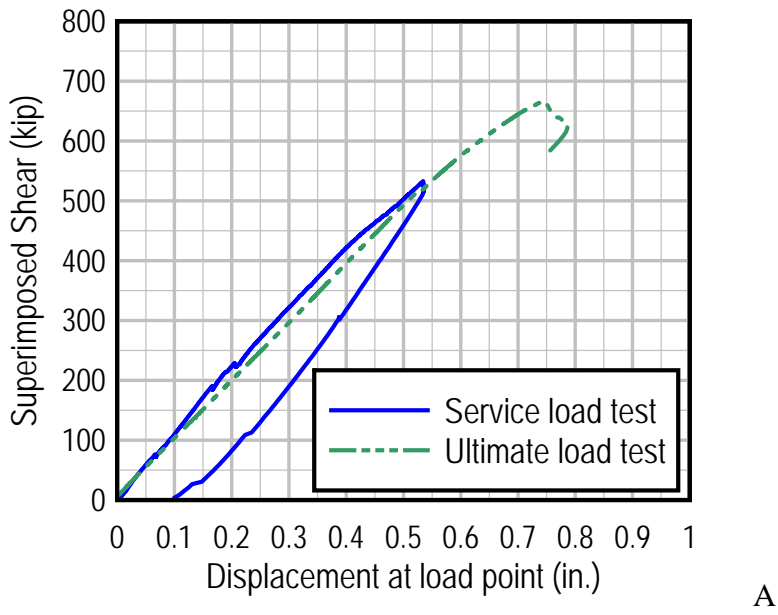
D.6.2.2 HU

Detailing of specimen HC (Figure 10) was effectively identical to the 2008 FDOT Interim Design Standards (FDOT, 2008), with the exception that no confinement reinforcement was placed in the bottom flange. Specimen HU had a bearing plate in the bottom flange, horizontal reinforcement in the end region, and the ‘design’ strand pattern (Figure 9) which included (39) fully bonded strands. Shear-displacement and crack pattern are shown in Figure 90.

Cracks in HU were first observed during the service load test at a shear of 215 kip. The first crack to be observed was a web crack inclined between the load point and support. Web cracks in specimen HU had a maximum width of 0.004 in. at a shear of 230kip, and partially closed to 0.002 in. after load was removed.

Following service load testing specimen HU was loaded to ultimate capacity. Stiffness decreased gradually as load increased beyond the level of the service load tests. Loss in stiffness is attributed to formation and growth of diagonal cracks. Web cracks that formed at lower loads were observed to spread into the bottom flange during the latter stages of testing. Flexural cracks were not observed.

Peak load in specimen HU corresponded to lateral-splitting failure in the bottom flange, which resulted in an abrupt loss of load (Figure 91, Figure 92). Specimen HU supported a maximum shear of 666 kip.



Release cracks not shown.

Initial crack shown bold in red

Final cracks shown blue.

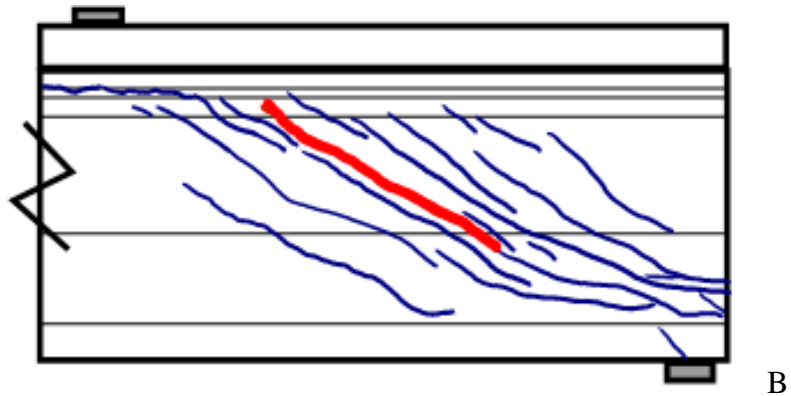


Figure 90–Specimen HU load test summary A) shear-displacement and B) crack pattern

Strand slip data are not shown in Figure 90. LVDT data indicate that strand slip was negligible at lower loads. At higher loads cracks caused shifting of the frame holding the LVDTs thereby compromising the strand slip data. Data from specimens with similar strand bond patterns and better instrumentation suggest that strand slip was not a contributing factor to in the failure of in specimens with the ‘design’ strand bond pattern.

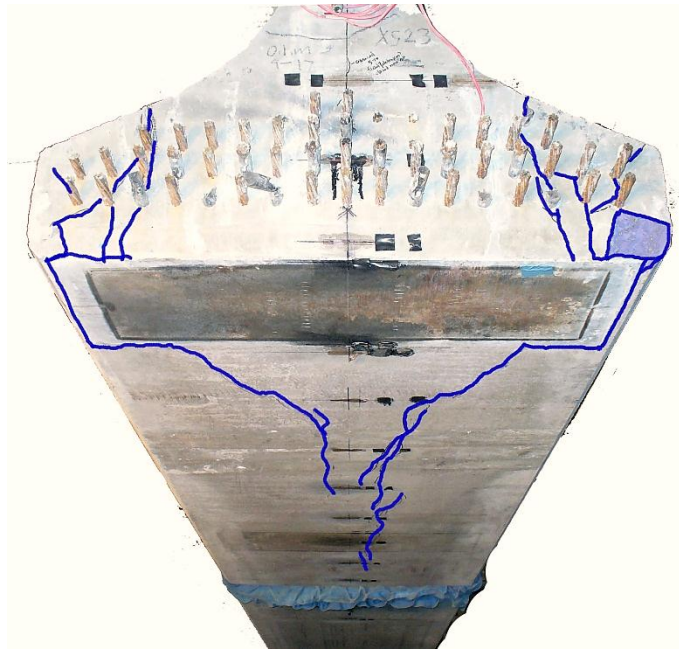


Figure 91–Bottom and end of HU after testing

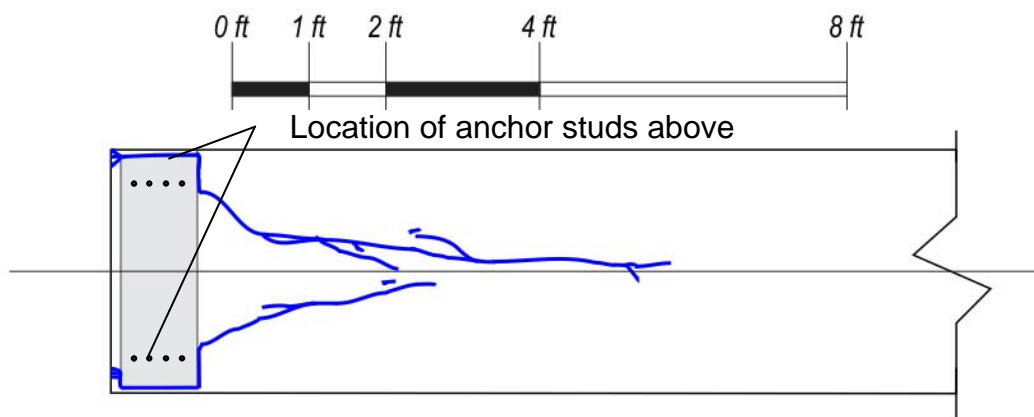
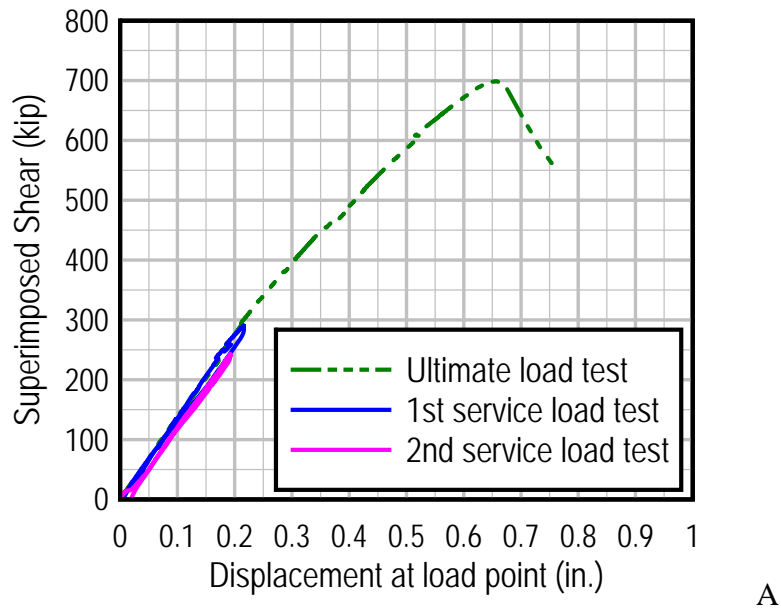


Figure 92–Bottom view of splitting cracks in HU

D.6.2.3 VC

Detailing of specimen VC (Figure 11) was similar to the 2008 FDOT Interim Design Standards (FDOT, 2008), with the exceptions that fewer vertical bars and no horizontal bars were placed in the end region. Other variables in specimen VC included FDOT specified confinement reinforcement and bearing plate in the bottom flange, and the ‘design’ strand bond

pattern (Figure 9) which included (39) fully bonded strands. Specimen VC failed in a web-shear failure mode. Shear-displacement and crack pattern are shown in Figure 93.



Release cracks not shown.
 Initial crack shown bold in red.
 Final cracks shown in blue.

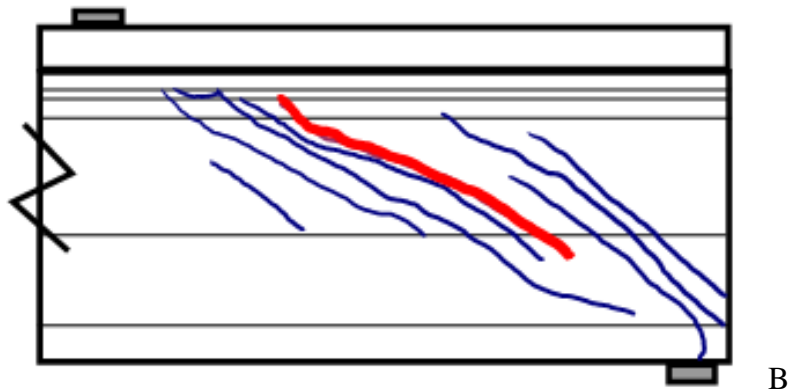


Figure 93–Specimen VC load test summary A) shear-displacement and B) crack pattern

Cracking in VC was first observed during service load testing at a shear of 240 kip. An inclined web crack between the load point and support was the first to be observed. Cracks in specimen VC partially closed during the unloading stage of the service load test. Web cracks in

VC had a maximum width of 0.014 in. at a shear of 290kip, and 0.002 in. after load was removed.

Following the service load testing specimen VC was loaded to ultimate capacity. Stiffness decreased gradually as load increased beyond the level of the service load tests. Because flexural cracks were not observed, the loss in stiffness is attributed to formation and growth of diagonal cracks. Ultimate capacity was signaled by web crushing followed immediately by movement of the portion of the specimen above the inclined cracks relative to that below the inclined crack (Figure 94). Areas of the web surface spalled due to the crushing. Spalling also occurred in the web below the load point, however this was a secondary effect occurring immediately after the load had dropped. No splitting cracks were observed on the bottom of the specimen.

Failure of VC is classified as a web-shear failure. Loss of capacity after the web-shear failure was abrupt. Specimen VC supported a maximum shear of 698 kip.

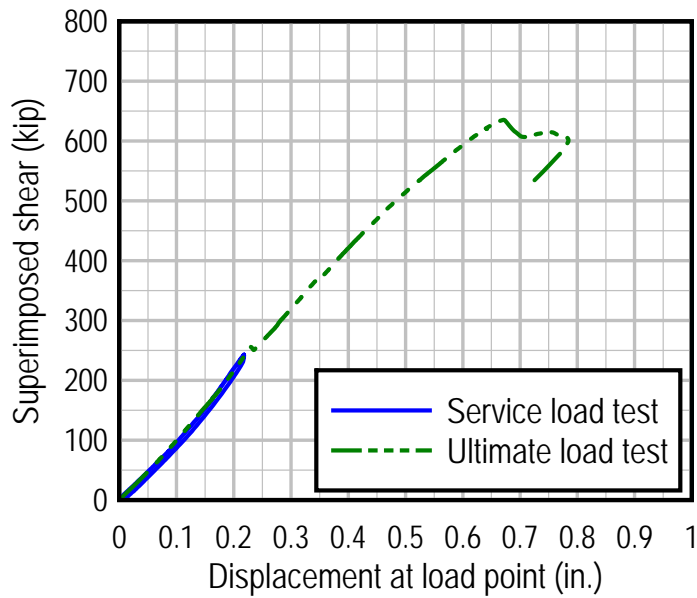
Strand slip data are not shown in Figure 93. LVDT data indicate that strand slip was negligible at lower loads. At higher loads cracks caused shifting of the frame holding the LVDTs thereby compromising the strand slip data. Data from specimens with similar strand bond patterns and better instrumentation suggest that strand slip was not a contributing factor to in the failure of in specimens with the 'design' strand bond pattern.



Figure 94–VC after load test

D.6.2.4 VU

Specimen VU (Figure 11) had the least amount of reinforcement of any specimen in the test program. Variables in specimen VU included no confinement reinforcement, no horizontal reinforcement and reduced vertical reinforcement in the end region. Specimen VU had a bearing plate in the bottom flange and had the ‘design’ strand bond pattern (Figure 9) which included (39) fully bonded strands. Shear-displacement and crack pattern are shown in Figure 95.

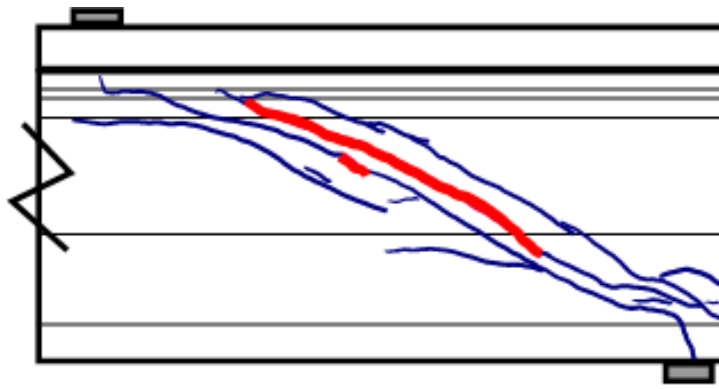


A

Release cracks not shown.

Initial cracks shown bold in red.

Final cracks shown blue.



B

Figure 95–Specimen VU load test summary A) shear-displacement and B) crack pattern

Cracks in VU were first observed during the service load test at a shear of 243 kip. The first crack to be observed was a web crack inclined between the load point and support. Web cracks in specimen VU had a maximum width of 0.001 in. at a shear of 243kip, and did not change in width as load was removed after the service load test.

Following service load testing specimen VU was loaded to ultimate capacity. Stiffness decreased gradually as load increased beyond the level of the service load tests. Loss in stiffness

is attributed to formation and growth of diagonal cracks. Web cracks that formed at lower loads were observed to spread into the bottom flange during the latter stages of testing. Flexural cracks were not observed.

Peak load in specimen HU corresponded to lateral-splitting failure in the bottom flange, which resulted in an abrupt loss of load (Figure 96). Specimen VU supported a maximum shear of 635 kip.

Strand slip data are not shown in Figure 95. LVDT data indicate that strand slip was negligible at lower loads. At higher loads cracks caused shifting of the frame holding the LVDTs thereby compromising the strand slip data. Data from specimens with similar strand bond patterns and better instrumentation suggest that strand slip was not a contributing factor to in the failure of in specimens with the ‘design’ strand bond pattern.

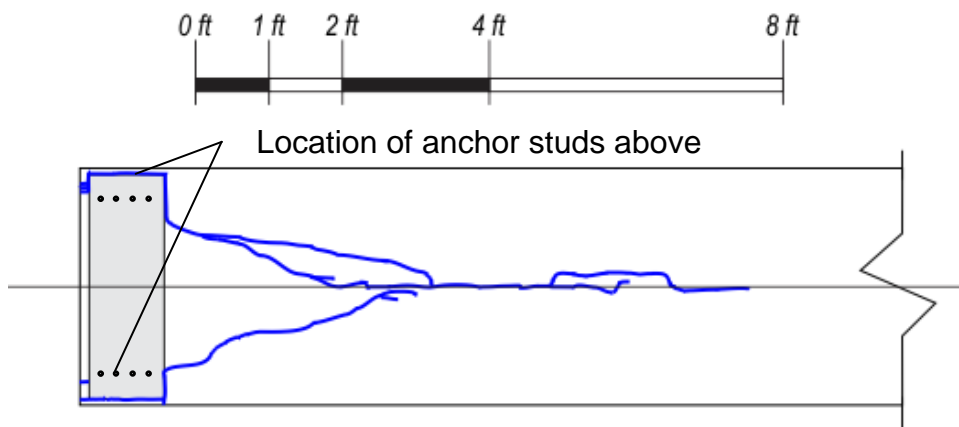
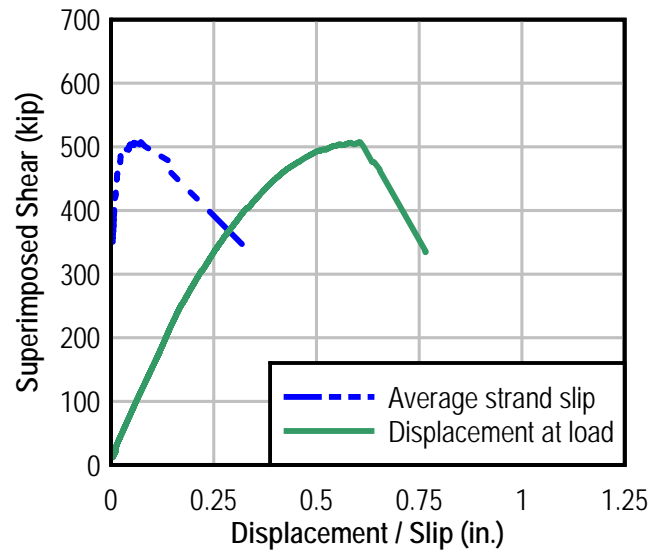


Figure 96–Bottom view of splitting cracks in VU

D.6.2.5 WN

The primary features of specimen WN (Figure 21) were the lack of an embedded bearing plate and the ‘web’ strand bond pattern (Figure 9) that placed (20) fully bonded strands below the web. Four additional strands were fully bonded at the edges of the flange, resulting in a total of (24) fully bonded strands. Other variables in WN included no horizontal bars in the end region and modified confinement reinforcement. The modified confinement scheme had fewer, but larger, bars than specified by the FDOT. Shear-displacement, shear-slip and crack pattern results for specimen WN are shown in Figure 97.

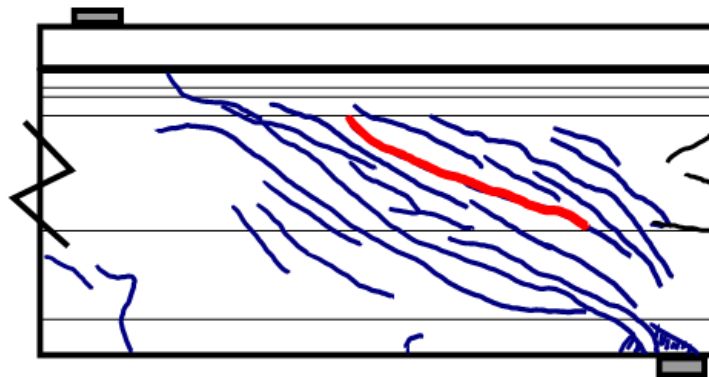


A

Release cracks shown black.

Initial crack shown bold in red.

Final cracks shown blue.



B

Figure 97–Specimen WN load test summary A) shear-displacement/slip and B) crack pattern

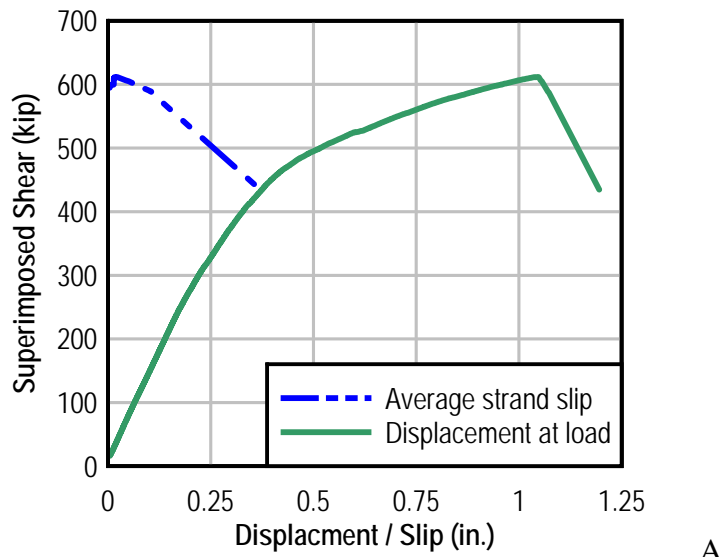
Cracking in WN was first observed during service load testing at a shear of 198 kip. An inclined web crack between the load point and support was the first to be observed. Cracks widths in specimen WN partially closed during the unloading stage of the service load test.

Following service load testing specimen WN was loaded to ultimate capacity. Stiffness decreased gradually as load increased beyond the level of the service load tests. Loss of stiffness is attributed primarily to flexural cracks which were first observed at a shear of 435 kip. Strand-slip initiated at approximately the same load. Popping sounds indicative of strand slip were

heard with increasing frequency as the load approached a peak shear of 507 kip. At peak shear, the strands slipped suddenly resulting in opening of the crack in front of the bearing pad and a subsequent loss of load. Capacity of WN was limited by strand-concrete bond, and failure of WN is labeled as a bond-shear failure.

D.6.2.6 WB

The primary feature of specimen WB (Figure 21) was the ‘web’ strand bond pattern (Figure 9) that placed (20) fully bonded strands below the web. Four additional strands were fully bonded at the edges of the flange, resulting in a total of (24) fully bonded strands. Other variables in WN included presence of an embedded bearing plate, and modified confinement reinforcement. The modified confinement scheme had fewer, but larger, bars than specified by the FDOT. Shear-displacement, shear-slip and crack pattern results for specimen WB are shown in Figure 98.



Release cracks shown black.
 Initial crack shown bold in red.
 Final cracks shown blue.

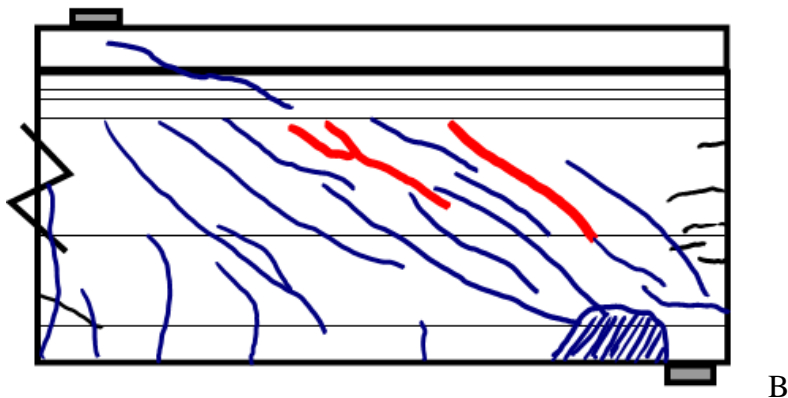


Figure 98–Specimen WB load test summary A) shear-displacement/slip and B) Crack pattern

Cracking in WB was first observed during service load testing at a shear of 175 kip. An inclined web crack between the load point and support was the first to be observed. Cracks widths in specimen WB partially closed during the unloading stage of the service load test.

Following service load testing specimen WB was loaded to ultimate capacity. Stiffness decreased gradually as load increased beyond the level of the service load tests. Loss of stiffness

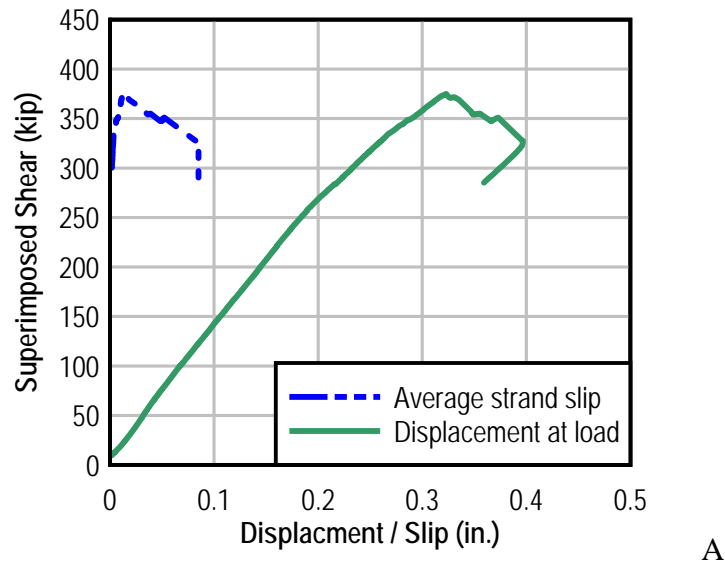
is attributed primarily to flexural cracks which were first observed at a shear of 380 kip. The first flexural crack occurred below the load and intersected cracks in the flange that had formed prior to load testing due to prestress transfer. Additional flexural cracks were observed at a shear of 494 kip.

Specimen WB had the greatest ductility and reached the largest displacement of any test specimen. The displacement at peak load was approximately 1.05in. Peak shear for WB was 612 kip. At peak shear the strands slipped abruptly and the crack in front of the bearing pad opened suddenly. Strand slip and cracking resulted in a sudden loss of load.

The bearing plate and confinement reinforcement in specimen WB maintained the structural integrity of the bottom flange above the bearing throughout load testing. Because the bottom flange held together above the bearing, the strand-concrete bond was also maintained at high load levels in WB. Capacity of the WB was governed by strand-concrete bond, and failure of WB is labeled as a bond-shear failure.

D.6.2.7 FN

The primary features of specimen FN (Figure 22) were lack of an embedded bearing plate and the 'flange' strand bond (Figure 9) pattern that placed (24) fully bonded strands in the outer portions of the bottom flange. Other variables in FN included no horizontal bars in the end region and modified confinement reinforcement. The modified confinement scheme had fewer, but larger, bars than specified by the FDOT. Shear-displacement, shear-slip and crack pattern results for specimen FN are shown in Figure 99.



Release cracks shown black.
 Initial crack shown bold in red.
 Final cracks shown blue.

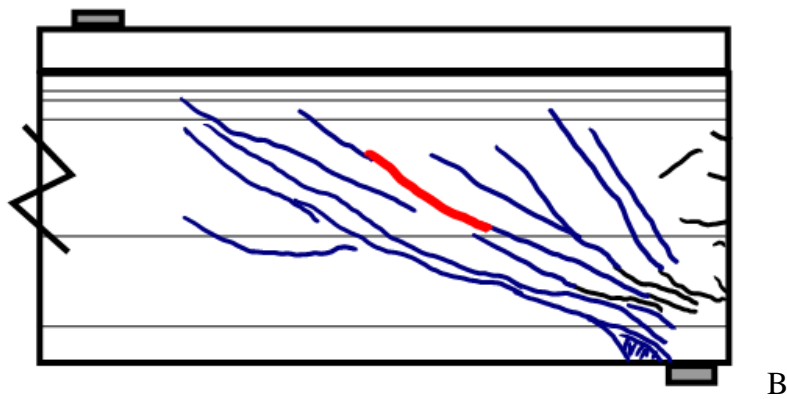


Figure 99–Specimen FN load test summary A) shear-displacement/slip and B) crack pattern

Cracking in FN was first observed during service load testing at a shear of 174 kip. An inclined web crack between the load point and support was the first to be observed. Additional inclined cracks formed and intersected splitting cracks in the bottom flange that had formed prior to load testing due to prestress transfer. Shear in the service load test reached 237kip, but for safety reasons the load was immediately removed and cracks were marked after the specimen was unloaded. The concern with specimen FN was that the strand bond pattern and lack of a

bearing plate could affect a sudden failure. Cracks widths in specimen FN partially closed during the unloading stage of the service load test.

Following service load testing specimen FN was loaded to ultimate capacity. Stiffness decreased as load increased beyond the level of the service load tests, but not to the degree observed with other specimens. Loss of stiffness is attributed to formation and growth of diagonal cracks. Web cracks that formed at lower loads were observed to spread into the bottom flange during the latter stages of testing. Flexural cracks were not observed.

Specimen FN reached a peak shear of 375 kip. This was the smallest peak of any specimen in the test program. At peak shear the strands slipped suddenly and the crack in front of the bearing opened. Slip and cracking was accompanied by a subsequent drop in load. Failure of specimen FN is labeled as a lateral-splitting failure because failure occurred in large part due to transverse splitting cracks in the bottom flange.

Failure of specimen FN can be understood by considering the strut-and-tie model shown in Figure 100. During latter stages of the ultimate load test, shear load was carried through the web into the bottom flange by concrete compression struts. Once in the bottom flange the load split into three separate load paths. The two outer paths connected to nodes at the fully bonded outer stands. The inner path was in the same plane as the web and connected to an inner node above the centerline of the bearing pad. At outer nodes equilibrium in the y-direction was maintained by tie forces in the strands. Y-direction equilibrium at the inner node was maintained by tension force in the concrete. At peak load strands at the outer nodes slipped and the crack in front of the bearing pad propagated into the center of the bottom flange thereby cutting the concrete tie (Figure 101).

The strut-and-tie concept shown in Figure 100 is supported by strain data from the confinement reinforcement which formed the transverse tie between the outside nodes. Strain in the confinement reinforcement increased after peak load. Once the concrete tension tie failed at peak load, force from the inner load path transferred to the outer load paths. Accordingly, additional force was generated in the confinement reinforcement to maintain x-direction equilibrium at the outer nodes. This additional force is responsible for the post-peak increase in strain observed in the confinement reinforcement (Figure 102).

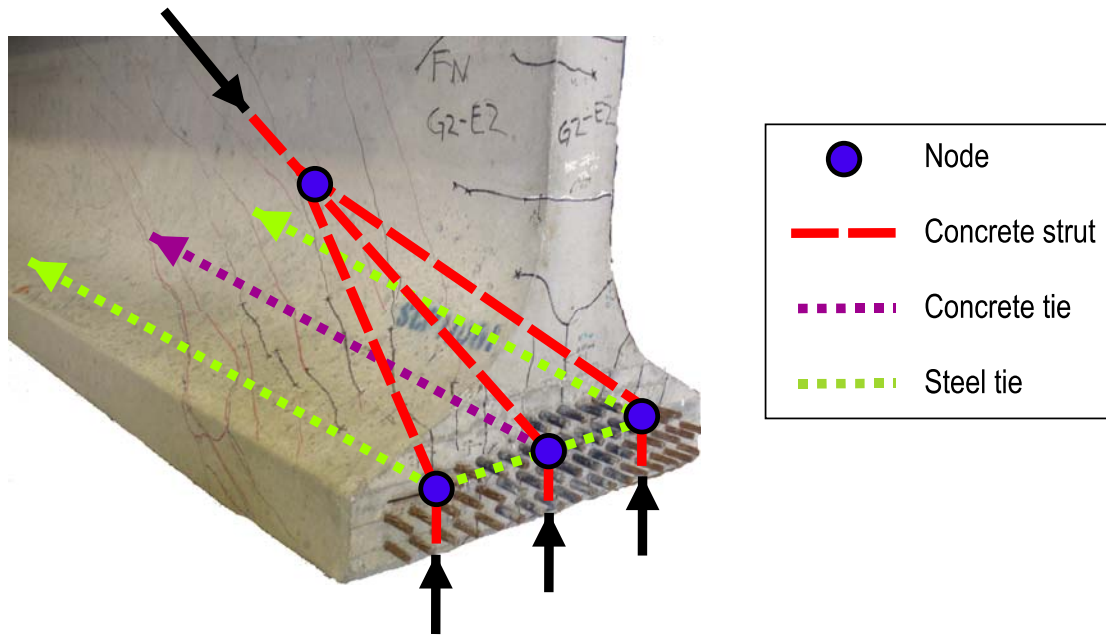


Figure 100–Strut and tie behavior specimen FN

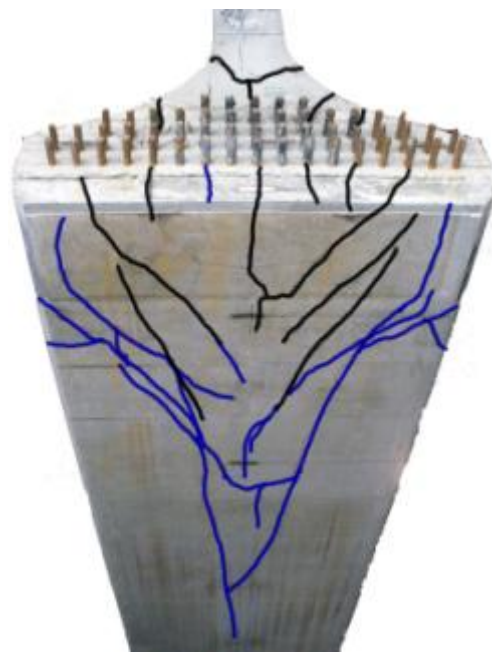


Figure 101–Longitudinal splitting cracks on bottom of specimen FN (release cracks shown black; final cracks shown blue)

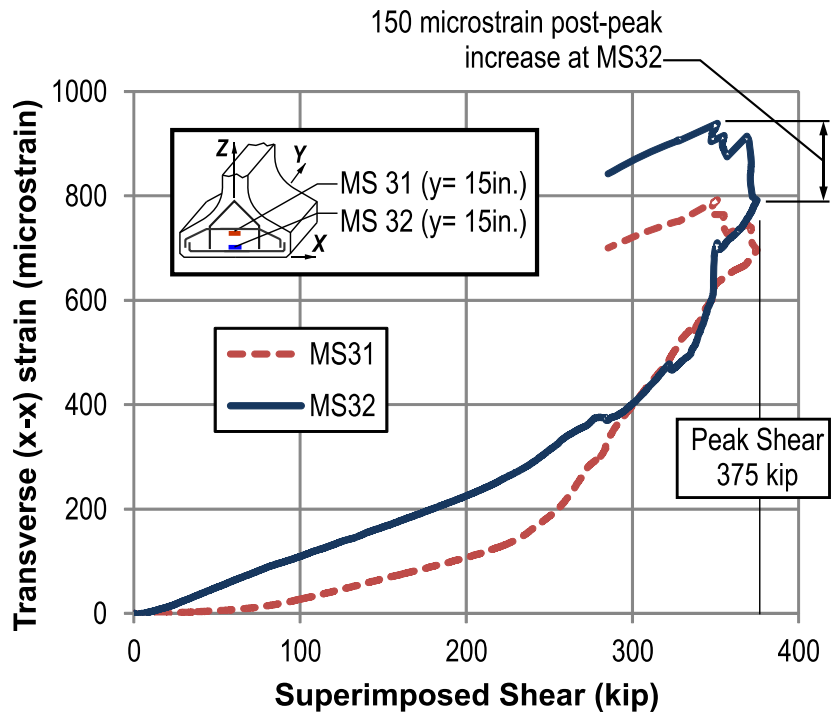


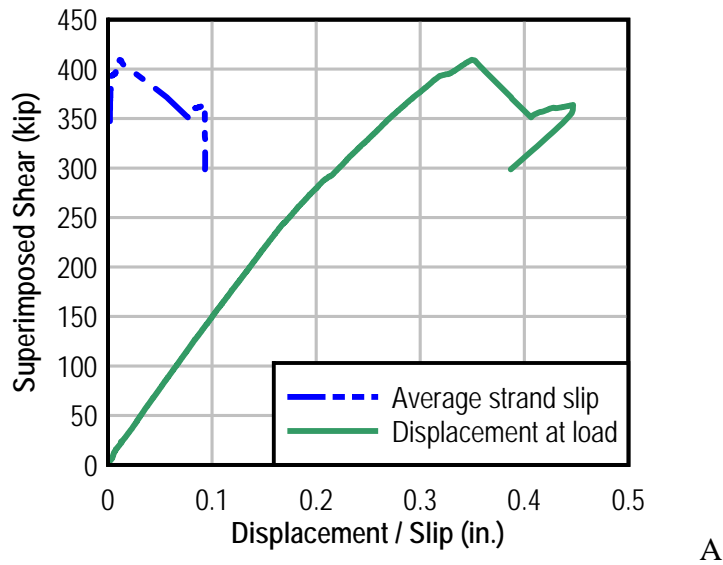
Figure 102–Confinement reinforcement strain specimen FN

D.6.2.8 FB

The primary features of specimen FB (Figure 22) were an embedded bearing plate and the ‘flange’ strand bond pattern (Figure 9) that placed (24) fully bonded strands in the outer portions of the bottom flange. Other variables in FB included no horizontal bars in the end region and modified confinement reinforcement. The modified confinement scheme had fewer, but larger, bars than specified by the FDOT. Shear-displacement, shear-slip and crack pattern results for specimen FB are shown in Figure 103.

Cracking in FB was first observed during service load testing at a shear of 158kip. An inclined web crack between the load point and support was the first to be observed. Cracks widths in specimen FB partially closed during the unloading stage of the service load test.

Following service load testing specimen FB was loaded to ultimate capacity. Specimen FB reached a peak shear of 409 kip. Failure of FB is categorized as a later-splitting failure. Circumstances and failure behavior of specimen FB were the same as those reported for specimen FN. As such, a detailed description of the failure mode is not repeated here.



Release cracks shown black.
 Initial crack shown bold in red.
 Final cracks shown blue.

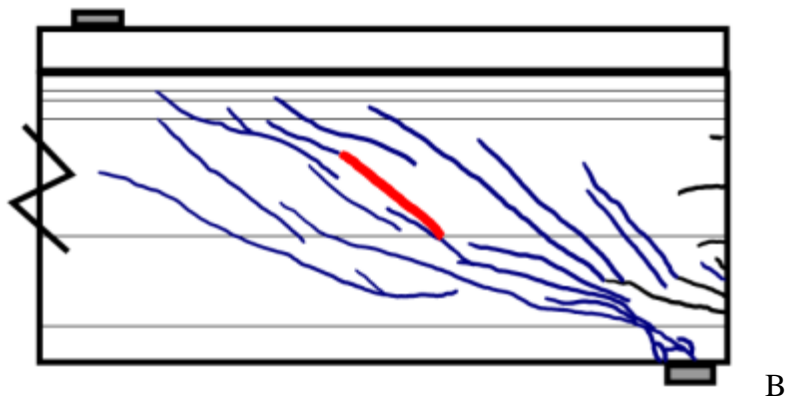


Figure 103–Specimen FB load test summary A) shear-displacement/slip and B) crack pattern

D.6.2.9 DC

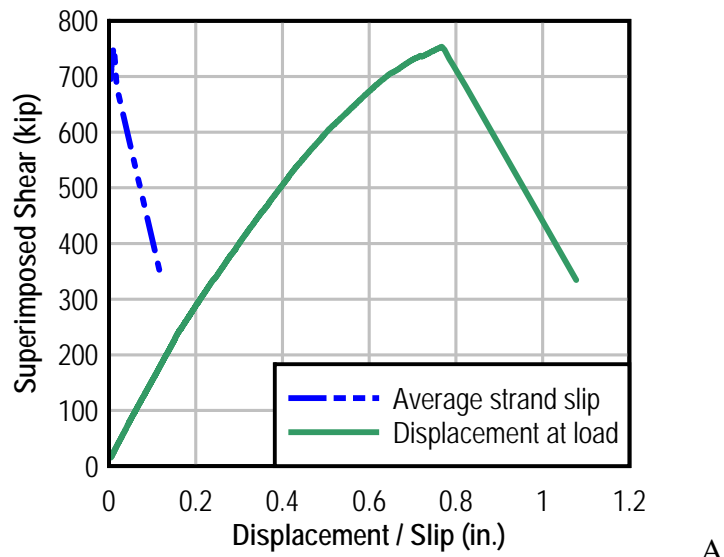
Specimen DC (Figure 23) was detailed according to the 2010 FDOT Interim Design Standards (FDOT, 2010). Variables in specimen DC included FDOT specified confinement reinforcement and bearing plate in the bottom flange, no horizontal reinforcement in the end region, and the ‘design’ strand pattern (Figure 9) which had (39) fully bonded strands. Shear-displacement, shear-slip, and crack pattern are shown in Figure 104.

Cracks in DC were first observed during the service load tests at a shear of 174 kip. Inclined web cracks between the load point and support were the first to be observed. Cracks partially closed during the unloading stage of the service load test.

Following service load testing specimen DC was loaded to ultimate capacity. Stiffness decreased gradually as load increased beyond the level of the service load tests. Because flexural cracks were not observed, the loss in stiffness is attributed to formation and growth of diagonal cracks.

Ultimate capacity was signaled by web crushing followed immediately by movement of the portion of the specimen above the inclined cracks relative to that below the inclined crack. This failure is classified as a web-shear failure. Loss of capacity after the web-shear failure was abrupt. Specimen HC supported a maximum shear of 753 kip.

Figure 104 shows that strand slip in specimen DC was negligible prior to the peak load. Strand slip reported in the figure after peak load was likely exaggerated by cracking of the bottom flange at the end of the load test. Lack of slip observed in DC and other specimens with the 'design' strand bond pattern is attributed to the relatively large quantity of strands.



Release cracks shown black.
 Initial crack shown bold in red.
 Final cracks shown blue.

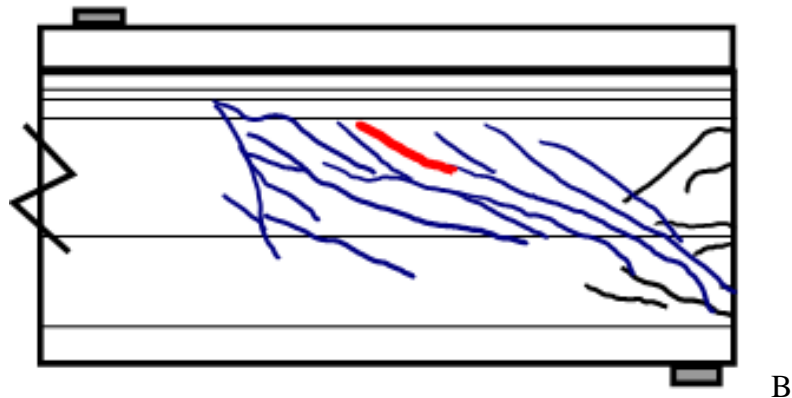


Figure 104–Specimen DC load test summary A) shear-displacement/slip and B) crack pattern

D.6.2.10 DM

Detailing of specimen HC (Figure 23) was effectively identical to the 2010 FDOT Interim Design Standards (FDOT 2010), with the exception that the modified confinement reinforcement scheme was used in the bottom flange. Modified confinement had fewer, but larger, bars than specified by the FDOT. Other variables in specimen DM included a bearing plate in the bottom flange, no horizontal reinforcement in the end region, and the ‘design’ strand

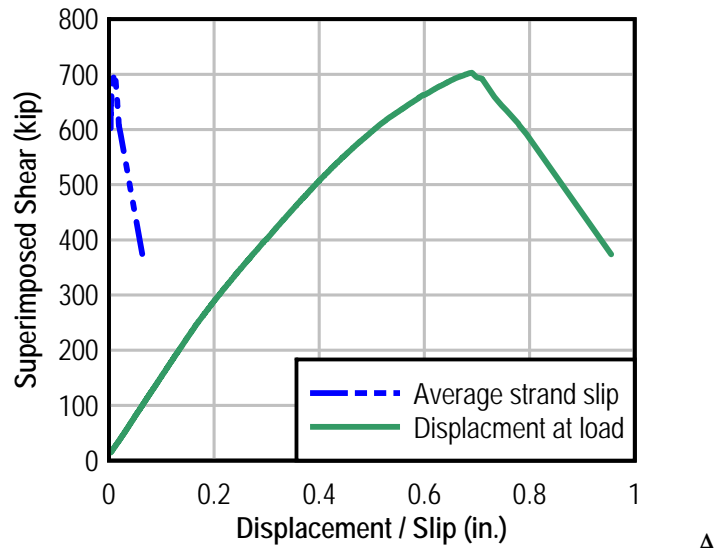
pattern (Figure 9) which had (39) fully bonded strands. Shear-displacement, shear-slip and crack pattern results for specimen DM are shown in Figure 105.

Cracks in DM were first observed during the service load tests at a shear of 166 kip. Inclined web cracks between the load point and support were the first to be observed. Cracks partially closed during the unloading stage of the service load test.

Following service load testing specimen DM was loaded to ultimate capacity. Stiffness decreased gradually as load increased beyond the level of the service load test. Because flexural cracks were not observed, the loss in stiffness is attributed to formation and growth of diagonal cracks.

Failure of specimen DM was a hybrid between lateral-splitting and web-shear. At peak load one of the inclined cracks had a suddenly increased in width. The load dropped approximately 5 kip after the crack opened. Opening of the crack and loss in load occurred in-part due to peeling movement of the bottom flange. Loading continued for approximately 15 sec until the web crushed and the load fell abruptly. After web crushing the top portion of the specimen slid along the cracking plane relative to the lower portion. Concrete spalled away from the web on both sides of the specimen during the web failure. Specimen DM supported a maximum shear of 703 kip. Longitudinal splitting cracks were observed on the bottom of DM after testing, indicative of lateral-splitting failure.

Figure 105 shows that strand slip in specimen DM was negligible prior to the peak load. Strand slip reported in the figure after peak load was likely exaggerated by cracking of the bottom flange at the end of the load test. Lack of slip observed in DM is attributed to the relatively large quantity of strands.



Release cracks shown black.
 Initial crack shown bold in red.
 Final cracks shown blue.

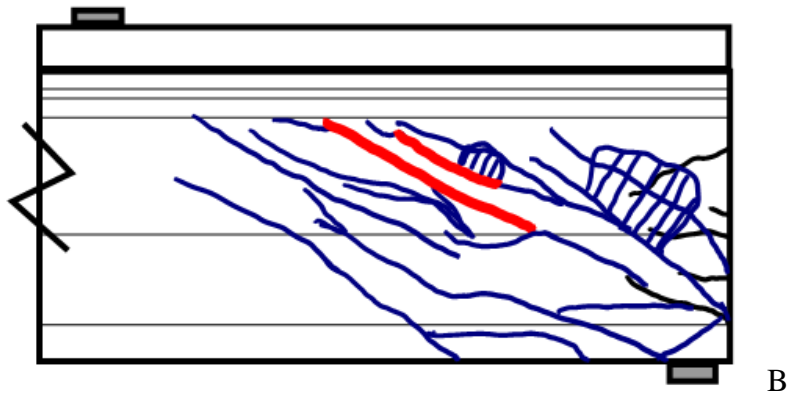


Figure 105–Specimen DM load test summary A) shear-displacement/slip and B) crack pattern

D.6.3 Confinement Reinforcement and Bearing Plates

Strain gages were used to monitor bearing plates and select confinement reinforcement assemblies during load testing. Strain data were then used to calculate stresses and forces in the confinement reinforcement and bearing plates. Stresses and forces were calculated at a shear of 375 kip and at each specimen’s maximum capacity. Analyses were conducted at a shear of 375 kip because this force corresponds to the maximum capacity of specimen FN. It is also near the factored shear force in the prototype bridge from which some the specimens were designed.

D.6.3.1 Girders W and F

Confinement reinforcement strain in specimens WN, WB, FN, and FB was monitored during prestress transfer and during load testing. Bearing plate strain was also monitored in WB and FB. Strain from prestress transfer and load testing were superimposed to determine total strain in the confinement reinforcement and bearing plates. It was assumed that strain did not change between prestress transfer and load testing. Although it is unlikely that strain was constant, it is necessary to make this assumption in order to estimate total strain.

Specimens WN, WB, FN, and FB each had the modified confinement reinforcement scheme (Figure 15) which placed five assemblies of confinement reinforcement above the bearing. Three of the five assemblies in each specimen were instrumented with gages (Figure 106). Gages were placed to measure the transverse (x-x) strain.

Combined strain from prestress transfer and load testing was multiplied by the steel modulus of elasticity to determine stress in the confinement reinforcement. Data indicate that confinement stresses were typically less than yield stress. One bar in specimen FN and one bar in WN had reached yield stress as ultimate load. Average stresses for each specimen at a shear force of 375 kip are shown in Figure 107. Figure 108 shows average stresses at ultimate capacity.

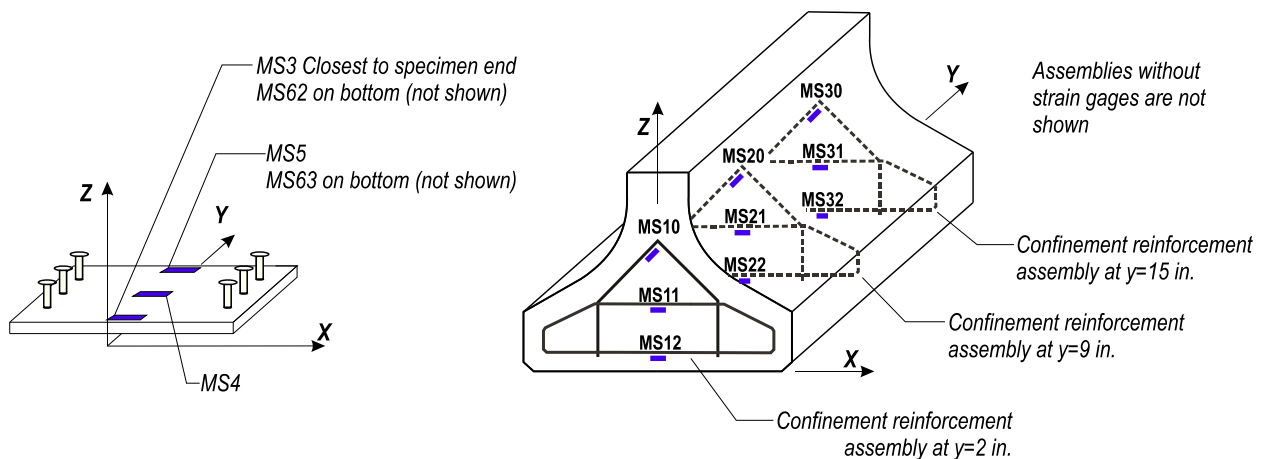


Figure 106–Strain gage placement girders W, F, and D

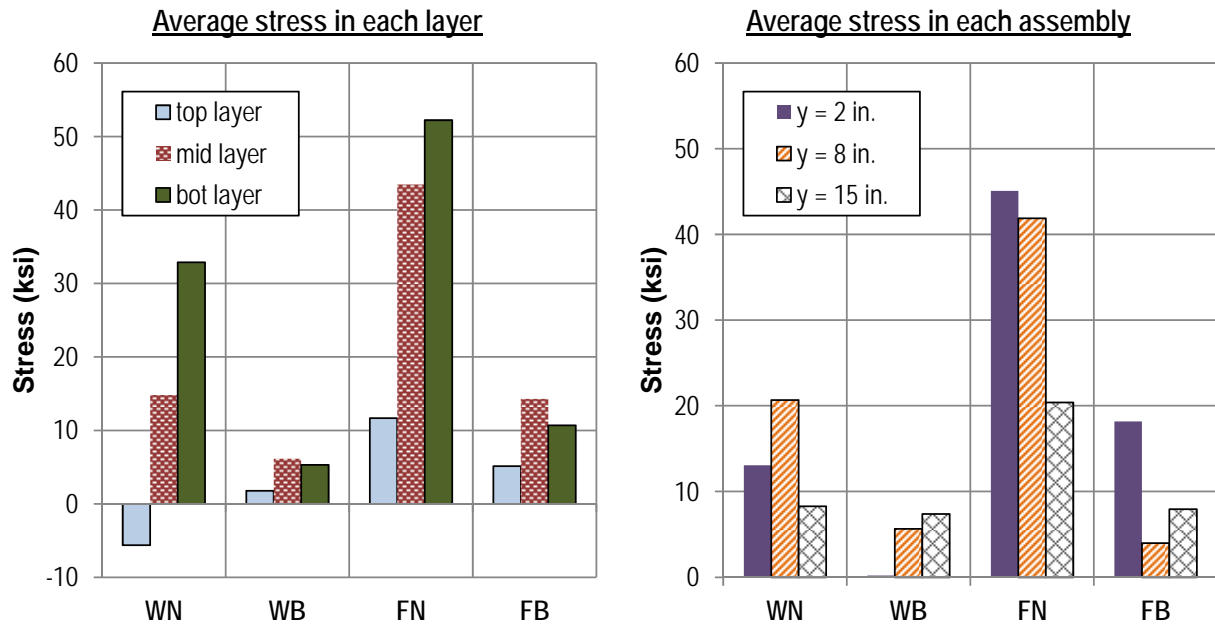


Figure 107–Confinement stress at shear = 375 kip

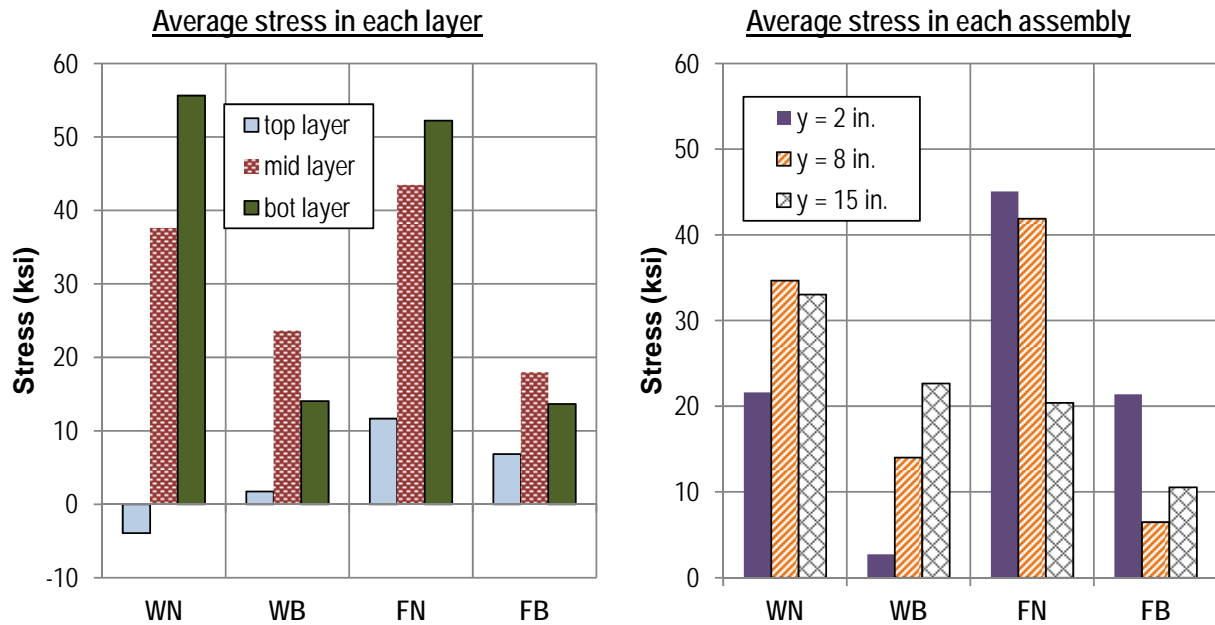


Figure 108–Confinement stress at ultimate capacity

The largest stresses occurred in specimens WN and FN, which did not have bearing plates. At a shear of 375 kip, the average confinement stress in WN and FN was 3.5 times

greater than the average stress in the specimens with bearing plates (WB and FB). At ultimate load the average stress in WN and FN was 2.5 times greater than WB and FB. These differences in stress are attributed to the presence of the steel bearing plate in WB and FB. The stiffness of the plate attracted transverse forces thereby reducing the forces (and stress) in the confinement reinforcement.

Average confinement stress varied according to the reinforcement layer. Average stresses in the middle and bottom layers were 6 to 8 times greater than stress in the top layer. It is believed that tension formed in the bottom flange as shear was delivered from the relatively narrow web to the wider bearing pad. This tension was likely the cause of the greater stress in the bottom and middle layers of confinement. Analytical modeling is presented in Chapter 8 to explore this effect.

Stress distribution in the confinement reinforcement also varied in the y-direction. For specimens with fully bonded strands placed below the web (WN and WB) the average stress in reinforcement at 8in. and 15in. was 1.6 to 2.1 times greater than the stress in reinforcement at 2in. The opposite trend was observed in specimens with fully bonded strands placed in the outer flange (FN and FB). Average stress in reinforcement 2in. from the end of FN and FB was typically 2 times greater than average stress in reinforcement placed at 15in. Similar trends were noted in confinement behavior at prestress transfer as discussed in Chapter D.6. The mechanics presented in Figure 58 and Figure 59 are believed to be culpable in the stress changes observed in stress in the y-direction. Discussion of these mechanics can be found in Chapter D.6 and are not repeated here.

Strand bond pattern also affected the magnitude of the average stresses. At a shear of 375 kip, confinement reinforcement in specimens FN and FB had an average stress that was 2.5 times greater than the average stress in WN and WB. The additional stress in FN and FB is attributed to strand bond pattern which placed fully bonded strands in the outer portion of the flange. This pattern caused transverse tension as described in Figure 84.

Transverse forces in confinement reinforcement and bearing plates (WB and FB only) were estimated by multiplying transverse stresses by the respective cross-sectional areas. Linear interpolation was used to estimate forces in the confinement assemblies that were not monitored with gages. Results are presented in Table 31. Forces from reinforcement with compressive

stress were not included in the results. Only the x-direction components of forces in the top layer were included.

Total transverse force between specimens WN and WB was consistent, suggesting that the presence of a bearing plate did not change the transverse force demand in these specimens.

Transverse forces in specimens FN and FB were not consistent. The bearing plate specimen (FB) had approximately 50% less transverse force. The difference in force between FB and FN is attributed to the bearing plate mechanics in specimen FB. Experimental data indicate that the bearing plate in FB carried an in-plane bending moment during loading. This behavior resulted in tensile and compressive forces in the bearing plate (Figure 109). The causes of the in-plane moment are the force and eccentricity of the outside strands (Figure 84). By carrying in-plane moment, the plate reduced the magnitude of transverse forces typically associated with the outer strands. In-plane bending of the plate in Specimen WB was not observed.

Table 31–Transverse forces in W and F specimens

		WN (kip)	WB (kip)	FN (kip)	FB (kip)
Shear of 375 kip	Confinement reinforcement	50	15	107	27
	Bearing plate	0	36	0	30
	Total	50	51	107	58
Ultimate load	Confinement reinforcement	95	40	107	35
	Bearing plate	0	70	0	30
	Total	95	111	107	65

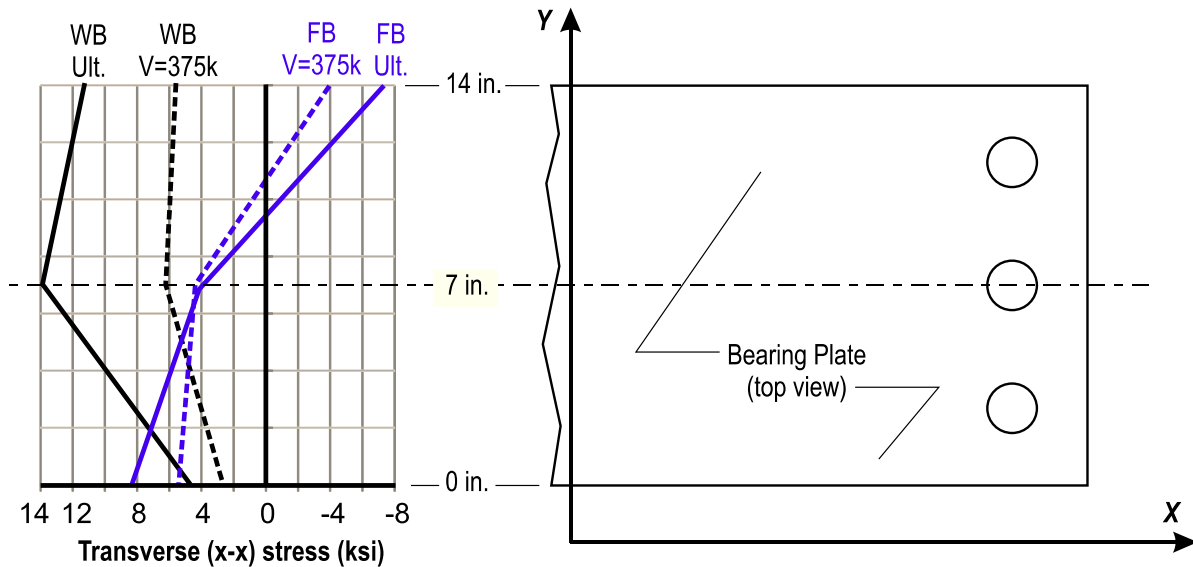


Figure 109–Transverse (x-x) stress profiles at bearing plate centerline

D.6.3.2 Girders H and V

Strain gages were placed on confinement reinforcement and bearing plates in specimens HC and VC to monitor strain during loading (Figure 110). Stresses and forces in these elements were estimated in the same manner as was done for specimens in girders W and F. Forces at ultimate load are shown in Figure 111, and are due to applied load only. Confinement strain data were not collected during prestress transverse in specimens VC and HC, and the effects of transfer are not included in Figure 111. In calculating the forces it was assumed the total strain in the confinement and plates was less than the yield strain. This assumption appears valid for HC and VC because yielding was only reached in two of the 36 bars that were monitored in girders W and F, and because the yielded bars occurred in specimens without bearing plates.

The estimated tensile force carried by all confinement reinforcement was 25.7 kip and 30.3 kip for specimens HC and VC, respectively. These forces equate to approximately 4% of the reaction at ultimate load. The largest confinement reinforcement forces occurred near the end of the specimens. At locations farther away from the end, the confinement reinforcement carried compressive forces, thus confirming the theoretical behavior presented in Figure 84.

The transition from tensile to compressive action in the confinement reinforcement is estimated to have occurred at distances approximately 40in. and 50in. from the specimen ends (Figure 111). The flexural depth (d) of the non-composite member was 49in. Comparing the distribution of confinement forces with the flexural depth shows that all tension in the

confinement reinforcement occurred within d of the member end. Current AASHTO LRFD requirements specify that confinement reinforcement must extend at least $1.5d$ from the member end. The experimental results suggest that this requirement is conservative, and that more effective placement of confinement reinforcement is possible. Other researchers (Tadros et al. 2010) have also suggested that the required distribution of confinement reinforcement should be reduced to less than $1.5d$.

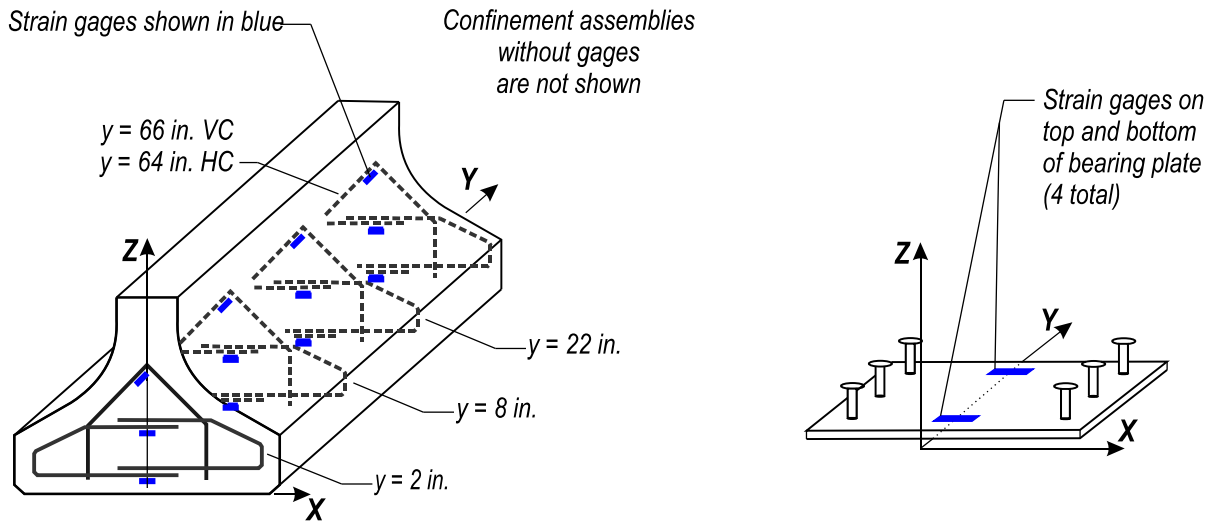
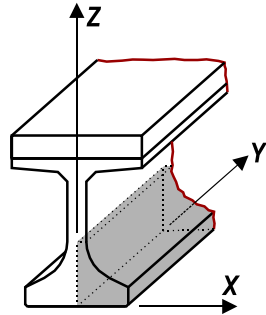
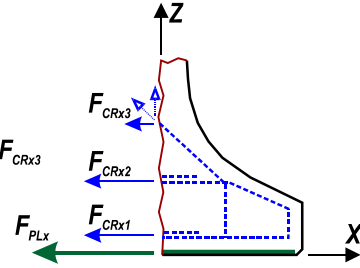


Figure 110—Strain gage placement girders H and V

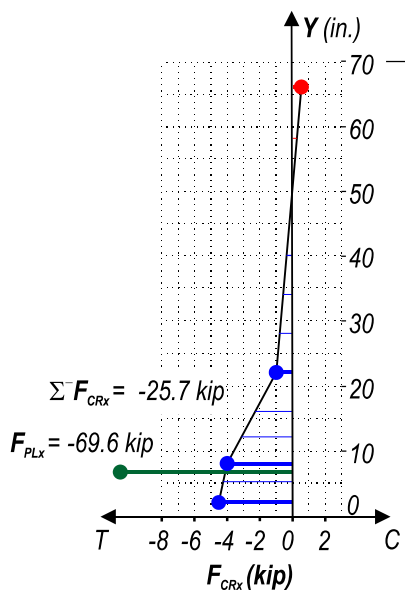


End region
isometric view

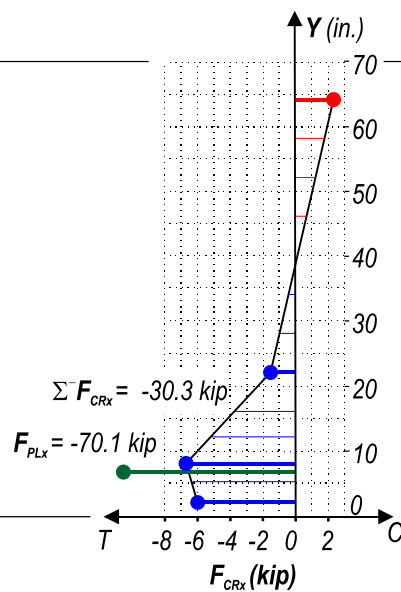
$$F_{CRx} = F_{CRx1} + F_{CRx2} + F_{CRx3}$$



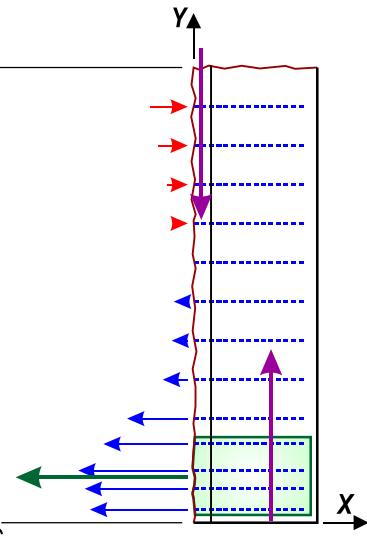
Bottom flange section
end view



Bottom flange forces
specimen HC



Bottom flange forces
specimen VC



Bottom flange section
partial plan view

Figure 111—Specimens HC and VC confinement reinforcement and bearing plate transverse (x-x) forces due to maximum applied load

D.6.3.3 Bearing Plates

Eight of the ten experimental specimens had embedded steel bearing plates. Strain in each bearing plate was monitored during load testing. Average stresses in the bearing plates were calculated by multiplying the average experimental strain by the elastic modulus. Bearing plate stresses due applied load (effects of prestress transfer not included) are presented in Figure 112. At ultimate load the average stresses ranged from 2.4 ksi (FB) to 10.6 ksi (VU). The

relatively low average stress in specimen FB was due to in-plane bending of the plate as discussed previously.

Bearing plate forces were calculated by multiplying the average stresses by the cross-section areas (Figure 113). Net tension force in the bearing plates at ultimate load ranged from 96.2 (VU) to 16.5 kip (FB). The average tension force at ultimate load was 62.9 kip.

Tension forces in the bearing plates are compared to the total transverse force in Figure 114. For this figure the total transverse force is defined as the combined transverse force in the bearing plate plus confinement reinforcement. Forces in Figure 114 are due to applied loads only. On average the bearing plates carried 60% to 71% of the total transverse force due to the applied load.

The portion of transverse force carried by the bearing plates at prestress transfer was evaluated using data from specimens WB and FB. As shown in Figure 115, contribution of the bearing plate at prestress transfer was affected by the strand bond pattern. The bearing plate in specimen FB (bonded strands in outer flange) carried almost 77% or the total transverse force at prestress transfer, whereas the plate in specimen WB (inner strands bonded) carried 52% of the transverse force at transfer.

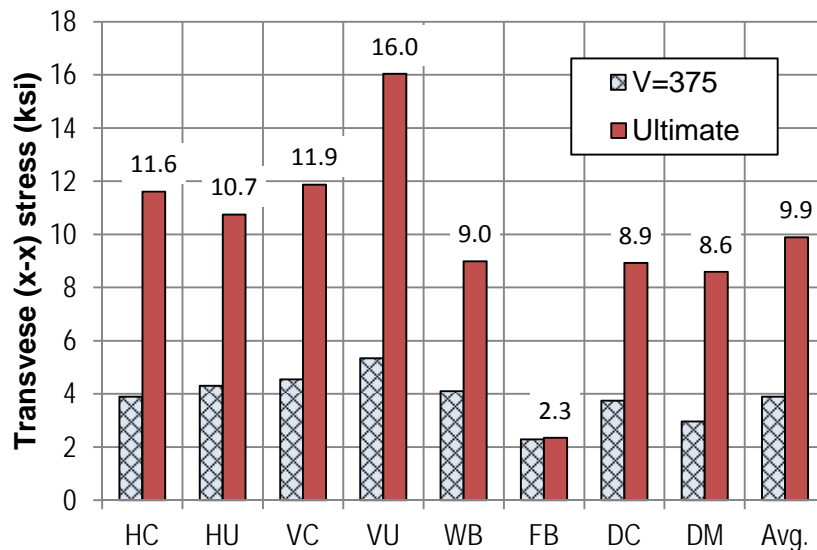


Figure 112–Bearing plate stress due to applied load

Experimental data presented in this section indicate that bearing plates in FIB girders will typically carry more than 50% of transverse splitting forces. Thus for purposes of designing

confinement reinforcement it is conservative to assume that the bearing plate will carry no more than 50% of transverse force.

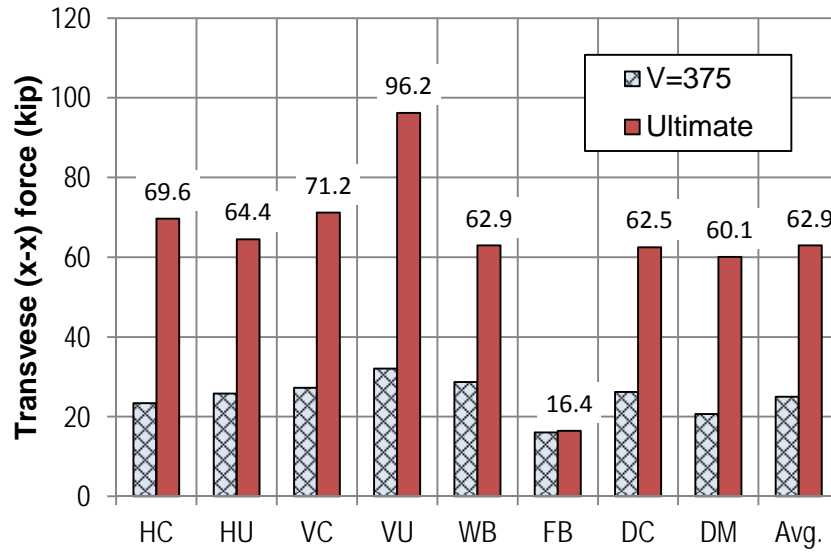


Figure 113–Bearing plate force due to applied load

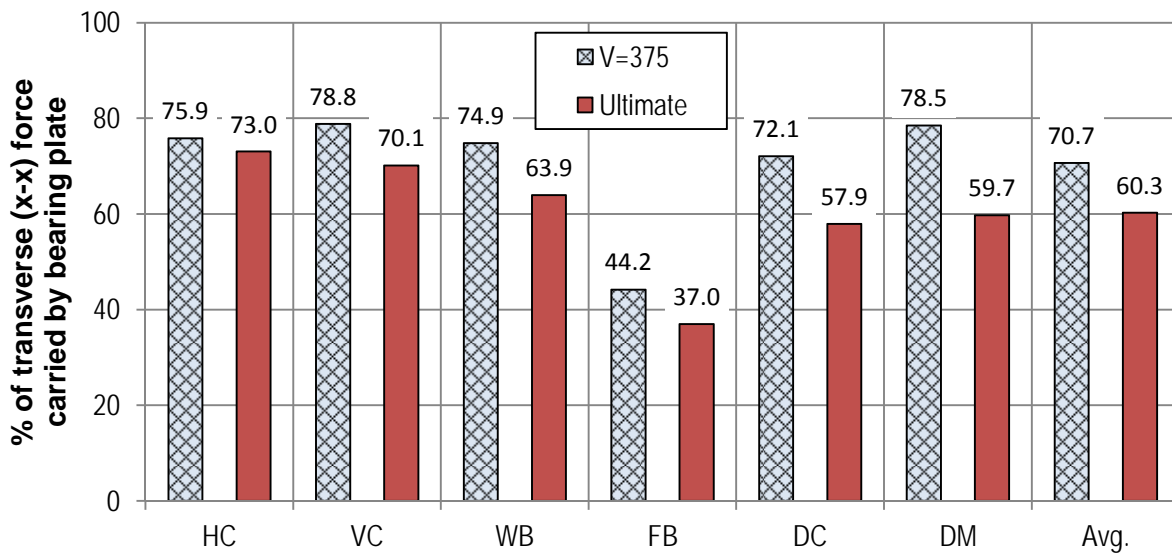


Figure 114–Percent of transverse force due to applied loads carried by bearing plate

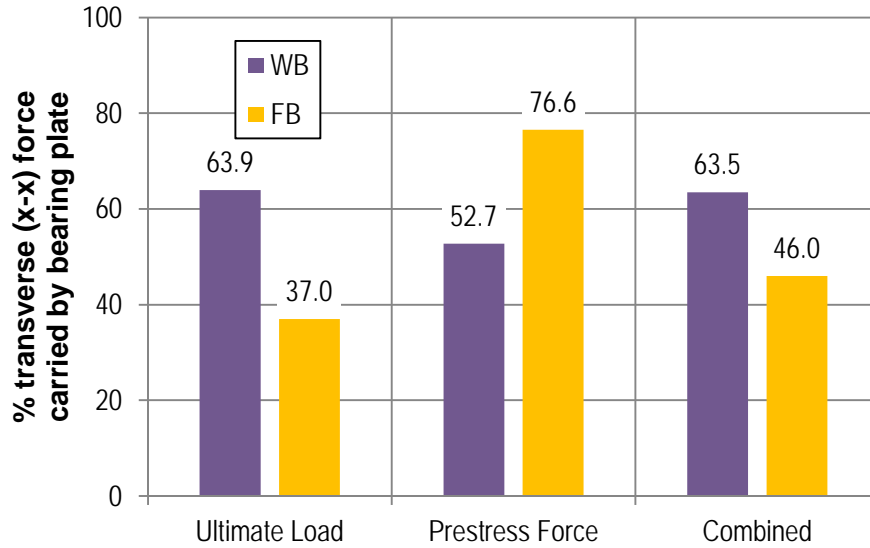


Figure 115–Percent of transverse force carried by bearing plate in WB and FB

D.6.4 Variable Comparisons

Maximum superimposed shear for each specimen are reported in Figure 116 and Table 32. Values ranged from a high of 766 kip (HC) to a low of 375 kip (FN), with an average of 612 kip. The large degree of variation in these results is a testament to the effect that detailing can have on end region behavior and capacity, even for members having the same cross-section and materials properties. Effects of the variables are discussed below and are summarized in Table 33.

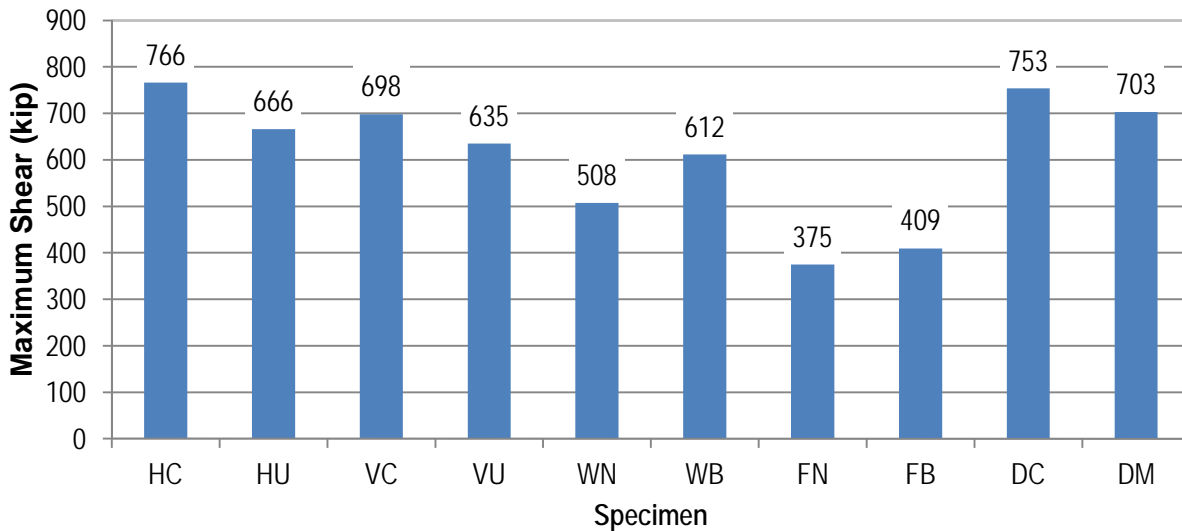


Figure 116–Maximum superimposed shear

Table 32–Maximum superimposed shear

Specimen	Maximum superimposed shear (kip)	Maximum shear / average shear
HC	766	1.25
HU	666	1.09
VC	698	1.14
VU	635	1.04
WN	507	0.83
WB	612	1.00
FN	375	0.61
FB	409	0.67
DC	753	1.23
DM	703	1.15
Average	612	1.00

Table 33–Variable comparisons

Variable	Relevant specimens	Result
Horizontal reinforcement	HC, DC	Negligible effect on end region capacity in specimens failing in web-shear
Bearing plate	WN, WB, FN, FB	9% to 21% capacity increase from bearing plate
FDOT vs. no confinement reinforcement	HC, HU, VC, VU	13% capacity increase from FDOT confinement reinforcement
FDOT vs. modified confinement reinforcement	DC, DM	7% capacity increase from FDOT confinement reinforcement
Strand quantity	All	Average capacity increase of 18.4 kip / bonded strand
Strand placement	WN, WB, FN, FB	43% capacity increase for strands placed near centerline relative to strands placed in outer flange

D.6.4.1 Horizontal Reinforcement

The 2008 FDOT interim standard for FIB-54 girders (FDOT 2008) called for horizontal bars to be placed in girder end regions. For reasons unrelated to the current test program, this detail was changed such that the 2010 FDOT interim design standard (FDOT 2010) eliminated horizontal bars. Effects of the horizontal reinforcement can be evaluated using results from specimens HC and DC. Specimens HC and DC were effectively identical with the exception of horizontal reinforcement placed in HC. Failure loads of these specimens were within 2% of each other, and both specimens failed in a web-shear mode. This result suggests that the relatively small amount of horizontal reinforcement placed in specimen HC had negligible effect on behavior or capacity.

Previous research by the authors (Ross et al. 2011) has shown that horizontal reinforcement improves ductility in girders having a critical failure mode of bond-shear. Specimens HC and DC failed in web-shear, thus indicating that horizontal reinforcement had negligible impact when web-shear was the critical failure mode.

D.6.4.2 Embedded Steel Bearing Plate

FDOT details call for embedded steel plates to be placed at the end of I-girders above the bearing location. Inclusion of the plates in the FDOT detail was based on recommendations by Cook and Reponen (2008), and was implemented to prevent cracks at the bottom corner of girders during fabrication. Embedded steel bearing plates were included as a variable in the current test program to evaluate the effects of bearing plates on bottom flange confinement.

Specimens WB and WN had identical detailing with the exception of the bearing plate which was excluded from specimen WN. Specimen WB had a bearing plate and a capacity of 612 kip. This was 21% greater than the 507 kip capacity of WN. Both specimens failed in bond-shear mode. The additional capacity in specimen WB is attributed to the confining effect of the bearing plate that helped maintain structural integrity of the bottom flange above the bearing. Because the bottom flange held together, strand-concrete bond in WB was maintained at loads beyond which specimen WN (no bearing plate) lost strand-concrete bond.

Specimens FB and FN also had identical detailing with exception of the bearing plate which was excluded from FN. Specimen FB had a bearing plate and a capacity of 409 kip. This was 9% larger than the 375 kip capacity of specimen FN. Both specimens failed in laterally-splitting mode. The additional capacity of specimen FB is attributed to the bearing plate, however the effect of the bearing plate was not as pronounced as the effect between specimens WN and WB.

D.6.4.3 Confinement Reinforcement

Three different confinement reinforcement schemes (Figure 15) were used in the test specimens. The current FDOT confinement scheme was used in specimens HC, VC, and DC. A modified confinement scheme was used in specimens WN, WB, FN, FB, and DM. The modified confinement scheme had fewer but larger bars than the FDOT scheme. Specimens HU and VU had the final scheme, in which confinement reinforcement was totally omitted.

FDOT vs. No Confinement. Specimens HC, VC, HU, and VU contained comparable variables and can be used to evaluate FDOT confinement relative to specimens with no confinement. HC and VC had FDOT confinement reinforcement and failed in a web-shear mode. The capacity of HC and VC was on average 13% larger than the capacity of HU and VU which had no confinement reinforcement. HU and VU failed in a later-splitting mode. Thus omission of confinement reinforcement allowed lateral-splitting failure of the bottom flange and

decreased capacity by 13%. Or, conversely, the presence of confinement reinforcement forced failure away from the bottom flange, thereby increasing capacity by an average of 13%.

FDOT vs. Modified Confinement. Detailing of specimens DC and DM (Figure 13) was identical with the exception of confinement reinforcement. DC had FDOT confinement reinforcement and a capacity of 753 kip, whereas DM had modified confinement reinforcement and a capacity of 703 kip. Failure mode was different between these specimens. In specimen DC the FDOT confinement reinforcement was sufficient to prevent lateral-splitting failure, thereby forcing a web-shear failure. Confinement reinforcement in DM was insufficient to prevent lateral-splitting of the bottom flange. Thus the current FDOT detail for confinement provides more effective confinement at ultimate load than the modified scheme. One reason that the FDOT scheme was superior is because it placed confinement bars in front of the bearing where they can act as stirrups. Confinement reinforcement as stirrups was postulated by Csagoly (1991). Confinement bars were not provided away from the bearing in the modified scheme. This allowed propagation of cracks in front of the bearing of specimen DM (Figure 117).

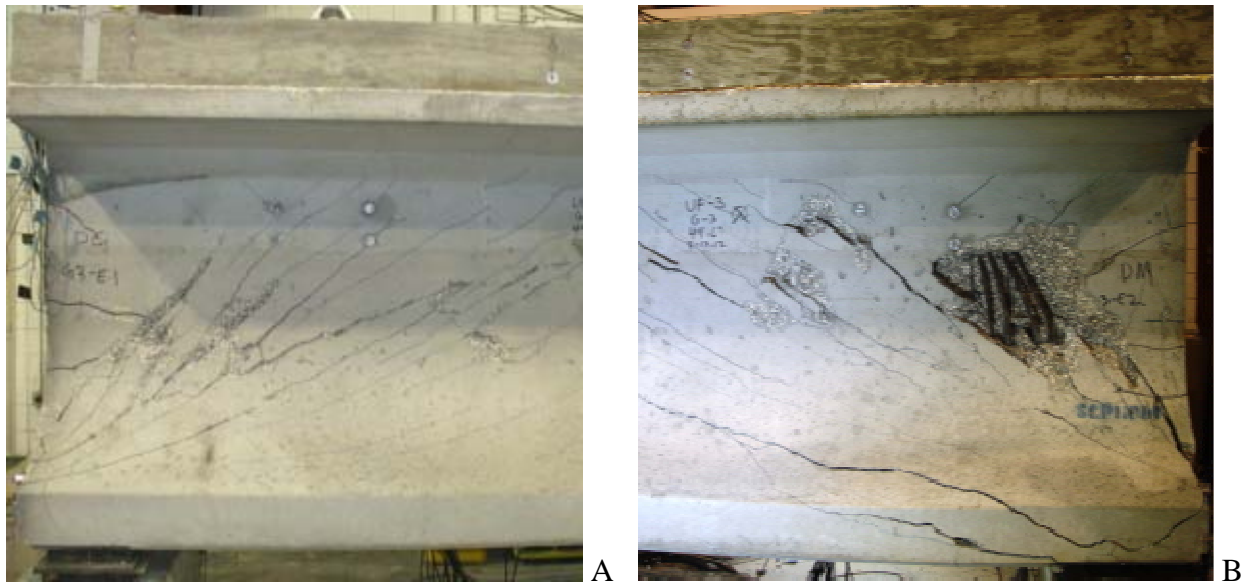


Figure 117–Girder D bottom flange cracking A) specimen DC with limited bottom flange cracking in front of bearing and B) specimen DM with severe bottom flange cracking in front of bearing

D.6.4.4 Strand Quantity

Strand quantity had a greater effect on specimen capacity than any other variable in the test program. Average capacity of specimens with (39) fully bonded strands was 48% greater than the average capacity of specimens with only (24) fully bonded strands. The relationship between strand quantity and experimental capacity is described in Figure 118. The figure shows a linear trend line that was fit to the experimental data. The trend line has an R^2 value of 0.69, indicating a reasonable degree of correlation between experimental capacity and strand quantity.

Current AASHTO LRFD requirements limit the quantity of partially shielded strands to 25% of the total strand count. Providing limits on strand shielding is considered good practice in light of the experimental results. Based on experimental data, every strand that was shielded resulted in a roughly proportional decrease in capacity. The data also suggest, however, that the means by which AASHTO LRFD limits strand shielding can be improved. Rather than limiting shielding to an arbitrary percentage, it is more rational to limit shielding according to the total number of bonded strands required to provide the necessary end region capacity. If sufficient strands are available to support the required capacity, than shielding of the remaining strands can reasonably be permitted. As will be discussed later, the minimum longitudinal reinforcement requirements of AASHTO section 5.8.3.5 can be employed to determine the necessary strand quantity for a given load demand.

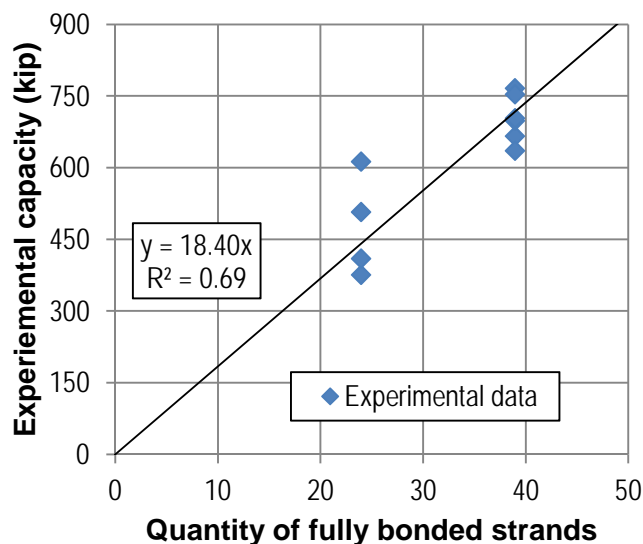


Figure 118—Relationship between strand quantity and end region capacity

D.6.4.5 Strand Placement

Strand placement can be evaluated using results from WN, WB, FN, and FB. Fully bonded strands in WN and WB were placed primarily in the center of the bottom flange below the web. In FN and FB, fully bonded strands were placed in the outer portions of the flange (Figure 9). Specimens WN and WB (strands below the web) failed in a bond-shear failure mode and at an average load that was 43% greater than specimens FB and FN (fully bonded strands in the outer flange). Specimens FB and FN failed in lateral-splitting mode. Crack patterns associated with the different strand patterns and failure modes are shown in Figure 119.

To maximize end region capacity and prevent lateral-splitting failures it is desirable to place strands as close to the cross-section centerline as practical. Doing so minimizes the horizontal eccentricity between prestressing forces and the equal but opposite internal force. This in-turn reduces the propensity for lateral-splitting in the bottom flange.



Figure 119–Comparison of FB (left) and WB (right)
(release cracks shown black; final cracks shown blue)

D.6.5 Code Comparisons

Experimental moments and shears in this section include both the applied load *and* self-weight of the specimens. Experimental moment is denoted as M_{exp} and is defined as the maximum moment occurring during testing at the section below the point load. Experimental shear is denoted as V_{exp} and is defined as the maximum shear occurring during testing at the near support.

Nominal capacities were calculated using the material properties listed in Table 34. These values are representative of the tested properties of materials in the experimental girders. The following paragraphs explain the calculation procedures used to determine nominal capacities.

Table 34—Material properties for capacity calculations

Property	Value
Prestressing strands ultimate strength	285 ksi
Vertical reinforcement yield strength	68 ksi
Concrete deck compressive strength	6500 psi
Concrete girder compressive strength	11000 psi

Nominal Moment Capacity. None of the experimental specimens failed in flexure; however nominal moment capacities were still calculated for reference purposes. Capacity was calculated using principals of strain compatibility and equilibrium. Typical assumptions for concrete in flexure were applied. Nominal moment capacity is denoted as M_n . Shear associated with nominal moment is denoted as V_{Mn} .

AASHTO LRFD Nominal Shear Capacity. Concrete contribution to shear capacity was calculated using the General Procedure from section 5.8.3.4.2 of AASHTO LRFD (2007). This procedure is based on the modified compression field theory (MCFT). Steel contribution was calculated using AASHTO LRFD Equation 5.8.3.3-4. AASHTO LRFD nominal shear capacity is denoted as V_{nLRFD} .

ACI Nominal Shear Capacity. Concrete contribution was calculated using section 11.3.3 of ACI 318 (2011). Provisions in this section are commonly referred to as the ACI detailed method. Steel contribution was calculated using the provisions of section 11.4.7. ACI nominal shear capacity is denoted as V_{nACI} .

Nominal Tie Capacity (Minimum longitudinal reinforcement). Nominal tie capacity calculations are based on the minimum longitudinal steel requirement in AASHTO LRFD 5.8.3.5. Equation 5.8.3.5-2 requires that sufficient longitudinal reinforcement be provided to carry tie forces at the bearing. Bond-shear failure is likely when the tie is insufficient. Procedures from Ross et al. (2011) were used to calculate the shear force that accompanies the nominal tie capacity. These procedures encompass the AASHTO LRFD requirements, but were derived for application to test specimens. Shear associated with nominal tie capacity is denoted as V_{nT} . In making the tie calculations, an available development of 22 in. was assumed. Forces in the strands were then calculated using the bi-linear relationship from AASHTO LRFD for strand development.

For each specimen the experimental moment was less than the calculated nominal moment capacity (Table 35). This result is in agreement with experimental specimens, in which no flexural failures were observed. Most specimens carried experimental moments that were between 60% and 75% of their nominal moment capacity.

Table 35–Experimental moments and nominal moment capacities

Specimen	M_{exp} (kip-ft)	M_n (kip-ft)	V_{exp} (kip)	V_{Mn} (kip)	M_{exp}/M_n
HC	7384	10295	793	1098	0.72
HU	6478	10295	697	1098	0.63
VC	6746	10295	725	1098	0.66
VU	6155	10295	662	1098	0.60
WN	4954	6570	534	700	0.75
WB	5939	6570	639	700	0.90
FN	3716	6720	402	716	0.55
FB	4035	6720	436	716	0.60
DC	7262	10295	780	1098	0.71
DM	6793	10295	730	1098	0.66

Nominal and experimental shear capacities are compared in Table 36. The AASHTO LRFD and ACI nominal shear capacities are based on web-shear failure, which was only observed in four of ten specimens. Bond-shear failure, the assumed failure mode of the AASHTO tie capacity, was only observed in two of the ten specimens. Because of

inconsistencies between code-assumed and experimentally observed failure modes, the comparisons shown in Table 36 are useful for relative comparisons only.

Table 36–Experimental shear and nominal shear capacities

Specimen	V_{exp} (kip)	AASHTO Shear		ACI Shear		AASHTO Tie	
		V_{nLRFD} (kip)	V_{exp} / V_{nLRFD}	V_{nACI} (kip)	V_{exp} / V_{nACI}	V_{nT} (kip)	V_{exp} / V_{nT}
HC	793	590	1.34	490	1.62	754	1.05
HU	697	590	1.18	490	1.42	754	0.92
VC	725	590	1.23	490	1.48	658	1.10
VU	662	590	1.12	490	1.35	658	1.01
WN	534	528	1.01	454	1.18	553	0.97
WB	639	528	1.21	454	1.41	553	1.16
FN	402	528	0.76	454	0.89	563	0.71
FB	436	528	0.83	454	0.96	563	0.77
DC	780	590	1.32	490	1.59	754	1.03
DM	730	590	1.24	490	1.49	754	0.97
Average			1.12		1.34		0.97

Although inconsistent with failure modes, calculated nominal capacities were typically conservative relative to the experimental results. ACI shear calculations were the most conservative, and resulted in nominal capacities 34% less on average than the experimental results. AASHTO shear capacity was an average of 12% less than the experimental results. AASHTO tie nominal capacity was an average of 3% greater than the ultimate strength.

Specimens FN and FB were the only specimens with calculated nominal capacities significantly greater than the experimental shear forces. These specimens failed in lateral-splitting. This type of failure is not explicitly considered in ACI or AASHTO code provisions. Because ACI and AASHTO codes do not account for lateral-splitting failure, code-based capacities for specimens FN and FB were unconservative (i.e. greater than experimental capacity). This result demonstrates the need for code provisions that account for lateral-splitting failure.

The nominal tie method was the most accurate method for calculating end region capacity of the experimental specimens. Average strength calculated by the nominal tie method was 3% greater than the average of the experimental capacities. It must be noted, however, that nominal capacity calculated by the tie method is highly dependent on the values that are assumed for the required and available development lengths. The AASHTO LRFD code does not give

specific requirements for selecting these values. Rather the code states, “Any lack of full development length shall be accounted for.” In spite of the ambiguity in code language, the agreement shown between experimental and nominal tie capacities demonstrate the utility of this method for designing I-girder end regions. In particular, this method is useful in determining the number of bonded strands required at the girder end to preclude a bond-shear failure.

D.7 Summary and Conclusions

Ten uniquely detailed FIB-54 specimens were load tested in three-point bending at a shear span-to-depth (a/d) ratio of 2.0. Variables in the test program included:

- Presence/absence of confinement reinforcement
- Quantity and configuration of confinement reinforcement
- Presence/absence of horizontal reinforcement
- Quantity of vertical reinforcement
- Presence/absence of embedded steel bearing plates
- Strand quantity
- Strand placement

The following conclusions are made:

- Differences in detailing have significant effect on the end region capacity, even for members having the same cross-section. All test specimens used the FIB-54 cross-section, yet experimental capacities ranged from a maximum of 766 kip to a minimum of 375 kip.
- Horizontal reinforcement in the end region has negligible effect on the capacity of members failing in web-shear. The test specimen with horizontal reinforcement had no significant increase in capacity relative a comparable specimen without horizontal reinforcement.
- Embedded steel bearing plates provide confinement to the bottom flange, thereby improving end region capacity. Test specimens with bearing plates had 9% to 21% greater capacity relative to comparable specimens without bearing plates.
- Confinement reinforcement can be used to mitigate lateral-splitting failure, thereby improving end region capacity. Test specimens with confinement reinforcement per current FDOT specifications failed in web-shear mode and at an average load 13% higher than comparable specimens without confinement. Specimens without confinement failed in lateral-splitting.
- To mitigate lateral-splitting failure confinement reinforcement must have sufficient quantity and effective placement. Lateral-splitting failure was observed

in specimens with confinement reinforcement placed only above the bearing. A comparable specimen with confinement placed throughout the strand transfer length failed in web-shear and at a 7% higher load.

- Bearing plates carry a significant portion of transverse splitting forces. Up to 79% of the transverse tension was carried by bearing plates in the test program.
- For purposes of designing confinement reinforcement it is conservative to assume that bearing plates carry 50% or less of the transverse splitting force.
- Girders with fully bonded strands in the outer flange have greater transverse splitting forces than due girders with fully bonded strands placed below the web. In the test program, transverse force in confinement reinforcement was up to 2.5 times larger in specimens with strands in the outer flange relative to those with strands below the web.
- Strand quantity had the greatest effect on end region capacity of any variable in the test program. Specimens with 39 fully bonded strands had an average capacity that was 43% greater than specimens with 24 fully bonded strands.
- There was a reasonable degree of correlation ($R^2=0.69$) between quantity of fully bonded strands and experimental end region capacity. As such, design of strand shielding based on longitudinal tie capacity appears to be a rational design approach. This approach may give better results than the arbitrary shielding limits imposed by current AASHTO LRFD specifications.
- There is need for code provisions that explicitly address lateral-splitting failure. Current shear and longitudinal tie provisions resulted in nominal capacities that were unconservative (too large) for some specimens failing in lateral-splitting.

Appendix E–FIB-63 Tests

Table of Contents

E.1	Introduction	363
E.2	Test Specimen Design and Construction.....	365
E.2.1	Descriptions and Labels.....	365
E.2.2	Design.....	366
E.2.3	Construction	373
E.2.4	Material Properties	383
E.3	Test Procedures	386
E.3.1	Fabrication.....	386
E.3.2	Load Testing.....	387
E.3.3	Coordinate System.....	390
E.4	Instrumentation.....	392
E.4.1	Types and Descriptions	392
E.4.2	Strain Gage Coordinates	398
E.5	Test Results and Discussion	400
E.5.1	Strain during Post-Tensioning	400
E.5.2	Strain and Cracking during Prestress Transfer	403
E.5.3	Web Cracks	409
E.5.4	Prestress Losses	416
E.5.5	Load Tests	417
E.5.6	Code Comparison	425
E.6	Summary and Conclusions	428

List of Figures

Figure 1–Web splitting cracks (enhanced in blue).....	363
Figure 2–Formation of splitting forces	363
Figure 3–Test specimen labels.....	366
Figure 4–Specimen orientation in stressing bed	366
Figure 5–Cross-section FIB-63.....	367
Figure 6–Strand layout and prestressing details	368
Figure 7–Strand bond and shielding patterns.....	368
Figure 8–Longitudinal stress due to prestress and self-weight	369
Figure 9–Reinforcement for specimens CT and SL.....	370
Figure 10–Reinforcement for specimens PT and LB.....	371
Figure 11–Reinforcement and bearing plate details.....	372
Figure 12–Jacking frame (left), and steel bulkhead (right).....	374
Figure 13–Tension pattern	375
Figure 14–Specimen CT reinforcement.....	375
Figure 15–Specimen SL reinforcement	376
Figure 16–Specimen PT reinforcement	376
Figure 17–Specimen LB reinforcement.....	377
Figure 18–Top (left) and bottom (right) of post-tension rods in specimen PT	377
Figure 19–Top (left) and bottom (right) of all-thread rods in specimen LB	378
Figure 20–Form placement	378
Figure 21–Form release application (left) and form cross-ties (right).....	379
Figure 22–Concrete delivery (left) and placement (right)	379
Figure 23–Top flange finish (left) and tarp covers (right)	379
Figure 24–Post-tensioning specimen PT (left) and load cells and anchor plate (right)	381
Figure 25–Strand cutting pattern.....	382
Figure 26–Girder lifted by crane.....	382
Figure 27–Test girder transported by truck.....	383
Figure 28–Test setup.....	388
Figure 29–Support conditions at bearing	389
Figure 30–Support conditions at load point for specimen LB	389
Figure 31–Support conditions at load point for specimens CT, SL, and PT.....	389
Figure 32–View of test specimen and load frame from above (left) and side view of specimen (right)	390
Figure 33–Coordinate system relative to load and supports	391
Figure 34–MS gage installation showing A) gage before protective covering and B) protective cover and label.....	393
Figure 35–XS gage installation.....	393
Figure 36–ES gage installation	394
Figure 37–V gage installation (view from above)	394
Figure 38–S gage installation on bottom flange (left) and close-up (right).....	395
Figure 39–LVDT placement and labels	395
Figure 40–LVDT and support frame	396
Figure 41–Strands monitored by potentiometers	397
Figure 42–Aluminum brackets and linear potentiometers on strands.....	397
Figure 43–Load cells below hydraulic actuators	398
Figure 44–Variation in load during post-tensioning process	400
Figure 45–Strain measured by V1 gage during the post-tensioning process	401
Figure 46–Gages at FIB-63 specimens	402
Figure 47–Strain due to post-tensioning process in XS gages.....	403
Figure 48–Estimated stress profile in web due to post-tensioning (tension positive).....	403

Figure 49–Strand cutting pattern groups.....	404
Figure 50–Concrete strain in specimen CT during prestress transfer	405
Figure 51–Concrete strain in specimen SL during prestress transfer	406
Figure 52–Concrete strain in specimen PT during prestress transfer	406
Figure 53–Concrete strain in specimen LB during prestress transfer	407
Figure 54–Cracks after prestress transfer.....	407
Figure 55–Estimated stress profile in web of specimen PT after transfer (tension positive).....	408
Figure 56–Strain and subsequent apparent transfer length	409
Figure 57–Crack growth in specimen CT (flexural cracks in top flange not shown)	410
Figure 58–Photo of end region cracks (cracks enhanced in blue)	411
Figure 59–Specimen CT end region cracks prior to load testing.....	411
Figure 60–Specimen SL end region cracks prior to load testing	412
Figure 61–Specimen PT end region cracks prior to load testing	412
Figure 62–Specimen LB end region cracks prior to load testing.....	413
Figure 63–Web crack measurements (view from end of specimen).....	414
Figure 64–Web crack measurements (view from side of specimen)	414
Figure 65–Web splitting crack length and area.....	415
Figure 66–Web splitting crack widths	415
Figure 67–Ultimate load test shear-displacement for all specimens.....	418
Figure 68–Ultimate load test shear-strand slip for specimens CT, SL, and PT	418
Figure 69–Strain gage and typical first crack location.....	419
Figure 70–Specimen CT after load tests	420
Figure 71– Punching failure and hook breakout at load point.....	420
Figure 72–Bond shear failure of specimen SL.....	422
Figure 73–Bottom flange cracking at SL bearing	422
Figure 74–Cracking specimen PT.....	423
Figure 75–Punching failure specimen LB	424
Figure 76–Punching shear failure in specimen SL	425
Figure 77–Punching failure from above (left) and below (right).....	425

List of Tables

Table 1–Specified material properties	373
Table 2–Fabrication chronology	374
Table 3–Post-tensioning force measured in specimen PT	381
Table 4–Tested concrete compressive strengths	384
Table 5–Prestressing steel properties	384
Table 6–NASP test results	384
Table 7–Steel reinforcement properties	385
Table 8–Construction events and inspection dates	387
Table 9–Load test chronology.....	387
Table 10–Instrumentation types and labels.....	392
Table 11–Specimen CT strain gage coordinates	399
Table 12–Specimen SL strain gage coordinates	399
Table 13–Specimen PT strain gage coordinates	399
Table 14–Specimen LB strain gage coordinates	399
Table 15–Girder fabrication stages.....	404
Table 16–Recommend action for web splitting cracks (Tadros et al. 2010).....	415
Table 17–Experimental and code prestress losses	417
Table 18–First cracks during service load testing.....	419
Table 19–Code comparison with experimental shear forces	426

1 Introduction

Web splitting cracks (Figure 1) typically form during prestress transfer, or in the days and weeks following transfer. They occur due to tensile stresses that are induced as prestressing forces in the bottom flange are distributed through the cross-section (Figure 2).



Figure 1–Web splitting cracks (enhanced in blue)

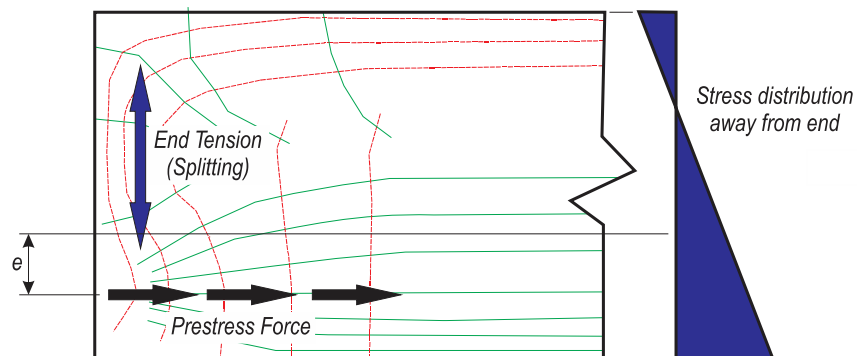


Figure 2–Formation of splitting forces

Some degree of cracking is expected and generally accepted in the end region of pretensioned girders. Indeed, one veteran quality control manager at a precast facility indicated that “My first day on the job I was sent out to monitor web splitting cracks. Years later that’s what I’m still doing.” Web-splitting cracks have also received a good deal of attention in the

research literature, much of which is summarized in Appendix A. Previous research has focused on the causes, design models, reject/repair criteria, and controlling of web-splitting cracks. The current research adds to the body of knowledge by comparing various methods for controlling and/or preventing web splitting cracks. Methods in the current study include: traditional vertical reinforcement, large diameter vertical reinforcement, vertical post-tensioning, and 45% partial strand shielding.

While some cracking is expected, it is also generally accepted that if the cracking is not excessive, then it will not typically impair the girder capacity. It does, however, present serviceability and service life problems. This is particularly true for bridges over salt water. Consequently, this portion of the research project is focused on evaluating methods that may eliminate or reduce this end cracking.

Vertical end zone reinforcement for controlling web splitting cracks is required by AASHTO LRFD Bridge Design Specification (hereafter “LRFD”) section 5.10.10 (2007). Note that in LRFD 2007, web splitting is referred to as “bursting.” Section 5.10.10 requires that vertical reinforcement be placed in pretensioned anchorage zones in sufficient quantity to resist 4% of the prestressing force at transfer ($0.04 * P_u$). Stress is limited to 20 ksi and it is placed as close to the end as practicable. These requirements are to be applied at the service limit state.

FDOT has additional requirements for end zone reinforcement beyond those in AASHTO LRFD. Section 4.3.1.D of the FDOT Structures Design Guidelines requires that end zone reinforcement be placed to carry the forces listed below:

- 3% P_u from the end of the beam to $h/8$, but not less than 10 in.
- 5% P_u from the end of the beam to $h/4$, but not less than 10 in.
- 6% P_u from the end of the beam to $3h/8$, but not less than 10 in.

This requirement is to reduce crack sizes.

2 Test Specimen Design and Construction

Two 63-in. deep Florida I-Beam (FIB-63) girders were fabricated and tested to evaluate the effects of end region detailing on web splitting and ultimate capacity. Each end of each girder was uniquely detailed and is referred to in this document as a distinct specimen. This section presents specimen details, construction procedures, and material properties. The labeling convention used to identify specimens is also presented

2.1 Descriptions and Labels

Four specimens were fabricated, each with different end region details (Figure 3). Specimen CT served as the control specimen and followed current Florida Department of Transportation (FDOT) details (2010). Vertical end zone reinforcement in CT consisted of (16) #5 bars placed within 16.5 in. of the member end. Of the (16) bars, (12) per placed within 9.5 in. of the member end. Quantity and placement of these bars complied with the AASHTO LRFD requirements governing web splitting reinforcement.

Specimen SL had the same end region reinforcement as specimen CT. Strands in SL, however, were 45% partially shielded. Because they were partially debonded, concrete stress associated with transfer length was moved away from the end region. This had the effect of reducing vertical end tension in the web.

LRFD 5.11.4.3 limits the number of shielded strands to 25% of the total number of strands. It also places limits on the number of shielded strands in a row and the number of strands that can have shielding terminate at the same section. Although specimen SL violated these code requirements, it was designed to provide information on the relative effectiveness of strand shielding on limiting web splitting cracks. Specimen SL also allowed for the implications of violating LRFD strand shielding provisions to be evaluated. SL was located on the same girder but at the end opposite of CT.

The end of specimen PT was vertically post-tensioned prior to prestress transfer. The post-tension force was designed to counteract vertical tensile stresses in the web. Vertical reinforcement at the end of PT consisted of the post-tension rods and traditional reinforcing bars. The area of vertical reinforcement was reduced by 33% relative to CT. The post-tension concept used in specimen PT was proposed by the FDOT Structures Design Office.

The fourth and final specimen, LB, had 1-in. diameter threaded rods as vertical end reinforcement. Because it used larger reinforcement, LB had 30% more end reinforcement than CT. Specimen LB was located on the same girder but opposite end as specimen PT.

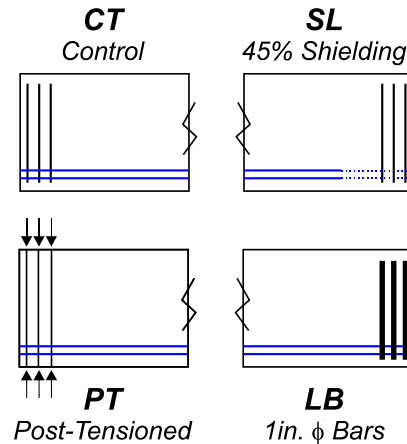


Figure 3–Test specimen labels

2.2 Design

FIB-63 specimens were constructed at the same time and in the same bed as the FIB-54 test girders, which were used in elsewhere in this project (Figure 4) (Appendix D). Since the FIB-54 girders were the primary test specimens in this project, their design dictated strand size, placement, and quantity.

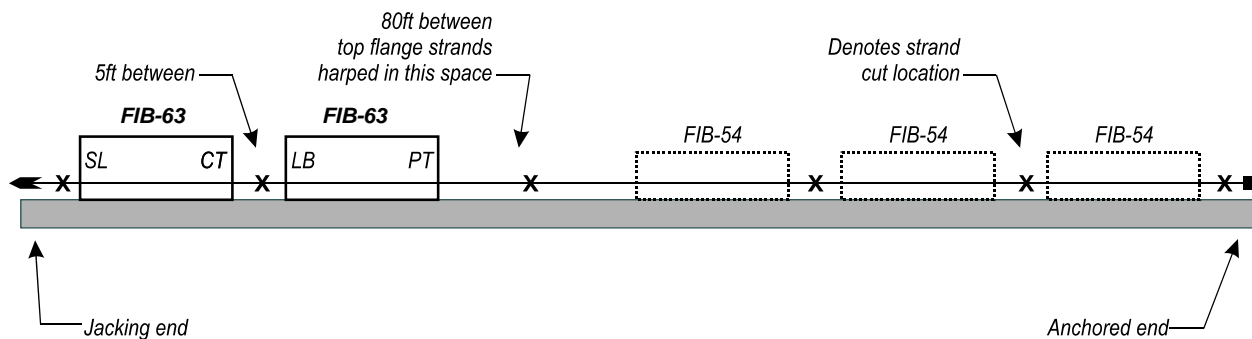


Figure 4–Specimen orientation in stressing bed

Test specimens used the FIB-63 cross-section (Figure 5) and had a total length of 49 ft-6 in. This length was selected to facilitate transport and load testing. Production girders with the same cross-section typically have span lengths over 125 ft.

Specimens had (52) 0.6-in. diameter prestressing strands in the bottom flange and (4) 3/8-in. diameter strands in the top flange (Figure 6). Strands in specimens CT, PT, and LB were fully bonded, whereas strands in SL were 45% partially shielded (Figure 7). The “checker board” shielding pattern used in SL was based on FDOT specifications that prohibit shielding of adjacent strands. As discussed in the previous section, the shielding pattern for SL violated strand shielding provisions of LRFD.

Calculated and allowable longitudinal stresses due to prestressing and self-weight are shown in Figure 8 for the girder with specimens PT and LB. Allowable stresses were calculated according to FDOT and AASHTO LRFD requirements. Specimen CT had the same calculated stresses as those shown in the figure. As demonstrated by Figure 8, specimens CT, PT, and LB exceeded the allowable stress limits in tension and compression. This was intentional to ensure that cracks formed within the end region and to test the detailing schemes under extreme conditions.

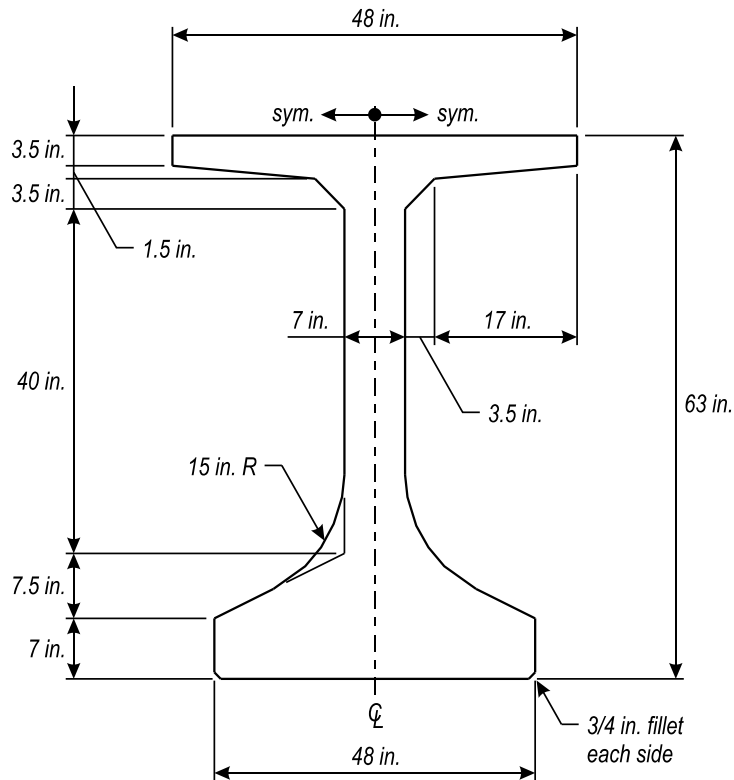


Figure 5—Cross-section FIB-63

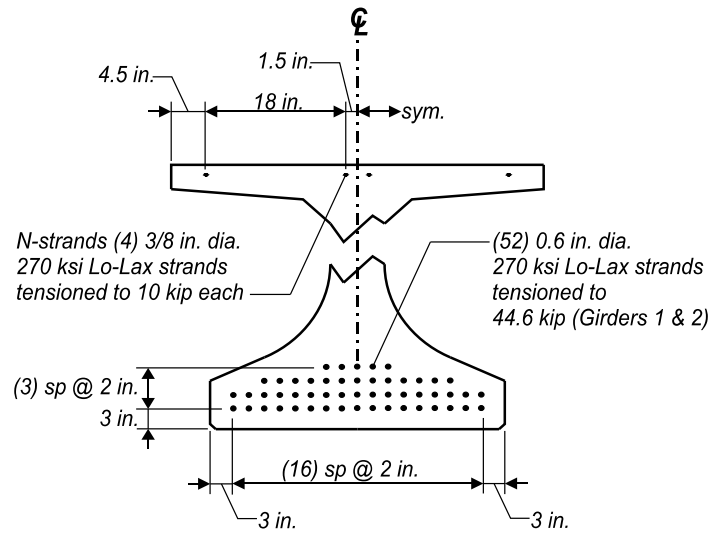


Figure 6—Strand layout and prestressing details

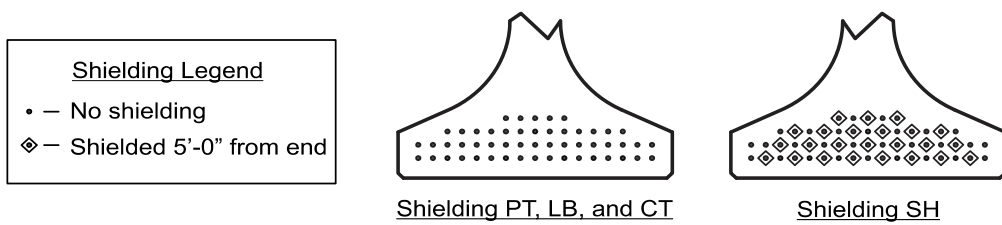


Figure 7—Strand bond and shielding patterns

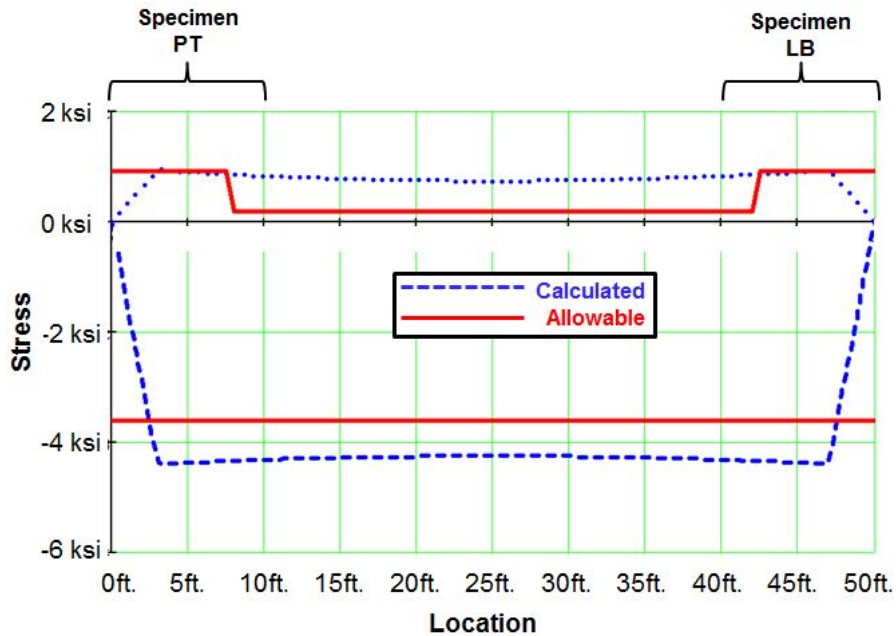


Figure 8—Longitudinal stress due to prestress and self-weight

Mild reinforcement in each specimen (Figure 10 and Figure 11) was based on FDOT FIB-63 Interim Standard Details (FDOT, 2010). Bar labels used in Figure 10 and Figure 11 are typically the same as those used in the FDOT standards. The numeric portion of each label indicates the size of bar (i.e. 5A is a #5 bar). Reinforcement bending and bearing plates details are shown in Figure 11.

Reinforcement labels 8G, 5R, 5Rs, 5T, 5Yt, and 8Y were unique to the test program and are not used in FDOT standards. Unique labels were used to distinguish bars in the FIB-63 girders from bars used in the FIB-54 girders that were fabricated simultaneously. Descriptions of the unique bars are given in the paragraphs below. Descriptions of typical bars are given in Appendix D.

8G. Bars placed longitudinally in the top flange. These bars were included to control cracking in the top flange after prestress transfer, and are not specified in FDOT standards. The G bars did not extend into the end regions where load testing and crack monitoring took place.

5R and 5Rs. Bars placed vertically in the web with hooks top and bottom. These bars were intended to act as shear reinforcement. In production beams these bars have a K label and protruded through the top flange to help develop composite action with the cast-in-place deck. Because a deck was not poured on the test girders, top hooks were embedded in the top flange.

The bottom hook on 5R bars was 16-in. long to assist in constructability. The bottom hook on 5Rs bars was 6-in. long. To eliminate any incidental confinement effects from the bottom hooks, 5Rs bars were used in lieu of 5R bars within the end region.

5T. Bars bundled with 5Rs bars at girder ends. These bars were used to control web splitting cracks.

5Yt. All-thread rods used to post-tension the end of specimen PT. These rods were placed inside of PVC pipes that acted as post-tensioning ducts.

8Y. Vertical all-thread rods placed at the end of specimen LB to control web splitting cracks. Heavy nuts were placed top and bottom to assist in development.

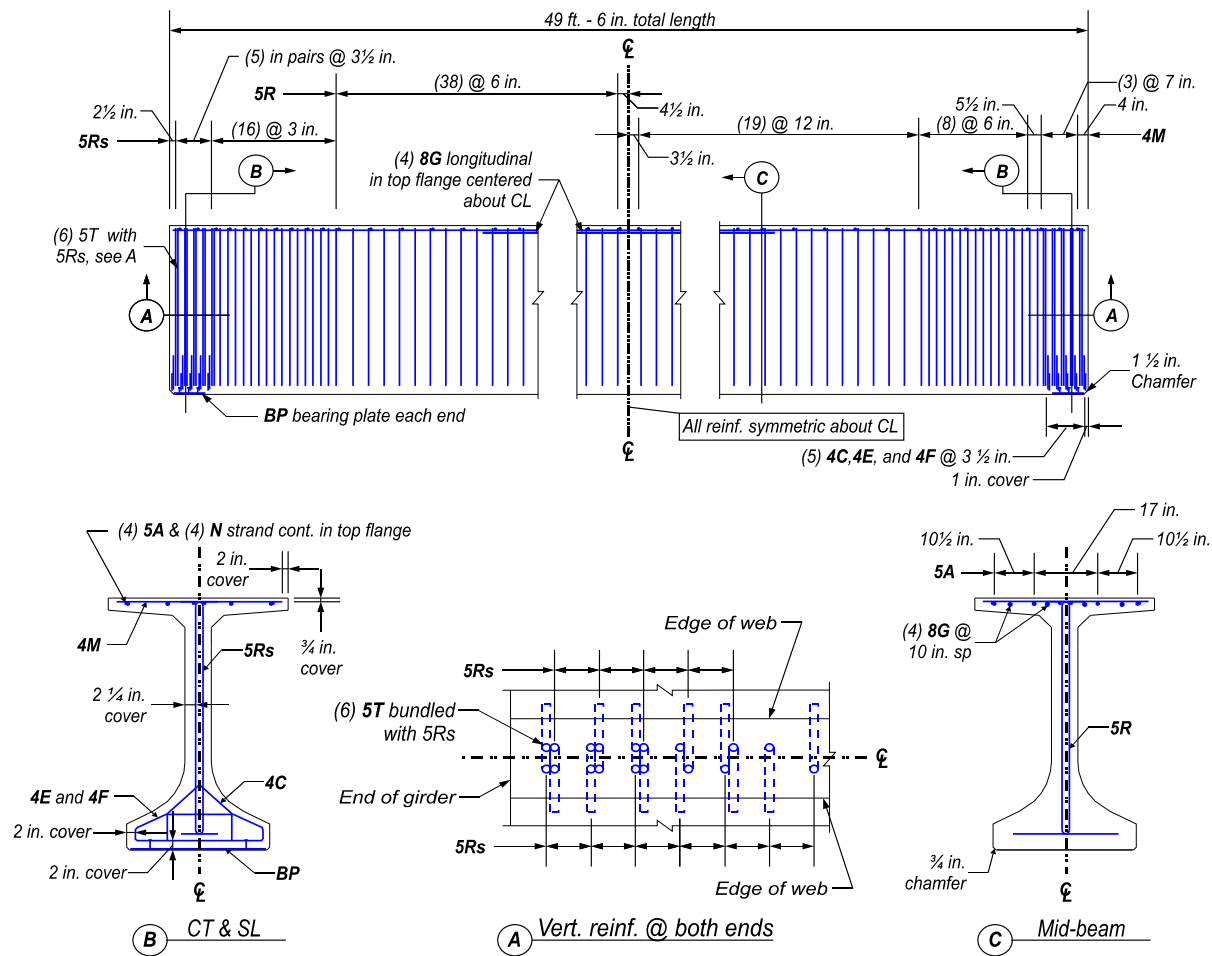


Figure 9–Reinforcement for specimens CT and SL

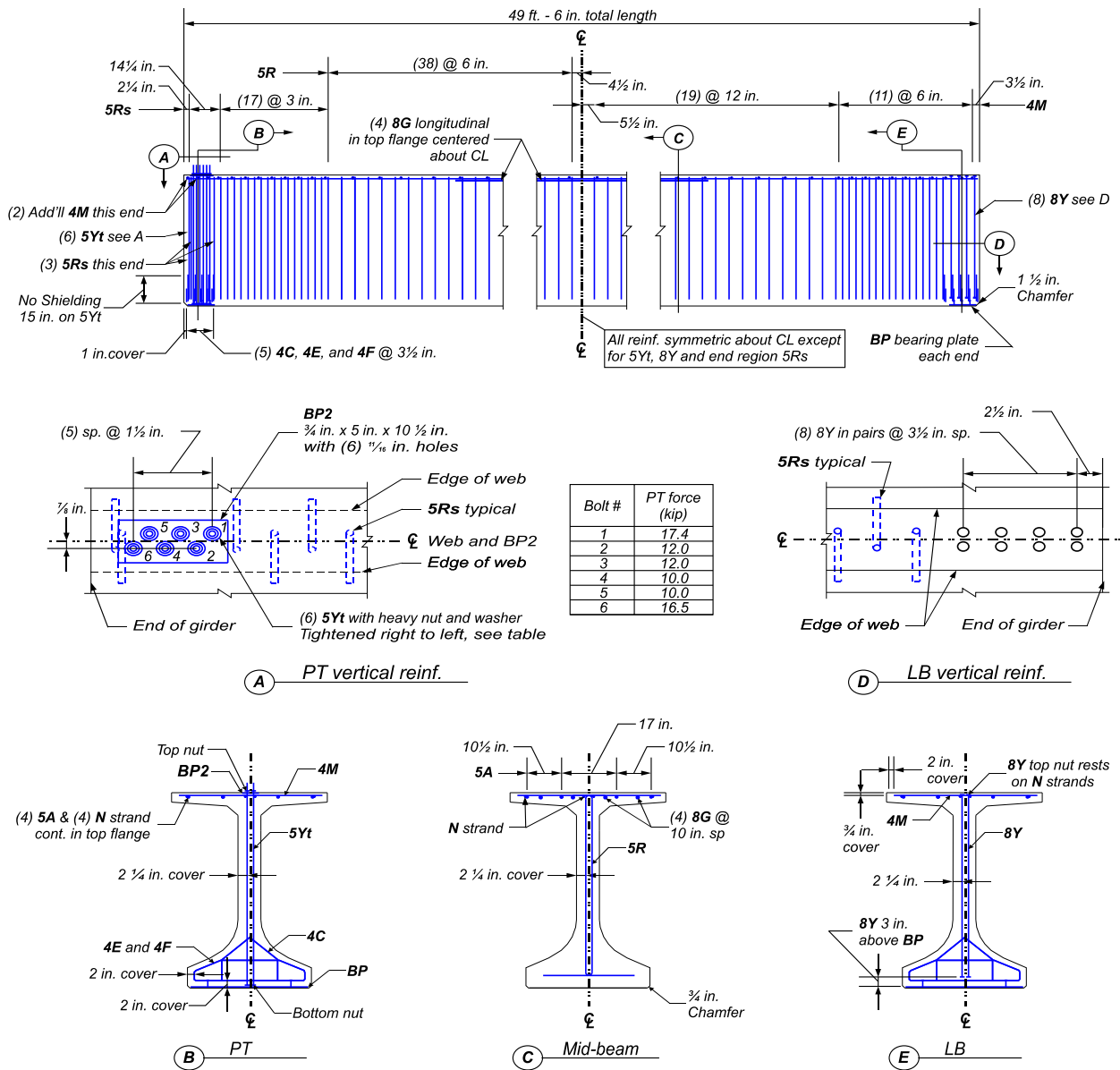


Figure 10–Reinforcement for specimens PT and LB

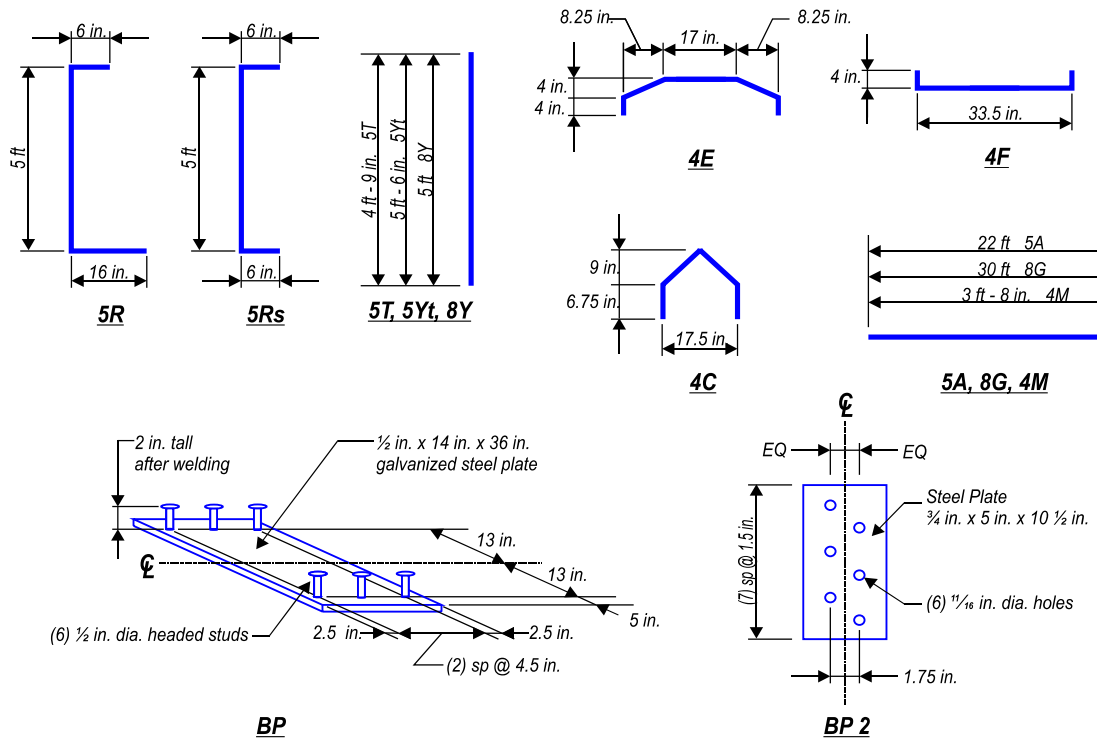


Figure 11–Reinforcement and bearing plate details

Specimens CT and SL both had (16) #5 vertical bars placed within 16.5 in. of the end. Of these bars, (12) were placed within 9.5 in. of the end. Vertical reinforcement in CT and SL satisfied the AASHTO LRFD requirements.

Specimen LB had (8) 1-in. diameter all-thread rods as vertical reinforcement in lieu of the FDOT specified #5 bars. Heavy nuts were placed at the top and bottom of each rod to aid in development, and were necessary because the test specimen did not have sufficient space for standard hooks of #8 bars. In other words, the all-thread rods with nuts allowed development of 1-in. diameter vertical reinforcement where development of hooked bars was not possible. The area of vertical reinforcement at the end of specimen LB was 30% greater than the reinforcement in specimens CT and SL.

Vertical reinforcement at the end of specimen PT also varied from the FDOT standard. In lieu of the standard #5 bars specimen PT had (6) 5/8-in. diameter post-tensioned all-thread rods. PVC pipes were used as post-tensioning ducts in the web. The PVC stopped 15 in. above the bearing plate to allow for development of the rods. To further aid in development, heavy nuts were placed at the bottom of each rod. The top of the rods passed through a 3/4 in. thick

steel plate, which served as a bearing plate for the post-tensioning force. Post-tensioning sequence and forces are shown in Figure 10. Grout was not placed in the PVC pipes.

Detailing of the confinement reinforcement in each specimen was modified from the FDOT standard. The modified confinement reinforcement detail used #4 bars in lieu of the FDOT specified #3 bars. Additionally, all confinement bars were placed directly over the bearing in the modified scheme. The modified confinement reinforcement scheme was used for convenience, as it matched the FIB-54 girders that were built simultaneously.

The test FIB-63 specimens were designed for testing without cast-in-place decks. The decision to test without decks was made because it was believed that decks would increase shear capacity of the specimens beyond the capabilities of the available load test equipment. Because decks were not used, vertical reinforcement was developed using hooks in the top flange. The top flange did not provide code-specified cover requirements for the hooks, but was the best possible solution given the test equipment and fabrication constraints.

Specified material properties matched FDOT standards. Specifications are listed in Table 1. Tested material properties will be discussed in a later section.

Table 1–Specified material properties

Material	Specification
Girder Concrete	FDOT class VI 8500 psi 28-day compressive strength 6000 psi compressive strength at prestress transfer
Prestressing Strand	ASTM A416 270 ksi ultimate strength Low relaxation
Mild Reinforcement	ASTM A615 60 ksi yield strength
All-thread rods (specimens LB and PT)	ASTM A193 Grade B7

2.3 Construction

Specimens were constructed at Standard Concrete Products in Tampa, FL in February 2012. A time line of construction events is provided in Table 2. Construction began with tensioning of the prestressing strands followed by placement of steel bulkheads. Plastic tubes for strand shielding were placed on the strands prior to tensioning. A hydraulic jack was used to

tension the strands. Jacking force was determined from pressure in the hydraulic line and was verified periodically by measuring strand elongation. Dormant strands in the top flange were tensioned first followed by strands in the bottom flange, which were stressed from the bottom-to-top and outside-in (Figure 13).

Table 2–Fabrication chronology

Event	Phase 2 Date
Strands tensioned	February 13, 2012
Concrete poured	February 17, 2012
Concrete exceeds release strength	February 20, 2012
Forms removed	February 20, 2012
Specimen PT post-tensioned	February 21, 2012
Prestress released	February 21, 2012
Moved to storage	February 22, 2012
Trucked to FDOT laboratory	June 1, 2012
Load testing	June 5, 2012 to June 13, 2012



Figure 12–Jacking frame (left), and steel bulkhead (right).

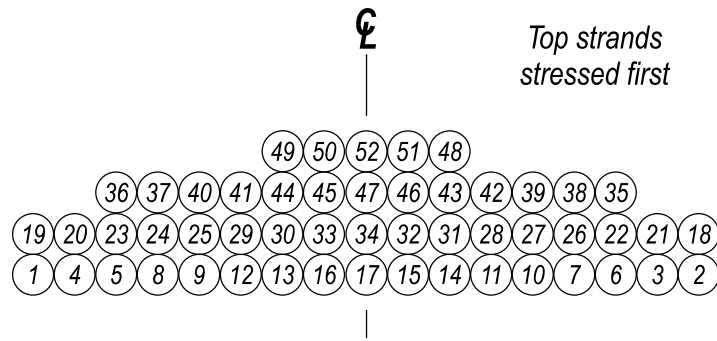


Figure 13–Tension pattern

After tensioning, mild steel reinforcement was placed in each specimen. Select bars were instrumented with strain gages prior to placement in the girders. Figure 14 to Figure 17 show the reinforcement in each specimen. Diagonal strands shown in the web in the pictures are from the lifting loops. Close-ups of the post-tensioning system used in specimen PT are shown in Figure 18. As shown in Figure 18 pipes were placed at the top of two rods to act as spacers for load cells. Close-ups of the 1-in. diameter vertical bars in specimen LB are shown in Figure 19.



Figure 14–Specimen CT reinforcement



Figure 15–Specimen SL reinforcement



Figure 16–Specimen PT reinforcement



Figure 17—Specimen LB reinforcement



Figure 18—Top (left) and bottom (right) of post-tension rods in specimen PT



Figure 19–Top (left) and bottom (right) of all-thread rods in specimen LB

Once reinforcement and internal instrumentation were installed and checked, steel forms were oiled, placed, and squared (Figure 20 and Figure 21). Concrete was mixed at an on-site batch plant and was transported and poured using the fabricator’s mix truck and delivery equipment (Figure 22). A self-consolidating concrete mix was used and vibration was not necessary. One batch of concrete was used for both FIB-63 test girders. Concrete test cylinders were taken by the fabricators and by the research team. The top surface of each FIB-63 girder was trowel smooth (Figure 23). Girders were covered with heavy tarps during curing (Figure 23).



Figure 20–Form placement



Figure 21–Form release application (left) and form cross-ties (right)



Figure 22–Concrete delivery (left) and placement (right)



Figure 23–Top flange finish (left) and tarp covers (right)

Forms were removed three days after casting and prestress force was transferred to the girders the day after form removal. The time between form removal and prestress transfer was

used to install surface-bonded foil strain gages, connect the data acquisition system, and apply post-tensioning to specimen PT.

Two 4x8 field cured cylinders were tested on the day of prestress transfer. The average compressive strength was 7320 psi, which was greater than the specified release strength of 6500 psi.

Specimen PT was post-tensioned a few hours prior to prestress transfer (Figure 24). The post-tensioning force was applied by hand using a socket wrench. A pipe was placed over the wrench to increase leverage. Even with the increased leverage the process required the strength of two men.

Rods were tensioned sequentially starting with the rod farthest from the end, and finishing with the rod closest to the end (Figure 10). Load cells were used to monitor force in the first and final rods during post-tensioning. Forces in the other rods were estimated using the turn-of-the-nut method. Turn-of-the-nut estimations were calibrated using data from the load cells and from linear-elastic mechanics principles. Load cell data were particularly helpful in determining the number of turns beyond snug-tight that were required to engage the rods. Measured and estimated loads are shown in Figure 10 and listed in Table 3.

Forces in the individual rods were influenced by the relative difficulty of the post-tensioning process. In spite of these difficulties a total post-tensioning force of 77.9 kip was obtained. This value is within the acceptable range as determined from preliminary analysis conducted prior to fabrication. The total applied post-tension force was approximately 3.4% of the initial pretension forces.



Figure 24–Post-tensioning specimen PT (left) and load cells and anchor plate (right)

Table 3–Post-tensioning force measured in specimen PT

Rod number (corresponds to stressing sequence)	Post-tension force (kip)	Measurement method
1 (farthest from end)	17.4	Load cell
2	12.0	Turn-on-the-nut
3	12.0	Turn-on-the-nut
4	10.0	Turn-on-the-nut
5	10.0	Turn-on-the-nut
6 (closest to end)	16.5	Load cell
Total	77.9	

Flame cutting was used to release the prestressing strands. Individual strands were cut simultaneously at points shown in Figure 4. Dormant strands in the top flange were cut first, followed by the bottom strands, which were cut from the outside-in and from bottom-to-top (Figure 25). This release pattern was selected because it is relatively easy to execute and because it is typical of precast girders in Florida. Strand cutting was stopped intermittently at multiple stages to obtain strain readings from vibrating wire strain gages and to check for cracking.

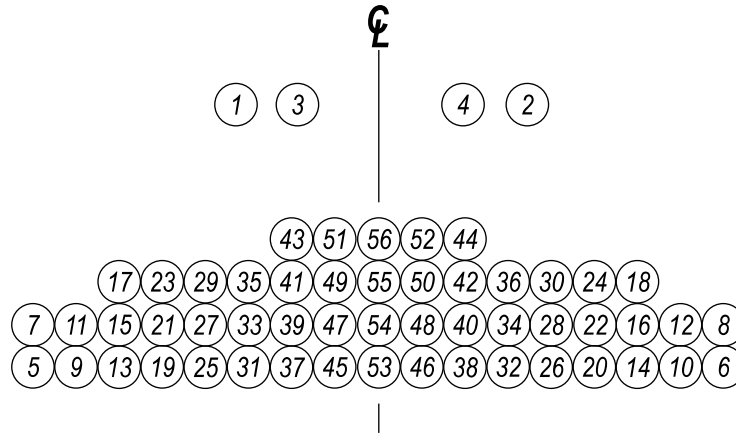


Figure 25–Strand cutting pattern

The girders shifted slightly (less than 1 in.) along the length of the stressing bed multiple times during prestress transfer. Movement events always corresponded to strand cuts.

Girders were moved from the stressing bed to storage yard the day after prestress was transfer (Figure 26). While in storage the girders were examined periodically for cracking. After three months in storage girders were trucked (Figure 27) to the Marcus H. Ansely FDOT structures laboratory in Tallahassee, FL for load testing.



Figure 26–Girder lifted by crane



Figure 27–Test girder transported by truck

2.4 Material Properties

Concrete, mild steel, and prestressing strand were selected to match FDOT specifications. FDOT class VI concrete ($f'_c = 8500$ psi) was specified for the girders. Concrete compressive strength was tested using both 4x8 and 6x12 cylinders. Table 4 presents the tested concrete strengths.

Prestressing strands were Grade 270 low-relaxation, conforming to ASTM A416. Tested strand properties are shown in Table 5.

Bond capacity of the prestressing strands was tested in accordance with the proposed standard recommended by the North American Strand Producers (NASP 2009). Table 6 lists results of the NASP tests.

Table 7 presents the tested material properties for mild steel reinforcement. All reinforcement was ASTM A615 grade 60.

Table 4–Tested concrete compressive strengths

Material	Cast date	Test date	Average strength (psi)	Sample size	Testing agent*	Cure Method
Phase 2 Girder Concrete	2-17-12	2-20-12	7050	(2) 4x8 cylinders	1	Wet
		2-21-12	7330	(2) 4x8 cylinders	1	Field
		3-02-12	8790	(2) 4x8 cylinders	1	Wet
		3-16-12	8250	(3) 6x12 cylinders	2	Wet
		3-16-12	9210	(3) 4x8 cylinders	1	Wet
		5-30-12	10,520	(3) 6x12 cylinders	3	Field
* 1. Tested by girder fabricator 2. Tested by FDOT State Materials Office 3. Tested by FDOT Structures Research Center						

Table 5–Prestressing steel properties

Material	Stress at 1% elongation	Ultimate stress	Elongation at ultimate stress	Testing agent*
Prestressing Strand	261 ksi	287 ksi	5.38%	1
	259 ksi	285 ksi	NA	2
* 1. Strand supplier 2. FDOT State Materials Office (average of 4 samples)				

Table 6–NASP test results

Test Number	Load at 0.1-in. strand slip (lb)
1	26400
2	21600
3	23400
4	24400
5	21300
6	28200
Average	24200

Table 7–Steel reinforcement properties

Material	Yield Stress	Ultimate Stress	Elongation at Ultimate Stress	Testing agent*
#4 confinement rebar	70.0 ksi	109.1 ksi	11%	1
	76.4 ksi	106.8 ksi	11%	2
#5 vertical rebar	64.5 ksi	103.2 ksi	11%	1
	63.2 ksi	103.5 ksi	13%	2
* 1. Rebar supplier 2. FDOT State Materials Office (average of 2 samples minimum)				

3 Test Procedures

3.1 Fabrication

This section describes the procedures used to collect strain and crack data during fabrication. Data were collected during post-tensioning of specimen PT, during prestress transfer, and while the specimens were in storage awaiting transport.

Specimen PT Post-tensioning. It was assumed that post-tensioning of specimen PT did not affect the other specimens so data were only collect from specimen PT during this process. Prior to applying the post-tensioning, specimen PT was examined for cracks and null readings were taken from all instruments. Data from strain gages were monitored and logged using a computerized data acquisition system powered by portable generators. Data from vibrating wire strain gages were monitored using an electronic readout box and logged manually. The data acquisition systems were placed in a van adjacent to the stressing bed. Cracks were not observed during post-tensioning so no crack data were collected during this phase.

Prestress transfer. Strain and crack data were collected from each specimen during prestress transfer. Prior to transfer girders were examined for cracks and null readings were taken from all instruments. Data from strain gages were monitored and logged using a computerized data acquisition system powered by portable generators. Data from vibrating wire strain gages were monitored using an electronic readout box and logged manually. The data acquisition systems were placed in a van adjacent to the stressing bed. Strand cutting was paused at various times during prestress transfer to allow for visual inspection of the specimens and to take readings from the vibrating wire gages. Visual inspections and vibrating wire readings were also conducted after prestress transfer was complete. Crack locations were marked with a crayon or marker and documented by photograph. Crack widths were measured at few locations using a microscope that was precise to +/- 0.001 in. Crack lengths were determined by visual inspection with the naked eye.

Storage. Specimens received periodic visual inspections while they were in storage at the precast facility. During these inspections cracks were marked then documented by photograph. Crack widths were measured by microscope at few locations on each end region crack. Dates of visual evaluations are listed in Table 8. Vibrating wire gage data were also collected while the girders were in storage.

Table 8–Construction events and inspection dates

Event	Inspection Date	Days after prestress transfer
Form Removal	February 20, 2012	--
Prestress Transfer	February 21, 2012	0
In storage immediately after lifting	February 22, 2012	1
In storage	February 23, 2012	2
In storage	February 24, 2012	3
In storage	March 6, 2012	14
In storage	March 22, 2012	30
In storage	April 9, 2012	48
Prior to load testing	June 1, 2012	101

3.2 Load Testing

Load tests were conducted at the FDOT M. H. Ansley Structures Research Center in Tallahassee, FL. Test dates are listed in Table 9. Load tests were conducted on both ends of each girder. After the first end (specimen) was tested, the supports and load point were moved and the opposite end was tested.

Table 9–Load test chronology

Specimen	Test Date (service and ultimate)
PT	06/06/2012
LB	06/05/2012
CT	06/13/2012
SH	06/11/2012

Each specimen was loaded at least twice. The first loading simulated a service load of approximately 500 kip. Once the service load was reached, the load was held constant and cracks were identified and marked. After the cracks were marked the load was removed. The second loading was intended to determine each specimen’s ultimate strength. A load-displacement plot was monitored real-time during the ultimate load test. Load was applied until it was apparent from the load-displacement plot that peak capacity had been reached, or until the capabilities of the test equipment were reached. Cracking was documented after the ultimate load test was complete.

Load and support geometry are shown in Figure 28. Each support consisted of a 10-in. x 32-in. reinforced bearing pad. Pads were “Type E” pads constructed according to FDOT design

interim design standards (FDOT 2009). The bearing pad at the near support was centered below the embedded steel bearing plate (Figure 29).

Load was applied to the specimen using side-by-side hydraulic actuators. The load rate was controlled by adjusting a pump that pressurized the hydraulic system. The combined load rate varied from 0.1 kip/sec to 0.6 kip/sec, with the typical rate being approximately 0.4 kip/sec. Load was spread from the actuators to the girders through steel plates and a 10 in. x 30 in. reinforced neoprene bearing pad. The orientation of the bearing pad and steel plate at the load point for specimen LB is shown in Figure 32. This orientation affected an undesirable failure mode in LB, so the bearing pad and plate orientation were changed for the remaining tests. The modified load point setup oriented the bearing pad parallel with span length of the specimen and placed an additional steel spreader beam to distribute the load (Figure 31). A reaction frame was used to transmit load from the actuators to the strong floor (Figure 32).

Load, displacement, strand slip, and strain data were continuously collected during the service and ultimate load tests. Strain from the vibrating wires strain gages was collected at discrete points during load testing. Concrete samples were tested in conjunction with the load tests to determine compressive strength at the time of load testing.

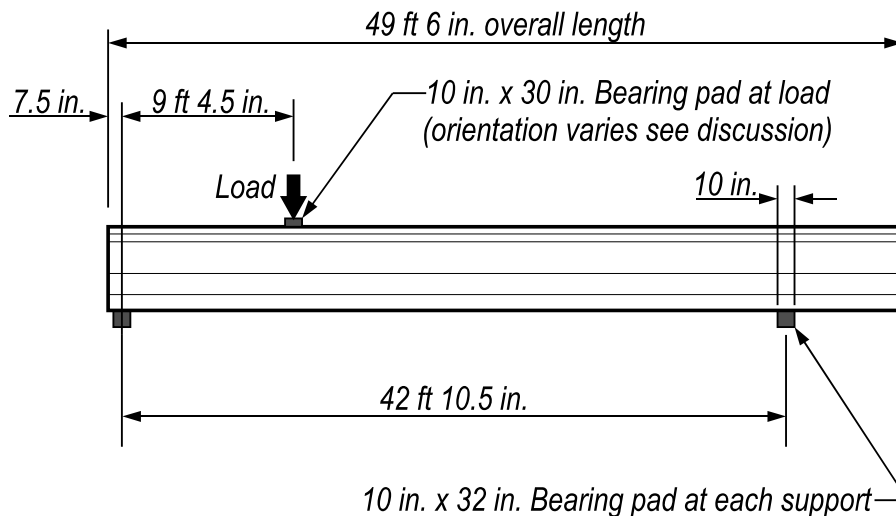


Figure 28–Test setup



Figure 29–Support conditions at bearing



Figure 30–Support conditions at load point for specimen LB



Figure 31–Support conditions at load point for specimens CT, SL, and PT



Figure 32–View of test specimen and load frame from above (left) and side view of specimen (right)

3.3 *Coordinate System*

A consistent coordinate system is used throughout this document to define instrumentation locations and to identify the direction of strains, stresses, and forces. The origin for the coordinate system is placed at the centerline of the cross-section, at the bottom of the girder, and at the girder end (Figure 33). The z-direction is vertical, the x-direction is horizontal across the width of the girder, and the y-direction is horizontal along the span length. The support nearest the origin is denoted as the near support, and the opposite end is denoted as the far support.

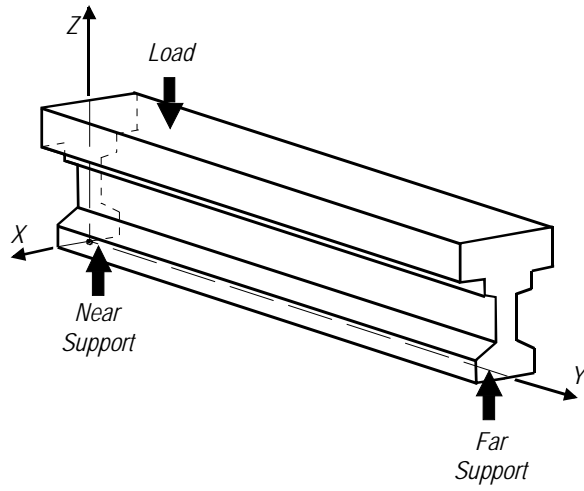


Figure 33—Coordinate system relative to load and supports

4 Instrumentation

Strain, displacement, force, and crack data were collected during fabrication and load testing. This chapter describes the instrumentation used to collect data and the labeling scheme used to identify the various instruments.

4.1 Types and Descriptions

Data were collected using load cells, LVDTs, linear potentiometers, variable resistance strain gages and vibrating wire strain gages. Table 10 lists the different types of instrumentation and the associated labels. With the exception of the vibrating wire strain gages, all data were logged electronically. Vibrating wire gage data were logged manually from an electronic readout box.

Table 10–Instrumentation types and labels

Label	Type	Placement
MS	Foil strain gage	Reinforcement
XS	Foil strain gage	Concrete surface
ES	Embedded strain gage	Concrete interior
V	Vibrating wire strain gage	Concrete interior
S	Foil strain gage	Concrete surface
L	Linear variable displacement transducer (LVDT)	Load point and supports
P	Linear potentiometer	Strands
--	Load Cell	Load point / post-tension rod

MS strain gages were attached to select mild reinforcement prior to placement in the test girders (Figure 34). MS gages had a gage length of 5mm and were used to monitor strain during load testing.

XS strain gages (Figure 35) were attached to the surface of test girders immediately after formwork was removed. These gages were used to measure concrete strains during prestress transfer. XS gages had a 60mm gage length.

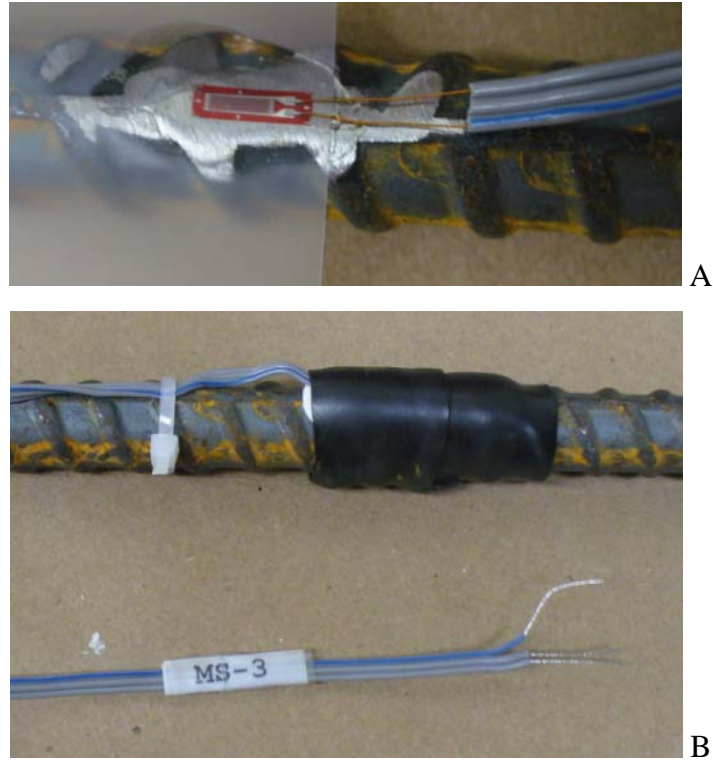


Figure 34–MS gage installation showing A) gage before protective covering and B) protective cover and label

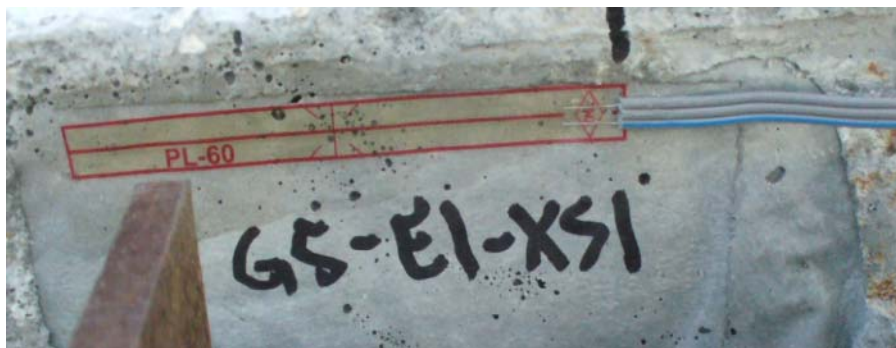


Figure 35–XS gage installation

ES gages were embedded in the test girders and were used to monitor concrete strain during prestress transfer and load testing. ES gages had a gage length of 60mm. Figure 36 shows ES gage installation prior to concrete placement. Wire leads from ES gages were routed along reinforcement and exited from the top flange. A label was placed at the end of each wire lead for identification purposes.

V series gages were vibrating wire strain gages which were embedded in the test girders. These gages had a gage length of 152mm and were used to measure concrete strain during all phases of fabrication and load testing. Figure 37 shows a V series gage installation prior to concrete placement. Because vibrating wire gages do not experience electronic drift over time, they were particularly useful in monitoring prestress losses.



Figure 36–ES gage installation



Figure 37–V gage installation (view from above)

S series strain gages were installed at discrete locations on girder surfaces (Figure 38). These gages had 60mm gages lengths and were used to monitor concrete strain during load testing.

L series instruments were LVDTs used to monitor vertical displacement during load tests. Labels and locations of the LVDTs measuring vertical displacement are shown in Figure 39. LVDTs were mounted to fixed support structures as shown in Figure 40.

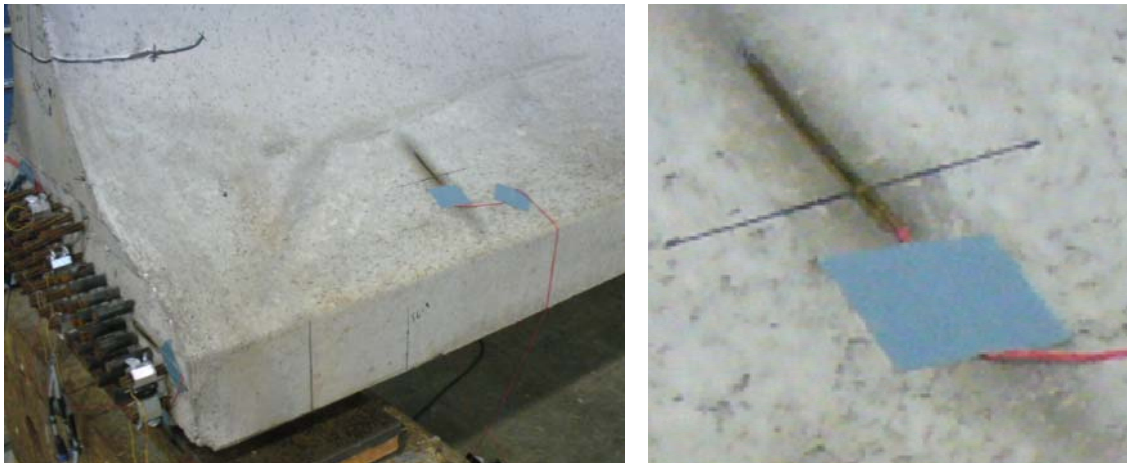


Figure 38–S gage installation on bottom flange (left) and close-up (right)

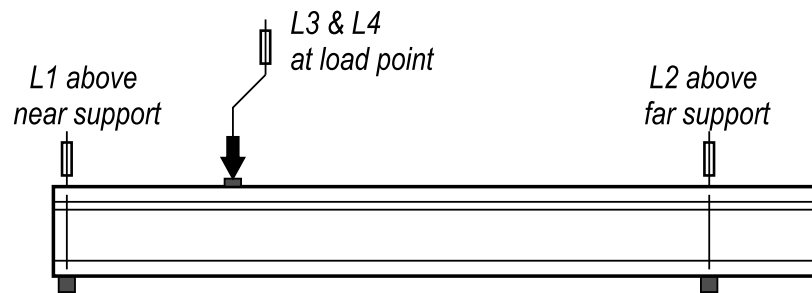


Figure 39–LVDT placement and labels



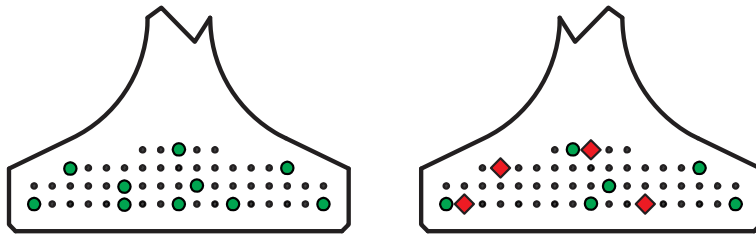
Figure 40–LVDT and support frame

P series variable resistant potentiometers were used to measure strand slip. Instrumented strands are shown in Figure 41. P series instruments were mounted directly to the strands using custom-machined aluminum brackets and set-screws (Figure 42).

Load cells (Figure 43) were used to measure the force applied during the load tests. A hydraulic system was used to apply the loads, and a pressure transducer was used to measure pressure in the hydraulic line during testing. Both force and pressure data were logged electronically, along with displacement and strain data from the other instruments.

Specimens PT, LB, and CT

Specimen SH



- – Fully bonded strand monitored by potentiometer
- ◆ – Partially bonded strand monitored by potentiometer

Figure 41–Strands monitored by potentiometers

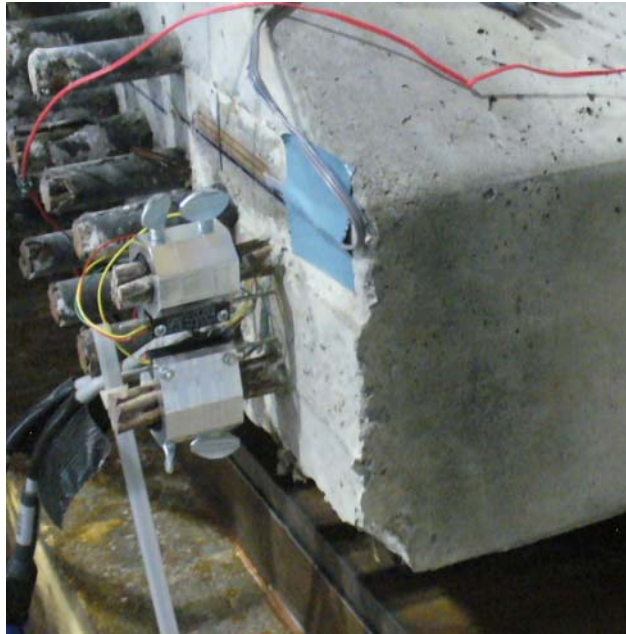


Figure 42–Aluminum brackets and linear potentiometers on strands



Figure 43–Load cells below hydraulic actuators

4.2 *Strain Gage Coordinates*

Figures in this document presenting strain data typically also contain information regarding the location of gage(s) from which the data were collected. Information in the figures gives a general idea of the gage orientation and position but doesn't always give specific coordinates. Table 11 through Table 14 give specific coordinates of gages referenced in this document. Coordinates are based on the system defined in Figure 33. Many gages used in the experimental program are not specifically referred to in this document.

Table 11–Specimen CT strain gage coordinates

Instrument	X (in.)	Y (in.)	Z (in.)	Orientation	Reference(s)
XS2	3.5	0.5	24	Z	Figure 50
XS3	3.5	4.25	24	Z	Figure 50
XS4	3.5	12	23.5	Z	Figure 50
XS5	19	6	6	Y	Figure 56
XS6	19	12	6	Y	Figure 56
XS7	19	17.5	6.25	Y	Figure 56
XS8	19	24	6.25	Y	Figure 56
XS9	19	29.75	6.25	Y	Figure 56
XS10	19	35.25	6	Y	Figure 56
V2	0	297	7.75	Y	Table 17
S4	3.5	72	36	Y-Z	Table 18

Table 12–Specimen SL strain gage coordinates

Instrument	X (in.)	Y (in.)	Z (in.)	Orientation	Reference(s)
XS2	3.5	0.5	24	Z	Figure 51
XS3	3.5	4.0	24	Z	Figure 51
XS4	3.5	12.0	24	Z	Figure 51
V2	0.0	297.0	7.5	Y	Table 17
S4	3.5	72.0	36.0	Y-Z	Table 18

Table 13–Specimen PT strain gage coordinates

Instrument	X (in.)	Y (in.)	Z (in.)	Orientation	Reference(s)
XS1	1.5	0	62.5	X	Figure 47
XS2	3.5	1.5	24.0	Z	Figure 47, Figure 52
XS3	3.5	4.0	24.0	Z	Figure 47, Figure 52
XS4	3.5	12.0	24.0	Z	Figure 47, Figure 52
V1	0.0	1.5	17.0	Y	Figure 45
V2	0.0	296.0	8.5	Z	Table 17
S4	3.5	72.0	36.0	Y-Z	Table 18

Table 14–Specimen LB strain gage coordinates

Instrument	X (in.)	Y (in.)	Z (in.)	Orientation	Reference(s)
XS2	3.5	0.5	23.5	Z	Figure 53
XS3	3.5	4.0	24.5	Z	Figure 53
XS4	3.5	12.0	23.5	Z	Figure 53
V2	0.0	298.0	8.5	Z	Table 17
S4	3.5	72.0	36.0	Y-Z	Table 18

5 Test Results and Discussion

5.1 Strain during Post-Tensioning

Vertical rods at the end of specimen PT were post-tensioned prior to cutting of the prestressing strands (Figure 10). Strain data from the concrete, as well as force data from the rods were collected during the post-tensioning process. Strain and load data are documented in this section.

Force data are presented in Figure 44 for rods #1 and #6. Time zero in the figure corresponds to the start of the post-tensioning. Rod #1 was farthest from the specimen end and was stressed first. Rod #6 was closest to the end as was stressed last. Tension in rod #1 reached a peak of 18 kip. At the end of post-tensioning the tension in #1 had reduced to 17.4kip. Loss of tension is the result of elastic losses as the other rods were being tensioned. Tension in #6 was 16.5 kip at the end of the post-tensioning process. Elastic losses did not affect rod #6 as it was the last rod to be tensioned.

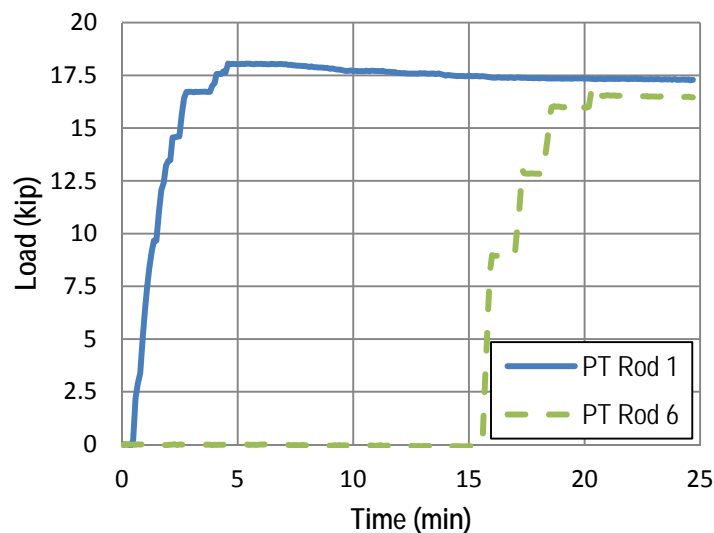


Figure 44–Variation in load during post-tensioning process

Tension in rods #2 though #5 were estimated using the turn-of-the-nut method. Tension force resulting from each turn was calibrated using data from rods #1 and #6 and was verified using linear elastic analysis of the rod elongation. The total post-tension force was estimated to

be 78kip. Dividing this number by the total number of turns suggests that post-tensioning was applied at a rate of approximately 6 kip/turn.

Strain effects from each turn-of-the nut are plotted in Figure 45. Strain in Figure 45 is from the vibrating wire gage placed vertically in the bottom flange (Figure 46). Strain at this location increased as the cumulative number of turns increased throughout the post-tensioning process. Abrupt jumps in the data at 2.2 turns and at 6.5 turns occurred during pauses in the post-tensioning. The strain-per-turn rate increased towards the end of the process as rods closer to the vibrating wire gage were tensioned.

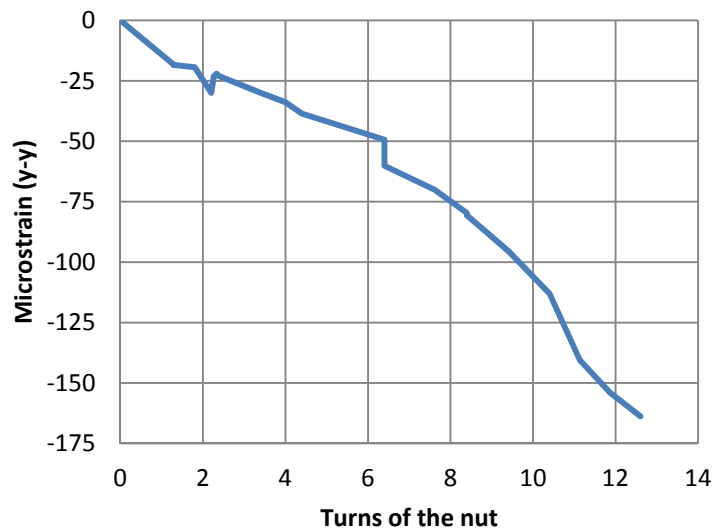


Figure 45–Strain measured by V1 gage during the post-tensioning process

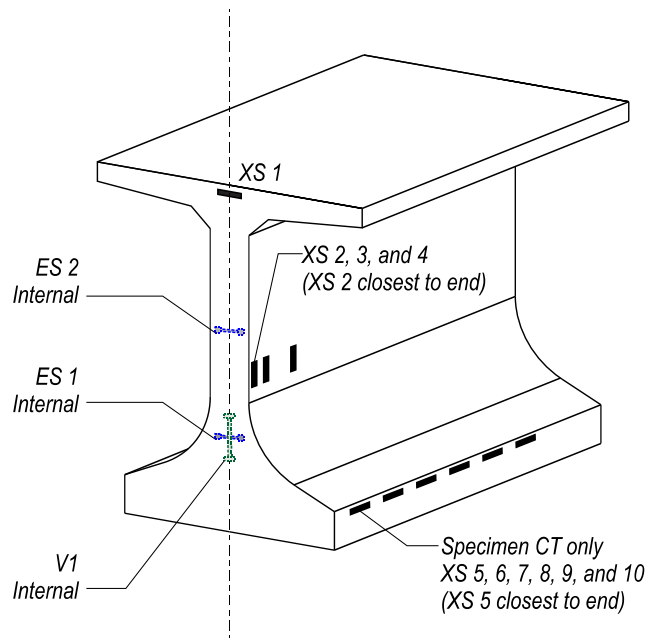


Figure 46–Gages at FIB-63 specimens

Strain gages placed on the concrete surface near the vibrating wire gage reported a similar magnitude of strain as the rods were post-tensioned (Figure 47). At the end of post-tensioning the vertical compressive strain at the end of the web was approximately 210 microstrain. Multiplying the experimental strains by an assumed a modulus of elasticity of 4750 ksi (based on measured compressive strength and empirical ACI equations) results in the stress profile shown in Figure 48. The location of zero stress at 17 in. was selected such that integrating the stress profile through the web results in 79kip which is close to the estimated post-tension force. This approximation is based on limited data, but does suggest that the post-tensioning was most significant at the end of the member and was effective over a finite distance of approximately 17 in. from the end.

Gage XS1 was placed horizontally at the end of the specimen near the post-tension bearing plate. This gage reported tension due to bursting action from the post-tension force. Although tensile strains were reported, no cracks were observed during or immediately after post-tensioning. Based on the experimental strain data it is estimated that the tensile strain at XS1 was approximately 585 psi at the end of post-tensioning.

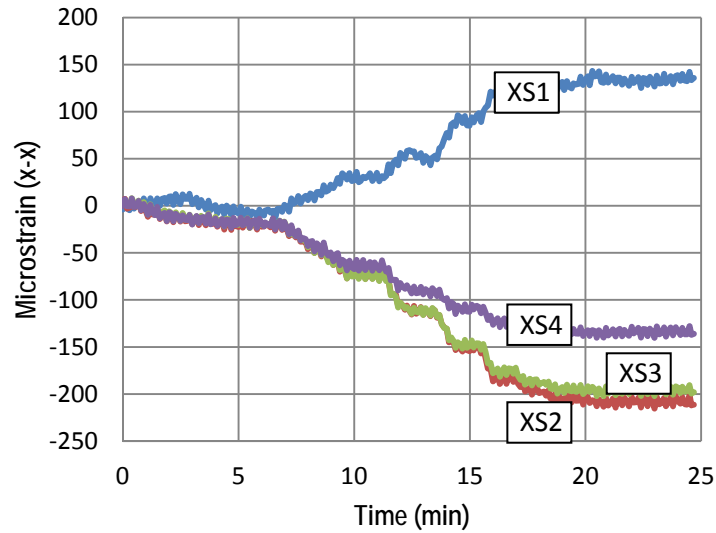


Figure 47–Strain due to post-tensioning process in XS gages

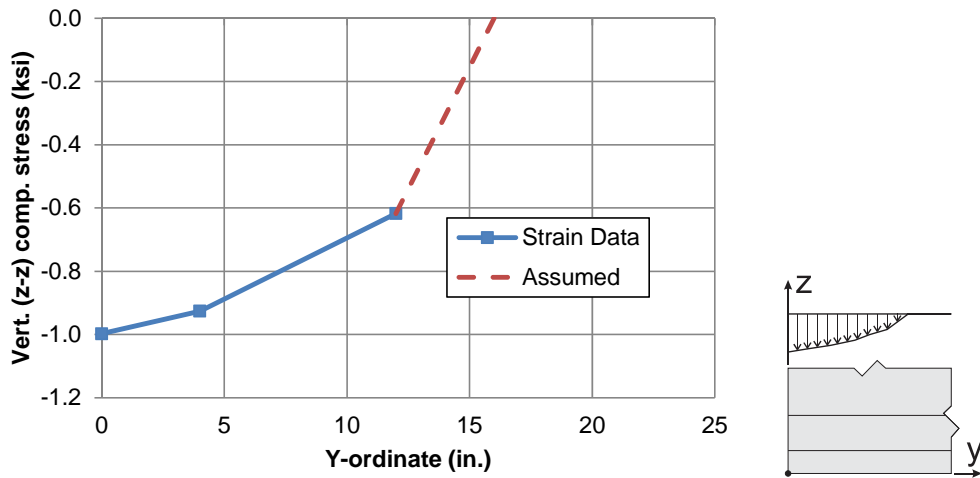


Figure 48–Estimated stress profile in web due to post-tensioning (tension positive)

5.2 Strain and Cracking during Prestress Transfer

Strain and crack data were collected during prestress transfer. To facilitate discussion of strain data, strand cutting events were broken into the stages listed in Table 15. Strand cutting events listed in Table 15 are keyed to the strand cutting pattern shown in Figure 49.

Table 15–Girder fabrication stages

Stage	Event
J	strands 1-4 cut
K	strands 5-30 cut
L	Pause
M	strands 30-56 cut
N	all strands cut

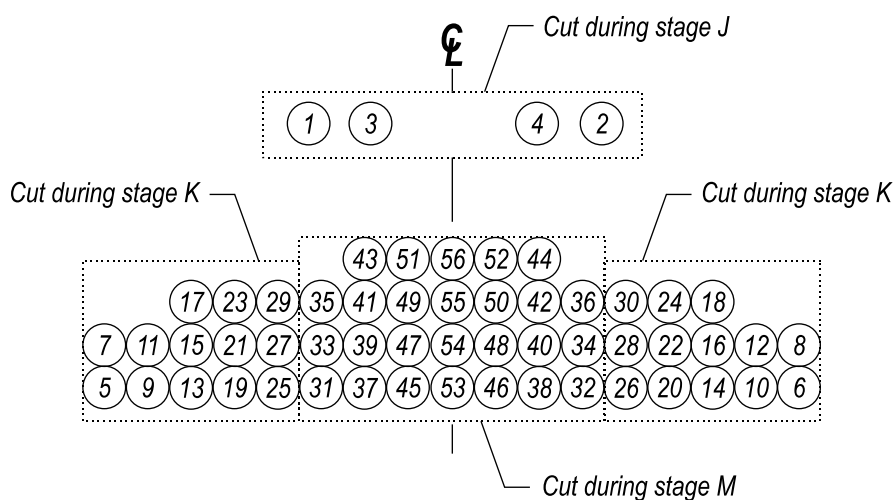


Figure 49–Strand cutting pattern groups

Vertical strain in the web became increasingly tensile in each specimen as prestress force was transferred to the girders (Figure 50 through Figure 53). Data indicate that strain was typically largest at the end of the girder (XS2) and smaller away from the end (XS4). For example, vertical strain in specimens CT at gage XS2 was 190 microstrain during stage L and only 90 microstrain at XS4.

Cracks were visually observed in specimen CT immediately after prestress transfer (Figure 54). Abrupt changes in strain behavior at approximately 57 minutes suggest that the cracks formed during stage M (Figure 50).

Cracks were also observed immediately after transfer in specimen LB (Figure 54). As with specimen CT, abrupt changes in strain behavior at approximately 57 minutes suggest that

the cracks formed during stage M (Figure 53). Cracking may have initiated during stage K as suggested by the abrupt changes at approximately 18 min.

Cracks were not observed in specimens SL or PT during or immediately after prestress transfer. The lack of cracking in these specimens is consistent with strain behavior demonstrated by the vertical gages. With the exception of XS2 on specimen SL, no abrupt changes in strain were observed in SL or PT. Lack of cracking in SL is attributed to the lower stresses affected by strand shielding. Lack of cracking in PT is attributed to the pre-compression in the web introduced by the post-tensioning.

For specimen PT, vertical strain at the beginning of transfer was initially compressive (Figure 52) due to the post-tension force discussed in the previous section. Strain reported by gages XS2 and XS3 became tensile as the outer strands were cut during stage M. Multiplying the final strain during stage N by an elastic modulus of 4750 ksi gives an estimated stress profile in the web (Figure 55). Integrating the tensile stress portion over the web area results in an estimated net tension force of 9.2kip.

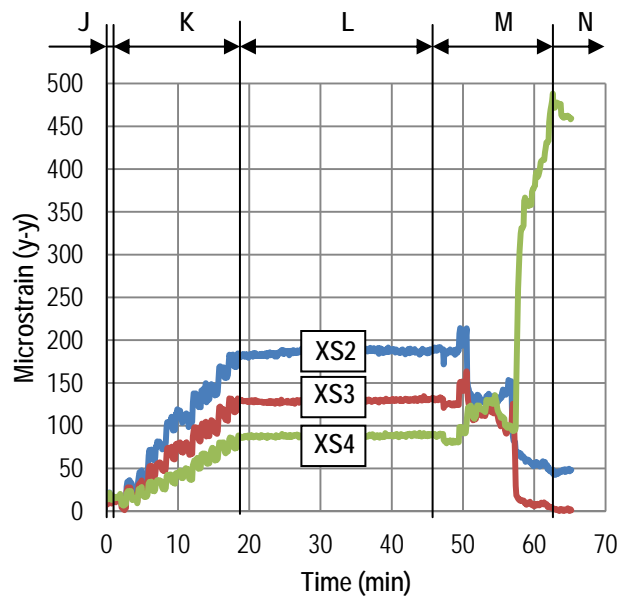


Figure 50–Concrete strain in specimen CT during prestress transfer

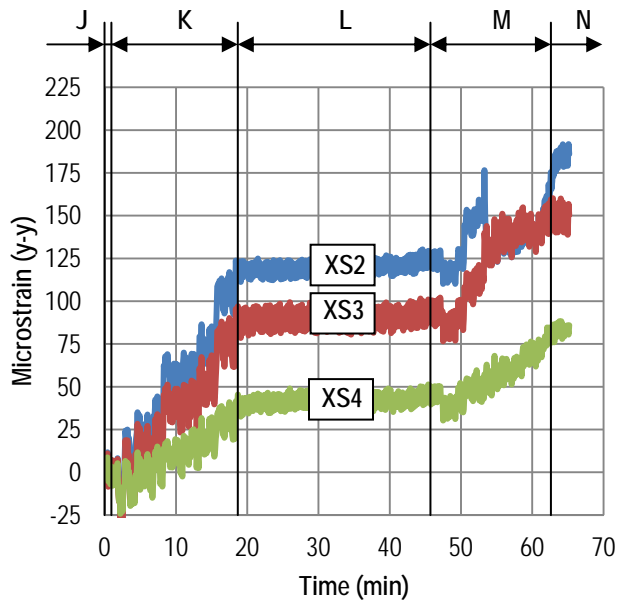


Figure 51–Concrete strain in specimen SL during prestress transfer

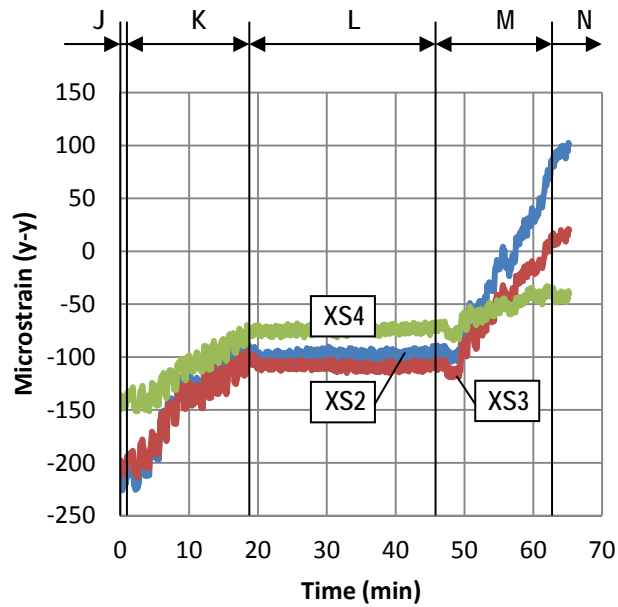


Figure 52–Concrete strain in specimen PT during prestress transfer

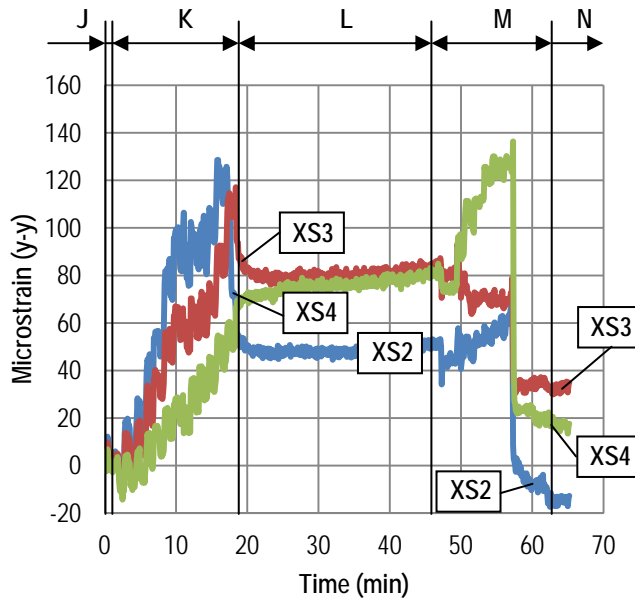


Figure 53–Concrete strain in specimen LB during prestress transfer

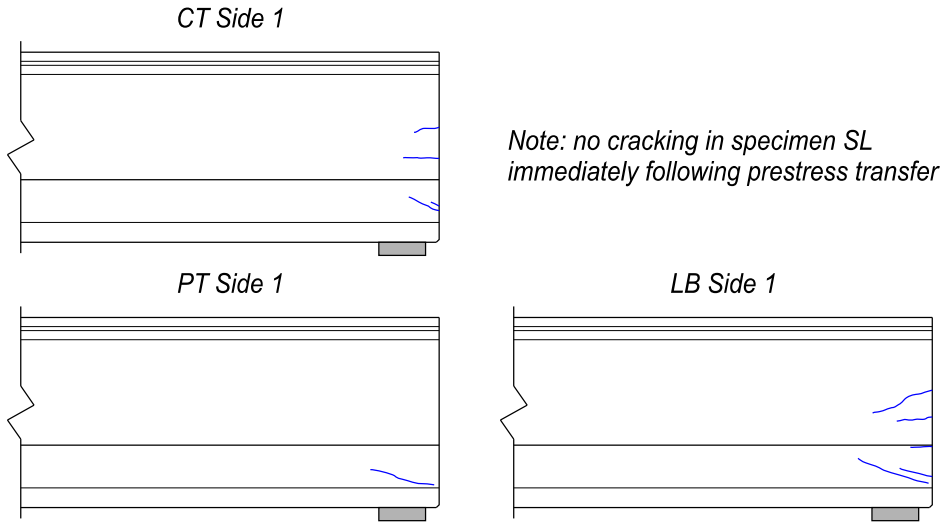


Figure 54–Cracks after prestress transfer

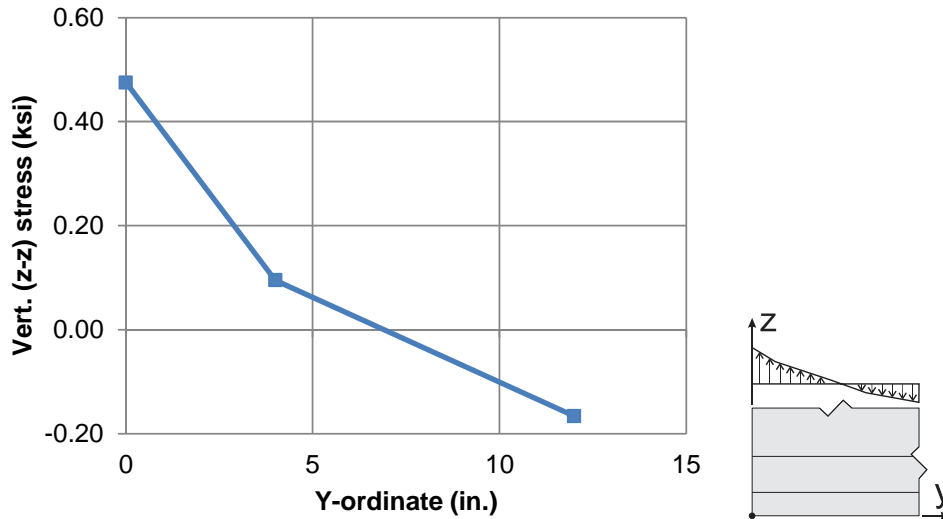


Figure 55–Estimated stress profile in web of specimen PT after transfer (tension positive)

Strain gages XS5 through XS10 (Figure 46) were placed on the bottom flange of CT to experimentally evaluate the transfer length. When sufficient data are available, the 95% Average Maximum Strain (AMS) Method is a well-established method for determining transfer length from experimental strain data (Russell and Burns 1996). The available strain data in the current study were insufficient to apply the AMS method, but were still sufficient to give an estimate of transfer length.

Strain data from stage N (all strands cut) are shown in Figure 56 for gages XS5 through XS10. Blue diamond markers indicate values from the gages. A bilinear curve representing the apparent strain is also shown. Gages reported increasing strain with increased distance from the girder end. The rate of increase dropped after 30 in. suggesting the end of the transfer length. A 30 in. estimated transfer length is consistent data from the FIB-54 girders fabricated at the same time (see Appendix D).

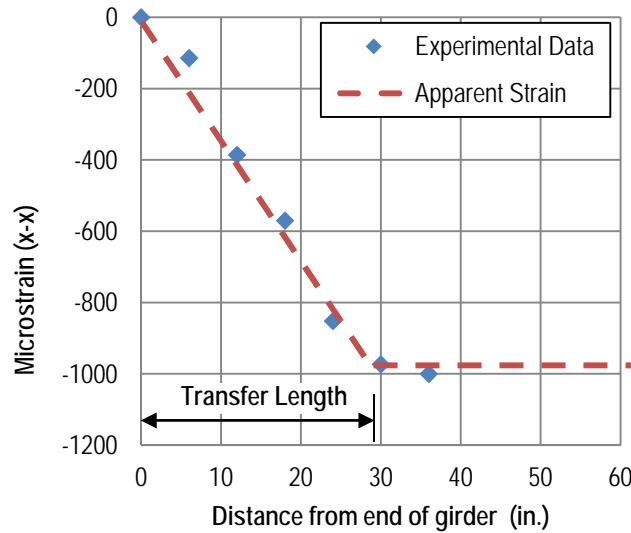


Figure 56–Strain and subsequent apparent transfer length

5.3 Web Cracks

Specimens were inspected for cracking during prestress transfer and during the days and weeks following transfer (Table 8). Cracks were first observed to form during prestress transfer. The initial cracks grew and additional cracks formed during the days and weeks following prestress transfer. Figure 57 shows the formation and propagation of cracking in specimen CT. Crack quantity and length also grew over time in the other specimens. Figures documenting cracking in the other specimens are included in Appendix H.

The observed crack patterns varied among specimens as shown in the photos in Figure 58. Cracks in the end region were observed in the top flange, web and bottom flange. Flexural cracks were also observed throughout the span lengths but are not shown in the figures. Cracks in each specimen prior to load testing are shown in Figure 59 through Figure 62. Web splitting cracks are the primary focus of the FIB-63 test program and are discussed in the proceeding paragraphs.

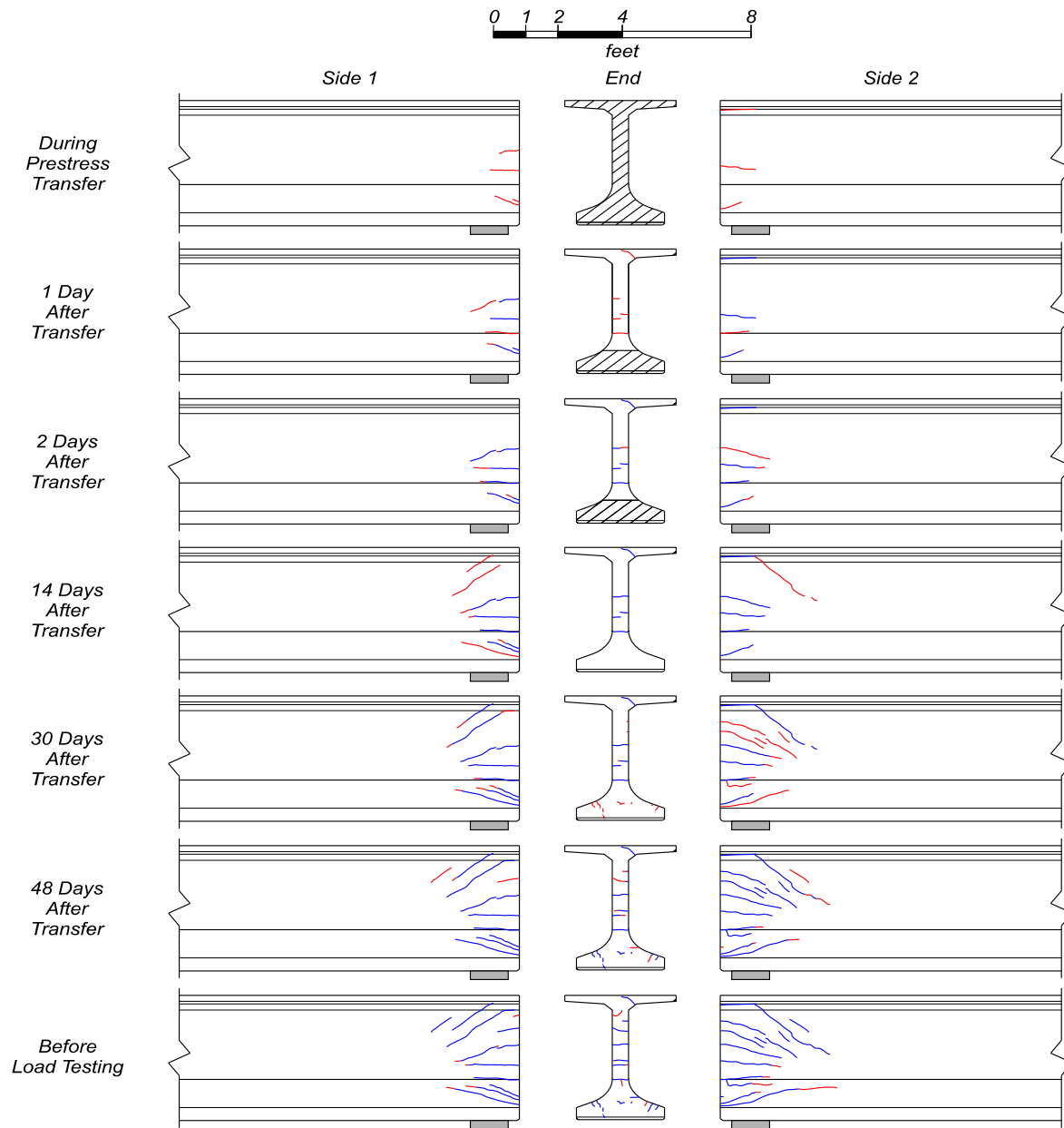


Figure 57–Crack growth in specimen CT (flexural cracks in top flange not shown)

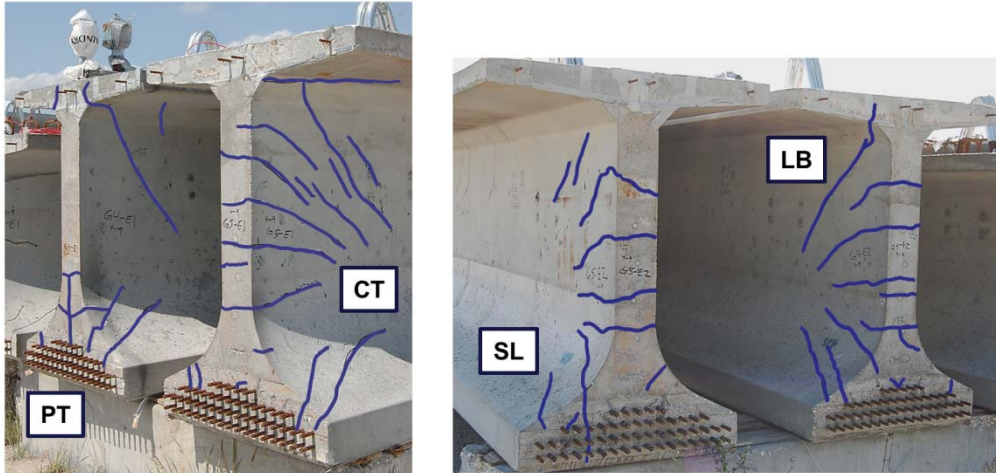


Figure 58–Photo of end region cracks (cracks enhanced in blue)

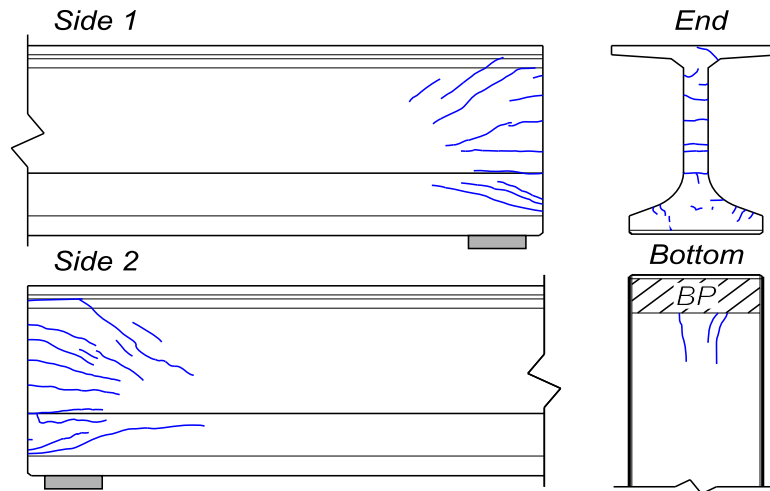


Figure 59–Specimen CT end region cracks prior to load testing

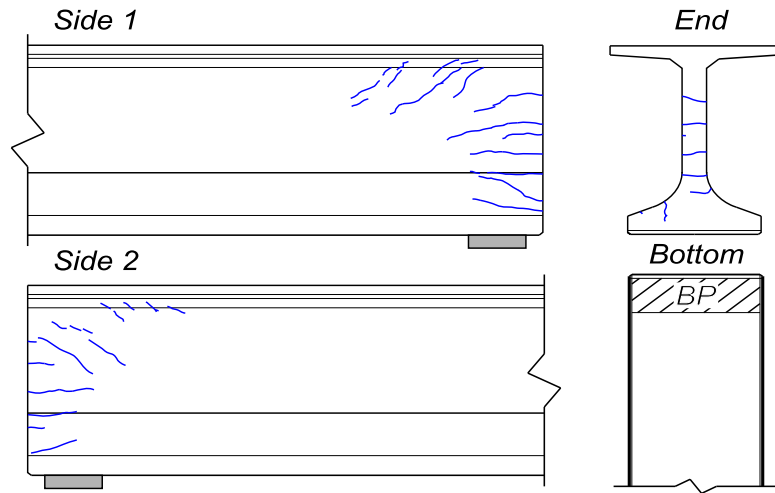


Figure 60—Specimen SL end region cracks prior to load testing

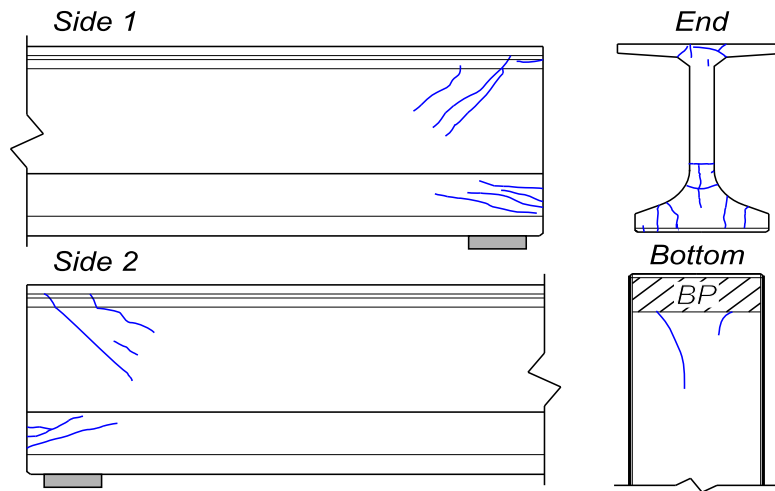


Figure 61—Specimen PT end region cracks prior to load testing

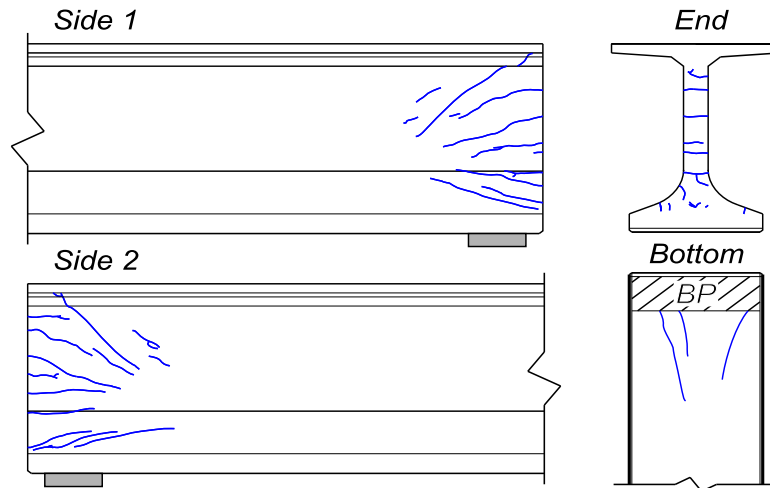


Figure 62–Specimen LB end region cracks prior to load testing

Web crack data from each specimen are quantified in Figure 65 and Figure 66. Four metrics are used for comparison: total length, total area, average width and maximum width. Total length was calculated by the summing the length of all individual web cracks in a specimen. Total area is the summation of areas from the individual web cracks, which was calculated by multiplying the individual crack lengths by a representative width. Average width was calculated by dividing the total area by the total length. Finally, maximum crack width was taken as the maximum width observed by the microscope readings.

Representative widths used to calculate crack area were derived from width measurements taken by microscope. The means of determining the representative width was different depending on the crack location. For the portion of a crack on the end face of a specimen, the representative width was taken as the measured width (Figure 63). Where multiple measurements were taken for the same crack on the end face, the representative width was taken as the average of the measurements. For the portion of a crack on the side of a specimen (Figure 64) the representative width was taken as the average of all widths measured along the crack. Only a single measurement was taken for some cracks on the specimen sides. The single measurements typically occurred near the end face where cracks had their greatest width. In these cases, the representative width was taken as one-half of the measured width.



Figure 63–Web crack measurements (view from end of specimen)

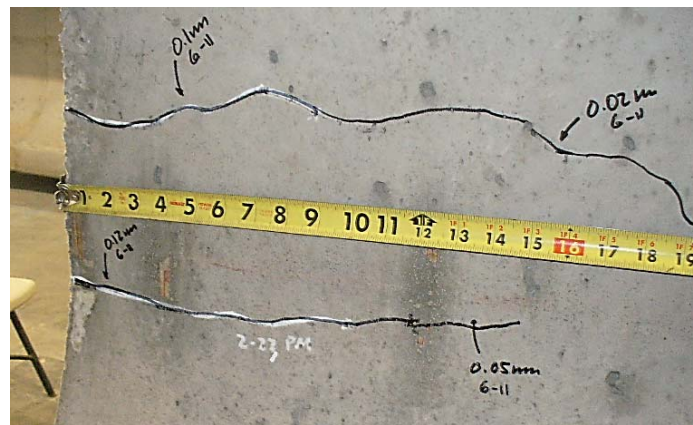


Figure 64–Web crack measurements (view from side of specimen)

Some degree of cracking is expected and generally accepted in the end region of pretensioned girders. Tadros et al. (2010) presented criteria for evaluating crack widths and determining when web cracks should be repaired (Table 16). According to these criteria, web splitting cracks wider than 0.012 in. require corrective action. Cracks with widths less than 0.012 in., though undesirable, do not warrant corrective action. Web crack widths in this test program were less than 0.012 in. and would not require corrective action according to the Tadros et al. criteria. FDOT specifications contain similar repair criteria, requiring corrective action for web cracks greater than 0.012-in. wide (FDOT 2011). For girders used in environments characterized as extremely aggressive, FDOT specifications requires corrective action for all web splitting cracks regardless of width.

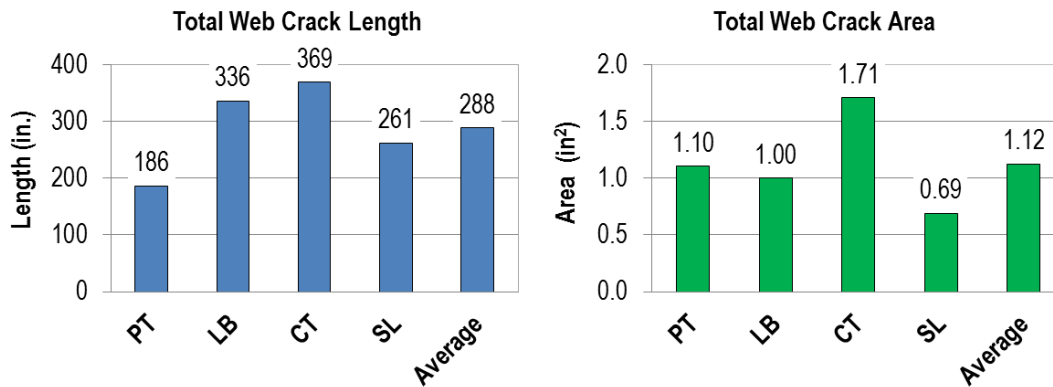


Figure 65–Web splitting crack length and area

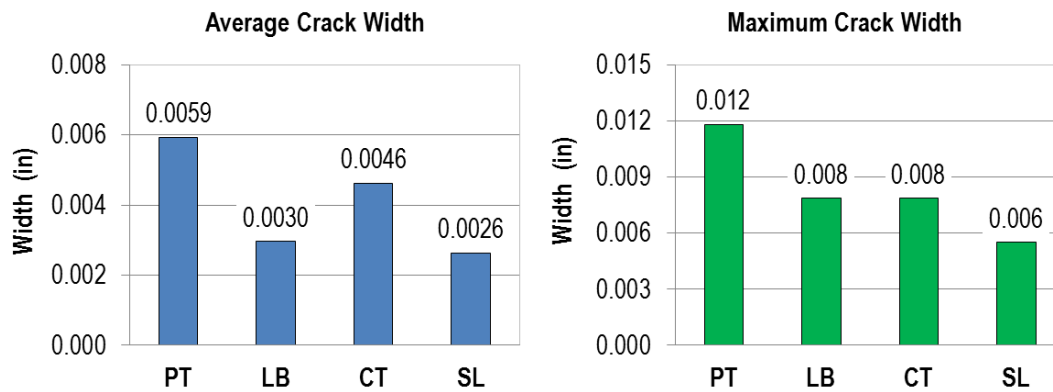


Figure 66–Web splitting crack widths

Table 16–Recommend action for web splitting cracks (Tadros et al. 2010)

Crack Width (in.)	Required Action
Less than 0.012	None
0.012 to 0.025	Fill cracks with cementitious material and apply surface sealant to end 4 ft of girder
0.025 to 0.05	Fill cracks with epoxy and apply surface sealant to end 4 ft of girder
Greater than 0.05	Reject girder unless shown by detailed analysis that structural capacity and long-term durability are sufficient

Data presented in Figure 65 and Figure 66 are useful for comparing the relative effectiveness of the different detailing schemes in controlling web cracks. Based on the metrics of total length and total area, the control detail (specimen CT) was the least effective in

controlling web splitting cracks. Specimen CT at had 28% more length and 53% greater area than the average of all specimens.

Specimen SL was the most effective detail according each metric except total length. SL had 59% less area, and 44% smaller average width than the control specimen. The reduction in crack length, area, and width observed in specimen SL is attributed to the partial strand debonding which reduced tensile stresses in the end region.

In terms of crack length, the post-tensioning detail of specimen PT was the most effective for controlling web splitting cracks. Web splitting crack length in specimen PT was 50% less than the control specimen. Figure 61 shows that the post-tensioning effectively mitigated all web cracks at the end surface of the member. Web cracking did, however, occur away from the end surface.

Web cracks away from the end of specimen PT extended diagonally into the web from the post-tensioning anchor plate. Forces introduced at the plate are believed to have contributed to the formation of the diagonal cracking in specimen PT. The diagonal web crack in PT had the greatest width of web crack in the test program. Specimen PT also had the largest average web crack width of approximately 0.006 in. This value was 30% greater than the control specimen.

Detailing of specimen PT had negative effect on the bottom flange spitting cracks. Referring to Figure 61, it can be observed that PT was the only specimen to have a vertical splitting crack on the end surface. This crack is attributed to development of the post-tensioning rods in the bottom flange.

Specimen LB compares well against the control specimen in every metric except maximum crack width, for which LB and CT both had a maximum crack width of 0.008 in. For LB, the total web crack length was 10% smaller and the average web crack width 35% smaller, than in the control specimen.

5.4 Prestress Losses

Vibrating wire strain gages were placed longitudinally near mid span to experimentally evaluate prestress losses. The gage in the girder PT/LB malfunctioned before valid data could be collected. The gage in girder CT/SL also malfunctioned, but not before sufficient data were collected to evaluate elastic losses. Experimental and code-calculated prestress losses are presented in Table 17.

Experimentally determined elastic loss in the girder with specimens CT and SL was higher than the AASHTO and PCI calculated elastic losses. The experimental long term losses, however, were less than half of those calculated by the code methods. This is likely due to the fact that the experimental long term losses were not actually long term; they were taken over a two week period. The AASHTO and PCI long term losses assume a much longer time period. Based on the experimental results it is believed that total losses were approximately 30% at the time of load testing. FIB-54 girders fabricated at the same time the FIB-63 specimens reported 12%-17% elastic losses and 22%-30% total losses (see appendix D).

Table 17–Experimental and code prestress losses

Prestress Losses	Experimental		Code	
	CT and SL*	PT and LB**	AASHTO	PCI
Elastic Losses (%)	18.9%	N/A	15.1%	11.8%
Long Term Losses (%)	9.2%	N/A	15.0%	26.9%
Total Losses (%)	28.2%	N/A	30.1%	38.7%
Measurement Period (Days)	14	-	-	-
Initial Prestress (kip)	2354			

* Gage malfunction at 14 days

** Gage malfunction

5.5 Load Tests

Load tests were conducted to evaluate the effects of each detailing scheme on end region capacity. Specimens were loaded in 3-point bending and an a/d ratio of approximately 2. Test results are presented in terms of superimposed shear, which is defined as the shear due to the applied load at the near support. Self-weight is not included in the superimposed shear. Displacement results are presented as the vertical displacement at the load point. Results have been adjusted to remove the effects of bearing pad displacement.

Each specimen was loaded twice. The first test mimicked service loading and the second test determined ultimate capacity. Maximum shear force in the service load test was 390kip. Shear-displacement data from the ultimate load tests are presented in Figure 67, and shear-strand slip data are presented in Figure 68. Slip data is presented as the average slip of all monitored fully bonded strands. Specimen LB was excluded from Figure 68 due to minimal slip.

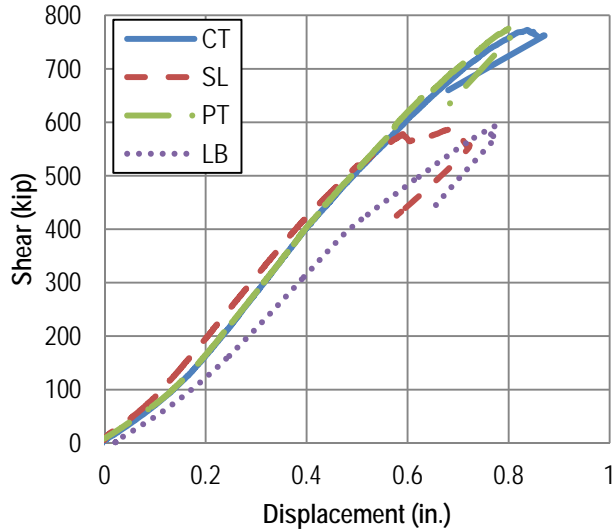


Figure 67–Ultimate load test shear-displacement for all specimens

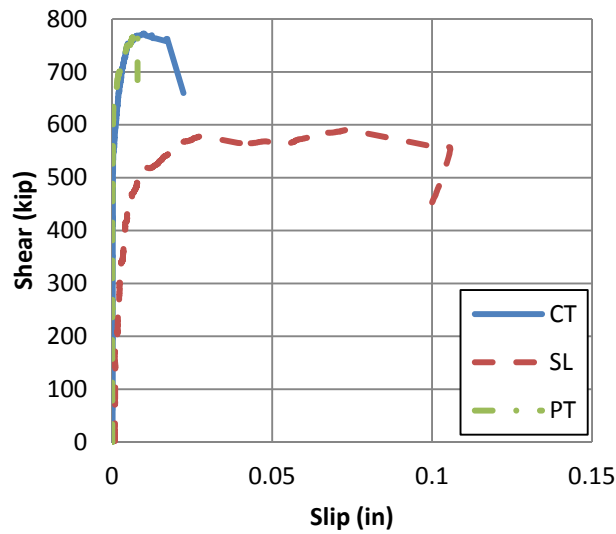


Figure 68–Ultimate load test shear-strand slip for specimens CT, SL, and PT

Shear forces associated with the first cracks during load testing are listed in Table 18. In three of the four specimens cracking was first reported by strain gage placed diagonally on the web (Figure 69) within the shear span. The first crack in each specimen was an inclined crack in the web. Discussions of load, slip, and crack data are presented in the following sections for each of the four specimens.

Table 18–First cracks during service load testing

Specimen	Shear at first crack observation	
	Gage (kip)	Visual (kip)
CT	350	345
SL	240	275
PT	350	370
LB	310	365

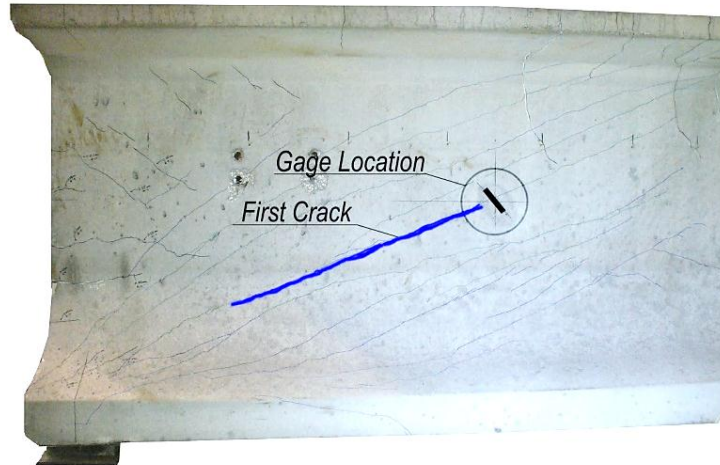


Figure 69–Strain gage and typical first crack location

5.5.1 CT

Vertical reinforcement in the end region of specimen CT (Figure 9) was based on FDOT standards. All (52) strands in specimen CT were fully bonded (Figure 7).

Load-displacement response of CT was approximately linear-elastic during service and ultimate loading (Figure 67). The first crack to form during the service load test occurred in the web at a superimposed shear of 350 kip. Additional web cracks formed at higher loads during the service and ultimate strength tests. Flexural cracks were not observed.

Strand slip in CT was negligible until the superimposed shear reached approximately 550 kip. Slip increased gradually beyond 550 kip, reaching a maximum slip of 0.016 in. at peak load.

Specimen CT failed in a brittle manner at a shear force of 773 kip. At this load the web crushed in dramatic fashion with concrete pieces spalling off the girder. Failure was categorized as a web-shear shear failure (Figure 70). After testing it was observed that the top hooks of the vertical reinforcement experienced breakout failure due to lack of sufficient cover (Figure 71). Top hooks from the vertical reinforcement were embedded in the relatively thin top

flange because a topping slab was not cast on the specimen. It is not known if the hook failure precipitated or was a by-product of the web failure. The bearing pad at the load point also punched through the top flange at peak load (Figure 71).

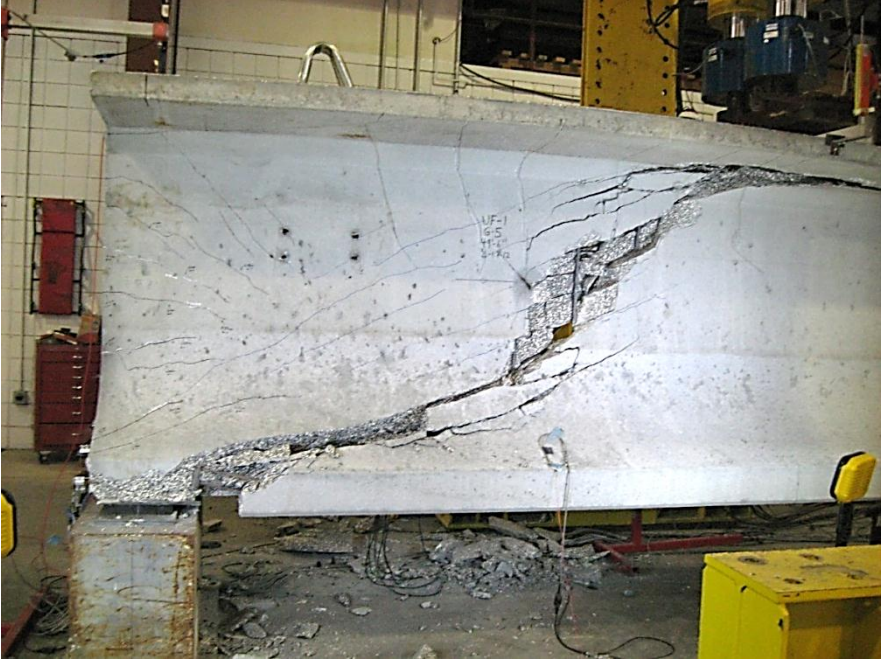


Figure 70–Specimen CT after load tests

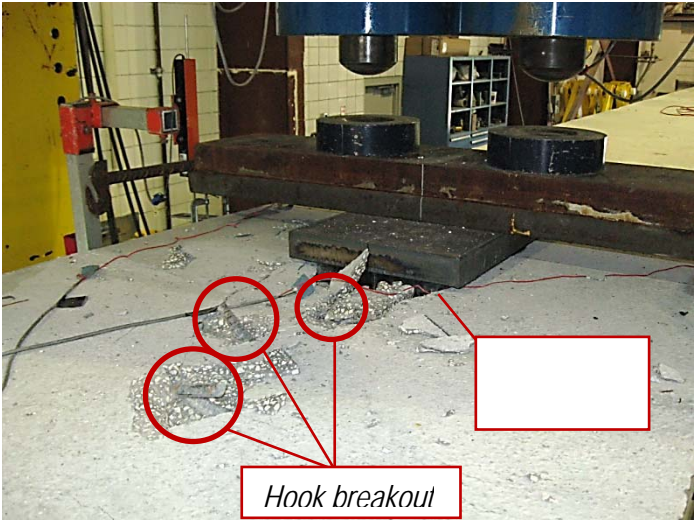


Figure 71– Punching failure and hook breakout at load point

5.5.2 SL

Vertical reinforcement in specimen SL (Figure 9) was based on FDOT standards. Of the (52) strands in SL, (23) were shielded for 5 ft from the specimen end (Figure 7).

Load-displacement response of SL was approximately linear-elastic during service load test and during the initial portion of the ultimate loading (Figure 67). The first crack to form during the service load test occurred in the web at a superimposed shear of 240 kip. Load at first crack was 30% to 45% lower than the other specimens. The lower cracking load is attributed to the reduced prestress force occurring at the end of specimen SL. This result demonstrates a potential serviceability problem with strand shielding. Although shielding reduces the vertical tensile stresses leading to web splitting cracks at prestress transfer, shielding also reduces the horizontal compressive stresses that acts to delay cracks in the web due to loading. Flexural cracks were not observed.

Additional cracks formed as the load increased beyond the initial cracking load. Some of these cracks entered the bottom flange thereby interrupting strand development and affecting strand slip. Popping sounds indicative of strand slipping were heard beginning at shear of approximately 390kip. Based on the shear-slip behavior shown in Figure 68 it is believed that strand slip started at approximately 300kip. Strands in SL began slipping at lower loads and slipped a greater distance than did strands in the other specimens. Peak load in SL corresponded to a strand slip event. As such, failure of SL was categorized as a bond-shear failure (Figure 72, Figure 73).

Specimen SL supported a maximum shear of 591kip, which was the smallest peak load of all the test specimens. The reduced number of fully bonded strands in SL was culpable for the bond-shear failure and lower capacity. Specimens CT, LB, and PT had almost twice as many bonded strands and were less affected by cracks interrupting the strand development length. As such bond-shear failure did not occur in these other specimens.

After reaching the maximum load, SL continued to carry load with a stick-slip behavior controlled by strand slip. Load was removed after it had become apparent from the load-displacement curve that peak load had been reached. Because of the stick-slip behavior, failure of SL was slightly more ductile than the other specimens (Figure 67).



Figure 72–Bond shear failure of specimen SL



Figure 73–Bottom flange cracking at SL bearing.

5.5.3 PT

The end of specimen PT (Figure 10) was vertically post-tensioned by tightening threaded rods prior to prestress transfer. PT also had a 33% reduction in vertical end region reinforcement relative to specimen CT. All of the (52) strands in PT were fully bonded (Figure 7).

Shear-displacement response of PT was approximately linear-elastic throughout the service and ultimate load tests (Figure 67). The first crack to form during the service load test occurred in the web at a superimposed shear of 350 kip. Additional web cracks formed at higher loads during the service and ultimate strength tests. Flexural cracks were not observed.

Strand slip behavior in specimen PT was similar to the control specimen (Figure 68). This result suggests that the vertical post-tensioning did not influence the strand-concrete bond

during ultimate load testing. Maximum slip in PT was approximately 0.01 in. occurring at peak load.

Specimen PT did not fail before reaching the capacity of the test apparatus and failure behavior could not be determined. Specimen PT was loaded to 782kip in shear, which was the greatest of any specimen. This result suggests that the post-tensioning had no adverse effect on the ultimate capacity. Multiple web cracks had formed in the web prior to peak load (Figure 74). Some of these cracks had propagated to the end of the specimen.



Figure 74—Cracking specimen PT

5.5.4 LB

Vertical end zone reinforcement in specimen LB (Figure 10) consisted of eight 1-in. diameter vertical threaded rods. These rods represented a 30% increase in vertical end region reinforcement relative to the control specimen CT. Each of the (52) strands in specimen LB was fully bonded (Figure 7).

Load-displacement behavior of LB was approximately linear-elastic throughout the ultimate load test (Figure 67). Apparent stiffness of LB was less than the other specimens. This difference is attributed to the orientation of the load point (Figure 30). Because the applied load was spread directly to the outer portions of the top flange, it is believed that the flange in specimen SL experienced a greater degree of displacement. The LVDTs monitoring vertical displacement (Figure 40, Figure 75) were placed at the edges of the flange and would have been sensitive to differences in displacement resulting from the load condition unique to LB.

Additional displacement due to the load condition affects the lower stiffness of LB relative to the other specimens.

The first crack to form during the service load test occurred in the web at a superimposed shear of 310 kip. Additional web cracks formed at higher loads during the service and ultimate strength tests. Flexural cracks were not observed.

Specimen LB failed in the top flange due to punching failure (Figure 75). Punching failure occurred because load was applied across the width of the relatively thin top flange. Cracking associated with punching failure is shown in the photos in Figure 76 and Figure 77.

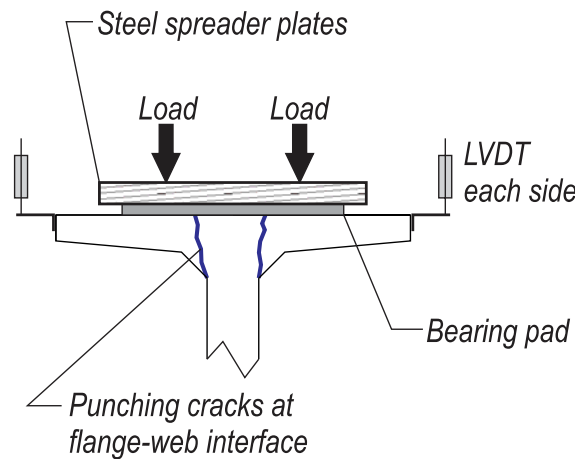


Figure 75–Punching failure specimen LB

Strand slip in specimen LB was negligible. Lack of slip was due to the relatively low loads supported by LB. Had LB supported similar loads to CT and PT, strand slip likely would have occurred.

Specimen LB supported a maximum shear of 594kip. Specimen LB was the first to be load tested. To prevent the reoccurrence of punching shear failure in the other specimens the load point configuration was adjusted.



Figure 76–Punching shear failure in specimen SL



Figure 77–Punching failure from above (left) and below (right)

5.6 Code Comparison

Experimental shear capacities were compared to nominal capacities calculated from three different procedures:

- Detailed procedure from ACI 318. (labeled as ACI V_n)
- General procedure from AASHTO LRFD. (labeled as LRFD V_n)
- End region tie requirement based on AASHTO LRFD 5.8.3.5. (labeled as Tie V_n)

All calculated capacities were based on the tested material properties and losses.

Calculations of the end region tie requirement followed the procedure proposed by Ross et al. (2011) for determining a nominal capacity based on AASHTO LRFD minimum tie requirements. A required development length 60 in. was assumed and an available development length of 25

in. was assumed. The nominal capacity due to the end region tension tie was lower for SL than for the other specimens because SL had fewer fully bonded strands to act as a tension tie.

The critical section for nominal shear capacity calculations (ACI and LRFD) occurred at the load point. At this section the prestressing force, reinforcement, and material properties were the same for each specimen, and all specimens have the same ACI and LRFD nominal capacities.

Nominal capacities from each method are presented in Table 19 along with maximum experimental shear forces. To facilitate comparison with nominal capacities, the maximum experimental shear forces listed in the table include the superimposed shear and the self-weight shear.

When comparing experimental and nominal capacities it is critical the failure behavior of the specimens be considered. Specimens CT failed in web-shear and can be directly compared to the ACI and LRFD nominal capacities which are based in-part on web-shear failure. Specimen SL failed in bond-shear and can be directly compared to the nominal capacity from the tie requirements which were derived assuming bond-shear failure. Specimen PT did not fail during testing and cannot be directly compared with any of the methods. Finally, specimen LB failed in flange punching shear which is not considered by any of the calculation methods.

Table 19–Code comparison with experimental shear forces

Specimen	V_{exp} (kip)	ACI V_n (kip)	LRFD V_n (kip)	Tie V_n (kip)	EXP / ACI	EXP / LRFD	EXP / TIE
CT	791	524	516	997	1.51	1.53	0.79
SL	609	524	516	673	1.16	1.18	0.90
PT	800	524	516	997	1.53	1.55	0.80
LB	612	524	516	997	1.17	1.19	0.61
Average					1.34	1.36	0.78

Important information can be gleaned from the comparisons in Table 19 in spite of the different failure modes exhibited by the specimens and assumed in the calculation procedures. First, the experimental capacities were always greater than nominal shear capacities calculated by ACI and LRFD. Thus the ACI and LRFD methods were conservative relative to the test results, regardless of failure behavior. Second, the experimental capacity of specimen SL was 10% lower than the nominal capacity based on the end region tie. It is critical to select

appropriate values for the available and required strand embedment as these the nominal tie capacity is sensitive to these values. Calculations for SL assumed 60 in. and 25 in. for the required and available strand embedment and these values appear to be slightly unconservative relative to the experimental results. LRFD section 5.8.3.5 which governs the end region tie requirements does not give explicit instructions regarding the available and required development to be used. Rather the LRFD says that “and lack of full development shall be accounted for.”

6 Summary and Conclusions

Four FIB-63 test specimens were fabricated and load tested to evaluate the effects of different end region detailing schemes on the control of web splitting cracks. Details in the test program included: 1) #5 vertical end region reinforcement per current FDOT standards (control specimen), 2) vertical reinforcement per FDOT and 45% partial strand shielding, 3) vertical end region post-tensioning, and 4) 1-in. diameter threaded rods as vertical reinforcement. Cracks and strains were monitored during prestress transfer and in the days and weeks following transfer. These data were used to compare the relative effectiveness of each detailing scheme in controlling web splitting cracks. Finally, specimens were load-tested in 3-point bending to determine what, if any, effect the end region detailing had on shear capacity and behavior. Key observations and conclusions are as follows:

- Partial strand shielding was an effective means of controlling the length, and width of web splitting cracks. Of the 52 strands in specimen SL 45% were shielded within the end region. Shielding resulted in a 29% reduction in web crack length and a 43% reduction in average web crack width relative to the control specimen.
- Vertical post-tensioning of specimen PT prevented web splitting cracks at the end surface, but affected other web cracks away from the end and in the bottom flange. The largest web cracks in the test program occurred in specimen PT.
- All web cracks in the test program had widths equal to or less than 0.012 in. Cracks above this width require corrective action based on FDOT requirements for moderate environments.
- Increasing the end region vertical reinforcement decreased the length and width of web splitting cracks. Specimen LB had 30% more vertical end region reinforcement than the control specimen, and had 10% less web crack length and 35% lower average web crack width.
- Experimental capacity of all specimens was greater than the ACI and LRFD calculated nominal shear capacities.

- Increased strand shielding in specimen SL resulted in a reduction in the experimental capacity of specimen SL. Because of strand shielding this specimen had insufficient fully bonded strands to prevent bond-shear failure after cracks formed in the above flange in front of the bearing.
- Vertical post-tensioning in the end region of specimen PT did not affect load capacity. Specimen PT supported the largest load of any specimen. Failure of PT could not be reached due to limitations of the testing equipment.
- Specimen LB experienced a punching shear failure in the top flange due to placement of the applied load. Consequently, the effect on load capacity of increased vertical reinforcement (relative to the control) in specimen LB could not be evaluated. It is assumed that the additional vertical reinforcement would not have had negative effect.
- During load testing, inclined cracking in specimen SL initiated at a load 30% to 45% lower than in the other specimens. The lower cracking load in SL occurred due to decreased end region compressive stresses affected by strand shielding.

Appendix F–Finite Element Analysis of End Region

Table of Contents

F.1	Modeling of End Region under Applied Loads	435
F.1.1	Model Configuration	435
F.1.2	Small Beam Model	440
F.1.3	Model Validation and Verification	442
F.1.4	Parametric Studies	446
F.1.5	Summary and Conclusions	463
F.2	Modeling of End Region during Prestress Transfer	466
F.2.1	Model Configuration	466
F.2.2	Model Validation and Verification	471
F.2.3	Transverse Force Quantification	476
F.2.4	Parametric Studies	478
F.2.5	Summary and Conclusions	497

List of Figures

Figure 1–Coordinate system relative to load and supports	435
Figure 2–FE model configuration	436
Figure 3–Rigid shell and link elements.....	436
Figure 4–Bearing pad model.....	438
Figure 5–End region model dimensions	438
Figure 6–FE model symmetry	439
Figure 7–FE model top view.....	439
Figure 8–Comparison of small beam test setup, FE model details, and FE mesh	440
Figure 9–Bearing pad axial stiffness.....	442
Figure 10–Transverse strain (x-x) at end of beam for proposed and refined mesh	443
Figure 11–Small beam transverse (x-x) strain profile (V = 15 kip).....	443
Figure 12–Small beam load vs. deflection at load point.....	444
Figure 13–Small beam load vs. strain S5 (y-y).....	445
Figure 14–Small beam load vs. average of strain S11 and S12 (y-y).....	445
Figure 15–Maximum principal tensile (P1) strain location	446
Figure 16–Sensitivity study maximum transverse (x-x) strain	447
Figure 17–FIB and rectangular section FE models.....	448
Figure 18–Location of maximum flexural strain (normalizing strain)	450
Figure 19–Bursting behavior	450
Figure 20–Normalized transverse (x-x) strain at end of FIB-8.....	450
Figure 21–Flexural behavior.....	451
Figure 22–Normalized transverse (x-x) strain at end of FIB-16.....	451
Figure 23–Normalized transverse (x-x) strain vs. bearing pad width.....	453
Figure 24–Normalized transverse (x-x) strain vs. bearing pad width in FIB.....	454
Figure 25–Normalized transverse (x-x) strain vs. bearing pad width in rectangular section.....	455
Figure 26–Normalized transverse (x-x) strain vs. bearing pad width in small beam.....	456
Figure 27–Steel bearing plate beam and model	458
Figure 28–Bearing plate discretization	459
Figure 29–Effect of bearing plate and bearing pad width on transverse (x-x) strain.....	459
Figure 30–Normalized transverse (x-x) strain vs. bearing pad width in FIB section with steel bearing plate.....	460
Figure 31–Integration area for transverse force	462
Figure 32–Element x-x stress and y-z area	462
Figure 33–Net transverse (x-x) tensile force vs. bearing geometry	463
Figure 34–Coordinate system and free-body diagram of girder after prestress transfer.....	467
Figure 35–FE model details	468
Figure 36–Strand layout and element mesh.....	470
Figure 37–Verification study mesh densities.....	472
Figure 38–Verification study principal tensile stresses	472
Figure 39–Displaced shape	473
Figure 40–Comparison of experimental and FE model strains at cracks.....	474
Figure 41–Comparison of experimental and FE model transverse (x-x) strain	475
Figure 42–Comparison experimental and FE model longitudinal (y-y) strain	476
Figure 43–Comparison of experimental and FE model vertical (z-z) strain.....	476
Figure 44–Area over which stress was integrated to determine lateral force	477
Figure 45–Element x-x stress and y-z area	478
Figure 46–Transverse (x-x) stress at stages of prestress transfer.....	479

Figure 47–Variation in transverse force as strands are cut	480
Figure 48–Transverse (x-x) stress distribution at stage 1 (outer strands cut) with bearing plate and without bearing plate	482
Figure 49–Transverse (x-x) stress distribution at stage 2 (all strands cut) with bearing plate and without bearing plate	483
Figure 50–Transverse force vs. length of prestress transfer	484
Figure 51–Transverse stress distribution with 17.5-in. transfer length (50% of strands cut)	486
Figure 52–Transverse stress distribution with 42.5-in. transfer length (50% of strands cut)	487
Figure 53–Length of tension area vs. transfer length (50% of strands cut)	488
Figure 54–Transverse (x-x) stress at MID section through bottom flange (30% of strands cut).....	488
Figure 55–Flange splitting cracks at girder end.....	489
Figure 56–Lines for stress calculations.....	490
Figure 57–FE model stresses at girder end (50% strands cut)	490
Figure 58–Transverse (x-x) stress at mid-flange line (50% strands cut)	491
Figure 59–Average transverse (x-x) stress at end of girder due to strand cutting	491
Figure 60–AASHTO Type IV FEA model and analysis lines.....	493
Figure 61–Transverse stress distribution in Type IV girder (maximum condition)	494
Figure 62–Transverse (x-x) stress due to self-weight.....	495
Figure 63–Transverse (x-x) stress due to self-weight.....	496

List of Tables

Table 1–Small beam FE model geometry	441
Table 2–Bearing stiffness sensitivity study details	447
Table 3–Model details: parametric study of bearing pad width.....	448
Table 4–Bearing pad properties	449
Table 5–Application of elastic loss.....	471
Table 6–Bearing plate study summary of transverse (x-x) stresses and forces	483
Table 7–Summary of transverse (x-x) stress at girder end due to strand cutting.....	492
Table 8–Summary of transverse (x-x) force at girder end due to strand cutting (FIB).....	492
Table 9–Summary of transverse (x-x) force at girder end due to strand cutting (Type IV)	493
Table 10–Transverse (x-x) stress due to self-weight	496

1 Modeling of End Region under Applied Loads

FE (finite element) modeling was conducted to 1) provide a better understanding of the elastic behavior of the end region prior to cracking and 2) to evaluate the effects of bearing pad stiffness and width on end region elastic stresses. The FEA (finite element analysis) program Adina (R&D 2009) was used to conduct all modeling and analysis. All models were linear elastic. Strain gage and displacement data from experimental work reported in Appendix B were used to validate the FEA model. Hereafter the beams reported in Appendix B are referred to as the “small beams.”

1.1 Model Configuration

The FE model was configured to be computationally efficient, yet able to capture the overall behavior of the beam as well as the local behavior of the end region. The ability of the model to capture the distribution of transverse tensile strain in the end region was of particular interest. The model was also designed such that the geometric and material properties could be adjusted to evaluate the sensitivity of the end region behavior to such parameters.

The coordinate system defined in Appendix D was also used in the FE models (Figure 1). The origin was located at the end of the beam nearest the point load, at the centerline of the cross-section, and at the bottom of the beam. The X axis was oriented horizontally across the cross-section, the Y axis was oriented horizontally along the length of the beam, and the Z axis was oriented vertically.

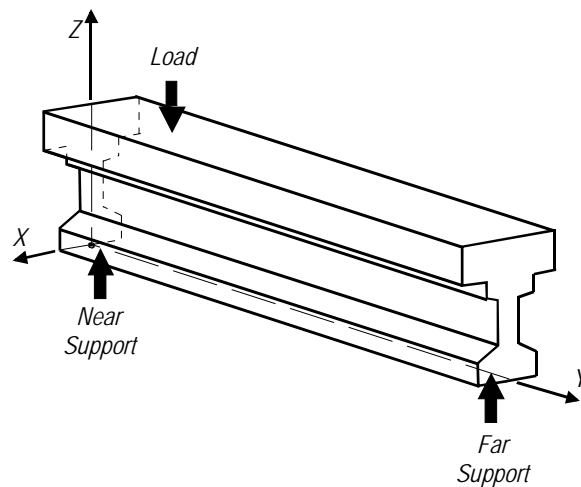


Figure 1—Coordinate system relative to load and supports

Figure 2 shows the model configuration. The shear span (distance from the load to the near support) and a small distance beyond the shear span were modeled with 27-node 3D solid elements on a primarily rectangular mesh. The remainder of the beam was modeled with 1D beam elements, with the transition from beam to solid elements made using rigid 2D shell elements and 1D rigid links. Rigid shell and link elements (Figure 3) coupled the displacements of the 3D solid elements with the displacements and rotations of the 1D beam elements. Transitioning to beam elements reduced the computational demand of the model while still modeling the global beam behavior and boundary conditions. Beam elements were placed at the centroid of the cross-section and were assigned cross-sectional properties equivalent to the physical beam. At the far support, a rigid link was provided to connect the beam elements to the physical location of the bearing pad at the bottom of the beam.

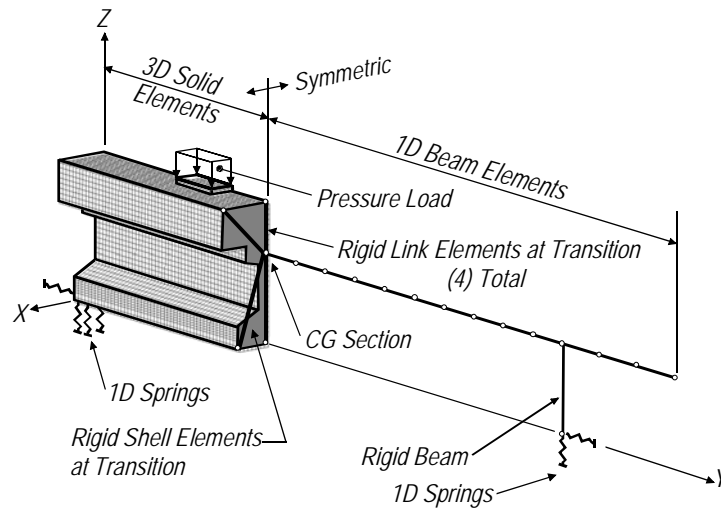


Figure 2–FE model configuration

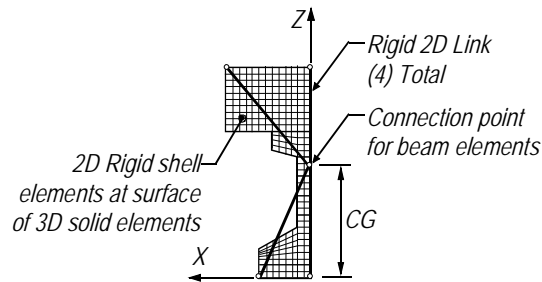


Figure 3–Rigid shell and link elements

Axial and shear stiffness of the bearing pad at the far support were modeled with 1D springs in the Z and Y directions respectively. At the near support, the axial and shear stiffness of the bearing pad was modeled with multiple spring elements in each of the X, Y, and Z directions. Position and quantity of spring elements matched the discretization of the solid elements used to model the beam (Figure 4). Stiffness was assigned to each spring in proportion to the tributary area represented by the spring.

Figure 5 defines key geometric variables of the model end region. Geometric variables were setup to allow variation of features such as shear span-to-depth ratio, bearing pad size and location, span length, and the location of the applied load. Additional geometric variables were defined on the cross section shown in Figure 6.

The cross-section, boundary conditions and load were symmetrical about the Y-Z plane, allowing for only half of the beam to be considered in the FE model (Figure 6). A top view of the model, shown in Figure 7, gives the position of the model relative to the physical geometry of the beam.

Concrete modulus of elasticity used for each model was 5300ksi, and the Poisson's ratio was defined as 0.2. The modulus of elasticity value was chosen to match the tested material properties from the physical beams used for model validation.

The typical model configuration described above was validated by comparison with experimental data, and was then used in more general investigations of the stress and strain state in the end region. Details of the validation and general investigations are contained in the proceeding sections.

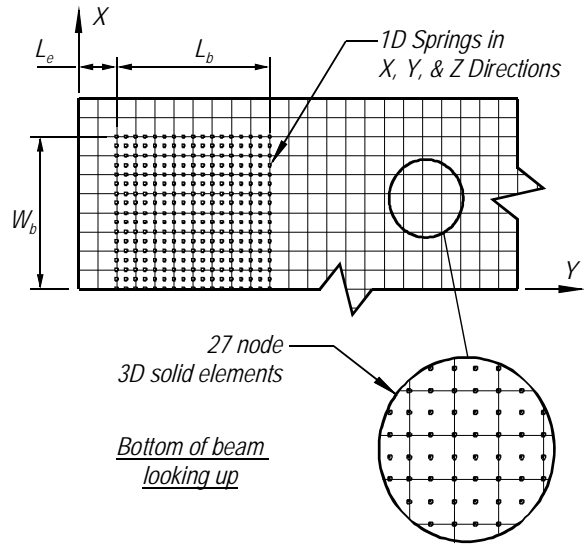


Figure 4–Bearing pad model

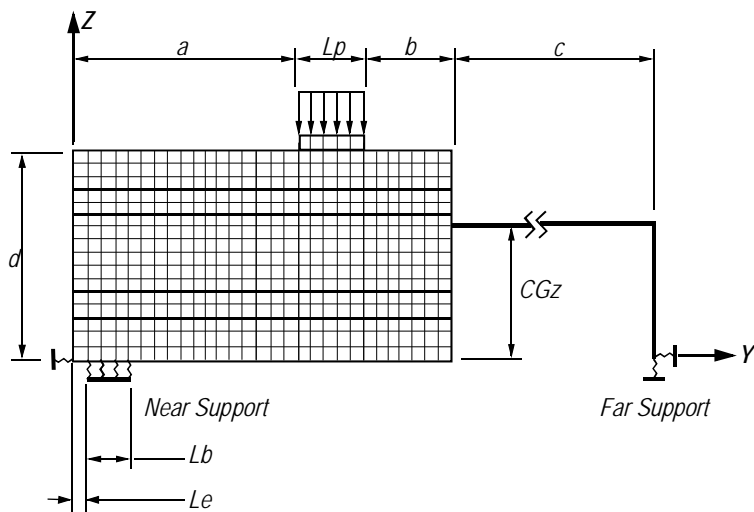


Figure 5–End region model dimensions

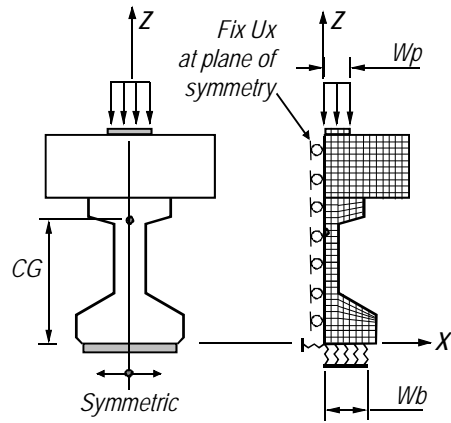


Figure 6–FE model symmetry

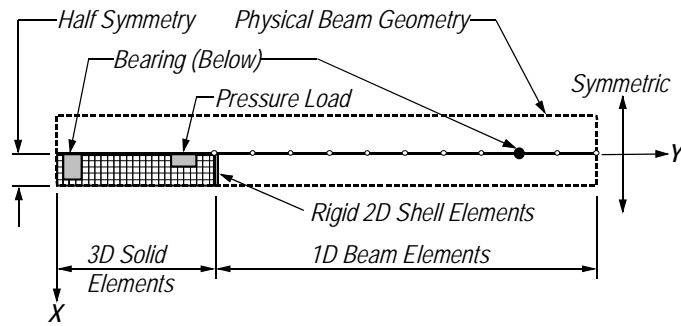


Figure 7–FE model top view

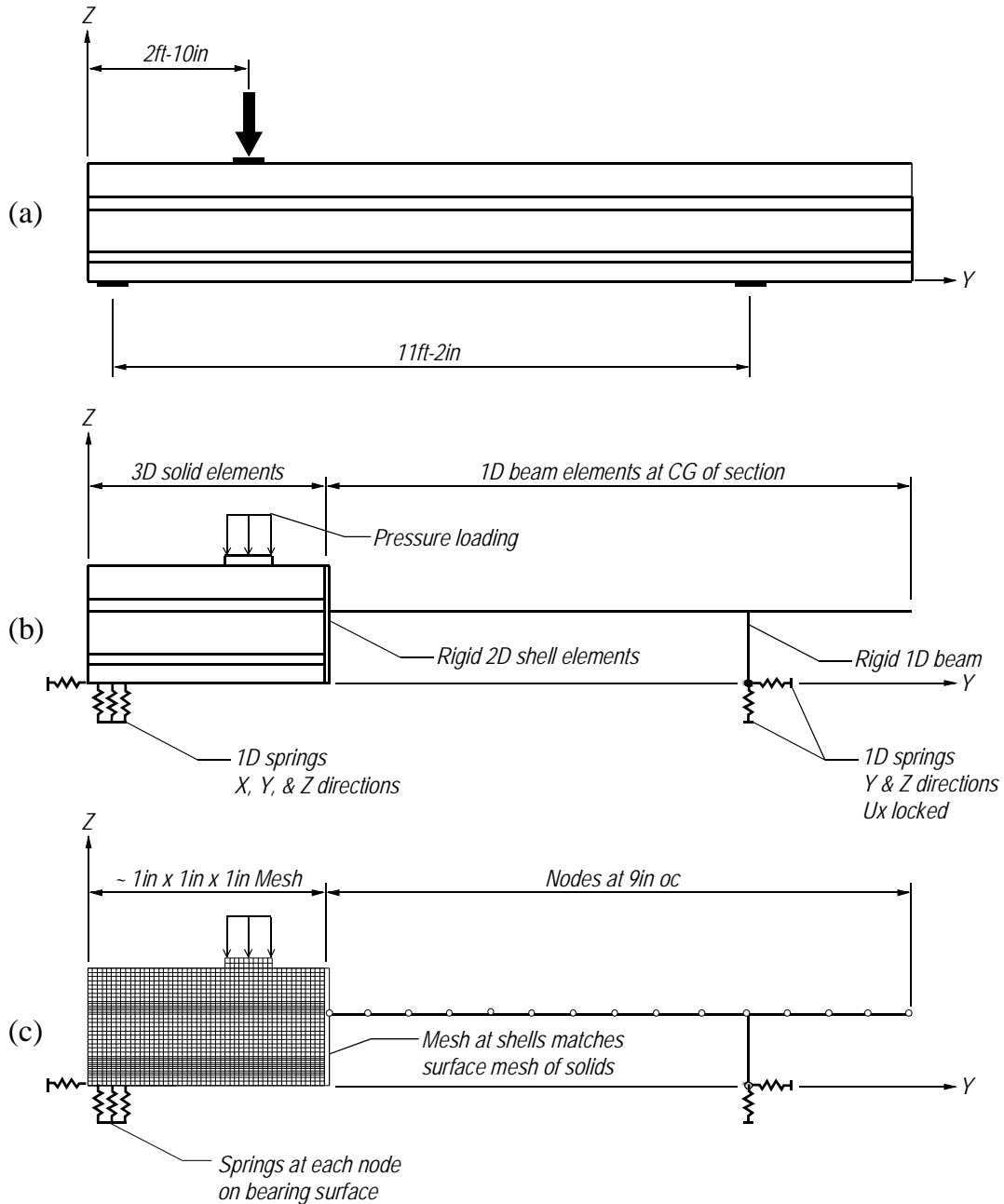


Figure 8—Comparison of small beam test setup, FE model details, and FE mesh

1.2 Small Beam Model

The configuration described above was used to model the small beam tests reported in Appendix B. Dimensions, element sizes, and spring properties of the model are listed in Table 1. Variables in this table are defined in Figure 5 and Figure 6. The experimental test setup being modeled, element types, and element density are shown in Figure 8. Stiffness values for the

springs in the Z direction were based on experimental load-displacement data from LVDTs located over the bearing pads on the small beam tests (Figure 9). From these data, a representative axial stiffness of 1150 kip/in was chosen. At the far support, the full axial stiffness was assigned to the single spring at the bearing point. At the near support the axial stiffness was distributed to the springs based in proportion to tributary area. Stiffness of springs at both the near and far supports in the pad shear directions (X & Y) were based on properties reported for similar sized bearing pads (Yura et al. 2001).

Table 1–Small beam FE model geometry

Dimension/Property	Value
A	29 in
B	11 in
C	90 in
D	28 in
CGz	17 in
Lp	10 in
Wp	5 in
Lb	7 in
Wb	6.5 in
Le	2 in
Near support Ka	8 kip/in
Near support Kv	0.05 kip/in
Far support Ka	1150 kip/in
Far support Kv	10 kip/in
3D solid element size	Approximately rectangular 1 in x 1 in x1 in
2D shell element size	Approximately square 1 in x 1 in
1D beam element size	9 in

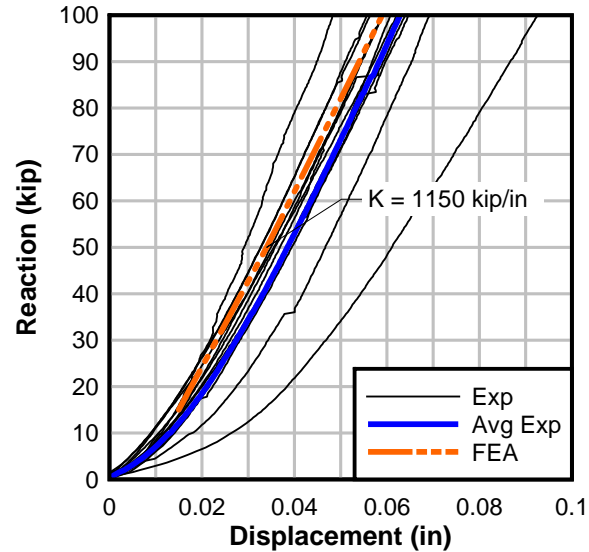


Figure 9–Bearing pad axial stiffness

1.3 Model Validation and Verification

Prior to comparing FE results with experimental data, convergence of the FE solution was verified by comparing the proposed model with a model containing a more refined mesh. Figure 10 shows the transverse (x-x) strain in the bottom bulb at the near support for the proposed and refined mesh densities. Note that the section geometry and strain values were symmetric about the Y-Z plane, and that only half of the bottom bulb is shown in the figure. The strain values and strain distributions were similar for both models, with the maximum transverse strain occurring at the centerline of the beam directly above the bearing pad ($Z=0, X=0$). The refined model reported a maximum strain that was only 0.1% greater than the maximum value from the proposed model. Based on the degree of correlation with the refined mesh, element sizes used in the proposed model were considered appropriate.

Comparison with experimental data indicated that the FE model did an adequate job of capturing both the global and local linear elastic behavior of the physical test beams. Global behavior is compared in the load-displacement plot in Figure 12. Displacement in the figure (both experimental and analytical) was the vertical displacement at the load point, which was corrected to remove displacement due to deformation of the bearing pads. Within the elastic range, the FE model stiffness was 23% less stiff than the average experimental beam stiffness, but was still within the scatter of the experimental data.

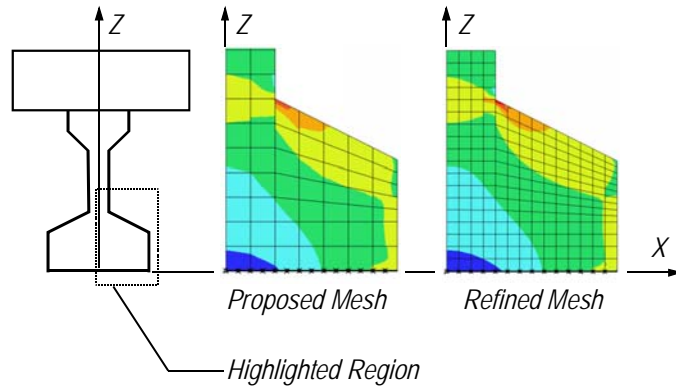


Figure 10–Transverse strain (x-x) at end of beam for proposed and refined mesh

The profile of the transverse (x-x) strain at the near end of the beam is shown in Figure 11. Strain profiles were compared at a load of 15 kip, as this load was well within the elastic range for each of the test beams. Experimental data came from strain gages mounted at the end of the beams 5 in. above the beam bottom. Shape of the strain profile was consistent between experimental data and the FE model, with the peak occurring at the centerline of the beam. Strain values calculated by the FE model were larger than the average of the experimental data, but were still within the scatter of the data.

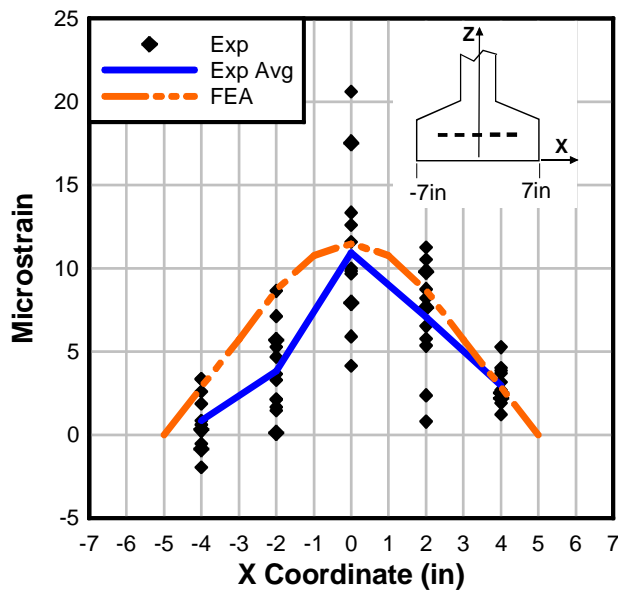


Figure 11–Small beam transverse (x-x) strain profile (V = 15 kip)

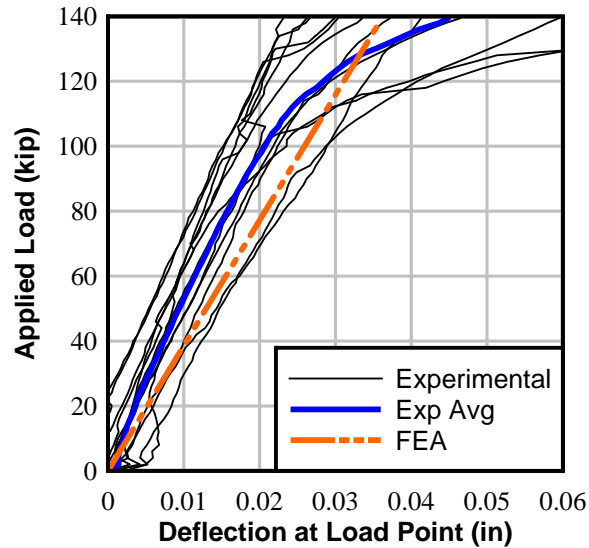


Figure 12–Small beam load vs. deflection at load point

Figure 13 shows the load versus strain relationship for gage S5, which was oriented longitudinally on the bottom of the beam directly below the applied load. Experimental data from gage S5 was consistent between tests. At the location of S5, the slope of the load-strain curve from the FE model was 20% less than the average slope of the experimental data.

Figure 14 shows the load versus strain relationship for gages S11 and S12. These gages were located on the top of the beam on either side of the applied load. Values from gages S11 and S12 were averaged to form the curves for the individual tests. Values reported by the FE model at the locations of S11 and S12 were identical because the FE model employed symmetry about the Y-Z plane. The slope of the load-strain curve reported by FE model was 5% greater than the average slope of the experimental data.

Finally, the maximum principal tensile strain was compared over the region shown in Figure 15. The maximum principle tensile strain occurred at the intersection of the web and the bottom bulb (Figure 15). The strain concentration at the web-bulb interface correlates with the location of cracks observed during testing.

The proposed FE model captured the general behavior of the physical beam, as well as the local behavior of the end region. In most cases, the FE results were within the scatter of the experimental data. Based on the correlations presented above, the proposed FE model was considered adequate for conducting more general evaluations of the concrete girder end region.

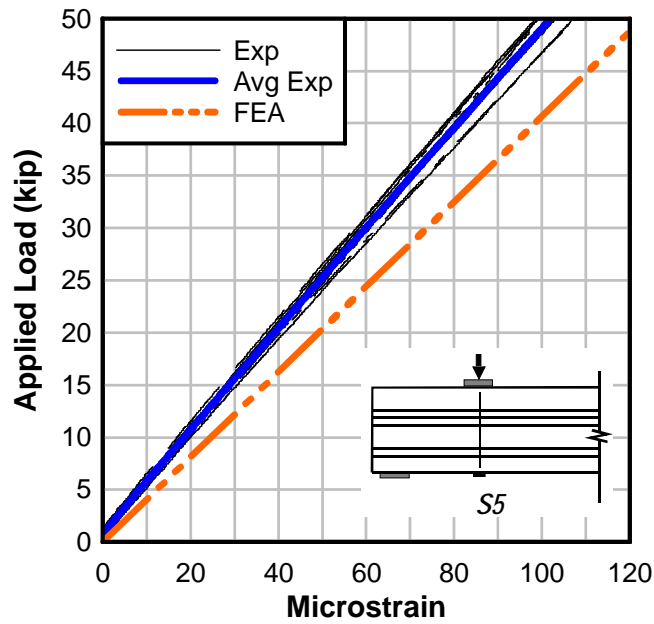


Figure 13–Small beam load vs. strain S5 (y-y)

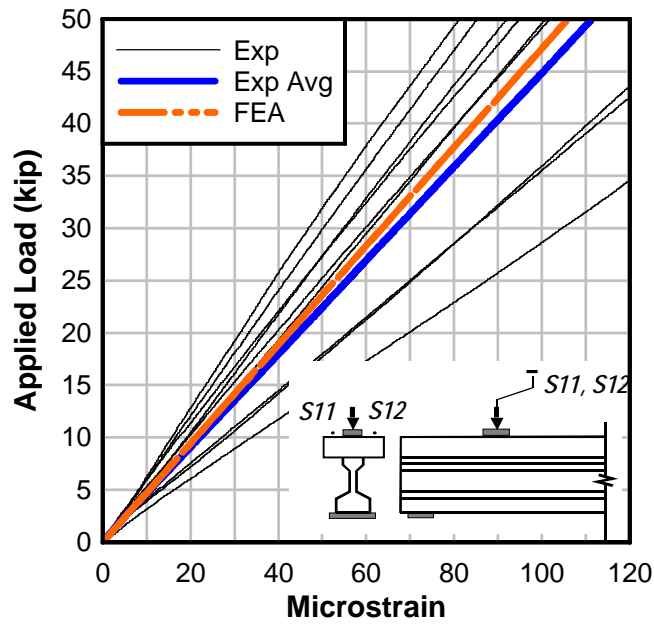


Figure 14–Small beam load vs. average of strain S11 and S12 (y-y)

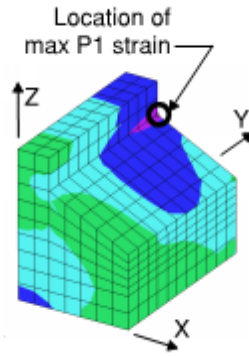


Figure 15–Maximum principal tensile (P1) strain location

1.4 Parametric Studies

The FE model configuration presented previously was used to evaluate parameters affecting the strain state in the end region including bearing pad stiffness, cross-section geometry, steel bearing plates, and bearing pad geometry.

1.4.1 Bearing Pad Stiffness

Four additional models were created to evaluate sensitivity of the end region strains to changes in bearing pad stiffness. In these models, the axial or shear stiffness of the bearing pad was either doubled or halved relative to the stiffness of the original model. By using half or double the stiffness properties of the original small beam model, the additional models cover the range of stiffness values for similar sized bearing pads reported by Yura et al. (2001). Details and results from the additional models are presented in Table 2. Information regarding the original model is also included in the table for reference.

Strain results were evaluated over the region shown in Figure 16. For each model, the maximum transverse tensile strain was located at the centerline of the beam directly above the bearing pad (Figure 16). Changes to bearing pad shear stiffness (K_v) had negligible effect on maximum transverse (x-x) strain over the range of values tested. However, changes to the axial stiffness (K_a) of the bearing pads did affect the maximum transverse strain. For the region considered, doubling the axial stiffness resulted in a 2.7% reduction in maximum transverse strain whereas halving the axial stiffness resulted in a 1.5% increase in maximum transverse strain.

Table 2–Bearing stiffness sensitivity study details

Model ID	Axial stiffness (kip/in)	Shear stiffness (kip/in)	Max tensile transverse strain (ϵ_x) for V = 15 kip (microstrain)	Change in max tensile transverse strain
Original	1150	10	26.64	--
x1/2 Axial stiffness	575	10	27.03	+1.5%
x2 Axial stiffness	2300	10	25.91	-2.7%
x1/2 Shear stiffness	1150	5	26.67	+0.1%
x2 Shear stiffness	1150	20	26.61	-0.1%

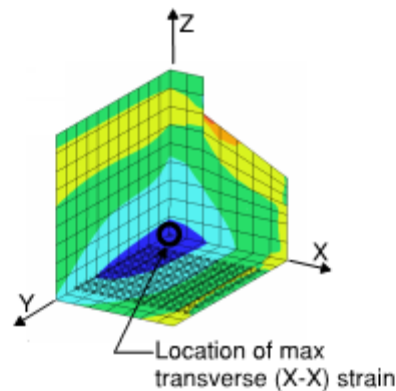


Figure 16–Sensitivity study maximum transverse (x-x) strain

1.4.2 Bearing Pad Geometry

To evaluate the effect of bearing pad width on the transverse strain in the end region, FE models of the Florida I-Beam (FIB) and a rectangular cross-section (Figure 17) were created using the modeling configuration described previously. Details of the models are given in Table 3. The bearing pad width, W_b , was varied from 8.55 in. to 16.15 in. Because half-symmetry models were used, the bearing pad width, W_b , was equal to half of the total bearing pad width. Thus the FE model with W_b of 16.15 in. corresponded to a total bearing pad width of 32.3 in. This dimension is similar to the 32 in. width specified in the FDOT design standards (FDOT 2009).

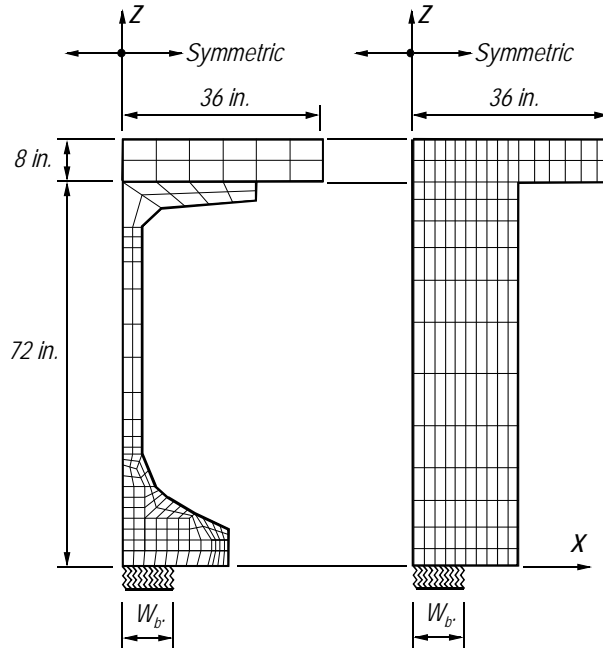


Figure 17–FIB and rectangular section FE models

Table 3–Model details: parametric study of bearing pad width

a	120 in
b	32 in
c	1032 in
d	80 in
CGZ	47.7 in
Lp	16 in
Wp	6 in
Lb	10 in
Wb	Varies

For convenience, models were assigned a label based on cross-section shape and nominal W_b dimension. For example, the label FIB-10 was assigned to the model with the FIB cross-section and a bearing pad width of 10.45 in. The label R-15 was given to the model with the rectangular cross-section and a bearing with of 15.20 in.

Stiffness and spacing of the individual springs comprising the bearing pad at the near support were held constant even as the bearing pad width varied. However, the total stiffness of the bearing pad changed as additional springs were added or removed to change the width of the bearing pad. Individual spring stiffness and total bearing pad stiffness are listed in Table 4. In each model, total the stiffness of the far support matched the stiffness of the near support.

Table 4–Bearing pad properties

	Half Symmetry			Total	
	Wb	Ka	Kv	Ka	Kv
FIB-8, R-8	8.55 in.	2710 kip/in.	5.4 kip/in.	5420 kip/in.	10.8 kip/in.
FIB-9, R-9	9.50 in.	2995 kip/in.	6.0 kip/in.	5990 kip/in.	12.0 kip/in.
FIB-10, R-10	10.45 in.	3280 kip/in.	6.6 kip/in.	6560 kip/in.	13.2 kip/in.
FIB-11, R-11	11.40 in.	3565 kip/in.	7.2 kip/in.	7130 kip/in.	14.4 kip/in.
FIB-12, R-12	12.35 in.	3850 kip/in.	7.7 kip/in.	7700 kip/in.	15.4 kip/in.
FIB-13, R-13	13.30 in.	4135 kip/in.	8.3 kip/in.	8270 kip/in.	16.6 kip/in.
FIB-14, R-14	14.25 in.	4420 kip/in.	8.9 kip/in.	8840 kip/in.	17.8 kip/in.
FIB-15, R-15	15.20 in.	4710 kip/in.	9.4 kip/in.	9420 kip/in.	18.8 kip/in.
FIB-16, R-16	16.15 in.	4995 kip/in.	10.0 kip/in.	9990 kip/in.	20.0 kip/in.
Axial stiffness of individual springs at near support = 31.7 kip/in.					
Shear stiffness of individual springs at near support = 0.0635 kip/in.					

Transverse (x-x) strain results from the models were normalized by the maximum flexural ($\epsilon_{y,max}$) tensile strain from the FIB model. The maximum flexural strain was located at the bottom of the beam below the load point (Figure 18). The value of $\epsilon_{y,max}$ was slightly different for the FIB and rectangular cross-sections; for a given section, however, it did not vary as the bearing pad width changed. For a half-symmetry applied load of 67 kip (experimental load of 134 kip), $\epsilon_{y,max}$ was 91 microstrain for the FIB model, and for the same load was 61 microstrain for the rectangular section model. The transverse strains for each model were normalized by $\epsilon_{y,max}$ from the FIB model.

For the FIB cross-section, two types of behavior were observed as the bearing pad width was adjusted. First, when the pad width was narrow, the transverse strains were distributed in a bottle shape between the bearing pad and the bottom of the web (Figure 19). This was denoted as ‘bursting’ behavior. The mechanics of bursting behavior are similar to a split cylinder test, with transfer tensile strain forming perpendicular to compressive loads. The maximum transverse strain occurred above the bearing pad, as shown in Figure 20. As the pad width increased, flexural strains increased at the bottom edge of the flange as the load spread to the far edge of the bearing pad (Figure 21). This is denoted as ‘flexural’ behavior. For ‘flexural’ behavior, the maximum transverse strain occurred at the bottom of the section as shown in Figure 22.

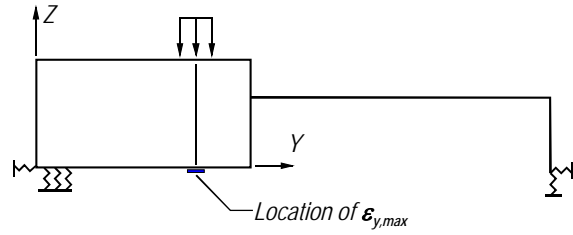


Figure 18–Location of maximum flexural strain (normalizing strain)

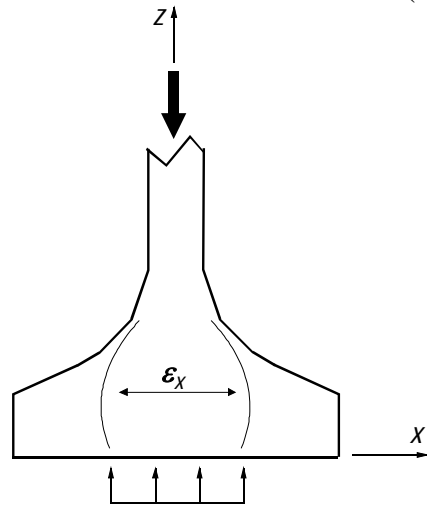


Figure 19–Bursting behavior

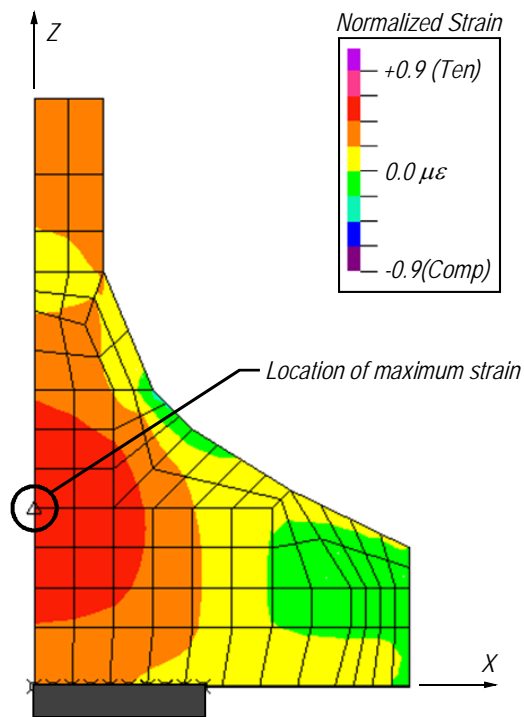


Figure 20–Normalized transverse (x-x) strain at end of FIB-8

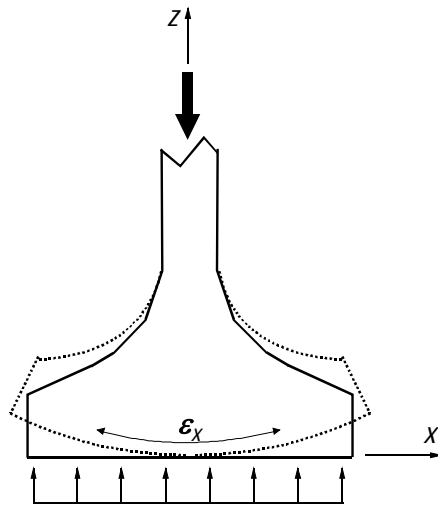


Figure 21–Flexural behavior

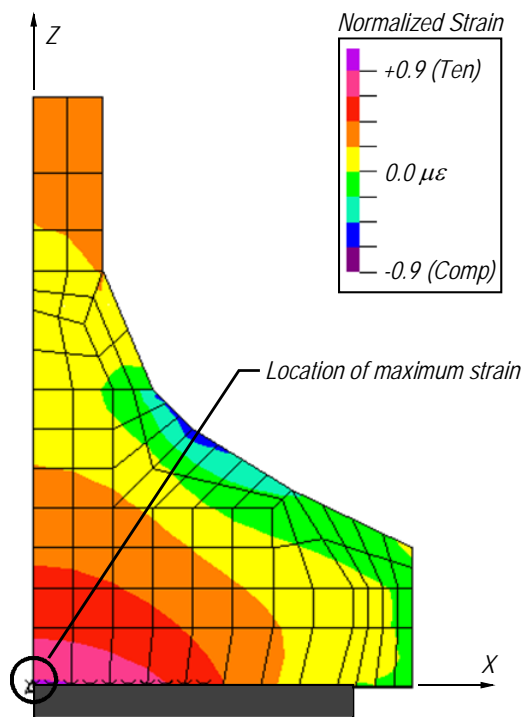


Figure 22–Normalized transverse (x-x) strain at end of FIB-16

To further investigate the relationship between transverse strain and bearing pad width, strain at three points on the end of the beam were plotted against the bearing pad width (Figure 23). Points were located at the end of the beam ($Y=0$ in.) along the plane of symmetry ($X=0$ in.) at Z coordinates of 0 in., 5 in., and 9 in. Looking first at the point $Z = 0$ in., it can be seen that

the maximum transverse strain increased as the bearing pad width also increased. This condition was a consequence of flange-bending behavior. For the point at $Z = 9$ in., the transverse strain increased as the bearing pad width decreased. Thus the strain at $Z = 9$ in. was maximum when the beam experienced bursting behavior, and was smaller when flange bending dominated the behavior. The strain at $Z = 5$ in. remained fairly constant as the pad width changed. The optimum bearing pad width, i.e. the width that minimized the transverse strain, was approximately 21 in. This coincides with the width where the behavior changed from bursting to flexural behavior.

Figure 24 shows the normalized transverse strains in the end region for four models with varying bearing pad widths. Variations in the transverse strain between the different models only occurred in portions of the beam adjacent to the bearing pad. In these portions of the beam, the ‘bursting’ and ‘flexural’ behavior were evident in both the Z-Y and Z-X planes. Regardless of pad width, the greatest transverse strains always occurred at the end of the beam.

Transverse strain distributions in the end region of the rectangular section are shown in Figure 25 for models with four different bearing pad widths. As previously noted, the transverse strains were normalized by $\epsilon_{y,\max}$ from the FIB model. The scale and color contours are different from earlier figures of the FIB section. The figure shows that the magnitudes of the strains in the rectangular section were considerably less than for the FIB section. For instance, the maximum normalized transverse strain in the R-8 model was only 38% of the maximum from the FIB-8 model. For R-16, the maximum normalized transverse strain was only 14% of the maximum from model FIB-16.

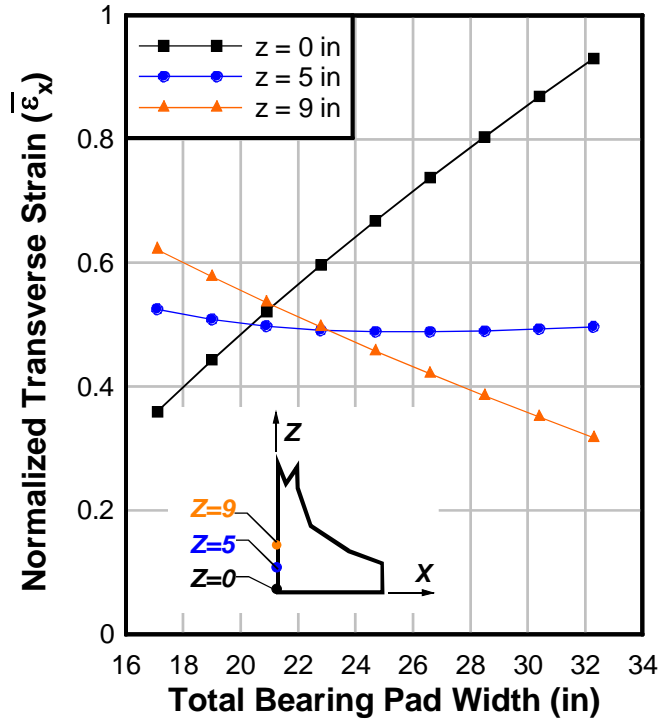


Figure 23–Normalized transverse (x-x) strain vs. bearing pad width

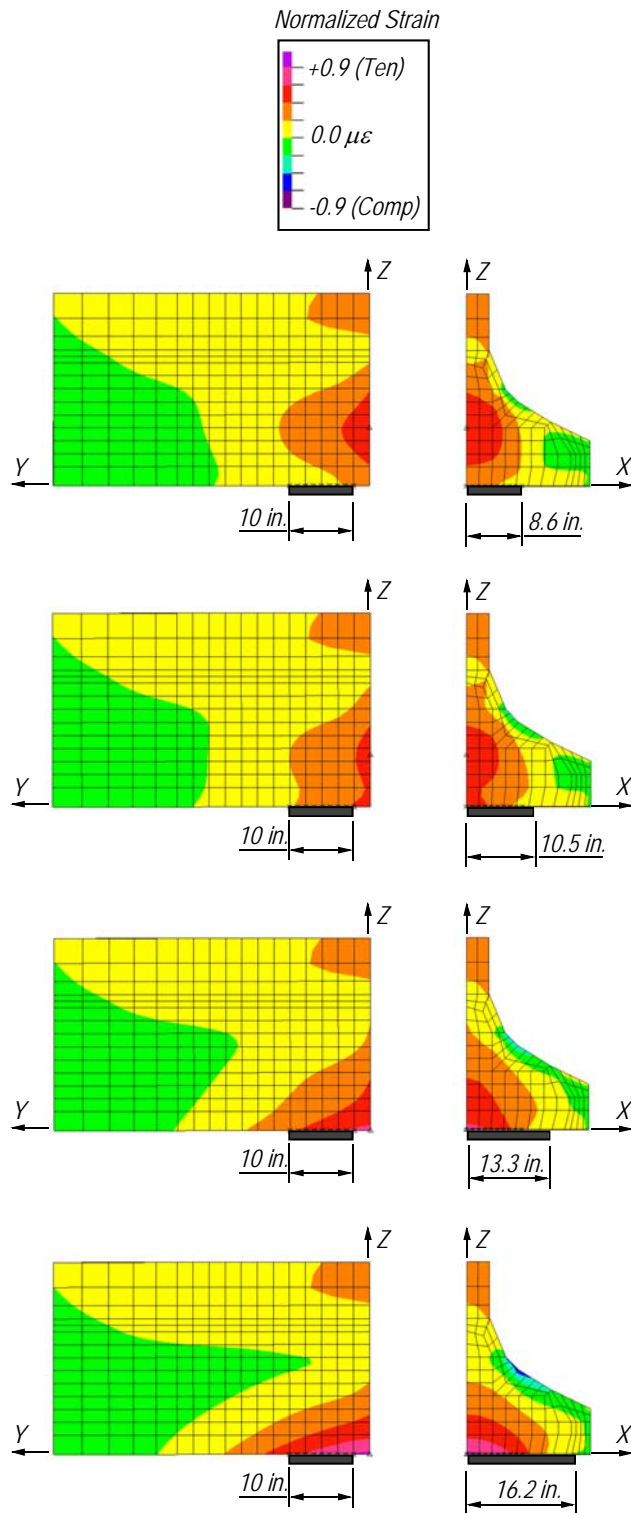


Figure 24—Normalized transverse (x-x) strain vs. bearing pad width in FIB

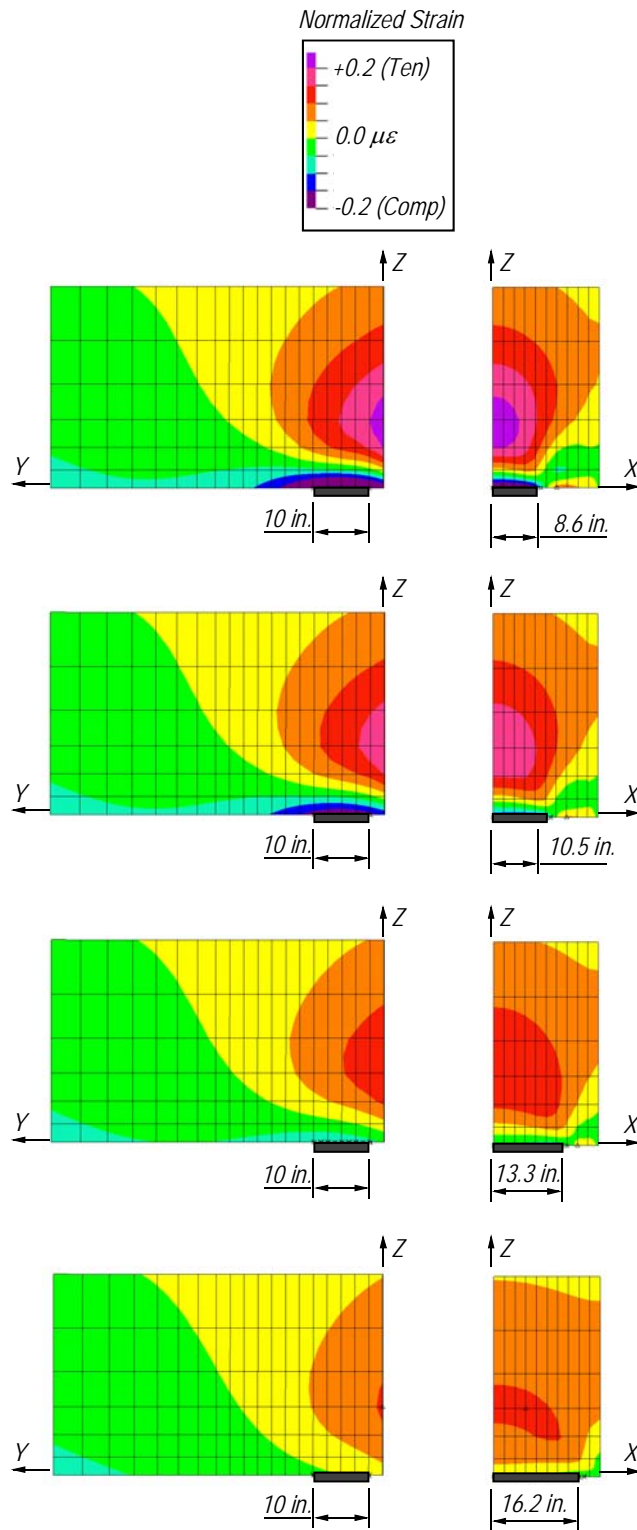


Figure 25–Normalized transverse (x-x) strain vs. bearing pad width in rectangular section

The greatest strain in the rectangular section models occurred in the model with the narrowest bearing pad. Conversely, the transverse strains were least in the model with the greatest pad width. Although the transverse strain varied as the pad width changed, the location of the maximum transverse strain always occurred at the end of the beam.

A parametric study of bearing pad width was also conducted using the small beam FE model (Figure 26). Results were similar to the FIB model. Regardless of bearing pad width, maximum transverse strain always occurred at the end of the beam. Under the flexural mode, maximum transverse strain occurred at the end of the beam at bottom of the section. For the bursting mode, maximum strain occurred at the end of the beam and at a distance of approximately 60% of the flange depth above the bearing pad. The transition between bursting and flexural behavior occurred when the bearing pad width was approximately twice the web width. This pad width also corresponded to the lowest value of peak transverse strain.

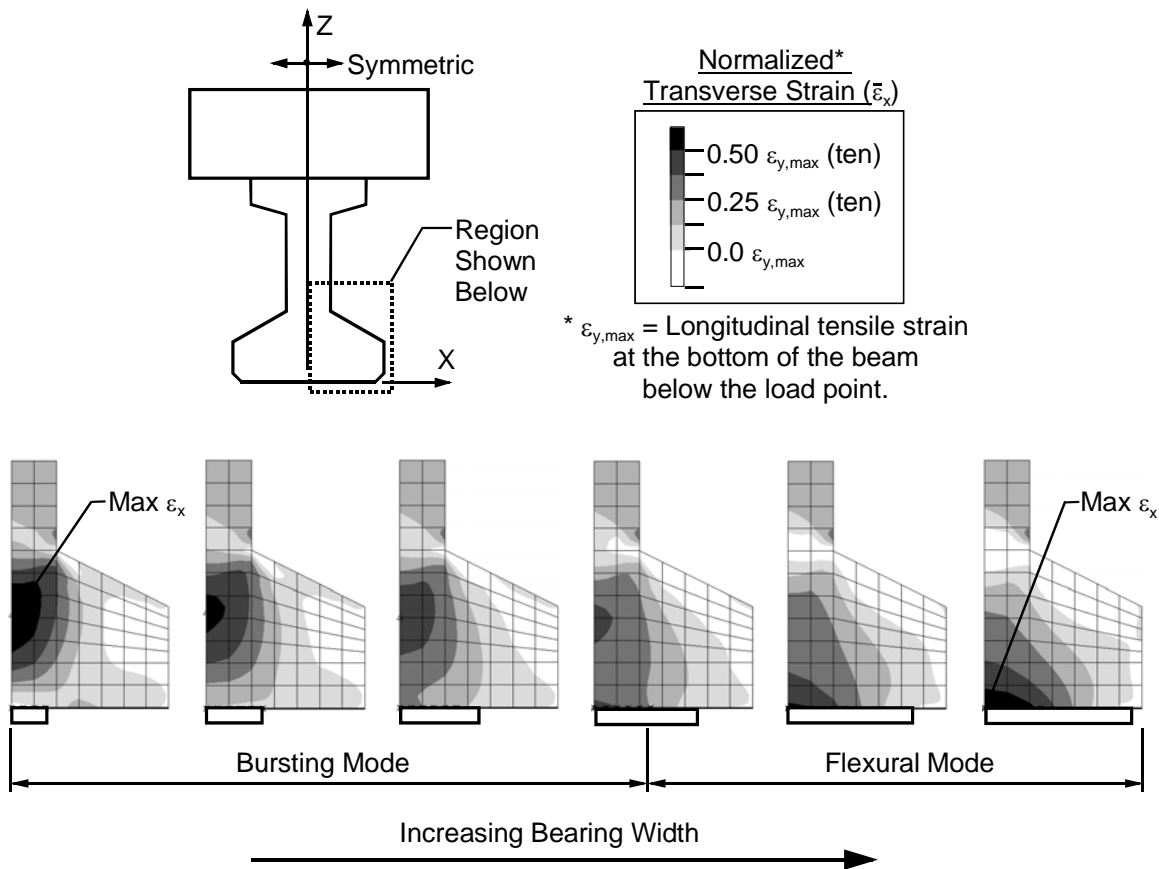


Figure 26–Normalized transverse (x-x) strain vs. bearing pad width in small beam

1.4.3 Effect of Steel Bearing Plate

The FDOT standard detail for the FIB end region specifies (FDOT 2009) a ½ in. thick x 12 in. x 36 in. steel bearing plate be embedded where the beam contacts the bearing pad. The bearing plate protects concrete in the region of high bearing stresses, and can be configured to aide in the constructability of skewed and/or sloped girders. Due to the location of the plate, its effect on the transverse (x-x) strain was of interest. To evaluate the effects of the bearing plate, the plate was added to the FIB models used in the previous section. The bearing plate was modeled with 4 node 2D shell elements positioned at the bottom of the beam (Figure 27). The bearing plate discretization was double that of the adjacent 27 node solid elements, thus each node from the plate elements aligned with a node from the adjacent solid element (Figure 28). Full composite behavior between the bearing plate and the concrete was assumed in the model. The parametric study of bearing pad width presented in the previous section was repeated for the model with the bearing plate.

Figure 29 shows the normalized transverse strain at the end of the beam vs. the bearing pad width for models with and without the steel bearing plate. As was done previously, the strain values in the figure were normalized by the maximum flexural tensile strain ($\epsilon_{y,max}$) (Figure 18) below the load point. Figure 29 shows that the presence of the steel bearing plate reduced the transverse strain at point Z=0. At a bearing pad width of 17 in., the model with the bearing plate reported 20% less transverse strain at point Z=0 than the model without the bearing plate. The reduction in strain was more pronounced at greater pad widths. For example, the bearing plate model reported 33% less transverse strain at a bearing pad width of 32 in. Results also indicated that the influence of the bearing plate was limited to those portions of the beam closest to the plate. At point Z =9, the presence of the bearing plate had insignificant effect on transverse strain.

Figure 30 shows the transverse strain distribution for models with different bearing pad widths. Similar to the FIB model that did not include the bearing plate, Figure 30 shows that the bearing plate models also experienced ‘bursting’ and ‘flexural’ behavior for narrow and wide bearing pad widths, respectively.

When compared to the model without the bearing plate, the reduction of transverse strain is attributed to the additional confinement provided by the plate. This effect was most significant when the bearing pad was at its widest, and when the maximum transverse strain occurred

closest to the plate. The models evaluated the effect of the plate in the range of elastic behavior, and did not consider post-cracking behavior.

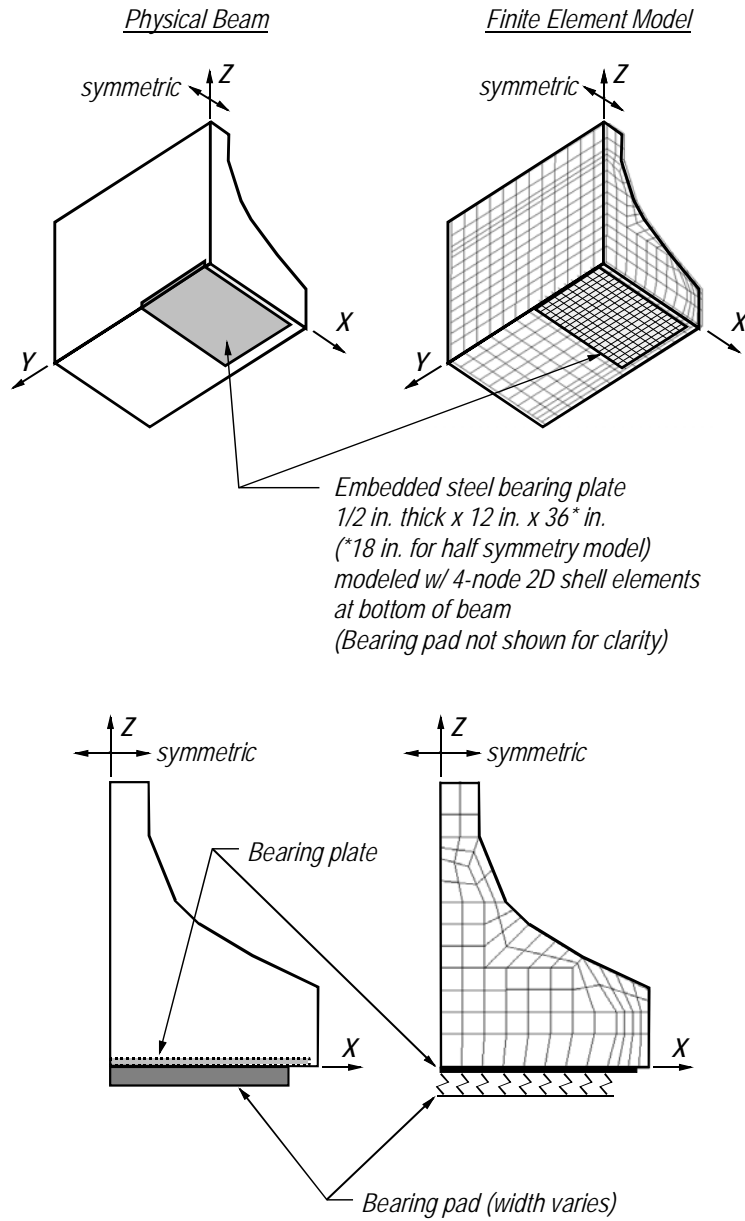


Figure 27–Steel bearing plate beam and model

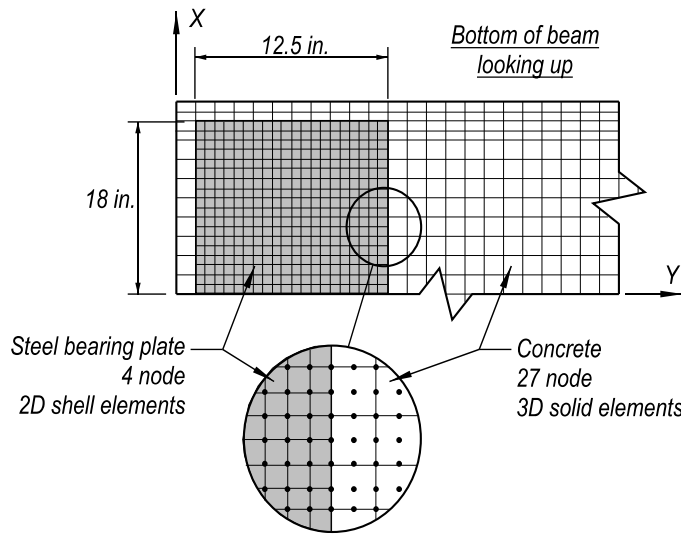


Figure 28–Bearing plate discretization

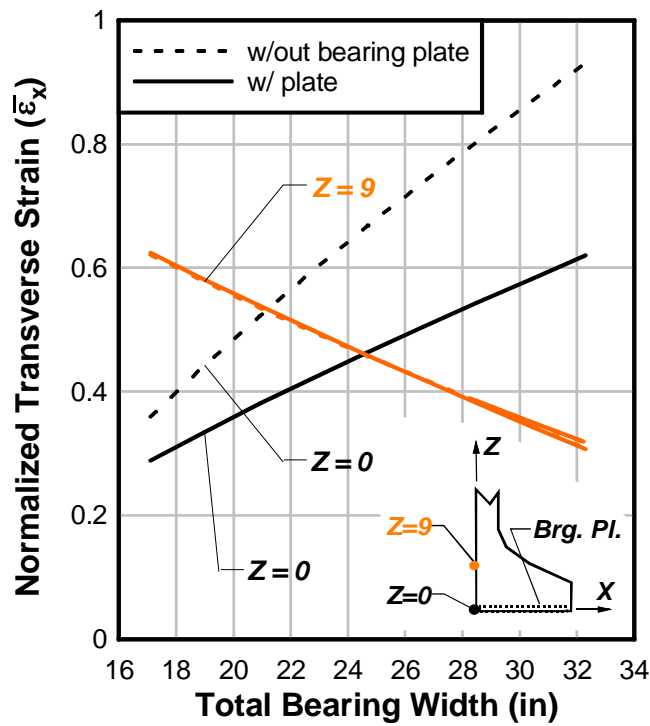


Figure 29–Effect of bearing plate and bearing pad width on transverse (x-x) strain

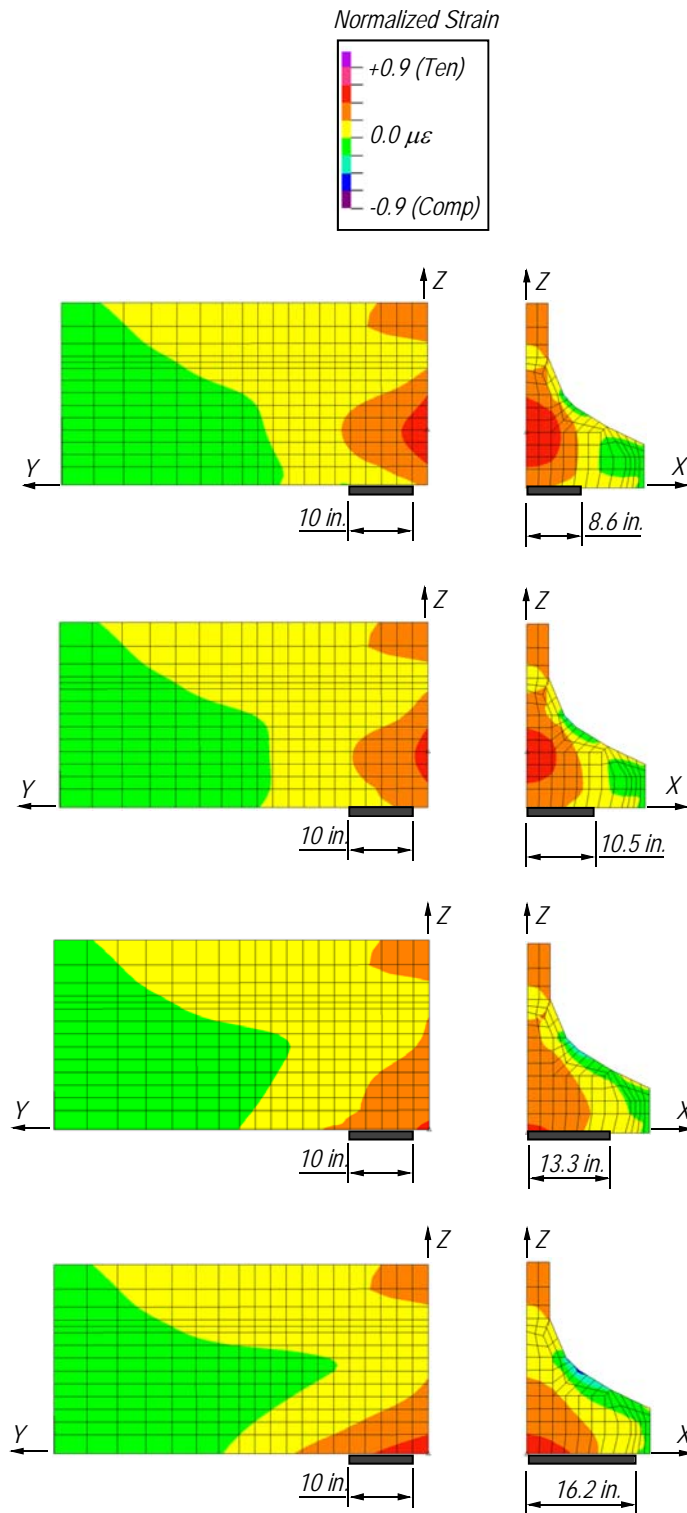


Figure 30–Normalized transverse (x-x) strain vs. bearing pad width in FIB section with steel bearing plate

1.4.4 Bearing Pad Width Effect on Transverse Force

Small beam, FIB, and FIB with bearing plate FE models developed in previous sections were used to evaluate the relationship between bearing pad width and transverse force. As with all models in this chapter, the analysis was linear-elastic and considered the effects of applied loads only.

Transverse force was calculated by integrating transverse stress over the area shown in Figure 31. Boundaries of the integration area were selected to capture those portions of the girder near the bearing pad subjected to steep strain/stress gradients due to the reaction force, and to include portions of the bottom flange where confinement reinforcement is placed to carry transverse tension. Stress distributions beyond the integration area were not significantly affected by changes in bearing pad width. Analyzing transverse forces over the selected area gave a broad picture of pad width effects in the end region, whereas analysis of strain data in previous sections only looked at maximum effects and effects at discrete points.

The integration area used in transverse force calculation was located at the centerline of the considered cross-section. Dimensions of the integration area were determined as a function of the bottom flange width (W_f) so that similar integration calculations could be conducted on beams with different geometries.

Discrete normal (x-x) stress values from center nodes in the integration area were multiplied by the associated y-z areas to obtain the transverse (x-x) force (Figure 32). Total transverse tensile force was taken as the sum of all element tensile forces. Compressive forces (when they occurred) were ignored in calculations of the total transverse force. This approach was taken because the transverse compressive forces were assumed to be resisted by concrete and transverse tensile forces resisted by confinement reinforcement.

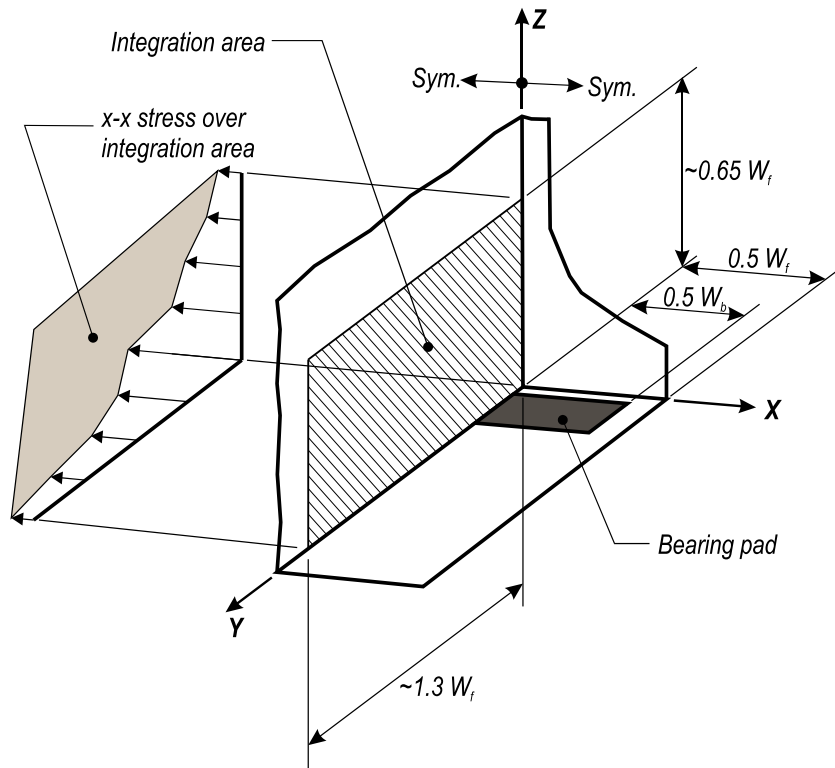


Figure 31–Integration area for transverse force

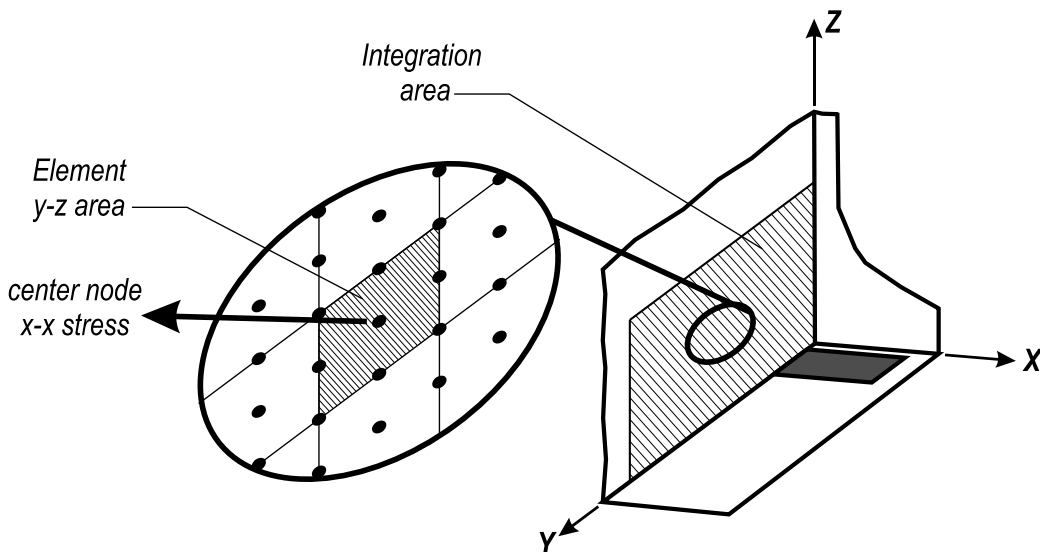


Figure 32–Element x-x stress and y-z area

Figure 33 presents the variation in net transverse tensile force as a function of the bearing pad width in the FE models. For the considered models and geometries, the transverse force was equal to 13% to 28% of the reaction force. Transverse force was smallest relative to the reaction

force when the bearing pad width was approximately 60% of the flange width. This ratio of bearing-to-flange width also corresponded to the change in behavior between bursting and flexural behavior as discussed in previous sections. For bearing pad-to-flange width ratios greater than 0.5, the FIB model including the bearing plate had the lowest normalized transverse force. This is attributed to the stiffness of the bearing plate, which attracted transverse force when the bearing pad width approached the flange width. Transverse force in the bearing plate is not included in the data presented in Figure 33.

FDOT design standards (FDOT 2009) for FIB girders resulted in a bearing pad-to-flange width ratio of 0.84. For this ratio, the calculated transverse tensile force in the bottom flange was equal to approximately 25% of the reaction force in the model without a plate, and approximately 17% of the reaction force in the model with a plate. These relationships reflect linear-elastic behavior and would likely change after cracks form in the bottom flange.

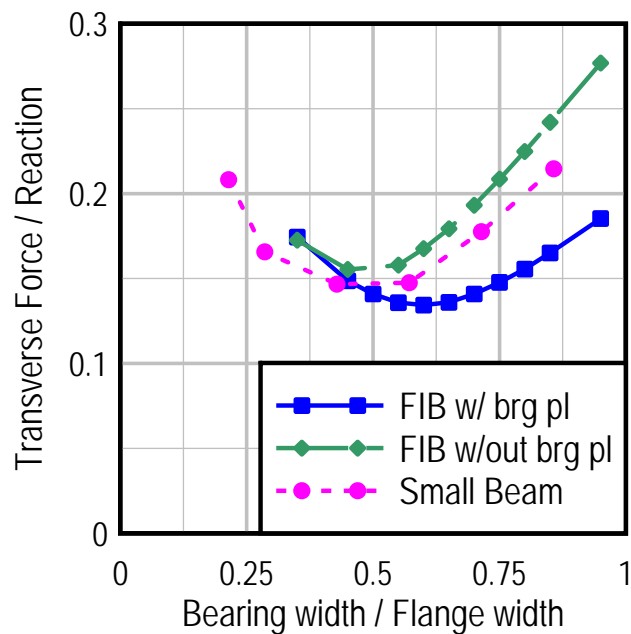


Figure 33–Net transverse (x-x) tensile force vs. bearing geometry

1.5 Summary and Conclusions

Linear-elastic FE models were used to evaluate the effects of applied load on I-beam and rectangular shaped end regions. Variables in the models included bearing pad width, bearing pad stiffness, cross-section shape, and the presence of embedded steel bearing plates. The following conclusions are based on results of the evaluations:

- The location of maximum transverse strain occurs at the end of the beam regardless of bearing conditions or cross-section.
- Due to Saint Venant's principle, changes to the bearing conditions have little effect beyond those portions of the beam nearest to the bearing.
- For the range of stiffness values reported for neoprene bearing pads, variations in pad shear stiffness have negligible effect ($< 0.1\%$) on the transverse strain in the end region. However, variations in pad axial stiffness can change the transverse strain by $\pm 3\%$.
- Depending on the width of the bearing pad, two types of strain distributions (behaviors) occur in the end region I-girders. A behavior denoted as 'bursting' occurred when the bearing pad width was narrow, and the transverse strain was distributed in a bottle-shaped manner. However, 'flexural' behavior occurred when the pad width was large, and transverse strain was dominated by flexural strains in the flange.
- When 'flexural' behavior occurred, the transverse strain increased as the bearing pad width increased.
- When 'bursting' behavior occurred, the transverse strain increased as the bearing pad width decreased.
- The transition between 'bursting' and 'flexural' behavior occurred when the bearing pad width was approximately equal to 60% of the bottom flange width. This pad width also corresponded to the optimal width for minimizing transverse tensile strain.
- The magnitudes of transverse strain in rectangular sections were 14% to 38% of those in similarly dimensioned I-shaped flanged sections. This reduction in transverse strain was one of the benefits of using end blocks on girders with I-shaped sections.
- When the bearing pad width was less than the web width (as in the rectangular models), the transverse strains increased as pad width decreased.
- Steel bearing plates reduced the magnitude of transverse strain in the concrete nearest to the plate location. This effect was most pronounced when the bottom flange was acting in the 'flexural' mode.

- Transverse force in the bottom flange above the bearing pad and due to applied load was minimized when the bearing pad width was approximately equal to 60% of the flange width.
- For the conditions investigated in this analytical study the transverse force in the bottom flange above the bearing pad was approximately 25% of the reaction force.

2 Modeling of End Region during Prestress Transfer

This chapter presents FE modeling that was conducted to 1) provide a better understanding of the elastic behavior of the end region during and immediately after prestress transfer, 2) quantify lateral forces in the bottom flange within the end region, and 3) evaluate the effects of variables such as transfer length and embedded steel bearing plates on end region behavior. The FE program ADINA (R&D 2009) was used to conduct the modeling. Analyses were conducted using linear elastic properties and were intended to model pre-cracked behavior. Strain gage and displacement data from construction of girders H and V from Appendix D were used to validate the FE model. The Hoyer effect was not considered in analyses presented in this section, but is addressed in Appendix G as part of the development of the end region design model.

2.1 Model Configuration

Figure 34 shows the coordinate system used for FE models in this chapter. The FE model configuration was designed to be computationally efficient, yet able to capture the overall behavior of girders as well as local behavior of the end region. Distribution of transverse ($x-x$) tensile strain in the bottom flange was of particular interest

Behavior during and immediately after prestress transfer was modeled as shown in Figure 34b. Transfer of prestress created negative bending moments of sufficient magnitude to overcome girder self-weight and cause the girders to camber upward. At this stage the boundary conditions were selected such that the girder model had vertical (Z -direction) supports at each end. While friction forces generally develop between test girders and the stressing bed, friction forces were assumed to be small and were thus neglected in development of the FE model. The restraining force from uncut strands was also assumed to be negligible. These assumptions appear valid based on comparison with experimental data, as presented in the next section.

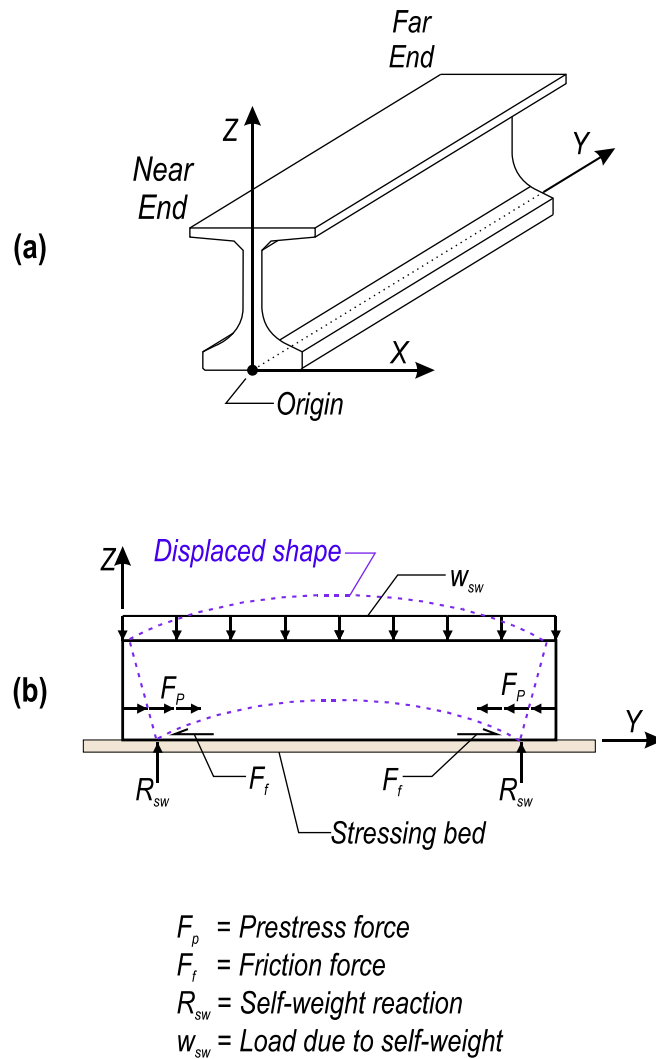


Figure 34—Coordinate system and free-body diagram of girder after prestress transfer

Figure 35 shows the details of the FE model and boundary conditions used to analyze the girder. A rectangular mesh of 27-node 3D solid elements was used to build the portion of the model representing the end region. The portion of the model that used solid elements was selected to fully capture the effects of the prestress and bearing forces on the end region. Beam elements were used in the remainder of the beam with the transition from beam to solid elements made using rigid 2D shell elements and 1D rigid links. Rigid shell and link elements coupled the displacements of the 3D solid elements with the displacements and rotations of the 1D beam elements. Transitioning to beam elements reduced the computational demand while still modeling the global girder behavior and boundary conditions. Beam elements were placed at the centroid of the cross-section and were assigned cross-sectional properties equivalent to the FIB-

54 test girders. A rigid link was provided to connect the beam elements to the physical location of the bearing at the bottom of the girder at the far end. The embedded steel bearing plate at the near end was modeled using shell elements.

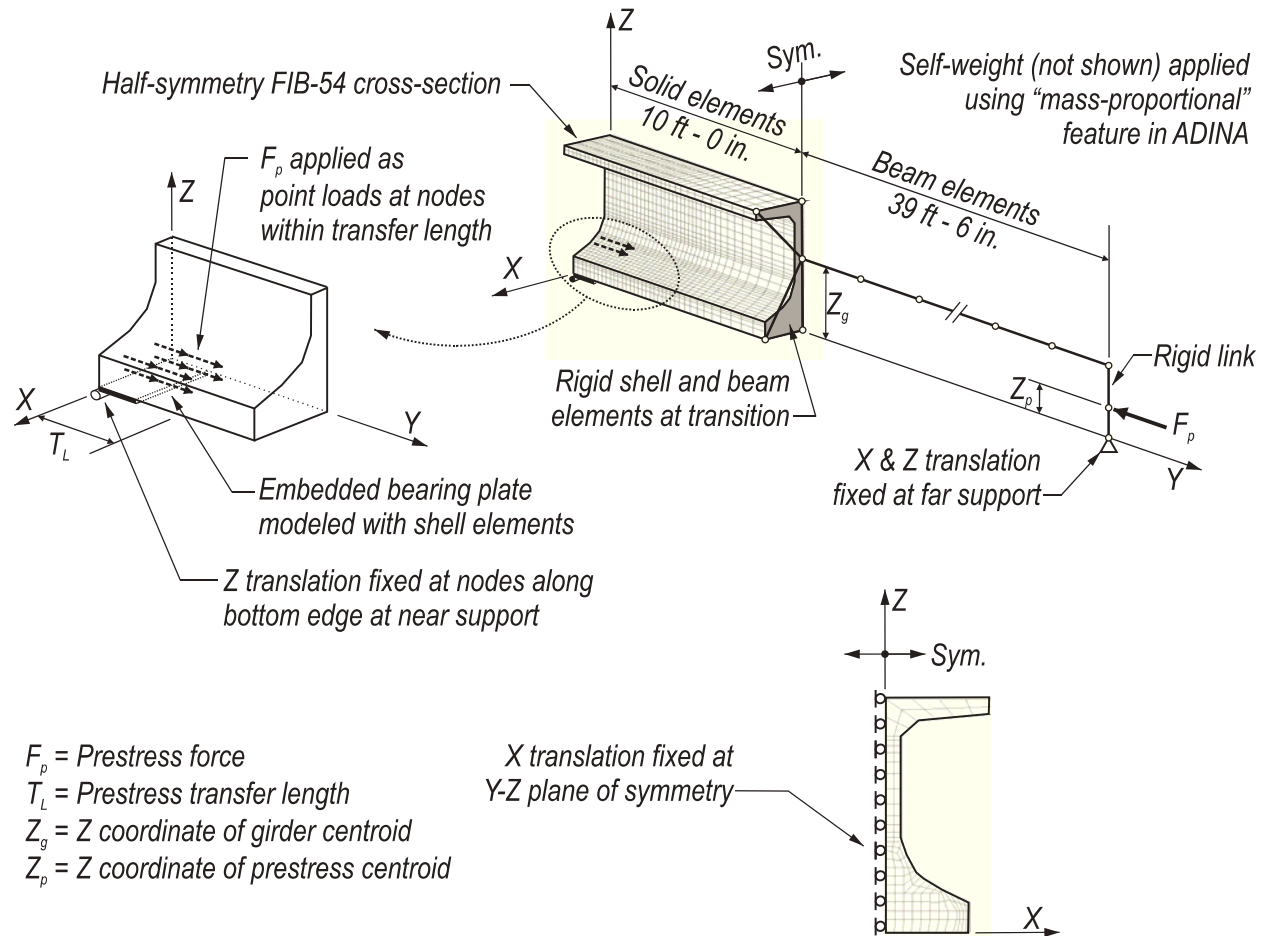


Figure 35-FE model details

Boundary and loading conditions of the FE model were consistent with the conditions of the physical test girders during and after prestress release. Vertical displacement was restrained along the bottom edge of the model at the near support and at the bottom of the rigid link at the far end. Prestressing forces were applied to both ends of the model. Application of prestressing at the near end is discussed in detail later in this section. At the far end, prestressing was applied as a single point load at a height equal to the Z-centroid of the prestressing force.

The cross-section, boundary conditions and loads were symmetrical about the Y-Z plane, allowing for half of the beam to be considered in the FE model. As such, transverse (x-x) translations were restrained at all nodes on the plane of symmetry.

Self-weight was modeled using the “mass-proportional” load feature in ADINA. This feature was employed by assigning mass density to the materials in the model, and assigning the direction and magnitude of gravity, and then allowing ADINA to calculate the body forces associated with self-weight.

The FE model was developed such that nodes in the bottom flange mesh aligned with the prestressing strand layout. Because element nodes coincided with the strand locations, the prestressing force could be applied as point loads to nodes within the transfer length (Figure 35). Prestressing in the FE model was based on test girders H and V that contained (39) fully bonded 0.6-in. diameter prestressing strands (Figure 36). Prestressing forces occurring at the centerline of the cross-section (plane of symmetry) were reduced by 50% to account for the model symmetry. Forces from the partially debonded strands were not included in the model. This simplification appeared reasonable based on the validation presented in the next section. It is further justified by considering that the partially debonded strands in the test girders did not transfer loads within the end region, which was the area of primary interest. Individual steel strands were not explicitly included in the model.

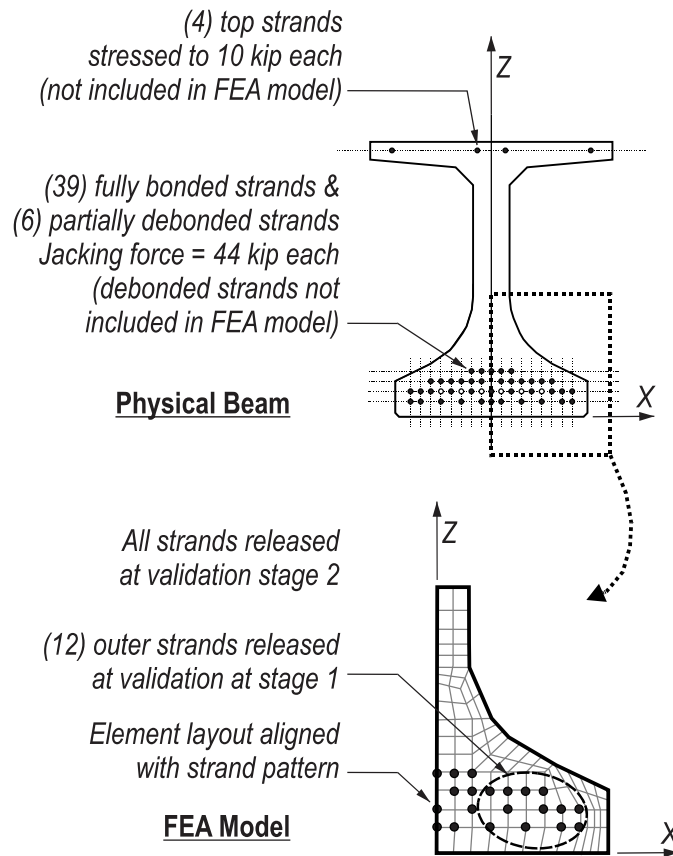


Figure 36–Strand layout and element mesh

A transfer length of 17.5 in. was used. This length was approximately half of the transfer length calculated using AASHTO LRFD provisions. A shorter length was used for multiple reasons. First, strand transfer lengths were shortest during and immediately after transfer (Barnes et al, 1999), which was the time that strain data were taken for validation. Second, the AASHTO LRFD transfer lengths were conservatively long relative to experimental data (Barnes et al., 1999). The transfer length in the FE model was denoted as T_L to distinguish it from the physical and code calculated transfer lengths.

Based on experimental data, the elastic prestress loss after all strands were released was approximately 10%. Elastic loss was indirectly considered in the FE model by reducing the magnitude of the applied prestress forces. As with the test girders prestress forces were applied sequentially to the model. As additional forces were applied, the elastic loss was assumed to be proportional to the number of released strands. To demonstrate how elastic losses were applied,

Table 5 lists some of the stages of prestressing, prestress forces and elastic losses considered in the FE model.

Table 5–Application of elastic loss

Stage	Initial prestress force	Assumed elastic loss (percentage)	Assumed elastic loss (force)	Prestress applied to model (initial minus losses)
4 of strands released	176 kip	2.0%	3.5 kip	172.4 kip
10 (half) strands released*	440 kip	5.0%	22.0 kip	418.0 kip
17 strands released	748 kip	8.7%	65.0 kip	683.0 kip
All strands released**	1716 kip	10.0%	171.6 kip	1544.4 kip
*Verification stage 1				
** Verification stage 2				
All forces for half symmetry FIB-54 model				

The concrete modulus of elasticity for each model was set at 4700ksi, and the Poisson’s ratio was set at 0.2. The modulus of elasticity value was chosen to match tested material properties from test girders used for validation.

The model configuration was validated by comparison with experimental data, and was then used in more general investigations of the stress and strain state in the end region. Details of the verification and validation are contained in the next section.

2.2 Model Validation and Verification

A verification study was conducted to determine that the mesh used in the proposed FE model had sufficient density to capture the end region behavior. Figure 37 shows the proposed mesh density and a refined mesh density, which was used for comparison. The refined mesh was twice as dense (i.e. 4 times more elements) as the proposed mesh.

Principal tensile stress results from the proposed and refined models are compared in Figure 38. Differences between refined and proposed meshes occurred primarily in elements adjacent to the applied prestress forces. Locations away from the prestress forces had similar stress magnitudes and distributions for both meshes. Based on this comparison the proposed mesh was deemed acceptable for evaluating behavior away from the prestress forces, and the refined mesh was required for evaluations near the prestress forces.

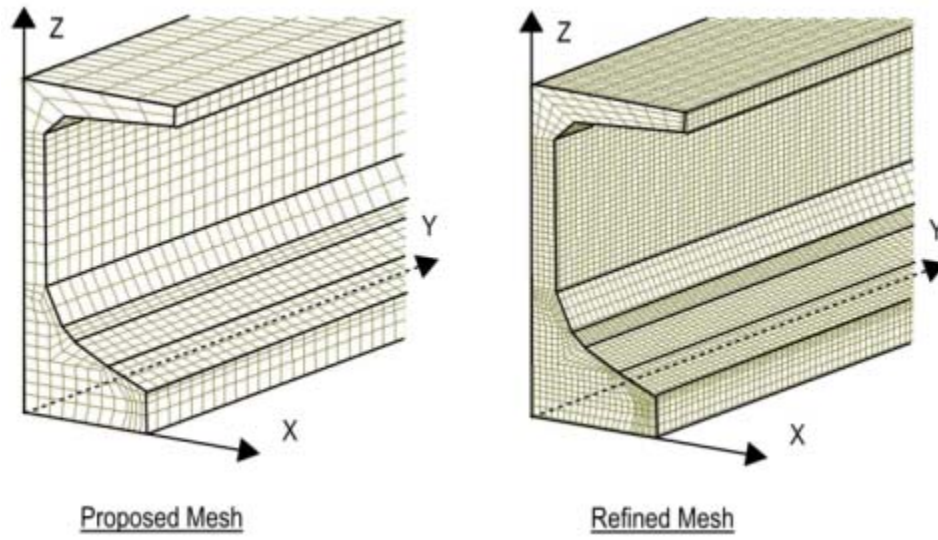


Figure 37–Verification study mesh densities

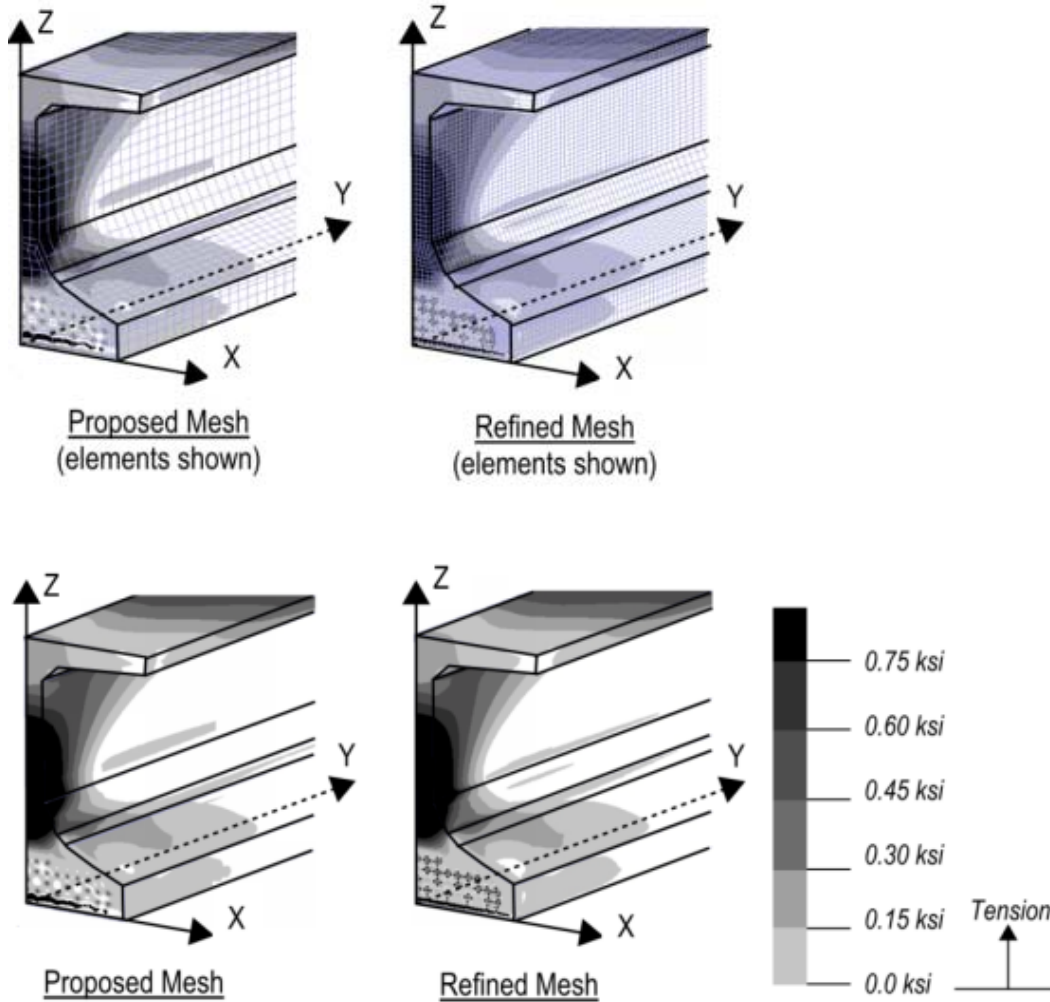


Figure 38–Verification study principal tensile stresses

Test girders H and V were selected for use in validating the FE model. During prestress transfer in these, strands farthest away from the girder centerline were cut first with subsequent strand cuts made progressively closer to the centerline. Based on the release pattern, two stages were considered in the model validation. During stage 1 only the outer strands were released. During stage 2 all strands were released.

Comparisons with the experimental data indicate that the FE model did an adequate job of capturing both the global and local linear elastic behavior of the physical test beams. The exaggerated displaced shape calculated by the FE model is shown in Figure 39 for stage 2 (all strands cut). Camber at mid-span calculated by the FE model was 0.90 in., which was within 2 % of the experimentally measured camber of 7/8 in.

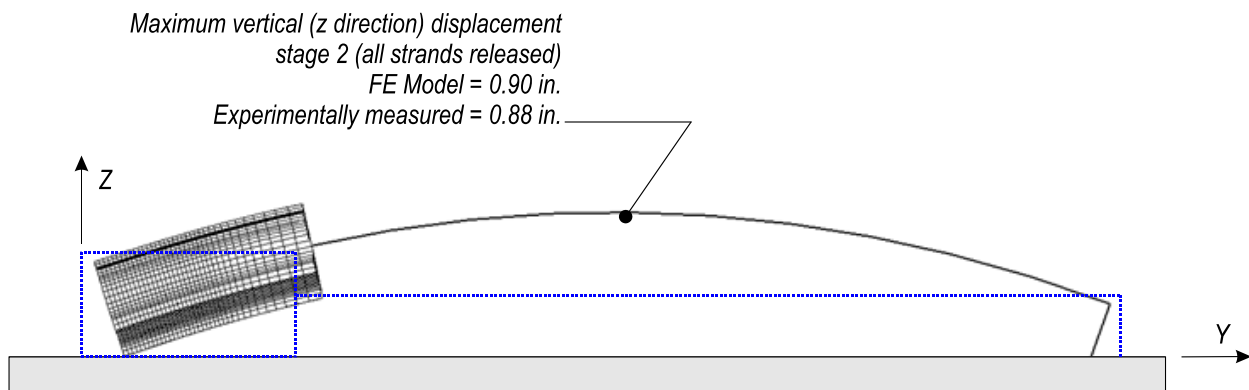


Figure 39–Displaced shape

Although cracking was not observed visually during or immediately after prestress transfer in girders H and V data from strain gages indicated that cracking may have occurred in the physical girders as the prestressing strands were being cut. Figure 40 shows that the magnitude of tensile strain reported by the gages exceeded the expected concrete rupture strain of 132 microstrain. The expected rupture strain was derived from empirical relationships for elastic modulus and rupture strain in ACI 318 (2011). Based on the location and magnitude of the tensile strains calculated by the FE model, it is not surprising that strain gages reported strains greater than the expected cracking strain. This result suggests that the FE model captured the behavior of the physical girders at both stages of prestress transfer.

With the exception of the locations presented in Figure 40, the calculated linear-elastic FE model strain values at most locations were below the experimental rupture strain. Experimental data from most strain gages also demonstrated linear-elastic behavior. Data from these gages were used to validate the linear-elastic strains calculated by the FE model.

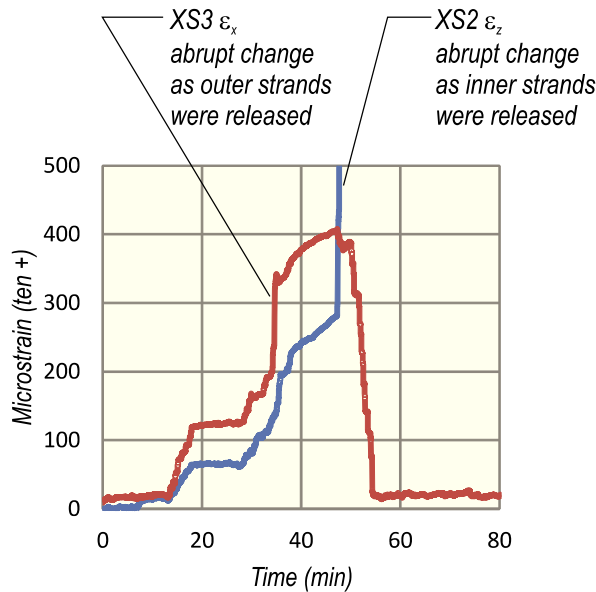
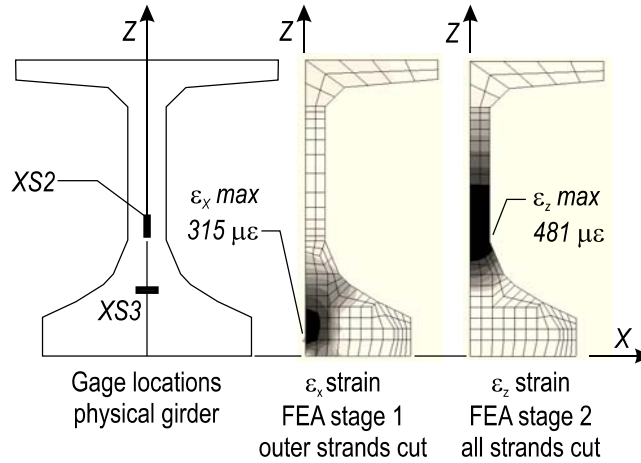


Figure 40–Comparison of experimental and FE model strains at cracks

Transverse (x-x) strain was of particular interest because transverse concrete behavior is coupled with confinement reinforcement behavior. Strain data from gages embedded in the physical girders are presented in Figure 41 along with strain data from the FE model. As demonstrated in the figure, the FE model was in good agreement with the experimental data

throughout the end region and at both stages. Gages located at $Y = 2$ in. were near the cracking that occurred prior to stage 1, hence the variability in those data points.

Longitudinal (y-y) strains at the edge of the bottom flange are compared in Figure 42. Strains predicted by the FE model were within the scatter of the strain data at stages 1 and 2. The good agreement between the FE model and the longitudinal experimental data suggest that the transfer length used in the model (17.5 in.) was consistent with the transfer length in the physical girders.

Figure 43 compares the vertical (z-z) strain from the FE model and the test girders. Trends and magnitudes were consistent between FE model and experimental data. The largest vertical strains occurred at the end of the girder ($y = 0$ in.) Vertical strains were larger during stage 2 than stage 1.

Strain and displacement data from the FE model were in good agreement with experimental data. The occurrence and location of cracking in the experimental girders were consistent with the locations of maximum tensile strains calculated by the FE model. It was concluded that the model accurately captured the global and local behavior of the physical girders at multiple stages of prestress transfer and that the model was adequate for more general parametric studies.

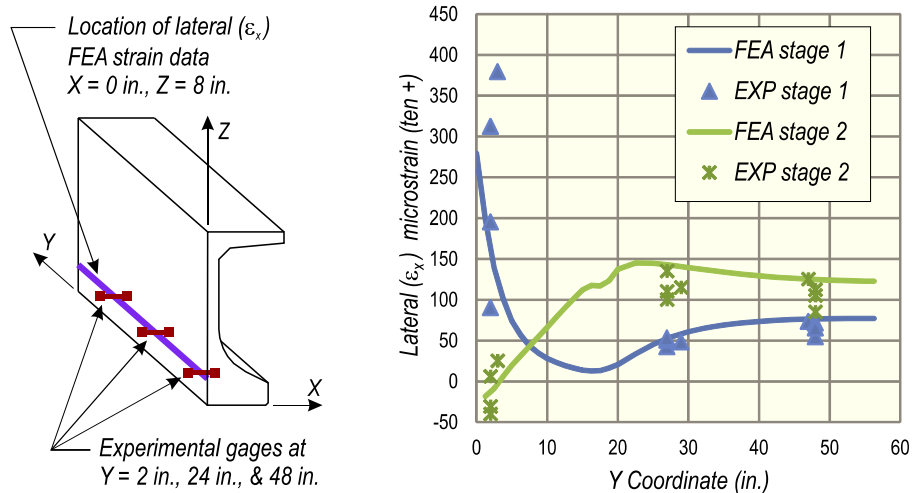


Figure 41–Comparison of experimental and FE model transverse (x-x) strain

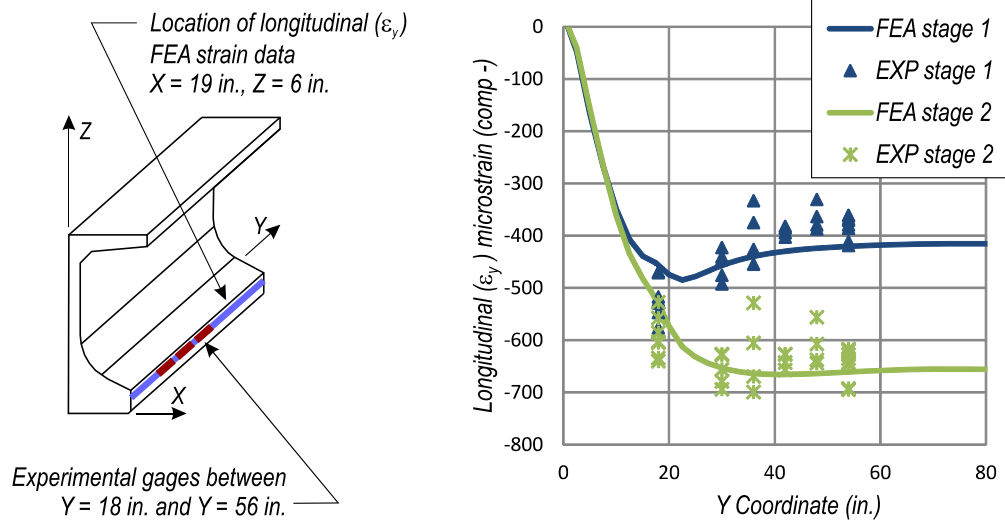


Figure 42–Comparison experimental and FE model longitudinal (y-y) strain

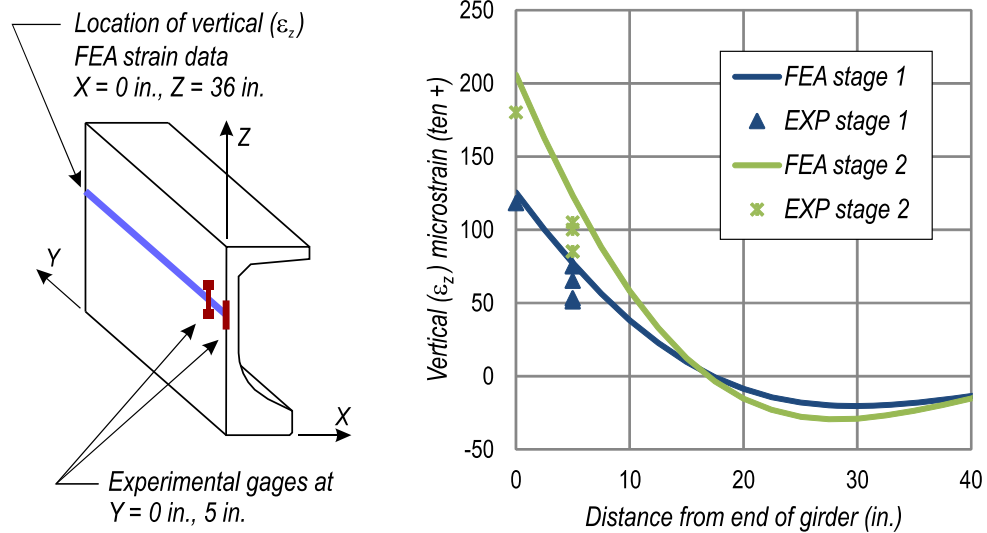


Figure 43–Comparison of experimental and FE model vertical (z-z) strain.

2.3 Transverse Force Quantification

Transverse tension forces in the bottom flange at the near support were of interest because they are resisted by confinement reinforcement in the event that the concrete cracks. This section describes the procedure used to quantify the transverse (x-x) force from the validated FE model.

Transverse force was calculated by integrating transverse stress over the area shown in Figure 44. This was the same area previously used for investigating the effects of bearing pad

width (Figure 32). Boundaries of the integration area were selected to capture those portions of the girder end subjected to steep stress gradients due to prestressing. Boundaries were also selected to include portions of the bottom flange where confinement reinforcement is placed to carry transverse tension. Boundaries of the integration area were defined as a function of bottom flange width (W_f) so that similar integrations could be performed on girders with varied cross-sections.

Discrete x-x stress values from center nodes in the integration area were multiplied by the associated y-z areas to obtain transverse forces (Figure 45). The total transverse tensile force was calculated as the sum of all element tensile forces. Lateral force in the steel bearing plate was calculated in a similar manner. Compressive forces (when they occurred) were ignored in calculations of transverse force. I.e., transverse tensile force equaled the gross tension and was not reduced by compressive forces. This approach was taken because transverse compressive forces are supported by concrete and do not typically lead to cracking of concrete or tension loading of confinement reinforcement.

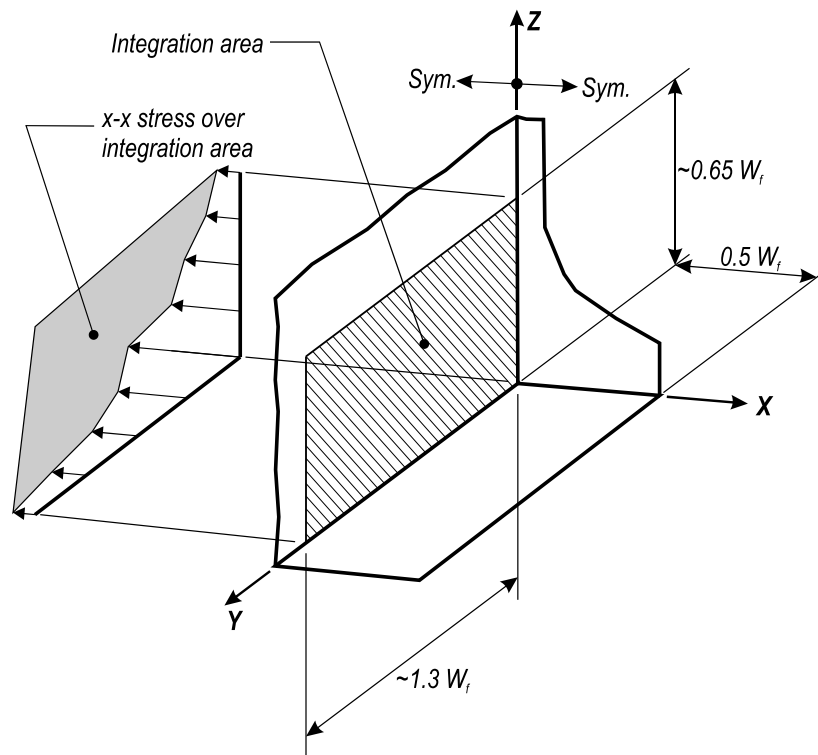


Figure 44—Area over which stress was integrated to determine lateral force

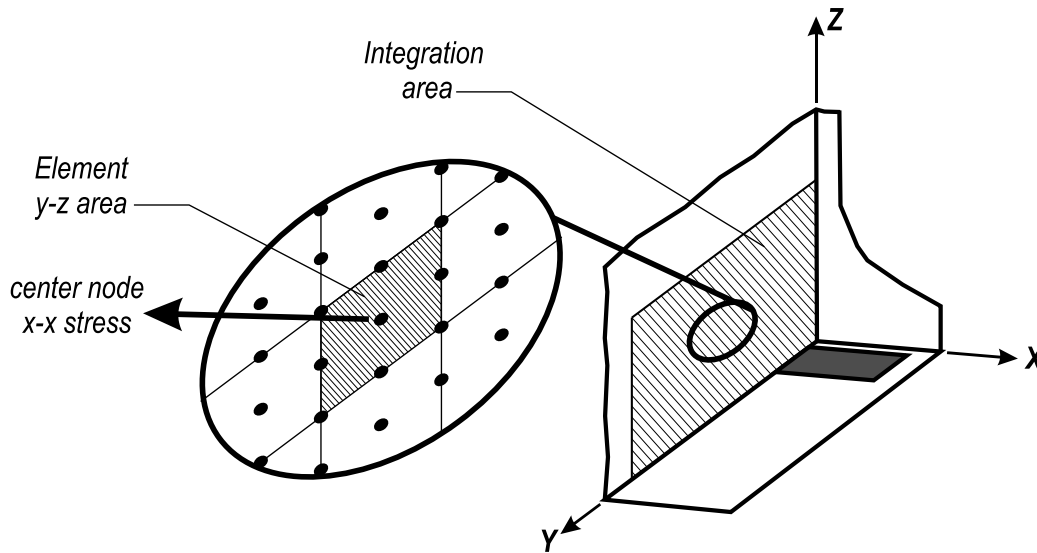


Figure 45–Element x-x stress and y-z area

2.4 Parametric Studies

2.4.1 Strand Release Parametric Study

Transverse (x-x) stresses and forces changed throughout prestress transfer as strands were sequentially cut. A parametric study was conducted to investigate the relationship between transverse force and the quantity of cut strands. This study used FE models of girders with FIB-54 and AASHTO Type IV cross-sections. The AASHTO girder model had the same configuration as the FIB model (Figure 35), with the exception of having cross-section dimensions of an AASHTO Type IV girder. Prestressing forces were applied as point loads over a transfer length of 17.5 in. Steel bearing plates were not included.

Elastic prestress losses were considered in the models. Losses were assumed to vary linearly from 0% when no strands were released to 10% when all strands were released. This magnitude of elastic loss was consistent with experimental data from girders H and V.

Strands in the experimental FIB girders were released from outside-in and bottom-to-top. To model this process, prestressing forces were added sequentially to FE models beginning at the location of outermost strands. Figure 46 show the locations of prestressing forces at different phases of prestress transfer in the FIB-54 model. Transverse (x-x) stress distributions are also shown. When only outer strands were released, the tensile stresses were concentrated within 10 in. of the girder end. Tensile stresses reduced in magnitude, but occurred over a greater portion

of the integration area after inner strands were released. Stresses shown in the figure were due to prestressing forces and self-weight.

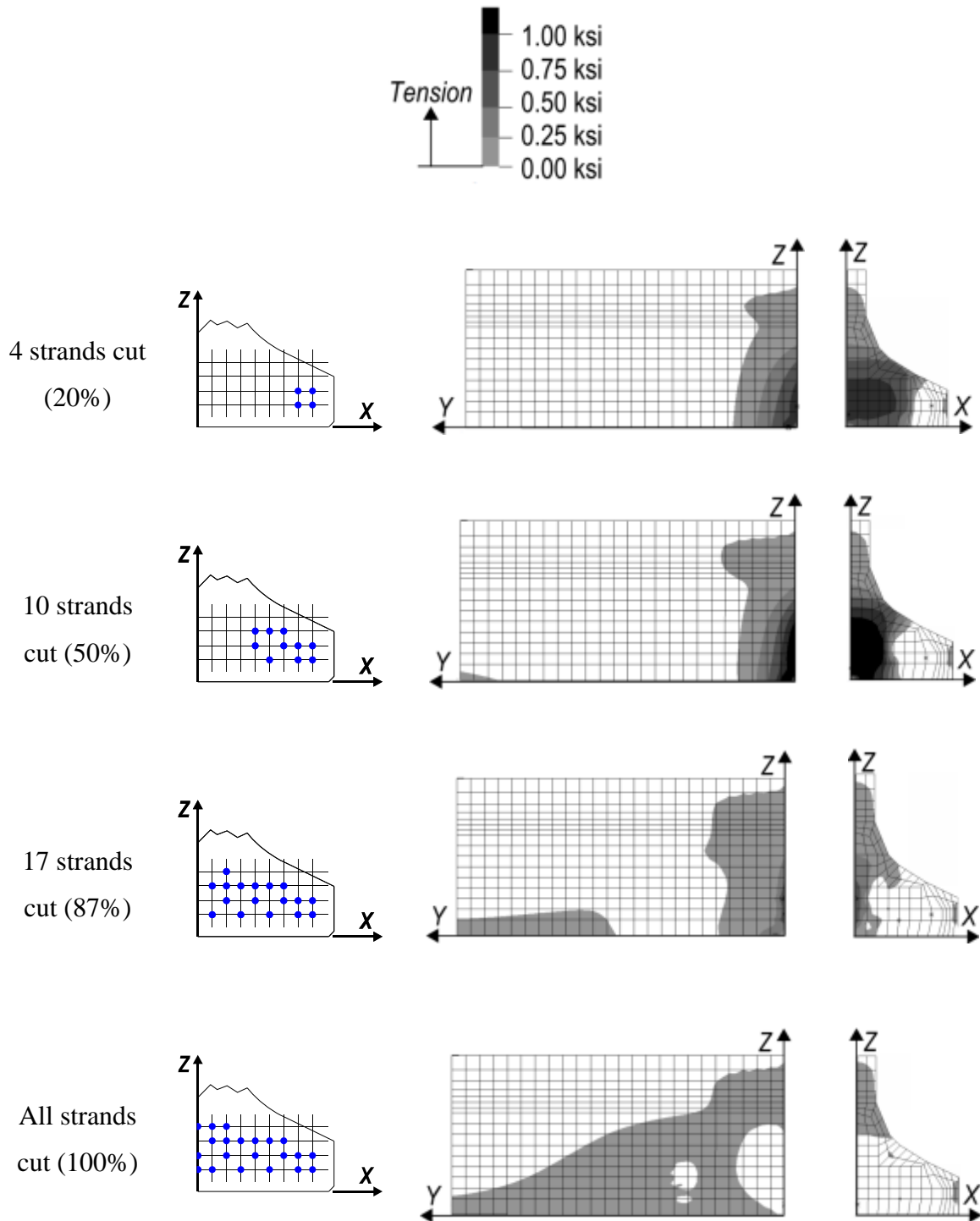


Figure 46–Transverse (x-x) stress at stages of prestress transfer

The bottom flange of the AASHTO Type IV section houses fewer strands than the FIB bottom flange. To normalize this difference, the quantity of strands in both AASHTO and FIB

models was designed to be approximately 50% of the maximum possible strand quantity for the given section. Strand locations in the FIB model also matched the experimental girders H and V.

The transverse tensile force at the cross section centerline was calculated at each stage of prestress release following the previously described integration procedure. Calculated forces are plotted as a function of the percentage of cut strands in Figure 47. The calculated forces presented in the figure were normalized by the final prestress force for each girder.

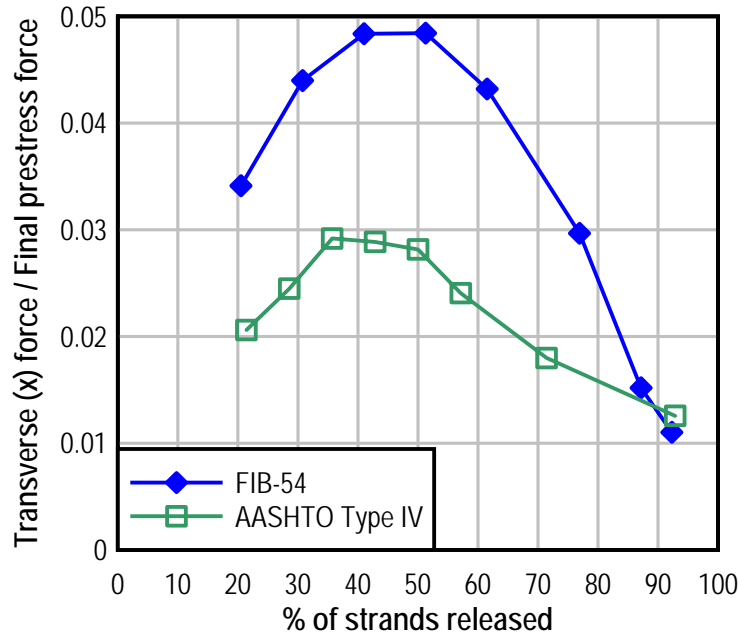


Figure 47–Variation in transverse force as strands are cut

For both girders the largest transverse tensile force occurred when approximately 40% of the strands were released. This percentage corresponds to the stage when only the strands in the outer portion of the flange had been cut. Transverse force decreased as the inner strands were cut. This observation is consistent with experimental strain data that reported the largest transverse tensile strains when the outer strands were released and a commensurate reduction in those tensile strains as the inner strands were released.

The FIB-54 model had higher ratios of transverse force to final prestress force than the AASHTO Type IV model. This was attributed to the FIB section’s relatively wide and slender bottom flange. Because of the greater width, strands in the FIB flange had a greater moment arm about the cross section centerline than did strands in the AASHTO flange.

Figure 47 also demonstrates the problem of partially debonding inner strands and fully bonding outer strands. In this circumstance, inner strands do not transfer prestress force at the end of the girder and consequently do not reduce the transverse tensile force at the centerline. This situation occurred in the experimental program in specimens FN and FB. Flange splitting cracks formed at the end of these girders at the centerline of the cross section. A similar situation and similar cracks were observed in experimental AASHTO Type IV girders by Llanos et al. (2009).

2.4.2 Bearing Plate Contribution

The validated FE model was used to evaluate transverse force carried by embedded steel bearing plates due to prestressing forces. This evaluation considered the same stages of prestress transfer as were used in model validation. For stage 1 only the outer strands were released. For stage 2 all of the strands were released. The presence or absence of the steel bearing plate was also included as a variable, resulting in four unique variable combinations.

Figure 48 and Figure 49 present the transverse (x-x) stress distributions along the plane of symmetry for each of the four variations considered. Transverse force was calculated using the previously described integration procedure. Table 6 lists the maximum stresses and total forces of each model variation. Calculated force in the bottom flange was approximately 67 kip at stage 1. When the steel bearing plate was present, it attracted approximately 7 kip, or 10% of the transverse force. The steel bearing plate also changed the transverse stress distribution in the concrete adjacent to the plate, but did not change the total transverse force.

Calculated transverse force during stage 2 was approximately 27 kip. When the embedded steel plate was present it attracted 3 kip, or approximately 10% of the force. This percentage is similar to stage 1. Presence of the steel plate changed the stress distribution in the concrete near the plate but it did not significantly affect the total transverse force at the end of the girder.

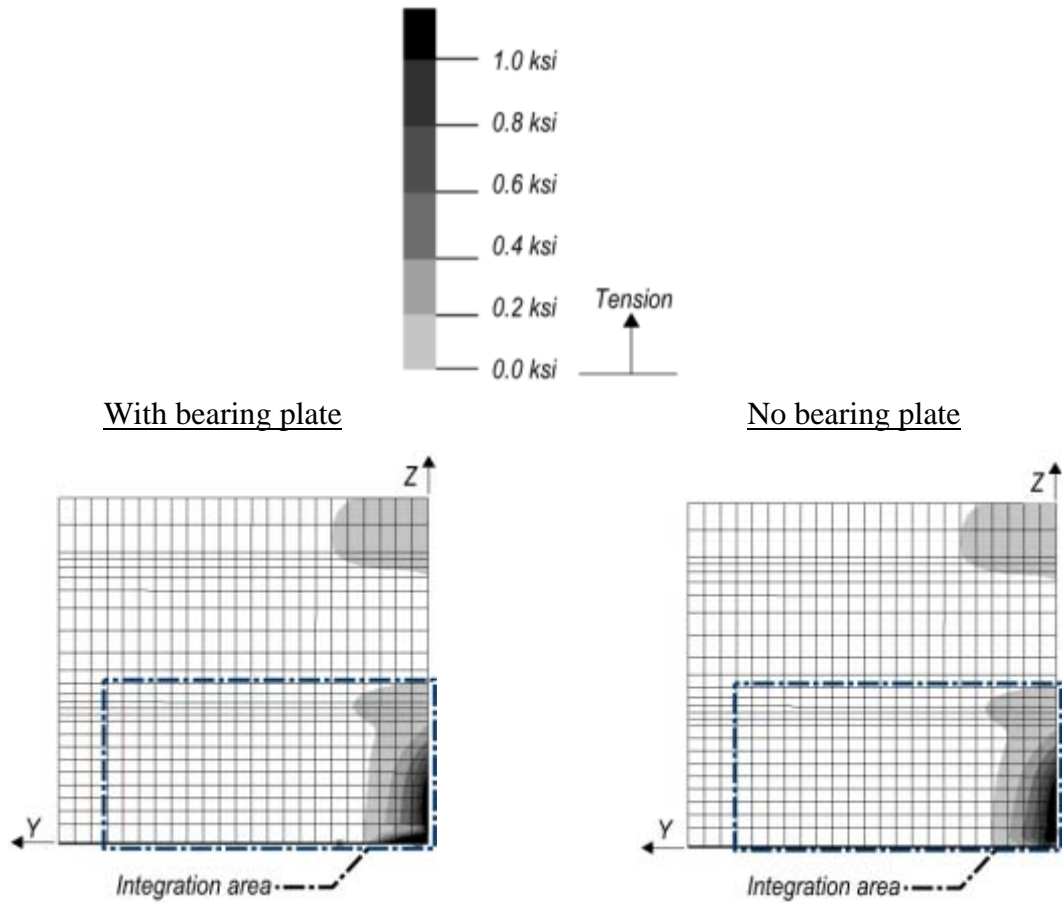


Figure 48–Transverse (x-x) stress distribution at stage 1 (outer strands cut) with bearing plate and without bearing plate

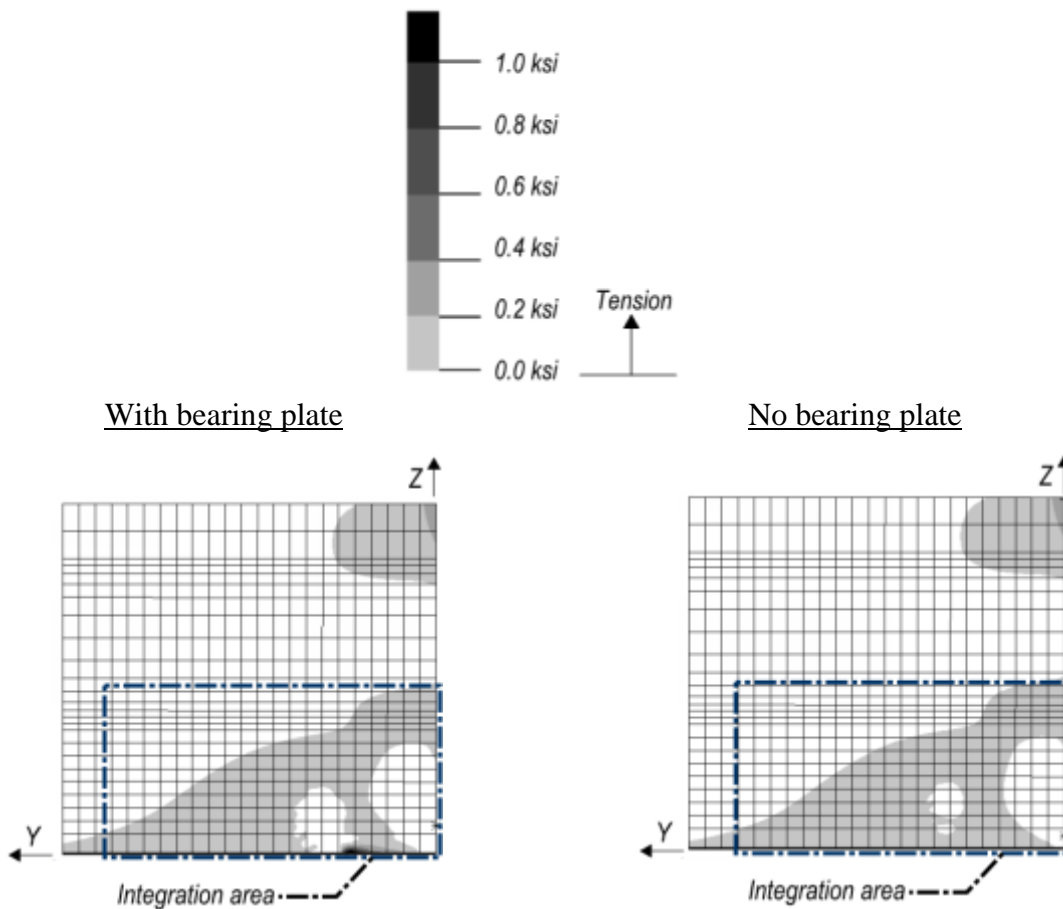


Figure 49–Transverse (x-x) stress distribution at stage 2 (all strands cut) with bearing plate and without bearing plate

Table 6–Bearing plate study summary of transverse (x-x) stresses and forces

	With bearing plate		No bearing plate	
	Max x-x stress at integration point (ksi)	Transverse tension force (kip)	Max x-x stress at integration point (ksi)	Transverse tension force (kip)
Outer strands cut (stage 1)	0.94	60.2 concrete 6.6 plate 66.8 total	1.16	66.9
All strands cut (stage 2)	0.15	24.9 concrete 3.0 plate 27.9 total	0.15	26.6

2.4.3 Transfer Length Parametric Study

This section presents results of a parametric study investigating the effect of transfer length on the magnitude of the transverse tensile force. FE models were created with transfer lengths that varied from 12.5 in. to 47.5 in. This range included lengths shorter than were observed in the experimental program as well as lengths longer than calculated using the AASHTO LRFD code.

The FIB model without a steel bearing plate was used in this study. Models considered the stage shown in Figure 46 when 50% of the strands were cut. This stage was selected because it corresponded to the largest transverse tensile forces.

The previously described integration procedure was used to calculate transverse tensile forces at the cross-section centerline. Transverse force at the centerline had an approximately linear relationship with the transfer length (Figure 50). The largest force corresponded to the shortest transfer length. Transverse tensile force decreased as the transfer length is increased. Thus, physical girders with relatively short transfer lengths have greater transverse forces and stresses than girders with longer transfer lengths.

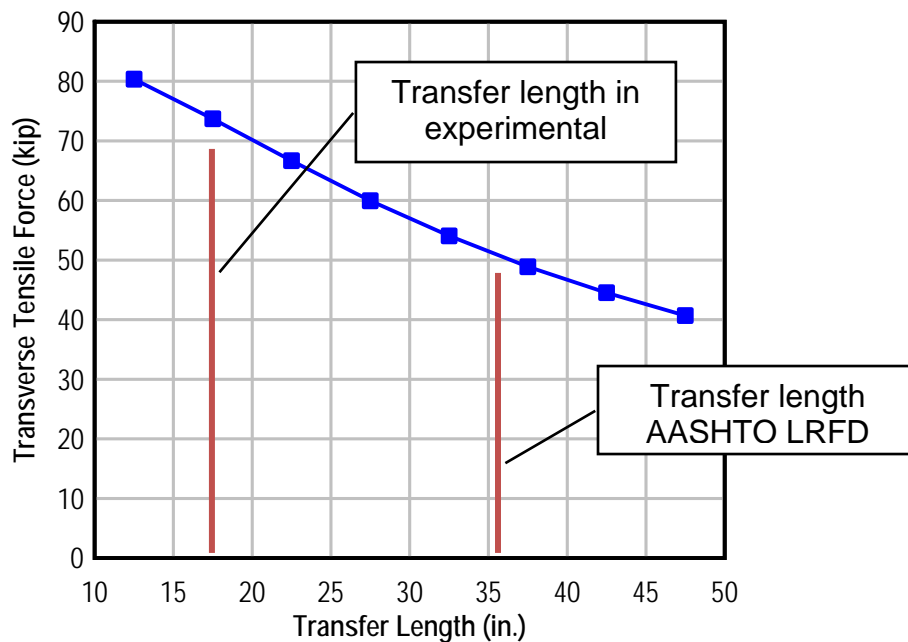


Figure 50–Transverse force vs. length of prestress transfer

According to the data in Figure 50, a 50% reduction in transfer length affected a 50% increase in transverse tensile force. For example, reducing the transfer length 50% from 40 in. to 20 in. resulted in an approximately 50% increase of transverse force from 48 kip to 70 kip.

Transverse tensile stresses due to prestressing forces are shown in Figure 53 and Figure 51 for sections through the centerline (CL) and bottom flange (MID). Tensile stresses formed near the member ends regardless of transfer length. The y-dimension of the tensile stress area was linearly related to the transfer length used in the FE models (Figure 53). Phase 1 experimental girders had a transfer length near 18in. For this transfer length, the FE model calculated that transverse tensile stress at the MID section of the bottom flange had a y-dimension of approximately 11in.

Transverse stress at the MID section is plotted as a function of y-coordinate in Figure 54 for transfer lengths of 17.5 in. and 42.5in. Stresses shown in the figure are from the condition when 30% of the strands had been cut. This condition produces the largest stresses on the MID section, and is a different condition that shown in Figure 51 and Figure 52. Figure 51 and Figure 52 show stresses for the stage when 50% of the strands have been cut. Shapes of the stress distributions in Figure 54 were representative of other bottom flange locations when only the strands outboard of the given location have been cut. For this condition, transverse tensile stresses were largest near the member end and were distributed in an approximately triangular shape. Also, tensile stresses for this condition were spread over a length of approximately 10 in. from the member end.

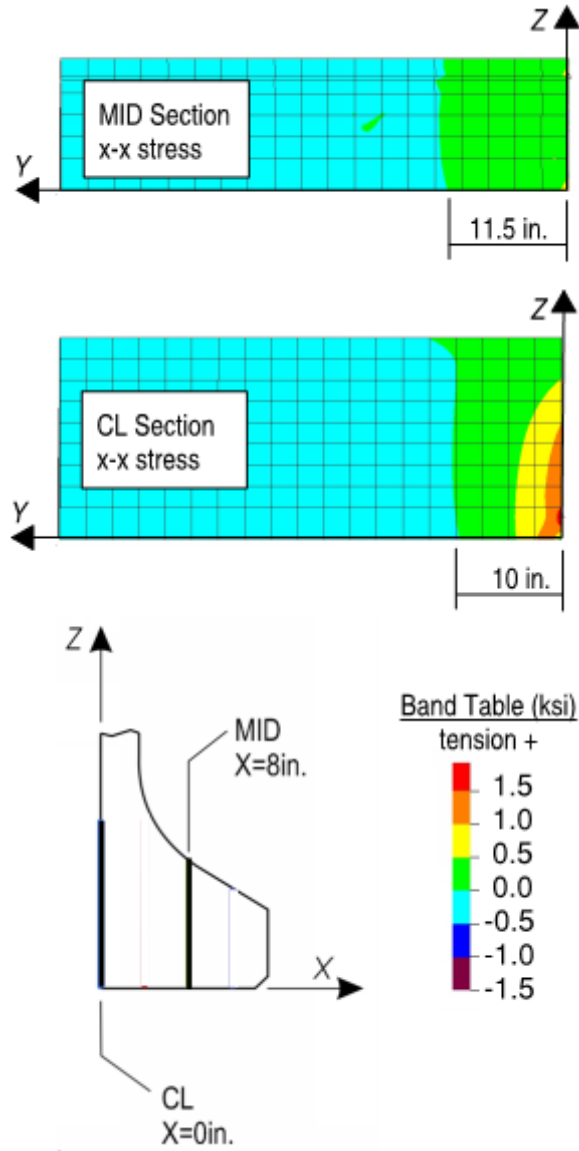


Figure 51–Transverse stress distribution with 17.5-in. transfer length (50% of strands cut)

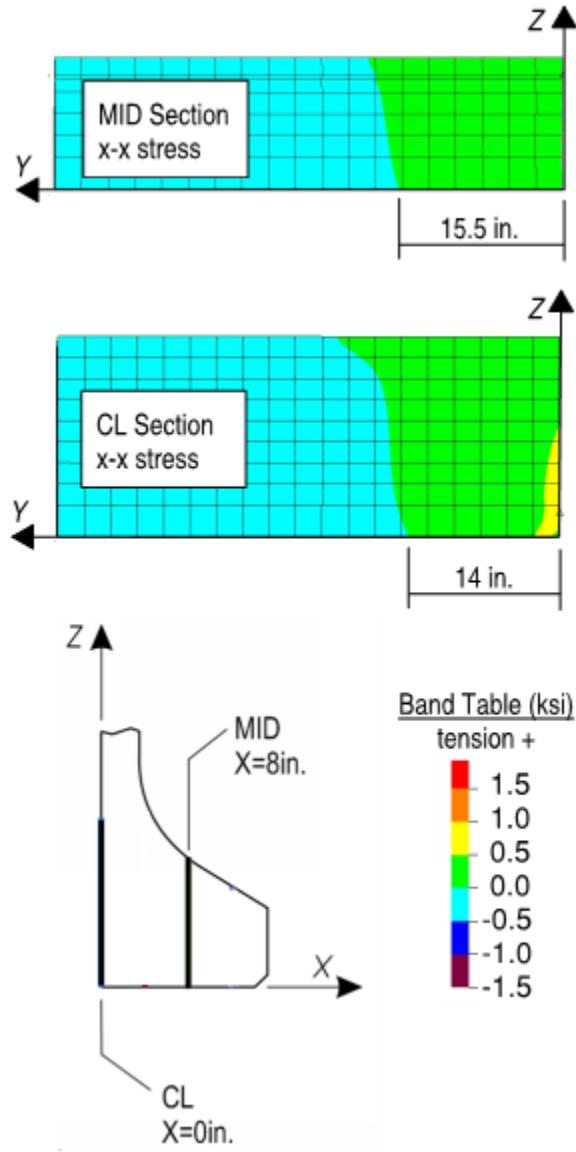


Figure 52–Transverse stress distribution with 42.5-in. transfer length (50% of strands cut)

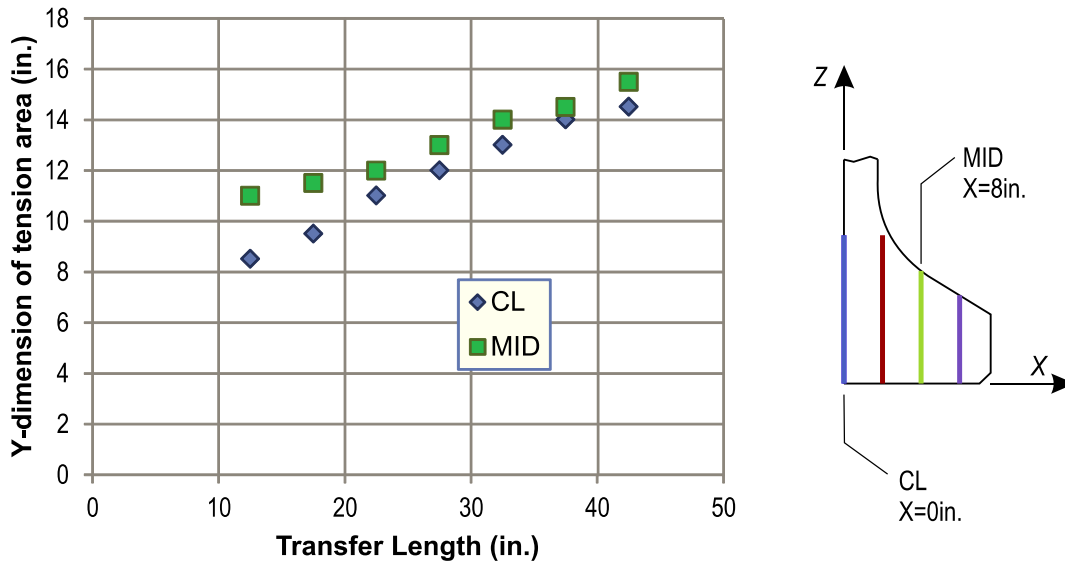


Figure 53–Length of tension area vs. transfer length (50% of strands cut)

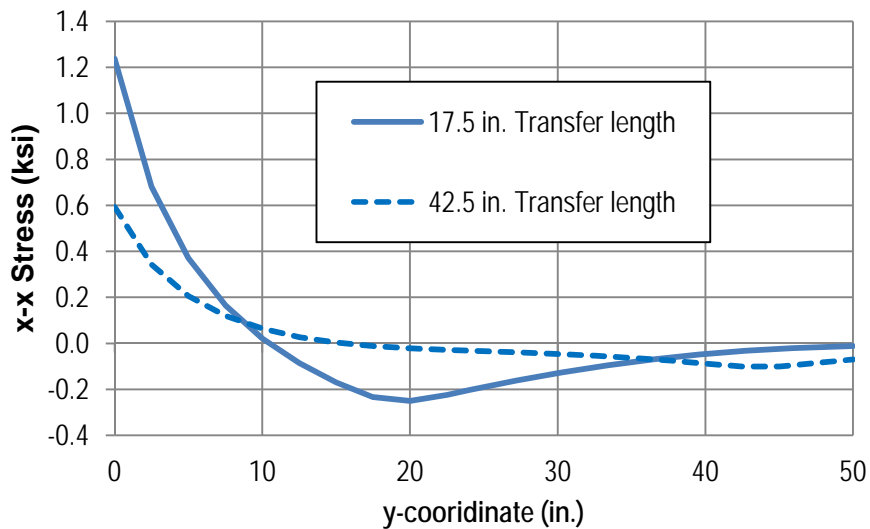


Figure 54–Transverse (x-x) stress at MID section through bottom flange (30% of strands cut)

2.4.4 End Stresses due to Prestress Forces

Analytical results have shown that the largest stresses from the prestressing force occur at the girder end surface (Figure 46). In the experimental program, flange splitting cracks were often observed at the end surface (Figure 55). This section presents a study of stresses at the end surface due to prestressing forces. Results from this study will later be used in development of a model for serviceability design of bottom flanges.

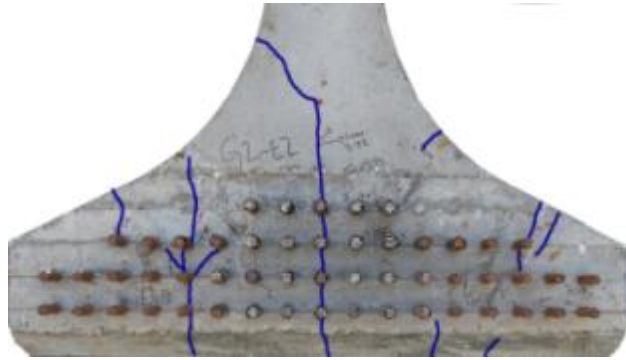


Figure 55–Flange splitting cracks at girder end

The FIB model without a steel bearing plate was used to study end stresses. Self-weight was eliminated to isolate the effects of the prestressing force on the section. A transfer length of 17.5 in. was used in the models. This length was chosen because previous results demonstrated that short transfer lengths produced the largest transverse effects. The refined mesh (Figure 38) was used in this study because stresses near the prestress forces (strands) were used in results interpretation. Strand pattern and strand cutting sequence demonstrated in Figure 46 was used in this study. This strand layout and cut pattern matched girders H, V, and D from the experimental program.

Four lines at the end surface of the model were selected for evaluation (Figure 56). Lines were selected based on the location of cracks observed in the test girders (Figure 55) and to give a representative analysis of the entire bottom flange end. A height of 15in. was used for the centerline (CL) and the web line (WEB) based on the height of flange splitting cracks in test girders. Height of the mid-flange (MID) and flange edge (EDGE) lines were limited by the flange height at those locations.

Transverse (x-x) stresses were considered along each line. This was done because tension stresses at the end of the bottom flange primarily acted in the x-direction. This was evident from the vertical orientation of cracks in the experimental girders (Figure 55). It was also observed in comparisons of transverse (x-x) and principal tension stresses at the end of the FE model (Figure 57). Transverse and principal tension stresses were effectively the same at areas away from the prestressing forces.

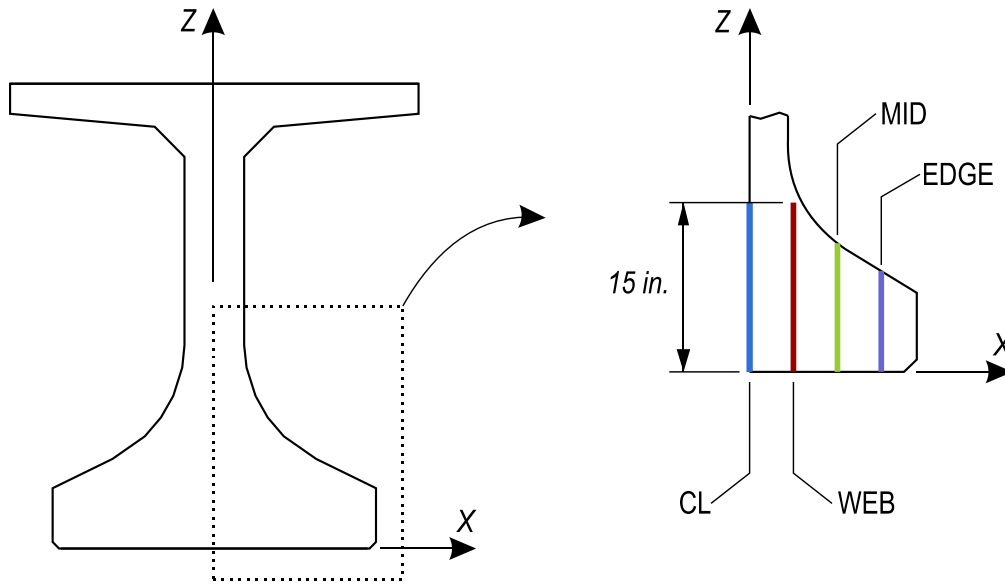


Figure 56—Lines for stress calculations

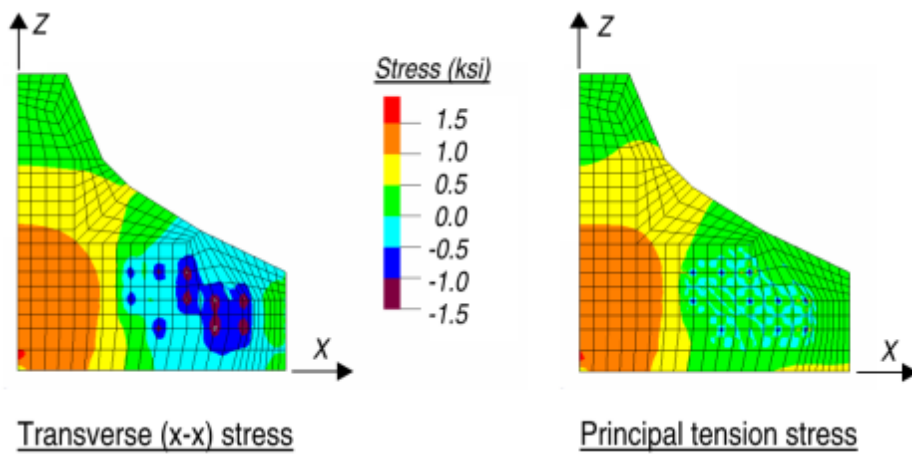


Figure 57—FE model stresses at girder end (50% strands cut)

Stresses along each line were calculated at each stage of prestress transfer using an outside-to-in strand cutting pattern. Stress concentrations occurred in the FE model at nodes where prestress forces were applied (Figure 57). In lieu of the concentrated stress values, stresses at these nodes were taken as the average stress from the adjacent nodes. This resulted in stress distributions such as that shown in Figure 58. Figure 58 shows the stress distribution at the mid-flange line for the stage when 50% of the strands had been cut. During this stage the two strands located on the mid-flange line were cut and resulted in compressive stresses near the strand locations.

The average stress along each line varied with the different stages of strand cutting as shown in Figure 59. The box markers on Figure 59 indicate the stage when strands on an individual line were cut. Average stress on a given line fell abruptly when strands along that line were cut. For example, average stress at the centerline went from 170 psi tension prior to cutting the centerline strands to 680 psi compression after the centerline strands were cut.

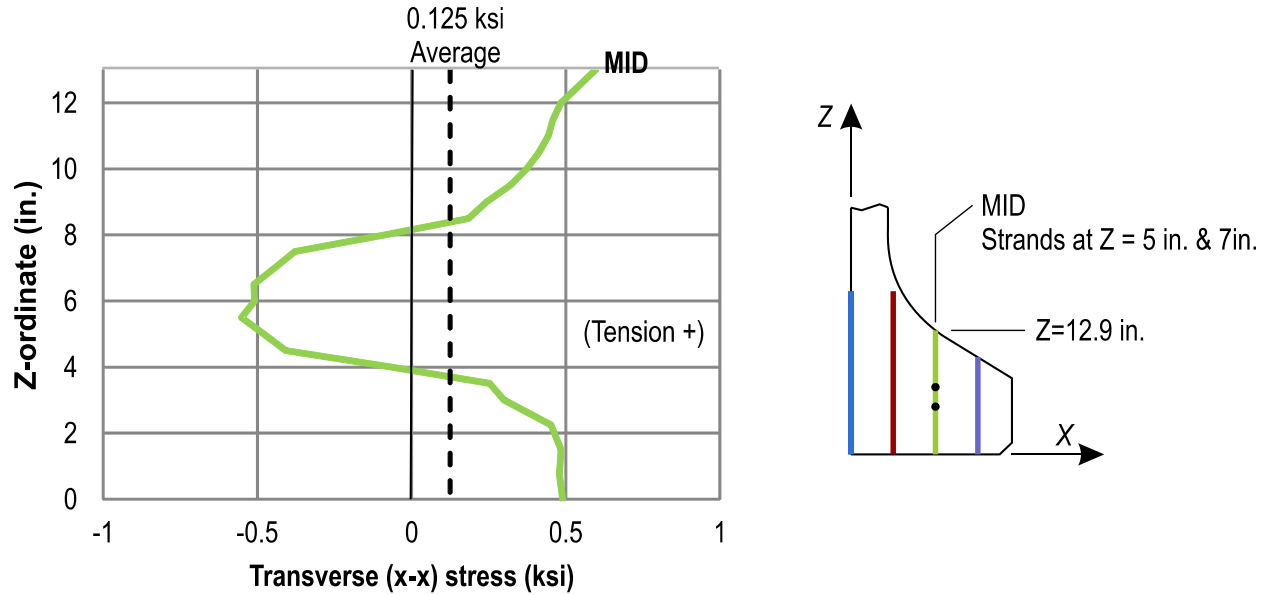


Figure 58–Transverse (x-x) stress at mid-flange line (50% strands cut)

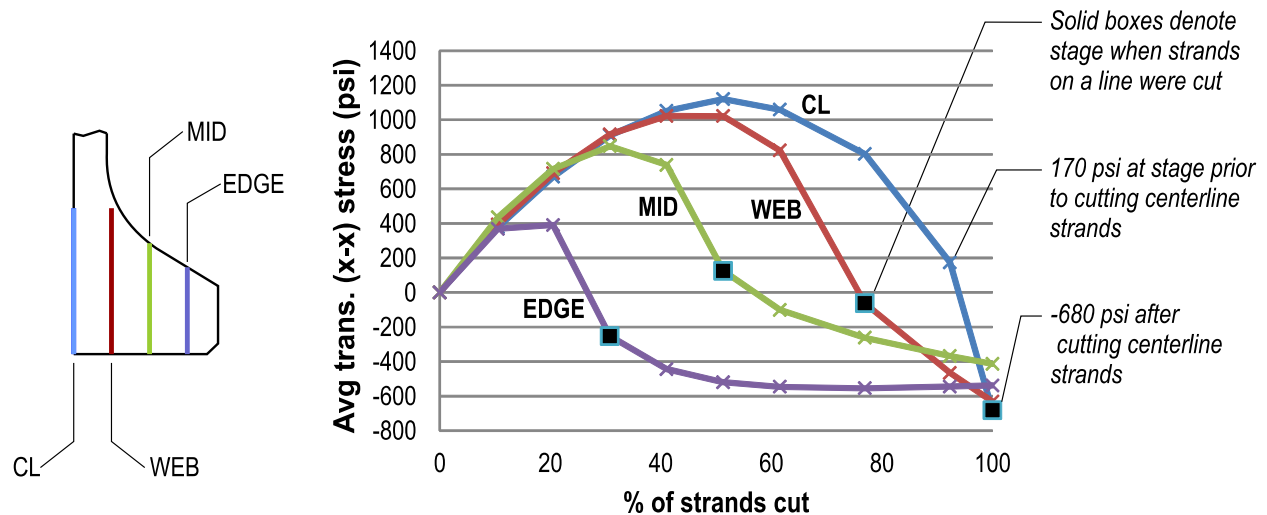


Figure 59–Average transverse (x-x) stress at end of girder due to strand cutting

Average stresses are summarized in Table 7 for each evaluation line. Tensile stress on a given line was greatest when only the strands outboard (closer to outside of flange) of the line

had been cut. Maximum tensile stresses ranged from 1.12 ksi to 0.39 ksi. The largest compressive stresses occurred after all strands had been cut. Maximum compressive stresses ranged from -0.68 ksi to -0.41 ksi. The average compressive stress after all strands had been cut was -0.57 ksi.

Table 7–Summary of transverse (x-x) stress at girder end due to strand cutting

Line	Maximum stress at any stage (ksi)	Stress at stage when strands on line were cut (ksi)	Stress after all strands were cut (ksi)
CL	1.12	-0.68	-0.68
WEB	1.02	-0.06	-0.63
MID	0.85	1.25	-0.41
EDGE	0.39	-0.25	-0.54
Average	0.85	-0.22	-0.57

2.4.5 Transverse Force through Flange Sections

The models used in the previous section were utilized to calculate the transverse force acting on the MID and EDGE lines (Figure 56) through the bottom flange. These locations were of particular interest because of their proximity to flange splitting cracks observed in the experimental girders. The typical integration procedure was used to calculate the transverse tension force at these locations. Results are summarized in Table 8. The maximum transverse force at each location occurred when strands outboard of that location had been cut. Cutting of strands along each location reduced the transverse tension force by 45% at the MID line and 28% at the EDGE line.

Table 8–Summary of transverse (x-x) force at girder end due to strand cutting (FIB)

Section	Maximum force at any stage (kip)	Force at stage when strands on line were cut (kip)
MID	36.1	20.3
EDGE	15.8	11.3

The same procedure was used to investigate transverse tensile forces in the bottom flange of AASHTO Type IV girders. Strand pattern, element mesh, and analysis locations are shown in Figure 60 for the Type IV girder model. A transfer length of 18 in. was used for applying the prestressing forces. Strands were cut sequentially from outside-in. The transverse force on the

WEB and FLANGE lines were calculated at each stage of cutting. Results are listed in Table 9. For both locations, the maximum force occurred when only the strands outboard of the that location were cut. For example, the maximum force on the WEB section occurred when only the outermost six strands had been cut.

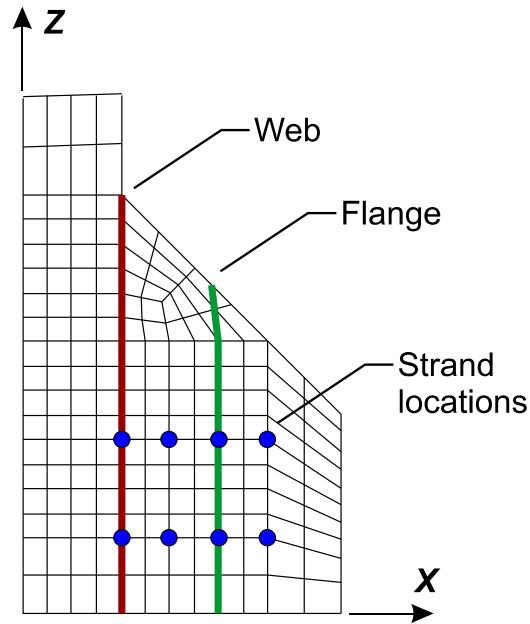


Figure 60–AASHTO Type IV FEA model and analysis lines

Table 9–Summary of transverse (x-x) force at girder end due to strand cutting (Type IV)

Section	Maximum force at any stage (kip)	Force at stage when strands on line were cut (kip)
WEB	11.4	7.0
FLANGE	5.9	5

As with the FIB model (Figure 54), tensile stresses in the Type IV model at the maximum stress condition are also distributed over a length of approximately 10in. from the member end. This is demonstrated by the stress distributions shown in Figure 61. Maximum stress for the WEB condition occurs when the outer six strands have been cut. Maximum stress at the FLANGE section occurs when the outer two strands have been cut. The maximum stress conditions are reported in the figure.

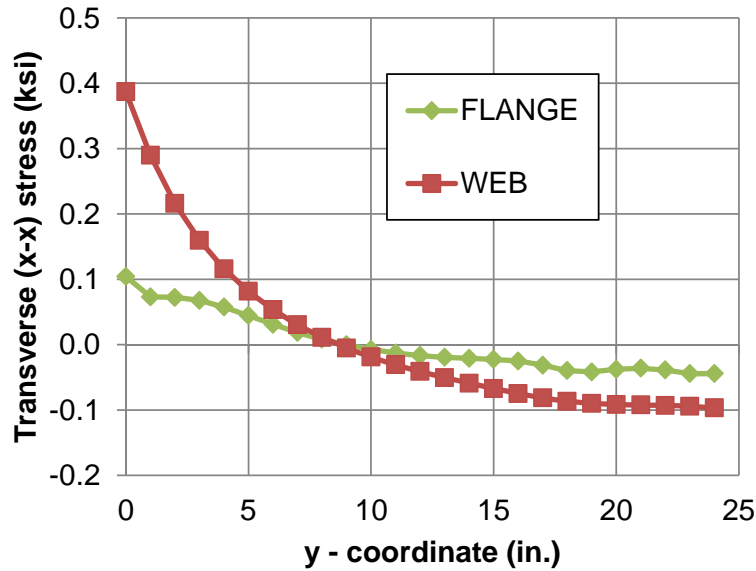


Figure 61–Transverse stress distribution in Type IV girder (maximum condition)

2.4.6 Transverse Action due to Self-Weight

The test girders cambered upward during prestress transfer after the girder self-weight was overcome by the prestressing moment. In this condition the girders were supported vertically at the bottom edge at each end (Figure 34). The FIB FE model was used to evaluate the transverse stresses and forces that occurred due to the self-weight during this condition. Prestress loads in the model were removed leaving only the mass-proportional load which modeled the girder self-weight. Boundary conditions remained the same as previous models in this chapter. Because prestress loads were removed and self-weight remained, the displaced shape of the model was sagging rather than cambering.

Figure 62 shows the transverse (x-x) stresses at the centerline and end due to self-weight. Transverse tensile stresses were largest at the bottom of the girder near the end. Magnitudes of transverse stress due to self-weight were small relative to transverse stress due to prestressing as calculated in the previous section. This is in-part because the self-weight model was based on test girders H and V which were only approximately 35% as long as typical production girders with the same cross-section. Thus the self-weight stresses reported in Figure 62 were also only 35% of stresses in typical production girders.

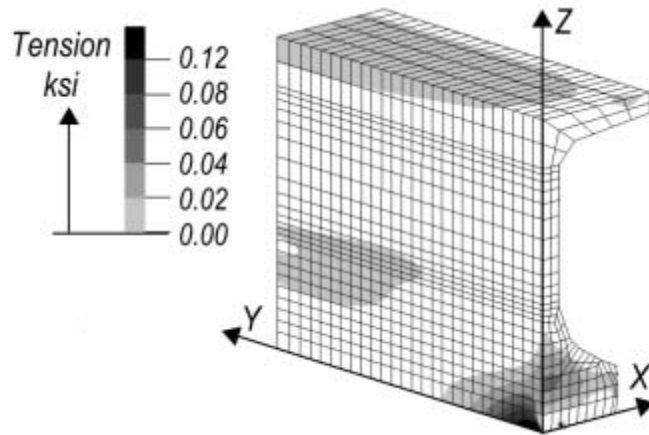


Figure 62–Transverse (x-x) stress due to self-weight

The typical integration procedure was used to calculate a transverse force of 6.7kip at the centerline. Self-weight reaction in the half-symmetry FE model was 12.0 kip. This reaction corresponded to a full reaction of 24 kip in the physical test girders. Thus the transverse force was equal to 28% of the physical reaction. This result is similar to the relationship derived between reaction force and transverse force shown in Figure 33.

Transverse stresses at the girder end were calculated at the same four lines (Figure 56) that were previously used to evaluate the effects of prestressing forces. Figure 63 shows stress that occurred at each line. Stresses below $Z=2\text{in.}$ are not shown because numerical errors occurred in the FE model near the boundary condition.

Maximum and average stresses at each line are summarized in Table 10. Average stresses in the table conservatively ignored compressive stresses below $Z=2\text{in.}$ The maximum tension stress was greatest at the centerline and was 3.4 times larger than at the line through the flange edge. The centerline section also had the largest average tension stress. At lines through the outer flange (MID and EDGE) the average stress was negligible or compressive. Average stresses at lines through the inner portion of the flange (CL and WEB) were tensile. Average tensile stresses at the CL and WEB lines were related to the reaction force by a factor of 1000. For example, the reaction force in the physical girders was 26 kip and the average tensile force on the inner lines was approximately 26 psi.

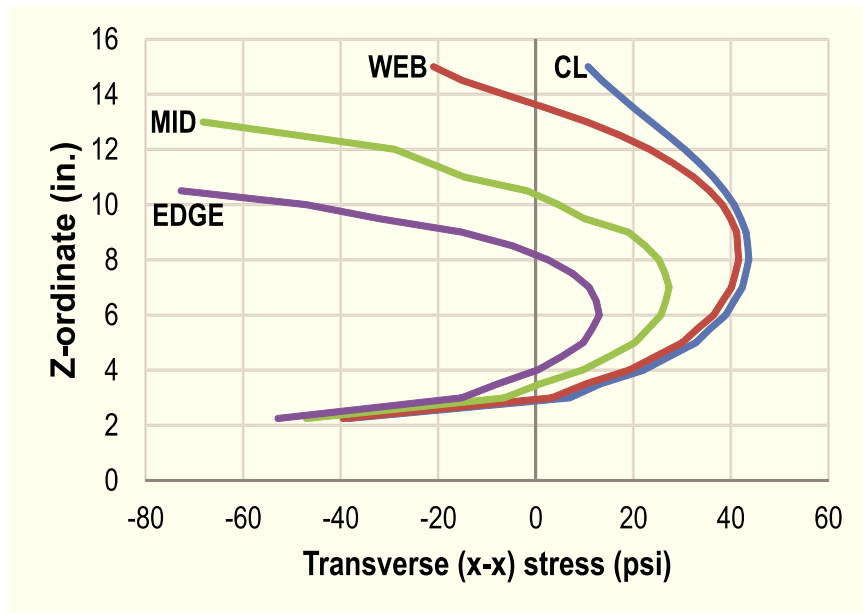
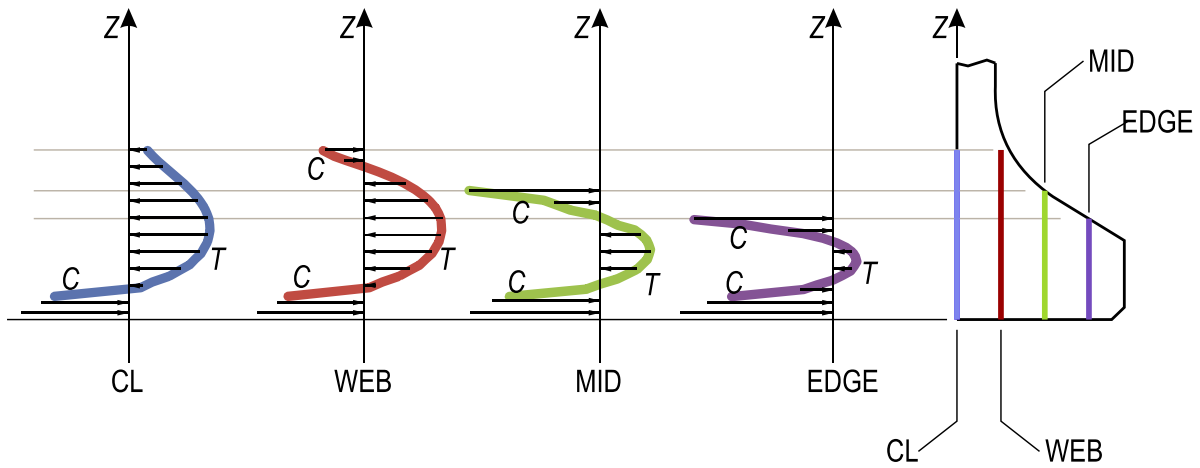


Figure 63–Transverse (x-x) stress due to self-weight

Table 10–Transverse (x-x) stress due to self-weight

	CL	WEB	MID	END
Maximum tension (psi)	44	42	27	13
Average stress (psi)	28	21	0.9	-10 (comp.)

2.5 Summary and Conclusions

Linear-elastic finite element modeling was used to evaluate stresses and forces in the bottom flange of Florida I-girders during prestress transfer. Each stage of prestress transfer (strand cutting) was considered in the models. Stresses and forces due to girder self-weight were also evaluated. Stresses due to the Hoyer effect were not considered in this chapter. Thus the conclusions below were based only on the effects of the prestress force and girder self-weight. Conclusions assumed strand cutting from outside-to-inside. The following conclusions were made based on results of the evaluations:

- For the given release sequence, the largest transverse (x-x) tensile stresses during prestress transfer occurred at the centerline of a section at the girder end. Centerline tension stresses were greatest when only the strands in the outer portion of the flange have been cut. Cutting of inner strands reduced this transverse tension.
- Embedded steel bearing plates carried transverse tension during and after prestress transfer. In the linear-elastic range plates in FIB girders carried 10% of the tension force due to prestressing. The portion carried by the plates does not vary during different stages of strand cutting.
- Transverse stress and forces were inversely proportional to strand transfer length. Thus the greatest transverse effects occurred in girders with the shortest transfer lengths. A 50% reduction in transfer length affected an approximately 50% increase in transverse tension.
- During prestress transfer the maximum transverse tensile stress on an arbitrary vertical line through the bottom flange occurred when only the strands outboard (closer to edge) of the line have been cut. Cutting of strands along or inboard (closer to centerline) of a line relieved tensile stresses on that line.
- Transverse stresses at the end of the bottom flange were compressive after all strands have been cut. An average compressive stress of 570 psi was calculated by the finite element models for conditions in experimental girders H and V.
- Self-weight reaction produced transverse tension forces in the bottom flange above the bearing. For Florida I-beams, the transverse tension force due to self-weight equaled 28% of the reaction.

Appendix G–End Region Design Models

Table of Contents

G.1	Confinement Reinforcement Design Model.....	502
G.1.1	Model Derivation.....	505
G.1.2	Model Comparison with Experimental Results.....	512
G.1.3	Ultimate Strength Design of Confinement Reinforcement	515
G.1.4	Summary and Conclusions	516
G.2	Serviceability Model	517
G.2.1	Causes of Bottom Flange Splitting at Prestress Transfer	517
G.2.2	Transverse Splitting Stress Model Derivation.....	521
G.2.3	Stress Calculations for Experimental Girders.....	536
G.2.4	Model Comparison with Experimental Crack Data.....	539
G.2.5	Summary and Conclusions	541

List of Figures

Figure 1–Local and general zones	504
Figure 2–Illustration of transverse and frictional forces caused by the Hoyer effect	504
Figure 3–Transverse tie force strut-and-tie models	505
Figure 4–Node layout	507
Figure 5–Strand anchorage force	509
Figure 6–Design model compared to nominal strength of experimental girders	513
Figure 7–Design model compared to experimental girders at maximum shear.....	515
Figure 8–Design model compared to experimental girders at maximum shear (external bearing plates considered)	515
Figure 9–Hoyer effect A) strand before stressing, B) strand after prestressing, C) concrete cast around strand, and D) stresses and forces after transfer.....	519
Figure 10–Flange tension due to outer strands	520
Figure 11–Camber due to prestress force	521
Figure 12–Self-weight reaction effects.....	521
Figure 13–Flange splitting in experimental girder.....	522
Figure 14–Strand cutting conditions.....	523
Figure 15–Strand physical analog (based on Oh et al. 2006)	524
Figure 16–Calculated radial stress (p) distribution (based on Oh et al. 2006).....	524
Figure 17–Effect of cover distance on calculated radial stress (p)	526
Figure 18–Concrete stress distribution due to Hoyer effect.....	527
Figure 19–Stresses at plane cut through strand and concrete	528
Figure 20–Bottom flange free body diagram.....	530
Figure 21–Analysis locations for determining F_{tos}	532
Figure 22–AASHTO girder FE model and analysis locations.....	533
Figure 23–Analysis sections for FIB bottom flange	536
Figure 24–Strand bond and shielding pattern specimen WN.....	536
Figure 25–Transverse (x-x) splitting stress at end of specimen WN.....	538
Figure 26–Calculated transverse splitting stress vs. experimental crack length.....	540
Figure 27–Calculated transverse splitting stress vs. experimental crack area	541

List of Tables

Table 1–Strand and concrete properties of experimental girders.....	527
Table 2–Model vs. FE for maximum peeling stress condition	532
Table 3–Model vs. FE for combined stress condition.....	532
Table 4–Model vs. FE for maximum peeling stress condition	533
Table 5–Model vs. FE for combined stress condition.....	534
Table 6–Hoyer stresses end of specimen WN	536
Table 7–Peeling stresses at end of specimen WN.....	537
Table 8–Transverse splitting stresses and splitting crack data.....	539

G.1 Confinement Reinforcement Design Model

The 2007 AASHTO LRFD Bridge Design Specifications contain prescriptive requirements for the quantity and placement of confinement reinforcement located in the bottom flange of pretensioned concrete I-girders. This chapter proposes a rational model that can be used to design confinement reinforcement as an alternative to the prescriptive requirements of AASHTO LRFD. The model considers a wide range of conditions and variations, yet is intended to be practical enough for use by bridge design engineers. Variables in the design model include: flange and bearing geometry, strand size and placement, effective prestress force, concrete and steel material properties, and the effects of steel bearing plates. Derivation of the model is presented, and the model is compared to experimental results from the published literature.

The proposed design model can be used to calculate the quantity of confinement reinforcement required to prevent lateral-splitting failure at ultimate load. The model is formulated to capture the multitude of variables that exist in pretensioned girders, but be practical enough for use by bridge designers. The model does not consider the function of confinement reinforcement in controlling cracks during prestress transfer. This topic, however, is covered in section G.2.

Experimental and analytical work from the previous chapters has shown that confinement reinforcement carries transverse tension forces due to prestressing and applied loads. By carrying these forces the confinement reinforcement functions to prevent lateral-splitting failure and provides a normal force whereby strand tension forces can be transferred to the concrete once strut-and-tie behavior has initiated. The ultimate strength design model considers both of these functions. Forces generated due to these functions are referred to as the transverse tie force (F_{TT}), and the strand anchorage force (F_{SA}).

Strand anchorage and transverse tie functions of confinement reinforcement are analogous to the local zone and general zone reinforcement in post-tensioned (PT) structures. Figure 1 shows the manner in which the anchorage zone in a post-tensioned (PT) structure is partitioned into local and general zones. The local zone is a highly stressed region that resides immediately under the anchorage device and requires significant confinement reinforcement to prevent bursting stresses from causing localized failure. It is within the local zone that PT forces

are transferred to the concrete. The general zone in a PT structure is the area where PT forces are transmitted throughout the member.

Conceptually the end region of a pretensioned beam can be divided into a local and general zone (Figure 1). General zone size is comparable to that of a PT anchorage and can be designed by the same approach as is used for PT anchorage zones. Pretensioned local zones, however, are longer because force transfer occurs gradually throughout the transfer length rather than through an anchorage device. Large, very localized lateral bursting stresses that are present immediately under the anchorage in a PT local zone are thus avoided in pretensioned end regions.

In pretensioned local zones the concrete immediately surrounding a prestressing strand is subjected to radial stresses from the Hoyer effect, which is illustrated in Figure 2. The Hoyer effect occurs due to Poisson expansion of the strands in the lateral direction when the strands are cut at prestress transfer. The beneficial effect of this expansion is to generate sufficiently large frictional forces at the concrete-strand interface to transfer the prestressing force into the concrete. As illustrated in Figure 1 this has been shown to occur in a relatively uniform manner over the transfer length.

Confinement reinforcement is typically placed such that some bars support loads from both local and general zones. Accordingly, confinement force due to the transverse tie is also utilized as the force required for strand anchorage. The proposed design procedure calculates the load demand on confinement reinforcement as the larger of the local and general zone loads. Or in other words, the model calculates confinement reinforcement required for the greater of the strand anchorage or transverse tie force.

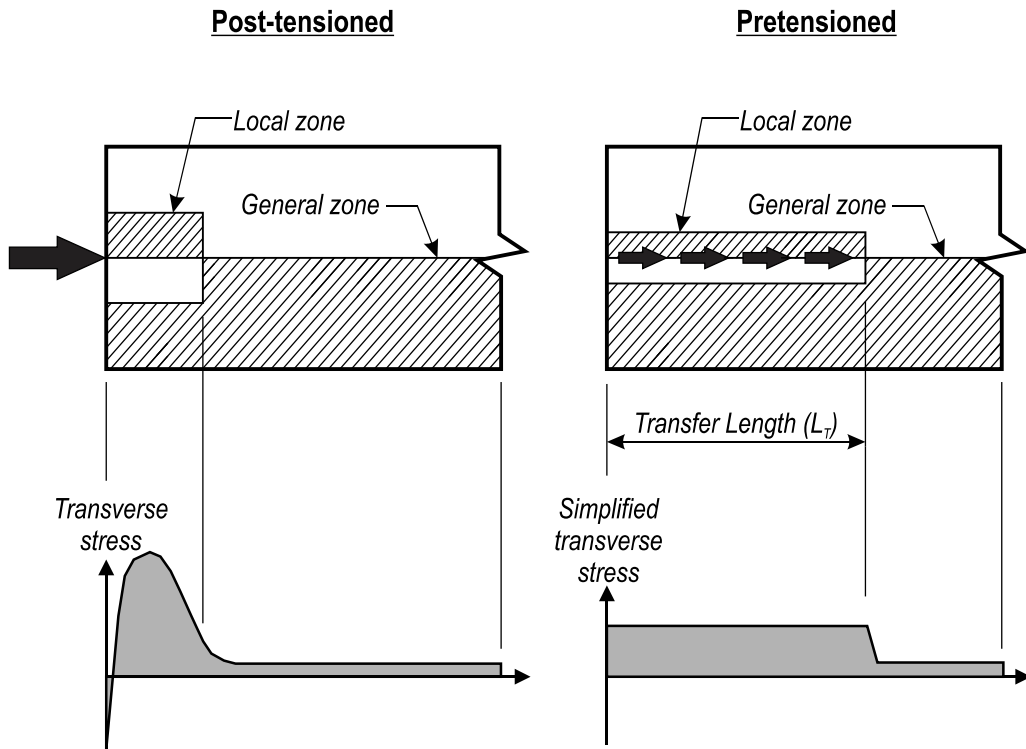


Figure 1—Local and general zones

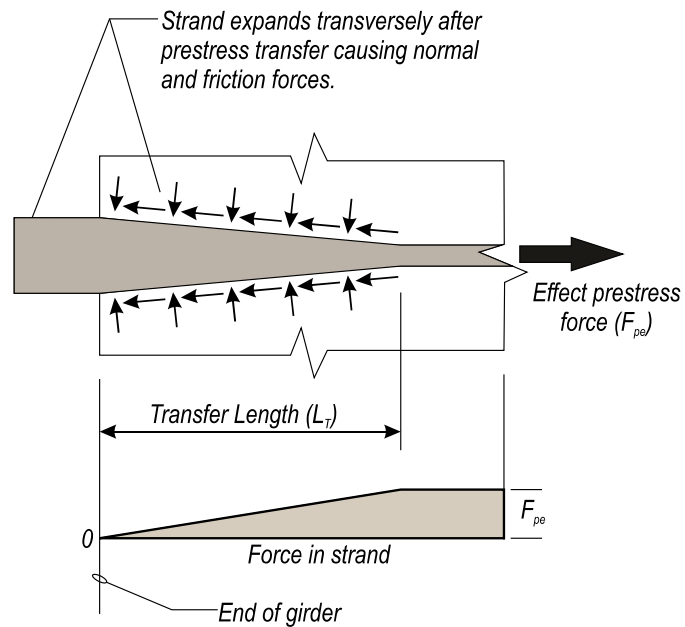


Figure 2—Illustration of transverse and frictional forces caused by the Hoyer effect

G.1.1 Model Derivation

G.1.1.1 Transverse Tie Force

Calculation of the transverse tie force is based on the strut-and-tie models shown in Figure 3. This figure describes transfer of the ultimate reaction (R_u) from the web, through the bottom flange and into the bearing pad. The struts and ties are symmetric about the z (vertical) axis.

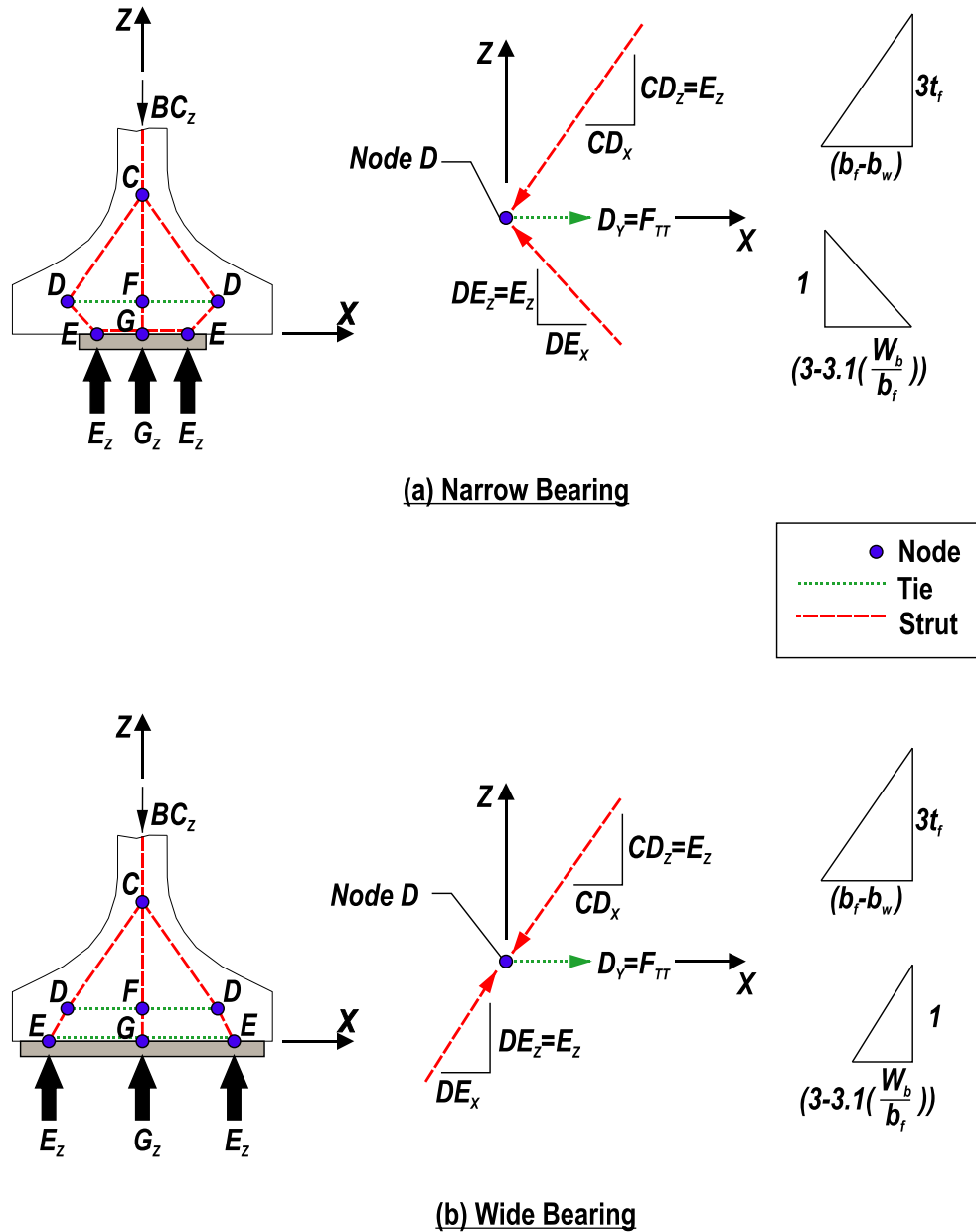


Figure 3–Transverse tie force strut-and-tie models

Compressive force BC_Z equals the ultimate reaction and is carried to the support through three separate load paths. Force in each path is assumed to be proportional to the quantity of strands associated with that path; strands in the flange are assumed to connect to D nodes and strands below the web are assumed to connect to node F . Thus the vertical (z-direction) component of load traveling path $C-D-E$ can be calculated by Equation 1-1:

$$CD_Z = DE_Z = E_Z = R_u \left(\frac{n_f}{n_{strand}} \right) \quad 1-1$$

Where:

$CD_Z =$ z-component of force in member CD

$DE_Z =$ z-component of force in member DE

$E_Z =$ Reaction at node E

$R_u =$ Factored reaction force

$n_f =$ number of strands in the flange

Using the strut and tie model shown in Figure 4a the slope of strut CD can be determined as follows:

$$Slope_{CD} = \frac{3t_f}{(b_f - b_w)} \quad 1-2$$

Where:

$t_f =$ Minimum thickness of bottom flange

$b_f =$ Bottom flange width

$b_w =$ Web width

Cross-sections from AASHTO, FDOT, Nebraska Department of Roads, and Washington State Department of Transportation were used to determine Equation 1-2. If exceptionally slender bottom flanges such as that shown in Figure 4b are used, then Equation 1-2 does not apply and the angle must be calculated directly.

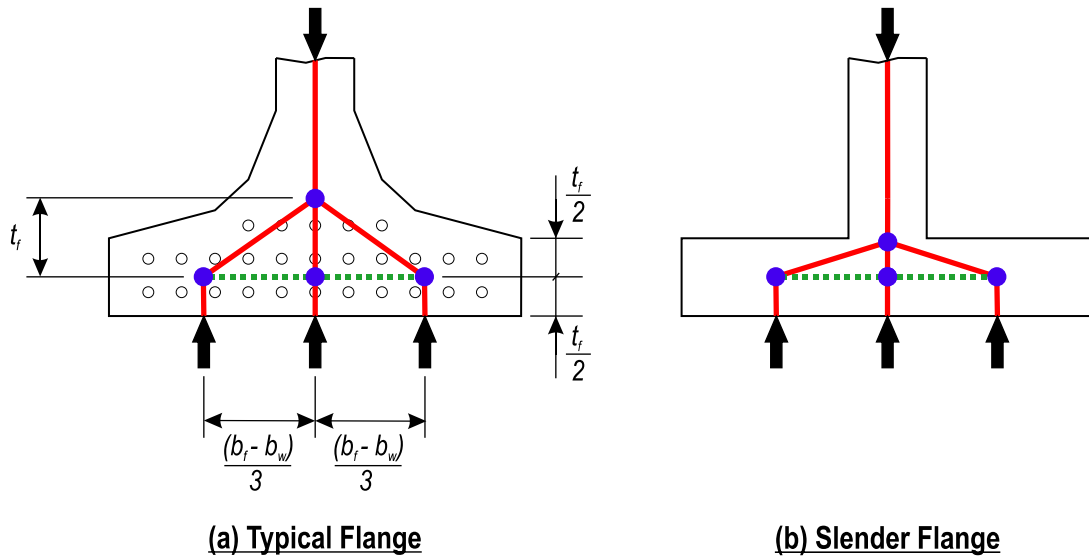


Figure 4–Node layout

Member DE slope can be calculated by Equation 1-3. When the bearing width is close to the flange width (Figure 3a), the slope calculated by Equation 1-3 is positive indicating that x-component of force in member DE acts in the positive x-direction. When the bearing width is smaller than the flange width (Figure 3b), the slope of member DE is negative, indicating that the x-component acts in the negative direction.

$$Slope_{DE} = \frac{1}{\left(3.1 \left(\frac{W_b}{b_f}\right) - 3\right)} \quad 1-3$$

Where:

$W_b =$ Width of bearing

The horizontal (x-direction) force components in members CD and DE are calculated by Equations 1-4 and 1-5, respectively. These equations are derived from the vertical (z-direction) force component from Equation 1-1 and the slopes from Equations 1-2 and 1-3.

$$CD_x = R_u \left(\frac{n_f}{n_{strands}}\right) \left(\frac{(b_f - b_w)}{3t_f}\right) \quad 1-4$$

$$DE_x = R_u \left(\frac{n_f}{n_{strands}}\right) \left(3.1 \left(\frac{W_b}{b_f}\right) - 3\right) \quad 1-5$$

The transverse tie force is equal to the force in member DF , and can be calculated from equilibrium in the x -direction at node D :

$$F_{TTu} = CD_X - DE_X \quad 1-6$$

Substituting for CD_X and DE_X and simplifying, Equation 1-6 can be rewritten as:

$$F_{TTu} = R_u \left(\frac{n_f}{n_{strands}} \right) \left[\frac{(b_f - b_w)}{3t_f} - 3.1 \left(\frac{W_b}{b_f} \right) + 3 \right] \quad 1-7$$

G.1.1.2 Strand Anchorage Force

Strand anchorage force refers to the normal force required to generate strand forces through friction. This force must be resisted by the concrete tensile strength, the confinement reinforcement, or both to ensure that the frictional force transfer between strands and concrete is maintained. If the concrete tensile strength and confinement are not sufficient bond is lost and the strand slips.

In addition to friction, force transfer between strands and concrete also occurs due to adhesion, mechanical interlock. Adhesion and mechanical interlock, however, are relatively small and are conservatively neglected. Also, it is thought unlikely that adhesion and mechanical interlock are significant at ultimate load after concrete around the strands has cracked.

At ultimate load it is assumed that internal forces in the end region can be described by strut-and-tie modeling as was done in calculating the transverse tie force. Strut-and-tie models conservatively neglect concrete tensile strength. This assumption will also be made in calculation of the strand anchorage force. Concrete around the strands will be assumed to have cracked and not be available to provide the normal force required to generate friction at the strand-concrete interface. In calculating the strand anchorage force, it is assumed that all of the normal force is supplied by confinement reinforcement.

Aknoukh (2010) presented a similar friction-based approach for designing confinement reinforcement. The Aknoukh model considered strand anchorage through on a horizontal section using a friction coefficient of 1.4. The proposed method is distinct from Aknoukh because it considers anchorage forces on vertical sections through the bottom flange, and because it uses a more conservative (and realistic) friction coefficient of 0.4. The proposed model is also distinct in that transverse tie forces are considered.

Equilibrium in the direction of the strand length requires that the total frictional force at the strand-concrete interface be equal and opposite of the effective prestress in the strand. The normal force required to generate the frictional force is equal to the frictional force divided by the friction coefficient at the strand-concrete interface. Based on this rationale, the normal force required to develop the effective prestress in an individual strand can be calculated by Equation 1-8:

$$F_N = \frac{A_{ps} f_{pe}}{\mu} \quad 1-8$$

Where:

- $F_N =$ Normal force on an individual strand required to develop prestress
- $A_{ps} =$ Cross-sectional area of prestressing strands
- $f_{pe} =$ Effective prestress
- $\mu =$ Coefficient of friction between concrete and strand, taken as 0.4

Although seven-wire strand does not have a circular cross section, it is believed that this simplification does not significantly affect the results of the strand anchorage force model. The same assumption was made by Oh et al (2006) in the development of a strand transfer length model. Using this assumption the Oh model correlated well with experimental data. The round strand assumption is also considered reasonable for the current model derivation.

Figure 5 illustrates the idealized normal stress acting on a single strand within the transfer length. The normal stress (f_N) can be calculated by assuming that the normal force (F_N) required to prevent strand slip is distributed evenly around the circumference and along the transfer length.

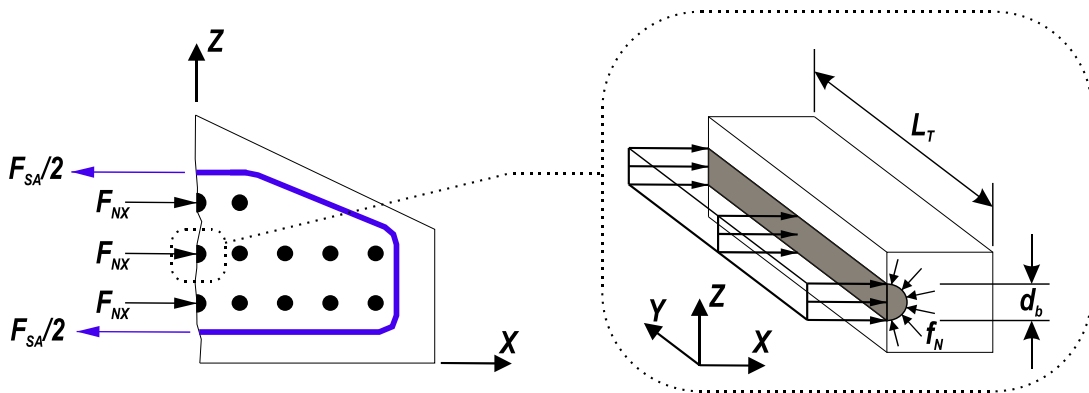


Figure 5–Strand anchorage force

The geometric properties of the strand can then be used to form equation 1-9:

$$f_N = \frac{F_N}{d_p L_T \pi} \quad 1-9$$

Where:

$$f_N = \text{Normal stress at strand-concrete interface}$$

$$d_p = \text{Diameter of prestressing strand}$$

Substituting Equation 1-8 into Equation 1-9 into gives:

$$f_N = \frac{A_{ps} f_{pe}}{d_p L_T \pi \mu} \quad 1-10$$

The transverse (x-direction) component of the normal force on an individual strand can be calculated using a pressure vessel analogy by multiplying the stress in Equation 1-10 by the projected area of the strand over the transfer length:

$$F_{Nx} = f_N d_p L_T \quad 1-11$$

Where:

$$F_{Nx} = \text{Transverse normal force on an individual strand}$$

Substituting Equation 1-10 into Equation 1-11 and simplifying gives:

$$F_{Nx} = \frac{A_{ps} f_{pe}}{\pi \mu} \quad 1-12$$

The total x-direction force along an arbitrary section can be determined from the product of the transverse component and the number of strands along the section. This force is defined as the strand anchorage force and is given as:

$$F_{SA} = F_{Nx} n_c = \frac{A_{ps} f_{pe} n_c}{\pi \mu} \quad 1-13$$

Where:

$$F_{SA} = \text{Strand anchorage force}$$

$$n_c = \text{Number of strands along critical section}$$

Equation 1-13 can be used to calculate the strand anchorage force on any arbitrary section. The maximum strand anchorage force occurs through the section that intersects the maximum number of strands.

G.1.1.3 Quantity and Placement

Preceding sections have presented equations for calculating the transverse forces resisted by confinement reinforcement at ultimate load. The design force in the confinement reinforcement is equal to the greater of the transverse tie or strand anchorage forces:

$$F_{CRu} = \text{maximum } (F_{SA}, F_{TTu}) \quad 1-14$$

Where:

F_{CRu} = Factored design force in confinement reinforcement

The reason for using the greater for the transverse tie or strand anchorage forces can be understood by considering the forces acting on a node in the bottom flange strut-and-tie model. For example, forces acting on node D in Figure 3 come from struts in the concrete and ties in the reinforcement. In deriving the transverse tie force it was shown that the forces at node D are based on equilibrium and geometric properties. The same forces acting on node D are also the forces that generate the strand forces (acting in the y-direction at node D) through friction. Additional strand anchorage force is not required. Thus confinement reinforcement capacity need only be the greater of the strand anchorage force or the transverse tie force.

The quantity of confinement required at ultimate load is equal to the confinement reinforcement design load divided by the specified yield stress of the reinforcement:

$$A_{CR} = \frac{(F_{CRu})}{f_{yCR}} \quad 1-15$$

Where:

A_{CR} = Required area of confinement reinforcement

f_{yCR} = Yield stress of confinement reinforcement

Data from the experimental program demonstrate that steel bearing plates contribute confinement to the bottom flange at ultimate load. To account for this, the proposed design model allows the bearing plate to replace up to 50% of the confinement required by Equation 1-15. The plate is not allowed to totally replace confinement reinforcement because the confining influence of the plate on its own was not enough to prevent lateral-splitting failure in

experiments. Bearing plates should not be considered as confinement reinforcement unless the bearing width and the spacing between plate anchorage points are *both* greater than 75% of the flange width. These requirements ensure that the bearing plate is in tension (Figure 3b), and is sufficiently anchored to provided confinement.

The confining effect of end diaphragms has also been shown to prevent splitting failures in experimental tests (Ross et al. 2011). End diaphragms, however, are not present during prestress transfer and therefore do not constitute a replacement for confinement reinforcement.

Results from the experimental program demonstrate that confinement reinforcement is most effective when placed near the end of the girder. As such, confinement reinforcement required by Equation 1-15 should be placed as close to the end of the girder as reasonable, but should also be placed over a distance of at least the transfer length.

G.1.2 Model Comparison with Experimental Results

In this section the proposed design model is evaluated against experimental data from 41 unique tests of pretensioned concrete girders reported in the literature (Appendix B, Appendix D, Llanos et al. 2009, Morcous et al. 2010, Tadros et al 2010, Deatherage et al 1994). Figure 6 compares confinement reinforcement installed in each test girder with the required confinement reinforcement calculated using the proposed model (Equation 1-15). The factored reaction force used to calculate the transverse tie force (F_{TT}) was taken as the nominal shear strength. Provided confinement reinforcement, plotted on the vertical axis, was taken as the area of confinement reinforcement placed within the transfer length. If present, the embedded steel bearing plate area was allowed to contribute up to 50% of the confinement requirement. Prestress losses were assumed to be 20 percent.

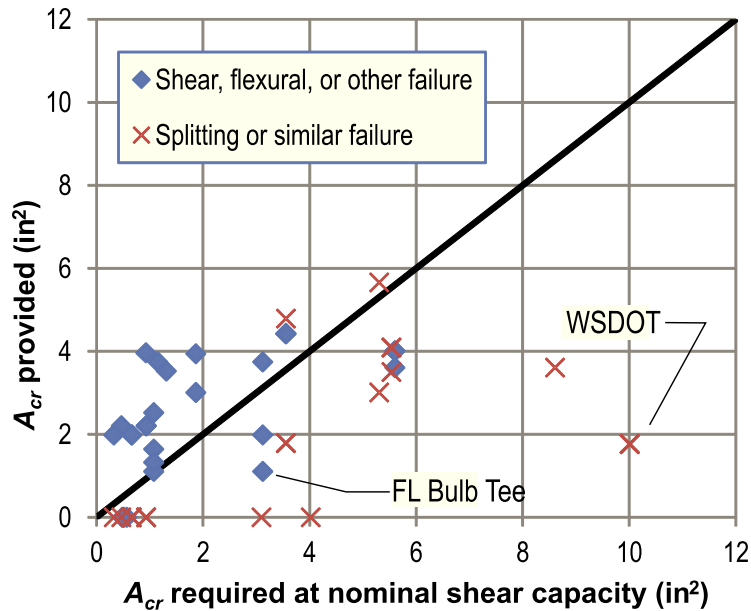


Figure 6–Design model compared to nominal strength of experimental girders

Points that fall below the solid line have less confinement than calculated by the model, and are predicted to fail due to splitting or lateral-bursting. The proposed model correctly identified all but two of the specimens that failed in lateral-splitting, bearing, or similar modes. Splitting and similar failures are denoted by the ‘X’ markers. The model incorrectly predicted failure in eight cases, as denoted by the diamond shaped markers that fall below the solid line. In most cases where the failure mode was not accurately predicted, the provided confinement reinforcement was within 1.5 in² of the calculated requirement, indicating a desirable degree of conservatism in the model.

The point marked “FL Bulb Tee” on Figure 6 shows the greatest level of disagreement with the proposed model. This data point represents a Florida Bulb Tee section (Tadros et al. 2010), which had only 35% of the calculated confinement reinforcement, but still did not fail due to lateral-splitting. Shear reinforcement in this specimen terminated in a hook at the bottom of the beam. Hook tails were placed under the strands, were oriented transverse to the axis of the beam, and extended to the edge of the bottom flange. Additional splitting resistance demonstrated by the specimen is attributed in-part to the confinement provided by these hook tails. Confining effects from hooks are neglected in the proposed model due to inadequate hook development. The Florida Bulb Tee was supported on a steel plate during testing. Splitting resistance of the specimen is also attributed to frictional force between the girder and plate.

Friction force at the bearing is thought to have had a greater impact on the bottom flange confinement than the hook tails from the vertical reinforcement.

The point label “WSDOT” on Figure 6 represents four tests of Washington wide flange girders (Tadros et al. 2010); each girder had identical calculated and provided confinement reinforcement. Numerous strands were located in the outer portion of the slender bottom flanges. During prestress transfer, it was observed that splitting cracks formed in the bottom flanges. Although not explicitly identified in the research, photographs of the failed beams suggest that lateral-splitting action occurred during testing.

The ultimate strength design model was also compared to the experimental data pool using the maximum shear force. For each data point, the maximum shear force reported in the literature was substituted into the model in lieu of the factored reaction force. As with the comparison at nominal shear capacity, the model also compares well with the maximum experimental shear forces (Figure 7). Points on the figure labeled “FL Bulb Tee” and “PC Bulb Tee” did not exhibit splitting failure in spite of having less confinement than calculated by the model. As with the FL Bulb Tee section discussed in Figure 6, the indicated specimens in Figure 7 were also supported on steel plates during testing. These plates were not embedded plates and were not considered in the model calculations; however they are thought to have provided additional splitting resistance to the FL and PC Bulb Tee specimens. This result indicates that the model may be conservative for girders that are supported on rigid surfaces such as steel plates or concrete bent caps.

Figure 8 shows the data set if the external steel bearing plates used in the tests were considered to provide confinement similar to embedded steel bearing plates. The external steel bearing plates were only considered if they were wide enough to provide confinement (Figure 3b). External steel bearing plates were not considered in specimens that also had embedded plates. Accuracy of the model in categorizing failure model improved when the external bearing plates were considered. All but one of the incorrectly categorized results was within 0.5 in^2 of the solid black line that denotes the border between failure modes.

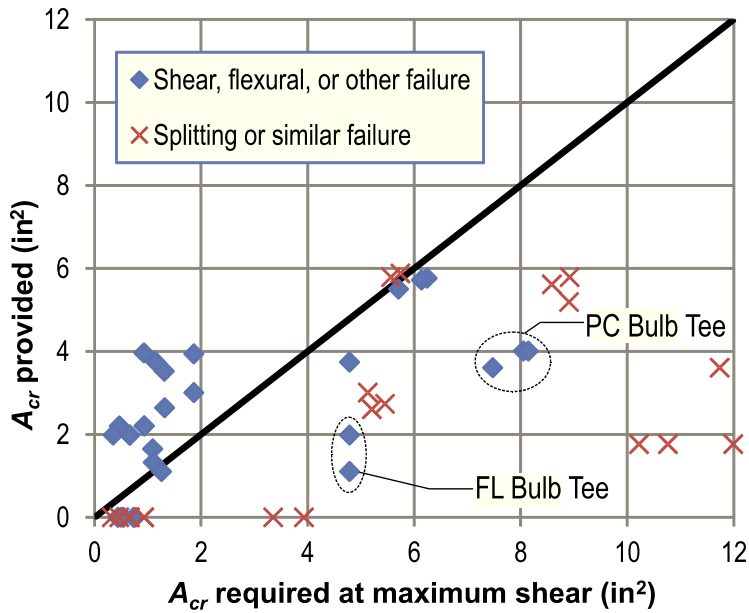


Figure 7–Design model compared to experimental girders at maximum shear

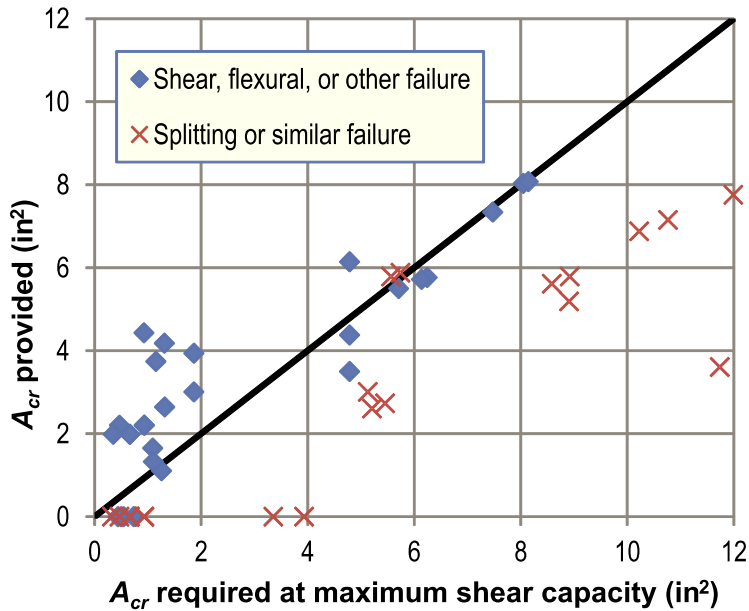


Figure 8–Design model compared to experimental girders at maximum shear (external bearing plates considered)

G.1.3 Ultimate Strength Design of Confinement Reinforcement

The ultimate strength model derived previously can be used for LRFD design using 1-16:

$$\phi A_{CR} f_{yCR} = F_{CRu} \quad 1-16$$

Where:

$A_{CR} =$	Required area of confinement reinforcement
$f_{yCR} =$	Yield stress of confinement reinforcement
$\phi =$	Resistance factor

The required area of confinement reinforcement is such that the confinement reinforcement must provide a design strength greater than the force generated by the strand anchorage or the transverse tie. The resistance factor should be determined using the LRFD reliability analysis of the limit states. In lieu of this it is reasonable to treat this reinforcement the same as tension steel in an anchorage zone ($\phi = 1.0$).

G.1.4 Summary and Conclusions

A rational design model was developed for designing confinement reinforcement at ultimate strength. The model considers strand anchorage and transverse tie requirements, which are analogous to local and general zone requirements in post-tensioned concrete members. The ultimate strength model was compared to 41 unique tests of pretensioned concrete girders reported in the literature. The model was found to have good agreement with the published test results. The model is recommended for the design of confinement reinforcement and bearing plates at ultimate load.

G.2 Serviceability Model

Experimental and analytical research presented in previous Appendices demonstrates that transverse tensile stress in the bottom flange of pretensioned I-girders can lead to flange splitting cracks during fabrication. It is believed that the following behaviors contribute to tensile stress and flange cracking:

- Hoyer effect
- Eccentric prestress forces
- Self-weight reaction

Flange splitting cracks can reduce the durability of concrete I-girders by allowing contaminants to enter the bottom flange and initiate corrosion of prestressing steel or chemical attack on the interior concrete. A serviceability design model is presented in this chapter for quantifying bottom flange splitting stress. The model is derived from a variety of sources including the work of other researchers, finite element modeling, and basic mechanics. Stress from the model can be compared to concrete tensile capacity to determine the likelihood of bottom flange splitting cracks.

Experimental and analytical research indicates that the largest transverse tensile stresses in the bottom flange occur at the member end. The majority of flange-splitting cracks in the experimental girders were located at or close to the specimen ends. Accordingly, the serviceability model provides equations for calculating the worst-case transverse tensile stress occurring at member ends. Calculated stresses at the member end can be compared to concrete tensile strength criteria to evaluate the likelihood of flange splitting cracks. Possible strength criteria are discussed later in this chapter.

In the final section of this chapter, experimental cracks data are compared to stresses calculated from the proposed model. The model and data are found to have a high degree of correlation.

G.2.1 Causes of Bottom Flange Splitting at Prestress Transfer

Flange splitting cracks in the bottom flange are caused by transverse splitting stresses that occur due to a combination of the Hoyer effect, eccentric prestress forces, and the self-weight reaction. The following sections describe the mechanics associated with each of these effects.

G.2.1.1 Hoyer Effect

The diameter of a prestressing strand decreases during pretensioning due to the Poisson effect (Figure 9a and b). When tension is released during prestress transfer the strands expand towards their original diameter. Expansion is partially restrained by the surrounding concrete resulting in normal stresses and proportional frictional forces at the strand-concrete interface. This behavior was named for Ewald Hoyer, the German Engineer who first wrote of radial expansion of prestressing strands (Hoyer 1939).

Expansion of prestressing strands is greatest at the edge of the concrete where strand tension is zero after prestress transfer (Figure 9d). At locations beyond the transfer length the strand expansion is negligible because strand tension is nearly the same before and after release. Change in radial expansion is approximately linear between the concrete edge and the end of the transfer length (Oh et al. 2006). Consequently, radial and annular stresses in the concrete also vary linearly along the transfer length.

Variable expansion of the strands leads to a wedge-like shape after prestress transfer. This shape creates mechanical bond between strand and concrete. Additional bond improvement comes from the radial stresses at the interface, which allow the generation of frictional forces. Wedge action and frictional forces are thus beneficial consequences of the Hoyer effect because they enable the transfer of prestress forces. The Hoyer effect can also have detrimental consequences on the behavior and capacity of pretensioned girders. Concrete surrounding strands cracks when stresses due in-part to the Hoyer effect exceed concrete tensile capacity.

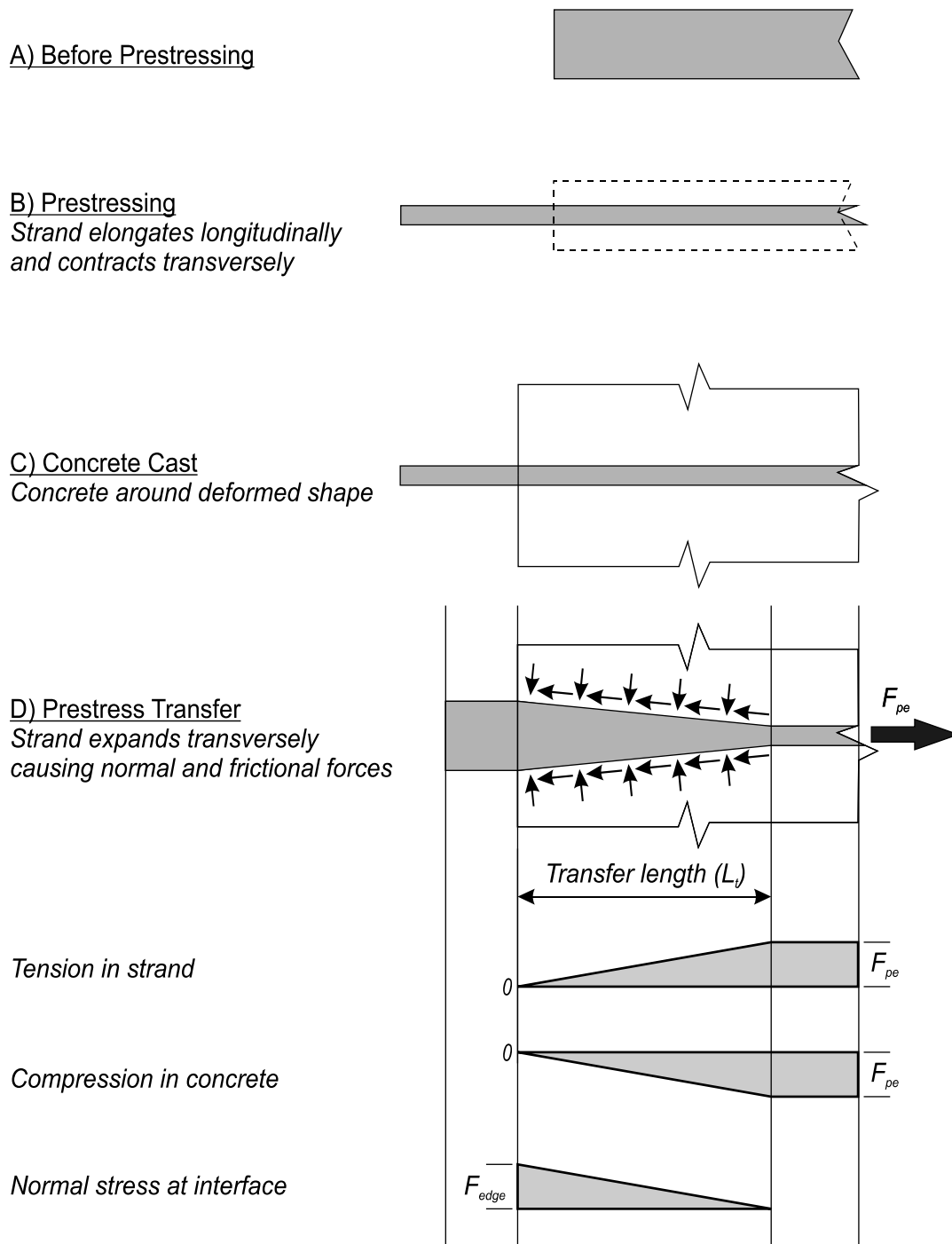


Figure 9–Hoyer effect A) strand before stressing, B) strand after prestressing, C) concrete cast around strand, and D) stresses and forces after transfer

G.2.1.2 Eccentric Prestress Forces

Tension forms in the bottom flange as prestressing forces from the outer strands are transferred to the concrete (Figure 10). This tension forms in response to the eccentricity

between prestressing forces from outer strands and the equal and opposite resultant force in the member. Tension is partially relieved as inner strands are released. This process has been demonstrated experimentally and analytically in previous chapters and is dependent on the strand bond pattern and strand cutting pattern. Tension stress due to eccentric prestress forces is referred to as “peeling” stress because they act to peel the outer portion of the bottom flange away from the web. Strands in the experimental program and in analytical models were cut from the outside-in. This detensioning pattern is assumed in the equations derived in this chapter.

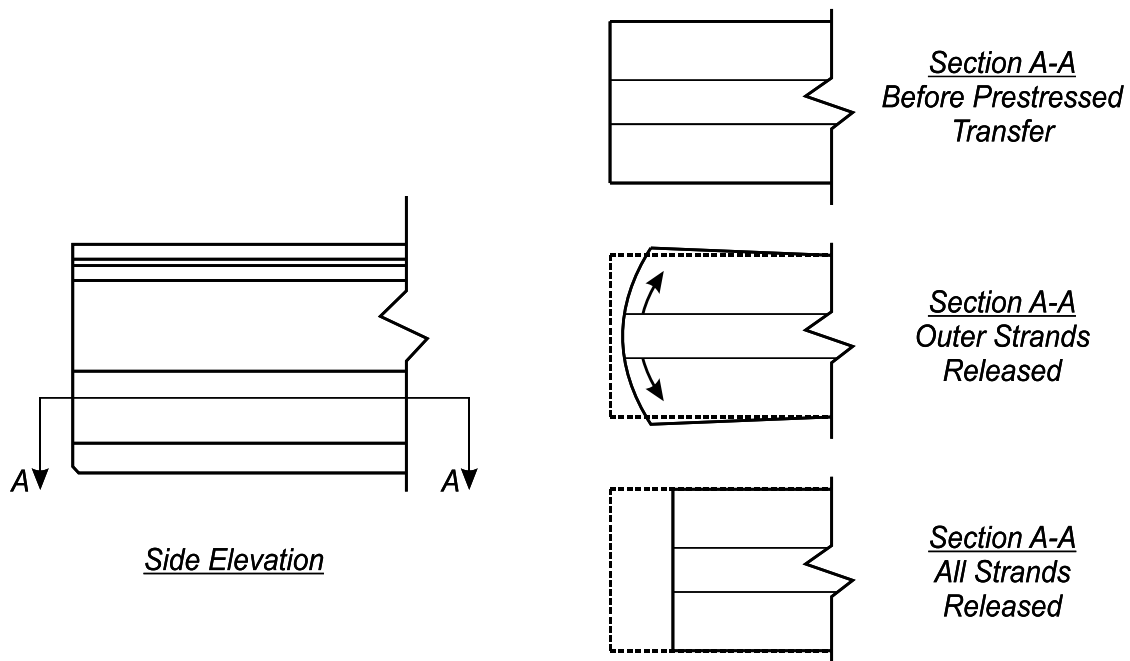


Figure 10–Flange tension due to outer strands

G.2.1.3 Self-Weight Reaction

Girders camber upward during prestress transfer after the prestressing moment exceeds the self-weight moment (Figure 11). After cambering, girders are supported by reactions at each end. Tensile stresses form in the bottom flange above the reaction points due to the flange bending illustrated in Figure 12.

Previous FE analyses show that self-weight reactions produce tensile and compressive transverse stresses in the FIB bottom flange (See Appendix F). Analysis also demonstrate that self-weight reaction stresses are small relative to peeling stresses, and that average stress on sections through the outer flange is near zero or slightly compressive. Because of this, self-

weight reaction stresses on sections through the outer portion of the FIB bottom flange are conservatively neglected in the proposed serviceability model. This assumption may not be reasonable for other cross-sections and for long-span FIB girders.

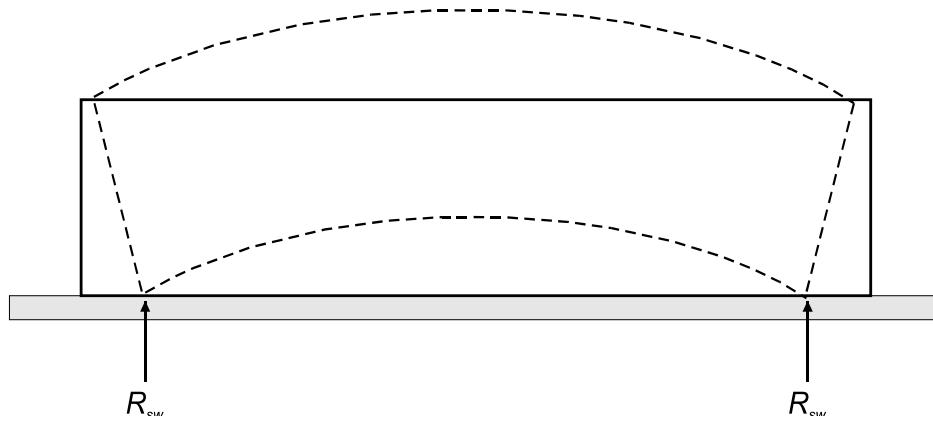


Figure 11–Camber due to prestress force

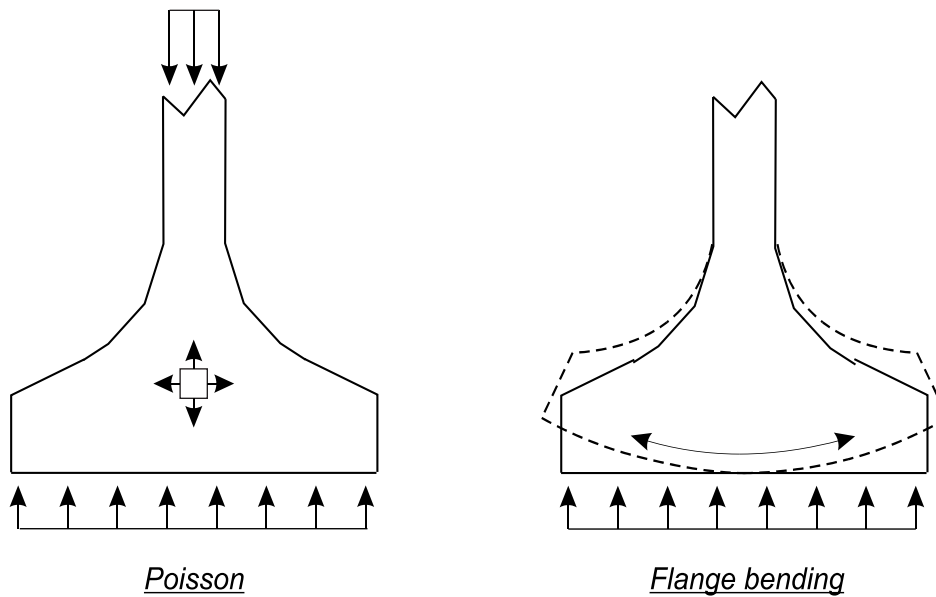


Figure 12–Self-weight reaction effects

G.2.2 Transverse Splitting Stress Model Derivation

Experimental results indicate that vertical splitting cracks can occur at multiple locations in the bottom flange (Figure 13). The proposed model focuses on splitting cracks through the

outer portion of the flange. Bottom flange splitting cracks below the web are not considered because they are associated with extreme strand bond patterns that are not permitted in FDOT production girders. Splitting cracks below the web were observed in the experimental program, but only in specimens with bonding patterns that placed fully bonded strands in the outer flange and shielded strands below the web.

An outside-in cut pattern is commonly used in FDOT production girders. As such, the serviceability model assumes an outside-in cut pattern. This pattern was used in construction of the experimental girders, as well as the FE models used to develop the serviceability model. The model does not apply to girders with other cut patterns.

Two critical conditions are considered in the design model:

- **Maximum Peeling.** Previous experimental and analytical research show that the maximum peeling stress along a given section occurs when only the outboard (closer to the outside edge) strands are cut (Figure 14). This condition is referred to as the “maximum peeling” condition.
- **Combined.** This condition occurs when strands along a given section are cut and Hoyer stresses are superimposed with peeling stress. It is referred to as the “combined” condition.

The model does not consider stress conditions when inboard (closer to the centerline) strands have been cut. Previous analytical work shows that cutting of inboard strands reduces peeling stresses on a given section.



Figure 13–Flange splitting in experimental girder.

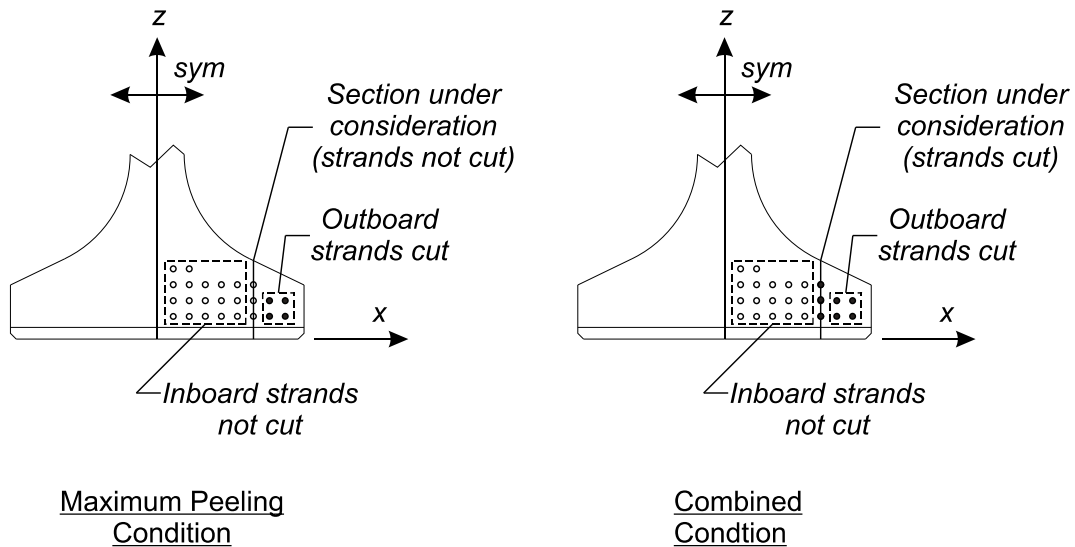


Figure 14–Strand cutting conditions

G.2.2.1 Hoyer Stress

Hoyer stress is calculated using a model developed by Oh et al. (2006). The Oh model is based on equilibrium, material constitutive properties, and strain compatibility. It assumes radial expansion of a steel cylinder surrounded by concrete (Figure 15). Equation 2-1 is for calculating radial stress at the steel-concrete interface. Figure 16 shows the radial stress distribution calculated from Equation 2-1 for a strand in the experimental girders. As described by the Hoyer effect, radial stress is greatest at the member end and reduces to near zero at the end of the transfer length.

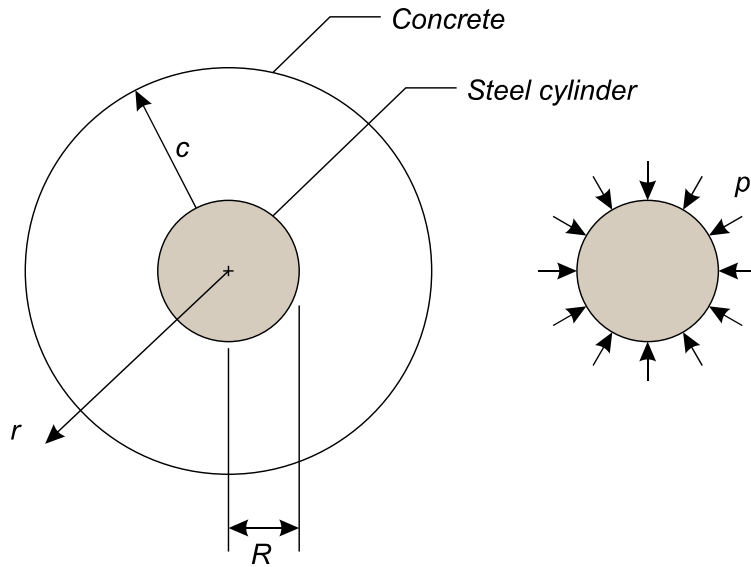


Figure 15–Strand physical analog (based on Oh et al. 2006)

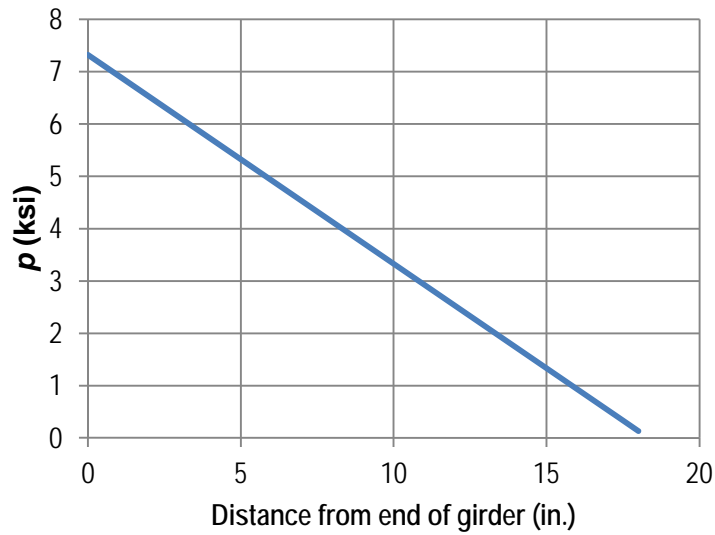


Figure 16–Calculated radial stress (p) distribution (based on Oh et al. 2006)

$$p = \frac{r_0(1 - \nu_p f_{pz}/E_p) - r_j(1 - \nu_c f_{cz}/E_c)}{(1 - \nu_p) r_0/E_p + [\nu_c - (r_j^2 + c^2)/(r_j^2 - c^2)] r_j/E_c} \quad 2-1$$

Where:

- p = Radial stress at strand-concrete interface
- r_o = Strand radius before pretensioning
- ν_p = Strand Poisson ratio
- f_{pz} = Axial stress in strand

- E_p = Strand Elastic Modulus
- r_j = Strand radius immediately after pretensioning
- ν_c = Concrete Poisson ratio
- f_{cz} = Concrete stress in direction parallel to strand
- E_c = Concrete Elastic Modulus
- c = Concrete cover distance

The equation above assumes linear-elastic behavior. Recognizing the possibility of concrete cracks forming near the strand, the Oh model also includes features to calculate the average stress in cracked concrete. Applying these features results in stresses that are smaller than those calculated by assuming linear-elastic behavior. Cracking features in the Oh model are neglected in the current model development. This approach allows superposition of Hoyer stresses with stresses derived from linear-elastic finite element modeling.

Stress calculated by Equation 2-1 is not sensitive to concrete cover (c) distance for cover values greater than approximately 10 times the strand diameter (Figure 17). By assuming that the cover distance is large relative to the strand diameter, the term $(r_j^2 + c^2)/(r_j^2 - c^2)$ in the denominator of Equation 2-1 approaches negative one, and Equation 11-1 can be simplified to:

$$p = \frac{r_0(1 - \nu_p f_{pz}/E_p) - r_j(1 - \nu_c f_{cz}/E_c)}{(1 - \nu_p) r_0/E_p + (\nu_c + 1)r_j/E_c} \quad 2-2$$

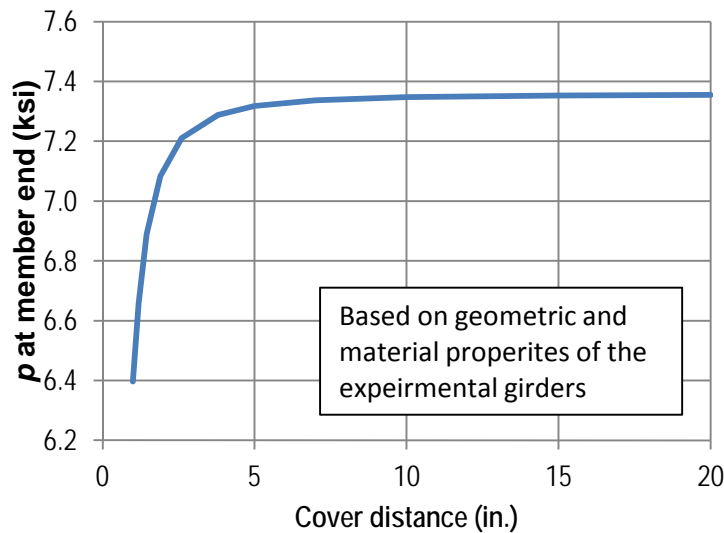


Figure 17–Effect of cover distance on calculated radial stress (p)

Assuming large concrete cover distance is conservative and results in slightly higher calculated stresses. For typical strand diameters and minimum cover dimensions, this assumption increases the calculated stress by less than 2%.

The serviceability model considers stresses at the girder end. At this location, strand expansion and the associated Hoyer stresses are at their maximum. Axial stress in the strand ($f_{pz} = 0$) and concrete ($f_{cz} = 0$) are equal to zero at the member end, which reduces Equation 2-2 to:

$$p_{edge} = \frac{r_0 - r_j}{(1 - \nu_p)r_0/E_p + (\nu_c + 1)r_j/E_c} \quad 2-3$$

Where:

p_{edge} = Radial stress at strand-concrete interface at end of member

Concrete circumferential stresses are a function of the interfacial stress, strand size, concrete cover, and distance from the strand. Oh et al. provide the following equation for calculating circumferential stresses:

$$\sigma_{\theta}(r) = \frac{-p(1/c^2 + 1/r^2)}{(1/c^2 + 1/R^2)} \quad 2-4$$

Where:

σ_{θ} = Radial stress at strand-concrete interface at end of member
 r = Ordinate in the radial direction
 R = Radius of prestressing strand

Figure 18 shows the concrete stress distribution calculated by Equations 2-3 and 2-4 for a single strand in the experimental girders. Values used to calculate the stress distribution are listed in Table 1. The maximum concrete stress is 7.35ksi and occurs adjacent to the strand. Stress decreases rapidly with increasing distance from the strand. At locations 2in. from the strand-concrete interface the stress is less than 0.125ksi.

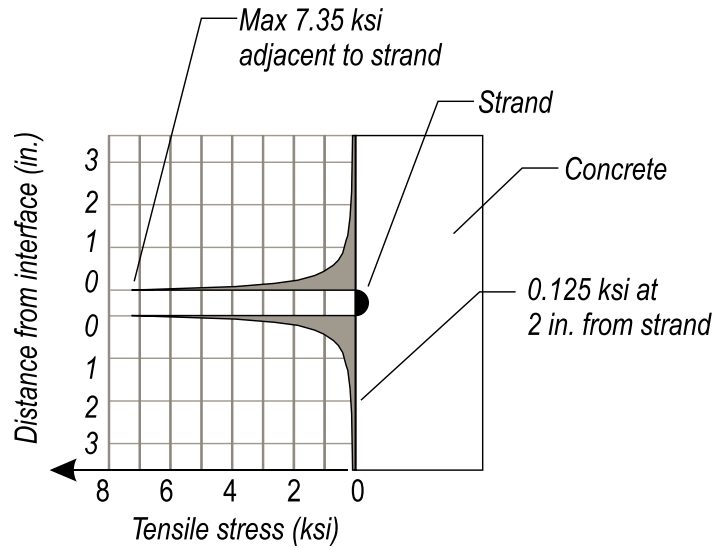


Figure 18–Concrete stress distribution due to Hoyer effect

Table 1–Strand and concrete properties of experimental girders

Concrete Elastic Modulus	4700 ksi
Concrete Poisson Ratio	0.2
Strand Elastic Modulus	29,000 ksi
Strand Poisson Ratio	0.3
Strand radius prior to jacking	0.3 in.
Strand radius after jacking	0.2994 in.

Large Hoyer stress adjacent to strand can cause local damage and cracking in the concrete. If tension through the flange is sufficient, then the localized cracking may propagate and form a crack through the entire flange. For this reason it is important to check the average stress due to the Hoyer effect through the flange thickness.

Rather than calculating average stress from the stress distribution described by Equation 2-4, average stress in the model is calculated indirectly using the interfacial stress. This is done to simplify the design model for design purposes and to avoid integration of concrete stress such as shown in Figure 18. Average stress calculated indirectly from the interfacial stress is the same as average stress calculated by integrating Equation 2-4.

Applying equilibrium to an idealized strand, the interface stress must equal the internal stress in the strand (Figure 19a). Equilibrium can also be applied along a section cut through the strand and concrete (Figure 19b) to show that the resultant force acting on the strand is equal and opposite the concrete force. This equilibrium condition is described by Equation 2-5.

$$\Sigma F_x = 0 = -pd_b d_y + f_{hs}(h_f - d_b)d_y \quad 2-5$$

Where:

- d_b = Strand diameter
- d_y = Differential length in y direction
- f_{hs} = Average Hoyer stress on the section from a single strand
- h_f = Thickness of flange at section under consideration

Rearranging Equation 2-5, average stress due to the Hoyer Effect can be described as:

$$f_{hs} = \frac{p d_b}{(h_f - d_b)} \quad 2-6$$

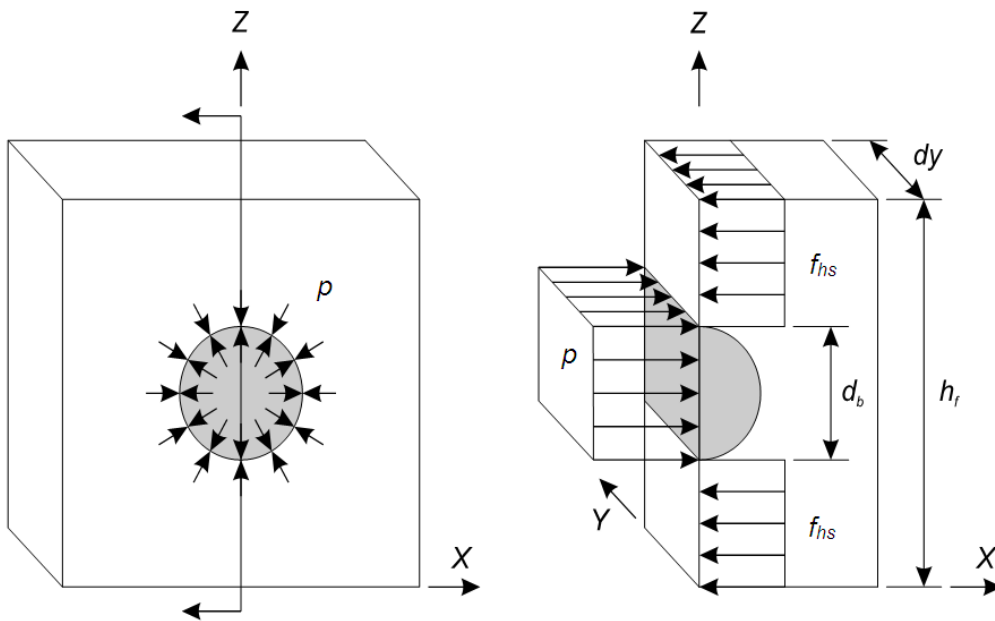


Figure 19–Stresses at plane cut through strand and concrete

The average Hoyer stress on a given line is a function of the quantity of strands on that line. For sections with multiple strands the average stress can be calculated by multiplying the stress from Equation 2-6 by the number of strands. Both shielded and bonded strands along a section displace the area of concrete that carries Hoyer stresses. The denominator in Equation 2-7 is adjusted to account for displaced concrete due to all strands:

$$f_h = \frac{n_s p d_b}{(h_f - n_{st} d_b)} \quad 2-7$$

Where:

- f_h = Average stress on the section due to Hoyer Effect
- n_s = Quantity of fully bonded strands on section under consideration
- n_{st} = Quantity of all strands on section under consideration

The serviceability model considers stress at the end of the member. At this location the interfacial stress between the strand and the concrete can be calculated using Equation 2-3. Substituting Equation 2-3 into Equation 2-7 results in Equation 2-8 for calculating the average Hoyer stress on a line through the bottom flange at the member end:

$$f_h = \frac{n_s d_b}{(h_f - n_{st} d_b)} \left[\frac{r_0 - r_j}{(1 - \nu_p) r_0 / E_p + (\nu_c + 1) r_j / E_c} \right] \quad 2-8$$

G.2.2.2 Peeling Stress

Peeling stress calculations are based on the free body diagram shown in Figure 20. This diagram is a simplified illustration of forces acting on the outer portion on a bottom flange during prestress transfer. Prestressing forces from the eccentric outer strands (F_{pos}) create a moment about the Z-axis. Moment equilibrium is maintained by x-direction tensile stresses in the concrete acting on the Y-Z cut plane. This equilibrium condition is described in equation 2-9:

$$\Sigma M_Z = 0 = F_{pos} x_p - F_{tos} l_y \quad 2-9$$

Where:

- F_{pos} = Prestressing force from strands outboard of cut plane
- x_p = Distance from cut plane to centroid of prestressing force
- F_{tos} = Transverse tension force acting on cut plane due to eccentric prestressing
- l_y = Internal moment arm in y-direction

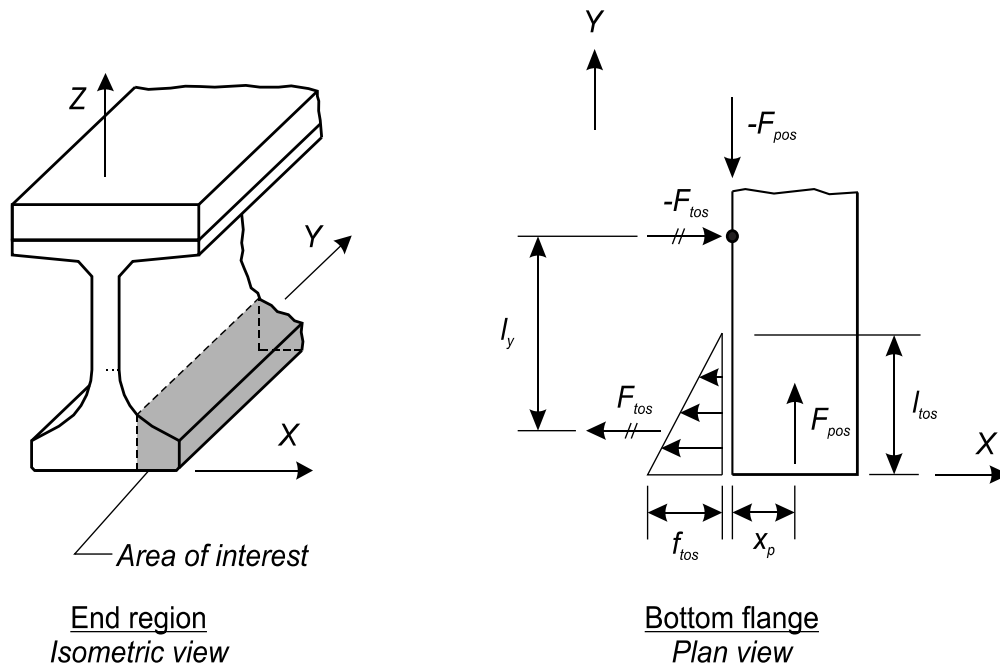


Figure 20–Bottom flange free body diagram

Rearranging Equation 2-9 results in the following equation for the transverse tension force due to the eccentric strands:

$$F_{tos} = \frac{F_{pos}x_p}{l_y} \tag{2-10}$$

Transverse tensile force in Equation 2-10 is the resultant of peeling stress in the concrete at the member end, which is assumed to have a triangular tensile stress distribution. Peeling stress is assumed to be largest at the member end and zero at a distance l_{tos} from the end (Figure 20). Previous FE modeling shows that a triangular stress distribution and a value of 10in. for l_{tos} are reasonable assumptions cross-sections with outer strands cut (See Appendix F). The following equation of equilibrium ensures that the resultant force from the assumed peeling stress distribution is equal the transverse tensile force:

$$F_{tos} = \frac{F_{pos}x_p}{l_y} = \frac{1}{2}f_{tos}l_{tos}h_f \tag{2-11}$$

Where:

f_{tos} = Peeling stress

l_{tos} = Length of the assumed tensile stress distribution

h_f = Thickness of the flange at the section under consideration

Equation 2-11 can be rearranged to solve for the peeling stress at the member end:

$$f_{tos} = \frac{2F_{pos}x_p}{l_y l_{tos} h_f} \quad 2-12$$

Strands along a given section displace the concrete area that carries peeling stress. The denominator in Equation 2-12 must be adjusted to account for the area displaced by shielded and bonded strands. Doing so results in:

$$f_{tos} = \frac{2F_{pos}x_p}{l_y l_{tos} (h_f - n_{st} d_b)} \quad 2-13$$

The term l_y in Equation 2-13 is the length of the internal moment arm in the y-direction. The value of l_y varies according to the quantity of cut strands, shape of the cross-section, and location within a given cross-section. Equation 2-14 and 2-15 are empirical equations for calculating l_y in FIB girders. These equations were found to give values of l_y -and consequently of F_{tos} - that are in agreement with previous FE results.

$$l_{y1} = 36 \frac{\sqrt{h_f}}{\sqrt{x}} \quad 2-14$$

$$l_{y2} = 53 \frac{h_f}{x} \quad 2-15$$

Where:

l_{y1} = Internal moment arm in the y-direction for maximum peeling condition

l_{y2} = Internal moment arm in the y-direction for combined condition

h_f = Thickness (z-dimension) of the flange at the section under consideration

x = x-ordinate of the section under consideration

Transverse forces calculated using Equation 2-13 and Equation 2-14 or Equation 2-15 are compared with previous FE results (see appendix F) in Table 2 and Table 3. Results are compared for the MID and EDGE sections (Figure 21), for the ‘design’ strand bond pattern used in the FIB-54 experimental program. Values from the model equations are within 1% of FE results for all but the combined condition at the MID section, for which the model is 7%

conservative. Consistency between the model and FE results indicates that Equations 2-14 and 2-15 are acceptable approximations for calculating l_y in FIB girders.

Table 2–Model vs. FE for maximum peeling stress condition

Section	h_f (in.)	x (in.)	l_{y1} (in.)	F_{tos} Model (kip)	F_{tos} FE (kip)	Model / FE
EDGE	10.5	12	46.4	11.4	11.3	1.01
MID	12.9	8	85.5	20.6	20.3	1.01

Table 3–Model vs. FE for combined stress condition

Section	h_f (in.)	x (in.)	l_{y2} (in.)	F_{tos} Model (kip)	F_{tos} FE (kip)	Model / FE
EDGE	10.5	12	33.7	15.7	15.9	0.99
MID	12.9	8	45.7	38.5	36.1	1.07

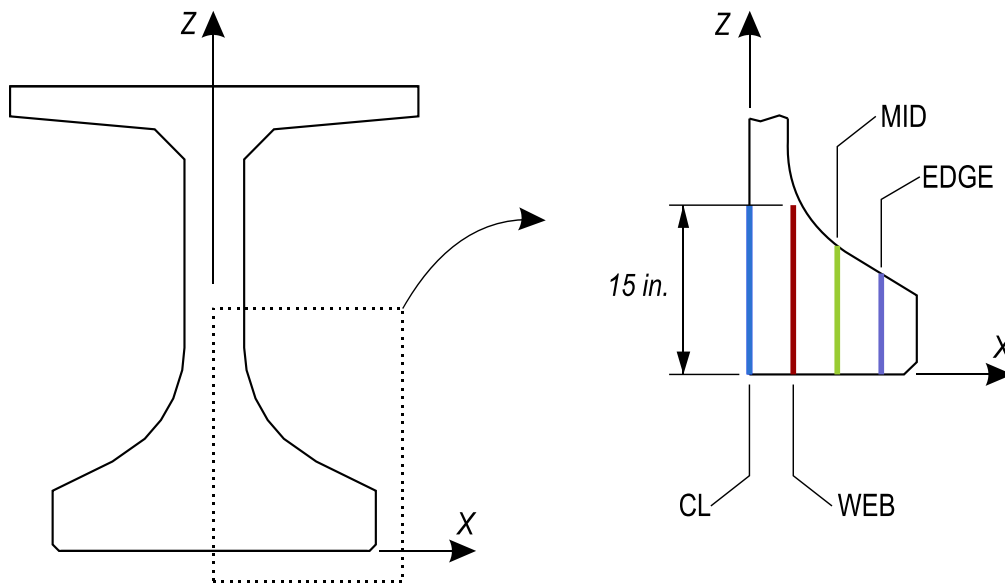


Figure 21–Analysis locations for determining F_{tos}

Equations 2-14 and 2-15 are empirically derived for FIB girders and are assumed reasonable for any girder with a similar flange aspect ratio. Different equations are needed for calculating l_y in girders with relatively stocky flanges, such as AASHTO girders. Equations 2-16 and 2-17 are for use with relatively stocky girders. These equations are empirically derived by comparison with previous FE results. Figure 22 shows the FE mesh, strand locations, and bottom flange sections used for the comparison. See appendix F for additional information on

the FE modeling. Transverse forces calculated using Equation 2-13 and Equations 2-16 or 2-17 are compared with FE results in Table 4 and Table 5. At the FLANGE section, the design model results in transverse forces that are within 1% of the FE results. The model is more conservative at the WEB section, resulting in values that are 7% to 9% larger than the FE model. Based on these favorable comparisons, Equations 2-16 and 2-17 are considered acceptable approximations for calculating l_y in AASHTO girders and other girders with stocky flanges.

$$l_{y1} = 19 \frac{h_f}{x} \tag{2-16}$$

$$l_{y2} = 1.85 \frac{h_f^2}{x} \tag{2-17}$$

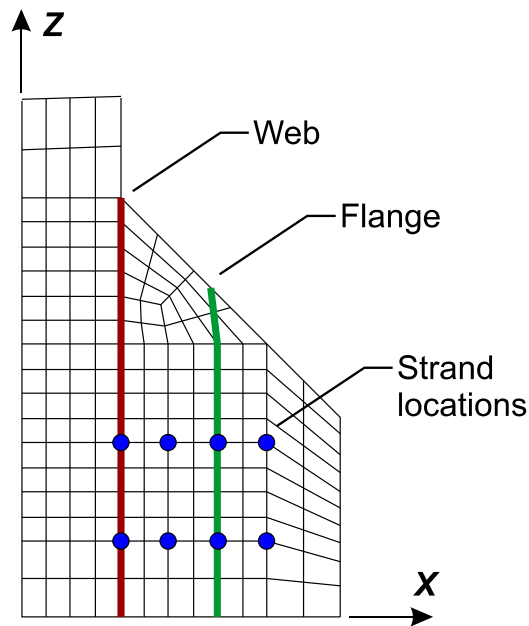


Figure 22–AASHTO girder FE model and analysis locations

Table 4–Model vs. FE for maximum peeling stress condition

Section	h_f (in.)	x (in.)	l_{y1} (in.)	F_{tos} Model (kip)	F_{tos} FE (kip)	Model / FE
WEB	17	4	80.8	12.4	11.4	1.09
FLANGE	12	8	28.5	5.0	5.9	1.00

Table 5–Model vs. FE for combined stress condition

Section	h_f (in.)	x (in.)	l_{y2} (in.)	F_{tos} Model (kip)	F_{tos} FE (kip)	Model / FE
WEB	17	4	133.7	7.5	7.0	1.07
FLANGE	12	8	33.3	5.0	5.0	1.00

Substituting l_{y1} and l_{y2} in into Equation 2-13 results in Equations 2-18 and 2-19. These equations are calibrated for sections through the outer portion of the bottom flange in FIB girders. They should not be used in conjunction with other girder shapes, or at sections in the FIB bottom flange that are below the web.

$$f_{tos1} = \frac{2F_{pos}x_p}{l_{y1}l_{tos}(h_f - n_{st}d_b)} \quad 2-18$$

$$f_{tos2} = \frac{2F_{pos}x_p}{l_{y2}l_{tos}(h_f - n_{st}d_b)} \quad 2-19$$

G.2.2.3 Self-Weight Reaction Stress

Analytical modeling has shown that self-weight reaction stress at the end surface of FIB girders can be neglected at locations in the outer portion of the bottom flange. As such, the self-weight reaction stress (f_{sw}) in the serviceability model is assumed to be zero. This assumption may not be reasonable for all cross-sections.

G.2.2.4 Superposition of Stresses

Horizontal spitting stress is defined as the superposition of Hoyer, peeling, and self-weight reaction stresses:

$$f_{hsp} = f_h + f_{tos} + f_{sw} \quad 2-20$$

Where:

- f_{hsp} = Horizontal splitting stress
- f_h = Average Hoyer effect stress
- f_{tos} = Peeling stress
- f_{sw} = Self-weight reaction stress

As previously discussed, stress due to self-weight reaction is negligible at the end face of the FIB bottom flange. Self-weight reaction is included in Equation 2-20 only as a reminder that self-weight effects may be critical in some long-span girders and in girders with other cross-sections. For FIB girders, Equation 2-20 can be reduced to:

$$f_{hsp} = f_h + f_{tos} \quad 2-21$$

Two critical conditions have been discussed for horizontal splitting stresses. The maximum peeling condition occurs when only the strands outboard of a section are cut. Strands at the section in question are not yet cut in the maximum peeling condition and Hoyer stress on the section is assumed to be zero. The combined condition occurs when strands on a section have been cut and peeling stress is superimposed with Hoyer stress. The maximum horizontal splitting stress on a given section is the greater of the stress from the maximum peeling or combined conditions:

$$f_{hsp1} = f_{tos1} \quad 2-22$$

$$f_{hsp2} = f_h + f_{tos2} \quad 2-23$$

Where:

- f_{hsp1} = Horizontal splitting stress for maximum peeling condition
- f_{hsp2} = Horizontal splitting stress for combined condition

In FIB girders transverse splitting stresses is checked for the five outermost columns of strands (Figure 23). Stresses are checked at strand locations because Hoyer stresses are greatest near prestressing strands, and because splitting cracks in the experimental program were observed to intersect strands. Stress is checked at each of the five locations for both of the critical stress conditions. Maximum stress from these locations and conditions is compared to concrete tensile strength criterion, which is discussed later.

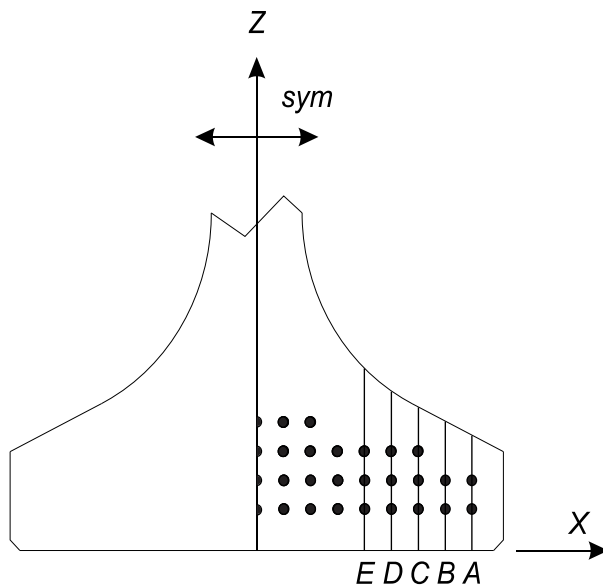


Figure 23–Analysis sections for FIB bottom flange

G.2.3 Stress Calculations for Experimental Girders

In this section the serviceability model is used to compute stresses at the end of specimen WN (Figure 24). The end of specimen WN had two fully bonded strands placed at the outside of the flange. All other strands in the outer flange were shielded.

Hoyer stresses were calculated using Equation 2-8 and are summarized in Table 6. The value of interfacial pressure (p) listed in Table 6 was calculated using Equation 2-3 and the values from Table 1. The calculated Hoyer stress is zero for all but section A. This is because the model assumes that Hoyer stresses from shielded strands are negligible.

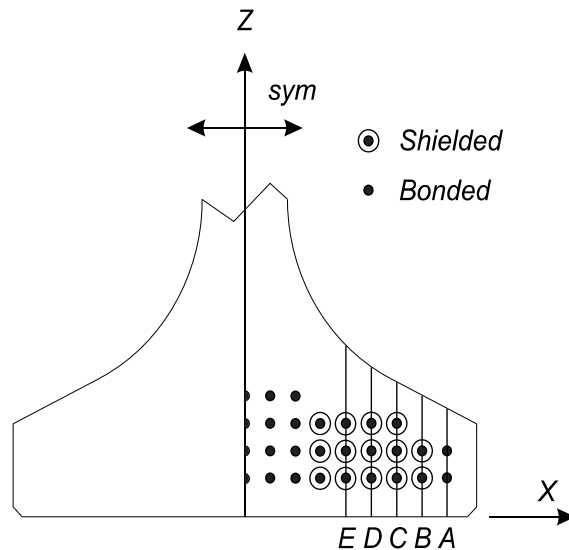


Figure 24–Strand bond and shielding pattern specimen WN

Table 6–Hoyer stresses end of specimen WN

Section	n_s	p (ksi)	d_b (in.)	n_{st}	h_f (in.)	f_h (ksi)
A	2	7.36	0.6	2	8.5	1.21
B	0	7.36	0.6	2	8.5	0
C (EDGE)	0	7.36	0.6	3	8.5	0
D	0	7.36	0.6	3	8.5	0
E (MID)	0	7.36	0.6	3	8.5	0

Peeling stresses were calculated using Equations 2-18 and 2-19 and are summarized in Table 7. Peeling stresses at section B require additional discussion. The maximum peeling condition is intended to have the maximum peeling stress, however, it has a lower peeling stress than the combined condition at section B. This is because empirical equations for the internal moment arm resulted in a shorter arm, and consequently at larger peeling stress, for the combined condition. This limitation of the model only affects section B and is of little concern. As shown later in the chapter, splitting stress at section B does not govern in any of the stress calculations for the experimental specimens. Also, this limitation makes the model is conservative at section B because it superimposes the larger peeling stress with the Hoyer stress.

Horizontal splitting stresses were calculated using Equations 2-22 and 2-23 and the stresses from Table 6 and Table 7. Results are presented graphically in Figure 25. The maximum calculated splitting stress at the end of WN occurs at section A during the combined condition. Because no peeling stress occurred at section A, the entire calculated splitting stress is due to the Hoyer effect. Splitting stresses at the other sections in WN are smaller than at section A because Hoyer stress from the shielded strands is assumed to be negligible. Calculated splitting stresses at sections B through E are solely due to peeling stresses caused by the bonded strands at section A.

Table 7–Peeling stresses at end of specimen WN

Section	F_{pos} (kip)	x_p (in.)	x (in.)	h_f (in.)	n_{st}	d_b (in.)	l_{y1} (in.)	l_{y2} (in.)	f_{tos1} (ksi)	f_{tos2} (ksi)
A	NA	NA	16	8.5	2	0.6	NA	NA	0	0
B	88	2	14	9.5	2	0.6	43.7	36.0	0.097	0.118
C (EDGE)	88	4	12	10.4	3	0.6	38.7	45.9	0.212	0.178
D	88	6	10	11.6	3	0.6	33.4	61.5	0.322	0.175
E (MID)	88	8	8	13.2	3	0.6	28.0	87.5	0.441	0.141

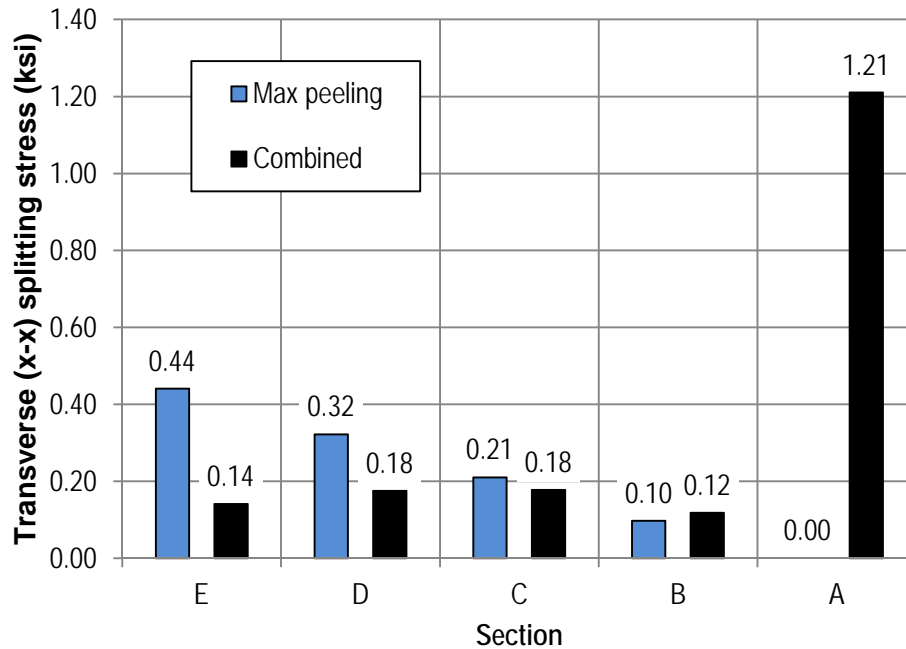


Figure 25–Transverse (x-x) splitting stress at end of specimen WN

The same procedures used above for WN were also used calculate transverse splitting stresses for each specimen in the FIB-54 and FIB-63 experimental programs. The serviceability model was derived for calculating stresses at the end of pretensioned I-girders. To test the applicability of the model to other locations, it was also used to estimate stress in specimens WN, WB, and SL where shielding terminated.

The maximum transverse splitting stress for each specimen and location are listed in Table 8, along with the governing section, governing stress condition, and flange splitting crack data. When stresses were calculated at two locations on the same specimen, crack data were assigned to the location where the cracks were observed in the physical girder. For example, no splitting cracks were observed at the end of specimen WN and the table lists zero for the crack length and area. Splitting cracks were observed 10 ft away from the end of WN, and the table lists the length and area of those cracks in the row labeled “WN (10 ft.)”.

Table 8–Transverse splitting stresses and splitting crack data

Specimen	Max transverse splitting stress (ksi)	Section	Critical Condition	Length of flange splitting cracks (in.)	Area of flange splitting cracks (in ²)
HC	1.29	C	Combined	0	0
HU	1.29	C	Combined	40	0.112
VC	1.29	C	Combined	0	0
VU	1.29	C	Combined	41	0.087
WN (10 ft.)	1.63	C	Combined	32	0.05
WB (10 ft.)	1.63	C	Combined	99	0.292
WN (end)	1.21	A	Combined	0	0
WB (end)	1.21	A	Combined	0	0
FN	1.73	D	Combined	190	0.469
FB	1.73	D	Combined	115	0.295
DC	1.29	C	Combined	104	0.239
DM	1.29	C	Combined	41.5	0.112
PT	1.81	C	Combined	142	0.316
LB	1.81	C	Combined	183	0.429
CN	1.81	C	Combined	175	0.368
SL	1.25	C	Combined	73	0.144
SL (5 ft.)	0.99	D	Combined	0	0

Table 8 shows that the combined stress condition governs for each specimen and location. For the combined condition Hoyer stress accounted for 85% of the splitting stress, on average. The remaining 15% (on average) was from peeling stress. This result indicates the significance that the Hoyer effect has on flange splitting cracks.

Section C has the governing (maximum) stress in 12 of 17 specimens and locations. Experimental observations support this result. Flange splitting cracks were more likely to be observed at section C than at any other location in the experimental program. The governing stress from the model never occurs at sections B or E. This result supports the previous statement that model limitations at section B do not impact overall results.

G.2.4 Model Comparison with Experimental Crack Data

Stresses calculated using the serviceability model correlate well with crack data from the experimental girders (Table 8 and Figure 26). This can be seen from the linear curve in Figure 26 that is fit to the stress and crack data from the specimen ends. The line has an R² value of 0.85, indicating a high degree of correlation between calculated stresses and experimental crack lengths. When stress and crack data away from the ends (WN, WB, and SL) are included,

correlation drops to 0.73. This suggests that the model is more accurate for calculating stress at member ends than at sections away from the end. Additional data are required, however, to quantify the degree to which the model can reasonably be applied to locations away from the member end.

A high degree of correlation is also observed when the calculated stresses are compared to the area of the flange splitting cracks in the experimental girders (Figure 27). Considering the random nature of cracking in concrete this level of correlation suggests that the model does an excellent job of capturing the physical phenomenon which cause bottom flange splitting cracks.

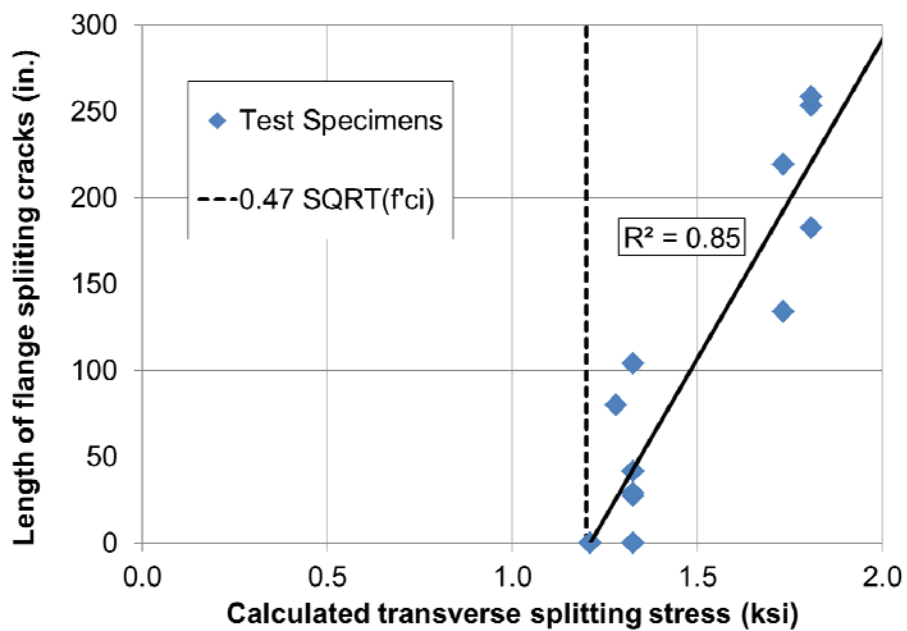


Figure 26–Calculated transverse splitting stress vs. experimental crack length

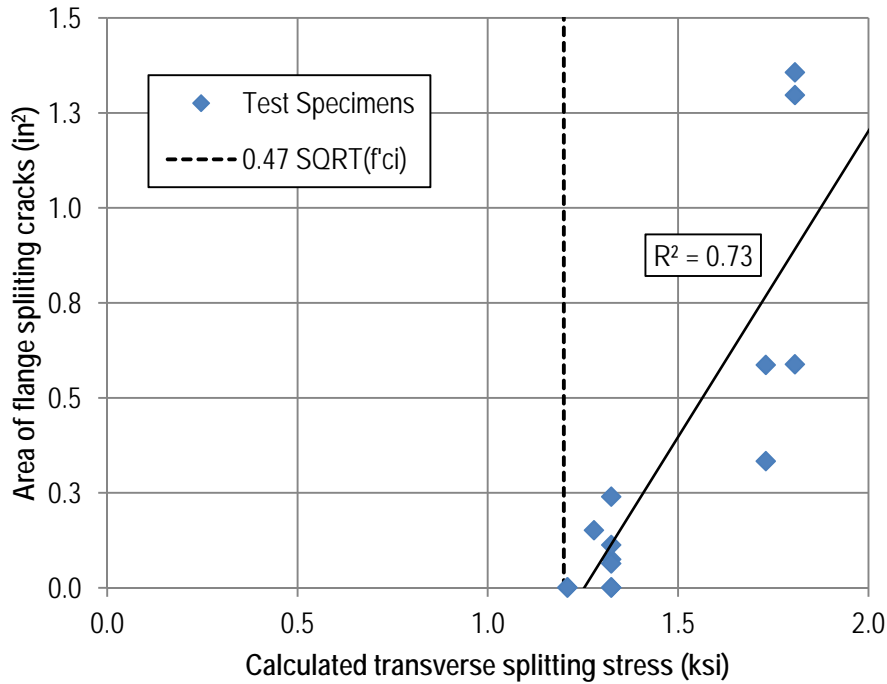


Figure 27–Calculated transverse splitting stress vs. experimental crack area

It is common in prestressed concrete design to compare concrete tensile stress to the square root of the compressive strength. Dashed vertical lines in Figure 26 and Figure 27 indicate 1.20ksi which is equal to $0.47\sqrt{f'_{ci}}$ (for f'_{ci} in ksi). This value is approximately equal to the x-intercept of the linear curves fit to the data. The x-intercept corresponds to the stress below which flange cracking are unlikely according to the sample data. All but one of the specimens and locations in the sample have stresses higher than this value. The lone location below this value, SL (5ft.), did not have flange splitting cracks in the experimental girder. A more conservative stress limit, and one that is already used in other circumstances by AASHTO LRFD, is $0.24\sqrt{f'_{ci}}$. This is approximately half of the limit indicated by the experimental data. Additional data are required to calibrate the reliability associated with different splitting stress criteria. Nevertheless, available data suggest that the proposed model is an adequate tool for calculating transverse splitting stress in the bottom flange of FIB girders.

G.2.5 Summary and Conclusions

A model was derived for calculating transverse splitting stresses in the bottom flange of concrete I-girders. The model considers contributions to splitting stress from the Hoyer effect

and from the horizontal eccentricity of strands in the outer flange. Stresses due to these effects are referred to as Hoyer stresses and peeling stresses, respectively. Self-weight also contributes to transverse splitting stress, however effects of self-weight are considered negligible in the outer flange. The work of Oh et al (2006) was utilized to derive an equation for Hoyer stress. An equation for peeling stress was derived using FE modeling and basic mechanics. The equation for peeling stress also contains empirical relationships that were derived by comparison with FE analyses.

The model was compared to crack data from the experimental girders and was found to have a high degree of correlation with said data. An R^2 value of 0.80 was obtained for linear trend line that was fit to the calculated and experimental data. Analysis indicates that flange splitting cracks are likely when the calculated splitting stress exceeds $0.45\sqrt{f'_{ci}}$ (for f'_{ci} in ksi). A lower threshold stress is recommended for controlling flange splitting cracks. One possible threshold is $0.24\sqrt{f'_{ci}}$, which is currently used by AASHTO LRFD to limit concrete tensile stresses in situations similar to the FIB bottom flange.

Appendix H–Support Data

Table of Contents

H.1	SR-72 Support Data	547
H.1.1	Original Plans	547
H.1.2	Core Testing	550
H.1.3	X7 Instrumentation	554
H.1.4	X4 Instrumentation	556
H.1.5	I2A Instrumentation.....	558
H.1.6	I2B Instrumentation.....	560
H.1.7	I4 Instrumentation	562
H.1.8	I6 Instrumentation	564
H.2	FIB-54 Support Data	567
H.2.1	Vertical Reinforcement Strain	567
H.2.2	Standard Test for Strand Bond	568
H.3	FIB-63 Support Data	574
H.3.1	Gage Coordinates	574
H.3.2	Strain during Post-Tensioning	575
H.3.3	Strain during Prestress Release.....	575
H.3.4	Web Cracks	578
H.3.5	Load Tests	581

List of Figures

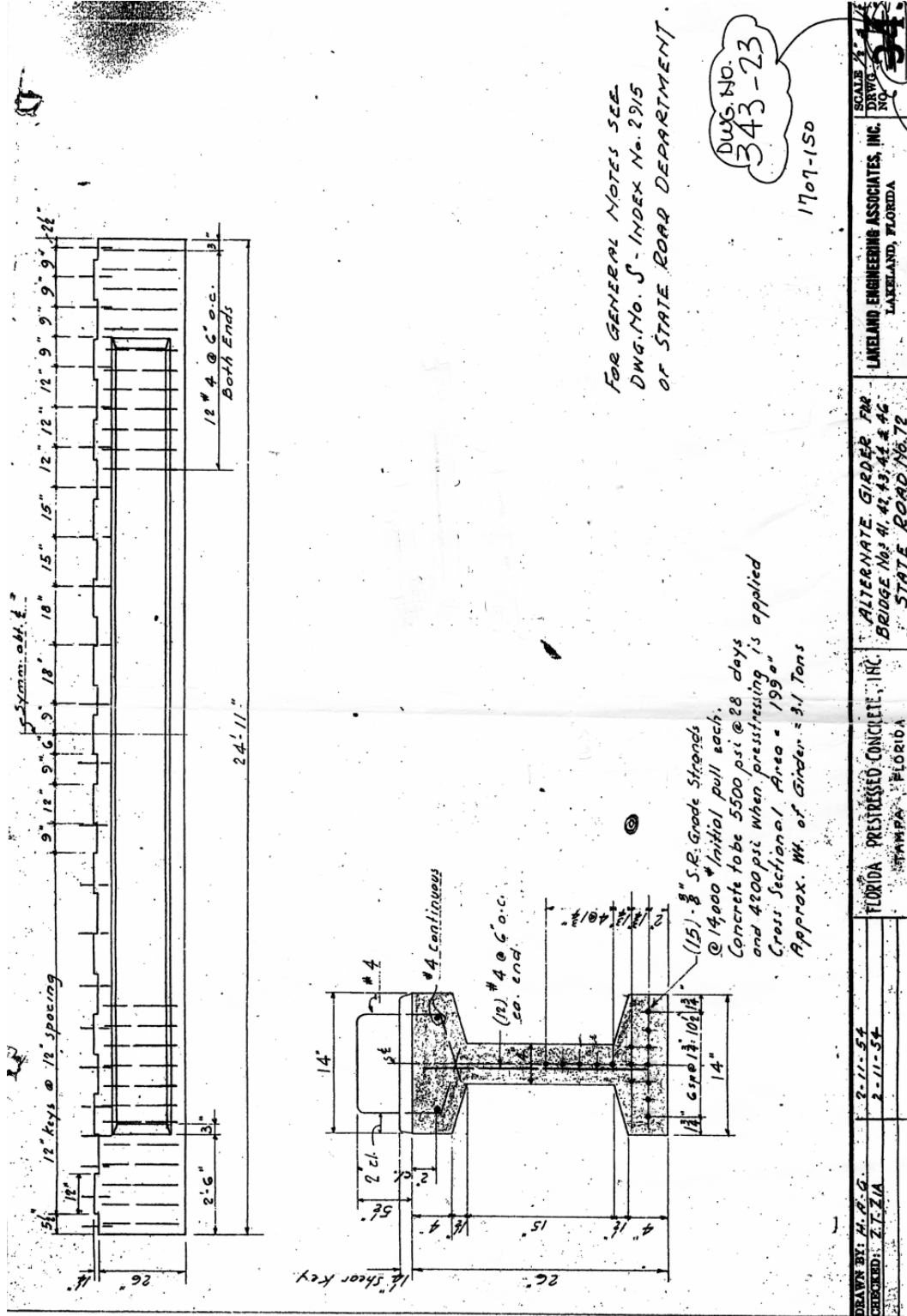
Figure 1–X7 instrumentation	554
Figure 2–X7 instrumentation at plane A-A (5'-6" from near end)	554
Figure 3–X7 instrumentation at plane B-B (load point)	555
Figure 4–X7 instrumentation at plane C-C (centerline of span)	555
Figure 5–X4 instrumentation	556
Figure 6–X4 instrumentation at plane A-A (12'-6" from near end)	556
Figure 7–X4 instrumentation at plane B-B (load point)	557
Figure 8–X4 instrumentation at plane C-C (5'-6" from near end)	557
Figure 9–I2A instrumentation	558
Figure 10–I2A instrumentation at plane A-A (5 ft-6 in. from far end)	558
Figure 11–I2A instrumentation at plane B-B (load point)	559
Figure 12–I2A instrumentation at plane C-C (5 ft-6 in. from near end)	559
Figure 13–I2B instrumentation	560
Figure 14–I2B instrumentation at plane A-A (load point)	560
Figure 15–I2B instrumentation at plane B-B (7 ft from near end)	561
Figure 16–I2B instrumentation at plane C-C (5 ft from near end)	561
Figure 17–I2B instrumentation at plane D-D (5 ft from near end)	561
Figure 18–I4 instrumentation	562
Figure 19–I4 instrumentation at plane A-A (load point)	562
Figure 20–I4 instrumentation at plane B-B (4 ft-2 in. from near end)	563
Figure 21–I4 instrumentation at plane C-C (3 ft-0 in. from near end)	563
Figure 22–I4 instrumentation at plane D-D (1 ft-8 in. from near end)	564
Figure 23–I6 instrumentation	564
Figure 24–I6 instrumentation at plane A-A (load point)	565
Figure 25–I6 instrumentation at plane B-B (5 ft-4 in. from near end)	565
Figure 26–I6 instrumentation at plane C-C (3 ft-0 in. from near end)	566
Figure 27–Mixer for small batches (left), large batches (right)	569
Figure 28–Wood frame and NASP samples (left), in cure room (right)	570
Figure 29–Stand lateral support at top of tube	570
Figure 30–NASP test setup	571
Figure 31–Strain due to prestress release in ES gages in specimen CT	576
Figure 32–Strain due to prestress release in ES gages in specimen SL	576
Figure 33–Strain due to prestress release in ES gages in specimen PT	577
Figure 34–Strain due to prestress release in ES gages in specimen LB	577
Figure 35–Crack growth in specimen SL (flexural cracks in top flange not shown)	578
Figure 36–Crack growth in specimen PT (flexural cracks in top flange not shown)	579
Figure 37–Crack growth in specimen LB (flexural cracks in top flange not shown)	580
Figure 38–Service load test strain data for specimen CT	581
Figure 39–Service load test strain data for specimen SL	581
Figure 40–Service load test strain data for specimen PT	582
Figure 41–Service load test strain data for specimen LB	582

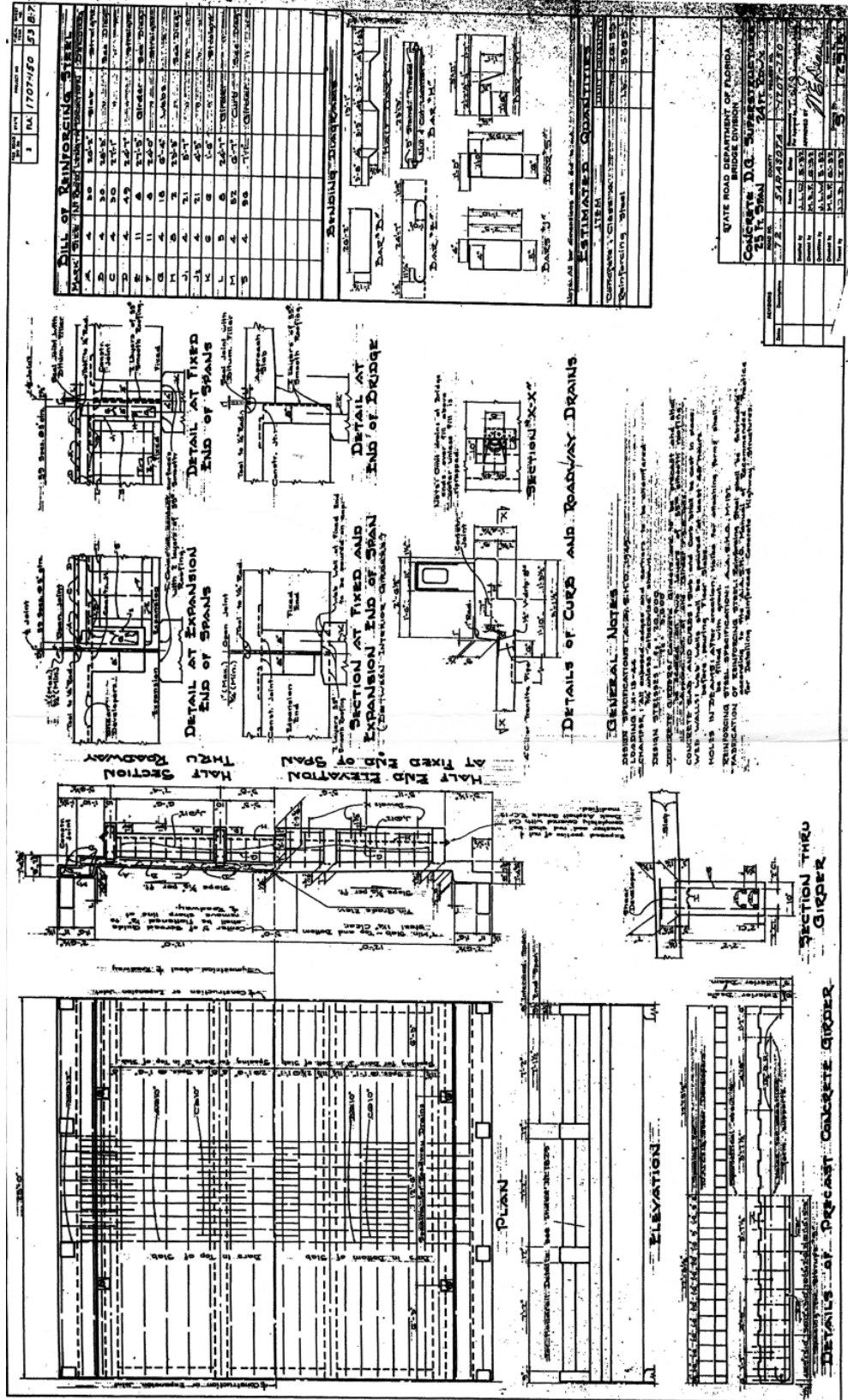
List of Tables

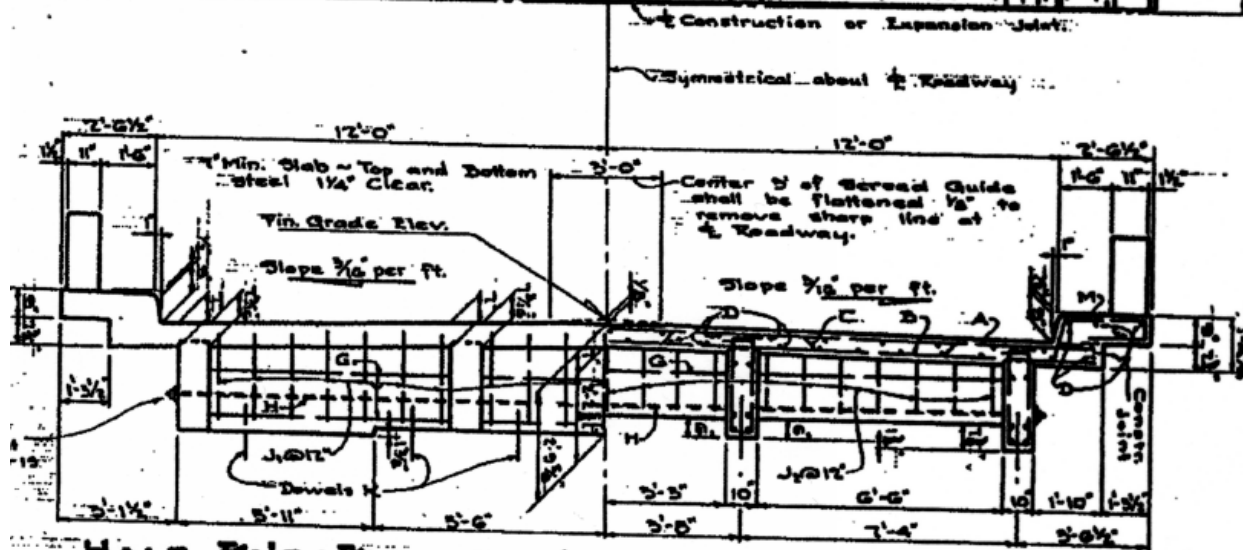
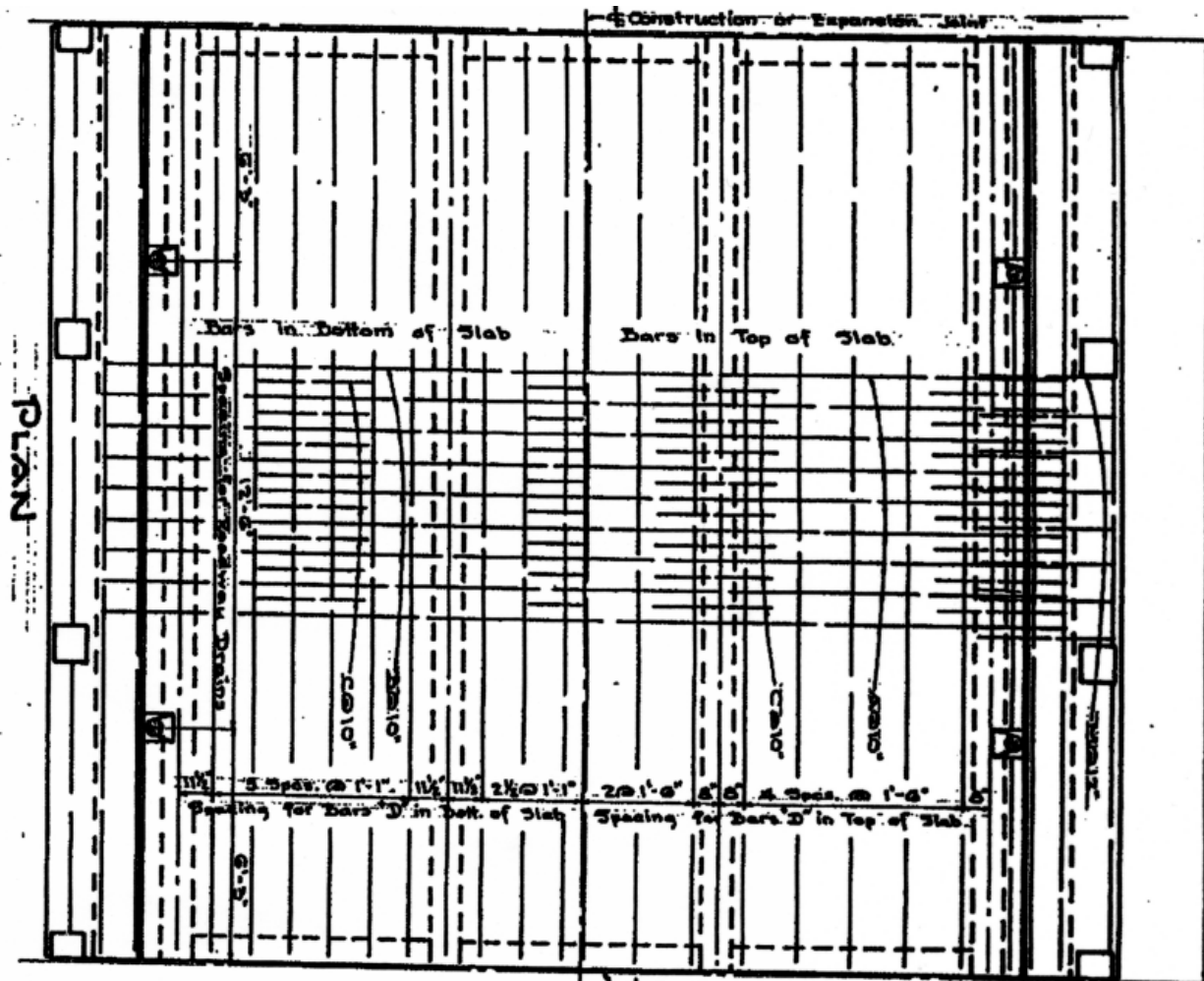
Table 1–Gage location on vertical reinforcement.....	567
Table 2–Strain in vertical reinforcement	568
Table 3–NASP test trial grout batches.....	568
Table 4–Gage coordinates for specimen CT.....	574
Table 5–Gage coordinates for specimen SL	574
Table 6–Gage coordinates for specimen PT	574
Table 7–Gage coordinates for specimen LB.....	575
Table 8–Stress due to post-tensioning during tensioning process in specimen PT.....	575

H.1 SR-72 Support Data

H.1.1 Original Plans







H.1.2 Core Testing



10600 Endeavour Way
Largo, Florida 33777
Office: (727) 541-3144
Fax: (727) 541-1510
www.williamsearthsciences.com

September 19, 2006

Timothy J. Farrell, P.E.
EC Driver & Associates, Inc.
500 N. Westshore Boulevard, Suite 500
Tampa, Florida 33609

Subject: Bridge Concrete Core Testing
SR 72 Bridge Nos. 170042, 170043, 170044, 170046, 170941
District-Wide Bridge Engineering Services
Financial Project ID 412550-1-32-02
Contract No. C-8C41
Williams Project No. 1305-000-05

Dear Mr. Farrell,

Williams Earth Sciences, Inc. (Williams) has completed the field and laboratory work for the above referenced project. This work was accomplished under the District-Wide Bridge Engineering Services contract C-8C41.

The field work consisted of taking concrete cores through the deck beams of five bridges along SR 72. The concrete cores were 2-inch nominal diameter and approximately 4 to 4.5 inches in length. Four cores were taken at predetermined span and core locations for each bridge. Sketches illustrating the core locations are attached. The cores were retrieved using a hand-held coring machine. This resulted in shape imperfections, as seen in the attached photographs. It is our opinion that these shape imperfections had insignificant effects on the compression and split tension break results. The coring was performed in August and September, 2006.

The concrete core samples were transported to our laboratory facility for compressive and tensile strength testing. The compressive strength cores were capped using a neoprene pad prior to testing. The specimen height, diameter and load at failure have been input into a spreadsheet and the corrected unconfined compressive strength or the splitting tensile strength has been calculated. The tests were performed in general accordance with ASTM Designation C 39/C 39M-05 and C 496/C 496M-04 for the compressive strength and splitting tensile strength, respectively. The spreadsheets illustrating the core measurements and test results are attached. Photographs were taken of each core sample before and after breaking. The photographs are attached.

Tables 1A through 4A contain a summary with the span number, beam number, core number, concrete test performed, resulting strength, and fracture pattern. Tables 1B through 4B contain the statistics of the breaks. The Designations for the cores represent the span, beam and core number. For example, core designation 3-4-1 represents Span 3, Beam 4, and core 1 for a particular bridge.

On Bridge 170044 Myakka River, core specimen 1-4-1, a 2-inch long crack about 1/8 inch wide was observed along one side. Additional photographs were taken to illustrate this characteristic. Williams did not observe any other fractures or other detrimental characteristics on the remaining concrete cores with the naked eye.



Geotechnical Engineering • Materials Testing and Inspection • Foundation Studies • Technical Training
Fort Lauderdale, Florida • Jacksonville, Florida • Largo, Florida • Panama City, Florida

Table 1: Summary of Test Results.

Specimen ID	Span Number	Beam Number	Core Number	Test Type (UC or ST)	Test Result (psi)	Failure Mode
Bridge No. 170042						
1-1-1	1	1	1	UC	4,068	3
3-4-1	3	4	1	UC	2,331	3
1-4-1	1	4	1	ST	362	3
3-1-1	3	1	1	ST	507	3
Bridge No. 170043						
1-1-1	1	1	1	UC	5,139	4
3-4-1	3	4	1	UC	2,928	3
1-4-1	1	4	1	ST	827	3
3-1-1	3	1	1	ST	517	3
Bridge No. 170044						
1-1-1	1	1	1	UC	2,333	3
10-4-1	10	4	1	UC	4,192	3
1-4-1	1	4	1	ST	561	3
10-1-1	10	1	1	ST	522	3
Bridge No. 170046						
1-1-1	1	1	1	UC	4,088	3
3-4-1	3	4	1	UC	2,400	3
1-4-1	1	4	1	ST	641	3
3-1-1	3	1	1	ST	726	3
Bridge No. 170941						
1-1-1	1	1	1	UC	2,035	3
6-4-1	6	4	1	UC	2,683	3
1-4-1	1	4	1	ST	549	3
6-1-1	6	1	1	ST	536	3

Table 2A: Statistics of Concrete Core Breaks; Bridge No. 1370042 Myakka River Overflow.

Statistic	Compression Tests	Split Tension Tests
Number of Specimens	2	2
Average Result	3,200 psi	435 psi
Standard Deviation	1,228 psi	103 psi
High Result	4,068 psi	507 psi
Low Result	2,331 psi	362 psi

Table 2B: Statistics of Concrete Core Breaks; Bridge No. 170043 Myakka River Relief.

Statistic	Compression Tests	Split Tension Tests
Number of Specimens	2	2
Average Result	4,034psi	672 psi
Standard Deviation	1,563 psi	219 psi
High Result	5,139 psi	827 psi
Low Result	2,928 psi	517 psi

Table 2C: Statistics of Concrete Core Breaks; Bridge No. 170044 Myakka River.

Statistic	Compression Tests	Split Tension Tests
Number of Specimens	2	2
Average Result	3,263 psi	542 psi
Standard Deviation	1,315 psi	28 psi
High Result	4,192 psi	561 psi
Low Result	2,333 psi	522 psi

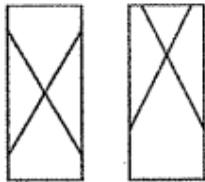
Table 3D: Statistics of Concrete Core Breaks; Bridge No. 170046 Deer Prairie Slough.

Statistic	Compression Tests	Split Tension Tests
Number of Specimens	2	2
Average Result	3,244 psi	684 psi
Standard Deviation	1,194 psi	60 psi
High Result	4,088 psi	726 psi
Low Result	2,400 psi	641 psi

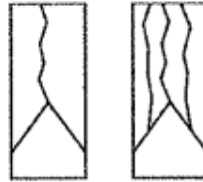
Table 3E: Statistics of Concrete Core Breaks; Bridge No. 170941 Cow Pen Slough.

Statistic	Compression Tests	Split Tension Tests
Number of Specimens	2	2
Average Result	2,359 psi	543 psi
Standard Deviation	458 psi	9 psi
High Result	2,683 psi	549 psi
Low Result	2,035 psi	536 psi

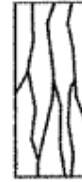
Typical Failure Patterns:



Type 1
Reasonably well-formed
cones on both ends,
less than 1 in (25 mm) of
cracking through caps



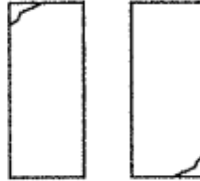
Type 2
Well-formed cone on one
end, vertical cracks running
through caps, no well-
defined cone on other end



Type 3
Columnar vertical cracking
through both ends, no well-
formed cones



Type 4
Diagonal fracture with no
cracking through ends;
tap with hammer to
distinguish from Type 1



Type 5
Side fractures at top or
bottom (occur commonly
with unbonded caps)



Type 6
Similar to Type 5 but end
of cylinder is pointed

Williams appreciates the opportunity to work with you on this project and we look forward to the next opportunity. If you have any questions regarding the results of this work, please contact the undersigned.

Sincerely,

WILLIAMS EARTH SCIENCES, INC.

Larry D. Spears, P.E.
Senior Geotechnical Engineer
Florida Registration No. 52105

Submittals: (3) Addressee

Attachments: Concrete Core Locations
Spreadsheet Results of Concrete Laboratory Testing
Photographs of Core Samples

H.1.3 X7 Instrumentation

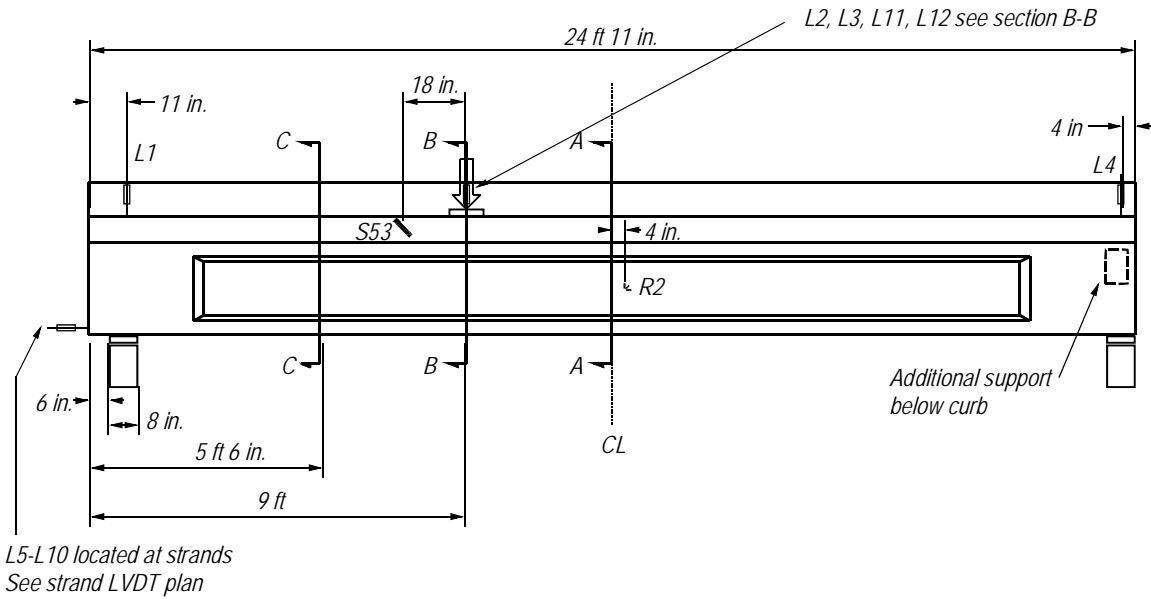


Figure 1-X7 instrumentation

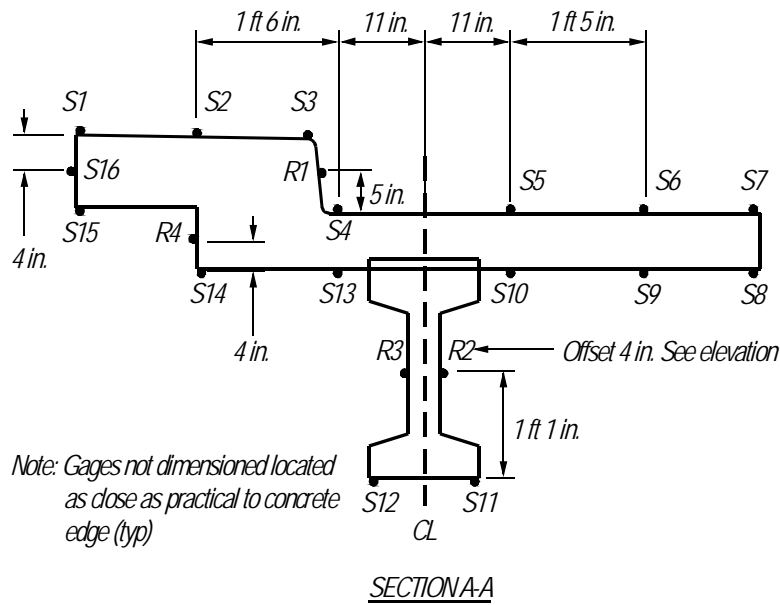


Figure 2-X7 instrumentation at plane A-A (5'-6" from near end)

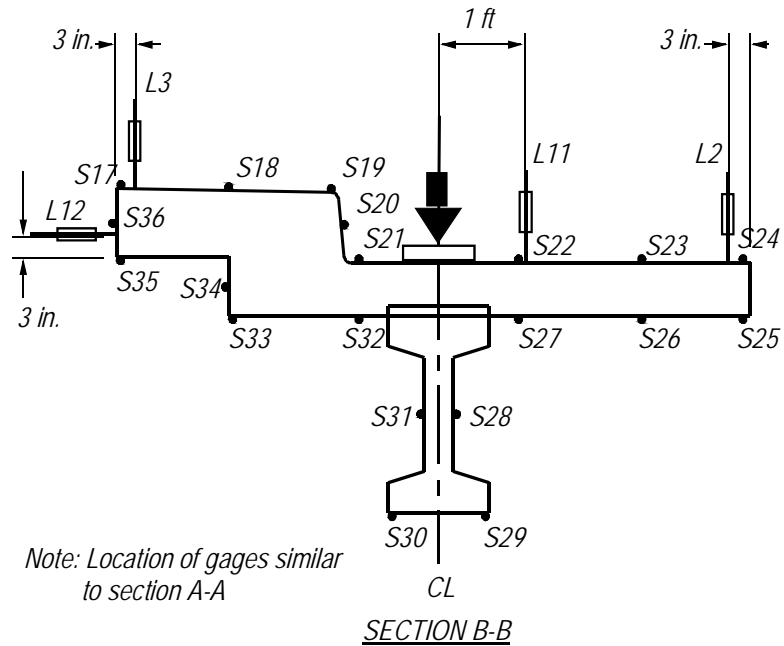


Figure 3-X7 instrumentation at plane B-B (load point)

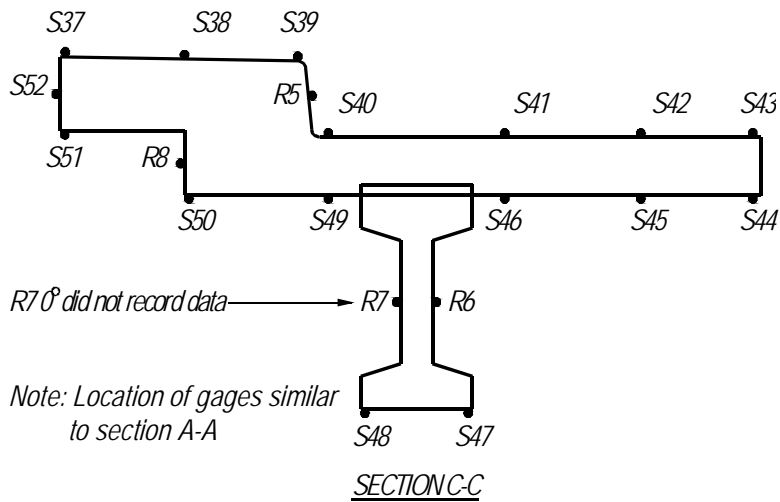


Figure 4-X7 instrumentation at plane C-C (centerline of span)

H.1.4 X4 Instrumentation

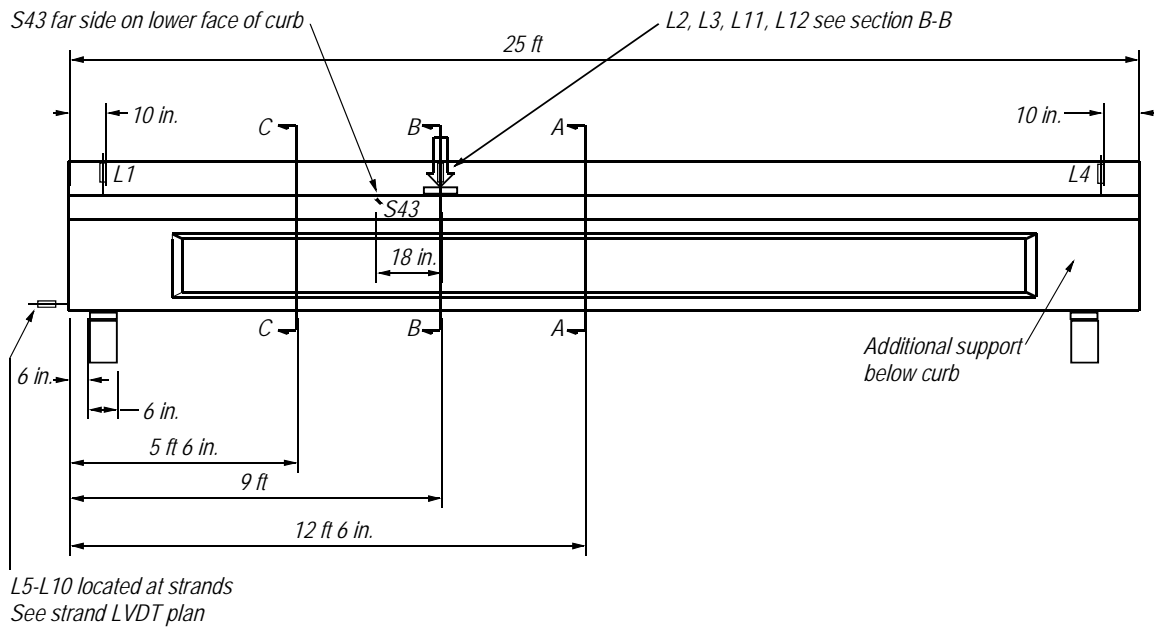


Figure 5—X4 instrumentation

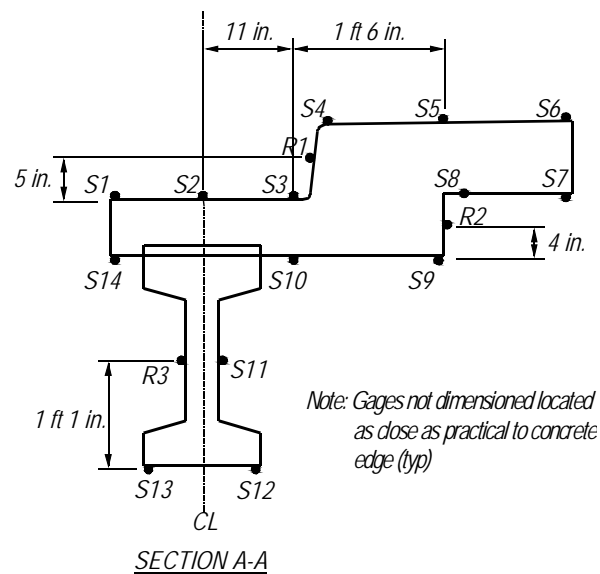


Figure 6—X4 instrumentation at plane A-A (12'-6" from near end)

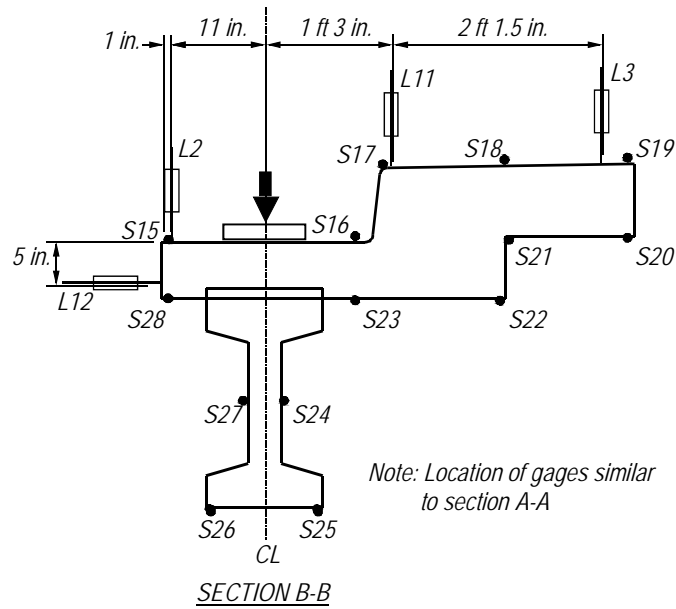


Figure 7-X4 instrumentation at plane B-B (load point)

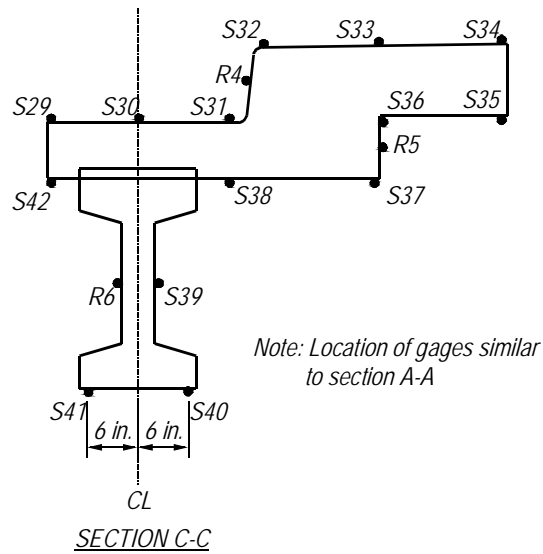


Figure 8-X4 instrumentation at plane C-C (5'-6" from near end)

H.1.5 I2A Instrumentation

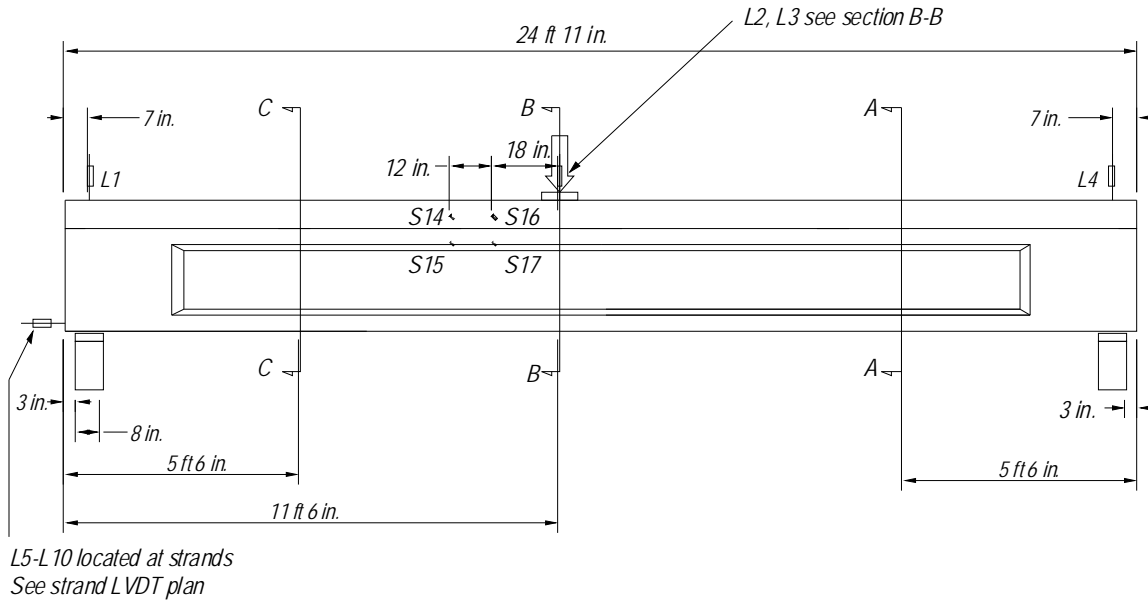


Figure 9-I2A instrumentation

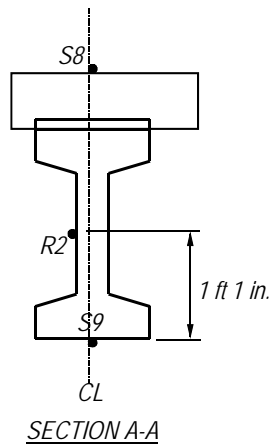


Figure 10-I2A instrumentation at plane A-A (5 ft-6 in. from far end)

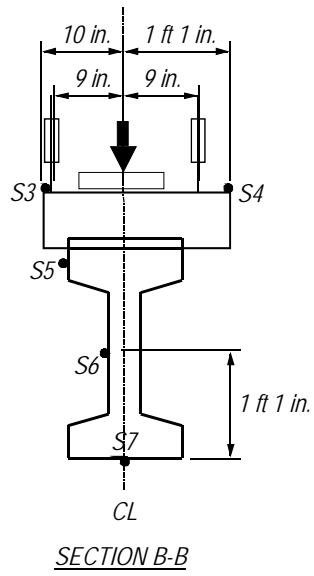


Figure 11-I2A instrumentation at plane B-B (load point)

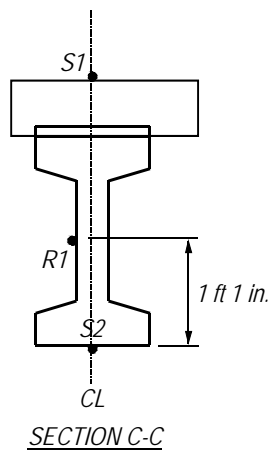


Figure 12-I2A instrumentation at plane C-C (5 ft-6 in. from near end)

H.1.6 I2B Instrumentation

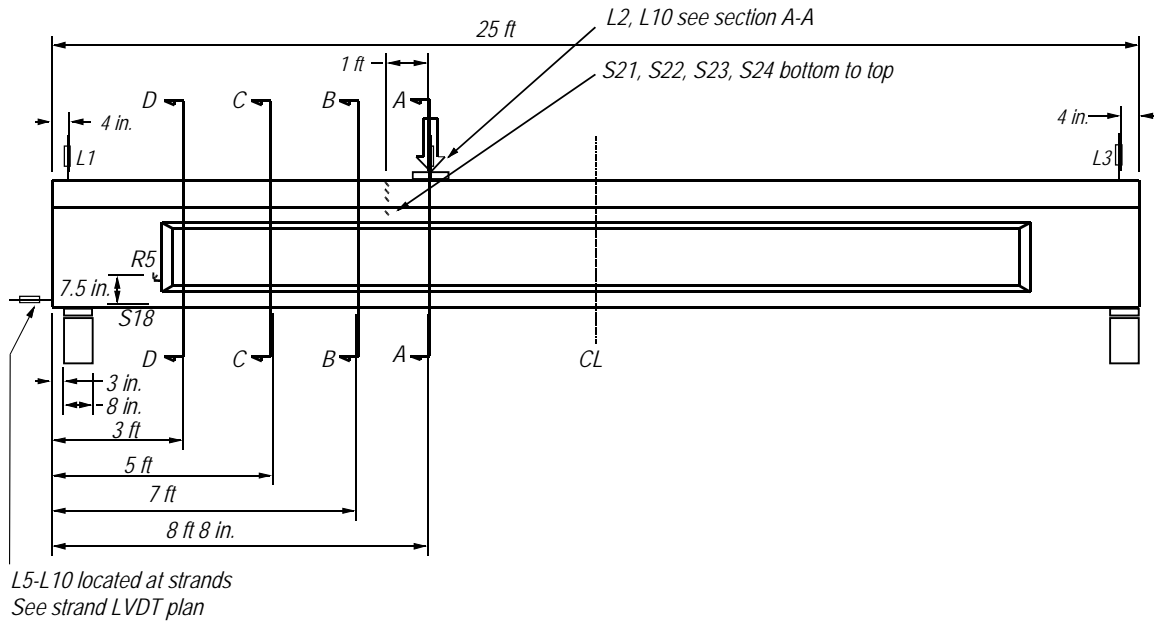


Figure 13-I2B instrumentation

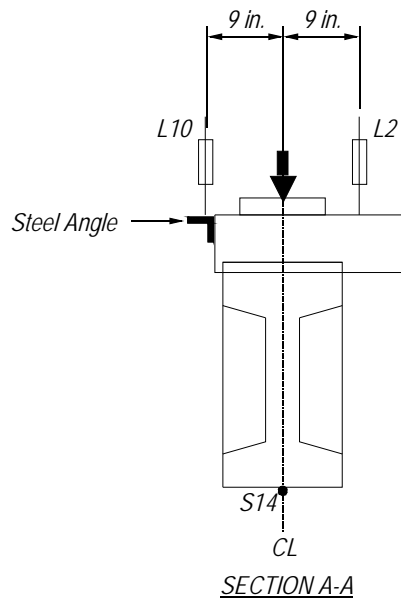


Figure 14-I2B instrumentation at plane A-A (load point)

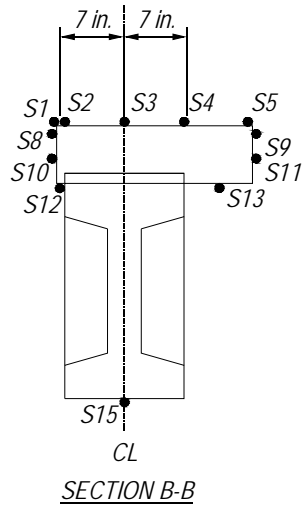


Figure 15–I2B instrumentation at plane B-B (7 ft from near end)

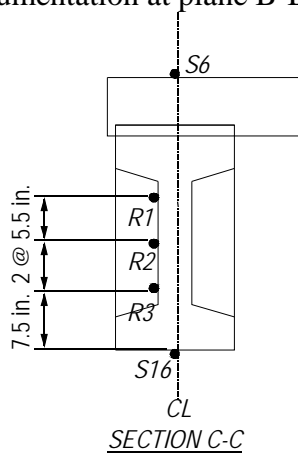


Figure 16–I2B instrumentation at plane C-C (5 ft from near end)

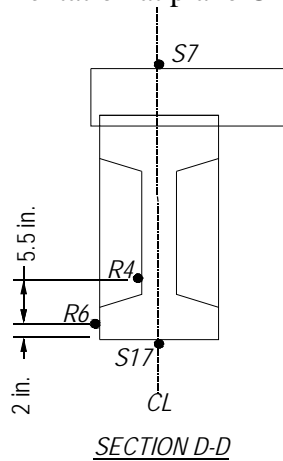


Figure 17–I2B instrumentation at plane D-D (5 ft from near end)

H.1.7 I4 Instrumentation

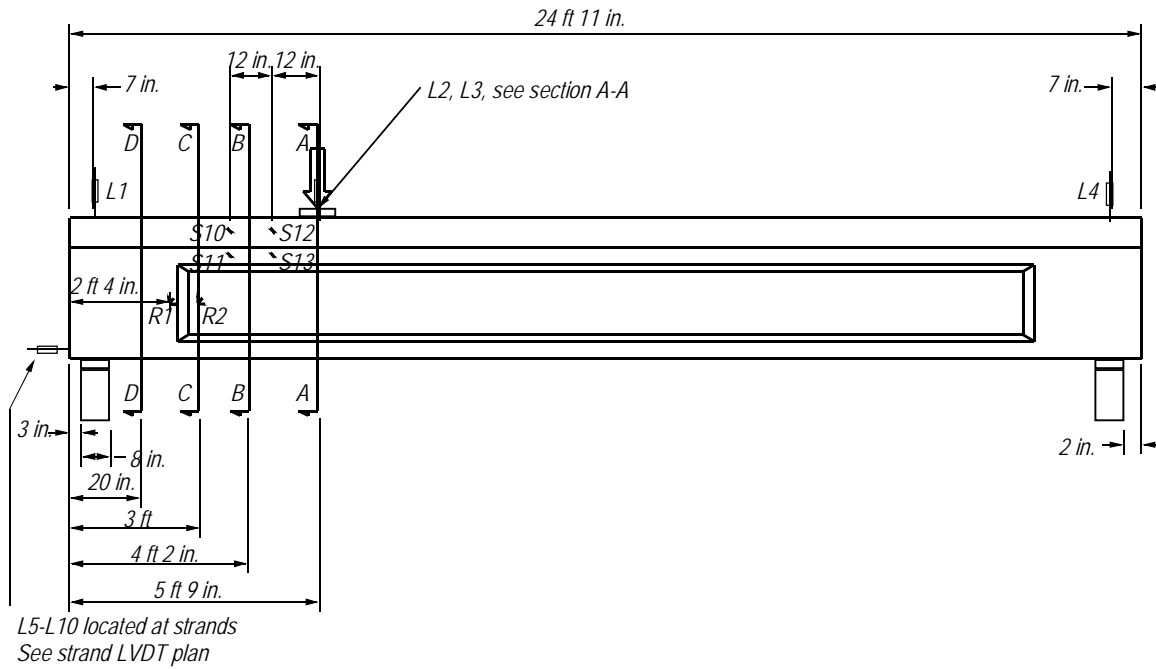


Figure 18-I4 instrumentation

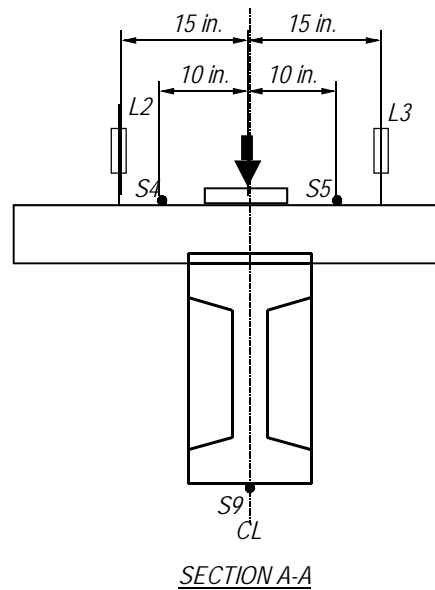
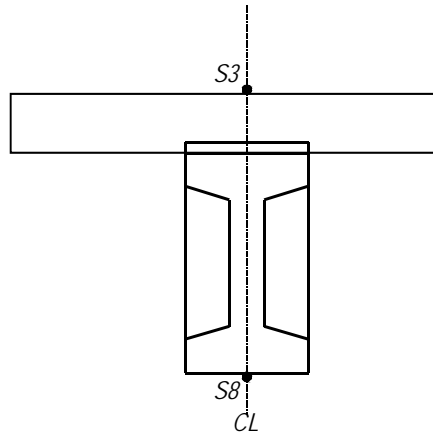
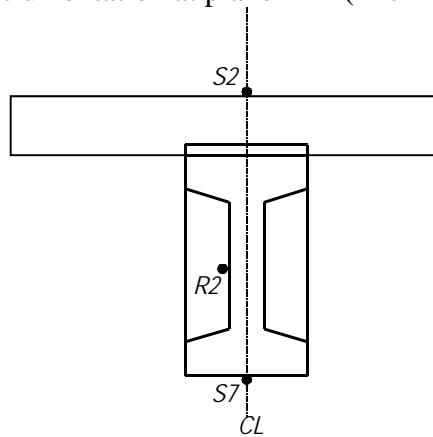


Figure 19-I4 instrumentation at plane A-A (load point)



SECTION B-B

Figure 20-I4 instrumentation at plane B-B (4 ft-2 in. from near end)



SECTION C-C

Figure 21-I4 instrumentation at plane C-C (3 ft-0 in. from near end)

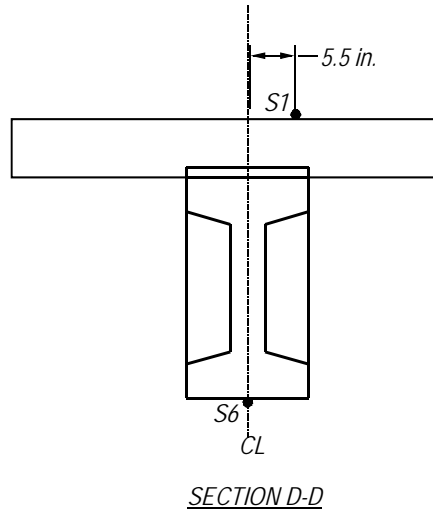


Figure 22-I4 instrumentation at plane D-D (1 ft-8 in. from near end)

H.1.8 I6 Instrumentation

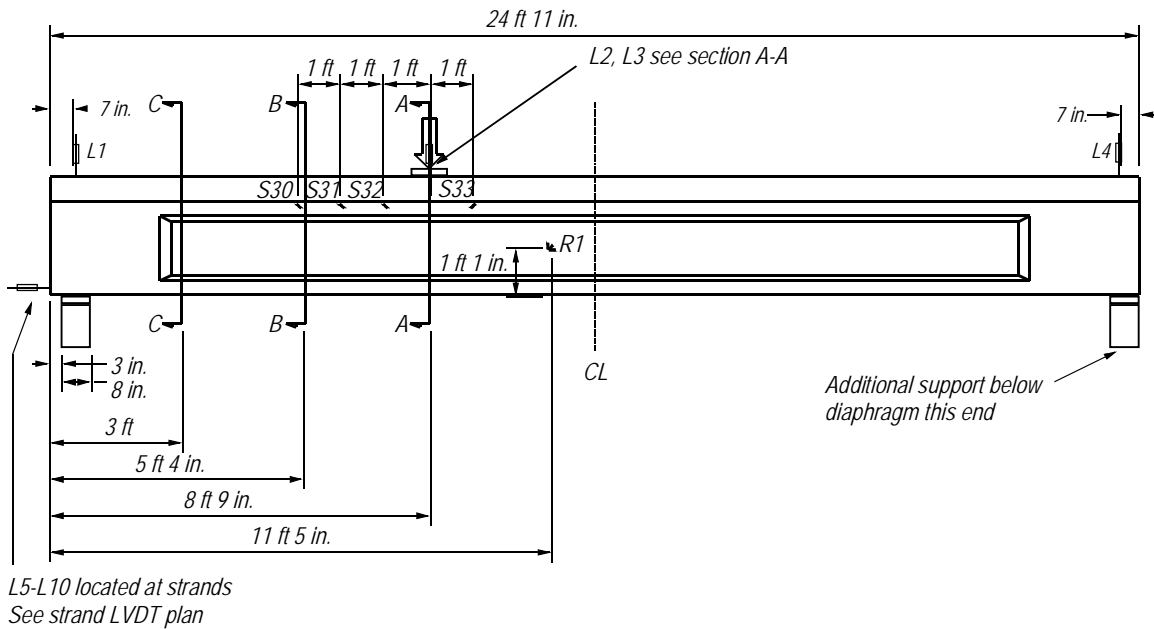


Figure 23-I6 instrumentation

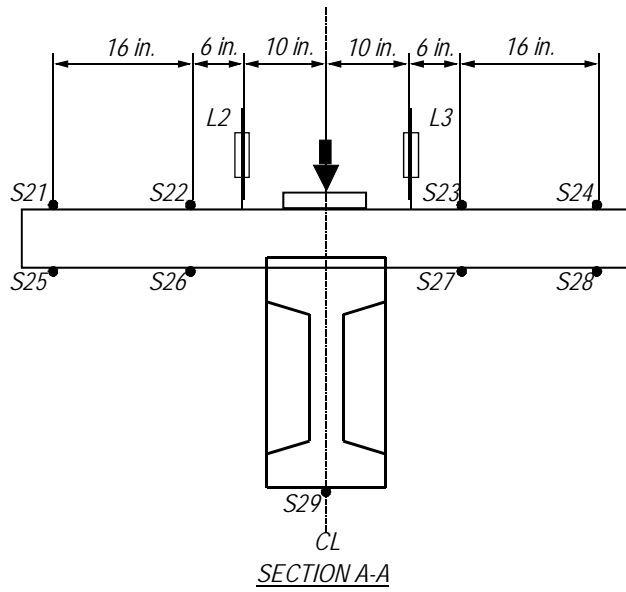


Figure 24-I6 instrumentation at plane A-A (load point)

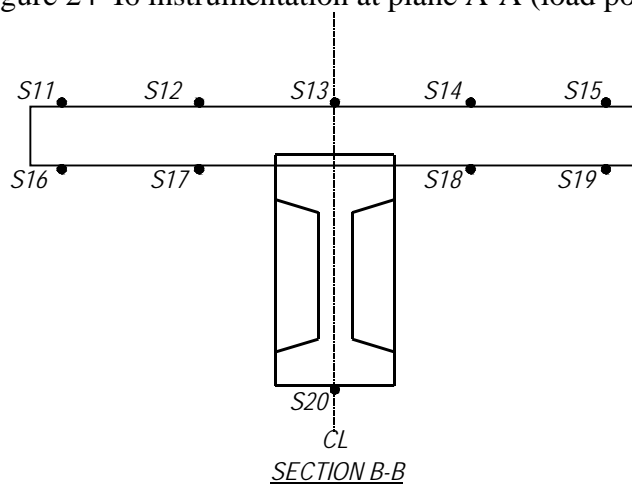


Figure 25-I6 instrumentation at plane B-B (5 ft-4 in. from near end)

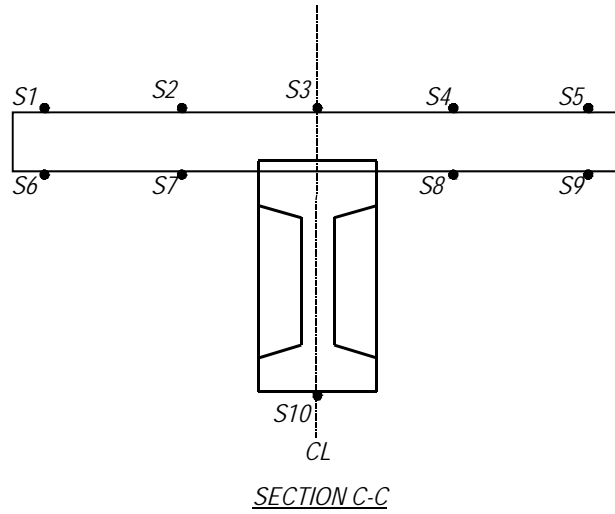


Figure 26-I6 instrumentation at plane C-C (3 ft-0 in. from near end)

H.2 FIB-54 Support Data

H.2.1 Vertical Reinforcement Strain

Strain data from select vertical reinforcement were collected from FIB-54 specimens during load testing. Locations of the strain gages on vertical reinforcement are provided in Table 1. Strain data from the gages are provided in Table 2.

Strain in the vertical reinforcement was not measured during prestress transfer but was estimated using the FE models from appendix F. By assuming strain compatibility between concrete and vertical reinforcement at prestress transfer, the strain in the reinforcement was assumed to equal the concrete strain taken from the FE models. Results are listed in Table 2.

Based on the strain data, stress in the vertical bars was estimated by multiply by the modulus of elasticity. Estimate stresses are listed in Table 2. Estimated stresses were limited to the test yield stress of the reinforcing bars. Stress data may be useful in developing strut-and-tie models of the end region at peak load.

Table 1–Gage location on vertical reinforcement

Specimen	Gage	X (in.)	Y (in.)	Z (in.)
WN	MS1	0	88.5	43.5
	MS2	0	52.5	25.3
WB	MS1	0	88.0	43.0
	MS2	0	52.5	25.5
FN	MS1	0	89.0	43.2
	MS2	0	53.0	25.5
FB	MS1	0	88.3	43.5
	MS2	0	52.5	25.5
DC	MS1	0	88.5	43.3
	MS2	0	52.5	25.5
DM	MS1	0	88.0	43.5
	MS2	0	44.5	25.5

Table 2–Strain in vertical reinforcement

Specimen	Gage	*Strain due to prestress transfer (microstrain)	Strain due to service load test (microstrain)	Strain due to ultimate load test (microstrain)	Total Strain at peak load (microstrain)	Stress at peak load (ksi)
WN	MS1	-8	184	1431	1607	46.6
	MS2	42	157	1170	1369	39.7
WB	MS1	-8	76	3867	3935	63.0
	MS2	42	38	1100	1180	34.2
FN	MS1	-8	74	545	611	17.7
	MS2	42	78	948	1068	31.1
FB	MS1	-8	241	2062	2295	63.0
	MS2	42	76	941	1059	30.7
DC	MS1	-13	130	7682	7799	63.0
	MS2	72	44	1973	2089	60.6
DM	MS1	-13	41	3188	3216	63.0
	MS2	72	79	1574	1725	50.0
*Based on FE model						

H.2.2 Standard Test for Strand Bond

Strain data Strand bonding capacity was tested according to the method proposed by the North American Strand Producers (NASP, 2009). This Appendix contains supplemental information on the materials, methods, and procedures used to carry out the tests.

In preparation for the NASP tests, numerous small and full size grout mixes were tested. Table 3 lists the proportions, flows, and strengths for each test mix. Small batches had a total mix weight of approximately 7 lb. Full batches had a total mix weight of approximately 225 lb. Prior to mixing the full batches, the mixer was “buttered” using a batch having a total weight of approximately 35 lb. The butter was discarded prior to mixing the grout batch. Mixers for the small and full batches are shown in Figure 27. All grout mixing and testing was conducted at the FDOT State Materials Office in Gainesville, FL.

Table 3–NASP test trial grout batches

Mix ID	Batch Size	Sand Proportion	Cement Proportion	Water Proportion	w/c ratio	s/c ratio	Flow	Strength at 24 hours
1	Small	0.645	0.239	0.116	0.485	2.703	124	NA

2	Small	0.695	0.206	0.100	0.485	3.378	65	NA
3	Small	0.656	0.231	0.112	0.485	2.838	112	4160 psi
4	Small	0.660	0.229	0.111	0.485	2.885	105	4310 psi
5	Small	0.659	0.230	0.111	0.485	2.872	111	4180 psi
6	Small	0.646	0.243	0.110	0.454	2.658	111	4640 psi
7	Small	0.646	0.243	0.110	0.454	2.658	104	4740 psi
8	Full*	0.645	0.244	0.110	0.452	2.639	96	4075 psi
9	Full	0.646	0.243	0.111	0.459	2.658	101.5	4310 psi
10	Full	0.644	0.246	0.110	0.449	2.618	105	4700 psi
11	Full	0.644	0.246	0.110	0.446	2.614	88.5	NA
12	Full	0.637	0.243	0.120	0.493	2.614	107.5	4250 psi
* The mixer for batch 8 was not “battered” prior to batching.								



Figure 27–Mixer for small batches (left), large batches (right)

Test samples were placed in a wood support frame to secure the strands and tubes during grout pouring and curing (Figure 28). Grout was placed in (3) lifts as specified by the test method. Grout was consolidated after each lift using a mechanical vibrator. Strands were supported vertically and laterally at the base of the wood frame. Additional lateral support was provided at the base and top (Figure 29) of the tube structure. Prior to placement in the tubes, the outer wires were cut shorter than the center wire (Figure 29). This was done to facilitate measurement of slip of the center wire, as required by the test method. Care was taken to maintain the surface condition of the strands from the time of collection in the prestressing yard, until they were embedded in grout.

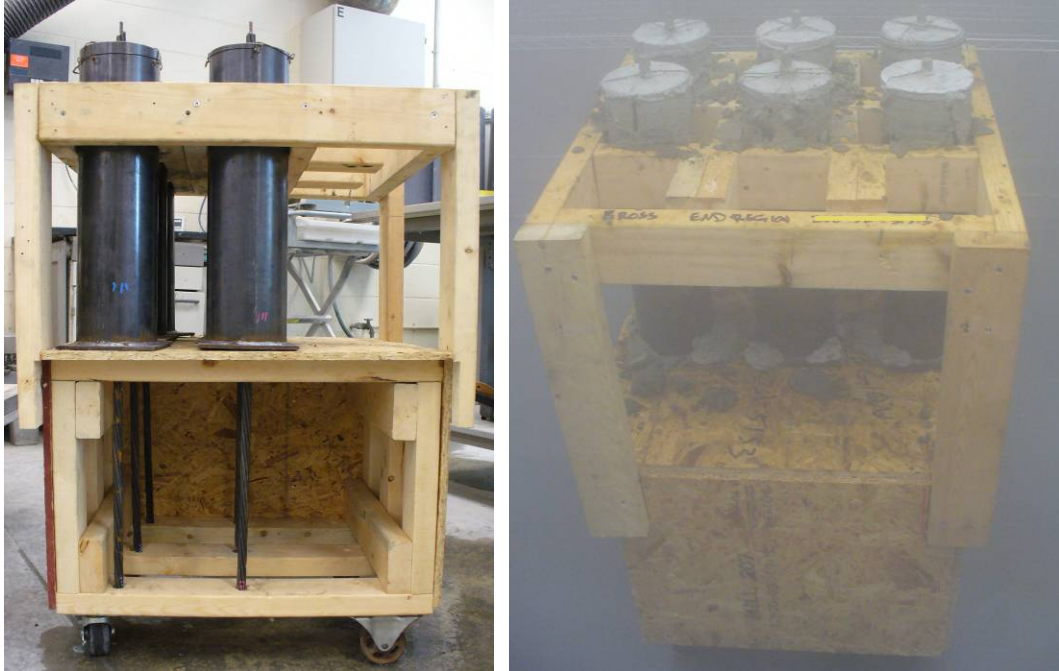


Figure 28–Wood frame and NASP samples (left), in cure room (right)



Figure 29–Stand lateral support at top of tube

The NASP pull-out tests were conducted the State Materials Office of the FDOT. The test setup is shown in Figure 30. The thrust bearing shown in the figure allows rotation of the strand (along its length) during loading, as required by the test method. No rotation of the strands was visually observed during testing.

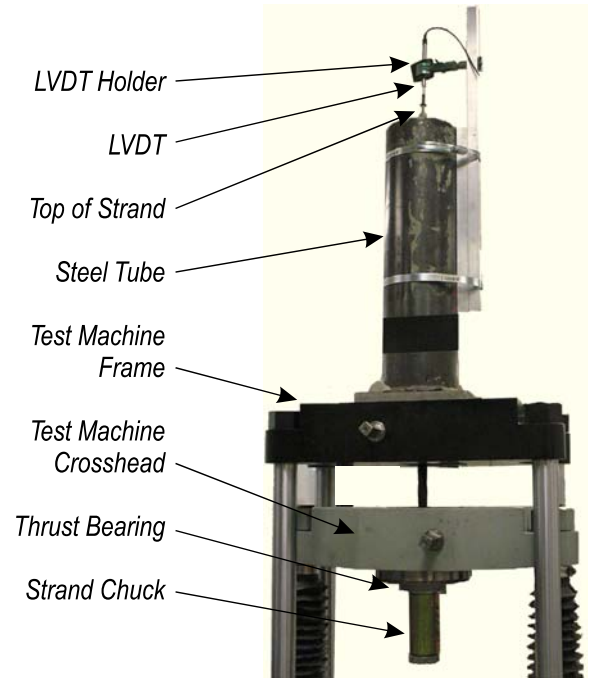


Figure 30–NASP test setup

Sand for NASP testing was donated by Florida Rock of Gainesville, FL. The particle size distribution for the sand was at edge of, but still within, the requirements of ASTM C33:



**Statistical Analysis 09/17/2010 - 10/15/2010 Production
1530-Grandin Sand Plant 76-349 301T-CONCRETE SAND**

Sample Id	Date	Status	#4 (4.75mm)	#8 (2.36mm)	#16 (1.18mm)	#30 (0.6mm)	#50 (0.3mm)	#100 (0.15mm)	#200 (75um)	PAN (0um)	FM																																																																																																			
1482582055	10/14/2010 13:26	Pass	99.8	97.9	86.5	57.1	25.4	5.0	0.33	0.00	2.28																																																																																																			
1481898021	10/15/2010 13:30	Pass	99.8	98.0	86.4	55.8	24.5	4.2	0.30	0.00	2.32																																																																																																			
1492884821	10/15/2010 13:32	Pass	99.7	97.9	86.0	55.1	24.6	3.1	0.27	0.00	2.33																																																																																																			
			<table border="1"> <thead> <tr> <th>#4 (4.75mm)</th> <th>#8 (2.36mm)</th> <th>#16 (1.18mm)</th> <th>#30 (0.6mm)</th> <th>#50 (0.3mm)</th> <th>#100 (0.15mm)</th> <th>#200 (75um)</th> <th>PAN (0um)</th> <th>FM</th> </tr> </thead> <tbody> <tr> <td>Count</td> <td>30</td> <td>30</td> <td>30</td> <td>30</td> <td>30</td> <td>30</td> <td>29</td> <td>30</td> </tr> <tr> <td>Min</td> <td>99.6</td> <td>96.6</td> <td>84.0</td> <td>52.5</td> <td>23.1</td> <td>2.2</td> <td>0.22</td> <td>2.22</td> </tr> <tr> <td>Max</td> <td>100.0</td> <td>98.3</td> <td>89.4</td> <td>60.1</td> <td>27.1</td> <td>5.2</td> <td>0.57</td> <td>2.40</td> </tr> <tr> <td>Range</td> <td>0.4</td> <td>1.7</td> <td>5.4</td> <td>7.6</td> <td>4.0</td> <td>3.0</td> <td>0.35</td> <td>0.18</td> </tr> <tr> <td>Mean</td> <td>99.8</td> <td>97.6</td> <td>85.8</td> <td>56.0</td> <td>25.1</td> <td>4.0</td> <td>0.30</td> <td>2.32</td> </tr> <tr> <td>Median</td> <td>99.8</td> <td>97.6</td> <td>85.7</td> <td>55.7</td> <td>25.0</td> <td>4.1</td> <td>0.30</td> <td>2.32</td> </tr> <tr> <td>St Dev</td> <td>0.1</td> <td>0.5</td> <td>1.3</td> <td>1.9</td> <td>1.2</td> <td>0.8</td> <td>0.08</td> <td>0.05</td> </tr> <tr> <td>CV</td> <td>0.0</td> <td>0.0</td> <td>0.0</td> <td>0.0</td> <td>0.0</td> <td>0.2</td> <td>0.3</td> <td>0.0</td> </tr> <tr> <td>Skewness</td> <td>0.8</td> <td>-0.6</td> <td>1.1</td> <td>0.3</td> <td>0.0</td> <td>-0.4</td> <td>2.3</td> <td>-0.2</td> </tr> <tr> <td>Kurtosis</td> <td>1.4</td> <td>-0.6</td> <td>0.9</td> <td>-0.8</td> <td>-1.3</td> <td>-0.7</td> <td>5.5</td> <td>-0.7</td> </tr> </tbody> </table>									#4 (4.75mm)	#8 (2.36mm)	#16 (1.18mm)	#30 (0.6mm)	#50 (0.3mm)	#100 (0.15mm)	#200 (75um)	PAN (0um)	FM	Count	30	30	30	30	30	30	29	30	Min	99.6	96.6	84.0	52.5	23.1	2.2	0.22	2.22	Max	100.0	98.3	89.4	60.1	27.1	5.2	0.57	2.40	Range	0.4	1.7	5.4	7.6	4.0	3.0	0.35	0.18	Mean	99.8	97.6	85.8	56.0	25.1	4.0	0.30	2.32	Median	99.8	97.6	85.7	55.7	25.0	4.1	0.30	2.32	St Dev	0.1	0.5	1.3	1.9	1.2	0.8	0.08	0.05	CV	0.0	0.0	0.0	0.0	0.0	0.2	0.3	0.0	Skewness	0.8	-0.6	1.1	0.3	0.0	-0.4	2.3	-0.2	Kurtosis	1.4	-0.6	0.9	-0.8	-1.3	-0.7	5.5	-0.7
#4 (4.75mm)	#8 (2.36mm)	#16 (1.18mm)	#30 (0.6mm)	#50 (0.3mm)	#100 (0.15mm)	#200 (75um)	PAN (0um)	FM																																																																																																						
Count	30	30	30	30	30	30	29	30																																																																																																						
Min	99.6	96.6	84.0	52.5	23.1	2.2	0.22	2.22																																																																																																						
Max	100.0	98.3	89.4	60.1	27.1	5.2	0.57	2.40																																																																																																						
Range	0.4	1.7	5.4	7.6	4.0	3.0	0.35	0.18																																																																																																						
Mean	99.8	97.6	85.8	56.0	25.1	4.0	0.30	2.32																																																																																																						
Median	99.8	97.6	85.7	55.7	25.0	4.1	0.30	2.32																																																																																																						
St Dev	0.1	0.5	1.3	1.9	1.2	0.8	0.08	0.05																																																																																																						
CV	0.0	0.0	0.0	0.0	0.0	0.2	0.3	0.0																																																																																																						
Skewness	0.8	-0.6	1.1	0.3	0.0	-0.4	2.3	-0.2																																																																																																						
Kurtosis	1.4	-0.6	0.9	-0.8	-1.3	-0.7	5.5	-0.7																																																																																																						
			<table border="1"> <thead> <tr> <th>Pay Factor</th> <th>Lower Target</th> <th>Upper Target</th> <th>Lower Spec (LSL)</th> <th>Upper Spec (USL)</th> <th>PWS</th> <th>Lower Limit (LCL)</th> <th>Upper Limit (UCL)</th> <th>PWL</th> </tr> </thead> <tbody> <tr> <td></td> <td>85</td> <td>65</td> <td>25</td> <td>5</td> <td>0</td> <td>0</td> <td>0</td> <td>2.05</td> </tr> <tr> <td></td> <td>100</td> <td>97</td> <td>70</td> <td>35</td> <td>7</td> <td>4</td> <td>4</td> <td>2.45</td> </tr> <tr> <td></td> <td>100.0</td> <td>100.0</td> <td>100.0</td> <td>100.0</td> <td>100.0</td> <td>100.0</td> <td>100.0</td> <td>99.8</td> </tr> <tr> <td></td> <td>99.6</td> <td>83.2</td> <td>52.2</td> <td>22.7</td> <td>2.4</td> <td>0.14</td> <td>0.00</td> <td>2.23</td> </tr> <tr> <td></td> <td>100.0</td> <td>98.6</td> <td>88.4</td> <td>27.5</td> <td>5.6</td> <td>0.46</td> <td>0.00</td> <td>2.41</td> </tr> <tr> <td></td> <td>99.8</td> <td>96.7</td> <td>95.8</td> <td>95.6</td> <td>96.0</td> <td>96.0</td> <td>100.0</td> <td>95.4</td> </tr> </tbody> </table>									Pay Factor	Lower Target	Upper Target	Lower Spec (LSL)	Upper Spec (USL)	PWS	Lower Limit (LCL)	Upper Limit (UCL)	PWL		85	65	25	5	0	0	0	2.05		100	97	70	35	7	4	4	2.45		100.0	100.0	100.0	100.0	100.0	100.0	100.0	99.8		99.6	83.2	52.2	22.7	2.4	0.14	0.00	2.23		100.0	98.6	88.4	27.5	5.6	0.46	0.00	2.41		99.8	96.7	95.8	95.6	96.0	96.0	100.0	95.4																																				
Pay Factor	Lower Target	Upper Target	Lower Spec (LSL)	Upper Spec (USL)	PWS	Lower Limit (LCL)	Upper Limit (UCL)	PWL																																																																																																						
	85	65	25	5	0	0	0	2.05																																																																																																						
	100	97	70	35	7	4	4	2.45																																																																																																						
	100.0	100.0	100.0	100.0	100.0	100.0	100.0	99.8																																																																																																						
	99.6	83.2	52.2	22.7	2.4	0.14	0.00	2.23																																																																																																						
	100.0	98.6	88.4	27.5	5.6	0.46	0.00	2.41																																																																																																						
	99.8	96.7	95.8	95.6	96.0	96.0	100.0	95.4																																																																																																						

Query Selections:
 Plant: 1530-Grandin Sand Plant 76-349
 Product: 301T-CONCRETE SAND
 Date Range: 09/17/2010 - 10/17/2010
 Sample Type: Production
 Sample Method: Production Cone
 Agency: Florida DOT
 Number of Tests: 30

Passing: 30
 Failures: 0

aggQC

Vulcan Materials Company

Cement for strand testing was donated by CEMEX of Brooksville, FL. As required by the NASP test method, the cement was high-early strength, Type III cement:



Brooksville South Plant
 10311 CEMENT PLANT ROAD
 Brooksville, FL 34601
 Phone (352) 799-7881 / FAX (352) 799-6088

CEMENT MILL TEST REPORT

Cement Identified as: TYPE III Portland Cement
 Plant: Cemex Brooksville Cement
 Location: Brooksville, FL
 Production Date: 9/1/10 - 9/30/10

Date of Report: 10/4/10

Silo 14

STANDARD CHEMICAL REQUIRMENTS (ASTM C114)	TEST RESULTS	SPECIFICATIONS	ASTM C-150	ASTM C-150	AASHTO M-85	ASTM C-150	ASTM C-1157
			AASHTO M-85			AASHTO M-85	
			TYPE I Low alkali	TYPE II Low alkali	TYPE II Low alkali	TYPE III	GU
Silicon Dioxide (SiO ₂) %	20.5	Minimum	---	---	20	---	---
Aluminum Oxide (Al ₂ O ₃) %	4.8	Maximum	---	6	6	---	---
Ferric Oxide (Fe ₂ O ₃) %	3.7	Maximum	---	6	6	---	---
Calcium Oxide (CaO) %	63.6		---	---	---	---	---
Magnesium Oxide (MgO) %	0.7	Maximum	6.0	6.0	6.0	6.0	---
Sulfur Trioxide (SO ₃) % **	3.2	Maximum	3.0	3.0	3.0	3.5 ***	---
Loss on Ignition (LOI) %	2.0	Maximum	3	3	3	3	---
Insoluble Residue (IR) %	0.56	Maximum	0.75	0.75	0.75	0.75	---
Alkalies (Na ₂ O equivalent) %	0.38	Maximum	0.60	0.60	0.60	0.60	---
Carbon Dioxide in cement (CO ₂) %							
Limestone % in cement (ASTM C150 A1)		Maximum	5	5	5	---	---
CaCO ₃ in limestone % (2.274 x %CO ₂ LS)		Minimum	70	70	70	---	---
Tricalcium Silicate (C ₃ S) %	55	Maximum	---	---	---	---	---
Dicalcium Silicate (C ₂ S) %	18		---	---	---	---	---
Tricalcium Aluminate (C ₃ A) %	7	Maximum	---	8	8	15	---
Tetracalcium Aluminoferrite (C ₄ AF) %	11		---	---	---	---	---
(C ₃ S + 4.75 C ₃ A)	86	Maximum	---	100	100	---	---
(C ₄ AF + 2C ₃ A) or (C ₄ AF + C ₂ F) %	24	Maximum	---	---	---	---	---
PHYSICAL REQUIRMENTS							
(ASTM C204) Blaine Fineness, cm ² /g	5812	Minimum	2800	2800	2800	---	---
(ASTM C204) Blaine Fineness, cm ² /g	5812	Maximum		4200 ⁽ⁱ⁾	4200 ⁽ⁱ⁾	---	---
(ASTM C430) -325 Mesh %			---	---	---	---	---
(ASTM C191) Time of Setting (Vicat)							
Initial Set, minutes	48	Minimum	45	45	45	45	45
Final Set, minutes	120	Maximum	375	375	375	375	420
(ASTM C185) Air Content of Mortar %	5.5	Maximum	12	12	12	12	---
(ASTM C151) Autoclave Expansion %	-0.020	Maximum	0.80	0.80	0.80	0.80	0.80
(ASTM C187) Normal Consistency %	26.0		---	---	---	---	---
(ASTM C1038) Expansion in Water %		Maximum	0.02	0.02	0.02	---	0.02
(ASTM C186) 7 day Heat of Hydration cal/g		Max. if specified					
(ASTM C109) Compressive Strength, psi (Mpa)							
1 Day	3050 (21.0)		---	---	---	1740 (12.0)	---
3 Days	4255 (29.3)	Minimum	1740 (12.0)	1450 (10.0)	1450 (10.0)	3480 (24.0)	1450 (10.0)
7 Days	5510 (38.0)	Minimum	2760 (19.0)	2470 (17.0)	2470 (17.0)	---	2465 (15.0)
28 Days	7590 (52.4)	Minimum	---	---	---	---	---

** The performance of Cemex Type III has proven to be improved with sulfur trioxide levels in excess of the 3.0% limit for Type II. As per footnote D (Table One ASTM C150) our Optimum SO₃ is 3.51% (ASTM C563-04). Cement tested according to C1038-4 showed 0.011 exp at 3.75% SO₃

*** Limit is 4.5 max. when C₃A is more than 8% FDOT Sec. 921
 (i) Does not apply if C₃S + 4.75C₃A is less than or equal to 90

The data shown above is typical of the cement produced at Brooksville, FL and currently being shipped from this silo. This Cement contains Limestone, except type III

Cemex hereby certifies that this cement meets or exceeds the chemical and physical Specifications of :

- ASTM C-150 for Type I and Type I low alkali
- ASTM C-150 for Type II and Type II low alkali
- ASTM C-150 and AASHTO M-85 for Type III
- ASTM C-1157 GU
- AASHTO M-85 for Type I and Type I low alkali
- AASHTO M-85 for Type II and Type II low alkali

Oliver H. Sohn
 Oliver H Sohn
 Quality Control Manager

Cemex is not responsible for the improper use or workmanship that may be associated with the use of this cement.

H.3 FIB-63 Support Data

H.3.1 Gage Coordinates

The gage coordinates used within this section listed by specimen in Tables

Table 4–Gage coordinates for specimen CT

Gage	X (in.)	Y (in.)	Z (in.)
ES1	0	3.5	18
ES2	0	3.5	36
SG1	-21	120	63
SG2	21	120	63
SG3	0	120	0
SG4	3.5	72	36
SG5	0	0	6
SG6	0	0.5	0.5

Table 5–Gage coordinates for specimen SL

Gage	X (in.)	Y (in.)	Z (in.)
ES1	0	3.75	16.75
ES2	0	3.75	34.5
SG1	-21	120	63
SG2	21	120	63
SG3	0	120	0
SG4	3.5	72	36
SG5	0	0	6
SG6	0	0.5	0.5

Table 6–Gage coordinates for specimen PT

Gage	X (in.)	Y (in.)	Z (in.)
ES1	0	2.25	17.5
ES2	0	2.25	36
SG1	-21	120	63
SG2	21	120	63
SG3	0	120	0
SG4	3.5	72	36
SG5	0	0	6
SG6	0	0.5	0.5
XS1	0	0	62.5

XS2	3.5	1.5	24
XS3	3.5	4	24
XS4	3.5	12	24
VG1	0	1.5	17

Table 7–Gage coordinates for specimen LB

Gage	X (in.)	Y (in.)	Z (in.)
ES1	0	18	2.5
ES2	0	36	3.5
SG1	-21	120	63
SG2	21	120	63
SG3	0	120	0
SG4	3.5	72	36
SG5	0	0	6
SG6	0	0.5	0.5

H.3.2 Strain during Post-Tensioning

Table 8–Stress due to post-tensioning during tensioning process in specimen PT

Tensioned Rods	VG1	ES1	ES2	XS1	XS2	XS3	XS4
Rods 1-3	-56.18	4.25	7.90	29.37	-69.81	-70.34	-61.76
All Rods	-163.76	65.67	23.59	134.11	-207.71	-195.63	-133.47
Axis	Y	Z	Z	Z	Y	Y	Y

H.3.3 Strain during Prestress Release

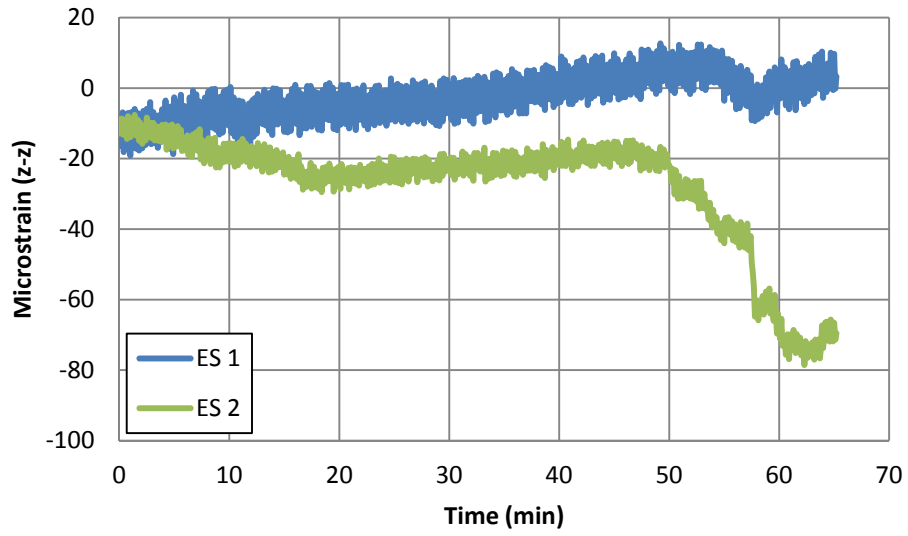


Figure 31—Strain due to prestress release in ES gages in specimen CT

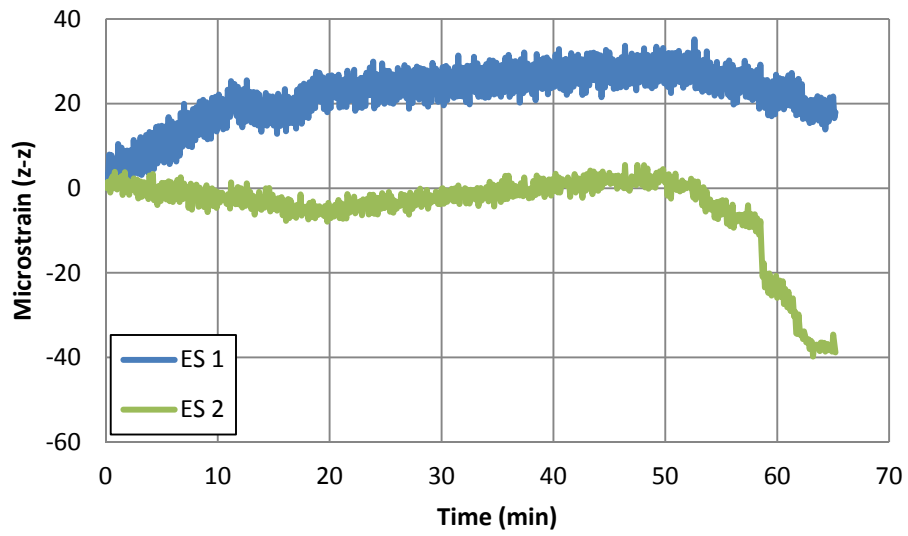


Figure 32—Strain due to prestress release in ES gages in specimen SL

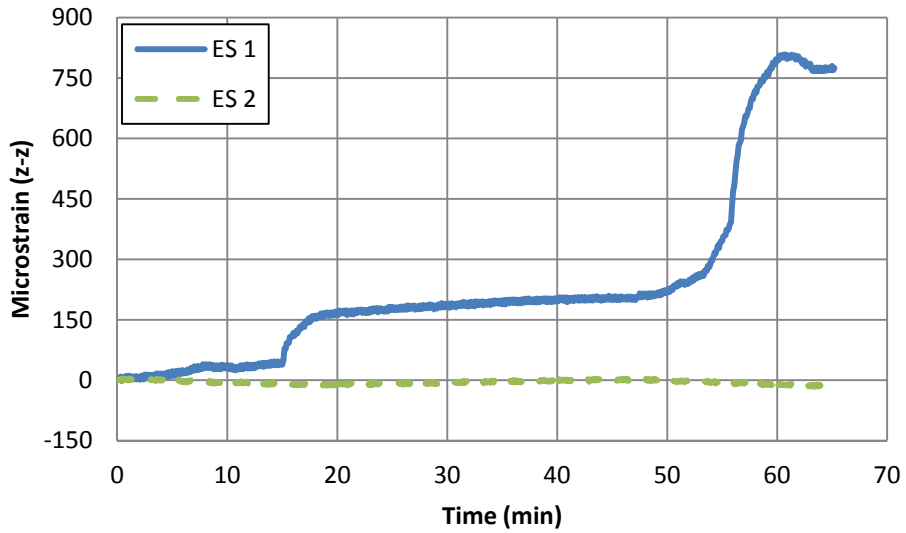


Figure 33—Strain due to prestress release in ES gages in specimen PT

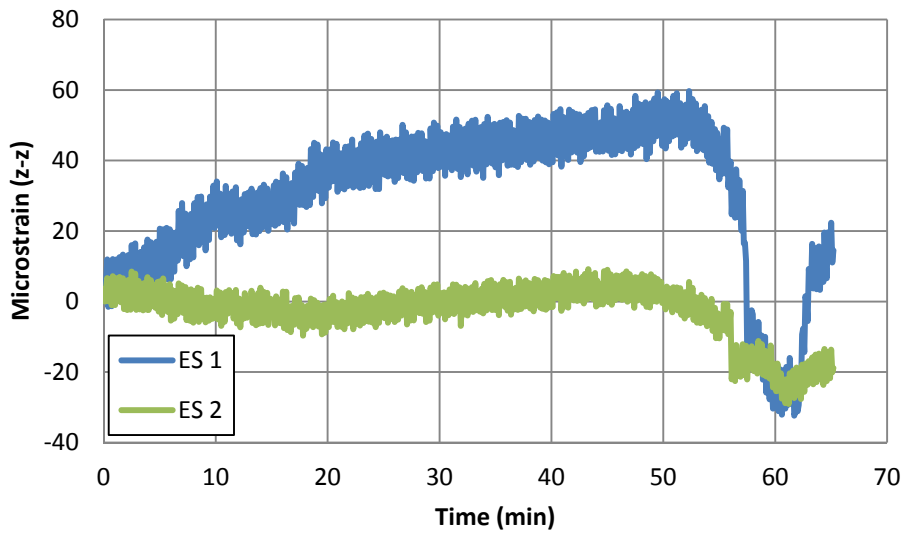


Figure 34—Strain due to prestress release in ES gages in specimen LB

H.3.4 Web Cracks

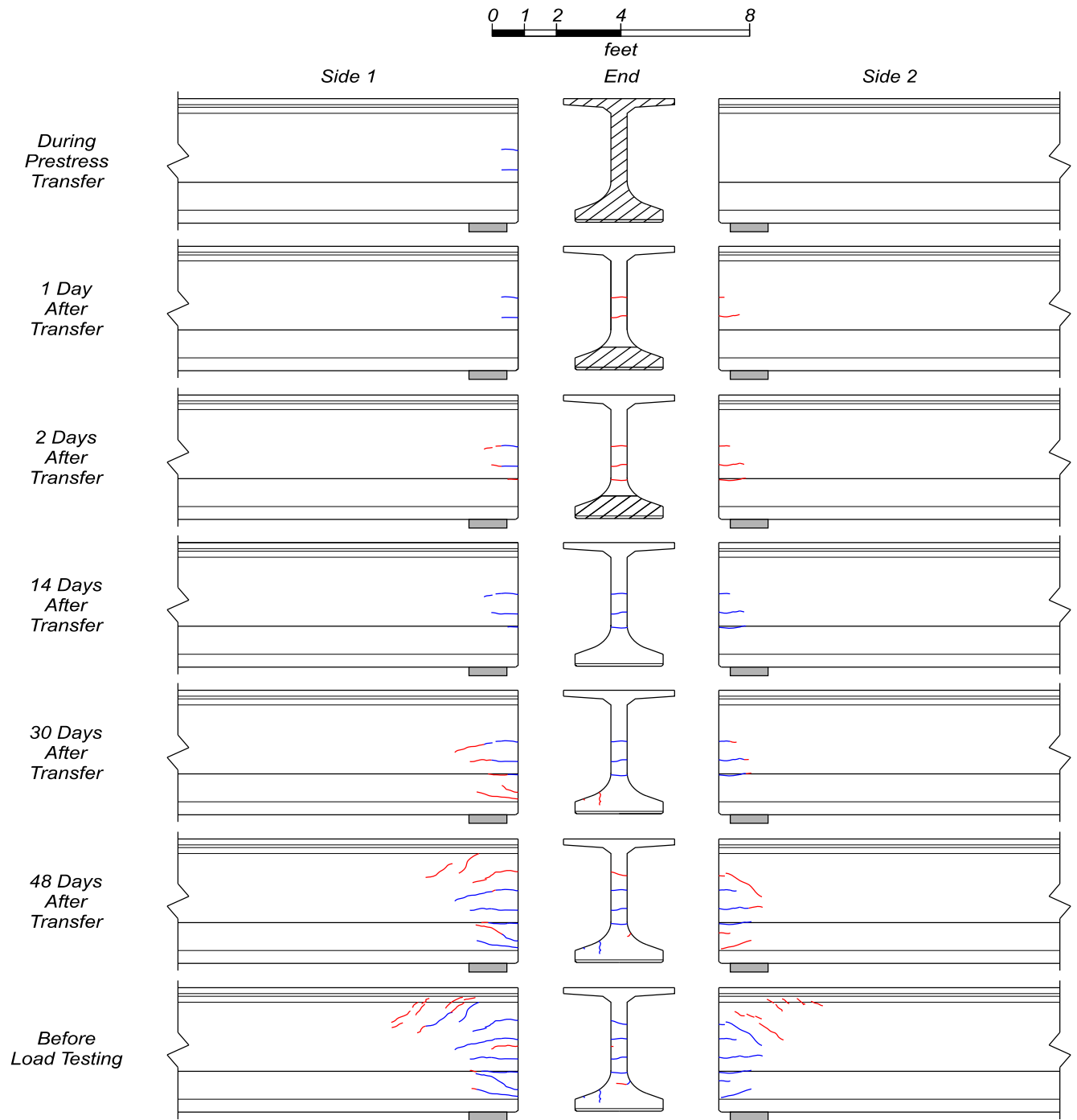


Figure 35—Crack growth in specimen SL (flexural cracks in top flange not shown)

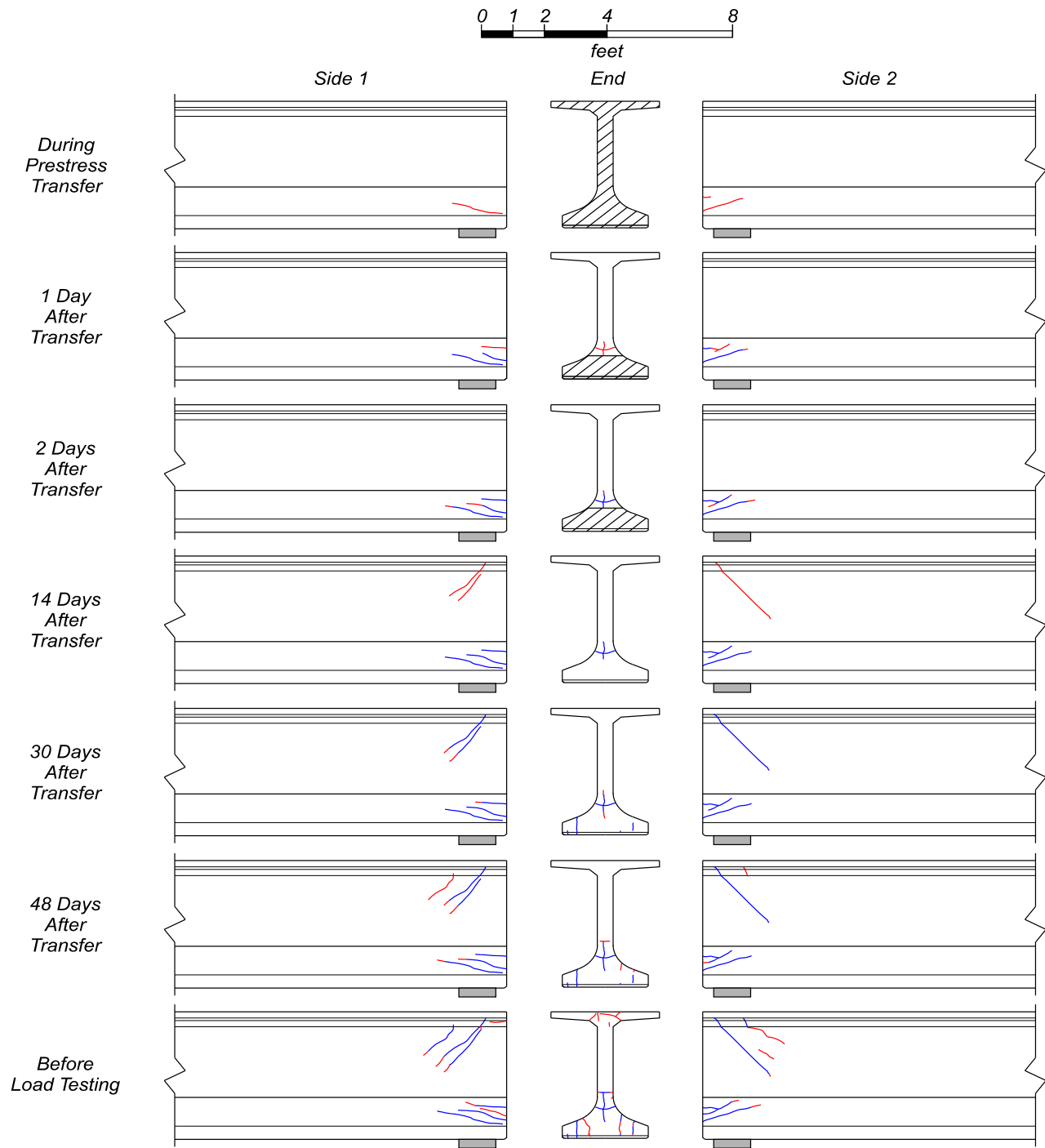


Figure 36–Crack growth in specimen PT (flexural cracks in top flange not shown)

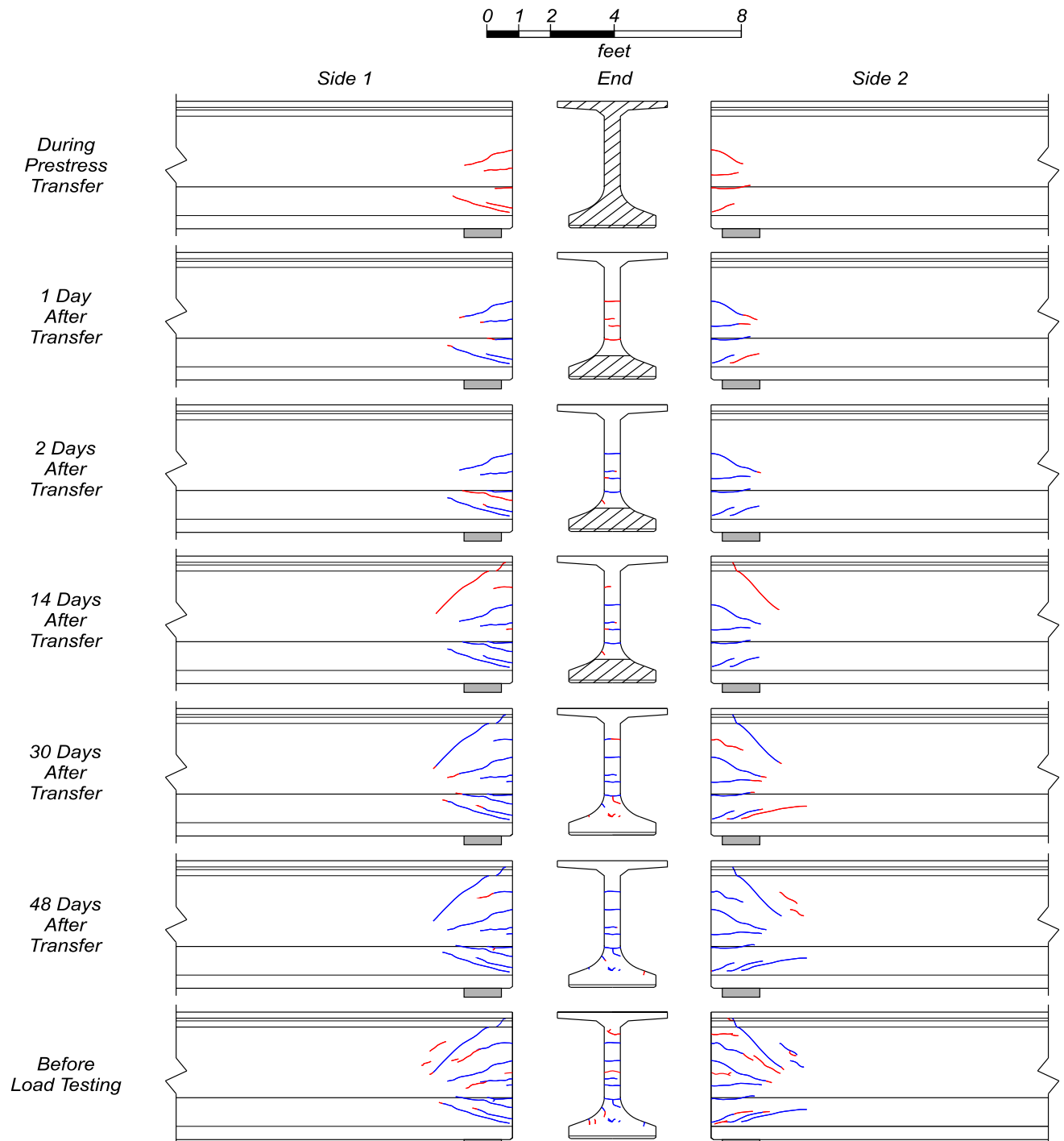


Figure 37–Crack growth in specimen LB (flexural cracks in top flange not shown)

H.3.5 Load Tests

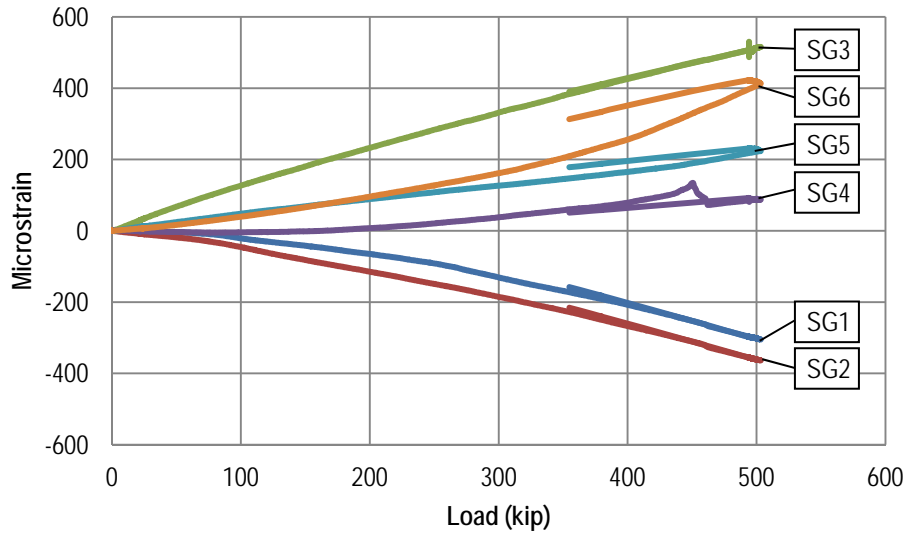


Figure 38–Service load test strain data for specimen CT

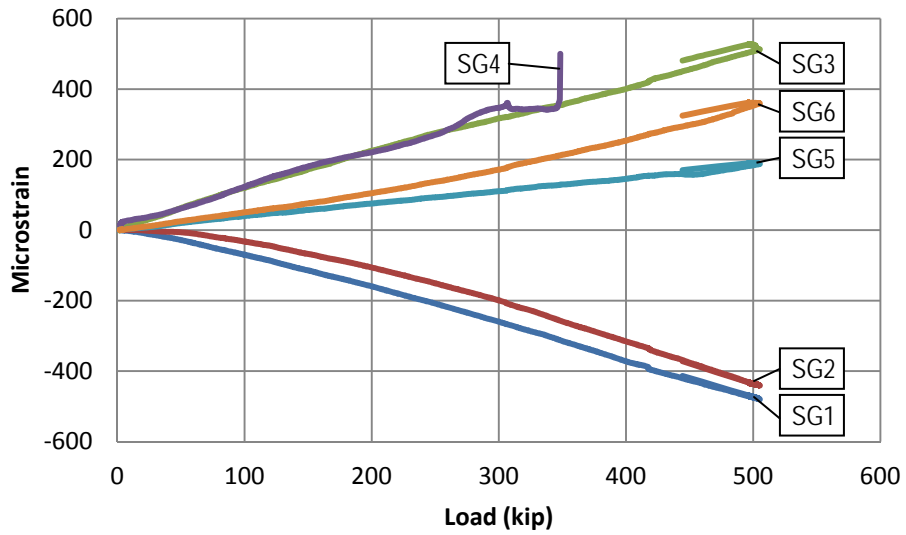


Figure 39–Service load test strain data for specimen SL

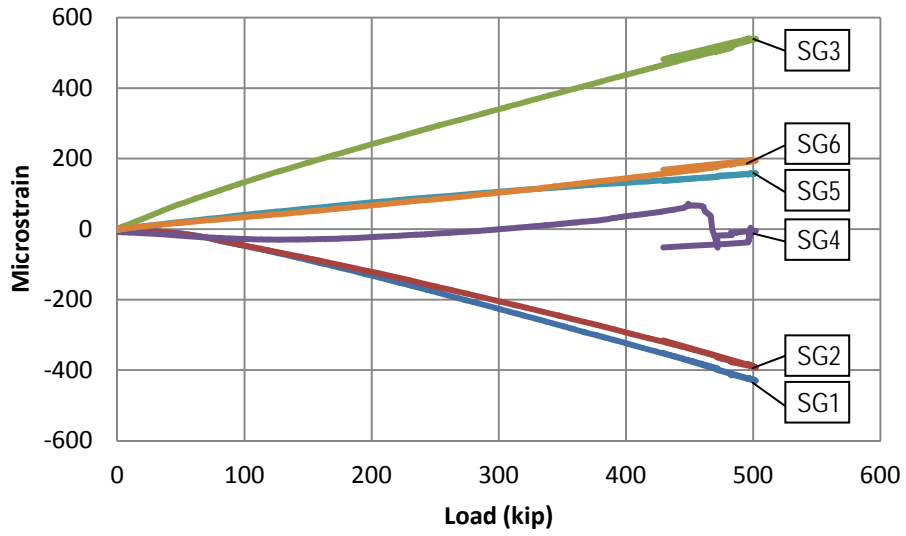


Figure 40–Service load test strain data for specimen PT

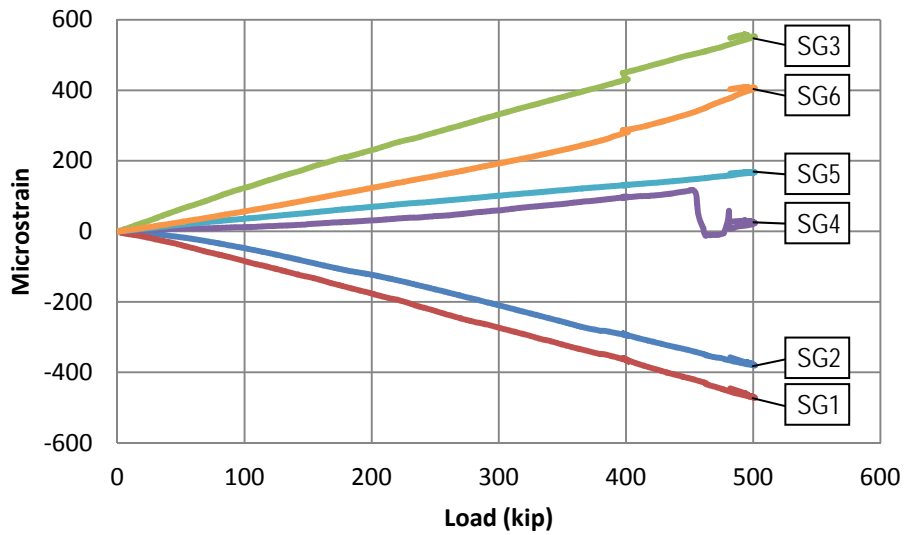


Figure 41–Service load test strain data for specimen LB